Multiscale Modeling of Morphology and Proton/Ion Transport in Electrolytes

A Dissertation Presented for the

Doctor of Philosophy

Degree

The University of Tennessee, Knoxville

Zhenghao Zhu

August 2024

Dedication

To all who are pursuing their dreams.

Acknowledgements

I offer my sincere acknowledgements to everyone who helped me throughout my Ph.D. journey at the University of Tennessee. This dissertation would not have been possible without their help and encouragement.

First and foremost, I would like to express my sincere gratitude to my advisor, Dr. Stephen Paddison, for his continuous support and guidance throughout my Ph.D. studies. His mentorship has been instrumental in my research and professional growth. His insights and advice have shaped my academic journey, and I am incredibly grateful for his belief in my potential.

I am also thankful to my dissertation committee members: Dr. Steven Abel, Dr. Belinda Akpa, Dr. Paul Dalhaimer, Dr. Haixuan Xu, and Dr. Alexei Sokolov. Their meaningful questions and practical advice have been helpful in my research. I also want to acknowledge the efforts of the knowledgeable faculty who have taught and guided me throughout my academic endeavors. Their wisdom and dedication have had a profound impact on my learning experience.

To my colleagues, including Dr. Hongjun Liu, Dr. Xubo Luo, and Mr. Ajay Dwivedi, thank you for the stimulating discussions and the camaraderie. Your support and collaboration have enriched my research and personal growth.

I would also like to extend my heartfelt gratitude to our collaborators: Dr. Mark Tuckerman, Dr. Tamar Zelovich, and Dr. Zhuoran Long from New York University; Dr. Klaus-Dieter Kreuer and Dr. Andreas Münchinger at the Max-Planck-Institute in Stuttgart; Dr. Linas Vilciauskas at Vilnius University; Dr. Alexei Sokolov and Dr. Ivan Popov from Oak Ridge National Laboratory; Dr. Amanda Young-Gonzales and Mr. Md Dipu Ahmed from Chemistry; Dr. Reza Foudazi and Ms. Fatemeh Naderi Samani from the University of Oklahoma. I am sincerely thankful for the opportunity to work alongside you all. Your insights and expertise have been instrumental in my growth and development, and I am truly grateful for the knowledge and wisdom you've shared.

Additionally, I appreciate the financial support from the National Science Foundation (NSF) and the ACCESS computing resources. This support has been crucial in enabling my research

and making this dissertation possible.

I am deeply grateful to my parents for their endless love and unwavering support. They have always cared about my well-being and happiness. They have provided me with a nurturing and open environment, allowing me the freedom to be myself and to think critically. Their encouragement has been instrumental in my pursuit of my dreams.

I am immensely thankful to my beautiful wife, Liu Cao, who has been my steadfast companion during the last decade of life's ups and downs. Her belief in me has been a constant source of inspiration, giving me the confidence to overcome challenges and persist in the face of adversity. Her support, both materially and emotionally, has been invaluable. Without her by my side, I would not be where I am today.

I give my deepest thanks to my parents-in-law for their support and kindness. Their encouragement has been a source of strength and comfort over these years.

Finally, I want to thank my friends. I am especially thankful for the memorable times spent swimming at SAC, cycling around campus, playing table tennis at the Student Union, hiking in the mountains, and sharing food at parties. These activities provided a relaxing break and a chance to bond with fellow students and friends like John, Robin, Dru, Bobby, Mary Kay, Lindon, Rebecca, Karthika, Xiaoyu, Xiaodong, Jiaqi, Jiani, Hao, Lu, Luna, Xianzhi, Shuyang, Di, Nan, Songyi, Dong, Huiwen, Nikhil, Apostolos, Steven, Xiaofei, J. P., and many others. Additionally, the music I enjoyed during these years helped me stay motivated and focused. Your companionship and shared experiences have made this journey enjoyable and enriching.

Abstract

Understanding structure-function relationships in electrolytes is essential for advancing energy conversion and storage. This dissertation employs multiscale modeling and simulations to study the morphology and proton/ion transport in various electrolytes for electrochemical systems, including anion exchange membranes (AEMs), protic ionic liquids (PILs), pure phosphoric acid (PA) and aqueous acid solutions, ionic liquids (ILs), and polymerized ionic liquids (polyILs).

Mesoscale dissipative particle dynamics (DPD) simulations were employed to study the hydrated morphology of polystyrene-*b*-poly(ethylene-co-butylene)-*b*-polystyrene (SEBS)-based AEMs. The results indicate that the choice of the functional group moderately affects the water distribution and has little influence on the backbone structure. The associated anion seems to have a greater impact on the size of exclusive water domains compared to the cationic groups.

The effect of the base on proton transfer in PA-based PILs was explored by using hybrid density functional theory (DFT) in conjunction with a continuum solvation model. Potential energy scans reveal that the bases with stronger proton affinity significantly influence the energetics of proton transfer between PA molecules. However, this effect diminishes when the potential shifts from a double-well to a single-well. *Ab initio* molecular dynamics (AIMD) simulations were performed to uncover the underlying mechanisms of proton transport in pure PA and aqueous acid solutions. The findings show that protons move by surprisingly short jumps of only ~0.5-0.7 Å, with these proton jumps being anticorrelated, resulting in suppressed conductivity. Furthermore, acid molecules exhibit different roles in proton transport in their aqueous solutions depending on their molecular structures and acidity.

Classical molecular dynamics (MD) simulations were utilized to elucidate ionic correlations and ion transport mechanisms in ILs and polyILs. For ILs, the relative ion mass significantly impacts distinct ion-ion correlations, swapping the relative amplitudes of distinct cation-cation and anion-anion correlations. In polyILs, ion transport mechanisms were systematically investigated to understand the effects of sidechain flexibility coupled with specific interactions,

revealing dynamical heterogeneity and stringlike cooperative motion. Importantly, distinct anion-anion correlations suppress conductivity in a barycentric reference frame but enhance it under a polycation-fixed reference frame. The cage escape emerges as the primary mechanism governing ion transport in these systems.

Table of Contents

Chapter 1 Introduction 1

1.1 Anion Exchange Membranes (AEMs) 4

1.1.1 Morphology 4

1.1.2 Ion Transport 7

1.2 Protic Ionic Liquids (PILs) 11

1.3 Pure H_3PO_4 and Aqueous Acids 13

1.3.1 Proton Transport in Acidic Water 14

1.3.2 Proton Transport in Pure H_3PO_4 16

1.3 Polymerized Ionic Liquids (PolyILs) 18

1.3.1 Ion Transport Mechanisms 19

1.3.2 Ion-Ion Correlations 22

1.4 Research Overview 25

1.4.1 Morphologies of AEMs 25

1.4.2 Proton Transfer in PILs 25

1.4.3 Proton Transport in Pure H_3PO_4 and Aqueous Acids 26

1.4.4 Ion Transport in ILs and polyILs 28

Chapter 2 Methods 30

2.1 Quantum Chemical Calculations 30

2.1.1 Hartree-Fock (HF) Method 32

2.1.2 Density Functional Theory (DFT) 33

2.2 *Ab Initio* Molecular Dynamics (AIMD) 34

2.3 Classical Molecular Dynamics (MD) 34

2.4 Dissipative Particle Dynamics (DPD) 35

2.4.1 Determining the Interaction Parameters 37
2.5 Ion-Ion Correlations 41
2.5.1 The Momentum Conservation Approach 41
2.5.2 The Onsager Transport Coefficients 43
Chapter 3 Morphology of Anion Exchange Membranes 45
3.1 Simulations 45
3.2 Effect of Functional Group 48
3.3 Effect of Associated Anion 53
3.4 Effect of Carbonation 55
Chapter 4 Proton Transfer in Protic Ionic Liquids 62
4.1 Computations 62
4.2 Optimized Structures of Base + nPA (n = 1 – 3) 64
4.3 Binding Energies of PA Molecules 67
4.4 Proton Transfer Energetics 71
Chapter 5 Beyond Proton Transfer: Proton Transport in Pure and Aqueous Acids 79
5.1 Simulation Setups 79
5.2 Proton Transport in Pure and Aqueous PA 80
5.2.1 Distribution of Protonated Species 80
5.2.2 Characteristic Relaxation Times 82
5.2.3 Proton Transport Mechanisms 88
5.2.4 Proton Correlations 90
5.3 Proton Transport in Aqueous Acids 92
5.3.1 Distribution of Protonated Species 92
5.3.2 Structure of H-Bonds 94

5.3.3 Solvation Structure of H_3O^+ 97
5.3.4 Solvation Patterns of H_3O^+ and H_2O 99
5.3.5 Energetics of Proton Transfer 102
5.3.6 Relaxation Time of H_3O^+ 103
5.3.7 H^+ (aq.) Transport Mechanism 107
Chapter 6 Ionic Correlations in Ionic Liquids 119
6.1 Simulations 119
6.2 Effect of Ion Mass Ratio 120
6.3 Effect of Alkyl Tail Length of Imidazolium 132
Chapter 7 Ion Transport in Polymerized Ionic Liquids 137
7.1 Simulation Details 137
7.2 Effects of Sidechain Flexibility and Specific Interactions 138
7.2.1 Structural and Ion Association Analysis 138
7.2.2 Anion Dynamical Correlations 142
7.2.3 Anion Dynamical Heterogeneity 148
7.2.4 Stringlike Cooperative Motion 156
7.2.5 Relaxation Time Underlying Anion Diffusivity 158
7.3 Effect of Electrostatic Interactions 159
7.3.1 Structural Highlights 159
7.3.2 Dynamic Anion-Anion Correlations 161
7.3.3 Dynamical Heterogeneity 163
7.3.4 Stringlike Cooperative Motion 163
Chapter 8 Conclusions 167
References 173

Appendices 191
Appendix A. Tables 191
Appendix B. Figures 196
Appendix C. List of Presentations and Publications 206
Appendix D. Reprints and Preprints of Publications 208
Vita 387

List of Tables

Table 3.1. Bead type, chemical structure, and volume. 46
Table 4.1. Proton affinities of the bases. 66
Table 4.2. Structural parameters[a] of phosphoric acid-based protic ionic liquids at the level of B3LYP/6-311G**/SMD. 69
Table 4.3. Energetics of phosphoric acid-based protic ionic liquids at the level of B3LYP/6-311G**/SMD. 70
Table 5.1. Details of AIMD simulation systems. 81
Table 5.2. Relaxation times obtained by fitting the Q-dependent $E_{max}(Q) = \hbar/\tau_R$ with $E_{max}(Q) = \hbar DQ^2/(1+D\tau Q^2)$ for pure PA and aqueous PA85 at different temperatures. 85
Table 5.3. Computed fractions (%) of acid and water molecules in their different states of protonation in the studied aqueous acid systems. 93
Table 5.4. Probability distribution (%) of solvation patterns. 100
Table 5.5. Probability distribution (%) of solvation patterns at $\delta_{\min} < 0.1$ Å. 101
Table 5.6. Calculated relaxation times (in ps) including and excluding rattling for hydronium ions in studied aqueous acid systems. The fitting results for the function excluding rattling are listed in parentheses. 106
Table 5.7. Diffusion coefficients of hydrated H^+ and H_2O (in Å^2/ps) and the computed conductivities of hydrated H^+ (in S/cm). 110
Table A.1. Bonded parameters in DPD simulations 191
Table A.2. Calculated conservative interaction parameters in DPD simulations. 192
Table A.3. Relaxation times obtained by fitting the self-intermediate scattering function with $ISF_s = a_1\exp(-t/\tau_1) + a_2\exp(-t/\tau_2) + a_3\exp[-(t/\tau_3)^\beta]$ for pure PA at 400 K. 193
Table A.4. Relaxation times obtained by fitting the self-intermediate scattering function with $ISF_s = a_2\exp(-t/\tau_2) + a_3\exp[-(t/\tau_3)^\beta]$ for pure PA at 383 K. 193
Table A.5. Relaxation times obtained by fitting the self-intermediate scattering function with $ISF_s = a_2\exp(-t/\tau_2) + a_3\exp[-(t/\tau_3)^\beta]$ for pure PA at 400 K. 194
Table A.6. Relaxation times obtained by fitting the self-intermediate scattering function with $ISF_s = a_2\exp(-t/\tau_2) + a_3\exp[-(t/\tau_3)^\beta]$ for aqueous PA85 at 390 K. 194
Table A.7. Relaxation times obtained by fitting the self-intermediate scattering function with $ISF_s = a_2\exp(-t/\tau_2) + a_3\exp[-(t/\tau_3)^\beta]$ for aqueous PA85 at 420 K. 195
Table A.8. Computed fractions (%) of special pair acid molecules in their different states of protonation in the studied aqueous acid systems. 195

List of Figures

Figure 1.1. Schematic summary of experimental and theoretical approaches used to study the effects of various chemical factors in pursuit of rational design strategies for novel electrolytes. 5

Figure 1.2. Hydrated morphology of SEBS-based AEMs in the alkaline form for λ = (a) 4, (b) 8, (c) 12, (d) 16, and (e) 20. Taken from ref.[44] 5

Figure 1.3. (A) Vehicular diffusion mechanism of OH^- in system a4 from a z-perspective. (B) Structural diffusion mechanism of OH^- in system b4 from a z-perspective. (C) Relationship between average diffusivity of OH^- and water density, inset: OH^- diffusivity *vs.* the hydration level. Taken and adapted from ref.[66] 10

Figure 1.4. Schematic representation of: (a) the vehicular mechanism; (b) proton hopping mechanism; and (c) collective chain-like proton transport (Grotthuss-like) mechanism, where charge moves much longer distance than individual proton hops. Taken from ref.[11] 12

Figure 1.5. Schematic representation of Eigen-Zundel-Eigen (EZE) proton transport mechanism. Taken from refs.[71, 118] 15

Figure 1.6. Snapshots of elementary steps in the concerted proton transport mechanism in water. Taken from ref.[69] 15

Figure 1.7. (A) Snapshots (a-d) of a few of the elementary steps of proton diffusion in PA as determined by AIMD simulations. These show the correlated proton transfer events and formation of an extended 'Grotthuss' chain, and the participation of other 'solvent' PA molecules. (B) Proton coupling correlation function $C_{pc}(n)$ in pure PA and PA/Imidazole mixture as a function of connectivity n (0, single H-bond; 1, adjacent H-bonds; 6, longest non-cyclic path in the H-bond network) and response time increment τ_{res}. Taken and adapted from refs.[77, 129] 17

Figure 1.8. (A) Activation energy for conductivity below T_g in various polyILs as a function of mobile ion radius. (B) Walden plot for poly(dimethylamino ethyl acrylate) functionalized with quaternary ammonium with various pedant groups. Taken from refs.[136, 142] 20

Figure 1.9. (A) Illustration of ion hopping types in polyIL electrolytes. (B) Percentage of hopping events in polyIL electrolytes (top); and decomposition of intrachain hopping events (type 1) assisted by N number of polymer chains (bottom). (C) Definition of effective hopping contributing to the long-range diffusion. (D) Probability of occurrence as a function of hopping type at four different temperatures when the ineffective ions were excluded. The inset is the definition of type 4: remaining intact (i.e. rattling). Taken and adapted from refs.[144, 145] 20

Figure 1.10. Schematic representation of: (a) the negative cation-cation correlations, in which charge transport short distance due to a correlated backflow of cations; and (b) positive cation-cation correlations that enhance conductivity, where charge moves much longer distance than individual cation hops. Taken from Ref.[11] 24

Figure 1.11. Chemical structures of the base molecules used to synthesize PILs: (a) TMA, (b) Imidazole, (c) Lidocaine, and (d) Creatinine. 27
Figure 1.12. Chemical structures of (a) phosphoric acid (PA), (b) sulfuric acid (SA), (c) nitric acid (NA), and (d) water (W). The p*K*a values for these acids are 2.1, –3, and –1.4, respectively. 27
Figure 1.13. Chemical structures of the polyILs consisting of polycations PMMA-C_x-[IM] with various linker lengths (x = 2 – 8) and four associated anions. 29
Figure 2.1. Schematic overview of multiscale modeling and simulations of various specific electrolytes providing their structural and dynamical properties. 31
Figure 2.2. Various pathways to obtain the Δa_{ij} for DPD simulations. Color codes: purple: handbook data; blue: atomic simulations with classical force fields; red: *ab initio* calculations; green: trial DPD simulations. 42
Figure 3.1. Coarse-grained model of a hydrated SEBS-based AEM in various forms. Each circle represents the specific bead/particle of the selected chemical group or collection of atoms. 46
Figure 3.2. Morphologies of the SEBS functionalized with different cationic groups in the alkaline form. There are two phases: hydrophilic and hydrophobic phases occurring at all hydration levels. For low λ, perforated and interconnected lamellae are formed; for high λ, disordered bicontinuous lamellas are formed and water droplets (blue regions) can be found. Color code: Bs and Bm (orange); Ph (mauve); TMM (green); TMA^+ (purple); TMP^+ (light orange); MIm^+ (dark blue); OH^- (cyan); and W (blue). 49
Figure 3.3. RDFs of the hydrated AEM in the alkaline form at λ = 8. The inset shows a magnified view of short-distance range. Color code: BsPh-BsPh (black); BsPh-Bm (red); Bm-Bm (green); and Cation-Cation (blue). Line scheme: SEBS-TMP (solid line); SEBS-MIm (dash-dotted line); SEBS-TMA (dashed line). 49
Figure 3.4. The coordination number (CN) of the cations as a function of cation distance across the various hydration levels: λ = 4 (black); λ = 8 (red); λ = 12 (blue); λ = 16 (green); and λ = 20 (pink). Line scheme: SEBS-TMP (solid line); SEBS-MIm (dash-dotted line); and SEBS-TMA (dashed line). The inset shows the cation-cation RDFs over the regions from 0 to 20 Å. The first minima of the RDFs lie around 9.5 Å 51
Figure 3.5. W-W RDFs for the AEMs functionalized with different cationic group in the alkaline form at various water contents. Color scheme: SEBS-TMP (black); SEBS-MIm (red); SEBS-TMA (blue). Line scheme: λ = 8 (solid line); λ = 12 (dotted line); λ = 16 (dash-dotted line); and λ = 20 (dashed). Zoom up shows the minimal radial distance where $g(r) = 1$ 51
Figure 3.6. Cluster size distributions of water and OH^- beads for (a) SEBS-TMP and (b) SEBS-MIm. Large clusters of water and OH^- beads are formed when $\lambda \geqslant 8$ for SEBS-TMP and SEBS-MIm. SEBS-TMP and SEBS-MIm have the almost same cluster sizes at $\lambda = 8$, while larger clusters form in SEBS-TMP than SEBS-MIm at λ = 12. 52

Figure 3.7. Five largest clusters of water and OH^- beads at $\lambda = 4, 8, 12, 16$ in: (a) SEBS-TMP; and (b) SEBS- MIm. 52
Figure 3.8. Simulated morphology of the SEBS-TMA in the alkaline form, in the chloride form, and in the bromide form at different hydration levels: $\lambda = 4, 8, 12, 16$, and 20. Color code: Bs and Bm (orange); Ph (mauve); TMM (green); TMA^+ (purple); OH^- (pink); Cl^- (light green); Br^- (red); and W (blue). . 54
Figure 3.9. Simulated morphology of the hydrated AEM in different forms at $\lambda = 8$. (a) TMA^+ in $Br^-(H_2O)_3$; (b) TMA^+ in $Cl^-(H_2O)_3$; (c) TMA^+ in $OH^-(H_2O)_3$. Color code: TMA^+ (purple); Br^- (red); Cl^- (light green); OH^- (pink); and W (blue). 54
Figure 3.10. W-W RDFs for the hydrated AEM in the alkaline (solid line), chloride (dash-dotted line), and bromide (dash line) forms at various levels of hydration. Color scheme: $\lambda = 8$ (black); $\lambda = 12$ (red); $\lambda = 16$ (green); and $\lambda = 20$ (blue). 56
Figure 3.11. Simulated morphology of the SEBS-TMA in the bicarbonate form, and in the carbonate form at different hydration levels: $\lambda = 4, 8, 12, 16$, and 20. Color code: Bs and Bm (orange); Ph (mauve); TMM (green); TMA^+ (purple); HCO_3^- (cyan); CO_3^{2-} (green-yellow); and W (blue). 56
Figure 3.12. Simulated morphology of the SEBS-TMA in the alkaline form with different percentages of carbonation, at two hydration levels: $\lambda = 8$ and 20. Color code: Bs and Bm (orange); Ph (mauve); TMM (green); TMA^+ (purple); OH^- (pink); HCO_3^- (cyan); and W (blue). 58
Figure 3.13. W-W RDFs for the hydrated SEBS-TMA (a) in the HCO_3^- form (solid line) and in the CO_3^{2-} form (dash-dotted line) at various hydration levels: $\lambda = 4$ (black); $\lambda = 8$ (red); $\lambda = 12$ (green); $\lambda = 16$ (blue); and $\lambda = 20$ (magenta); (b) in the alkaline form with different ratios of OH^- being carbonated 10% (black); 25% (red); 50% (green); and 75% (blue) at $\lambda = 8$ (solid line) and $\lambda = 20$ (dash-dotted line). 59
Figure 3.14. Cluster size distributions of water and anion beads for SEBS-TMA (a) in the HCO_3^- form and (b) in the CO_3^{2-} form at various hydration levels; in the alkaline form with different ratios of OH^- being carbonated at (c) $\lambda = 8$ and (d) $\lambda = 20$. Large clusters of water and anion beads are formed when $\lambda \geqslant 8$ for these systems. At low hydration ($\lambda = 8$), the carbonation generally enlarges the percolated clusters, while at high hydration ($\lambda = 20$), the effect of carbonation is minimum on the percolated clusters. 60
Figure 4.1. (a) CPU time needed for optimizing a typical cluster consisting of 55 atoms as a function of functionals and basis sets. (b) Energetics for proton transfer between first and second PA molecules in the system of CRT+3PA at the B3LYP/6-311G**/SMD level of theory. There is a minimal effect of the dielectric constant on the energetics for the proton transfer within a wide range of 11 to 61. 63
Figure 4.2. Fully optimized configurations of one PA molecule with (a) TMA, (b) IMI, (c) LDC, (d) CRT, and (e) CRT* (congener of CRT cluster) at the B3LYP/6-311G**/SMD level of theory. All values are reported in Å. The atomic color scheme in Figure 4.2 and 4.3 is: hydrogen (white), carbon (gray), nitrogen (blue), oxygen (red), phosphor (orange). CRT*+1PA is less energetic favorable than the structure of CRT+1PA by 1.1 kcal/mol. 66

Figure 4.3. Fully optimized configurations of cluster of three PA molecules with (a) TMA, (b) IMI, (c) LDC, (d) CRT, and (e) CRT* (congener of CRT cluster) at the B3LYP/6-311G**/SMD level of theory. All values are reported in Å. CRT*+3PA is more energetic favorable than the structure of CRT+3PA by 1.1 kcal/mol..... 68
Figure 4.4. Energetics for proton transfer from protonated base to PA in systems of cluster of (a) one PA molecules with TMA, IMI, LDC, and CRT; and (b) three PA molecules with TMA, IMI, LDC, and CRT at the B3LYP/6-311G**/SMD level of theory. The ionic pairs are energetically preferable and stable in these systems. 72
Figure 4.5. Energetics for proton transfer between the PA molecules in systems of (a) cluster of two PA molecules with TMA, IMI, LDC, CRT, and CRT*, and (b) cluster of two PA subunits flanked by two base molecules at the B3LYP/6-311G**/SMD level of theory. Note that the bases with stronger proton affinity exert greater influence on the energetics for proton transfer between individual PA molecules. However, the effects are minimal when the potential is shifted into the single-well from the double-well. The double-well potential recovers with deformations in various manners when one additional base molecule is added to the other side of these complexes forming $(\text{Base}\cdots\text{PA}\cdots\text{PA}\cdots\text{Base})$ clusters. 75
Figure 4.6. Energetics for proton transfer between: (a) first and second PA; and (b) second and third PA in systems of cluster consisting of three PA molecules with TMA, IMI, LDC, CRT, and CRT* at the B3LYP/6-311G**/SMD level of theory. Note that the neighboring cation Base-H^+ results in either a negligible energetic barrier or a single minimum between the first and second PA molecules. The energetics for proton transfer in systems of Base+3PA (Base = TMA, IMI, CRT*, and LDC) have similar trends in which the energies are monotonically increasing without the formation of a transition state. Barrierless proton transfer occurs in the system of CRT with several PA molecules. 75
Figure 5.1. The oxygen-hydrogen radial distribution function (g_{OH}) of PA. The shoulder on the left side of the 3rd peak corresponds to the distances between the proton and the oxygen atoms from the same PA molecule..... 81
Figure 5.2. Calculated fractions of PA and water in their different states of protonation in: (a) pure PA and (b) aqueous 85% PA systems. Note that the transiently shared protons are included..... 81
Figure 5.3. (a) Illustration of fitting the self-intermediate scattering function $ISF_s(Q,t)$ of protons with $ISF_s = a_1\exp(-t/\tau_1) + a_2\exp(-t/\tau_2) + a_3\exp[-(t/\tau_3)^\beta]$ for three different Q values probed at 400 K for pure PA. (b) Vibrational density of state (VDOS) for protons in pure PA system at 400 K. 83
Figure 5.4. Q dependence of the characteristic energy of the QENS relaxation process (open symbols) and corresponding simulation data from self-correlation of proton motion in MD (closed symbols) and their fit to jump-diffusion model (lines). The jump-diffusion model provides correct estimates of the proton diffusion and enables estimates of the proton jump length λ. The latter appears surprisingly short and comparable to the expected length for the proton transfer. The inset displays self-intermediate

scattering functions $ISF_s(Q,t)$ of protons with different Q values at 400 K for pure PA from AIMD simulations (upper) and QENS spectra (bottom). 85
Figure 5.5. (a) Proton transfer population correlation functions (both including and excluding proton rattling) and their triexponential fits for pure PA at 400 K. (b) The self-part of the van Hove function of the protons with three characteristic times obtained from triexponential fits of the population correlation functions in pure PA at 400 K. 87
Figure 5.6. Trajectory lines of an individual proton in pure PA at 400 K. Each colored cloud reflects the proton vibrational and rotational motions as the proton is associated with the same oxygen atom. The trajectory changes color when the proton transfers to a different oxygen atom. The center of mass of each cloud is connected by a black line to the center of mass of the next cloud. These black lines present averaged jumps of the proton transfers between the oxygen atoms. (Inset) The length of proton jumps between oxygen atoms (the length of the black lines). 89
Figure 5.7. Snapshots of the elementary steps of the mechanism for long-range proton diffusion in pure PA. The green ball represents the long-range diffusive proton, and the charged entities are highlighted. The arrows denote the associated proton transfers and the reorientations of the covalent OH bonds in the mechanism. The collaboration of proton transfers (a, b, d, f, and g) and large angular jumps (c, e, and h) facilitates the long-range diffusion of protons. 89
Figure 5.8. (a) Temperature dependence of the inverse Haven ratio for PA (blue symbols) and PA85 (red symbols) estimated using diffusion coefficients obtained from PFG-NMR[81, 82] (open squares) and BDS (closed squares). (b) Correlation functions of proton displacement vectors for pure PA at 400 K and the linear fit to obtain self-, distinct, and total diffusion coefficients. 91
Figure 5.9. RDFs of OO pairs from different species: Total (a and e); both from water species (b and f); oxygen atoms of water and acid molecules (c and g); and oxygen atoms of acid molecules (d and h). The oxygen atoms from the same molecule are excluded for clarity. 95
Figure 5.10. RDFs of O^* with other atoms: oxygen atom of water molecule (a and d); oxygen atom of acid molecule (b and e); and all hydrogen atom (c and f). 98
Figure 5.11. RDFs of the water oxygen atom with other atoms: oxygen atom of the water molecule (a and d); oxygen atom of the acid molecule (b and e); and all hydrogen atoms (c and f). 98
Figure 5.12. Energy profiles for proton transfer between different molecular species in (a) PA1H, (b) SA1H, (c) NA1H, (d) PA3H, (e) SA3H, and (f) NA3H. 104
Figure 5.13. Continuous population correlation functions $C_c(t)$ for H_3O^+ at two conditions: (a) including proton rattling; and (b) excluding proton rattling. 106
Figure 5.14. (a) RDFs of the central atom of the acid with the oxygen of H_3O^+ for the aqueous acid systems. The inset lists the percentage time the proton spends as A-H, H_3O^+, or Zundel ions. (b) A close-up view of the second peak seen in (a). 108

Figure 5.15. The mean squared displacement (MSD) of H_3O^+ decomposed into the continuous vehicular component; the discrete structural component; and the correlation between the two components in (a) PA1H; (b) SA1H; (c) NA1H; (d) PA3H; (e) SA3H; and (f) NA3H. 112
Figure 5.16. The average occurrence times per picosecond for three types of proton transfer as defined at the bottom: proton transfer from hydronium ion to water; from hydronium ion to acid molecule; and between acid molecules in the (a) 1:1 systems, and (b) 1:3 systems. 115
Figure 5.17. The occurrence probability for the distinct types of the acid functionality as defined on the left: Type 1: the acid molecule accepts the dissociated proton returns the proton; Type 2: the acid molecule accepts the dissociated proton and then passes the proton to a different water molecule; Type 3: the acid molecule accepts the dissociated proton and then passes another proton to the water molecule by rotating OH bond; and Type 4: the acid molecule accepts the dissociated proton and then passes a different proton to another water molecule. 117
Figure 6.1. Comparison of simulated (open symbols) and experimental (filled symbols) (Refs.[267, 268]) densities of [BMIM] [TFSI], [BMIM][PF_6], [BMIM][BF_4], and [BMIM][Br] ILs as a function of temperature. The densities from our simulations are in good agreement with experimental ones over the entire temperature range. 121
Figure 6.2. (a) Radial distribution functions of centers of mass of cations and anions in four BMIM-based ILs. (b) Coordination number functions of centers of mass of cations and anions in four BMIM-based ILs. 121
Figure 6.3. Spatial distribution functions of anions around the [BMIM] cation (top) and the [BMIM] cation around three anions (bottom). The SDFs were computed using TRAVIS program[269] and visualized by VMD program.[270] The contour surfaces are shown at the isovalues of 10 and 6 nm^{-3} for the top and bottom ones, respectively. 122
Figure 6.4. Snapshots of [BMIM][BF_4] at 400 K with (a) polar and nonpolar domains and tail groups; (b) polar domains only; and (c) tail groups only. The corresponding snapshots of [C_8MIM][BF_4] at 400 K are illustrated in (d – f). The polar domain is composed of the imidazolium ring, the methyl and methylene groups and the anion. The tail groups represent the nonpolar domains. The center of mass of the heavy atoms in the circles is shown. (g) Radial distribution functions of tail-tail to quantitively charaterize the clustering of the tail groups. The anion has a minimal effect on the clustering of tail groups. However, the increase of the tail length significantly enhances the aggregation of tail groups. 124
Figure 6.5. The self-diffusion coefficients of (a) cations and (b) anions of BMIM-based ILs as a function of temperature compared with the experimental data (closed symbols). 125
Figure 6.6. Temperature dependence of the DC conductivity obtained from the MD simulations and BDS experiments. 127
Figure 6.7. The inverse Haven ratio H^{-1} of [BMIM][TFSI], [BMIM][PF_6], [BMIM][BF_4], and [BMIM][Br] as a function of temperature compared with experimental data (closed symbols). 127

Figure 6.8. Contribution of distinct ion-ion correlations to conductivity normalized by σ_{NE} for: (a) [BMIM][TFSI]; (b) [BMIM][PF_6]; (c) [BMIM][BF_4]; and (d) [BMIM][Br] as a function of temperature compared with experimental data (closed symbols). 128
Figure 6.9. (a) The self-diffusion coefficient as a function of the anion-to-cation mass ratio, $x = M_-/M_+$, at 400 K obtained by MD simulations. (b) Contributions of distinct (closed symbols) and total (open symbols) ion-ion correlations to conductivity normalized by σ_{NE} of [BMIM][BF_4] ionic liquids as a function of the artificially changed anion-to-cation mass ratio, $x = M_-/M_+$, at 400 K. The green vertical line indicates the case in which the masses of anion and cation are equal. The solid lines present the theoretical prediction from the denoted equations, where we used $H^{-1} = 0.78$. 130
Figure 6.10. Spatial distribution functions of anions around the BMIM cation (top) and the BMIM cation around BF_4 anion (bottom) for [BMIM][BF_4] systems with artificially changed anion mass. The SDFs were computed using TRAVIS program[269] and visualized by VMD program.[270] The contour surfaces are shown at the isovalues of 10 nm^{-3} and 6 nm^{-3} for the top and bottom ones, respectively. 130
Figure 6.11. The continuous time correlation function, $S(t) = \langle H(t)h(0)\rangle/\langle h\rangle$, (solid), and the intermittent time correlation function, $C(t) = \langle h(t)h(0)\rangle/\langle h\rangle$, (dashed). $H(t)$ is assigned unity if an ion-association continuously retains from initial $t = 0$ to time t, while $h(t)$ is assigned unity if an ion-association occurs at time t. Ion-association is defined as the distance between cation and anion is within a cutoff of 8.0 Å that is the first local minimum of the cation and anion RDF. $S(t)$ provides insight into the average lifetime of the ion-association, while $C(t)$ reflects the relaxation behavior of all possible types of ion-associations including single ion-pairs, multiplets, and clusters.[144, 282] 131
Figure 6.12. Radial distribution functions of center of mass of cations and anions in TFSI-based ILs at 400 K..... 133
Figure 6.13. (a) Diffusion coefficient of cations and anions in TFSI-based ILs at 400 K. (b) Conductivity of TFSI-based ILs at 400 K..... 135
Figure 6.14. The inverse Haven ratio H^{-1} of TFSI-based ILs at 400 K. 135
Figure 6.15. Contributions of distinct ion-ion correlations to conductivity normalized by σ_{NE} of TFSI-based ILs as a function of the alkyl tail lengths of the cation at 400 K. 135
Figure 7.1. Distribution of the sidechain extended (solid lines) and projected (dotted lines) distances at 400 K..... 139
Figure 7.2. Radial distribution functions of the cation-anion at 580 K for (a) PMMA-C_x-IM[TFSI] (x = 2 – 8); and (b) PMMA-C_2-IM associated with various anions. 139
Figure 7.3. Probability of an anion coordinating with n cations, $P(n)$, for: (a) a broad range of linker lengths; and (b) four anions at 580 K. Probability of an anion associating with N cations, $P(N)$, for: (c) a broad range of linker lengths; and (d) four anions at 580 K. 141
Figure 7.4. The diffusion coefficients of the four anions as a function of linker length at 580 K. 143

Figure 7.5. (a) Contribution of anion-anion correlations as a function of linker length under (a) barycentric reference frame and (b) polycation-fixed reference frame at 580 K. 145
Figure 7.6. Categorization of the ion hopping types: Type 1 (intrachain); Type 2 (interchain); Type 3 (free ions without associated ions); and Type 4 (rattling) 147
Figure 7.7. Occurrence probability of the hopping types for [TFSI] with: (a) different linker lengths; and (b) various anions with the linker length of C2 at 580 K. 147
Figure 7.8. Average distance, d_p, between the nearest cationic groups from the same polymer chain and distinct polymers. Inset depicts the intermolecular distance (green dashed line) and the intramolecular distance (red dashed line) between the nearest cations, respectively. 149
Figure 7.9. (a) The time scale (t^*) for the non-Gaussian parameter (α_2) reaching its maximum as a function of the linker length at 580 K. The inset shows the non-Gaussian parameters as a function of time for [TFSI] with different linker lengths at 580 K. (b) Maxima of α_2 as a function of the linker length at 580 K. 149
Figure 7.10. Trajectory lines of an individual anion in: (a) PMMA-C_8-IM[TFSI]; and (b) PMMA-C_2-IM[Br] at 580 K. Different color lines represent different types of ion hopping. Thin and thick lines refer to the trajectories with a timestep of 10 ps and the characteristic time, respectively (130 ps for (a) and 860 ps for (b), respectively). The length of each anion hopping from one "cage" to another at the interval of the characteristic time in (c) PMMA-C_8-IM[TFSI] and (d) PMMA-C_2-IM[Br] at 580 K. 151
Figure 7.11. Self-part of the van Hove function, $G_s(r, t^*)$, for: (a) PMMA-C_x-IM[Br] systems and (c) four anions in PMMA-C_2-IM systems at 580K. Each curve in (a) is vertically shifted 0.5 for clarity. The vertical line represents the intersection of $G_s(r, t^*)$, (solid lines) and $G_{s,0}(r, t^*)$, (dotted lines), which is used as the r^* criterion to determine fast and slow anion populations. Distinct-part of the van Hove function, $G_d(r, t^*)$, for: (b) PMMA-C_x-IM[Br] systems and (d) four anions in PMMA-C_2-IM systems at 580K. 153
Figure 7.12. (a) Self-part of the van Hove function, $G_s(r, t^*)$, for PMMA-C_2-IM[Br] system to define the diffusive and hopping anions. (b) The fraction of hopping anions defined as the integral of the green area in (a) as a function of linker length for different anions. 155
Figure 7.13. (a) The string length distribution for Br^- with different chain lengths in the linker at 580 K. (b) The string length distribution for various mobile anions. (c) The average string length $\langle n_s \rangle$ as a function of chain length for the four anions. (d) The fraction of mobile anions defined by both temporal and spatial scales (t^* and r^*). 157
Figure 7.14. (a) Temperature dependence of cage time and average lifetime of ion association for various linker lengths. (b) Correlations of self-diffusivity and cage relaxation time or average lifetime of ion association for all studied systems. 160
Figure 7.15. Radial distribution functions of cation-anion at 500 K for PMMA-C_2-IM[TFSI] as a function of the relative permittivity. 160

Figure 7.16. Diffusion coefficients of the three anions as a function of relative permittivity at 500 K. 162
Figure 7.17. Contributions of anion-anion correlations as a function of relative permittivity for [TFSI] (black), [BF_4] (red), and [Br] (blue) at 500 K. 162
Figure 7.18. (a) Mean squared displacement (MSD) and the non-Gaussian parameters (α_2) for the anions as a function of the relative permittivity in PMMA-C_2-IM[TFSI] at 500 K. (b) Maxima of α_2 and the corresponding time when α_2 reaches the maximum as a function of the relative permittivity in PMMA-C_2-IM[TFSI] at 500 K. 164
Figure 7.19. (a) Self-part of the van Hove function, $G_s(r, t^*)$, for PMMA-C_2-IM[TFSI] system as a function of the relative permittivity at 500K. Each curve in (a) is vertically shifted 0.5 for clarity. The vertical line represents the intersection of $G_s(r, t^*)$ (solid lines) and $G_{s,0}(r, t^*)$ (dotted lines), which is used as the r^* criterion to determine fast and slow anion populations. (b) Distinct-part of the van Hove function, $G_d(r, t^*)$, for PMMA-C_2-IM[TFSI] system as a function of the relative permittivity at 500 K. 164
Figure 7.20. The string length distribution for PMMA-C_2-IM[TFSI] as a function of the relative permittivity at 500 K. Inset: average string length $\langle n_s \rangle$ as a function of the relative permittivity at 500 K..... 166
Figure A.1. Fully optimized configurations of cluster of two PA molecules with (a) TMA, (b) IMI, (c) LDC, (d) CRT, and (e) CRT* at the B3LYP/6-311G**/SMD level of theory. All values are reported in Å. CRT*+2PA is more energetic favorable than the structure of CRT+2PA by 0.16 kcal/mol. 196
Figure A.2. Self-intermediate scattering function $ISF_s(Q, t)$ of protons for different Q values probed at 400 K for pure PA (a), at 383 K for pure PA (b), at 390 K for aqueous PA85 (c), and at 420K for aqueous PA85. 197
Figure A.3. Correlation functions of proton displacement vectors excluding the protons from the same PA molecule. We obtained the inverse Haven ratio as $H^{-1} = 0.56$, that was slightly smaller than that computed by including all protons ($H^{-1} = 0.58$). 197
Figure A.4. The total RDFs of OO pairs of water and acid molecules and the split OO RDFs between 4 pairs: oxygen of H_2O (O_W) and unprotonated oxygen of acid molecules (O_A); oxygen of H_2O (O_W) and protonated oxygen of acid molecules (O_AH); oxygen of H_3O^+ (O^*) and unprotonated oxygen of acid molecules (O_A); oxygen of H_3O^+ (O^*) and protonated oxygen of acid molecules (O_AH) in (a) PA1H; (b) SA1H; (c) PA3H; and (d) SA3H. In PA1H, strong H-bonds mainly form between H_2O molecules and protonated/unprotonated O atoms of PA molecules. The addition of water molecules slightly affects this composition due to the similar proton affinity. In SA1H, however, the strongest H-bond forms between H_3O^+ and the unprotonated O atoms of the SA molecules significantly contributing to the first peak of the OO RDF between water and SA molecules and the shoulder on the right of the peak comes from the weaker H-bonds between H_2O and the unprotonated O of SA. Increasing the water content switches the intensities of these two peaks. 198

Figure A.5. Representative solvation patterns for active H_3O^+ ($\delta_{min} < 0.1$ Å) in the studied aqueous acid systems. The numbers displayed in the top-left corner represent the population percentages (%) of these solvation patterns. The green ball represents the transferring proton of the active H_3O^+. 199
Figure A.6. $P(R_{OO}, \delta)$ probability distribution for proton transfer between H_3O^+ and other species in (a) PA1H, (b) SA1H, (c) NA1H, (d) PA3H, (e) SA3H, and (f) NA3H. 200
Figure A.7. The mean squared displacement (MSD) for the: (a) water oxygen atoms; and (b) hydronium oxygen atoms. 200
Figure A.8. The MSD of the hydronium ion decomposed into: (a) continuous vehicular component; and (b) discrete structural component. 201
Figure A.9. The MSD of the hydronium ion decomposed into a continuous vehicular component; a discrete structural component; and the correlation between the vehicular and structural components in the slightly acidic water. 201
Figure A.10. Contour plots of sidechain conformation as a function of both distance and angle from polymer backbone at 480 K for (a) PMMA-C_2-IM[TFSI]; (b) PMMA-C_4-IM[TFSI]; (c) PMMA-C_6-IM[TFSI]; and (d) PMMA-C_8-IM[TFSI]. 202
Figure A.11. Occurrence probability of the hopping types for TFSI with (a) different linker lengths; and (b) various anions with the linker length of C2 at 480 K. 202
Figure A.12. The length of each anion hopping from one "cage" to another at the interval of 10 ps in (a) PMMA-C_8-IM[TFSI] and (b) PMMA-C_2-IM[Br] at 580 K. Color codes: blue: Type 1; green: Type 2; and red: Type 3. (c) The average jump length of $TFSI^-$ and Br^- as a function of linker length at 580 K. 203
Figure A.13. (a) Probability of a fast anion (solid lines) compared to a slow anion (dotted lines) (a) coordinating with *n* cations $P(n)$ and (b) associating with *N* cations $P(N)$ for a broad range of linker lengths for the PMMA-C_x-IM[TFSI] systems at 580 K. (c) Occurrence probability of the hopping types for fast anions (solid lines) compared with slow anions (dotted lines) for the PMMA-C_x-IM[TFSI] systems at 580 K. 204
Figure A.14. (a) Continuous time correlation function, $S(t)$, and (b) intermittent time correlation function, $C(t)$, at various temperatures for the PMMA-C_2-IM[TFSI] system. $S(t)$ was computed from trajectories sampled every 10 ps, while $C(t)$ was derived from trajectories sampled every 100 ps. Both functions are fitted to a stretched exponential function as shown in blue dotted lines. 205

Chapter 1 Introduction

This chapter is closely adapted from portions of the following publication:[1]

- Zhu, Z; Paddison, S. J., Perspective: Morphology and Ion Transport in Ion-Containing Polymers from Multiscale Modeling and Simulations. *Frontiers in Chemistry* **2022,** *10*, 981508.

Electrolytes are the key component in energy conversion and storage devices, electrodialysis for water treatment, and solar-driven desalination, in which they selectively conduct ions but not electrons. Next-generation electrolyte materials are being developed for fuel cells, lithium batteries, electrolyzers, and other electrochemical devices.[2-20] In fuel cells, a fuel such as: hydrogen, methane, or methanol is efficiently converted into electrical energy with the aid of catalysts with the typical byproduct being only water.[13] This is in contrast to solid-state Li-ion battery electrolytes where the presence of water must be avoided due to the reactivity of electrode materials. Therefore, the presence of water is a crucial parameter in distinguishing the electrolytes suitable for fuel cells from those employed in certain batteries. Differences in these materials, including the coupled dynamics of the mobile ions and the chains, result in varying ion transport mechanisms and consequently different design principles.

Over the past several decades, fundamental understanding and improvements in various types of electrolytes: proton exchange membranes (PEMs), anion exchange membranes (AEMs), polymerized ionic liquids (polyILs), low molecular weight ionic liquids (ILs), and acids and their aqueous solutions have advanced through experimental work and theoretical studies.[2-21] PEMs, in particular, were partially commercialized due to their high proton conductivity and first use in the Gemini space program in the early 1960s.[10] However, the requirement of expensive noble metal catalysts limits their real-world applications, prompting further research into alternative PEMs. AEMs have garnered significant attention as a viable alternative to PEMs in fuel cells because of the use of non-noble transition metals as electrocatalysts under the high OH^- environment, despite typically lower conductivity.[7-9] Thus, considerable effort has been directed toward understanding ion transport mechanisms and enhancing AEM conductivity. In the context of batteries, polyILs, in which each repeating unit may be charged,

unlike ionomers with a relatively small percentage of charged units, present a promising alternative to organic liquid-based electrolytes, which are toxic, flammable, and have limited electrochemical stability. PolyILs offer good mechanical stability, flexibility, improved safety, and durability. However, enhancing their ion conductivity to a sufficient degree for electrochemical applications remains challenging due to the sluggish local dynamics of polymer chains and the low dielectric constant of these materials.[6, 22]

The performance of these materials is influenced by various tunable factors, including: the functionalized end-groups, composition of block copolymers, polarity and rigidity of polymer backbones, molecular weight, conformational asymmetry, acidity etc. These factors provide opportunities to tailor the structural and dynamical properties of the materials, though they also present challenges in establishing broadly applicable design rules. We hypothesize that the origins of how these factors affect molecular packing and ion dynamics stem mainly from the relatively weak specific interactions in comparison to covalent bonds as they play a key role in block copolymers.[5] This provokes several important yet unanswered questions: How do these specific interactions affect the properties of ion-containing materials? Do these specific interactions have synergistic or uncooperative effects? Which interactions are dominant or the most important? Hence, the development of advanced ion-containing materials depends on a deeper understanding of specific interactions of polymer/polymer, polymer/solvent, acidic or basic group/solvent, and fixed-/counter- ions. These interactions including hydrogen bonding, ion-dipole interactions, Coulombic, and acid-base interactions may govern molecular arrangements, selectivity of ion uptake and transport, ion-ion correlations, and ion transference.

In determining the role of the specific interactions on the performance of a material, various experimental techniques have been employed to study the structural and dynamical properties of ion-containing materials at different length and time scales. Techniques such as small-angle X-ray scattering (SAXS), wide-angle X-ray scattering (WAXS), small-angle neutron scattering (SANS) have been widely applied to deduce hydrated morphology.[23] Quasi-elastic neutron scattering (QENS)[24, 25] and pulsed field gradient NMR (PFG-NMR)[26] are used to measure the self-diffusion coefficient of ions and water molecules, while broadband dielectric spectroscopy

(BDS)[27] may be used to derive among many things the ion conductivity. Additional techniques, including infrared (IR) spectroscopy,[28] Raman spectroscopy,[29] atomic force microscopy (AFM),[30] and transmission electron microscopy (TEM),[31, 32] provide insights into molecular interactions and direct images of surface and 3-D morphology.

Despite advances in technology offering robust tools for elucidating critical information on these materials, modeling and simulations are clearly necessary to complement experiment findings and guide further experimental directions. These efforts aim to enhance our understanding of morphology formation, proton/ion transport mechanisms, and the development of improved materials for electrochemical applications. Given the complex morphological and dynamical behavior of electrolyte materials, multiscale theoretical approaches are required to describe characteristics across a wide range of temporal and spatial scales. Quantum mechanical calculations and *ab initio* molecular dynamics (AIMD) simulations offer high accuracy in gaining information on static and dynamic properties by accounting for both electronic and nuclear degrees of freedom. This accuracy is particularly critical when studying proton/hydroxide ion diffusion, which involves the breaking and forming of covalent bonds. However, AIMD is limited to small time and length scales.

To extend the systems up to the size of a hydrophilic pore or domain, multistate empirical valence bond (MS-EVB)[33] and reactive ReaxFF[34] have been employed to study both vehicular and structural diffusion in hydrated ion exchange membranes. However, it remains challenging to capture the solvation structures of proton/hydroxide ions and to transfer the force fields to different chemical structures. For nonreactive systems such as polyILs and ILs, classical molecular dynamics (MD) simulations are suitable for investigating structure and ion transport at time scales up to microseconds, though polarization effects are difficult to accommodate. This issue can be addressed by developing a computationally expensive polarizable force field[35] or simply scaling the full atomic charges. The latter has proven effective in capturing polarizability effects on both structural and dynamic properties of polyILs.[36] Although classical MD simulations can predict transport phenomena and structures within a small region, they are limited to time scales of less than 1 μs and length scales of less than 10 nm. To model phase

separations within membranes, which typically require large length scales of 10 – 200 nm, coarse-grained MD and dissipative particle dynamics (DPD) simulations are widely utilized.[37] To capitalize on both experimental and theoretical strategies, a tight feedback loop between modeling and simulations with a broad spectrum of experimental techniques will serve as a protocol for the rational design of functional materials with optimal properties (**Figure** 1.1). The specific systems of interest in this study include AEMs, protic ionic liquids (PILs), pure phosphoric acid, aqueous acids, polyILs, and low molecular weight ILs.

1.1 Anion Exchange Membranes (AEMs)

The AEM is crucial in anion exchange membrane fuel cells (AEMFCs), facilitating hydroxide ion transport and fuel separation. AEMFCs provide a potential alternative to proton exchange membrane fuel cells (PEMFCs) because they utilize non-noble metal catalysts in alkaline conditions, avoiding the need for expensive noble metal catalyst required in acidic environments.[8, 9] Despite the stability of non-noble metal catalysts under alkaline conditions,[38, 39] AEMFCs still face challenges related to mechanical and chemical stability at high pH levels. While recent studies have achieved high OH^- conductivity,[9] the underlying mechanisms remain incompletely understood, prompting further research into the interplay between morphology and ion transport.

1.1.1 Morphology

Understanding nanophase separation in AEMs, particularly the characteristics of the hydrophobic domain compared to the ion-conducting phase, is crucial for designing highly conductive electrolytes with mechanical and chemical stability under various operating conditions. Recently, extensive investigations focused on the hydrated morphology of polystyrene-b-poly(ethylene-co-butylene)-b-polystyrene (SEBS)-based AEMs.[40-44] Findings indicate that quaternary ammonium (QA)-functionalized SEBS AEMs phase separate into a functionalized polystyrene-rich phase and a hydrophobic phase. The water content significantly influences the morphology, evolving from perforated and interconnected lamellae to perfect lamellae and eventually to disordered bicontinuous structures as the water content is increased (**Figure** 1.2).[44] Reducing functionalization and/or the percentage of styrene delays the

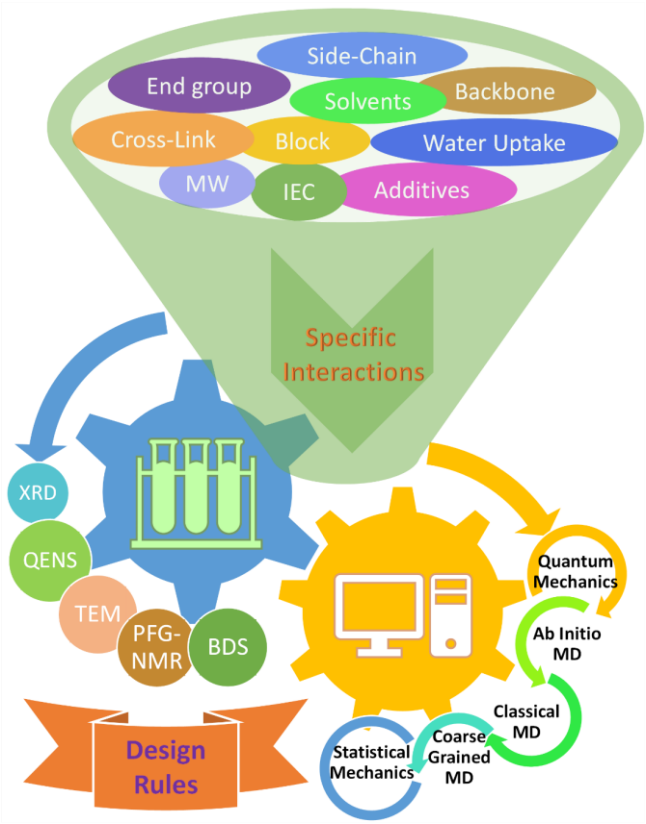

Figure 1.1. Schematic summary of experimental and theoretical approaches used to study the effects of various chemical factors in pursuit of rational design strategies for novel electrolytes.

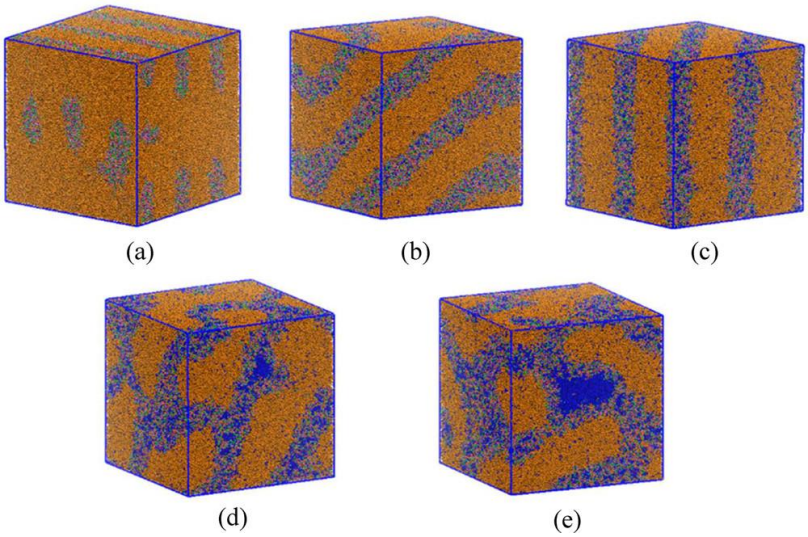

Figure 1.2. Hydrated morphology of SEBS-based AEMs in the alkaline form for λ = (a) 4, (b) 8, (c) 12, (d) 16, and (e) 20. Taken from ref.[44]

formation of large interconnected water domains, while increasing the styrene content facilitates percolation at lower hydration levels.[41] An alkyl spacer (C_4H_8) grafted between the backbone and functional QA group, whether as a linker, tail, or both, strongly affects the morphology, the domain spacing of the hydrophilic phase, the distribution of the backbone-TMA^+ distance, and the water clusters. Specifically, additional spacers may postpone the formation of percolated water domains and promote a uniform water distribution.[43]

Lee and coworkers[40, 45, 46] used DPD simulations to explore the effects of alkyl chain length, sidechain structure, hydrophilic and hydrophobic spacers, and sidechain distribution on the microstructure of polyphenylene oxide tetramethylammonium (PPO-TMA). They found that compared with PPO-based triblock copolymers, the SEBS-based materials undergo nano-segregation even without any sidechain modifications due to their greater hydrophobicity and flexible backbones. The comb-like structure distribution of the sidechains contributed to the formation of a lamellar structure. Short sidechains acting as spacers break the percolated water domain into smaller ones, highlighting the significant impact of alkyl spacers than alkyl extenders. Tailoring the pendant length or composition of sidechains can transform lamellar morphology into an interconnected water network.[45] Adding hydrophobic alkyl spacers enhances phase separation and promotes the formation of large water clusters, but excessive hydrophobicity of the sidechains (either alkyl spacers or alkyl extenders) can create bottlenecks that hinder anion mobility. Less hydrophobic alkoxy spacers may help to form narrower but more connected channels.[46] In contrast, adding hydrophilic spacers impedes ion and water transport due to the stretched sidechains dispersing in the hydrophilic phase.[40] This drawback may be resolved by altering multi-cation sidechains, which facilitate the formation of largely connected ion-conducting pathways.

Coarse-grained MD simulations of poly(ether ether ketone) (PEEK) membranes[47] showed better interconnected and smaller hydrophilic clusters with two QA groups than with a single QA, further improving alkaline stability. Li and coworkers[48] also found that grafting a tri-cation side-chain with a long hydrophobic extender and an additional hydrophilic side-chain significantly enhanced both OH^- conductivity and chemical/mechanical stability of PPO-based

AEMs. These results further demonstrate the success of multi-cations strategies for balancing ionic conductivity and chemical stability.[48-50] A delicate balance of hydrophilic and hydrophobic features in functional groups can also mitigate the bottleneck issues.[34, 51, 52]

Reactive force-field MD simulations on hydrated PPO-based homopolymers with five distinct QA cationic groups (R_1: $-CH_3$, R_2: $-C_2H_5$, R_3: $-C_3H_7$, R_4: $-C_6H_{13}$ and R_5: $-C_4H_8OCH_3$)[52] revealed that nanoscale water domains were connected by narrow channels, with channel size increasing with water content. For symmetrically modified cation groups, longer alkyl tails (i.e., $3R_3$) enhanced phase segregation large, less connected water clusters. In contrast, systems with asymmetric cationic groups ($2R_1R_4$ and $2R_1R_5$) had a narrower pore size distribution at a hydration level of 5. Enhancing hydrophilicity in $2R_1R_5$ by introducing an ether group resulted in a more uniform distribution of the size of the water channels in comparison to $2R_1R_4$, forming narrower connections between water domains. These findings indicate that the hydrophobicity of the functional groups should be sufficient for the desired nanophase segregation but not so strong as to create narrow bottlenecks between the water domains, e.g. $2R_1R_4$.[52]

While a high ion exchange capacity (IEC) enhances AEM ionic conductivity, it also causes swelling and reduces dimensional stability. Cross-linking can manage this swelling without sacrificing anion conductivity. Experiments show that cross-linking with *N,N,N',N'*-tetramethyl-1,6-hexanediamine (TMHDA) or rigid β-cyclodextrin[53] reduces water uptake and swelling in AEMs like poly(bromopropyl norbornene)-b-poly(butyl norbornene) copolymers[54] and the TMA-functionalized SEBS membranes.[55] However, few simulations have explored the impact of cross-linking on AEM morphology despite available algorithms.[56]

1.1.2 Ion Transport

Hydrated AEMs exhibit various hydrophilic ionic domains due to nanophase separation, in which different OH^- transport phenomena occur depending on the chemical structures of the ionomers. These hydrophilic ionic domains, and in some cases, channels are formed by pendant functional groups, water molecules, and OH^-, creating a complex confined environment for OH^- transport.

Given the disparate range of time and length scales involved in the phase-separated hydrated morphology and hydroxide ion transport within a local environment, it is challenging to properly describe OH^- transport (via structural diffusion) within a polymeric system and the conformation of a water network due to nanophase separation using a single model.[57] More importantly, OH^- transport occurs through the migration of charged defects in the hydrogen bond network via a sequence of elementary proton transfer reactions/events, necessitating a quantum mechanical description of covalent and hydrogen bond breaking and forming.[58, 59] Therefore, significant effort has been devoted to addressing these challenges.

To mimic the structural diffusion of OH^-, various techniques have been incorporated into classical MD simulations, including: MS-EVB;[60] bond order-based ReaxFF;[34] and quantum hopping (Q-HOP).[61] Recently, a combination of reactive and nonreactive polarizable MD simulations was used to study OH^- transport mechanisms in hydrated PPO-QA AEMs.[51] The morphology of these non-blocky AEMs at a hydration level of 10 exhibited narrow percolating channels connecting the water domains. It was found that a vehicular mechanism predominantly contributed to the conductivity in the water-rich domains, while structural diffusion was significant in crossing the bottlenecks between large water domains in the confined environment of a channel.[51, 52] Their findings demonstrate that structural diffusion of OH^- facilitates diffusion through these bottlenecks without loss of the anion solvation structure, while vehicular diffusion of OH^- through the bottlenecks requires a change in solvation structure, resulting in a high kinetic barrier. Notably, the decomposition of the total diffusivity into vehicular motion and discrete structural diffusion revealed that structural diffusion is dominant and anticorrelated with vehicular diffusion.[62]

To capture the delicate interplay of proton transfer and solvation structure, AIMD simulations are utilized, in which “on the fly” force fields obtained from DFT-based electronic structure calculations and enable one to accurately simulate the breaking and formation of covalent bonds. However, their high computational cost limits the accessible length and time scales, necessitating careful selection of simulated systems. Recent AIMD simulations examined OH^- transport in AEMs under varying hydration levels, cation spacing, and cell geometries.[63] These

simulations identified active 3-fold and inactive 4-fold OH^- structures (i.e., hydroxide ion coordinated by three or four water molecules), correlating with fast and slow processes, respectively. At low hydration, cations stabilize the 3-fold complex, acting as a fourth neighbor (shown in subplot a of **Figure** 1.3A), followed by the drift of this 3-fold complex toward water molecules forming a 4-fold planar structure (shown in subplot c of **Figure** 1.3A). This complex continues to move toward the nearby cation forming a stable 3-fold structure in the vicinity of the cation. Insufficient water causes vehicular movement of the 3-fold complex between the cations, while increased hydration creates a hydrogen bond network, facilitating a series of proton transfer events via structural diffusion (shown in **Figure** 1.3B). Three distinct diffusion regimes were identified under low-hydration conditions: a non-diffusive regime at very low effective water density, a vehicular diffusion regime at intermediate water density, and a mixed diffusion regime with higher water density (**Figure** 1.3C). Moreover, it is surprising to observe the non-monotonic temperature dependence of OH^- diffusivity in both theoretical and experimental studies.[64] This unexpected phenomenon was explained by transport mechanisms varying with hydration. Specifically, vehicular diffusion dominates at extremely low hydration ($\lambda = 2$), requiring high temperatures to break the hydrogen bonds of the stable solvated hydroxide ion clusters. At low hydration ($2 < \lambda < 5$), moderate temperatures enhance trivial proton rattling but the hydroxide ions are still trapped in the cell center, which requires high temperatures to overcome the bottleneck between the cations. High hydration ($\lambda > 5$) leads to layered water structures, with higher OH^- diffusivity in the upper layer than in the cation-containing layer. Therefore, the temperature threshold for high OH^- diffusivity occurs when the hydroxide ions can move to the upper layer where efficient structural diffusion is predominant.[64] These findings highlight the importance of water distribution and the OH^- solvation structure in proton transfer mechanisms. The combination of water density, cation spacing, and confinement creates complex local environments. Further study of the interplay of solvation patterns and diffusion mechanisms was undertaken by Zelovich and Tuckerman.[65] These interesting results offer new design avenues for high-performance AEMs by engineering the water within a nanoconfined environment.

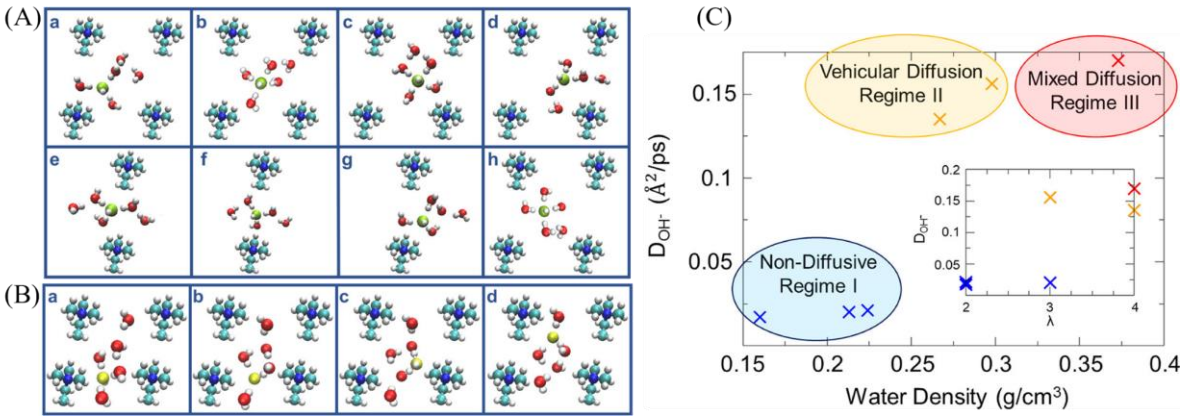

Figure 1.3. (A) Vehicular diffusion mechanism of OH^- in system a4 from a z-perspective. (B) Structural diffusion mechanism of OH^- in system b4 from a z-perspective. (C) Relationship between average diffusivity of OH^- and water density, inset: OH^- diffusivity *vs.* the hydration level. Taken and adapted from ref.[66]

1.2 Protic Ionic Liquids (PILs)

PILs are typically combinations of Brønsted-Lowry acids and bases.[12, 16] They are favored as anhydrous electrolytes used in fuel cells due to their promising properties, including high thermal and electrochemical stability, low vapor pressure, high open circuit voltage and efficiency.[12, 15, 16] Thus, there has been significant research into their transport properties and potential applications, including fuel cells, environmentally friendly organic synthesis, and various bio-related uses.[11, 13, 67]

Proton transport in PILs occurs via two main mechanisms: (1) vehicular in which a molecular entity "carries" the excess positive charge (**Figure** 1.4a); and (2) structural diffusion where protons move by being transferred through the connected hydrogen bond network through a change in the identity of the protons (**Figure** 1.4b).[67-73] The second one may be chain-like (similar to the original Grotthuss idea) where charge moves by collective hopping of protons within the hydrogen bond network (**Figure** 1.4c). The high efficiency of the latter is generally viewed to be the principal reason for the high proton conductivity in neat phosphoric acid and high diffusivity in slightly acidic water.[74-82]

Experimental investigations have provided insights into proton transport mechanisms in PILs. Hoarfrost and coworkers[83] found that the proton conductivity in the imidazolium bis(trifluoromethylsulfonyl)imide PIL was enhanced by both proton hopping and long-range transport, using pulsed-field gradient NMR and quasi-elastic neutron scattering techniques. Kreuer et al.[84] compared the self-diffusion coefficients of protons obtained experimentally with those calculated using the Nernst-Einstein relation in three imidazole doped systems, attributing the greatest contribution to the structural diffusion of protons.

Generally, it is expected that the chemical structure and orientation of the Brønsted-Lowry acid-base pair is responsible for the formation of hydrogen bond networks that facilitate fast proton diffusivity in PILs.[11, 58, 85, 86] However, in many cases, a proton is transferred from an acid to a base, and a vehicular mechanism dominates. Interestingly, in lidocaine-PA mixtures, proton conductivity remains high even in a glassy state where vehicular diffusion is frozen.[87] This raises the question of whether choosing the right acid-base pair can lead to a decrease in

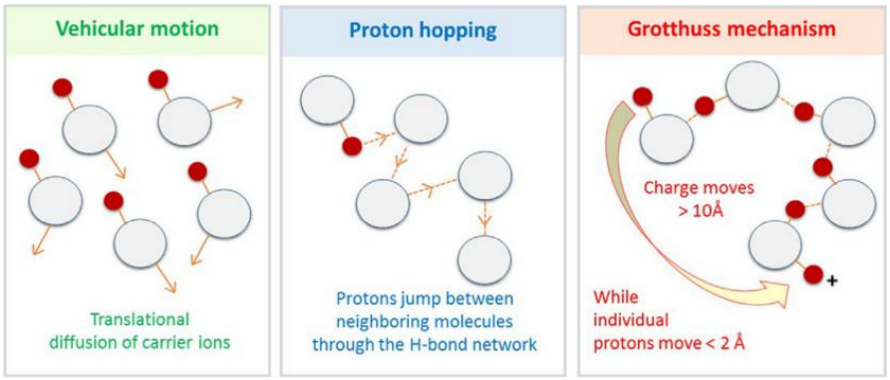

(a) (b) (c)

Figure 1.4. Schematic representation of: (a) the vehicular mechanism; (b) proton hopping mechanism; and (c) collective chain-like proton transport (Grotthuss-like) mechanism, where charge moves much longer distance than individual proton hops. Taken from ref.[11]

the energy barrier for proton transfer and then would lead to exceptionally high proton conductivity in PILs.

To further understand proton transfer in PILs at the molecular level, electronic structure calculations were utilized to study proton transfer, and hydrogen bond networks in a select series of PILs, as discussed in Chapter 4.

1.3 Pure H_3PO_4 and Aqueous Acids

Phosphoric acid (PA), sulfuric acid (SA), and nitric acid (NA) are three canonical acids, which are important chemicals in agriculture, food and cosmetic industries, and atmospheric science.[88-91] These acids possess distinct features including acidity, molecular structure, and proton donor/acceptor sites. PA, a weak acid with a pK_a of 2.1, has the highest intrinsic proton conductivity among many acids and features a peculiar molecular structure with three OH proton donors and one unprotonated oxygen proton acceptor. This makes PA an excellent model for studying proton transport mechanisms, and both pure PA and its solutions have been extensively investigated through experiments and simulations.[81, 82, 92-96]

SA, known as a strong acid with a pK_a of –3, displays high conductivity in dilute solutions.[97] NA, a monoprotic acid with a planar molecular structure, also has a strong acidity with a pK_a of –1.4. These acids are highly soluble in water, forming protonic defects like H_3O^+ upon dissociation, which contribute to their high conductivity. Consequently, these acids and their derivatives are widely used in electrochemical devices, such as phosphoric acid fuel cells (PAFCs)[19] and PA/SA/NA-doped polybenzimidazole (PBI).[98, 99]

The key to their high conductivity lies in the unique behavior of the protons. The proton is the only cation without electrons, and can readily be transferred along a hydrogen bond (H-bond). This simple chemical reaction is crucial in various fields ranging from biochemical processes to electrochemical technologies.[17, 20, 67, 100] This proton transfer involves two protonic defects (i.e. hydronium H_3O^+ and hydroxide OH^-) that act as charge carriers, providing ionic conductivity in many materials.[14, 18, 20, 67, 100]

These protonic defects can be transported via two primary mechanisms: (1) the vehicular mechanism where the defect moves via a molecular vehicle; and (2) the structural diffusion

mechanism, in which the defect diffuses structurally by sequentially transferring protons between molecules within a H-bond network.[67-72] The latter may involve collective proton transfers within a strong H-bond chain, an idea originally proposed by Grotthuss.[101, 102] Extensive research has focused on understanding these proton transport mechanisms by examining the molecular structures and dynamics in various environments, especially aqueous solutions.[1, 14, 33, 63, 69, 70, 77, 103-115]

1.3.1 Proton Transport in Acidic Water

Recent studies highlight several differences in the solvation structure and dynamics of hydronium and hydroxide ions. The hydroxide ion possesses four accepting and one donating H-bond forming a stable configuration that leads to slow transport.[116] However, the hydronium ion prefers to have three donating H-bonds forming an Eigen cation. Once a proton transfers to a neighboring water molecule from an H_3O^+, a transition state occurs where the proton is shared equally by two water molecules, known as the Zundel ion.[117] This transport mechanism is referred to as the Eigen-Zundel-Eigen (EZE) mechanism as shown in **Figure** 1.5.[71, 118, 119] However, more complex solvation structures of H_3O^+ have been observed in slightly acidic water.[111, 113-115, 118, 120] For instance, Tuckerman et al. proposed a concerted mechanism,[69] in which a proton-accepting water molecule begins to lose one of its acceptor H-bonds while the hydronium ion simultaneously accepts a new H-bond from a donor water molecule, leading to the proton transfer (**Figure** 1.6). Meanwhile, these results indicate that the Eigen ion is distorted with one strong and two weak H-bonds and the coordinated water in the strong H-bond is denoted as the "special pair". More importantly, this special pair is dynamically altering among the water molecules of the first solvation shell, referred to as the "special pair dance".[118] Recently, Voth et al. deconvoluted the distorted structures of a H_3O^+ and resolved an anisotropy reorientation relaxation time of 1 – 2 ps.[105]

The solvation and transport properties of hydrated protons are influenced by local environments such as confinement and hydration.[75, 78, 103, 104, 110, 121-123] Studies by Tuckerman et al. suggest that the functional groups in model PEMs is capable of participating in H^+ transport at low hydration levels, enhancing H_3O^+ diffusion.[103, 104, 124] Additionally, Paddison

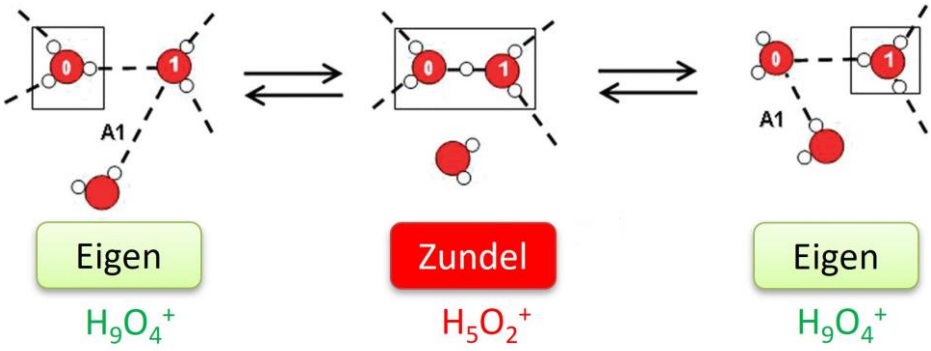

Figure 1.5. Schematic representation of Eigen-Zundel-Eigen (EZE) proton transport mechanism. Taken from refs.[71, 118]

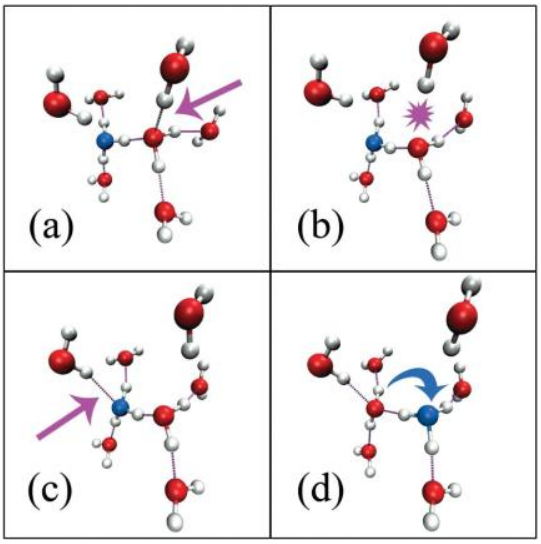

Figure 1.6. Snapshots of elementary steps in the concerted proton transport mechanism in water. Taken from ref.[69]

et al. demonstrated how confinement in bare and fluorinated carbon nanotubes affects proton transfer.[75, 123] Reactive MD simulations have also been used to explore charge transport in PEMs via vehicular and structural diffusion mechanisms.[60, 109, 125-127] These prior studies prompt several questions: What is the solvation structure of H_3O^+ in the presence of either strong or weak acid molecules? How does acid strength affect H^+ diffusion via vehicular and/or structural mechanisms?

In an aqueous acid system, acid molecules act as proton donors while water molecules act as proton acceptors, forming protonic defects that contribute to the protonic conductivity of the solution. The diffusion of protons is influenced by factors such as acid strength and water content. The stronger the acid, the more $H^+(H_2O)$ in the acid solution. Therefore, a strong acid solution may contain a greater number of H_3O^+, leading to a significant vehicular component in the transport of protons. Conversely, weak acids like acetic acid ($pK_a = 4.76$) retain protons, which may result in lower conductivity. Regarding water content, there exists a maximum with regard to acid concentration. This phenomenon has been observed in various acidic solutions.[94] To understand the diffusion of protons, it is necessary to take into consideration the chemical structure, the acidity, and the ability of the acid species to exchange protons with low energy barriers. Chapter 5 delves into the comprehensive study of proton transport within these aqueous acid solutions.

1.3.2 Proton Transport in Pure H_3PO_4

Recent advances in computational modeling, specifically AIMD simulations, have provided unprecedented insights into the proton transport mechanism of pure PA (**Figure** 1.7A).[77, 128] The simulations uncovered a collective chain-like mechanism for proton conduction, in which a 4-step proton conduction process is involved accompanying the reorganization of solvent molecules. Initially, correlated proton transfers initiate the formation of a 'Grotthuss' chain (**Figure** 1.7A (a)). Subsequently, depolarization occurs as one solvent PA molecule donates a proton to an oxygen atom in the chain, initiating a new H-bond (**Figure** 1.7A (b)). This process is followed by charge separation and successive proton transfers near the charged species (**Figure** 1.7A (c-d)), leading to long-range proton transport.

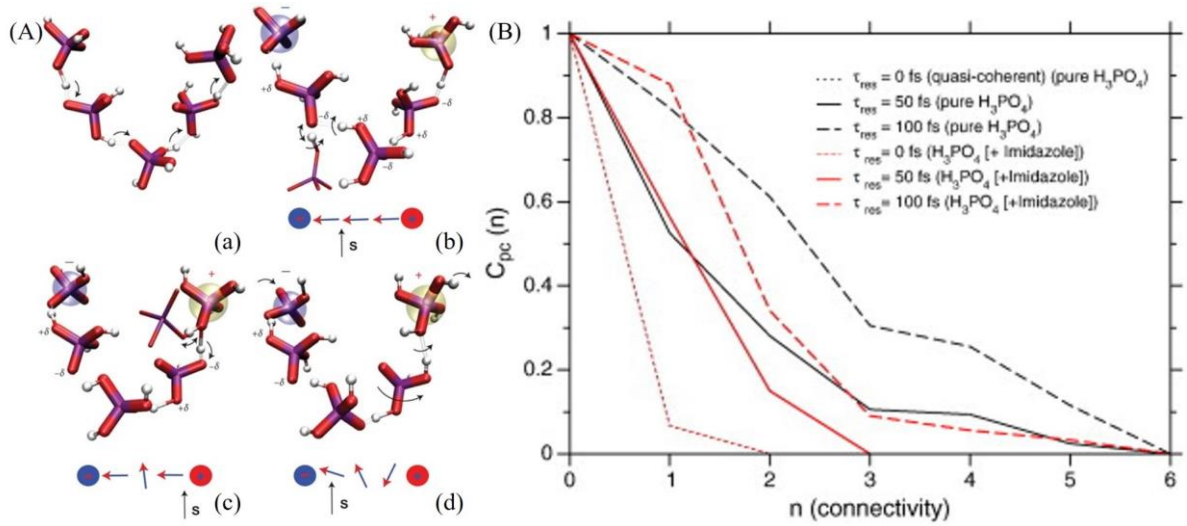

Figure 1.7. (A) Snapshots (a-d) of a few of the elementary steps of proton diffusion in PA as determined by AIMD simulations. These show the correlated proton transfer events and formation of an extended 'Grotthuss' chain, and the participation of other 'solvent' PA molecules. (B) Proton coupling correlation function $C_{pc}(n)$ in pure PA and PA/Imidazole mixture as a function of connectivity n (0, single H-bond; 1, adjacent H-bonds; 6, longest non-cyclic path in the H-bond network) and response time increment τ_{res}. Taken and adapted from refs.[77, 129]

To quantify the length of an extended "Grotthuss" chain and the time interval for each step in the chain formation, a correlation function was introduced. This function assesses the probability of correlation between two proton transfer events separated by a specific number of H-bonds in the chain.[77, 129] This approach not only reveals insight into the H-bonding but also elucidates the probability of correlated proton transfer events occurring instantaneously or within a certain response time. **Figure** 1.7B shows the calculated proton coupling correlation functions with respect to the H-bond connectivity *n* for pure PA and the mixture of PA/Imidazole (2:1), indicating that imidazole bases do not affect instantaneous proton transfer but reduce the overall connectivity of the H-bond network.[129]

Additionally, Tuckerman et al.[58] developed a statistical mechanical theory of proton transport kinetics in H-bonded networks based on population correlation functions. This theory establishes direct links between solvation structure, charge transfer kinetics, and structural diffusion mechanisms, offering valuable insight into many systems involving proton transfer reactions.[58, 63, 65, 66, 106, 130]

Our research extends these findings by also studying proton transport in pure PA, furthering our understanding of its unique conduction properties and potential applications. This study combined AIMD simulations with dielectric spectroscopy, quasielastic neutron, and light scattering, revealing that protons move by surprisingly short jumps of ~0.5-0.7 Å, comparable to proton transfer distances. These jumps are anticorrelated, resulting in a reduction in the conductivity, as discussed in Chapter 5.

1.3 Polymerized Ionic Liquids (PolyILs)

Polymerized ionic liquids (polyILs) continue to be of great interest as electrolytes in energy conversion and storage devices because they combine the ion transport behavior of ILs with the advantageous properties of polymers. These properties include robust mechanical integrity, low flammability, reduced leakage concerns, improved safety, and prolonged durability.[6, 22, 131, 132] However, polyILs exhibit low conductivity at room temperature primarily due to the sluggish segmental dynamics of the polymer chains and low dielectric constants, which impedes their widespread application.[6, 22]

To address these challenges and enhance ionic conductivity to ~10^{-3} S/cm, substantial efforts have been made to tailor the architecture of the polymer chain and the chemical structure of the ions.[1, 4, 6, 37, 131, 133, 134] Strategies include lowering the glass transition temperature of polyILs and decoupling ion mobility from the segmental dynamics of the polymer. Hence, advancing next-generation materials with superior properties strongly relies on acquiring a fundamental understanding of the role of molecular structure, morphology, ion transport mechanisms, and ionic correlations in charge transport.

1.3.1 Ion Transport Mechanisms

Recent studies[135-139] have unveiled a competition between electrostatic interactions and elastic forces, strongly influenced by factors such as mobile ion size, dielectric constant, and polymer backbone rigidity. This competition results in a non-monotonic trend in the activation energy of ion mobility versus the radius of the mobile ion within polyILs below their glass transition temperature (see **Figure** 1.8A).[136] Similar patterns are observed in properties like the glass transition temperature, segmental relaxation time, and counterion diffusivity, as evidenced by coarse-grained simulations.[138] These findings suggest that ion transport can potentially be enhanced by reducing the glass transition temperature via careful parameter adjustments. Furthermore, a decoupling of mobile ion transport from polymer segmental dynamics has been observed in polyILs, as depicted in a Walden plot (see **Figure** 1.8B).[140-143] Particularly, rigid polymers with small counterions exhibit pronounced decoupling behavior.

To explore molecular-level ion transport characteristics behind these intriguing phenomena, MD simulations were leveraged to elucidate ion transport mechanisms in polyILs. Specifically, Ganesan et al.[144] proposed that mobile ions transport through interchain, intrachain, and chain-to-free hopping pathways (see **Figure** 1.9A). Detailed analyses show that anion transport in polyILs is mainly governed by intra- and inter-chain ion hopping, facilitated through the breaking and forming of ion association involving four polymerized cationic groups from two polymer chains (see **Figure** 1.9B). This finding was confirmed by atomistic simulations that included polarizability effects.[36] More interestingly, the authors found that mobile ions tend to associate with three polycations from two polymer chains when refining the ion hopping

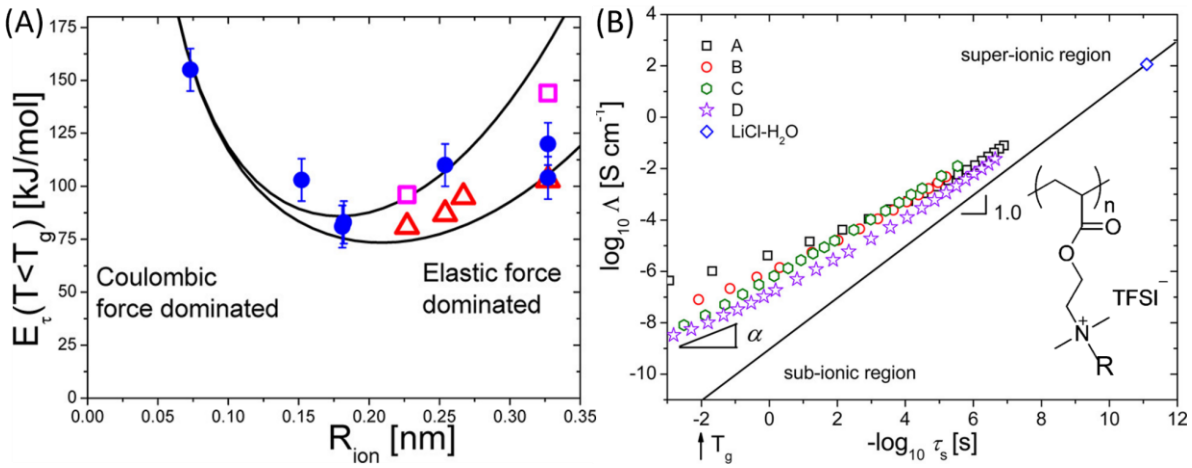

Figure 1.8. (A) Activation energy for conductivity below T_g in various polyILs as a function of mobile ion radius. (B) Walden plot for poly(dimethylamino ethyl acrylate) functionalized with quaternary ammonium with various pedant groups. Taken from refs.[136, 142]

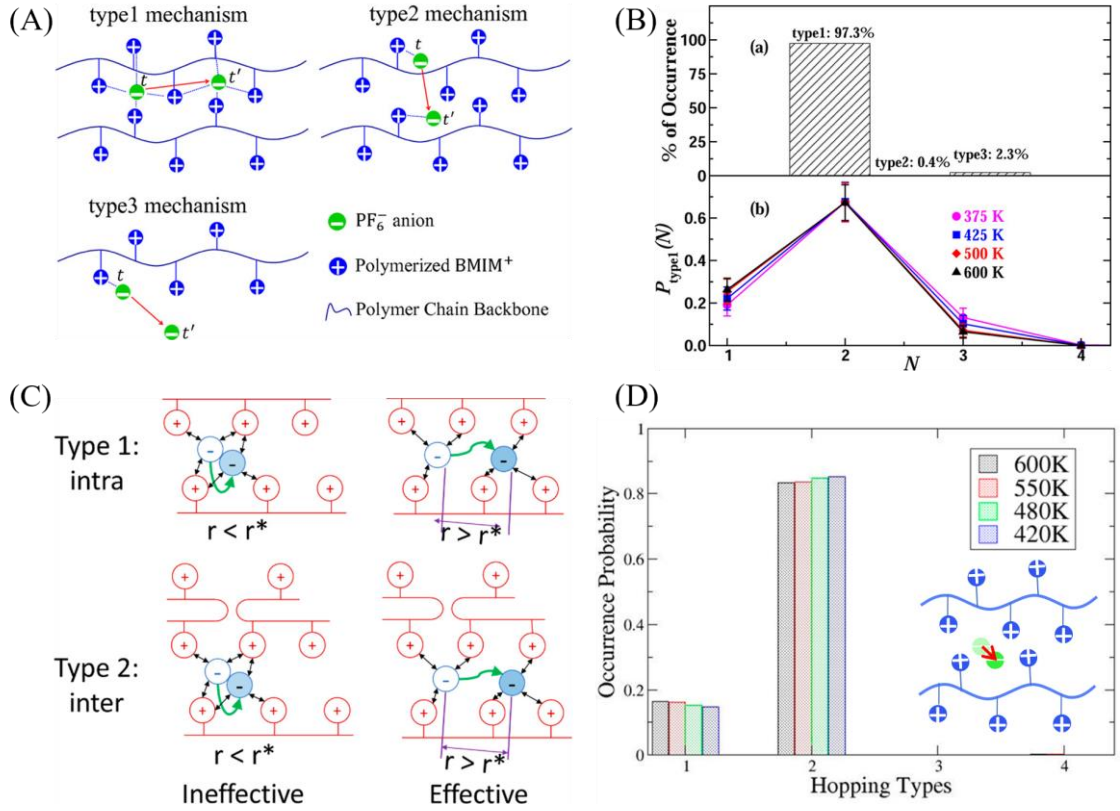

Figure 1.9. (A) Illustration of ion hopping types in polyIL electrolytes. (B) Percentage of hopping events in polyIL electrolytes (top); and decomposition of intrachain hopping events (type 1) assisted by N number of polymer chains (bottom). (C) Definition of effective hopping contributing to the long-range diffusion. (D) Probability of occurrence as a function of hopping type at four different temperatures when the ineffective ions were excluded. The inset is the definition of type 4: remaining intact (i.e. rattling). Taken and adapted from refs.[144, 145]

mechanism by excluding the rattling ions.[36] They determined that ion mobilities in imidazolium-based polyILs are directly correlated to the average lifetimes of the ion associations, while ion mobilities in pure ILs are correlated to structural relaxation time, indicating that anion hopping along the cation monomer chains underlies ion transport in polyILs.[144] These results conclusively imply that anion transport is decoupled from the slow segmental relaxations in imidazolium-based polyILs, which differs from observations in poly(ethylene oxide) and poly(propylene glycol) systems.[146, 147] This difference may be ascribed to the rigid polymer backbone that facilitates decoupling of ion transport from segmental dynamics.

However, it was subsequently argued that the breaking and forming of ion associations probably do not contribute to long-range ion transport because most ions merely "rattle" among the polymerized cationic monomers within a cage.[145, 148] No long-range transport may occur unless the ion escapes from its cage. MD simulations performed on both 1-butyl-3-methylimidazolium tetrafluoroborate ([BMIM]-[BF_4]) IL and poly(1-butyl-3-vinylimidazolium-tetrafluoroborate) (poly([BVIM]-[BF_4])) polyIL confirmed that anion diffusivity in polyILs is directly correlated with anion hopping among cages formed by the cationic groups. Thus, the trap time, during which an anion is confined within a cage, determines the timescale of anion transport rather than the ion association lifetime.[148] Nevertheless, the coupled motion of an anion and the surrounding ions governs the diffusivities of ions in the IL, i.e., the ion transport is correlated with the ion association lifetime. These phenomena were observed in additional all-atom MD simulations,[145, 149] improving the understanding of ion hopping mechanisms in polyILs.

Specifically, the ion transport mechanism in poly(C2Vim)TFSI polyIL was investigated by defining an additional ion transport mode: the intact type, corresponding to the rattling of an ion when trapped in a cage. As anticipated, a significant portion of intact anions (35-50%) were observed, implying that many mobile anions are trapped in cages and do not contribute to long-range transport. Examination of the self-part of the van Hove function of the anions at the characteristic time of the greatest dynamical heterogeneity shows the occurrence of a secondary

peak, quantitatively indicating diffusion via hopping among the cages.[145] The dynamical heterogeneity can be quantified with a non-Gaussian parameter (α_2), required to be large enough ($\alpha_2 > 1$) to distinguish the double peaks in the self-part of the van Hove function. When distinguishing effective mobile anions from slow "immobile" ones according to the distance criterion of the local minimum between the two peaks in the self-part of the van Hove function of the anions, categorization of only these effective mobile anions shows negligible intact anions and dominant inter-chain hopping over intra-chain events. This contrasts with the classification using a short sampling interval (**Figure** 1.9C, D). These results conclusively show that instant ion dissociation is necessary but not sufficient for effective hopping transport. Furthermore, the stringlike cooperative motion of the mobile ions was quantified according to the criterion: $\min\left[\left|r_i(t) - r_j(0)\right|, \left|r_i(0) - r_j(t)\right|\right] < r_s$, in which $r_i(t)$ and $r_j(t)$ are the coordinates of ith and j^{th} anions at time t, and r_s is the cutoff distance for the string collection. The average string length for the polyILs ranges from 1.6 to 2.2 anions, but close loops in the anion transport were not observed. This was hypothesized to be the consequence of the low ionic conductivity of polyILs.[136] Notably, the analysis methods employed in these studies, including the categorization of hopping types, the definitions of dynamic heterogeneity and string-like cooperative motion, can be extended to other ion-containing polymer systems.

1.3.2 Ion-Ion Correlations

Regardless of the ion transport mechanism, another indicator that shows the difference between ion transport and ionic conductivity is the inverse Haven ratio:

$$H^{-1} = \frac{\sigma_{DC}}{\sigma_{NE}}, \tag{1.1}$$

in which σ_{DC} is the ionic conductivity obtained from impedance spectroscopy, whereas σ_{NE} the estimated conductivity from the self-diffusivity of ions using the Nernst-Einstein (NE) equation:[150-153]

$$\sigma_{NE} = \frac{q^2}{k_B T} \sum_i n_i D_i^s, \tag{1.2}$$

where q is the charge of an ion, k_B is Boltzmann constant, T is temperature, n_i, and D_i^s are

the concentration and self-diffusion coefficient of ions, respectively.

In ILs, an $H^{-1} < 1$ is typically explained by the movement of the cation-anion pairs that contribute to ion diffusion but not to conductivity. This explanation, however, was challenged by results from atomistic MD simulations.[154] Further experimental studies of polyILs revealed that the primary mechanism suppressing ionic conductivity is due to the strongly correlated movement of mobile ions with like charges.[132] Recently, simulations of ILs and polyILs with various degrees of polymerization (N) demonstrated that strong distinct correlations between neighboring cations in the polyILs backbone lead to distinct cation-cation diffusivity that is greater than the self-diffusivity of cations in magnitude and independent of N at larger N.[155] Hence, the inverse Haven ratio shows a maximum at $N = 3$. Moreover, the ideal transference numbers decrease with increasing N for large N due to the cationic contribution to the conductivity, challenging the notion that pure polyILs are single-ion conductors.

Shen and Hall studied the effects of ion-polymer and ion-ion interactions on the correlation of anion and cation motions by modeling salt-doped homopolymers and block copolymers.[156] They found that increased ion-monomer interactions led to competing diffusion and ion correlation effects at low salt concentrations, progressively suppressing conductivity with increasing salt concentration. Stronger ion-ion interactions reduce ion conductivity regardless of ion concentration.[156]

Notably, ion-ion correlations reduce the ionic conductivity in these systems due to a seemingly correlated backflow of ions (**Figure** 1.10a), but enhance conductivity in superionic ceramics with charge displacement exceeding that of the ions (**Figure** 1.10b). One potential strategy is to turn negative ion-ion correlation into positive correlation by tailoring the structure of the ion channels and the specific interactions between the ions and the lattice. Excitingly, superionicity has been achieved in IL-based electrolytes by adding ether oxygens to the sidechains of IL cations.[157] This modification enhances the correlation between Li and IL cations but reverses the sign of the Li-anion correlation. However, it remains puzzling why these correlations enhance conductivity in superionic ceramics but strongly reduce ionic conductivity in polyILs. To develop a fundamental molecular-level understanding of the chemical and structural aspects

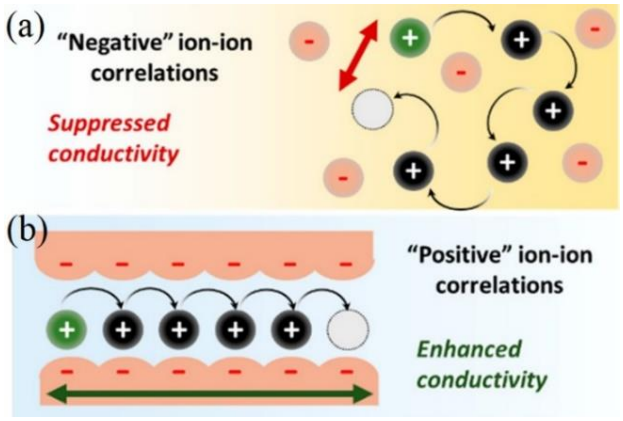

Figure 1.10. Schematic representation of: (a) the negative cation-cation correlations, in which charge transport short distance due to a correlated backflow of cations; and (b) positive cation-cation correlations that enhance conductivity, where charge moves much longer distance than individual cation hops. Taken from Ref.[11]

that control ion transport in polyILs and their low molecular weight ILs, extensive classical MD simulations are needed. These simulations should elucidate the role of the molecular geometry of mobile ions, pendant functional groups, specific interactions, and ionic correlations in charge transport, paving the way for the development of novel materials with superionic conductivity.

1.4 Research Overview

The main goal of the research performed in this dissertation is to develop a fundamental understanding of the interplay between molecular structure and the structural and dynamical properties of a wide range of electrolytes applied for clean energy technologies. To this end, multiscale modeling and simulations were employed to gain molecular-level insights into the behavior of these materials.

1.4.1 Morphologies of AEMs

AEMs based on the triblock copolymer SEBS can be functionalized with different cationic groups, with the coexisting anions varying depending on the synthesis route. The hydrated morphology of SEBS functionalized with various cationic groups offers a suitable platform for understanding the mechanism of anion transport and developing highly conductive and stable membranes. In this dissertation, the impact of different cationic groups on the morphology of SEBS-based AEMs across a broad range of hydration levels (4 – 20) was investigated using mesoscale DPD simulations. In addition, the effects of associated anions (OH^-, Cl^-, and Br^-) were examined. The effects of carbonate counter anions, resulting from a carbonation process, were also studied to better understand the change in the morphology of AEMs during the operation of AEMFCs under ambient air.

1.4.2 Proton Transfer in PILs

Recent studies[85, 87] have revealed exceptionally strong decoupling of proton conductivity from viscosity in a mixture of lidocaine (LDC) and PA. Proton conductivity in this mixture even exceeds that of PA at a similar viscosity. Both LDC and PA possess proton donor and acceptor sites, which are crucial for establishing a H-bond network with efficient proton transport. In comparison, trimethylammonium (TMA) has only one proton acceptor site, and its mixture

with PA exhibits significantly lower conductivity than the LDC and PA mixture at the same viscosity.[87] Therefore, it is necessary to develop a fundamental molecular-level understanding of the chemical and structural aspects that control proton transfer in these PILs.

Electronic structure calculations were performed on systems of PA paired with TMA, imidazole (IMI), LDC, and creatinine (CRT) to elucidate the role of molecular geometry, number of proton donor and acceptor sites, and H-bonds participating in the proton transfer within a select series of PILs (**Figure** 1.11). The findings aim to guide the development of novel materials exhibiting superionic conductivity.

1.4.3 Proton Transport in Pure H_3PO_4 and Aqueous Acids

The "Grotthuss" chain-like mechanism has been elucidated in liquid PA using AIMD simulation.[77] Theoretically, this mechanism should enhance conductivity. However, the inverse Haven ratio in these systems is approximately 0.5, which cannot be explained by a "Grotthuss chain-like mechanism" alone. This raises the question: is there another proton transport mechanism dominating proton conduction in these systems?

To shed light on this question, we combined AIMD simulations with dielectric spectroscopy, quasielastic neutron, and light scattering to determine the proton jump length and transport mechanisms in both pure and 85% aqueous PA. Furthermore, acids play an important role in electrolytes by either reacting with a base to form PILs or being tethered to a polymer backbone to form PEMs. The acid strength controls the local environment of proton transfer as well as long-range proton transport, suggesting that the dominant proton transport mechanism may vary with the strength of the acid.

Thus, the solvation and transport of protons in aqueous acids were studied using AIMD simulations. Aqueous solutions of PA, SA, and NA were examined at two different acid-to-water ratios: 1:1 and 1:3 to understand the similarities and differences in transport mechanisms in these aqueous acids (**Figure** 1.12). This comprehensive study aims to gain a fundamental understanding of the mechanisms underlying proton transport, including vehicular and structural diffusion, which may also help in understanding proton transport in PEMs.

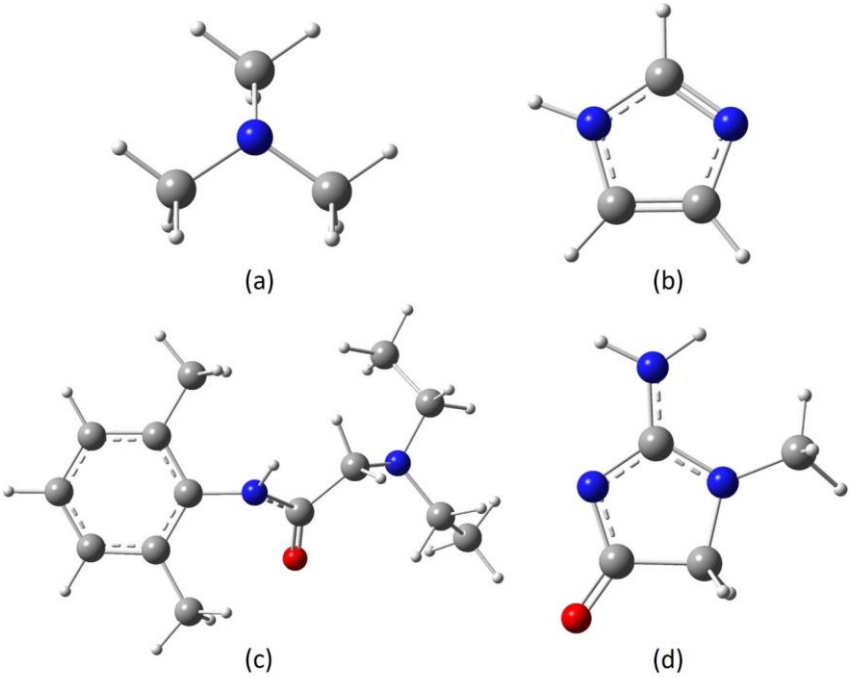

Figure 1.11. Chemical structures of the base molecules used to synthesize PILs: (a) TMA, (b) Imidazole, (c) Lidocaine, and (d) Creatinine.

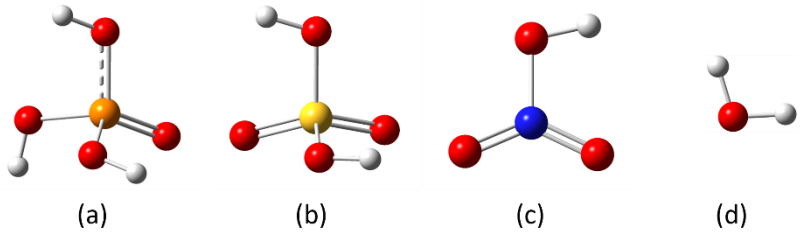

Figure 1.12. Chemical structures of (a) phosphoric acid (PA), (b) sulfuric acid (SA), (c) nitric acid (NA), and (d) water (W). The p*K*a values for these acids are 2.1, –3, and –1.4, respectively.

1.4.4 Ion Transport in ILs and polyILs

Ionic correlations and the mechanisms of ion transport in polyILs and their corresponding ILs were systematically studied by varying the molecular chemistry of the cation and anion using classical MD simulations.

First, to validate the momentum conservation approach for evaluating the distinct ion-ion correlations from experimental data, we directly calculated dynamic correlations from MD simulations using the Onsager transport coefficients. We selected a series of IL systems composed of the same cation, 1-butyl-3-methylimidazolium ([BMIM]), but different anions: bis(trifluoromethane)sulfonimide ([TFSI]), [PF_6], [BF_4], and [Br] to explore the impact of the relative ion mass on ion-ion correlations. The results were further verified by artificially tuning the mass of [BF_4] across a broad spectrum of molecular weights while maintaining the same force field. Additionally, we examined the effects of imidazolium alkyl tail lengths on ion-ion correlations by tailoring the two tails of imidazolium $[C_mC_nIM]^+$ (m = 1 and 2; n = 1 – 8).

Next, we explored ion-ion correlations and ion transport mechanisms in polyILs, focusing on the effects of sidechain flexibility coupled with specific interactions. For this study, we used polymethylmethacrylate (PMMA) attached with imidazolium and varied the sidechain length Cx ($x = 2 - 8$), selecting [TFSI], [PF_6], [BF_4], and [Br] as the anions (**Figure** 1.13). In addition, we investigated the role of electrostatic interactions by changing the dielectric constant of the simulated systems. This work provides insight into the design of highly ion-conductive polymer electrolytes.

This dissertation is organized as follows. Chapter 2 provides a brief introduction to the multiscale computational methods used in this research. Chapter 3 presents the hydrated morphologies of AEMs obtained from DPD simulations. In Chapter 4, hybrid DFT calculations were employed to elucidate the effects of the base on proton transfer between PA molecules in PILs. Chapter 5 explores the mechanisms of proton transport in pure PA and various aqueous acid solutions. Chapter 6 and 7 delve into ionic correlations and ion transport mechanisms, focusing on ILs and polyILs, respectively. Finally, Chapter 8 summarizes the significant findings of this research.

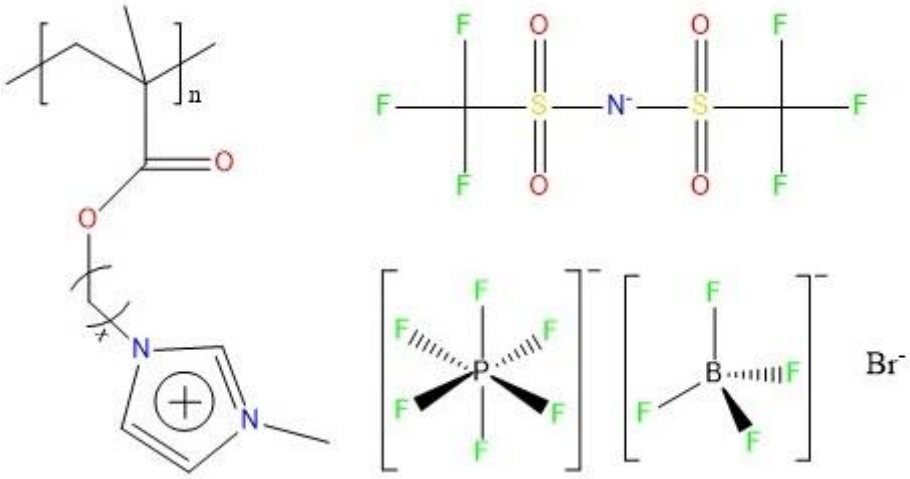

Figure 1.13. Chemical structures of the polyILs consisting of polycations PMMA-C_x-[IM] with various linker lengths (x = 2 – 8) and four associated anions.

Chapter 2 Methods

This chapter is closely adapted from portions of the following publication:[37]

- Zhu, Z; Luo, X; Paddison, S. J., Coarse-grained modeling of ion-containing polymers. *Chemical Reviews* **2022,** *122*, 10710-10745.

Modeling and simulations have been widely used as powerful and robust tools in conjunction with experimental techniques to elucidate important information on these electrolytes and guide further experimental directions with the purpose of enhancing our understanding of morphology formation and proton/ion transport mechanisms as well as the development of improved materials for electrochemical applications (**Figure** 2.1).[1, 37] Given the complex morphological and dynamic behavior of these electrolytes, multiscale approaches are required to describe characteristics over a wide range of temporal and spatial scales. Quantum mechanical calculations and *ab initio* molecular dynamics (AIMD) simulations are regarded as highly accurate methods to gain information on the static and dynamic properties allowing for both the electronic and nuclear degrees of freedom, which are critical when studying proton/hydroxide ion diffusion since the associated proton transfer involves the breaking and forming of covalent bonds. However, the use of AIMD simulation is limited to access small time and length scales. When dealing with nonreactive systems such as polyILs and ILs, classical MD simulations are suitable in investigating the structure and ion transport at time scales up to microseconds. Although classical MD simulations are capable of predicting transport phenomena and structures within a small region, due to the limitations of time (< 1 μs) and length (< 10 nm) scales, coarse-grained MD and dissipative particle dynamics (DPD) simulations are widely utilized in modeling phase separations within membranes that typically require large length scale of 10 – 200 nm.[37]

2.1 Quantum Chemical Calculations

Quantum chemical calculations are used to determine molecular cluster structure, interactions between molecular fragments, formation of hydrogen bonds, proton dissociation and transfer in electrolytes. The quantum chemistry aims to solve the time-independent Schrödinger equation:

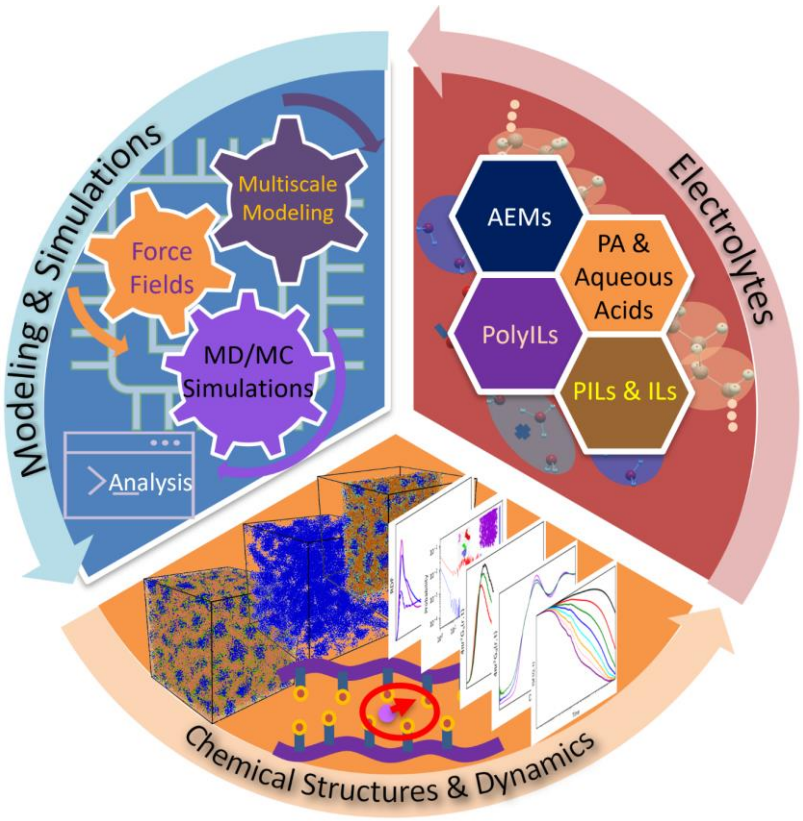

Figure 2.1. Schematic overview of multiscale modeling and simulations of various specific electrolytes providing their structural and dynamical properties.

$$\hat{H}\psi = E\psi\,, \tag{2.1}$$

where $\hat{H}$ is the Hamiltonian operator, ψ is the wave function/eigenfunction, and E is the energy/eigenvalue. The Hamiltonian is simply defined as the sum of the kinetic and potential energies of all electrons and nuclei:

$$\hat{H} = \hat{T}_e + \hat{T}_n + \hat{V}_{ee} + \hat{V}_{nn} + \hat{V}_{en}. \tag{2.2}$$

Here $\hat{T}$ and $\hat{V}$ represent the operators of kinetic and potential energies respectively and the subscripts *e* and *n* refer to electron and nucleus, respectively. The operators $\hat{V}_{ee}$, $\hat{V}_{nn}$, and $\hat{V}_{ne}$ represent the electron-electron, nucleus-nucleus, and nucleus-electron interactions, respectively. The explicit form in atomic units for N_e electrons and N_n nuclei is:

$$\hat{H} = -\frac{1}{2}\sum_{i}^{N_e}\nabla_i^2 - \sum_{k}^{N_n}\frac{1}{2M_k}\nabla_k^2 + \sum_{i}^{N_e}\sum_{j>i}^{N_e}\frac{1}{r_{ij}} + \sum_{k}^{N_n}\sum_{l>k}^{N_n}\frac{Z_k Z_l}{r_{kl}} - \sum_{i}^{N_e}\sum_{k}^{N_n}\frac{Z_k}{r_{ik}}, \tag{2.3}$$

where *i* and *j* denote to electrons, *k* and *l* denote to nuclei, M_k is the ratio of the mass of the kth nucleus to the mass of an electron, ∇^2 is the Laplacian operator, *Z* is the atomic number of the nucleus, and $r_{ab} = |r_a - r_b|$ is the inter-particle distance.

The Born-Oppenheimer (B-O) approximation was made based on the fact that the nuclei are much heavier than electrons by three orders of magnitude, which allows treating the nuclei as fixed in calculating electronic structure. Consequently, the Hamiltonian can be simplified as:

$$\hat{H} = \hat{H}_{elec} + V_{nn}\,, \tag{2.4}$$

where, $\hat{H}_{elec}$ is the electronic Hamiltonian in which the electron-electron interactions cannot be solved exactly except for the hydrogen molecule. Thus, a variety of approximations are made, although we will briefly describe the Hartree-Fock (HF) approximation and density functional theory that are widely used in this study.

2.1.1 Hartree-Fock (HF) Method

Under the HF approximation, it is assumed that each electron moves in an orbital within the mean field generated by all other electrons. To satisfy the requirements of antisymmetry, the trial wave function is expressed as a Slater determinant (SD) with orthonormal spin orbitals. The optimum wave function is obtained by variationally minimizing the energy. Consequently, we gain the HF equation for an arbitrary electron:

$$\hat{F}(1)\chi_i(1) = \varepsilon_i\chi_i(1), \tag{2.5}$$

where ε_i is the orbital energy and $\hat{F}$ is the Fock operator that is defined as:

$$\hat{F}(1) = \hat{h}_1 + \sum_j \left(\hat{J}_j(1) - \hat{K}_j(1)\right). \tag{2.6}$$

The first term of the Fock operator is the sum of the kinetic energy operator for an electron and its interaction with all the nuclei. The second term describes electron-electron repulsion, and the third term is exchange operator. The HF equation can be solved through the self-consistent field (SCF) method. Because HF theory lacks the description of the electron correlation, several post HF methods have been introduced.

2.1.2 Density Functional Theory (DFT)

DFT has been widely used to determine the ground state energy from the molecular electron probability density rather than the wave function. This dramatically decreases the number of variables from 3*N* spatial and *N* spin coordinates to only 3 spatial coordinates.

The central KS DFT equations are developed based on the existence theorem and the variational theorem:[158]

$$\hat{h}_i^{KS}\chi_i = \varepsilon_i\chi_i\,, \tag{2.7}$$

where χ_i and ε_i are the Kohn-Sham orbitals and orbital energy, respectively. The operator $\hat{h}_i^{KS}$ is the one-electron KS Hamiltonian defined as:

$$\hat{h}_i^{KS} = -\frac{1}{2}\nabla_i^2 - \sum_k^{N_n}\frac{Z_k}{r_{ik}} + \int\frac{\rho(r_j)}{r_{ij}}dr_j + V_{xc}\,. \tag{2.8}$$

The term V_{xc} is the functional derivative as:

$$V_{xc} = \frac{\delta E_{xc}}{\delta\rho}\,, \tag{2.9}$$

where V_{xc} is the exchange-correlation potential and the density is $\rho = \sum_{i=1}^{N}\langle\chi_i|\chi_i\rangle$. The KS equations are solved iteratively, similar to the SCF method in HF method. Because the exact $E_{xc}[\rho]$ functional form is unknown. Some approximations are made such as the local density approximation (LDA), the generalized gradient approximation (GGA), and the hybrid functional. One hybrid functional widely used in this study is B3LYP.[159]

2.2 *Ab Initio* Molecular Dynamics (AIMD)

There are various AIMD techniques, we will only briefly discuss Car-Parrinello approach that is used in our study. In Car-Parrinello molecular dynamics (CPMD),[160, 161] ionic dynamics could be run in parallel with fictitious electronic dynamics via the following Lagrangian:

$$L_{CP} = \sum_i \frac{1}{2}\mu_i\langle\dot{\psi}_i|\dot{\psi}_i\rangle + \frac{1}{2}\sum_i M_i\dot{\boldsymbol{R}}_{\boldsymbol{i}}^{\ 2} - E[\{\psi_i\},\{\boldsymbol{R}_{\boldsymbol{i}}\}]. \tag{2.10}$$

This Lagrangian constrained with the orthonormality conditions leads to the following equations of motion:

$$M_i\ddot{\boldsymbol{R}}_i^{\alpha} = -\frac{\partial E[\{\psi_i\},\{\boldsymbol{R}_{\boldsymbol{i}}\}]}{\partial \boldsymbol{R}_i^{\alpha}} = F_{\mathrm{CP_i}}^{\alpha}\,, \tag{2.11}$$

$$\mu_i|\ddot{\psi}_i\rangle = -\frac{\partial E[\{\psi_i\},\{\boldsymbol{R}_{\boldsymbol{i}}\}]}{\partial\langle\psi_i|}\,, \tag{2.12}$$

where M_i and $\boldsymbol{R}_{\boldsymbol{i}}$ represent the atom mass and position, respectively. ψ_i and μ_i denote the KS orbitals and the fictitious mass parameter, respectively. The KS energy is evaluated by minimizing the energy functional with respect to the K-S orbitals. Once this minimum is achieved, the forces on the nuclei are derived from the gradient of the energy with respect to the nuclear coordinates. These forces are then used to advance the nuclear dynamics to the next time step.

In this scheme, the nuclei and electrons evolve at different temperatures, with the nuclei at a higher physical temperature and the electrons at a much lower fictitious temperature, close to the Born-Oppenheimer surface. This adiabatic decoupling of the two subsystems is effective only if their vibrational densities of states do not overlap, making it a challenge for the original Car-Parrinello algorithm in metallic systems.

2.3 Classical Molecular Dynamics (MD)

Compared with AIMD, the interactions between atoms in classical MD are obtained from potential functions, which can be parametrized by fitting to the potential energy surface of electronic structure calculations or experimental data. The functional form of the force field for the classical MD is given by

$$
\begin{aligned}
U &= U_{\text{bonded}} + U_{\text{non-bonded}} \\
&= \sum_{\text{bonds}} k_b(b - b_0)^2 + \sum_{\text{angles}} k_\theta(\theta - \theta_0)^2 \\
&+ \sum_{\text{dihedrals}} k_\chi\left[1 + \cos\left(n\chi - \delta_\chi\right)\right] \\
&+ \sum_{\text{improper}} k_\psi\left[1 + \cos\left(n\psi - \delta_\psi\right)\right] \\
&+ \sum_{i=1}^{N-1} \sum_{i<j}^{N} \left\{ 4\epsilon_{ij} \left[\left(\frac{\sigma_{ij}}{r_{ij}}\right)^{12} - \left(\frac{\sigma_{ij}}{r_{ij}}\right)^{6} \right] + \frac{q_i q_j}{4\pi\varepsilon_0 \varepsilon_r r_{ij}} \right\},
\end{aligned}
\tag{2.13}
$$

where k_b, k_θ, k_χ, and k_ψ are the force constants for bond, angle, dihedral, and improper terms, respectively. b_0, θ_0, δ_χ, and δ_ψ denote the equilibrium values. The last two terms define Lennard-Jones and electrostatic interactions. In our simulations, the parameters are obtained from the General AMBER force field (GAFF)[162] and the partial charge on each atom is calculated through the restrained electrostatic potential (RESP) algorithm based on electronic structure results. The deficiency of this scheme is the difficulty in allowing for polarization effects, which is resolved by either developing a computationally expensive polarizable force field[35] or simply scaling the full charges by some fraction. The latter was recently proven to be capable of capturing polarizability effects on both structural and dynamic properties of polyILs based on the comparison of the results obtained from the scaled partial charge force field and the Drude oscillator polarizable force field.[36]

2.4 Dissipative Particle Dynamics (DPD)

The development of DPD can dates back to the 1990s, pioneered by Hoogerbrugge,[163] Espanol[164-166] and Avalos.[167] In 1997, Groot and Warren refined the DPD method, providing an algorithm and a case study of water, which established DPD as a practical simulation technique.[168] DPD has since been successfully applied to polymers and membranes.[169-178] The following briefly introduces the original DPD method, with comprehensive descriptions available in the works of Groot and Warren,[168] Espanol and Warren,[179] and Santo and Neimark.[180]

In the DPD model, several atoms are grouped into a single particle or "bead". The dynamics of these beads are governed by Newton's law, with all particle masses treated as unity to ensure meeting the requirement that the particles have similar sizes and masses. The equations of motion are:

$$\frac{d\boldsymbol{r_i}}{dt} = \boldsymbol{v}_i \quad and \quad \frac{d\boldsymbol{v_i}}{dt} = \boldsymbol{f}_i\,, \tag{2.14}$$

where $\boldsymbol{r}_i$, $\boldsymbol{v}_i$, and $\boldsymbol{f}_i$ are the position, velocity, and net force of the ith particle, respectively. The net force consists of three non-bonded pairwise interactions (conservative ($\boldsymbol{F}_{ij}^{C}$), dissipative ($\boldsymbol{F}_{ij}^{D}$), and random ($\boldsymbol{F}_{ij}^{R}$) forces) and an additional bonded interaction $\boldsymbol{f}_i^{bonded}$:

$$\boldsymbol{f_i} = \sum_{j\neq i}\left(\boldsymbol{F}_{ij}^{C} + \boldsymbol{F}_{ij}^{D} + \boldsymbol{F}_{ij}^{R}\right) + \boldsymbol{f}_i^{bonded} \tag{2.15}$$

$$\boldsymbol{F}_{ij}^{C} = \begin{cases} a_{ij}(1 - r_{ij})\boldsymbol{e}_{ij} & r_{ij} < r_c \\ 0 & r_{ij} \geq r_c \end{cases} \tag{2.16}$$

$$\boldsymbol{F}_{ij}^{D} = -\gamma_{ij}(1 - r_{ij})^2(\boldsymbol{e}_{ij} \cdot \boldsymbol{v}_{ij})\boldsymbol{e}_{ij} \tag{2.17}$$

$$\boldsymbol{F}_{ij}^{R} = \sigma_{ij}(1 - r_{ij})\xi_{ij}\frac{1}{\sqrt{\Delta t}}\boldsymbol{e}_{ij}\,. \tag{2.18}$$

The forces are dimensionless, using LJ units. The conservative force has a cutoff $r_c = 1$, where $\boldsymbol{F}_{ij}^{C}$ is linear to the distance between the two beads within r_c but becomes zero for the distances greater than r_c. The parameter a_{ij} specifies the interaction strength between pairs of beads and is material-specific. The distance between beads *i* and *j* is denoted by $r_{ij} = |\boldsymbol{r}_i - \boldsymbol{r}_j|$ The unit vector $\boldsymbol{e}_{ij}$ pointing from bead *i* to bead *j*, and the relative velocity $\boldsymbol{v}_{ij}$ are defined as $\boldsymbol{e}_{ij} = \frac{\boldsymbol{r}_i - \boldsymbol{r}_j}{|\boldsymbol{r}_i - \boldsymbol{r}_j|}$ and $\boldsymbol{v}_{ij} = \boldsymbol{v}_i - \boldsymbol{v}_j$, respectively. In the dissipative ($\boldsymbol{F}_{ij}^{D}$) and random forces ($\boldsymbol{F}_{ij}^{R}$), the dissipation constant γ_{ij} and noise amplitude σ_{ij} are related by $\sigma_{ij} = \sqrt{\gamma_{ij} 2k_bT}$, serving as a thermostat based on the fluctuation-dissipation theorem.[165] Typically, γ_{ij} and σ_{ij} have values of 4.5 and 3, respectively, with k_bT = 1 (dimensionless temperature), and ξ_{ij} is a uniformly distributed random number with zero mean and unit variance.

The bonded force, $\boldsymbol{f}_i^{bonded}$, describes the polymer chains where particles or beads are connected by covalent bonds, with angle constraints applied to consecutive bonds to control

chain flexibility.[181, 182] To achieve specific properties, the DPD model can be further adjusted to include additional interactions such as explicit Coulombic interactions,[181, 183] proton and hydroxide ion transport,[45, 184, 185] and the entanglement of polymer chains.[186-188]

2.4.1 Determining the Interaction Parameters

A DPD simulation begins with the crucial task of estimating the conservative a_{ij} parameters accurately. Initially, a specific bead is selected as the reference, and its self-interaction, denoted as a_{RR}, is determined to ensure sufficient fluctuation. Typically, the compressibility of water is reproduced by setting $a_{RR} = 25$ when coarse-graining a water molecule into a single bead. It is recognized that increasing the number of water molecules per DPD bead requires a higher a_{RR} to accurately represent physical properties in real units.[46, 189] However, this adjustment is primarily numerical and depends on the simulation's focus on structural properties; excessively high a_{RR} values can result in a system that is overly rigid.

For other types of molecules, a_{ij} parameters can be assigned based on intuitive chemical insights.[182, 189, 190] Alternatively, a widely adopted approach involves setting all $a_{ii} = a_{RR}$ for all the particles and relating the a_{ij} ($i \neq j$) to the Flory-Huggins χ-parameter. Warren and Groot established a relationship between χ and a_{ij}, showing that $0.286(a_{ij} - a_{ii}) = \chi$ for a numerical density of 3. The χ-parameter can be computed using the solubility parameters, δ_A and δ_B, from experimental data found in handbooks that catalog common solvents and equivalent polymer segments[191, 192] with this relationship:

$$\chi = \frac{V_{bead}}{RT} (\delta_A - \delta_B)^2 , \tag{2.19}$$

where R is the gas constant, and V_{bead} is the molar volume of the DPD bead, which is the same for all beads. This method, however, is limited by the availability of chemical data. When an exact match is not feasible, one must seek similar materials in the handbook to serve as substitutes for the desired DPD bead.

The χ-parameter can alternatively be estimated through atomistic simulations employing classical force fields. Early methodologies relied on cohesive energy or heat of vaporization to calculate the solubility parameter:[171-173, 175, 193, 194]

$$\delta_i = \sqrt{\frac{\Delta \mathrm{E}_{coh,i}}{V_i}} = \sqrt{\frac{\Delta H_i^{vap} - RT}{V_i}} \,. \tag{2.20}$$

Here, $\Delta \mathrm{E}_{coh,i}$, ΔH_i^{vap}, and V_i represent the cohesive energy, heat of vaporization, and molar volume of the ith species (bead type i), respectively. $\Delta \mathrm{E}_{coh,i}$ can be derived from atomistic simulations of the pure i^{th} species with this equation:

$$\Delta \mathrm{E}_{coh,i} = \mathrm{E}_{liquid,i} - n\mathrm{E}_{gas,i} \tag{2.21}$$

where $\mathrm{E}_{liquid,i}$ is the potential energy of i in the liquid state, n is the number of molecules in this liquid system, and $\mathrm{E}_{gas,i}$ is the potential energy of an isolated molecule.

Alternatively, the χ-parameter can also be computed from mixing energy using atomic Monte Carlo (MC) calculations:[195]

$$\chi = Z\left(\frac{\Delta \mathrm{E}_{12}}{RT}\right) \tag{2.22}$$

$$\Delta E_{12} = E_{12} - \frac{1}{2}(E_{11} + E_{22}) \,, \tag{2.23}$$

where Z denotes the coordination number, i.e., the number of potential interaction partners, ΔE_{12} is the heat of mixing of components 1 and 2, and E_{12} and $E_{11(22)}$ represent the energies of the mixture and pure systems, respectively. The estimation of Z involves placing the nearest neighbors around the center molecule, and E_{ij} is evaluated via all-atom MC calculations for a pair consisting of i and j. After sampling numerous orientations to maintain contact between their van der Waals surfaces, the Metropolis algorithm ensures acceptance.[196] This method has found application in studying copolymers and proton exchange membranes.[171-173, 175, 197]

Conceptually, deriving the χ-parameter from cohesive or mixing energies offers greater precision than relying on similarities found in material handbooks. However, conducting atomistic simulations can incur significant costs, particularly when dealing with numerous types of beads.

Vishnyakov et al.[198] proposed a method to match DPD repulsion parameters with infinite dilution activity coefficients (IDAC). Lee and coworkers further extended the IDAC approach to polymer chains and polymeric electrolytes for insoluble bead pairs.[40, 45, 46, 184] To calibrate $\Delta a_{ij} = (a_{ij} - a_{RR})$ with the IDAC, a series of hybrid DPD-MC simulations are conducted

using the Widom test particle insertion methodology.[199] For instance, a water bead is inserted into a pure 4-mer melt. The activity coefficient of the inserted species is calculated as follows:

$$\ln(\gamma_i^{\infty}) = \ln\langle\exp\left(-\frac{E_{i\to j}^{ins}}{k_B T}\right)\rangle - \ln\langle\exp\left(-\frac{E_{i\to i}^{ins}}{k_B T}\right)\rangle - \ln\left(\frac{n_j b_i \rho_{ij}}{n_i b_j \rho_{ii}}\right), \quad (2.24)$$

where γ_i^{∞} is the activity coefficient of dilute *i* in the solvent *j*, $E_{i\to j}^{ins}$ is the energy of randomly inserting one *i* bead to a bath of *j* molecules, n_j is the number of molecules represented by a coarse-grained molecule, b_i is the number of beads in a coarse-grained molecule, and ρ_{ij} is the numerical density of the simulation box after insertion (approximately 3). Insertion energies are calculated by performing trial DPD simulations with various Δa_{ij} values, yielding a series of $\ln(\gamma_i^{\infty})$ from Eq. (2.24). Typically, a linear correlation between $\ln(\gamma_i^{\infty})$ and Δa_{ij} is found. If γ_i^{∞} is known from experimental data or the COSMO-RS model,[200, 201] it is used to calculate $\ln(\gamma_i^{\infty})$, and the exact Δa_{ij} is obtained from a calibration curve.

These parameterization approaches highlight the versatility of different methodologies but are inadequate for charged beads. In DPD simulations of ion-containing polymers, one approach is to combine oppositely charged moieties into a single bead, which sacrifices a precise description of ion transport. Alternatively, the mobile charged bead can be treated as a special entity, interacting with opposite charged beads and water beads through an attractive short-range Morse potential $\mathbf{F}_{ij}^{(\mathrm{M})}$ in DPD simulations:[40, 45, 46, 184, 202]

$$\mathbf{F}_{ij}^{(\mathrm{M})}(r_{ij}) = -2\alpha_{IJ}K_{IJ}e^{\alpha_{IJ}r_{ij}}\{1 - e^{\alpha_{IJ}r_{ij}}\}\frac{\boldsymbol{r_{ij}}}{r_{ij}}, \text{at } r_{ij} < r_{ij}^{M}, \quad (2.25)$$

where K_{IJ}, α_{IJ}, and r_{ij}^{M} represent the effective strength parameter, the effective steepness of the Morse potential, and the cutoff distance for a Morse bond, respectively. These parameters are obtained by fitting the mobility of the simulated bead in bulk water and the degree of dissociation in dilute reference solutions to the experimental values. In these simulations, the electrostatic interactions between charged species are explicitly treated using a smeared charge approach, which increases computational cost and can lead to unphysical clustering phenomena in some systems.[184]

To address this issue, Fatemeh and Paddison introduced an *ab initio*-based method for treating charged beads, where electrostatic interactions are implicitly included, and the a_{ij} parameters retain some chemical specificity of ion-containing polymers.[203] This method involves sampling various orientations of two rigid clusters of atoms, identical to the DPD beads, and conducting DFT calculations for the interaction energy. The a_{ij} parameter is then estimated by fitting the excess energies with the distances between the two beads using:

$$U_{ij}^{ex} = U_{(i+j)} - U_{(i)} - U_{(j)} = \frac{a_{ij}^{int}}{2}\left(1 - r_{ij}\right)^2 + b_{ij}^{int}\,, \tag{2.26}$$

where $U_{(i+j)}$ and $U_{(i)}$ are the energies of the cluster of $i + j$ beads and the isolated i bead, respectively, and a_{ij}^{int} and b_{ij}^{int} are fitting parameters. These parameters are further scaled to obtain Δa_{ij} using:

$$\Delta a_{ij} = \frac{a_{ij}^{int}}{r_c^2 s} + \frac{b_{ij}^{int}}{s}\,, \tag{2.27}$$

where r_c is a value comparable to the cutoff distance in real units, and s is an arbitrary scaling factor. Although this method requires fine-tuning and careful scaling of the energy curves, it provides a comprehensive solution incorporating charged beads within the standard DPD model. In this research, we utilized this novel approach.

The fragmental molecular orbital (FMO) method also estimates the a_{ij} parameters from *ab initio* calculations[204, 205] and has been successfully applied in DPD simulations of ion-containing membranes by Okuwaki et al.[206] Although their initial work involved only neutral DPD beads, the FMO method is fundamentally capable of handling charged beads. This method follows a similar philosophy to Eqs. (2.22) and (2.23) but uses a modified relation for the χ-parameter and mixing energy:

$$\chi = \frac{(E_{12}Z_{12}S_{12} + E_{21}Z_{21}S_{21}) - (E_{11}Z_{11}S_{11} + E_{22}Z_{22}S_{22})}{RT}\,. \tag{2.28}$$

Here, Z_{ij}, E_{ij} and S_{ij} are the coordination number, energy of the bead pair, and the scaling factor of beads i and j, respectively. Z_{ij} is estimated from the configuration setup using the J-OCTA program.[207] The energy of the bead pair, E_{ij}, is derived from *ab initio* calculations for a polymer fragment and a cluster of small molecules, utilizing numerous FMO calculations with

tools like the ABINIT-MP program.[208] S_{ij} represents the anisotropy of the orientations for the two approaching fragments i and j, evaluated through MC sampling. S_{ij} equals unity when interactions between two fragments are uniform in all directions, otherwise, S_{ij} is less than one. It is noteworthy that for the same material (Nafion), the FMO method yielded a different set of a_{ij} parameters compared to classical MC calculations.[197, 206] This indicates that various parameterization strategies are applicable and that the derived DPD parameter set only needs to have relative trends instead of the unique values. **Figure** 2.2 summarizes the different pathways for computing or estimating the a_{ij} parameters. For readers interested in more detailed approaches, including those addressing electrostatic interactions and different bead volumes, we refer to a comprehensive review.[180]

2.5 Ion-Ion Correlations

To elucidate the role of ion-ion correlations in ionic conductivity, the contributions of distinct ion-ion correlations to conductivity can be estimated using experimental techniques and MD simulations.

2.5.1 The Momentum Conservation Approach

One simple momentum conservation approach was proposed by Schonert and developed in several papers,[132, 154, 209] assuming that the total momentum of all ions is conserved. Simply, the velocities of cations and anions in a simple system consisting of only two ions follow the equation:

$$M_+ \sum_i \boldsymbol{v}_{i+}(0) + M_- \sum_i \boldsymbol{v}_{i-}(0) = 0\,. \tag{2.29}$$

Multiplying Eq. (2.29) by $\boldsymbol{v}_{i+}(t)$ and $\boldsymbol{v}_{i-}(t)$, respectively, and taking the average yields the following pair of equations:

$$\begin{cases} M_+\left(D_+^s + \dfrac{D_{++}^d}{2}\right) = -\dfrac{M_- D_{+-}^d}{2}, \\ M_-\left(D_-^s + \dfrac{D_{--}^d}{2}\right) = -\dfrac{M_+ D_{+-}^d}{2}, \end{cases} \tag{2.30}$$

where D_+^s and D_-^s are self-diffusion coefficients of cations and anions, respectively; and D_{++}^d, D_{--}^d, and D_{+-}^d are distinct diffusion coefficients between ions. These coefficients can be

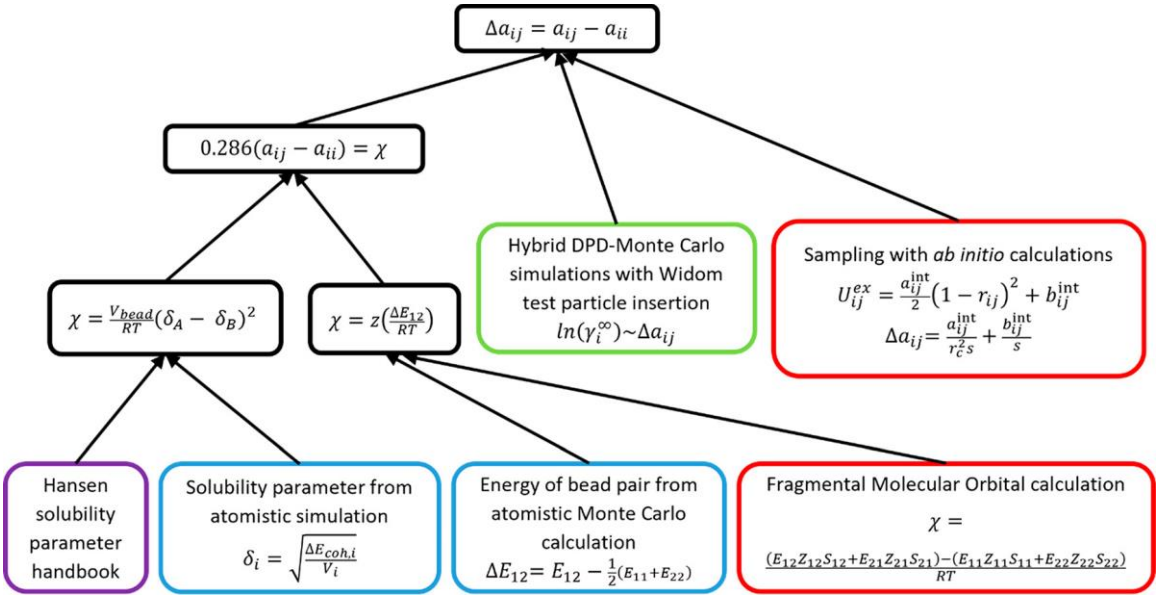

Figure 2.2. Various pathways to obtain the Δa_{ij} for DPD simulations. Color codes: purple: handbook data; blue: atomic simulations with classical force fields; red: *ab initio* calculations; green: trial DPD simulations.

defined by the following relationships:

$$D_{+}^{s} = \frac{1}{3}\int_0^\infty < \boldsymbol{v}_{i+}(t)\, \boldsymbol{v}_{i+}(0) > dt, \qquad D_{-}^{s} = \frac{1}{3}\int_0^\infty < \boldsymbol{v}_{i-}(t)\boldsymbol{v}_{i-}(0) > dt,$$

$$D_{++}^{d} = \frac{\varphi}{3}\int_0^\infty < \boldsymbol{v}_{i+}(t)\boldsymbol{v}_{j+}(0) > dt, \qquad D_{--}^{d} = \frac{\varphi}{3}\int_0^\infty < \boldsymbol{v}_{i-}(t)\boldsymbol{v}_{j-}(0) > dt,$$

$$D_{+-}^{d} = \frac{\varphi}{3}\int_0^\infty < \boldsymbol{v}_{i+}(t)\boldsymbol{v}_{j-}(0) > dt = \frac{\varphi}{3}\int_0^\infty < \boldsymbol{v}_{i-}(t)\boldsymbol{v}_{j+}(0) > dt. \tag{2.31}$$

Here φ is the total number of correlated ions in a local area, and $i \neq j$. The conductivity can be defined as a current-current correlation function:[152, 153, 210]

$$\sigma_{DC} = \frac{1}{3Vk_BT}\int_0^\infty \langle \boldsymbol{J}(0)\cdot\boldsymbol{J}(t)\rangle\, dt = \frac{1}{3Vk_BT}\int_0^\infty \langle \sum_i q_i\boldsymbol{v}_i(0)\cdot\sum_j q_j\boldsymbol{v}_j(t)\rangle\, dt\,. \tag{2.32}$$

Combination of Eqs. (2.30-32) gives contributions of distinct ion-ion correlations into conductivity as follows:[132, 154, 209]

$$\sigma_{DC} = \sigma_{NE} + 2\sigma_{+-}^{d} + \sigma_{++}^{d} + \sigma_{--}^{d} \tag{2.33}$$

$$\sigma_{NE} = \sigma_{+}^{s} + \sigma_{-}^{s}\,, \tag{2.34}$$

where the NE conductivity is the summation of the self-correlations of cations and anions, and the last three terms define contributions of conductivity from distinct anion-cation (σ_{+-}^{d}), cation-cation (σ_{++}^{d}), and anion-anion (σ_{--}^{d}), correlations. As a result, analytical expressions for the contributions of the ion-ion correlations in Eq. (2.33) can be obtained by solving Eqs. (2.30) and (2.32):[132, 154, 209, 211]

$$\sigma_{++}^{d} = \frac{1}{2}\frac{e^2n}{k_BT}D_{++}^{d} = \sigma_{DC}\left(\frac{M_-}{M_- + M_+}\right)^2 - \sigma_{+}^{s}, \qquad \sigma_{+}^{s} = \frac{e^2n}{k_BT}D_{+}^{s} \tag{2.35}$$

$$\sigma_{--}^{d} = \frac{1}{2}\frac{e^2n}{k_BT}D_{--}^{d} = \sigma_{DC}\left(\frac{M_+}{M_- + M_+}\right)^2 - \sigma_{-}^{s}, \qquad \sigma_{-}^{s} = \frac{e^2n}{k_BT}D_{-}^{s} \tag{2.36}$$

$$\sigma_{+-}^{d} = -\frac{e^2n}{k_BT}D_{+-}^{d} = \sigma_{DC}\frac{2M_+M_-}{(M_- + M_+)^2}. \tag{2.37}$$

These expressions offer a straightforward method for estimating distinct ion-ion correlations if the DC-conductivity and self-diffusion coefficient are measured experimentally. It is worth noting that these expressions can be further expanded to complex systems with solvents.

2.5.2 The Onsager Transport Coefficients

In addition, the Onsager transport theory can readily be adopted to quantify the effect of strong

dynamical correlations on the ionic conductivity in these concentrated ionic systems, which has been highlighted in recently published papers.[4] The Onsager transport theory will be briefly introduced as follows.

Based on the Green-Kubo relations, the Onsager transport coefficients, L^{ij}, can be expressed as follows:

$$L^{ij} = \frac{V}{3k_B T}\int_0^\infty \langle \boldsymbol{J}_i(0)\cdot\boldsymbol{J}_j(t)\rangle\, dt, \tag{2.38}$$

where $\boldsymbol{J}_i$ and $\boldsymbol{J}_j$ are the fluxes of species *i* and *j*, respectively. This equation can be written in terms of particle positions rather than velocities:

$$L^{ij} = \frac{1}{6k_B TV}\lim_{t\to\infty}\frac{d}{dt}\langle\sum_\alpha[\boldsymbol{r}_i^\alpha(t)-\boldsymbol{r}_i^\alpha(0)]\cdot\sum_\beta\left[\boldsymbol{r}_j^\beta(t)-\boldsymbol{r}_j^\beta(0)\right]\rangle, \tag{2.39}$$

in which $\boldsymbol{r}_i^\alpha$ represents the coordinate of particle *i* of species α. Then the diagonal terms of the transport matrix, L^{ii}, can be written as:

$$L^{ii} = \frac{1}{6k_B TV}\lim_{t\to\infty}\frac{d}{dt}\sum_\alpha\sum_\beta\langle[\boldsymbol{r}_i^\alpha(t)-\boldsymbol{r}_i^\alpha(0)]\cdot\left[\boldsymbol{r}_i^\beta(t)-\boldsymbol{r}_i^\beta(0)\right]\rangle. \tag{2.40}$$

This equation can be decomposed into the self- (L^{ii}_{self} for $i=j$) and distinct- (L^{ii}_{distinct} for $i\neq j$) diffusivity contributions:

$$L^{ii}_{\text{self}} = \frac{1}{6k_B TV}\lim_{t\to\infty}\frac{d}{dt}\sum_\alpha\langle[\boldsymbol{r}_i^\alpha(t)-\boldsymbol{r}_i^\alpha(0)]^2\rangle, \tag{2.41}$$

$$L^{ii}_{\text{distinct}} = \frac{1}{6k_B TV}\lim_{t\to\infty}\frac{d}{dt}\sum_\alpha\sum_{\beta\neq\alpha}\langle[\boldsymbol{r}_i^\alpha(t)-\boldsymbol{r}_i^\alpha(0)]\cdot\left[\boldsymbol{r}_i^\beta(t)-\boldsymbol{r}_i^\beta(0)\right]\rangle. \tag{2.42}$$

The self-contribution may be directly related to the self-diffusivity with this equation:

$$L^{ii}_{\text{self}} = \frac{D_i^s c_i}{k_B T}\ . \tag{2.43}$$

The physical interpretations of these Onsager transport coefficients were discussed in Reference.[4] These relationships provide us an approach to evaluate the ion-ion correlations from simulation trajectories. By employing these two methods, one can cross-verify findings, ensuring more accurate and comprehensive insights into ion-ion correlations.

Chapter 3 Morphology of Anion Exchange Membranes

This chapter is closely adapted from the following publication:[42]

- Zhu, Z; Luo, X; Paddison, S. J., DPD Simulations of Anion Exchange Membranes Functionalized with Various Cationic Groups and Associated Anions. *Solid State Ionics* **2019,** *340*, 115011.

This chapter presents mesoscale dissipative particle dynamics (DPD) simulations of AEMs based on the triblock copolymer polystyrene-b-poly(ethylene-co-butylene)-b-polystyrene (SEBS), which can be readily functionalized with different cationic groups. The coexisting anion, due to different possible synthetic routes can also be varied. The hydrated morphology of SEBS functionalized with various cationic groups provides a suitable platform for understanding the mechanism of anion transport and the route to preparing highly conductive and stable membranes. In this work, DPD simulations were utilized to study the morphology of various SEBS-based ionomers: SEBS-trimethylphosphonium (SEBS-TMP), SEBS-methylimidazolium (SEBS-MIm) and SEBS-trimethylammonium (SEBS-TMA) as a function of hydration level. Furthermore, the effects of the associated anion including OH^-, Cl^-, Br^-, HCO_3^-, and CO_3^{2-}, were explored, with the last two anions resulting from carbonation.

3.1 Simulations

Particles of analogous volume but of dihydratedmical structure were selected and coarse-grained to a bead, ignoring the detailed atomic information which is not deemed necessary for studying the morphological features of the hydrated materials. The selected structure of our coarse-grained model is shown in **Figure** 3.1 and the details are listed in **Table** 3.1. The SEBS-based backbone consists of polystyrene blocks and poly(ethylene-co-butylene) blocks which were modelled with two distinct bead types: the Bs ($(CH_2CH_2)_2$) bead and the Ph (phenyl group) bead. The middle blocks, however, are treated as polyethylene represented by a Bm bead. For the AEM ionomers, one end of the TMM (trimethylenemethane) beads is attached with Ph whereas the other end is linked to different cationic groups including trimethylphosphonium (TMP^+), methyl Imidazolium (MIm^+), and trimethylammonium (TMA^+) to compare the impact of the functional groups on the ionomers. To compare the effect of the associated anion on the

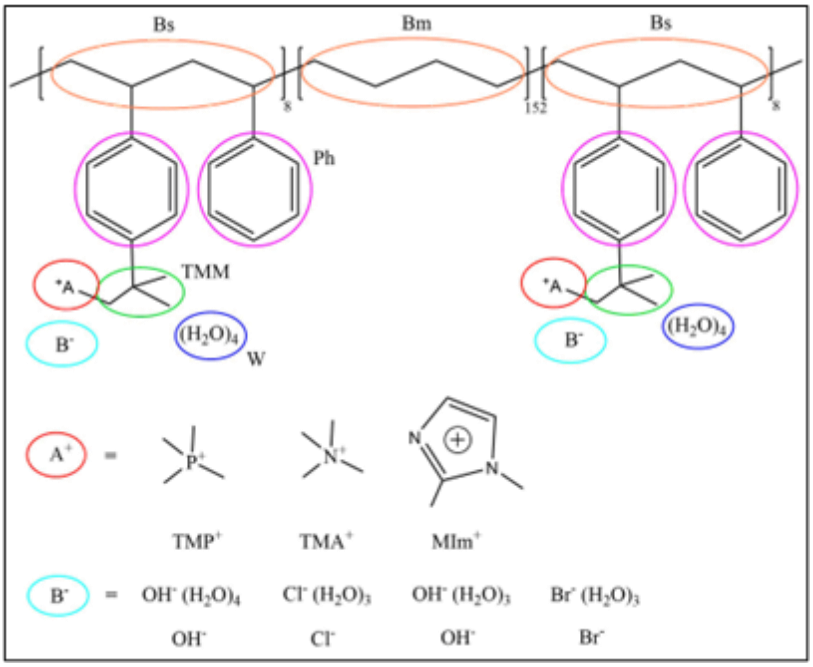

Figure 3.1. Coarse-grained model of a hydrated SEBS-based AEM in various forms. Each circle represents the specific bead/particle of the selected chemical group or collection of atoms.

Table 3.1. Bead type, chemical structure, and volume.

Bead type	Structure	Volume[a] (Å^3)
Bs, Bm	$[H](CH_2CH_2)_2[H]$	125.5
Ph	$C_6H_4[H_2]$	129.7
TMM	$[H]C(CH_3)_2CH_2[H]$	124.8
TMA^+	$[H]N(CH_3)_3$	121.8
TMP^+	$[H]P(CH_3)_3$	136.8
MIm^+	$[H]C_3N_2H_3CH_3$	130.9
W	$(H_2O)_4$	120.1
OH^-	$OH^-(H_2O)_4$	134.6
Cl^-	$Cl^-(H_2O)_3$	125.0
OH^-	$OH^-(H_2O)_3$	118.8
Br^-	$Br^-(H_2O)_3$	132.3
HCO_3^-	$HCO_3^-(H_2O)_3$	152.0
CO_3^{2-}	$CO_3^{2-}(H_2O)_3$	145.8

[a]Volumes were referred to or obtained using the same approach in our previous work.[44]

hydrated AEM, three associated anions were introduced: an OH^- bead for alkaline form, a Cl^- bead and a Br^- for the chloride and bromide precursor form, respectively. The OH^- bead is comprised of an hydroxide ion and three or four water molecules based on the primary hydrated structure[70, 212, 213] while the Cl^-, Br^-, HCO_3^-, and CO_3^{2-} beads consist of three water molecules along with a chloride, a bromide, a bicarbonate, and a carbonate anion, respectively. A water bead includes four water molecules. The hydrated OH^-, Cl^-, and Br^- structures were referred to previous literature[70, 213-215] which meet the criteria of similar volume (see **Table** 3.1). The bonded interactions and the DPD conservative interaction parameters were obtained from prior work[44] or calculated by a parameterization method (see **Table** A1 and A2).[203]

LAMMPS (large scale atomic/molecular massively parallel simulator)[216] was employed to perform all DPD simulations undertaken in this investigation on Stampede2 at the Texas Advanced Computing Center (TACC). Generation of random initial configurations were determined with the PACKMOL package.[217] In a typical simulation box, there were 648,000 beads in a 3-dimensional periodic unit cell of 60 DPD length units (42.7 nm) and a density of 3. The time step was fixed at 0.01 DPD time units, i.e., 38 fs, and the overall number of steps was typically 70,000,000 (i.e., a total of 2.68 μs of simulation time) to ensure each system reached equilibrium.

The AEM ionomers were constructed with a molecular weight (MW) of 11,830 g/mol with 29.63% composition of polystyrene end-blocks and 50% of the styrene being functionalized with the TMM and cationic groups as described above. All chains were built to have a similar MW. The impact of water content on morphology was assessed by simulating a broad range of hydration levels. Hence, the water content in the systems ranged from $\lambda = 4$ to 20, where λ is the number of water molecules per cationic functional group. Although it is not the focus of this study, it would be worthwhile to extend the hydration since ultra-low hydration gives rise to serious OH^--derived AEM degradation[218] and excessively high-water content causes electrode flooding and ionomer swelling that leads to substantial decrease of the mechanical integrity of an AEM.[219] Each system consists of water, anions, and more than two thousand macromolecules; the latter is determined by the degree of hydration. The numbers of positively

and negatively charged beads were constrained to be equal to ensure electroneutrality of each system.

3.2 Effect of Functional Group

Figure 3.2 illustrates the simulated morphologies of an SEBS ionomer functionalized with different cationic groups in the alkaline form over a broad range of hydration (λ = 4, 8, 12, 16, and 20). Generally, there are two clearly defined phases: hydrophilic and hydrophobic, which occur at all hydration levels. The hydrophilic domains consist of the functionalized polystyrene end-blocks (Bs, Ph, TMM, cationic groups, anions and water beads) whereas the other phase consists of backbone of AEMs. For the SEBS-TMP and SEBS-MIm, interconnected lamellae occur at very low hydration (λ = 4). The morphology gradually transforms into organized lamellae from interconnected lamellae, and then into disordered bicontinuous regions as the hydration level is increased. The SEBS-TMP reaches a perfect lamellae morphology at λ = 8, while the SEBS-MIm does not until λ = 12. With increased water content, the disordered bicontinuous domains are observed in both SEBS-TMP and SEBS-MIm, and the exclusive water clusters (blue regions) form simultaneously. Moreover, the water clusters in the SEBS-MIm are larger than that in the SEBS-TMP, which seems to suggest that the water is more uniformly distributed in SEBS-TMP. Comparing these results to our previous work,[44] we note that perforated lamellae do not seem to form at low hydration levels.

The RDFs of the hydrated SEBS-based polymers functionalized with three different cationic groups in the alkaline form at λ = 8 are depicted in **Figure** 3.3. The black lines are the BsPh-BsPh RDFs with solid, dash-dotted, and dashed lines corresponding to the SEBS-TMP, SEBS-MIm, and SEBS-TMA, respectively. The cation-cation RDFs, shown with the blue lines, are similar to that of the end-blocks at distances greater than 15 Å, which is expected as the cationic groups are attached to the end-blocks. The green lines correspond to the hydrophobic mid-blocks. The red lines correspond to the RDFs of the hydrophobic blocks and illustrate that the two phases are, as expected, repulsive to each other. The RDFs of the same pair with different cationic groups have a similar pattern, meaning these pendant functionalized groups appear to have little influence on the structures of the backbone. It is evident from the inset of **Figure** 3.3

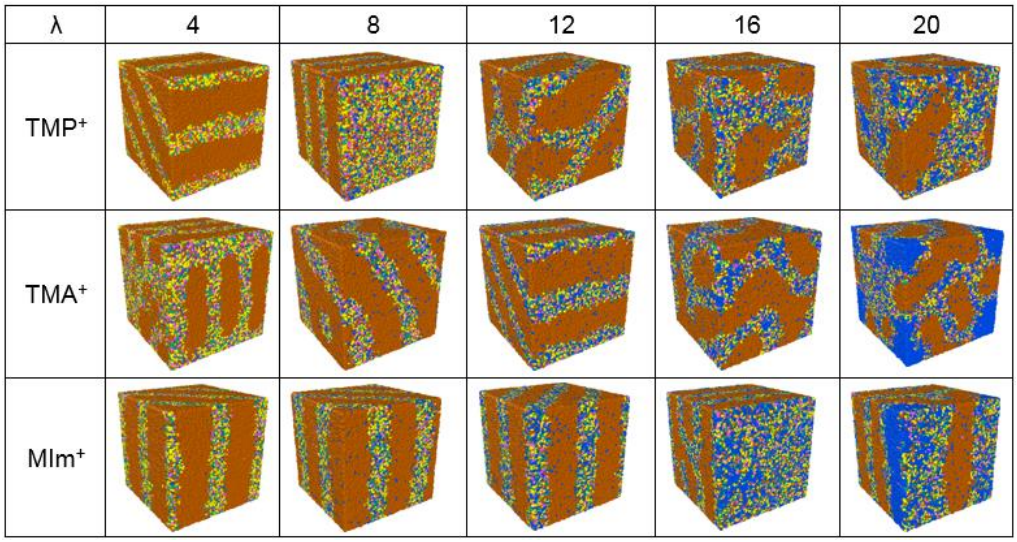

Figure 3.2. Morphologies of the SEBS functionalized with different cationic groups in the alkaline form. There are two phases: hydrophilic and hydrophobic phases occurring at all hydration levels. For low λ, perforated and interconnected lamellae are formed; for high λ, disordered bicontinuous lamellas are formed and water droplets (blue regions) can be found. Color code: Bs and Bm (orange); Ph (mauve); TMM (green); TMA^+ (purple); TMP^+ (light orange); MIm^+ (dark blue); OH^- (cyan); and W (blue).

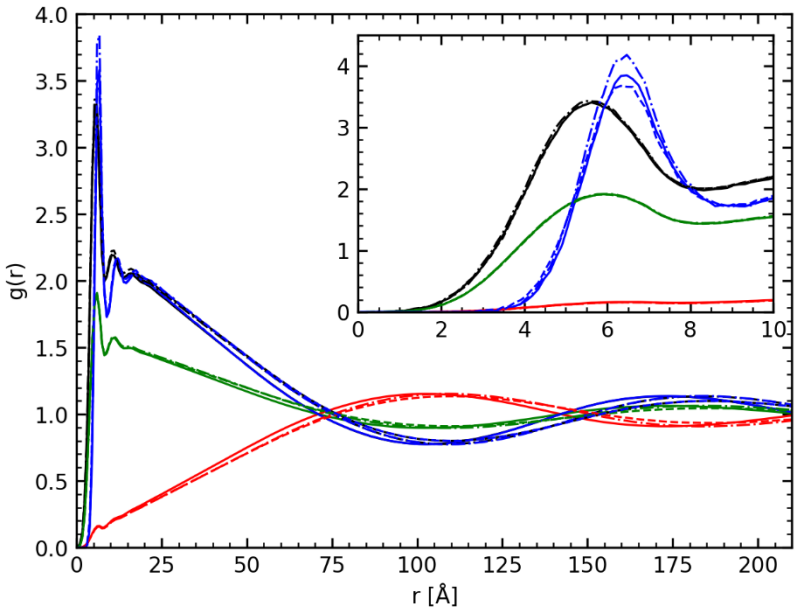

Figure 3.3. RDFs of the hydrated AEM in the alkaline form at λ = 8. The inset shows a magnified view of short-distance range. Color code: BsPh-BsPh (black); BsPh-Bm (red); Bm-Bm (green); and Cation-Cation (blue). Line scheme: SEBS-TMP (solid line); SEBS-MIm (dash-dotted line); SEBS-TMA (dashed line).

that the first peaks of the cation-cation RDFs shift to the right with shorter distance compared to the RDFs of the hydrophilic phase because of the repulsive coulombic force between them. Furthermore, the first peaks have different intensities for SEBS functionalized with different cationic groups: the SEBS-MIm has the highest value and SEBS-TMA the lowest one.

Figure 3.4 shows a plot of the coordination number (CN) of the cationic groups as a function of the distance from the cation group over a range of water content. The cation-cation CN shown in Figure 3.4 indicates that there is one other cationic group with the sphere radius of 5.5 – 6.5 Å, which can be treated as a characteristic length that the hydroxide ion needs to overcome if its trajectory is between the two cationic groups.[52] For all cases, at CN = 1, the separation between the immediate vicinity expands when the hydration level is increased. The SEBS-MIm always has the smallest distance when CN = 1 at various hydration levels in comparison with the SEBS-TMP and the SEBS-TMA whose separations are similar. It is clear that the cationic groups are separated by at least 4.0 Å.

Figure 3.5 shows the W-W RDFs of ionomers with different pendant cationic groups at hydration levels corresponding to λ = 8, 12, 16, and 20. The intensity of the peaks increases with increasing hydration for these three AEMs, indicating that the water is more structured at high hydration levels. At low levels of hydration (λ = 8 and 12), the effect of the cationic group is somewhat smaller. However, the affect becomes significant at the highest water contents: λ = 16 and 20, where the water in the SEBS-MIm is the most structured. The point where $g(r)$ first becomes 1 varies little for the three AEMs at the lowest water content, in contrast to what occurs at the highest water contents where there are substantial differences. This suggests that the cationic group affects the distribution of water but has little impact on the size of the exclusive water domains.

Figure 3.6 shows the distribution in water cluster size at the different water contents. In general, the left side of the cluster size distribution shifts to the left, while the right branch shifts to the right with increasing water content, suggesting there are increasing number of water beads contributing to the clusters. The snapshots of the five largest clusters at various hydration levels are shown in **Figure** 3.7. In the case of SEBS-MIm, the largest cluster consists of 823 beads at

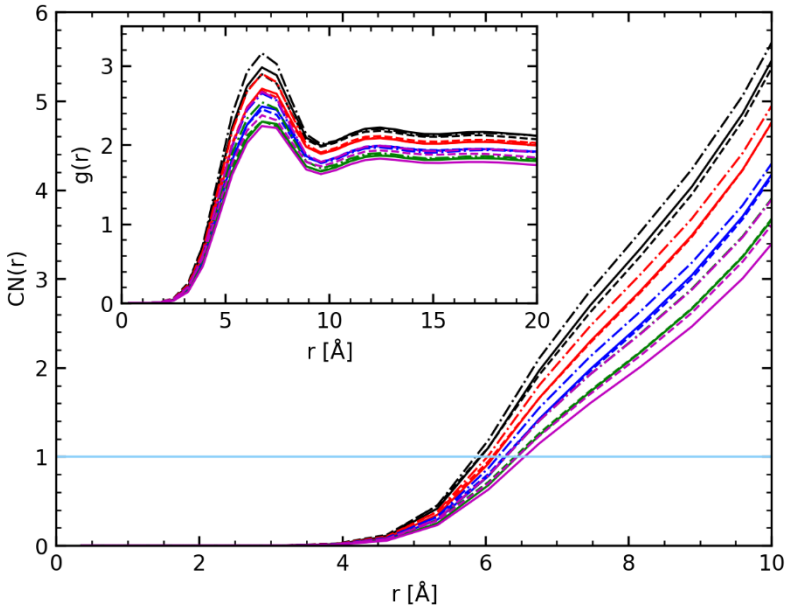

Figure 3.4. The coordination number (CN) of the cations as a function of cation distance across the various hydration levels: λ = 4 (black); λ = 8 (red); λ = 12 (blue); λ = 16 (green); and λ = 20 (pink). Line scheme: SEBS-TMP (solid line); SEBS-MIm (dash-dotted line); and SEBS-TMA (dashed line). The inset shows the cation-cation RDFs over the regions from 0 to 20 Å. The first minima of the RDFs lie around 9.5 Å.

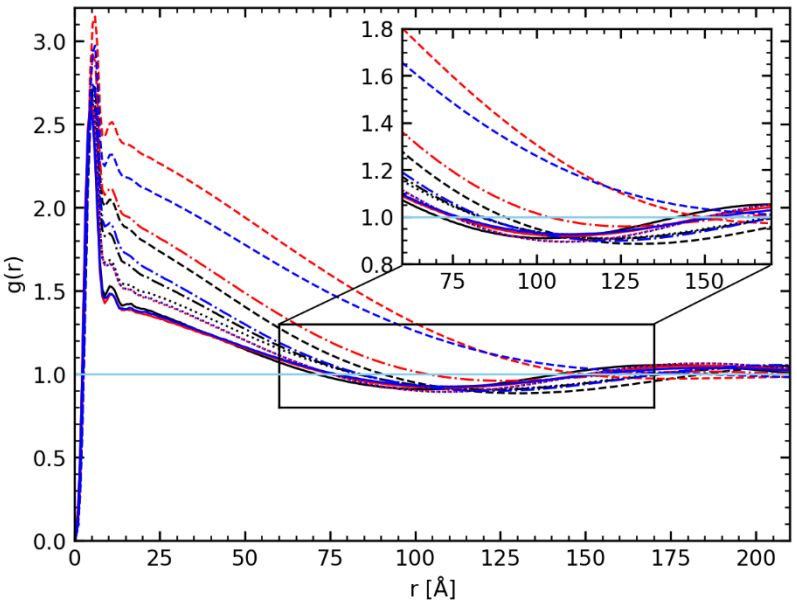

Figure 3.5. W-W RDFs for the AEMs functionalized with different cationic group in the alkaline form at various water contents. Color scheme: SEBS-TMP (black); SEBS-MIm (red); SEBS-TMA (blue). Line scheme: λ = 8 (solid line); λ = 12 (dotted line); λ = 16 (dash-dotted line); and λ = 20 (dashed). Zoom up shows the minimal radial distance where $g(r) = 1$.

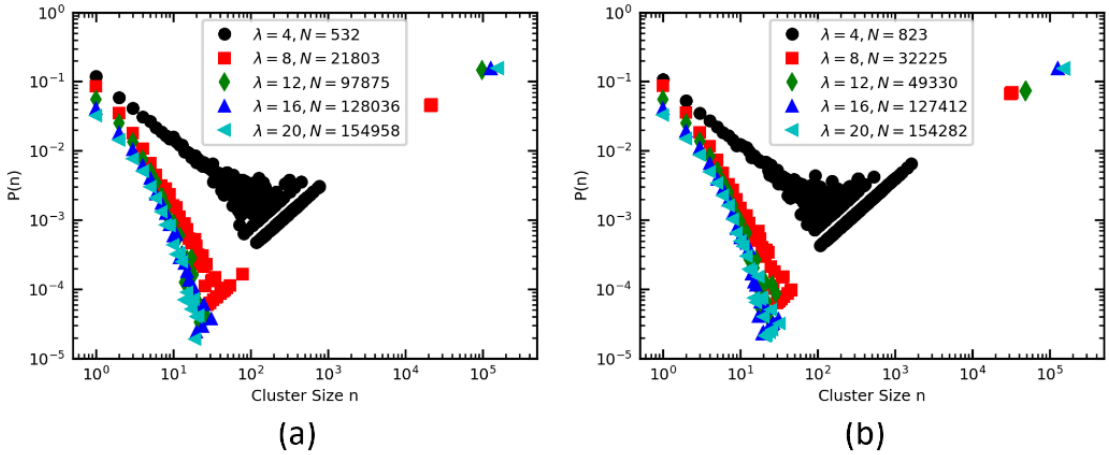

Figure 3.6. Cluster size distributions of water and OH^- beads for (a) SEBS-TMP and (b) SEBS-MIm. Large clusters of water and OH^- beads are formed when $\lambda \geq 8$ for SEBS-TMP and SEBS-MIm. SEBS-TMP and SEBS-MIm have the almost same cluster sizes at $\lambda = 8$, while larger clusters form in SEBS-TMP than SEBS-MIm at $\lambda = 12$.

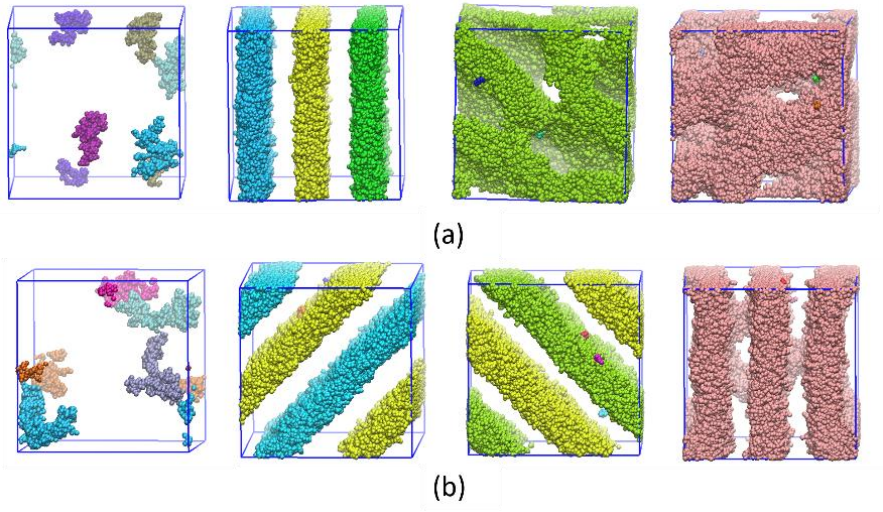

Figure 3.7. Five largest clusters of water and OH^- beads at $\lambda = 4, 8, 12, 16$ in: (a) SEBS-TMP; and (b) SEBS- MIm.

$\lambda = 4$. It is evident that no percolating domains emerge. The percolating domains begin to appear at $\lambda = 8$ and the size expands with increasing water content: 32,225 beads at $\lambda = 8$; 49,330 beads at $\lambda = 12$; and 127,412 beads at $\lambda = 16$. The structure of the clusters become bicontinuous at $\lambda = 12$ in the SEBS-TMP, but do not occur until the water content reaches 16 for SEBS-MIm. Clearly the more polar head group (TMP) facilitates a more connected network of water. The largest water clusters for the SEBS-TMP at different hydration levels are 532 beads for $\lambda = 4$, 21803 beads for $\lambda = 8$, 97875 beads for $\lambda = 12$, and 128036 beads for $\lambda = 16$.

3.3 Effect of Associated Anion

To investigate the effect of the associated anions, the hydroxide ion bead consisting of three water molecules was introduced instead of OH^- $(H_2O)_4$ to match the systems of Cl^- $(H_2O)_3$ and $Br^-(H_2O)_3$. The simulated morphology of the SEBS-TMA in the three different forms (hydroxide, chloride, and bromide) are shown in **Figure** 3.8. It is clear that phase separation occurred in all systems and perfect lamellae were observed at $\lambda = 8$ for the three different associated anions. At the lowest hydration level, perforated lamellae appeared in the cases of $OH^-(H_2O)_3$ and $Cl^-(H_2O)_3$, while perforated lamellae were not observed in the bromide form. This would seem to imply that it is easier to form the interconnected lamellae in the bromide form than in the other two forms. It is important to be aware of the lack of connectivity between isolated tiny hydrophilic clusters and the occurrence of the water-bridged double-hydroxide structures in the OH^- form when the hydration levels are extremely low ($\lambda < 4$) as shown in a recent study.[212]

In **Figure** 3.9, the morphology of a specific bead type at $\lambda = 8$ was presented for clarity. It is evident that the ionic species have similar distributions in all systems since there is strong coulombic attraction between the cationic groups and the associated anions. Most of the water is distributed within the same phase (i.e., inclusive of all ionic species), while some isolated water appears in the polyethylene phase. In the case of the Cl^- form, the perforated and interconnected morphology is shown, which does not emerge in the other two forms at $\lambda = 8$. This clearly indicates that different anion forms may exhibit qualitatively different hydrated morphologies.

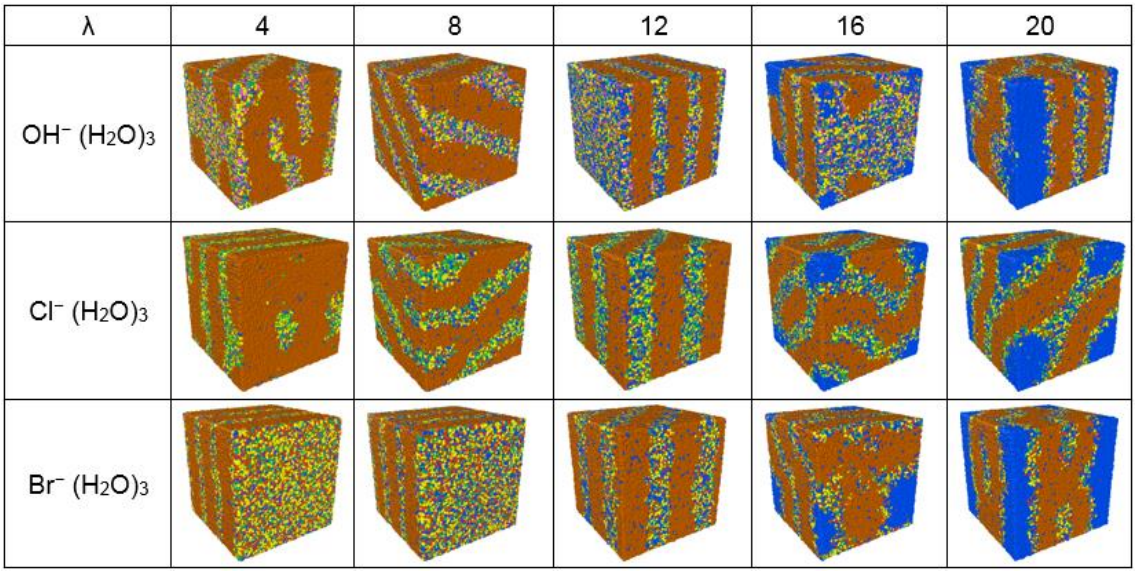

Figure 3.8. Simulated morphology of the SEBS-TMA in the alkaline form, in the chloride form, and in the bromide form at different hydration levels: λ = 4, 8, 12, 16, and 20. Color code: Bs and Bm (orange); Ph (mauve); TMM (green); TMA^+ (purple); OH^- (pink); Cl^- (light green); Br^- (red); and W (blue).

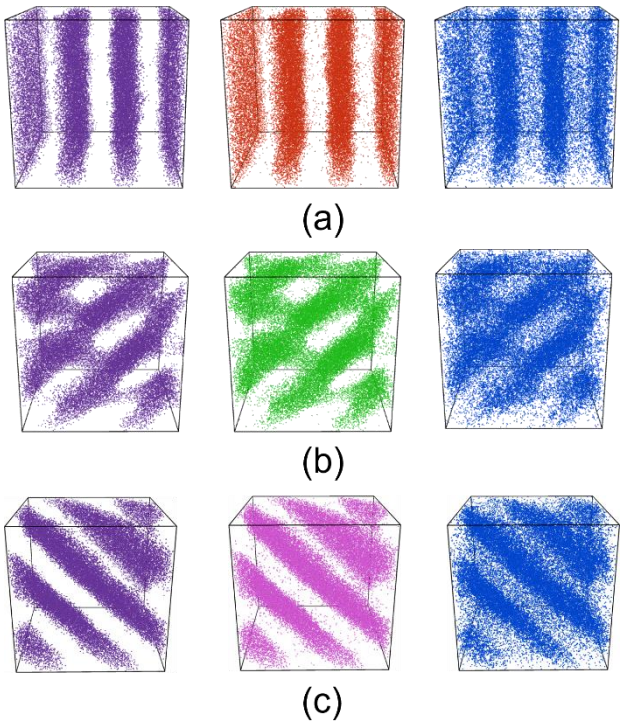

Figure 3.9. Simulated morphology of the hydrated AEM in different forms at λ = 8. (a) TMA^+ in $Br^-(H_2O)_3$; (b) TMA^+ in $Cl^-(H_2O)_3$; (c) TMA^+ in $OH^-(H_2O)_3$. Color code: TMA^+ (purple); Br^- (red); Cl^- (light green); OH^- (pink); and W (blue).

The water-water RDFs in the alkaline, the chloride, and the bromide forms as a function of water content are shown in **Figure** 3.10. Generally, the intensity of peaks in these three forms rises as the water content increases. The associated anion has little impact on the W-W RDFs at low hydrations (λ = 8 and 12). However, the effect becomes noticeable when the level of hydration is greater than 12. The distance the RDF reaches a value of one increases considerably at λ = 16 with the largest water domains occurring in the bromide form, in sharp contrast to the chloride form. It is interesting to note that the associated anion has more impact on the size of the exclusive water domains at the highest water contents in comparison to the somewhat minimal effect of the choice of the cationic group.

3.4 Effect of Carbonation

It is worth noting that carbonate counter anions are also important to study in order to better understand the adverse impact of ambient air feed (i.e., CO_2) on the performance of AEMFCs.[220, 221] As CO_2 can react with OH^- to form HCO_3^- and CO_3^{2-}, the effective anion conductivity in the AEM would be significantly decreased through the carbonation process. The following work focuses on simulations of AEM properties under the impact of carbon dioxide and carbonation products (bicarbonate and carbonate anions) to better understand the AEM behavior during operation of AEMFCs under ambient air.

Figure 3.11 illustrates the simulated morphology of SEBS-TMA in the bicarbonate and carbonate forms. Compared to the morphology of SEBS-TMA in the $OH^-(H_2O)_3$ form, perfect lamellae appear at λ = 4 and 8 in both bicarbonate and carbonate forms. Disordered bicontinuous structures occur at λ = 12 and 16 followed by exclusive water domains at λ = 20 in the bicarbonate form. However, in the carbonate form, exclusive water domains begin to appear at λ = 12, and these water droplets maintain similar sizes as the hydration level further increases. These morphologies clearly demonstrate that at low water contents, CO_3^{2-} and HCO_3^- have a moderate influence on the morphologies. In contrast, CO_3^{2-} exerts more influence on the exclusive domains than HCO_3^- when the hydration level is sufficiently high. This phenomenon may be attributed to the strong attraction between CO_3^{2-} and the pendant cations, forming large hydrophilic domains.

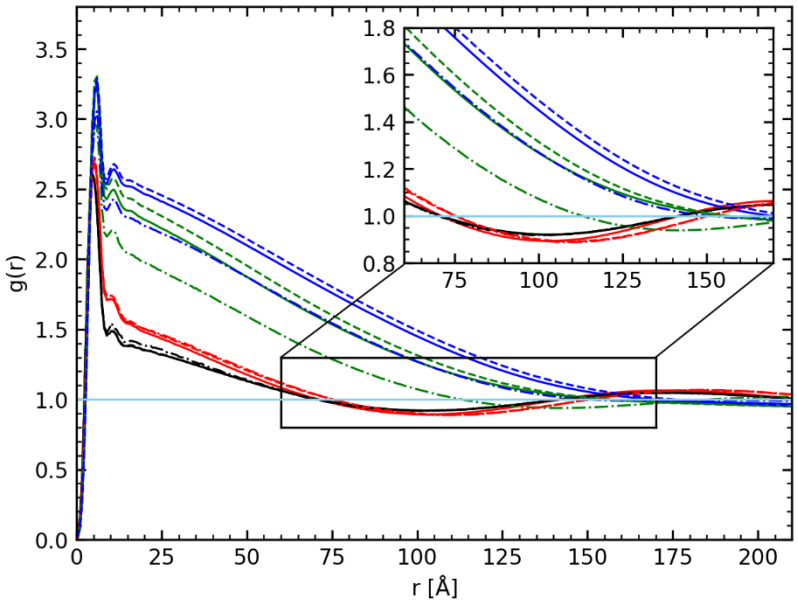

Figure 3.10. W-W RDFs for the hydrated AEM in the alkaline (solid line), chloride (dash-dotted line), and bromide (dash line) forms at various levels of hydration. Color scheme: λ = 8 (black); λ = 12 (red); λ = 16 (green); and λ = 20 (blue).

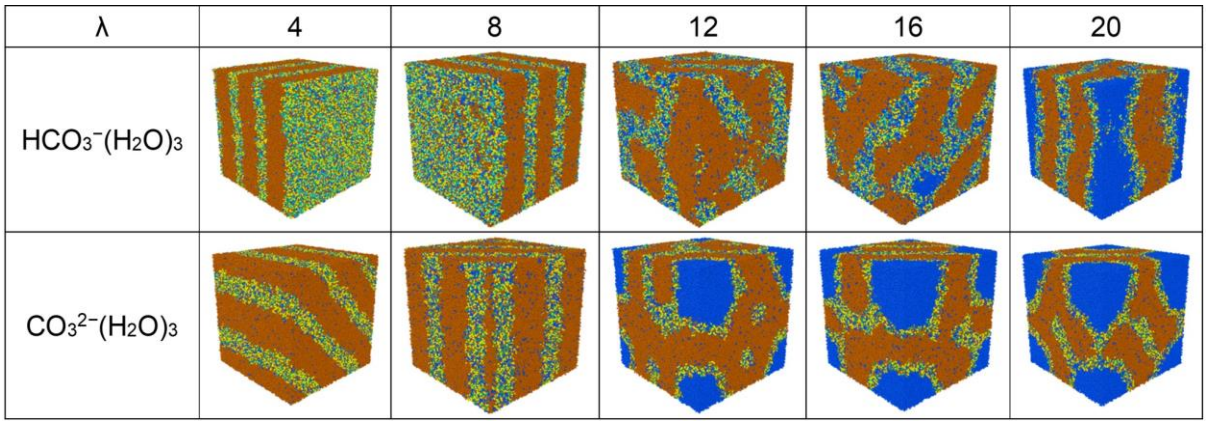

Figure 3.11. Simulated morphology of the SEBS-TMA in the bicarbonate form, and in the carbonate form at different hydration levels: λ = 4, 8, 12, 16, and 20. Color code: Bs and Bm (orange); Ph (mauve); TMM (green); TMA^+ (purple); HCO_3^- (cyan); CO_3^{2-} (green-yellow); and W (blue).

To further explore the effects of carbonation, the percentage of OH^- being carbonated was varied from 10 to 75%. It is important to note that only HCO_3^- anions are considered for simplicity, although CO_3^{2-} exists in real systems.[222] The hydrated morphologies with different percentages of OH^- being carbonated at λ = 8 and 20 are shown in **Figure** 3.12. At the low hydration level, perforated lamellas appear when 10% of the OH^- is carbonated, followed by perfect lamellae at 25 and 50%, and then disordered bicontinuous structures as the carbonation ratio increases to 75%. Interestingly, perfect lamellae reoccur when OH^- is fully carbonated. However, at a high hydration level, irregular lamellae appear at all percentages of carbonation, along with the formation of exclusive water domains. These results indicate that the interplay of the interactions between these ions and the water content results in the changes in the hydrated morphology.

The water-water RDFs in the bicarbonate and carbonate forms as a function of water content are depicted in **Figure** 3.13(a). In the HCO_3^- form, the intensity of peaks increases with increasing water content, while in the CO_3^{2-} form, the water is the most structured at λ = 12. Moreover, the RDFs do not show significant differences at λ = 4 and 8, especially for the position where RDF = 1. Nevertheless, at $\lambda \geq 12$, substantial differences in the RDFs appear between the two forms, and the position where the RDF first reaches one significantly shifts to a large distance, suggesting the formation of exclusive water domains. **Figure** 3.13(b) shows the water-water RDFs with various percentages of OH^- being carbonated at λ = 8 and 20. It is evident that the RDFs are not influenced by carbonation at λ = 8, while the effect becomes appreciable at λ = 20. Combining these results with the hydrated morphology, HCO_3^- has minimal influence on the structure of water, although it affects the shape of the hydrophilic region.

Figure 3.14(a and b) show the cluster size distributions of water and anion beads at different water contents for SEBS-TMA in the HCO_3^- and CO_3^{2-} forms, respectively. Percolated clusters of water and anion beads form at $\lambda \geq 8$ for both HCO_3^- and CO_3^{2-} forms, although the percolated cluster size extends from $\sim 10^4$ to 10^5 as the hydration level increases from λ=8 to λ=12. Furthermore, the distributions in water cluster size at the different ratios of OH^- being

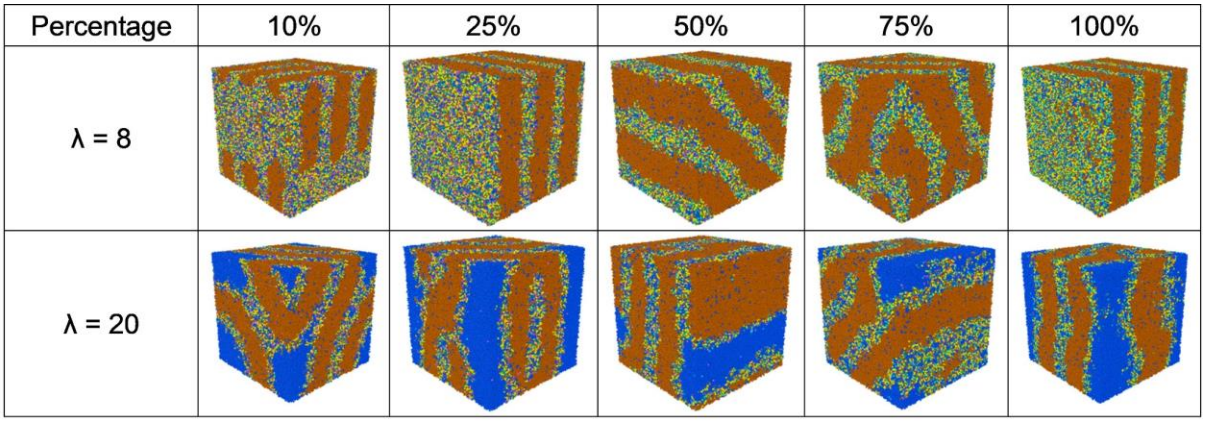

Figure 3.12. Simulated morphology of the SEBS-TMA in the alkaline form with different percentages of carbonation, at two hydration levels: λ = 8 and 20. Color code: Bs and Bm (orange); Ph (mauve); TMM (green); TMA^+ (purple); OH^- (pink); HCO_3^- (cyan); and W (blue).

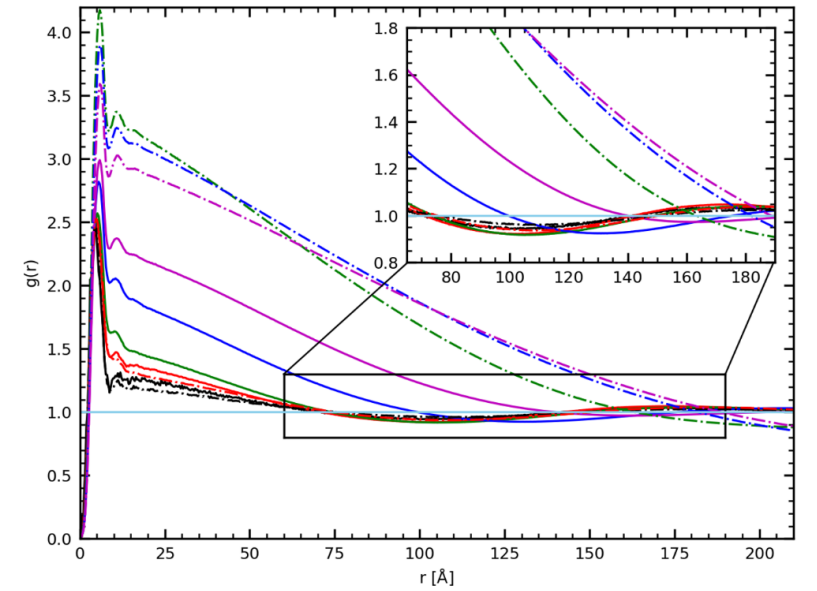

Figure 3.13. W-W RDFs for the hydrated SEBS-TMA (a) in the HCO_3^- form (solid line) and in the CO_3^{2-} form (dash-dotted line) at various hydration levels: λ = 4 (black); λ = 8 (red); λ = 12 (green); λ = 16 (blue); and λ = 20 (magenta); (b) in the alkaline form with different ratios of OH^- being carbonated 10% (black); 25% (red); 50% (green); and 75% (blue) at λ = 8 (solid line) and λ = 20 (dash-dotted line).

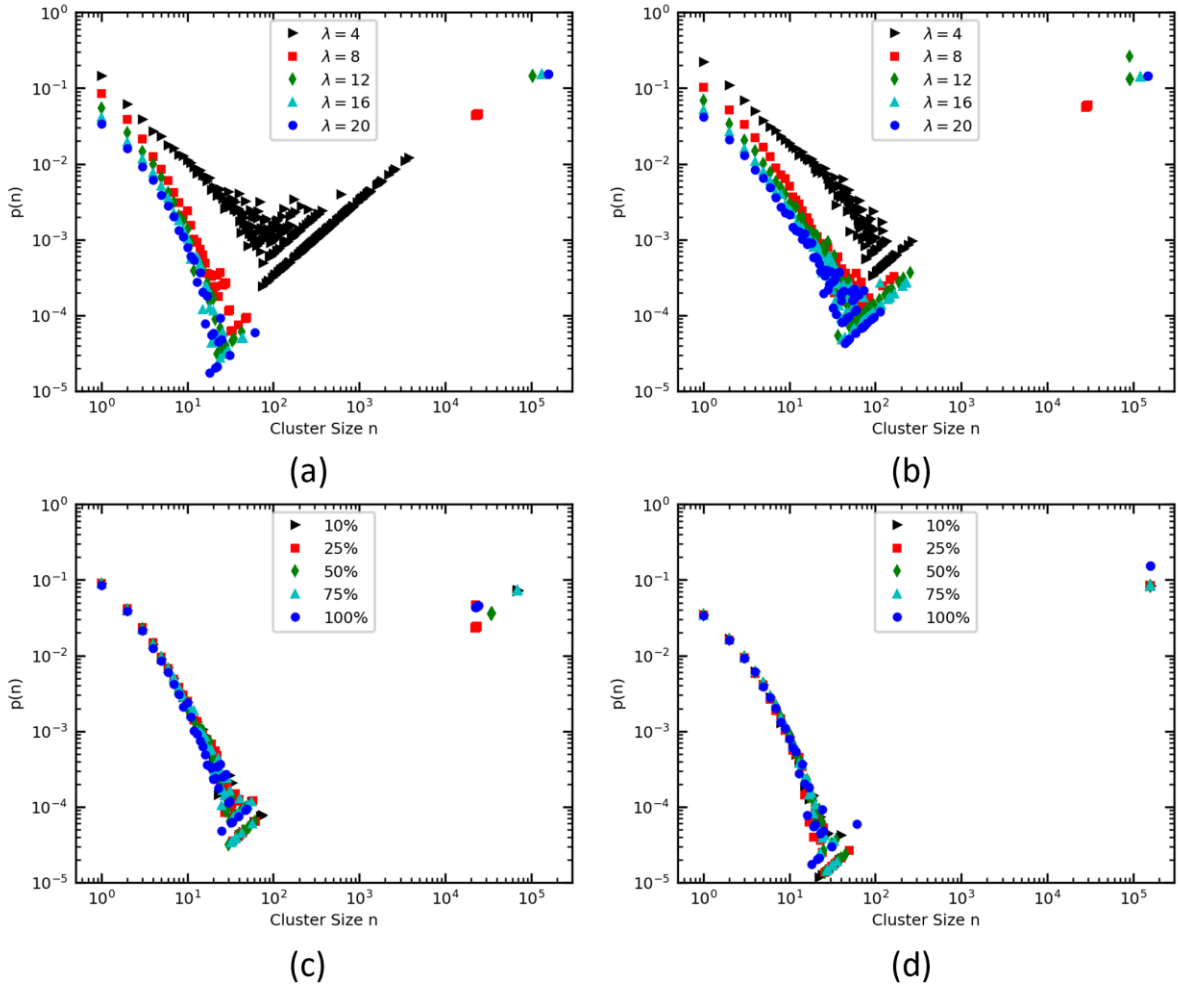

Figure 3.14. Cluster size distributions of water and anion beads for SEBS-TMA (a) in the HCO_3^- form and (b) in the CO_3^{2-} form at various hydration levels; in the alkaline form with different ratios of OH^- being carbonated at (c) $\lambda = 8$ and (d) $\lambda = 20$. Large clusters of water and anion beads are formed when $\lambda \geq 8$ for these systems. At low hydration ($\lambda = 8$), the carbonation generally enlarges the percolated clusters, while at high hydration ($\lambda = 20$), the effect of carbonation is minimum on the percolated clusters.

carbonated at λ=8 and 20 are depicted in **Figure** 3.14(c and d). At low hydration (λ=8), carbonation generally enlarges the percolated clusters, with sizes ranging from 10^4 to 10^5, while at high hydration (λ=20), carbonation has minimal effect on the size of the percolated clusters (~2×10^5 beads).

Chapter 4 Proton Transfer in Protic Ionic Liquids

This chapter is closely adapted from the following publication:[223]

- Zhu, Z; Luo, X; Sokolov, A. P.; Paddison, S. J., Proton Transfer in Phosphoric Acid-Based Protic Ionic Liquids: Effects of the Base. *The Journal of Physical Chemistry A* **2020,** *20*, 4141-4149.

This chapter focuses on the influence of the chemical composition and molecular geometry of several bases on proton dissociation and transfer in phosphoric acid (PA)-based protic ionic liquids (PILs). These results formed the basis for simulations of extended systems using *ab initio* molecular dynamics. Specially, in the reported studies here quantum chemical calculations were performed on systems of PA paired with trimethylamine (TMA), imidazole (IMI), lidocaine (LDC), and creatinine (CRT). The computations are briefly described in the following section followed by the results and discussion.

4.1 Computations

Electronic structure calculations were performed with the GAUSSIAN 09 suite of programs.[224] The molecular geometry optimizations of bases and acids were initially performed with Hartree-Fock theory and the 6-31G** split valence basis set[225, 226] with conjugate gradient methods[227] without symmetry constraints. Hybrid density functional theory (DFT) with Beck's 3 parameter functional (B3LYP)[159, 228-230] using the same basis set was employed to further optimize the electronic structures, followed by final refinement at the B3LYP/6-311G** level of theory.[231] This procedure was found to be the most efficient approach in obtaining fully optimized global minimum-energy structures. **Figure** 4.1(a) illustrates the computational time as a function of functionals with the split valence basis sets, indicating the reasonableness of utilizing the B3LYP/6-311** level of theory to perform the molecular orbital calculations. The effect of the dispersion interactions had been evaluated in a previous study[232] by comparing the results of the B3LYP functional to the dispersion-corrected B97D functional[233] and only minor differences in the optimized structures and energetics for proton transfer were observed. Subsequently, the density-based solvation model (SMD)[234] was implemented to all optimized structures to account for the effect of the environment of the phosphoric acid (i.e., at a high

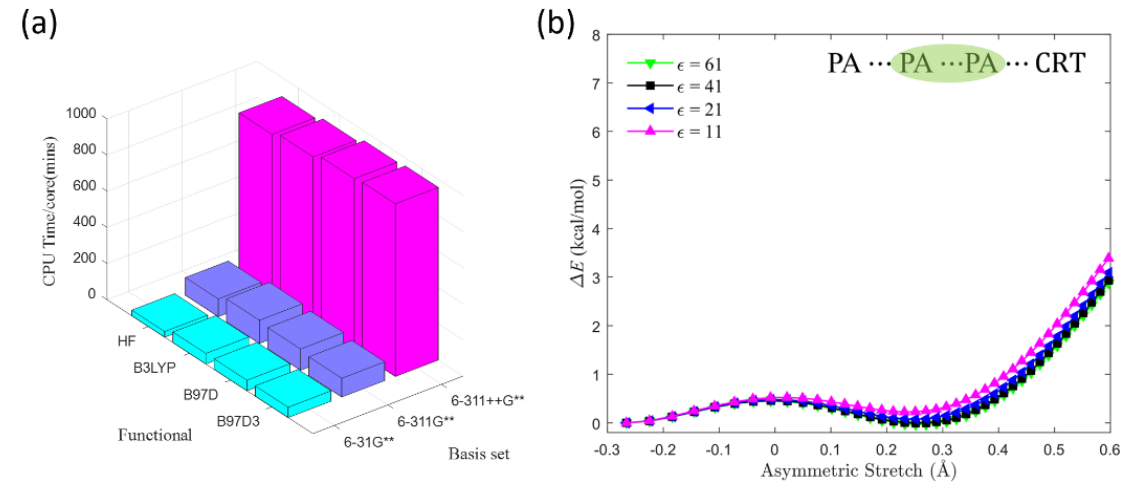

Figure 4.1. (a) CPU time needed for optimizing a typical cluster consisting of 55 atoms as a function of functionals and basis sets. (b) Energetics for proton transfer between first and second PA molecules in the system of CRT+3PA at the B3LYP/6-311G**/SMD level of theory. There is a minimal effect of the dielectric constant on the energetics for the proton transfer within a wide range of 11 to 61.

dielectric constant, $\varepsilon = 61$)[235] on the global minimum-energy structures and proton transfer. It is worth noting that there is only a minimal effect of the dielectric constant on the energetics for the proton transfer [see **Figure** 4.1(b)]. The choice of B3LYP/6-311G** with the SMD model is due to its success and reliability when applied to many systems.[236-240] The calculation of the frequencies at the same level of theory was undertaken to confirm a local minimum without imaginary frequency along with the zero-point energies (ZPEs) for each of the systems. Proton affinities of the bases and molecular binding energies of the PA molecules to different bases were calculated from the ZPE corrected total electronic energies.

In the present study, from 1 to 3 PA molecules were added to the fully optimized structures of each base starting from different initial configurations. We selected the lowest energy structure for each system as the "ground state" structure. The potential energy surface (PES) scan at the B3LYP/6-311G**/SMD level of theory was employed on the optimized structures of pairs and clusters of the PA molecules with the bases to determine the relative energetics (i.e., energetic barrier) associated with proton transfer from a proton donor to an acceptor site. The profiles of the energy associated with the proton transfer were obtained by incrementally changing the length of the O–H or N–H between the transferring proton and the oxygen or nitrogen accepting the proton with an incremental step size of 0.02 Å. This bond length is the only fixed parameter, and the optimization was undertaken over all other degrees of freedom without symmetry constraints at each step of the scan. A reverse set of scans was also implemented by decreasing the OH or NH bond length starting from the geometry obtained at the last step of the original scan. The energetic profiles were plotted by selecting the configuration with the lower energy at the same OH or NH bond length from the forward and reverse scans. A transition state (TS) structure was further optimized via the Berny algorithm[241] and confirmed by the determination of one imaginary frequency.

4.2 Optimized Structures of Base + nPA (n = 1 – 3)

The fully optimized configurations of one PA molecule paired with: (a) TMA; (b) IMI; (c) LDC; and (d) CRT were obtained at the B3LYP/6-311G** level with inclusion of an implicit solvent (SMD). The proton affinity is an important parameter indicating the entity's capability of

intrinsically attracting a proton.[242] Computed affinities in the gas phase and with the continuum solvation model are reported in **Table** 4.1. The results demonstrate that the inclusion of an implicit solvent noticeably increases the proton affinity of the four bases to various extents as the positively charged bases molecules are stabilized by the high dielectric constant solvent. Comparison with the experimental values of TMA and IMI in the gas phase shows that our computed affinities are in good agreement at the B3LYP/6-311G** level of theory. The order of the proton affinities calculated with the SMD model is as following: LDC > TMA > CRT > IMI. Generally, proton dissociation from PA occurs in the four systems resulting in the formation of ion pairs consisting of a positively charged base and negatively charged anion $H_2PO_4^-$ due to the relatively strong basicity of the bases and the effect of the high dielectric constant solvent on stabilizing the charge separation. In **Figure** 4.2(a), there is only one hydrogen bond of 2.62 Å in the open structure of TMA+1PA as the TMA molecule possesses only one proton accepting site. Although IMI has both proton donor and acceptor sites, only one hydrogen bond of 2.56 Å in length exists in the system of IMI + 1PA shown in **Figure** 4.2(b) because of the coplanar heterocycle of the IMI molecule. In **Figure** 4.2(c) and (d), the equilibrium structures show that the PA molecule adopts a similar orientation paired with LDC and CRT leading to a "ring-like" hydrogen bond network, though these two bases have different geometries. The critical differences in their configurations are that the PA molecule in the CRT+1PA cluster acts as both a hydrogen bond donor and acceptor with two hydrogen bonds of intermediate length (2.67 and 2.70 Å) while the PA molecule in the LDC + 1PA system plays a role of hydrogen bond donor forming a short hydrogen bond of 2.62 Å and a weak hydrogen bond of 2.77 Å. This demonstrates the characteristics of PA molecules: three proton donor sites and one proton acceptor site contributing to the configurational frustration in pure phosphoric acid.[77] It is worth noting that there is a congener of CRT*+1PA (distinguished by *) shown in **Figure** 4.2(e). In this case two hydrogen bonds formed with O1 and N1 of the CRT molecule instead of N1 and N2 atoms in the CRT+1PA pair, showing similar hydrogen bonding with the LDC+1PA system, except that the proton is still associated with PA in CRT*+1PA due to the interaction between O1 and N1 of the CRT molecule. This geometric isomer is less favorable

Table 4.1. Proton affinities of the bases.

	Proton Affinities /kcal mol^{-1}		
	Gas phase[a]	**SMD**[b]	**Exp.**
TMA	226.12	289.36	231.44[c]
IMI	227.46	283.97	229.95[c]
LDC (N1 site)	240.85	290.15	
LDC (O1 site)	222.45	264.11	
CRT (N1 site)	234.47	286.04	
CRT (O1 site)	230.63	273.09	

[a]ZPE corrected proton affinities at B3LYP/6-311G** level of theory in gas phase.

[b]ZPE corrected proton affinities at B3LYP/6-311G** level of theory with SMD model.

[c]From ref.[242]

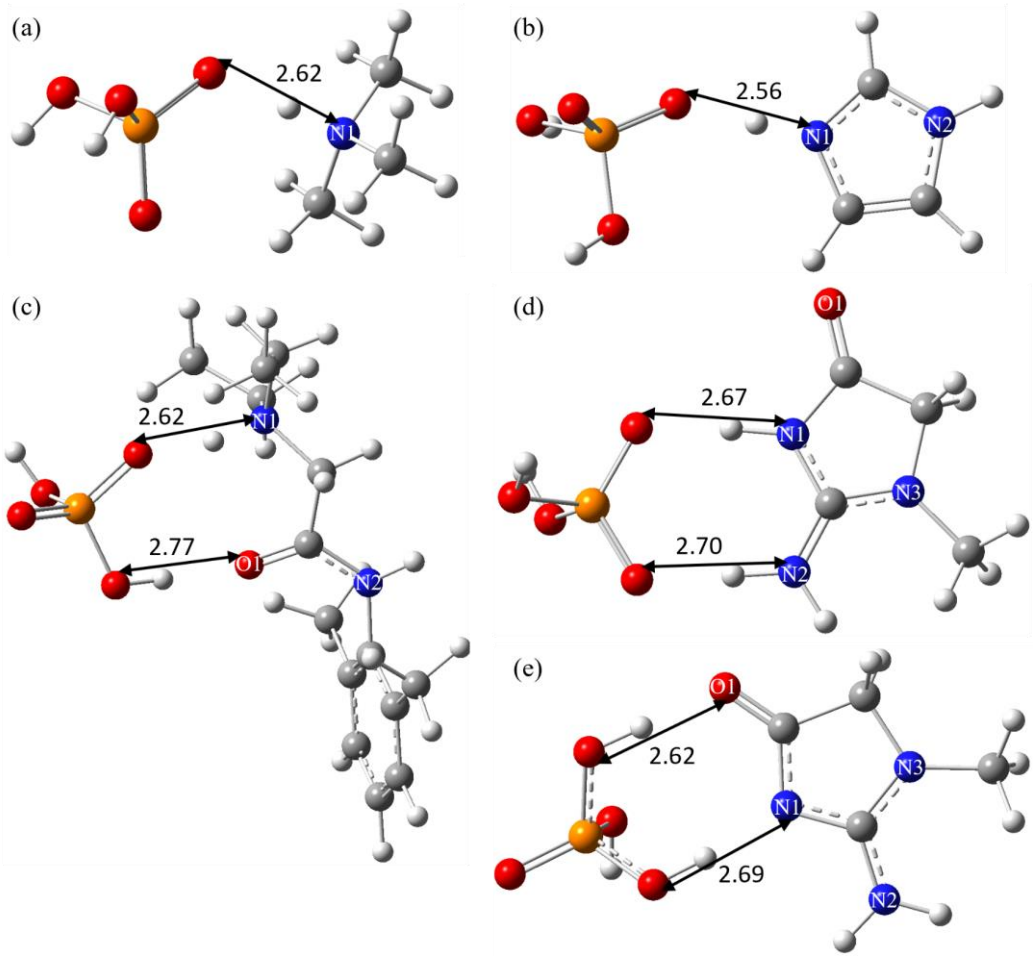

Figure 4.2. Fully optimized configurations of one PA molecule with (a) TMA, (b) IMI, (c) LDC, (d) CRT, and (e) CRT* (congener of CRT cluster) at the B3LYP/6-311G**/SMD level of theory. All values are reported in Å. The atomic color scheme in Figure 4.2 and 4.3 is: hydrogen (white), carbon (gray), nitrogen (blue), oxygen (red), phosphor (orange). CRT*+1PA is less energetic favorable than the structure of CRT+1PA by 1.1 kcal/mol.

in energy by 1.1 kcal/mol.

The fully optimized structures of TMA, IMI, LDC, CRT, and CRT* with the addition of two PA molecules were also determined (see **Figure** A.1). There is little difference in the hydrogen bonding between the bases and the PA molecules except for the observed increase in hydrogen bond length. It was noted that the second PA molecule preferentially forms "ring-like" hydrogen bonds ranging from 2.50 to 2.73 Å with the first PA molecule rather than with available hydrogen bond donor and acceptor sites of the base (based on the minimum energy structure at the B3LYP/6-311G**/SMD level of theory). As were the cases for the complexes of bases with subsequently adding the third PA molecule (see **Figure** 4.3); the hydrogen bond lengths continuously increase to some extent resulting in slight shortening of the covalent bond between the dissociated H atom and protonated N1 atom of the bases from various distances to the same final value of 1.05 Å (see **Table** 4.2). It is interesting to note that distances of the hydrogen bonds formed between the second and third PA molecules are the same (2.65 Å and 2.52 Å) for all of the Base+3PA systems [shown in **Figure** 4.3(a-c, and e)] except the CRT+3PA complex in **Figure** 4.3(d) with two comparable hydrogen bonds (2.58 Å and 2.59 Å), which implies that the hydrogen bonding between the second and third PA molecules are influenced by the base molecules even when separated by another PA molecule. In most of the studied systems, the charged ions are separated by a neutral PA molecule forming the complex: Base-$H^+ \cdots$ PA$\cdots$PA$^- \cdots$ PA, in which the excess charge is delocalized over the PA molecules through the hydrogen bond network. Specifically, the contact ion pairs were only observed in the system of CRT+3PA [see **Figure** 4.3(d)] in the form of CRT-$H^+ \cdots$ PA$^- \cdots$PA $\cdots$ PA because the original proton accepting oxygen of a PA in the proximity of $CRTH^+$ not only forms a hydrogen bond with the N2 atom of CRT molecule but also with the neighboring PA molecule.

4.3 Binding Energies of PA Molecules

Examination of the ZPE corrected binding energies of PA to the various bases (**Table** 4.3) indicates that the first PA molecule is most loosely bound to IMI, while the binding energy per PA molecule increases with the addition of PA molecules since the second and third PA molecules form double hydrogen bonds with the first PA. Although only one hydrogen bond is

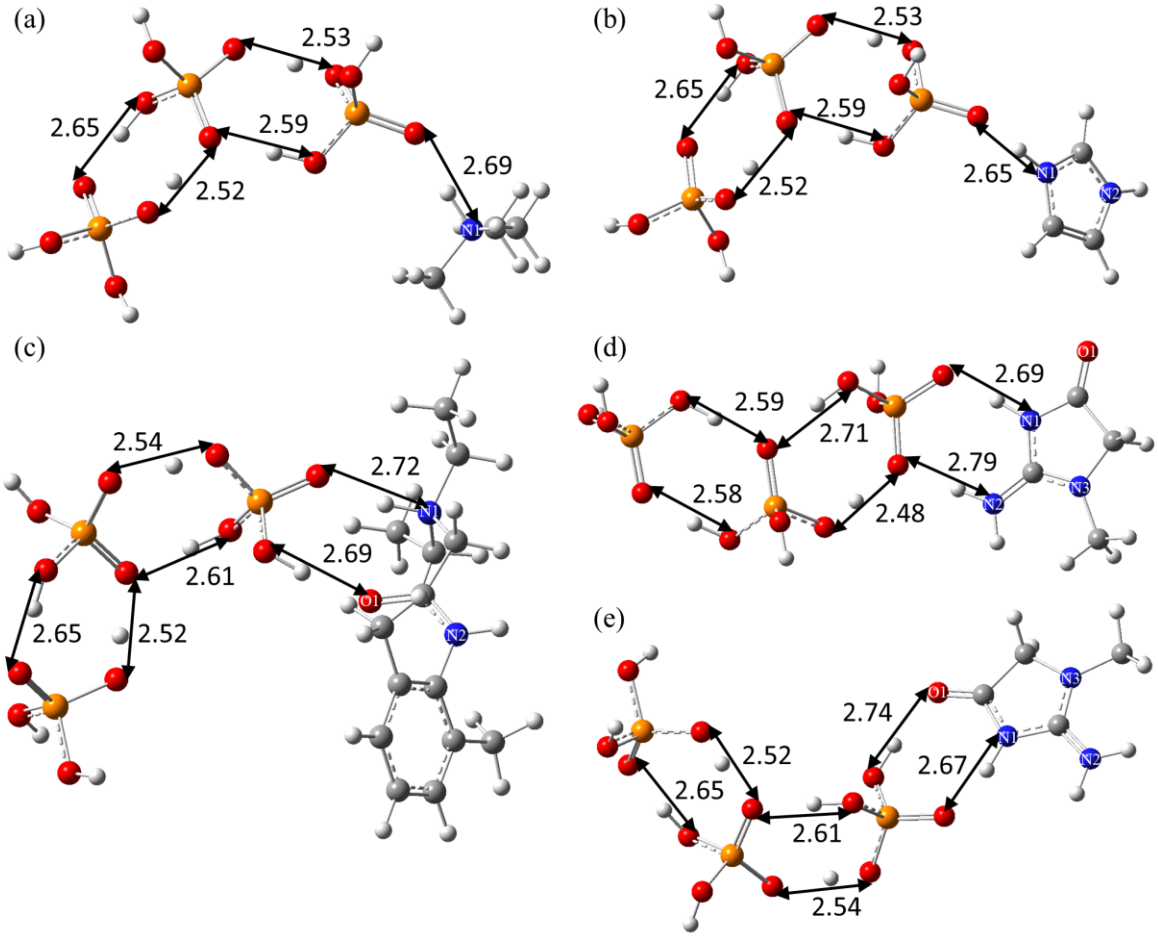

Figure 4.3. Fully optimized configurations of cluster of three PA molecules with (a) TMA, (b) IMI, (c) LDC, (d) CRT, and (e) CRT* (congener of CRT cluster) at the B3LYP/6-311G**/SMD level of theory. All values are reported in Å. CRT*+3PA is more energetic favorable than the structure of CRT+3PA by 1.1 kcal/mol.

Table 4.2. Structural parameters[a] of phosphoric acid-based protic ionic liquids at the level of B3LYP/6-311G**/SMD.

	r(**N1** ⋯ O)	**r**(**N2**/O**1** ⋯ O)	**r**(**O** ⋯ O)(1st and 2nd PA)		**r**(**O** ⋯ O)(2nd and 3rd PA)	
TMA-1PA	2.62 (1.07)[b]					
IMI-1PA	2.56 (1.09)					
LDC-1PA	2.62 (1.08)	2.77 (0.98)				
CRT-1PA	2.67 (1.06)	2.70 (1.05)				
CRT*-1PA	2.69 (1.01)	2.62 (1.01)				
TMA-2PA	2.68 (1.05)		2.51 (1.04)	2.53 (1.03)		
IMI-2PA	2.63 (1.06)		2.54 (1.02)	2.73 (0.99)		
LDC-2PA	2.71 (1.06)	2.69 (0.98)	2.54 (1.02)	2.55 (1.02)		
CRT-2PA	2.68 (1.05)	2.78 (1.04)	2.50 (1.04)	2.66 (0.99)		
CRT*-2PA	2.66 (1.06)	2.75 (0.98)	2.54 (1.03)	2.55 (1.02)		
TMA-3PA	2.69 (1.05)		2.53 (1.02)	2.59 (1.01)	2.52 (1.03)	2.65 (0.99)
IMI-3PA	2.65 (1.05)		2.53 (1.02)	2.59 (1.01)	2.52 (1.03)	2.65 (0.99)
LDC-3PA	2.72 (1.05)	2.69 (0.98)	2.54 (1.02)	2.61 (1.01)	2.52 (1.03)	2.65 (0.99)
CRT-3PA	2.69 (1.05)	2.79 (1.03)	2.48 (1.05)	2.63 (0.99)	2.58 (1.01)	2.59 (1.01)
CRT*-3PA	2.67 (1.05)	2.74 (0.99)	2.54 (1.02)	2.61 (1.01)	2.52 (1.03)	2.65 (0.99)

[a]All reported values are in the unit of Å.

[b]Values in parenthesis are the distances of covalent bond N-H or O-H.

Table 4.3. Energetics of phosphoric acid-based protic ionic liquids at the level of B3LYP/6-311G**/SMD.

	$\boldsymbol{E_{elec}}$ + ZPE[a]	$\Delta \boldsymbol{E}_{\mathrm{ZPE}}$[b]/kcal mol^{-1}	$\Delta \boldsymbol{E}^{c}$/kcal mol^{-1}
PA	-644.239902		
TMA	-174.413899		
LDC	-731.370596		
IMI	-226.229286		
CRT	-396.153573		
TMA-1PA	-818.682904	-18.26	-18.26
IMI-1PA	-870.491277	-13.86	-13.86
LDC-1PA	-1375.639985	-18.50	-18.50
CRT-1PA	-1040.427675	-21.46	-21.46
CRT*-1PA	-1040.425845	-20.31	-20.31
TMA-2PA	-1462.960320	-41.80	-20.90
IMI-2PA	-1514.765266	-35.26	-17.63
LDC-2PA	-2019.919933	-43.64	-21.82
CRT-2PA	-1684.699093	-41.24	-20.62
CRT*-2PA	-1684.699342	-41.39	-20.69
TMA-3PA	-2107.229423	-60.12	-20.04
IMI-3PA	-2159.036694	-55.02	-18.34
LDC-3PA	-2664.189472	-62.22	-20.74
CRT-3PA	-2328.966906	-58.74	-19.58
CRT*-3PA	-2328.968909	-60.01	-20.00

[a]Total electronic energy corrected for zero-point energy (ZPE) in Hartrees.

[b]Energy difference based on ZPE corrected electronic energies (i.e. $\Delta \boldsymbol{E_b} = \boldsymbol{E}[\boldsymbol{base}(\boldsymbol{H_3PO_4})_n] - \mathbf{n} \times \mathbf{E}[\boldsymbol{H_3PO_4}] - \boldsymbol{E}[\boldsymbol{base}]$).

[c]Binding energy per phosphoric acid molecule.

formed in the TMA+1PA complex, a much larger ZPE corrected binding energy of 18.26 kcal/mol is observed, meaning that the basicity of TMA is stronger than IMI, which is confirmed by the greater proton affinity of TMA (see **Table** 4.1). The ZPE corrected binding energies of PA to LDC increases followed by a slight decrease with additional PA molecules, implying that PA is more strongly bound to other PA molecules than to LDC. Similar magnitude in the binding energy per PA is observed in both systems of CRT + nPA and CRT* + nPA (n = 1 – 3), revealing that there is a small difference in binding energies between the PA molecules, and PA and CRT. It is important to recognize that the shorter the hydrogen bond, the stronger the binding energy when there is no accompanying covalent bond breaking and forming. The equilibrium structures show that the proton is initially covalently bonded to PA and then transferred to the base except in the complex of CRT*+1PA. Specifically, the smallest binding energy of the first PA paired with IMI through the shortest hydrogen bond $\mathrm{O}\cdots\mathrm{N1}$ results from the partially covalent bond between the proton and N1 of IMI, i.e. the proton in closest proximity to IMI is shared by the proton donor oxygen and the proton acceptor nitrogen.

4.4 Proton Transfer Energetics

The PES scans for proton transfer were performed with respect to the fully optimized structures. The relative energy profiles shown in **Figure** 4.4 are plotted as a function of the asymmetric stretch coordinate, $q_{\mathrm{asym}} = 1/\sqrt{2}\,(r_{\mathrm{D}\cdots\mathrm{H}} - r_{\mathrm{H}\cdots\mathrm{A}})$, where D indicates the nitrogen or oxygen atom initially covalently bonded to the proton, and A represents the nitrogen or oxygen atom acting as a proton acceptor. As indicated previously, the PA molecule has dissociated one proton to the base in all systems except the CRT*+1PA complex. Thus, it is necessary to investigate the proton transfer from the base to PA. The relative energy profiles for proton transfer from the protonated N1 atom of the base to PA through the hydrogen bond between them in systems of Base+1PA and Base+3PA were determined at the B3LYP/6-311G** level of theory with inclusion of the implicit SMD continuum solvation model are shown in **Figure** 4.4(a). All curves demonstrate that the bridging proton between the PA and the base has a marked propensity of remaining associated with the base. In both systems of TMA+1PA and CRT+1PA shown in **Figure** 4.4(a), the relative energy profiles reveal a

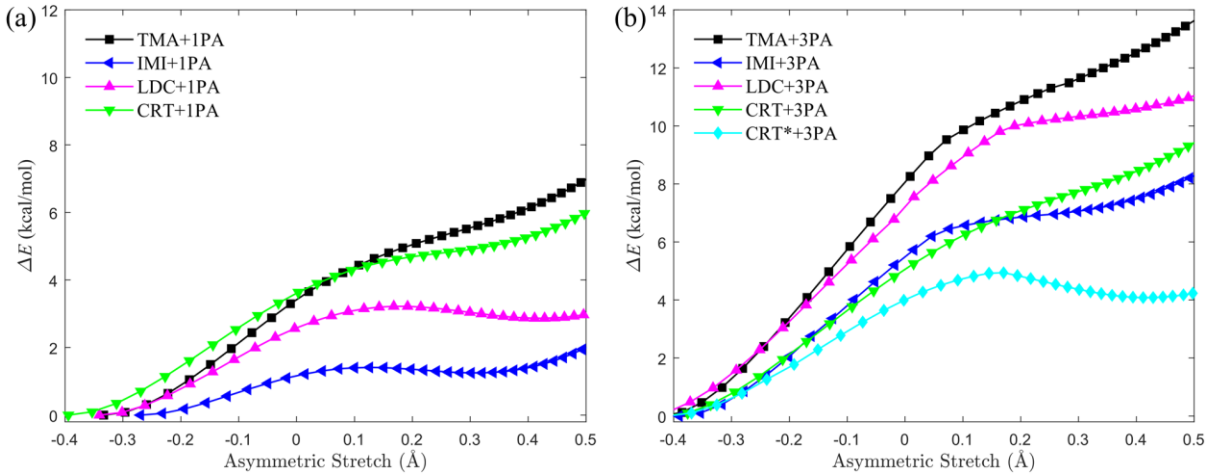

Figure 4.4. Energetics for proton transfer from protonated base to PA in systems of cluster of (a) one PA molecules with TMA, IMI, LDC, and CRT; and (b) three PA molecules with TMA, IMI, LDC, and CRT at the B3LYP/6-311G**/SMD level of theory. The ionic pairs are energetically preferable and stable in these systems.

monotonically increasing trend indicating there is only one minimum energy structure, i.e. the contact ion pair; $\mathrm{Base\text{-}H^{+}\cdots PA^{-}}$; which attributes its stability to the effect of the implicit continuum solvation and the strong basicity of the base. There is a very shallow minimum in the clusters of LDC+1PA and IMI+1PA. This is because in the LDC+1PA complex another hydrogen bond between the proton donor oxygen of the PA molecule and O1 atom of LDC stabilizes the charge distribution accompanying the proton transfer event, which can be confirmed by the contraction of the hydrogen bond $\mathrm{O\cdots O1}$ (from 2.77 Å to 2.61 Å) and the slight elongation of the O–H bond length (from 0.98 Å to 1.00 Å). It is important to note that the second hydrogen bond in the CRT+1PA pair strengthens the proton dissociation in PA since the N2 atom donates a hydrogen bond to PA, which causes higher endothermicity for proton transfer in CRT+1PA than LDC+1PA. However, in the IMI+1PA system, the lowest endothermicity for the transfer of a proton results from the weakening covalent bond between the proton and the N1 atom of IMI. On the other hand, these small wells may disappear when the ZPE corrected energies are included as the ground vibrational energy is probably higher than this tiny barrier.

Figure 4.4(b) illustrates the higher energetics for proton transfer from the protonated base to a PA molecule upon the addition of three PA molecules to various bases in comparison to those shown in **Figure** 4.4(a). It means that the extra PA molecules act to retain the proton on the bases. This observation is consistent with the AIMD results that there is no back-transfer of a proton from IMI-H^{+} to PA or PA^{-} occurring in phosphoric acid/imidazole (2:1) system.[129] It is interesting to note that the low energetics with a second well for proton transfer is observed in the congener of CRT*+3PA since there is proton transfer simultaneously occurring from the first PA to the second PA (see Figure 2S) and the reorientation of the hydrogen bonding, while this phenomenon is not shown in the cluster of LDC+3PA that possesses the analogous hydrogen bond network to the CRT*+3PA system. These differences may be caused in part, by two different situations in the proton affinity for LDC and CRT: one site of LDC with strong proton affinity and another site with considerably weak proton affinity (i.e. 290.15 kcal/mol vs. 264.11 kcal/mol); both sites of CRT molecule with medium proton affinities (i.e. 286.04

kcal/mol vs. 273.09 kcal/mol), as reported in **Table** 4.1. Another crucial factor is the huge difference in the geometries of LDC and CRT. It may be concluded that the ionicity of these PILs is reasonably high based on these calculations.

Of particular interest is the influence of the protonated bases (i.e. Base-H^+) on the energetics for proton transfer from one PA molecule to another. The relative proton-transfer energy profiles for both clusters of $(H_3PO_4)_2$ and $(H_3PO_4)_3$ are illustrated with a red line as a reference for comparison purpose in **Figure** 4.5 and **Figure** 4.6. Compared with the energetics for proton transfer within phosphoric acid clusters in the gas phase,[79] the trends are similar to each other, but the energetic barrier is almost equivalent for the $(H_3PO_4)_2$ cluster while much lower in the solvation SMD model than in the gas phase for the cluster of $(H_3PO_4)_3$. It should be pointed out that the proton transfer exactly occurs in the cluster of $(H_3PO_4 \cdot H_2PO_4)^-$ or $(H_3PO_4 \cdot H_3PO_4 \cdot H_2PO_4)^-$ in the proximity of a positively charged base molecule instead of the pure phosphoric acid clusters. To some extent, the cationic Base-H^+ may be treated as a substituent hydrogen bonded to the PA molecules, but it is more complex because the bases have different proton affinities and possess various proton acceptor and/or donor sites.

The energetics for transferring a proton between two PA molecules in the systems with two added PA molecules are shown in **Figure** 4.5(a). The curves indicate that the symmetric double-well potential for proton transfer are distorted to various extents leading to a considerable weakening of the barriers with small secondary wells in the systems of Base+2PA (Base = IMI, CRT, and TMA) and the single minimum potential in the complexes of Base+2PA (Base = LDC and CRT*). These changes may be ascribed to the different proton affinities of these bases: IMI < CRT < TMA < LDC (reported in **Table** 4.1). Although the proton affinity of a single site of CRT is somewhat smaller than TMA, the cooperative effects of the two proton acceptor sites rather than one acceptor and one donor strengthen the ability of attracting a proton. Interestingly, when the single-well potential appears, the differences are not discernible in comparison to the curves of LDC+2PA and CRT*+2PA, which will be further borne out by examining the energetic profiles for proton transfer between PA molecules in the systems of Base+3PA (see below).

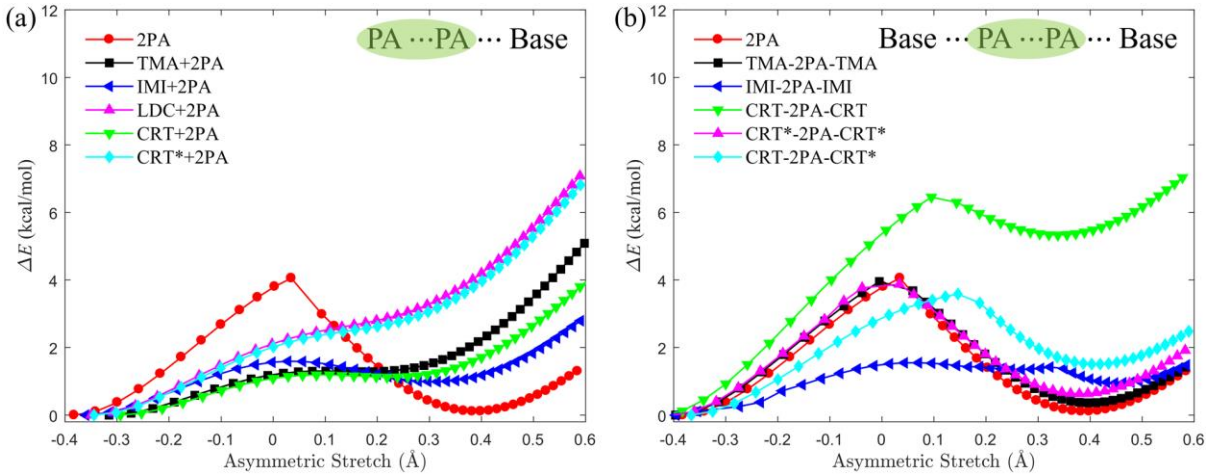

Figure 4.5. Energetics for proton transfer between the PA molecules in systems of (a) cluster of two PA molecules with TMA, IMI, LDC, CRT, and CRT*, and (b) cluster of two PA subunits flanked by two base molecules at the B3LYP/6-311G**/SMD level of theory. Note that the bases with stronger proton affinity exert greater influence on the energetics for proton transfer between individual PA molecules. However, the effects are minimal when the potential is shifted into the single-well from the double-well. The double-well potential recovers with deformations in various manners when one additional base molecule is added to the other side of these complexes forming (Base ··· PA···PA ··· Base) clusters.

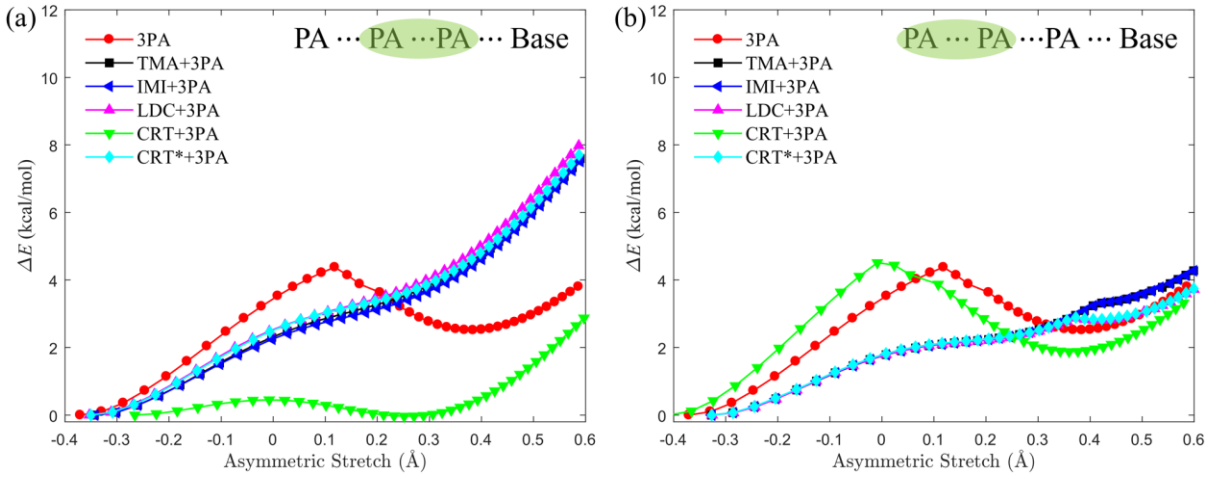

Figure 4.6. Energetics for proton transfer between: (a) first and second PA; and (b) second and third PA in systems of cluster consisting of three PA molecules with TMA, IMI, LDC, CRT, and CRT* at the B3LYP/6-311G**/SMD level of theory. Note that the neighboring cation Base-H^+ results in either a negligible energetic barrier or a single minimum between the first and second PA molecules. The energetics for proton transfer in systems of Base+3PA (Base = TMA, IMI, CRT*, and LDC) have similar trends in which the energies are monotonically increasing without the formation of a transition state. Barrierless proton transfer occurs in the system of CRT with several PA molecules.

To aid in understanding the effects of the base molecules, one additional base molecule was added to the 'other side' of these complexes forming (Base ⋯ PA⋯PA ⋯ Base) clusters (Base = TMA, IMI, CRT, and CRT*) including (CRT ⋯ PA⋯PA ⋯ CRT*). Note that the LDC was not included due to the enormous computational cost. It is not surprising to observe that the double-well potential recovers with deformations in various degrees. Firstly, the curves of the proton-transfer energetics coincide with the reference in the systems of (Base ⋯ PA⋯PA ⋯ Base) (Base = TMA and CRT*), which implies that the influence of the initial base molecule is exactly counterbalanced by the additional identical base. It should be noted that the energetic barrier is dramatically higher in the CRT ⋯ PA⋯PA ⋯ CRT system. This may be because the electron density of proton accepting oxygen atoms of PA molecules is shared by the proton donating N2 atoms leading to the attenuation of attracting the proton. In addition, the symmetry was distorted upon adding CRT to CRT*+2PA complex consequently giving rise to a slight decrease in the energetic barrier to proton transfer with a less energetically favorable configuration after transferring the proton. The relatively small penalty for proton transfer occurs in the system (IMI ⋯ PA⋯PA ⋯ IMI) due to the feasible moving of the bridging proton between the base and the PA molecule to stabilize the system during the proton transfer. The adjusting of the bridging proton is due to the moderate proton affinity of IMI.

Figure 4.6 displays the energetics for transferring a proton between the first and second PA molecules as well as between the second and third PA molecules in the complexes of a base paired with three PA molecules. It is worth noting that the neighboring cation Base-H^+ results in either a negligible energetic barrier or a single minimum for the proton-transfer energetics between the first and second PA molecules; shown in **Figure** 4.6(a). More specifically, the monotonically increasing curves are nearly coincident with each other in the Base+3PA complexes (Base = TMA, IMI, LDC, and CRT*). The similarity in these systems is that the base is hydrogen bonded to a PA via only one proton accepting site or two proton accepting sites. It may be concluded that the involvement of only proton accepting sites of the base molecule could lead to the analogous energetic situation on the proton transfer between the central PA subunits flanked by a cation and a neutral PA molecule. The endothermicity for

proton transfer is roughly 4 kcal/mol, a similar value to the barrier to transfer a proton in the cluster of $(H_3PO_4)_3$, if the asymmetric stretch coordinate where the second well resides in the pure cluster of $(H_3PO_4)_3$ are treated as the final (or end) position in the transfer. Nevertheless, the occurrence of a negligible barrier to proton transfer in the system of CRT+3PA does not mean that the small barrier would appear as long as there is a proton donating site of the base molecule involved in the neighboring hydrogen bonding networks. In terms of dynamics, the proton transfer in PA clusters could facilely happen when protonated base molecule approaches this cluster and forms such hydrogen bonding network at the cost of 2 kcal/mol (the difference in energy between the second minimum and endothermicity). Again, the monotonically increasing curves (i.e., in the cases with a single-well potential) of the proton transfer energetics between the second and third PA molecules in **Figure** 4.6(b) that nearly coincide, indicate that the effects of the protonated bases are quite insensitive to the specific molecular geometries and the proton affinities except for the case in which the proton donating site of a base molecule is involved. This pattern is further underscored by comparing the results of the CRT+3PA and CRT*+3PA systems in which the differences are the hydrogen bonds formed through different pairs of proton donor and acceptor sites. It is surprising to observe that the endothermicities decrease in comparison to the energetics for proton transfer between PA molecules in vicinity of the cations (shown in **Figure** 4.6(a)). The flattening of these curves may be the result of the better stabilization of charge by the neighboring PA molecule when in proximity to the bases. However, the curve of the proton-transfer energetics in the CRT+3PA complex resembles that in a pure (or neat) PA cluster but shifts to the left with a lower well. The formation of a contact ion pair in CRT+3PA may be responsible for the weakening influence of the base molecule on the energetics for proton transfer between the second and third PA molecules.

Assuming that the computed energetics in these small clusters reflect the behavior in the bulk systems, and that the entropic effects would not qualitatively change the observed trends, we can speculate about behavior of the proton transport in mixtures of phosphoric acid with the bases. According to the analysis in the present study, the proton transferred from a PA molecule to any of the bases examined here remains with the base (i.e., protonating the base), and might

not contribute significantly to the proton conductivity of the bulk system. At the same time, the presence of a protonated base and the existence of deprotonated PA molecules polarize the network of the hydrogen bonded PA molecules. As a result, the energy barrier for proton transfer between the neighboring PA molecules is decreased. Thus, changes of the proton conductivity in PA with specific bases might be caused by the changes in the energy barrier for the proton transfer between the PA molecules, rather than due to the proton transfer between the base and PA molecules. *Ab initio* molecular dynamic simulations on larger and extended systems should provide verification of this proposed idea.

Chapter 5 Beyond Proton Transfer: Proton Transport in Pure and Aqueous Acids

This chapter is based on the following papers:[243]

- Popov, I; Zhu, Z; Young-Gonzales, A. R.; Sacci, R. L.; Mamontov, E.; Gainaru, C.; Paddison, S. J; Sokolov, A. P., Search for a Grotthuss Mechanism through the Observation of Proton Transfer. *Communications Chemistry* **2023,** *6*, 77.
- Zhu, Z; Sokolov, A. P; Paddison, S. J., Proton Transport Mechanisms in Aqueous Acids: Insight from Ab Initio Molecular Dynamics Simulations. *Journal of Chemical Physics* **2024**, JCP24-AR-MD602024-02497, submitted.
- Popov, I.; Zhu, Z.; Singh, H.; Abdullah, M.; Sacci, R. L.; Mamontov, E.; Damron, J. T.; Gainaru, C.; Paddison, S. J.; Sokolov, A. P., Mechanisms of Proton Transport in Aqueous Acid Solutions. *Cell Reports Physical Science* **2024**, CR-PHYS-SCI-D-24-00474, submitted.

This chapter presents the results of an investigation of proton transport in pure and aqueous phosphoric acid (PA), aqueous sulfuric acid (SA), and aqueous nitric acid (NA) to elucidate proton transport mechanisms and proton correlations using *ab initio* molecular dynamics (AIMD) simulations. In Section 5.2, to accompany dielectric spectroscopy, quasielastic neutron, and light scattering, we determined that protons move by surprisingly short jumps of only ~0.5-0.7 Å, much smaller than the typical ion jump length in ionic liquids, and these proton jumps are anticorrelated resulting in the suppression of conductivity. In Section 5.3, we extensively investigate the similarities and differences in proton transport mechanisms in aqueous H_3PO_4, H_2SO_4, and HNO_3 at two ratios of acid to water: 1:1 and 1:3. The results elucidate the role of the various acid molecules in proton transport within their aqueous solutions, thereby advancing fundamental mechanistic understanding.

5.1 Simulation Setups

AIMD simulations were performed for pure phosphoric acid and a variety of aqueous acids. These systems contained ~420 atoms, which was proven to be the best balance between obtaining sufficient statistics and computational cost.[77, 129] The specifics of each system are

presented in **Table** 5.1. The initial systems were pre-equilibrated for over 10 ns using the GROMACS code.[244, 245] The methodology was established by using the general AMBER force field (GAFF) with the help of a published protocol.[246, 247] Classical MD simulations were undertaken for all these systems in a periodic cubic box with a time step of 2 fs. After obtaining the desired starting structures, AIMD simulations were performed using the CPMD code.[248, 249] The dispersion-corrected atomic core pseudopotentials (DCACP)[250, 251] were employed to account for dispersion forces within the Kohn-Sham formulation of density functional theory and the B-LYP exchange-correlation functional.[230, 252] A plane-wave basis set was used to expand the Kohn-Sham orbitals up to an energy cutoff of 80 Ry. In order to increase the adiabatic decoupling of nuclear and electronic dynamics, and allow a larger time step 4 au, the mass of deuterium was assigned to the hydrogen atoms and the fictitious electron mass set to $\mu = 500$ au. Each system was equilibrated at the targeted temperature using a massive Nose-Hoover chain thermostat,[253] followed by 15-20 ps of canonical (NVT) dynamics, also using a massive Nose-Hoover chain thermostat, finally followed by 60 - 107 ps of microcanonical (NVE) dynamics.

5.2 Proton Transport in Pure and Aqueous PA

5.2.1 Distribution of Protonated Species

PA has been treated as a model system to investigate proton transport mechanisms underlying the exceedingly high intrinsic proton conductivity.[73, 77, 79, 92, 94, 129, 254] Initially we examined the oxygen-hydrogen radial distribution function of pure PA and this presented in **Figure** 5.1. The first sharp peak corresponds to the covalent OH bond and the second small peak refers to the hydrogen bond. The shoulder on the left side of the 3rd peak corresponds to the distances between the proton and the oxygen atoms from the same PA molecule. Previous structural analysis[77, 92] revealed the strong hydrogen bond network in both pure PA and aqueous 85% PA, resulting in charged species due to fast proton transfer. The fractions of various species were calculated given that the individual protons are assigned as belonging to a particular oxygen atom. The results for pure PA and aqueous PA are presented in **Figure** 5.2. The fraction of $H_4PO_4^+$ is about 11% in pure PA due to the self-dissociation of PA. This decreases to 5% in

Table 5.1. Details of AIMD simulation systems.

System	Acid #	Water #	Density (g/cm^3)	wt%	Temperature (K)	Prod. Time (ps)
PA	54	0	1.88	100.0	400/383	60.7
PA1H	38	38	1.68	85.0	390/420	103.1
PA3H	24	72	1.48	65.0	390	102.4
SA1H	40	40	1.78	85.0	360	61.1
SA3H	26	78	1.56	65.0	360	60.9
NA1H	48	48	1.45	78.0	360	61.3
NA3H	30	90	1.33	54.0	360	61.1
H_3O^+	0	104	1.00	0.0	320	104.0

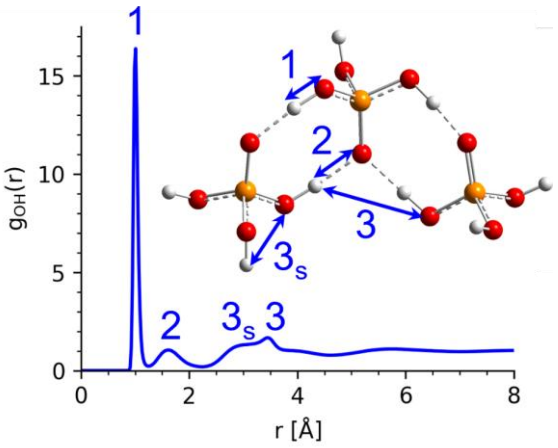

Figure 5.1. The oxygen-hydrogen radial distribution function (g_{OH}) of PA. The shoulder on the left side of the 3rd peak corresponds to the distances between the proton and the oxygen atoms from the same PA molecule.

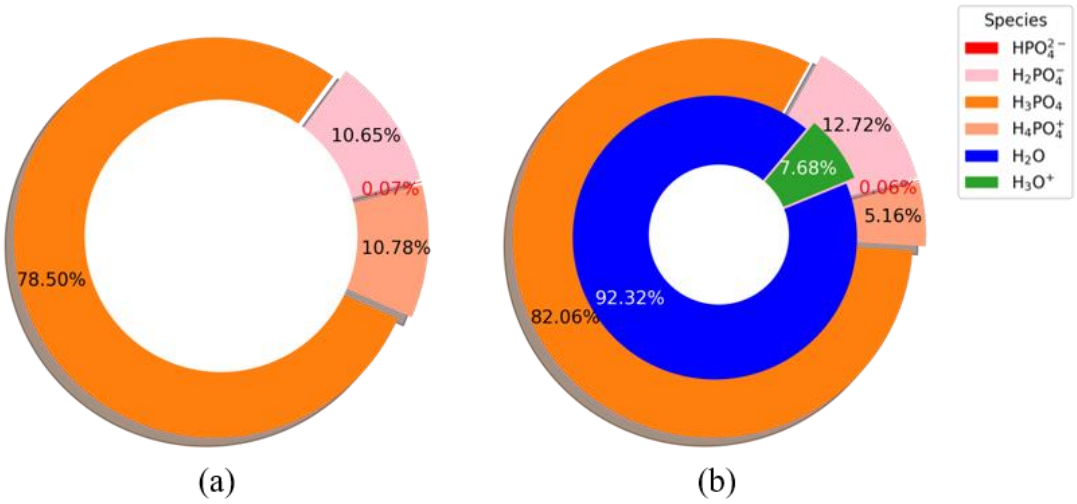

Figure 5.2. Calculated fractions of PA and water in their different states of protonation in: (a) pure PA and (b) aqueous 85% PA systems. Note that the transiently shared protons are included.

aqueous PA, suggesting that the presence of water molecules significantly reduces the self-dissociation of PA molecules. Although the proton affinities of both PA and water molecules are very similar, only a small portion of water molecules (7.7%) accept a proton from PA molecules forming hydronium ions. However, the total number of protonic charged species in aqueous PA is larger than in pure PA, which may enhance the vehicular transport of charged species. It is clear that there is only a very tiny fraction of HPO_4^{2-} in both systems.

5.2.2 Characteristic Relaxation Times

The self-part of the incoherent intermediate scattering function of protons can be computed with: $ISF_s(Q,t) = \langle \exp(i\boldsymbol{Q} \cdot [\boldsymbol{r}_i(t) - \boldsymbol{r}_i(0)]) \rangle$ from the AIMD simulation trajectories, in which i and $\boldsymbol{Q}$ are the imaginary unit and the reciprocal lattice vector, respectively, $\boldsymbol{r}_i$ is the coordinates of the ith proton. This function provides similar information to that obtained from QENS data, but can access a much higher Q range. To illustrate the major processes of proton motion, we first fitted the $ISF_s(Q,t)$ curves with two exponential terms and one stretched exponential term (i.e., $ISF_s(Q,t) = a_1 \exp(-t/\tau_1) + a_2 \exp(-t/\tau_2) + a_3 \exp[-(t/\tau_3)^{\beta}]$) for various Q values as shown in **Figure** 5.3(a). The fitting results are listed in **Table** A.3. The $ISF_s(Q,t)$ shows three processes. The fastest process occurs within the first 100 fs, which corresponds to the covalent bond vibration. This process can be further verified by examining the vibrational density of states (VDOS) for the protons in pure PA at 400 K [see **Figure** 5.3(b)], in which the relaxation time of the OD bond, τ_1, is in good agreement with the fastest mode obtained from the fitting of $ISF_s(Q,t)$. Note that this process only accounts for a very small proportion of the $ISF_s(Q,t)$, in particular for small Q values. Thus, we skipped this Q-independent vibrational mode in the latter fitting procedure by dismissing the first 100 fs, which improved the fitting results for small Q values but had a minimal effect on the ones for large Q values based on the comparison between the E_3 values from **Table** A.3 and **Table** A.5.

Besides the vibrational mode, $ISF_s(Q,t)$ bears a fast relaxation process and a slow relaxation process. The fast process also has a Q-independent time constant ~0.1–0.3 ps, suggesting a local process. Similar processes with characteristic times of ~0.1–0.3 ps were reported in simulations of water and imidazole, and assigned to proton rattling between two

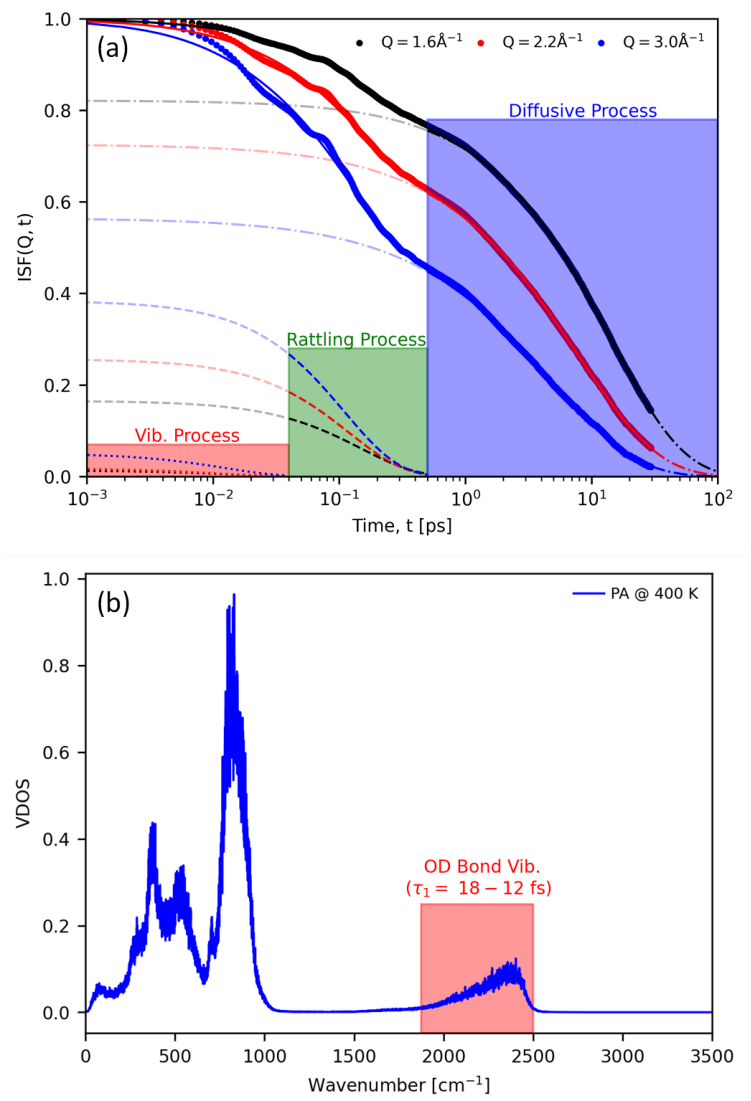

Figure 5.3. (a) Illustration of fitting the self-intermediate scattering function $ISF_s(Q,t)$ of protons with $ISF_s = a_1\exp(-t/\tau_1) + a_2\exp(-t/\tau_2) + a_3\exp[-(t/\tau_3)^\beta]$ for three different Q values probed at 400 K for pure PA. (b) Vibrational density of state (VDOS) for protons in pure PA system at 400 K.

oxygen/nitrogen atoms.[69, 106] Following this idea, we also ascribe this process to the rattling of protons between oxygen atoms in PA and PA85. Furthermore, the proton rattling process can be validated by computing proton transfer population correlation functions (PCFs), as discussed below. The slow process, however, exhibits a strongly Q dependent relaxation time, τ_3, indicating its diffusive nature. It can be well described by a stretched exponential decay, $\propto \exp\left[-(t/\tau_3)^{\beta}\right]$, with the stretching parameter $\beta \sim 0.7 \pm 0.2$. The latter agrees with the stretching determined from the QENS spectra.

To estimate the relaxation times, the $ISF_s(Q,t)$ curves were fit to a modified Kohlrausch-Williams-Watts function $ISF_s = a_2 \exp(-t/\tau_2) + a_3 \exp\left[-(t/\tau_3)^{\beta}\right]$ (**Figure** A.2). The fast process has an exponential form, while the slow diffusive process features a stretched exponential form. The characteristic slow process relaxation time is given by $\tau_R = \tau_3/\beta\,\Gamma(1/\beta)$, where Γ is the Gamma function. Subsequently, the half width of energy maximum (HWHM) of the relaxation spectra for the diffusive process E_3 can be calculated with $E_3 = \hbar/\tau_R$, where $\hbar$ is Planck's constant divided by 2π. The fitting parameters are presented in **Table** A.4-**Table** A.7. The HWHM exhibits the same Q dependence as the process observed in QENS (**Figure** 5.4 inset). The fit of the AIMD simulation results (**Figure** 5.4) provides estimates of the parameter $\langle\lambda_p\rangle = 0.7 \pm 0.2$ Å for pure PA and $\langle\lambda_p\rangle = 0.5 \pm 0.1$ Å for PA85, in excellent agreement with the QENS data analysis (see **Table** 5.2). Meanwhile, the estimated relaxation time, τ_{QENS}, exhibits a similar value to that obtained from the BDS spectra, indicating that proton dynamics probed by QENS governs the conductivity of these systems.[243]

To further verify the various relaxation time scales of proton motion, proton transfer PCFs were calculated from the trajectories. The PCF approach has proven capable of providing the characteristic time scales for proton transfer kinetics including proton rattling and long-range proton transport, which is defined as:

$$C_c(t) = \frac{\langle h(0) \cdot H(t)\rangle}{\langle h\rangle}, \tag{5.1}$$

where $h(0) = 1$ if a given oxygen atom is protonated and 0 otherwise, $H(t) = 1$ if the protonated oxygen atom keeps its identity up to time *t*. The decay of $C_c(t)$ can be fitted to a tri-exponential form:

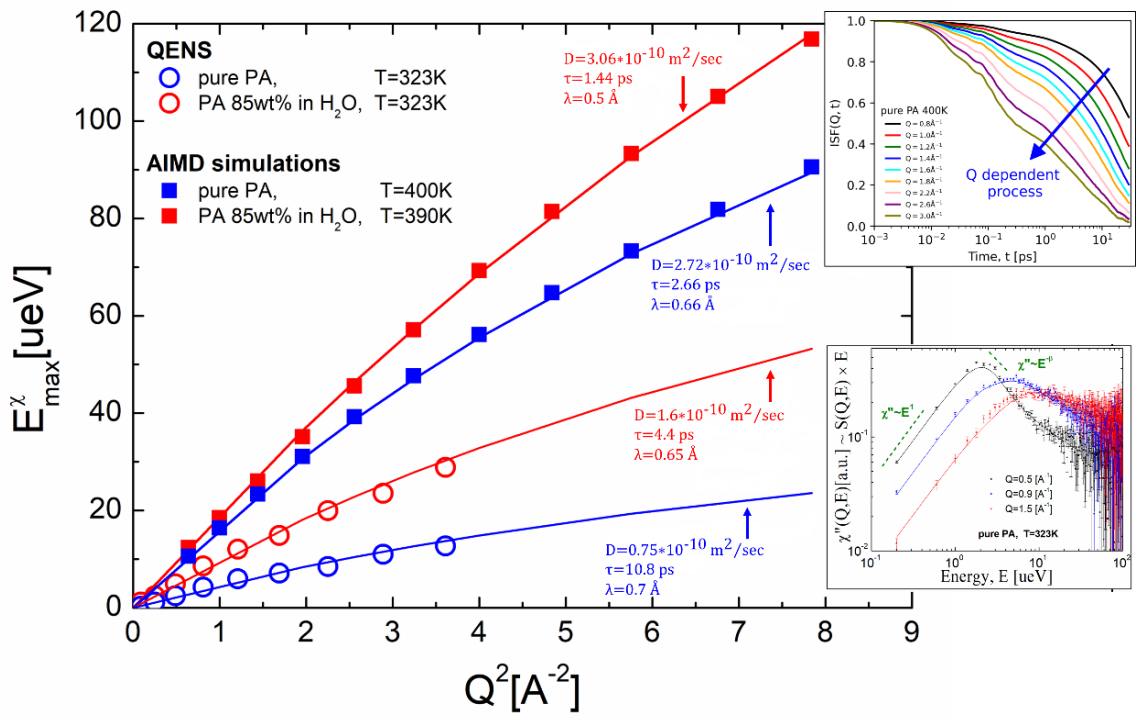

Figure 5.4. Q dependence of the characteristic energy of the QENS relaxation process (open symbols) and corresponding simulation data from self-correlation of proton motion in MD (closed symbols) and their fit to jump-diffusion model (lines). The jump-diffusion model provides correct estimates of the proton diffusion and enables estimates of the proton jump length λ. The latter appears surprisingly short and comparable to the expected length for the proton transfer. The inset displays self-intermediate scattering functions $ISF_s(Q,t)$ of protons with different Q values at 400 K for pure PA from AIMD simulations (upper) and QENS spectra (bottom).

Table 5.2. Relaxation times obtained by fitting the Q-dependent $E_{max}(Q) = \hbar/\tau_R$ with $E_{max}(Q) = \hbar DQ^2/(1+D\tau Q^2)$ for pure PA and aqueous PA85 at different temperatures.

System	T[K]	$1000/T$	D [$\times 10^{-10} m^2 s^{-1}$]	Error D	λ [Å]	Error λ	τ [ps]	Error τ
PA	383	2.611	2.78	0.0044	0.68	0.016	2.79	0.177
PA	400	2.500	2.72	0.0016	0.66	0.02	2.66	0.064
PA85	390	2.564	3.06	0.039	0.51	0.015	1.440	0.100
PA85	420	2.381	7.20	0.079	0.51	0.012	0.61	0.364

$$C_c(t) = \sum_{i=1}^{3} a_i \exp\left(-\frac{t}{\tau_i}\right), \tag{5.2}$$

where the time constants, τ_i, correspond to the different time-scale processes. The results for pure PA at 400 K are shown in **Figure** 5.5(a). The relaxation times are 0.32 ps, 2.20 ps, and 11.02 ps. The fastest relaxation time is typically assigned to proton rattling, which lies in the sub-picosecond regime as observed in the $ISF_s(Q,t)$. The slower one represents a hydrogen bond reorganization process, and the slowest one is derived from long-range proton transport, which is further confirmed by the similar characteristic relaxation time, τ_{QENS}, of 10.8 ps (**Figure** 5.4). It is important to note that the proton transfer PCFs cannot detect the vibrational motion because the proton transfer is the elementary step in this correlation function that has a larger time scale than vibrational motion. However, it is able to demonstrate more details about the proton behavior in terms of transfer events. Specifically, the hydrogen bond reorganization process can be easily detected via the proton transfer PCFs but difficult to distinguish from $ISF_s(Q,t)$ especially at small Q values. Interestingly, the fit of the proton transfer PCF that excludes proton rattling shows a single characteristic time (22.32 ps), meaning that there is only one slow process associated with this time scale.

The distribution of displacements of the protons can be quantified by computing the self-part of the van Hove function defined as:

$$G_s(r,t) = \frac{1}{N}\sum_{i=1}^{N} \langle \delta(r - |\boldsymbol{r}_i(t) - \boldsymbol{r}_i(0)|) \rangle, \tag{5.3}$$

where $4\pi r^2 G_s(r,t)$ is the probability that a particle has moved a distance *r* within the time *t*. The integral of $4\pi r^2 G_s(r,t)$ over all times must be unity, i.e.,

$$\int_0^{\infty} 4\pi r^2 dr G_s(r,t) = 1. \tag{5.4}$$

To estimate the length of proton transport at various characteristic times, the self-part of the van Hove functions at three characteristic time scales were determined and is shown in **Figure** 5.5(b). The van Hove functions demonstrate Gaussian behavior at short and long times, which correspond to local proton hopping and long-range proton diffusive motion. It is noted that there is a flat peak for the van Hove function at the intermediate time, which can probably be

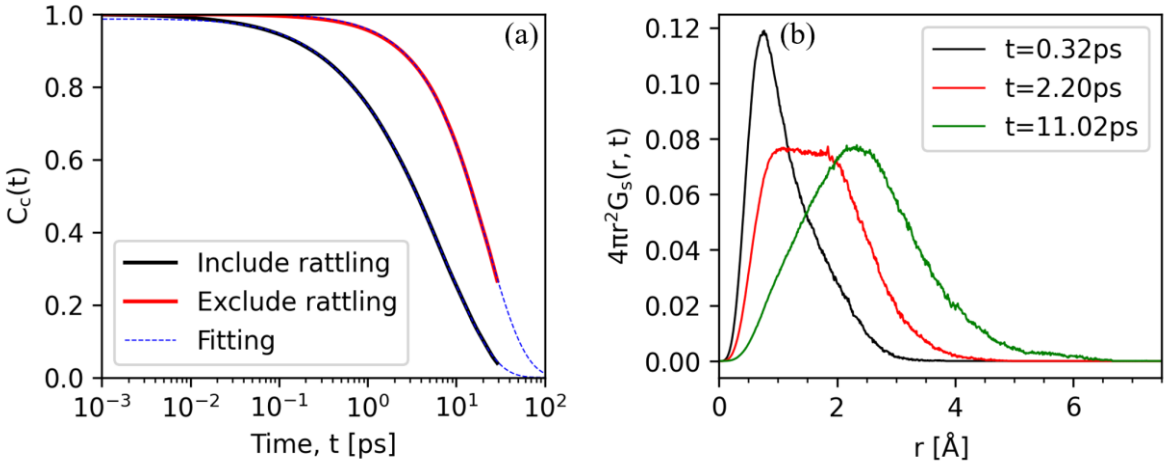

Figure 5.5. (a) Proton transfer population correlation functions (both including and excluding proton rattling) and their triexponential fits for pure PA at 400 K. (b) The self-part of the van Hove function of the protons with three characteristic times obtained from triexponential fits of the population correlation functions in pure PA at 400 K.

ascribed to the reorientation of the solvent molecules facilitating the escape of protons from the "cages". Importantly, the position of the peak for the shortest time scale is ~0.7 Å, which is in good agreement with the proton jump length. Indeed, this result illustrates that a short proton jump length is definitely due to proton transfer events.

Having established a clear relationship of the diffusive process in the simulations to the proton jumps observed in the QENS, we can now follow the trajectory of an individual proton during its diffusion over 40 ps (**Figure** 5.6). Trajectories show the vibrational and rotational motion of the proton within the same color cloud and proton jumps are defined as transfers from one oxygen atom to another oxygen atom. The center of mass of each cloud is connected by a black line to the center of mass of the next cloud. These black lines can be considered as average paths of the proton switching the oxygen atoms. Analysis of these proton jumps reveals that they are very short ~ 0.5 Å with only a few (~2-3 out of 50) large scale jumps ~ 2 Å (**Figure** 5.6 inset). This is smaller than that suggested earlier: ~2.8 Å.[82] Specifically, the short proton jumps are the proton transfers between the same pair of oxygen atoms although there are some trials involving rotations. However, the long jumps are associated with a rotation of the OH bond followed by an effective proton transfer, which is a much rarer event than individual proton jumps. Examination of the other protons in the PA system shows a similar distribution and average jump length.

5.2.3 Proton Transport Mechanisms

The AIMD simulations reveal that proton hopping/shuttling plays a key role in the long-range proton diffusion through the breaking and forming of hydrogen bonds (**Figure** 5.7). The structural characteristics of a proton with neighboring oxygen atoms show that the covalent OH bond and the hydrogen bond are the first peak at $r_{\mathrm{OH}} = 1.01$ Å and the second peak at $r_{\mathrm{OH}} = 1.61$ Å, respectively, in the radial distribution function g_{OH} (**Figure** 5.1). The proton (in green) first forms a strong hydrogen bond with a neighboring oxygen, which induces the proton associated with a neighboring oxygen to transfer to the solvent (neutral) PA molecule [**Figure** 5.7(a)]. Following the completion of the transfer of a proton from the neighboring oxygen to the solvent PA molecule, the proton transfers to the neighboring oxygen through a strong

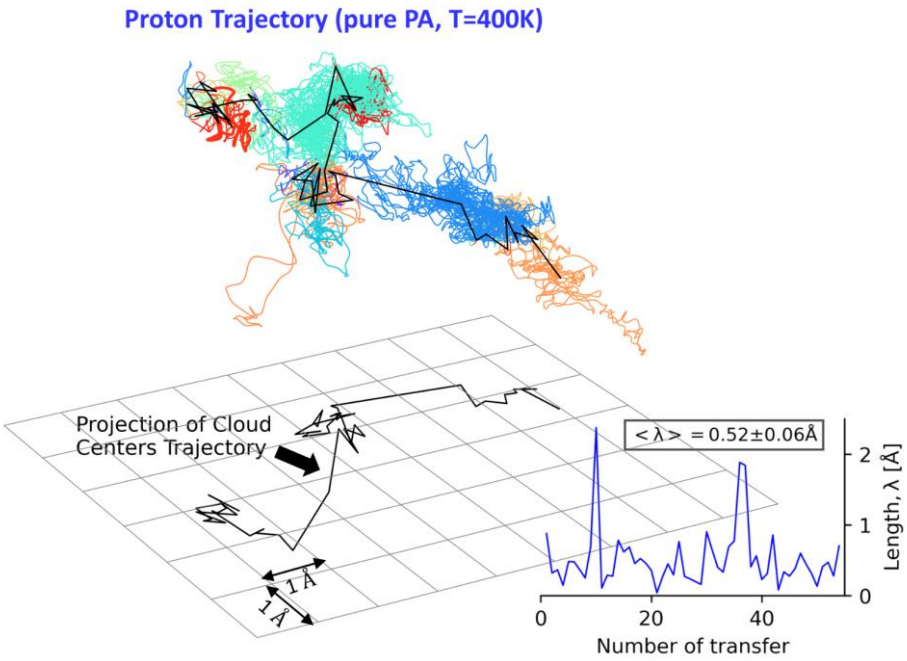

Figure 5.6. Trajectory lines of an individual proton in pure PA at 400 K. Each colored cloud reflects the proton vibrational and rotational motions as the proton is associated with the same oxygen atom. The trajectory changes color when the proton transfers to a different oxygen atom. The center of mass of each cloud is connected by a black line to the center of mass of the next cloud. These black lines present averaged jumps of the proton transfers between the oxygen atoms. (Inset) The length of proton jumps between oxygen atoms (the length of the black lines).

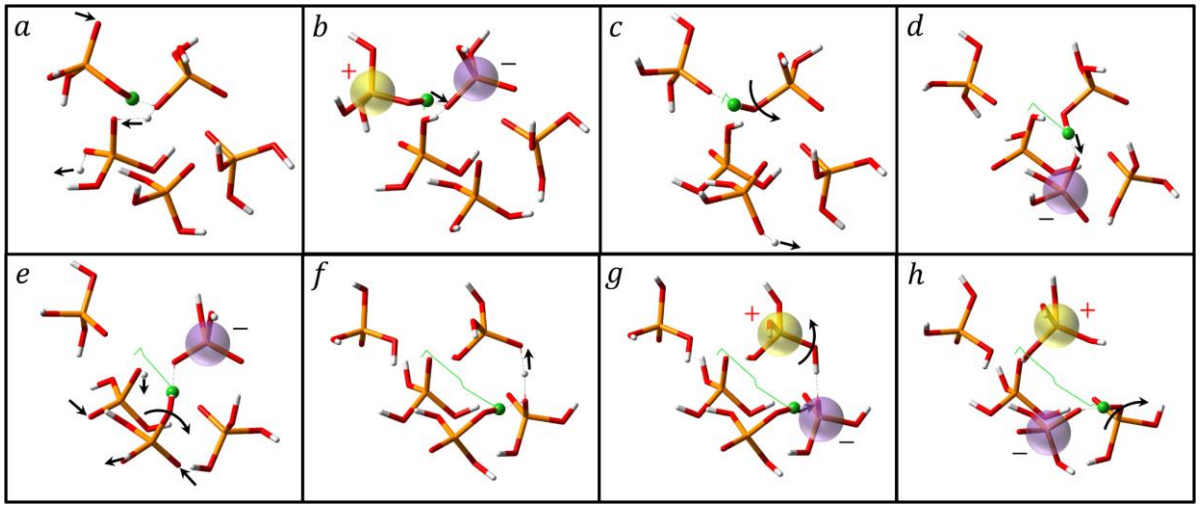

Figure 5.7. Snapshots of the elementary steps of the mechanism for long-range proton diffusion in pure PA. The green ball represents the long-range diffusive proton, and the charged entities are highlighted. The arrows denote the associated proton transfers and the reorientations of the covalent OH bonds in the mechanism. The collaboration of proton transfers (a, b, d, f, and g) and large angular jumps (c, e, and h) facilitates the long-range diffusion of protons.

hydrogen bond [**Figure** 5.7(b)]. These successive proton hopping events take place at the sub-picosecond time scale, followed by a long quiescent period, in which the proton is trapped in a cage formed by adjacent oxygen atoms via strong hydrogen bonds. This quiescent period corresponds to the hydrogen bond reorganization relaxation time (couple of picoseconds), which is also detected by the proton transfer PCFs [**Figure** 5.5(a)]. A large-angle proton jump due to the reorientation of the covalent OH bond causes the breaking of the original hydrogen bond and the forming of the nascent hydrogen bond with a new PA molecule [**Figure** 5.7(c, d)], which facilitates protons escaping the local "trap" formed by the strong hydrogen bonds. Subsequently, proton transfer occurs via the new hydrogen bond followed by another large-angle reorientation of the covalent OH bond [**Figure** 5.7(e, f)]. The proton transfer through this newly formed hydrogen bond induces the cleavage of the other hydrogen bond between the next acceptor oxygen and the surrounding solvent PA molecules by a large reorientation of a covalent OH bond [**Figure** 5.7(g, h)]. This mechanism indicates that the reorientation of an OH bond by large angular jumps is involved in the long-range diffusion of the protons.

5.2.4 Proton Correlations

Our experimental results reveal that $H^{-1} < 1$ over the entire temperature range [**Figure** 5.8(a)], suggesting that proton transfer between PA molecules is indeed correlated.[243] However, in contrast to the expected enhancement of conductivity for a Grotthuss-like mechanism, the correlated proton transfer events in PA lead to a decrease in conductivity. Thus, we hypothesize that the correlations between protons may be responsible for this suppression. To confirm this hypothesis, we analyzed distinct proton-proton displacement vector correlations from AIMD simulation trajectories. The self- and distinct- diffusivities of the protons can be obtained using the Einstein relation:

$$D_{ij} = \frac{1}{6}\lim_{t\to\infty}\frac{d}{dt}\langle\sum_{i=1}^{N}\sum_{j=1}^{N}[\boldsymbol{r}_i(t) - \boldsymbol{r}_i(0)]\cdot\left[\boldsymbol{r}_j(t) - \boldsymbol{r}_j(0)\right]\rangle, \tag{5.5}$$

where $\boldsymbol{r}_i$ and $\boldsymbol{r}_j$ are the coordinates of protons i and j, respectively. This Eq. can be decomposed into self- (D_{ii}^{self} for $i = j$) and distinct- (D_{ii}^{distinct} for $i \neq j$) diffusivity contributions. Assuming that the proton conductivity is the dominant contribution to the

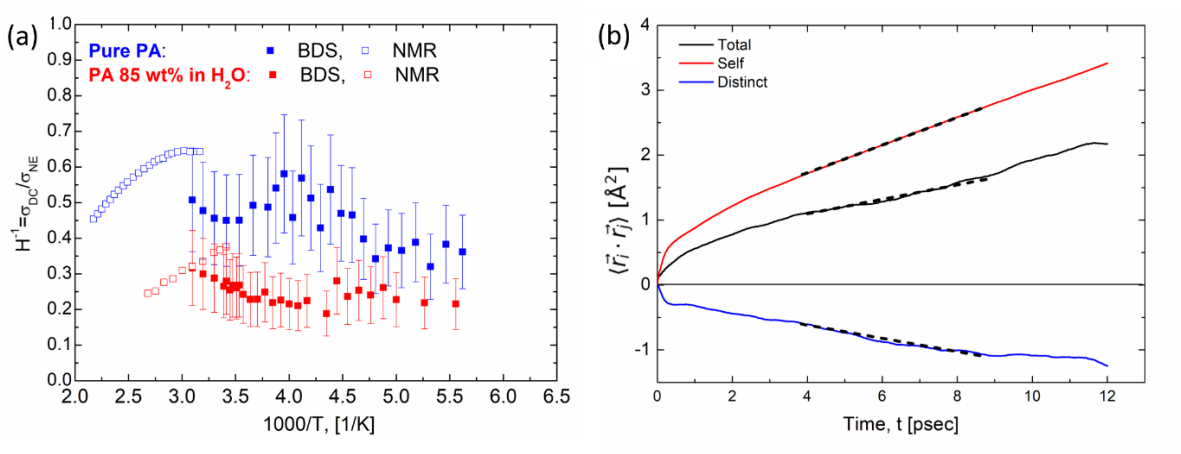

Figure 5.8. (a) Temperature dependence of the inverse Haven ratio for PA (blue symbols) and PA85 (red symbols) estimated using diffusion coefficients obtained from PFG-NMR[81, 82] (open squares) and BDS (closed squares). (b) Correlation functions of proton displacement vectors for pure PA at 400 K and the linear fit to obtain self-, distinct, and total diffusion coefficients.

conductivity of the system, the inverse Haven ratio can be computed via $H^{-1} = (D_{ii}^{\text{self}} + D_{ii}^{\text{distinct}})/D_{ii}^{\text{self}}$. These diffusivities were calculated from linear fitting to the proton displacement vector correlations ($\langle \boldsymbol{r}_i \cdot \boldsymbol{r}_j \rangle$. Indeed, the distinct proton correlations are negative, $D_{ii}^{\text{distinct}} = -1.53 \times 10^{-6}$ cm^2/s, leading to negative contribution to the conductivity [**Figure** 5.8(b)]. Given that the negative distinct correlation of a proton may arise through the rotation of PA molecules, we calculated the distinct correlation function of the proton displacement vectors from the same PA molecule and the results show that the distinct diffusivity of protons from the same PA molecule are very small with a positive value (see **Figure** A.3), suggesting that the translational motion of PA molecules may contribute more to the distinct proton diffusivity than the rotation of PA molecules, and both are much slower than the proton self-diffusivity. Notably, the self-diffusion coefficient of protons is in good agreement with that obtained from the intermediate scattering function ($D_{ii}^{\text{self}} = 3.59 \times 10^{-6}$ cm^2/s). The anticorrelation between protons definitely gives rise to the suppression of the conductivity in pure PA at 400 K ($H^{-1} = 0.58$). This combination of experimental and simulation results suggests that correlated proton transfer events in PA and PA85 form a kind of backflow with total charge displacement lower than in the case of uncorrelated proton transfer. Based on these results, we speculate that a Grotthuss-like enhancement mechanism of conductivity is impossible in bulk liquid state, most likely because of the requirement for momentum conservation.

5.3 Proton Transport in Aqueous Acids

5.3.1 Distribution of Protonated Species

AIMD simulations explicitly allow for the breaking and forming of covalent bonds, leading to an equilibrium distribution of the various protonated/deprotonated states of the acid and water molecules. In order to identify the protonated species in these systems, each hydrogen atom is assigned to its nearest particular oxygen atom. Oxygen atoms associated with two hydrogen atoms are identified as a water oxygen, $\mathrm{O_W}$, while oxygen atoms with three assigned hydrogen atoms are treated as hydronium ions denoted by $\mathrm{O^*}$. Similarly, the oxygen atoms belonging to the acid molecules are denoted as $\mathrm{O_A}$. The fraction of water and acid molecules in their various states of protonation were calculated and the results collected in **Table** 5.3.

Table 5.3. Computed fractions (%) of acid and water molecules in their different states of protonation in the studied aqueous acid systems.

Species	$H_4PO_4^+$/ $H_3SO_4^+$/ $H_2NO_3^+$	H_3PO_4/ H_2SO_4/ HNO_3	$H_2PO_4^-$/ HSO_4^-/ NO_3^-	HPO_4^{2-}/ SO_4^{2-}	H_3O^+	H_2O
PA1H	5.6	81.5	12.8	0.06	7.3	92.7
PA3H	2.3	81.9	15.7	0.05	4.5	95.5
SA1H	0.03	46.7	53.0	0.26	53.5	46.5
SA3H	-	10.1	88.9	1.03	30.3	69.7
NA1H	-	88.3	11.7	-	11.7	88.3
NA3H	-	49.0	51.0	-	17.0	83.0

There is a small number of positively charged acidic species in the aqueous PA systems due to the similar proton affinity of PA and H_2O. For the strong acids, these species are negligible, but the water appears to trap protons as H_3O^+ ions, which may consequently retard the structural diffusion of the protons. The increase in the ratio of water to an acid has minimal influence on the neutral species in aqueous PA but significantly decreases the neutral species in aqueous SA and NA. Although SA is a strong acid, SA molecules tend to donate only one proton to the water molecules even when the ratio of water to acid is 3. It is worth noting that there are about 10% neutral species in the SA3H system, in contrast to the findings of a previous study[97] where the authors stated that all sulfuric acid molecules were dissociated although short-lived neutral sulfuric acid molecules were observed because the transiently shared protons are included. In contrast, the addition of water to PA gives rise to a slight increase in neutral phosphoric acid from 81.5 to 81.9% due to the reduction of self-dissociation of the PA molecules, suggesting that the self-dissociation of PA decreases with increasing water content. With respect to H_3O^+, there is a small number of H_3O^+ in the PA systems due to its weak acidity. However, most water molecules are protonated in the SA systems and an increase in water further promotes the dissociation of protons by SA even facilitating dissociation of a second proton. The significant fraction of H_3O^+ in the aqueous SA systems contributes to the high conductivity via vehicular diffusion. The acidity of NA is moderately strong, and leads to a significant increase in the proton dissociation from NA molecules with the addition of water (i.e., NA3H).

5.3.2 Structure of H-Bonds

The primary aim of this work is to provide insight into how the acid molecules affect the solvation structure of the protons and H_2O and elucidating proton transport mechanisms in terms of molecular structure and acidity. To this end, we start with exploring the structural properties of the hydrogen bonding. **Figure** 5.9 shows the OO radial distribution functions (RDFs) excluding the intra-molecular pairs for clarity. To gain additional insight into the compositions of the peaks, we decomposed the OO RDFs into three pairs: both oxygen atoms from water molecules denoted by O_WO_W; one oxygen from a water molecule and the other from an acid molecule denoted by O_WO_A; and both oxygen atoms from acid molecules denoted

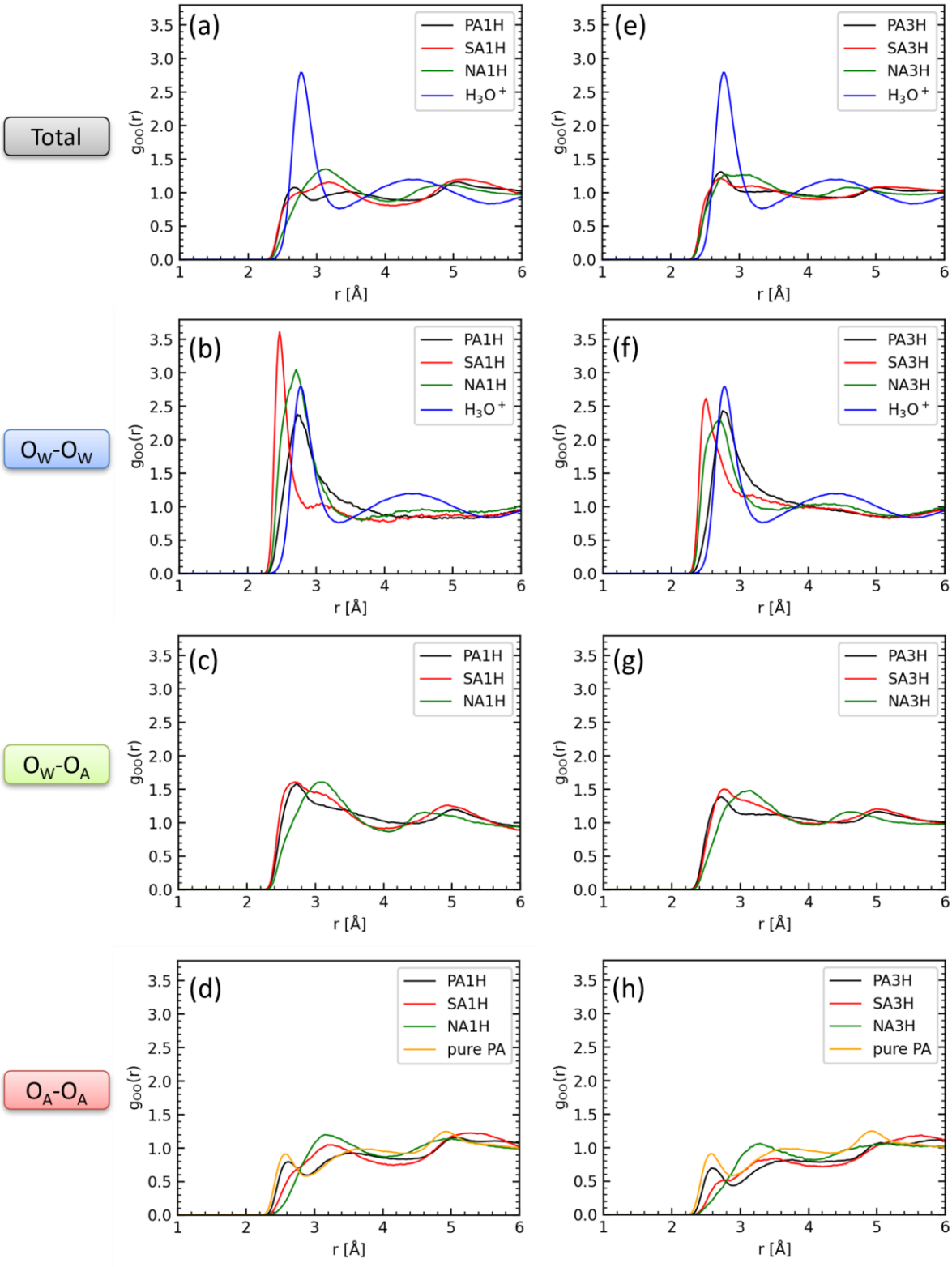

Figure 5.9. RDFs of OO pairs from different species: Total (a and e); both from water species (b and f); oxygen atoms of water and acid molecules (c and g); and oxygen atoms of acid molecules (d and h). The oxygen atoms from the same molecule are excluded for clarity.

by O_AO_A. Note that all oxygen atoms are not distinguished based on their protonation states, namely, the O_W includes neutral water and hydronium ion oxygen atoms. Compared to the OO RDF for the protonated water system, the first peak becomes weaker but shifts to shorter or longer distances to various extents. Specifically, the first peak is located at ~2.6 Å in the PA1H system while the first peak moves to 2.7 Å in PA3H which is identical to that in the protonated water system, indicating that the presence of water molecules at the ratio of 1:1 does not change the strong overall H-bonds but the addition of water molecules makes the overall H-bonds weaker.[77, 243] However, the corresponding peak for SA1H and NA1H systems is located at ~3.1 Å which is much longer than that in the protonated water system. Obviously, there is a shoulder on the left side of the peak in SA1H while the shoulder and the peak switch their roles in SA3H. A similar phenomenon occurs in the aqueous NA systems changing from a broad peak to two equivalent flat peaks.

In the aqueous acids, hydrogen bonds exist between the different species, leading to distinct local environments for the transfer of protons. **Figure** 5.9 (b-d) depict the OO RDFs of different species for the 1:1 aqueous acid systems. For the H-bonds between water species (including H_3O^+), the position of the first peak shifts to the left as the acidity increases, suggesting that there are more H_3O^+ ions in strong acids forming stronger H-bonds than between the water molecules. The H-bond between water and NA is the weakest while the H-bonds between water and PA or SA molecules are similar despite the difference in their acidities. The scenarios are different in the strong H-bonds between aqueous species and PA or SA molecules. In aqueous PA, the PA molecules donate protons to aqueous species (mainly H_2O) due to the high concentration of OH groups. SA molecules act as proton-acceptors in H-bonds with aqueous species (mainly H_3O^+) (see **Figure** A.4). It is commonly understood that neat PA has a high intrinsic proton conductivity because of the strong and polarizable H-bonds between the PA molecules.[77, 81, 82, 92, 94, 96, 254] **Figure** 5.9(d) shows that the position of the first peak is located at the shortest distance (2.62 Å) among these aqueous acids, implying that the strong H-bonds between the PA molecules are essentially not influenced by the presence of water molecules. Interestingly, the addition of water molecules alters the intensities of the first OO RDF peaks

but not the positions of the corresponding peaks [**Figure** 5.9(f-h)].

5.3.3 Solvation Structure of H_3O^+

Of particular interest is the influence of the acid on the solvation structure of the hydronium ions. For this purpose, we calculated the O^*O and O^*H RDFs for these aqueous acid systems as shown in **Figure** 5.10, in which O^* denotes the hydronium oxygen atoms, and O_W and O_A represent water and acid oxygen atoms, respectively. For comparison, the O_WO RDFs are also illustrated in **Figure** 5.11. As seen in **Figure** 5.11(a, d), the positions of the first peak for the three aqueous acids are similar but their intensities vary due to the different number of water molecules in these systems. The addition of water makes the difference in intensity smaller. The O^*H RDFs are shown in **Figure** 5.10(c and f), in which the first sharp peak clearly indicates the covalent bond OH, and the second one represents the H-bond that is consistent with the trend of the O^*O_W RDFs [**Figure** 5.10(a and d)]. It is worth noting that there is a small shoulder on the second peak of O^*H RDFs corresponding to the weak accepting H-bond of the H_3O^+ ions. A significant difference in the H-bonds appears in the pair of hydronium ion oxygen and acid oxygen atoms due to the various protonated states of the acid molecules. Specifically, the H-bond is stronger in the PA systems than in the other two aqueous acids partially because of the potent proton-donating capability of neat PA. In the aqueous SA and NA systems, there are two characteristic peaks related to the H-bond, which are located at identical positions but clearly possess distinct features. The first peak is dominant in aqueous SA while the second one is dominant in aqueous NA. The addition of water molecules weakens the difference between the two peaks in these two aqueous acids. These results clearly suggest that the H-bond structure is influenced by the acid molecules and the water content.

Figure 5.11 displays the RDFs of the water oxygen with other atoms from different molecular species. The position of the first peak of the O_WO_W RDFs is located at ~2.8 Å in good agreement with results from an X-ray diffraction measurements of 1.2 mol/L sulfuric acid solution at 20 °C,[255] indicating that the H-bonding between the water molecules is weaker than that between H_3O^+ and H_2O. This phenomenon is consistent with previous studies.[97, 113, 115, 256, 257] The acid has a very small influence on the hydrogen bonding between the water molecules.

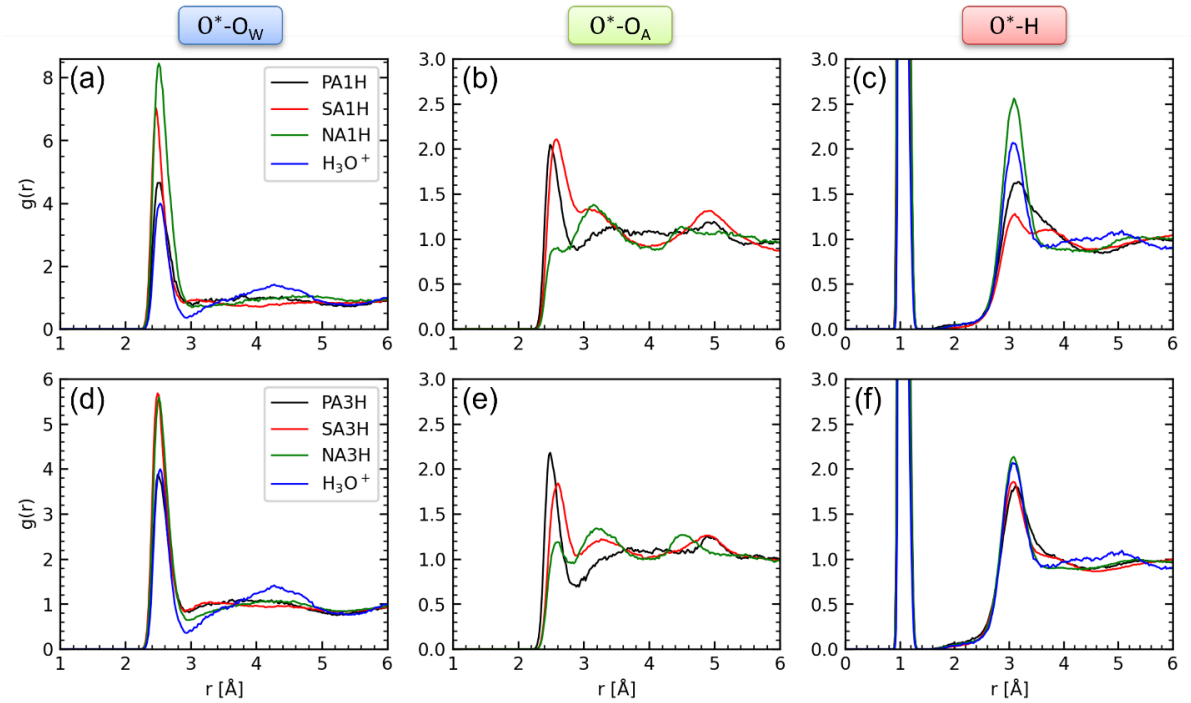

Figure 5.10. RDFs of O^* with other atoms: oxygen atom of water molecule (a and d); oxygen atom of acid molecule (b and e); and all hydrogen atom (c and f).

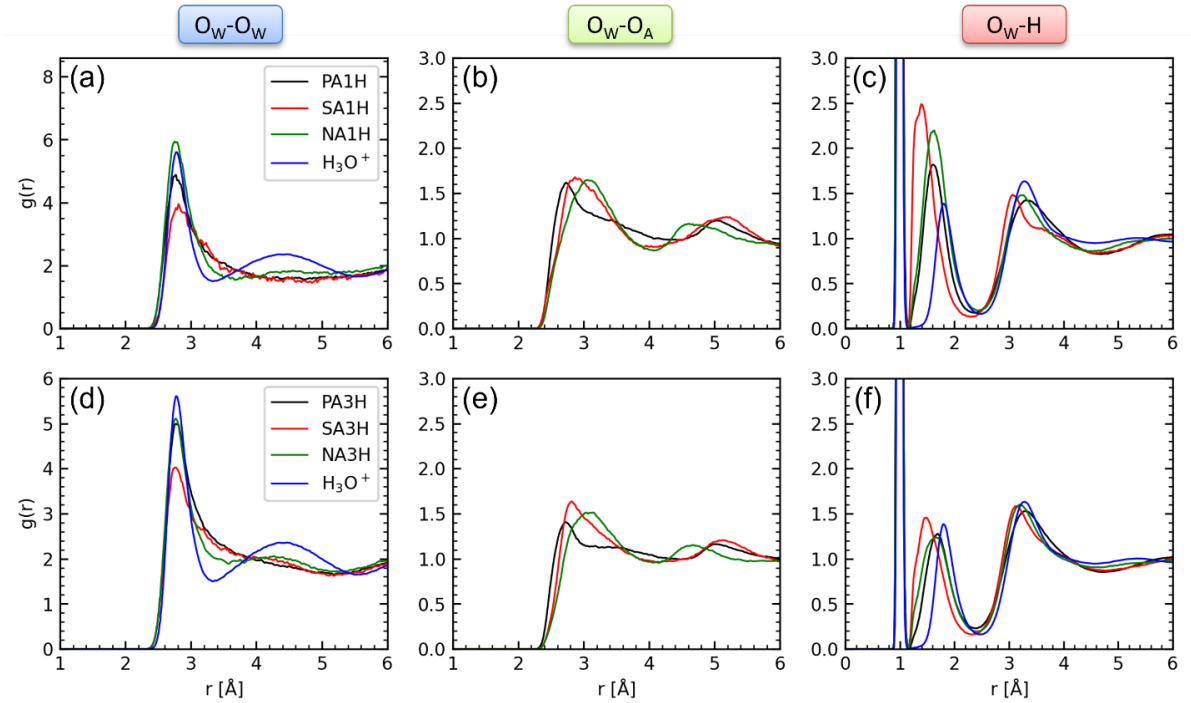

Figure 5.11. RDFs of the water oxygen atom with other atoms: oxygen atom of the water molecule (a and d); oxygen atom of the acid molecule (b and e); and all hydrogen atoms (c and f).

Figure 5.11(b and e) shows that the strength of the H-bonds between water and acid molecules is as follows: PA > SA > NA. It should be emphasized that this order is different from that of the acidity of these acid solutions (i.e., SA > NA >> PA). The first peak of the O_WH RDFs resembles that of the protonated water system where the covalent bonds in the water molecules are sharper than that of H_3O^+. However, the second peak moves a short distance to varying extents due to the number of H_3O^+ ions in the systems.

5.3.4 Solvation Patterns of H_3O^+ and H_2O

Proton transfer is significantly influenced by the solvation structure of H_3O^+ and neighboring H_2O.[33, 104, 115, 116, 258] To elucidate the local surrounding H-bond network of H^+(aq), probability distribution functions for the solvation pattern were calculated as the probability of finding a H_3O^+ or H_2O that donates *m* H-bonds and accepts *n* H-bonds (denoted as *m*D*n*A) according to the H-bond criteria: the distance between donating oxygen (O_d) and accepting oxygen (O_a) O_dO_a < 3.5 Å; the distance between accepting oxygen and donating hydrogen (H_d) O_aH_d < 2.5 Å; and the angle $\angle O_aO_dH_d$ < 30°. Furthermore, a reaction coordinate is defined as $\delta = |r(O_aH) - r(O_dH)|$ for proton transfer events occurring along the $O_a\cdots H - O_d$ H-bond. Previous studies[105, 118] revealed that H_3O^+ primarily forms three dynamic donating H-bonds with water or acid molecules in the first solvation shell, and one of the three H-bonds is stronger than the other two, referred to as the "special pair" (i.e., δ_{min}). The water molecule in this special pair, which acts as the proton acceptor, needs to adjust its coordination to readily receive the proton from a H_3O^+. These coordination fluctuations are the rate-limiting step for proton transport.[113-115] Therefore, it is also crucial to analyze the solvation pattern distribution for the H_2O in the special pair at the proton transfer transition state ($\delta_{min} < 0.1$ Å). The results are presented in **Table** 5.4 and **Table** 5.5 along with the representative solvation patterns for active H_3O^+ in these aqueous acid systems (**Figure** A.5).

In the slightly acidic water system, the solvation pattern of 3D0A is dominant (90.4%). This dominance of 3D0A is also evident in all the aqueous acid systems, albeit with varying percentages lower than in the acidic water system. At the proton transfer transition state, the prevalent solvation pattern for H_3O^+ remains 3D0A, although the population becomes lower.

Table 5.4. Probability distribution (%) of solvation patterns.

O*		**1D**	**2D**	**3D**	**4D**
PA1H	0A	0.09	8.86	85.54	0.26
	1A	0	0.29	4.96	0.01
PA3H	0A	0.07	7.28	83.56	0.2
	1A	0	0.46	8.4	0.01
SA1H	0A	0.36	14.09	83.31	0.62
	1A	0	0.17	1.44	0
SA3H	0A	0.08	7.4	87.74	0.32
	1A	0	0.27	4.18	0.02
NA1H	0A	0.13	9.27	84.55	2.09
	1A	0	0.26	3.62	0.07
NA3H	0A	0.03	5.38	86.16	1.64
	1A	0	0.24	6.45	0.08
H_3O^+	0A	0	1.09	90.44	0
	1A	0	0.09	8.37	0
O_W		**0D**	**1D**	**2D**	**3D**
PA1H	0A	0.16	0.5	0.47	0
	1A	2.96	19.28	29.76	0.32
	2A	1.33	13.07	31.43	0.27
	3A	0	0.11	0.32	0
PA3H	0A	0.29	1.05	0.89	0
	1A	2.63	18.13	29.41	0.25
	2A	1.28	13.27	30.94	0.24
	3A	0.03	0.4	1.18	0
SA1H	0A	0.07	0.12	0.11	0
	1A	3.81	25.92	41.6	0.63
	2A	1.05	8.27	18.06	0.31
	3A	0	0	0.03	0
SA3H	0A	0.11	0.39	0.36	0
	1A	2.27	19.58	41.01	0.48
	2A	0.88	9.59	24.72	0.26
	3A	0	0.08	0.23	0
NA1H	0A	0.17	0.54	0.38	0.01
	1A	4.77	23.26	26.46	0.83
	2A	2.28	15.61	24.57	0.8
	3A	0.02	0.11	0.18	0
NA3H	0A	0.18	0.82	0.71	0.02
	1A	2.54	18.54	32.68	0.93
	2A	1.14	12.33	28.38	0.82
	3A	0.02	0.21	0.67	0.02

Table 5.4. Continued.

O_W		0D	1D	2D	3D
H_3O^+	0A	0.08	0.41	0.45	0
	1A	0.65	7.59	16.73	0
	2A	0.48	12.18	54.82	0
	3A	0.01	0.68	5.71	0

Table 5.5. Probability distribution (%) of solvation patterns at $\delta_{min} <$ 0.1 Å.

O*		1D	2D	3D	4D
PA1H	0A	0.31	15.02	73.93	0.31
	1A	0	0.78	9.61	0.04
PA3H	0A	0.2	11.32	73.88	0.29
	1A	0	1.16	13.01	0.04
SA1H	0A	1.3	22.44	71.84	0.87
	1A	0.02	0.6	2.9	0.02
SA3H	0A	0.31	12.83	78.21	0.47
	1A	0	0.79	7.34	0.02
NA1H	0A	0.49	18.25	72.22	2.14
	1A	0	0.76	5.94	0.15
NA3H	0A	0.16	10.2	76.07	1.8
	1A	0	0.82	10.74	0.17
H_3O^+	0A	0	2.38	80.12	0
	1A	0	0.15	17.35	0
O_W^{1x}		0D	1D	2D	3D
PA1H	1A	0.43	16.96	68.93	0.54
	2A	0.02	1.46	11.52	0.02
PA3H	1A	0.34	14.33	70.81	0.25
	2A	0	1.52	12.41	0
SA1H	1A	1.76	25.96	66.02	0.79
	2A	0.04	1.17	4.27	0.04
SA3H	1A	0.56	15.81	73.15	0.57
	2A	0.03	1.21	8.6	0.04
NA1H	1A	1.15	22.37	67.82	1.77
	2A	0.06	1.18	5.55	0.07
NA3H	1A	0.36	13.01	70.83	1.88
	2A	0	1.12	12.51	0.17
H_3O^+	1A	0.07	3.48	73.62	0.07
	2A	0	0.35	22.33	0.02

Correspondingly, the special pair water exhibits the highest population of the 2D1A solvation pattern at the proton transfer transition state in all the systems we studied. This configuration corresponds to a Zundel ion, featuring two water molecules with the same solvation pattern (see **Table** 5.5). In this scenario, proton transfer occurs readily between the two water molecules with a very low energy barrier. These findings indicate that the dominate solvation pattern 3D0A of the H_3O^+ persists in the aqueous acids even at the transition state, when compared to its prevalence in acidic water. However, the solvation pattern distribution of H_2O is influenced by the presence of the acid molecules. Specifically, in acidic water, the dominant solvation configuration is 2D2A (54.8%), with 2D1A and 1D2A patterns having similar populations (16.7 and 12.2%, respectively). In the aqueous PA systems, the population of the 2D2A configuration remains the highest, but their values decrease to 31.4 and 30.9% in PA1H and PA3H, respectively. Nevertheless, as the acid strength increases, the highest population shifts from 2D2A to 2D1A, with the stronger acids favoring the dominance of the 2D1A solvation pattern. This trend is attributed to the reduced presence of water molecules in strong acid solutions and the steric hindrance imposed by the larger acid molecules, which hinders them from donating the second H-bond to H_2O. Interestingly, the active special pair water ($\delta_{\min} < 0.1$ Å) consistently exhibits the highest population of the 2D1A pattern in all systems. This suggests the occurrence of the Eigen-Zundel-Eigen (i.e., EZE) mechanism, even though the H_3O^+ ion forms three H-bonds with either water or acid molecules (i.e., an Eigen-like ion). For this Eigen-like ion, the special partner may involve acid molecules with various protonation states (see **Table** A.8).

5.3.5 Energetics of Proton Transfer

The H-bond structure between different molecular species has been discussed above. Proton transfer along the H-bonds is an elementary step in the structural diffusion of protons. Energy profiles, $A(\delta)$, provides energetics of proton transfer along the reaction coordinate δ, which may be defined as:

$$A(\delta) = -k_B T \ln P(\delta), \tag{5.6}$$

where k_B is the Boltzmann constant, and T is the absolute temperature. The reaction

coordinate is defined as $\delta = |r(O_aH) - r(O_dH)|$ for proton transfer events occurring along the H-bond: $O_a \cdots H - O_d$. $P(\delta)$ is the probability distribution of δ, which is affected by the proton donor-acceptor distance $R_{O_aO_d}$ (see **Figure** A.6). The computed free energy profiles for proton transfer are shown in **Figure** 5.12. Generally, the free energy profiles are symmetrical double-well shaped with barriers at $\delta = 0$. In the PA1H system, the energetic barrier for proton transfer from H_3O^+ to H_2O is ~1.1 kcal/mol while the barrier for proton transfer from an H_3O^+ ion to PA molecule is slightly lower (0.9 kcal/mol). Surprisingly, an increase in the number of water molecules per PA increases the barrier (1.2 kcal/mol) for proton transfer from H_3O^+ ion to H_2O but lowers the barrier (0.7 kcal/mol) for H_3O^+ to a PA molecule. The most probable δ values are almost identical (~0.48 Å). However, proton transfer barriers in proximity to PA molecules are much higher than those near H_3O^+ ions. It is interesting to note that the equilibrium distance for proton transfer between the PA molecules is ~0.65 Å which is similar to that in pure PA.[77] In the SA1H system, the proton transfer barrier from H_3O^+ to H_2O is the lowest amongst all aqueous acid systems (0.4 kcal/mol), while in the SA3H system, this energy barrier for proton transfer is ~0.8 kcal/mol which is twice as high as in the SA1H system. Moreover, there is a large penalty for transferring a proton back to the SA molecule from H_3O^+ due to the strong acidity of SA and weak basicity of HSO_4^-. The strong acidity of the SA molecules also gives rise to a very high barrier for proton transfer between the SA molecules. This phenomenon, not surprisingly, occurs in the aqueous NA systems although the NA is not as acidic as the SA. In addition, the aqueous NA system is the only one where the addition of water molecules slightly lowers the proton transfer barrier from H_3O^+ to H_2O.

5.3.6 Relaxation Time of H_3O^+

To elucidate the structural diffusion of the protons, it is important to estimate relaxation times, lifetimes, and reaction rates. Time-dependent population correlation functions have been extensively employed in a variety of systems.[58, 63, 66, 105, 106, 243, 259] Here the continuous correlation function for protons was calculated according to the following equation:

$$C_c(t) = \frac{\langle h(0) \cdot H(t) \rangle}{\langle h \rangle}, \tag{5.7}$$

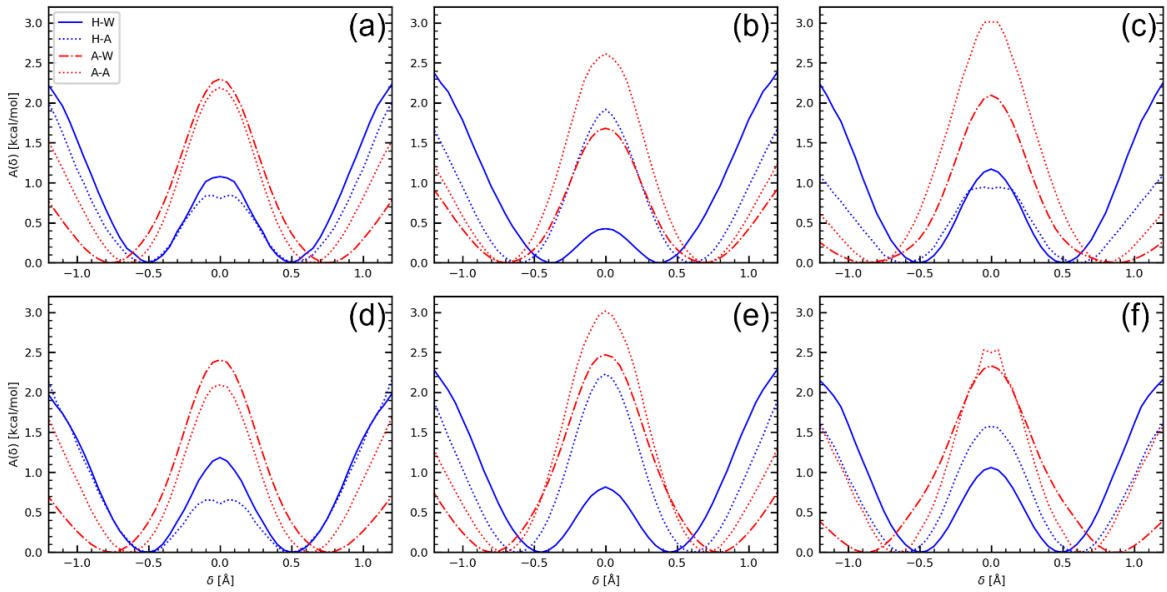

Figure 5.12. Energy profiles for proton transfer between different molecular species in (a) PA1H, (b) SA1H, (c) NA1H, (d) PA3H, (e) SA3H, and (f) NA3H.

where $h(0)$ and $H(t)$ are the indicators for the H_3O^+ at initial time $t = 0$ and t, respectively. If the targeted hydronium ion O* retains its identity during the period from time 0 to t, then $H(t) = 1$; otherwise, $H(t) = 0$. This "history-dependent" correlation function includes fast proton rattling and long-range proton diffusion behavior. Since proton rattling does not contribute to long-range diffusion, this process can be excluded by defining proton rattling as a proton transferring between two oxygen atoms without visiting a third oxygen atom. The relaxation time of these different time-scale events may be extracted by fitting the function to a bi-exponential function:

$$C_c(t) = a_1 exp\left[-\left(\frac{t}{\tau_1}\right)\right] + a_2 exp\left[-\left(\frac{t}{\tau_2}\right)\right], \tag{5.8}$$

where a_1 and a_2 are weighting factors satisfying $a_1 + a_2 = 1$, and τ_1 and τ_2 represent two separate relaxation times. The lifetime, τ_{exch}, of an H_3O^+ can be calculated with

$$\tau_{\text{exch}} = \int_0^\infty C_c(t)\, dt\,. \tag{5.9}$$

Figure 5.13(a) presents the continuous population correlation functions for H_3O^+ by including proton rattling. The continuous population correlation function including rattling for the six systems decays very quickly (~ 2 ps). In the aqueous strong acid systems, the hydronium ion has a long lifetime (**Table** 5.6), but the increase in water content makes it decay quickly. This may be because there are more acid molecules around the H_3O^+ in the 1:1 systems leading to a smaller probability for the hydronium ion to transfer a proton to a neighboring molecule. The addition of water molecules changes the local environment of the hydrated protons in which more water molecules coordinate with the H_3O^+ and the energetic penalty for proton transfer between an H_3O^+ ion and an H_2O is small as shown in **Figure** 5.12. However, in the weak aqueous PA systems, the barriers for a hydronium ion to transfer a proton to water or PA molecules are identically low, which gives rise to the fastest decay occurring in aqueous PA systems. The short lifetime caused by the fast rattling does not mean that the proton can transport fast via a 'Grotthuss' mechanism. Thus, the long timescale for proton diffusion is contained in the continuous population correlation functions excluding the rattling [**Figure** 5.13(b)]. In this case, the decay process becomes quite slow (beyond 30 ps for some systems).

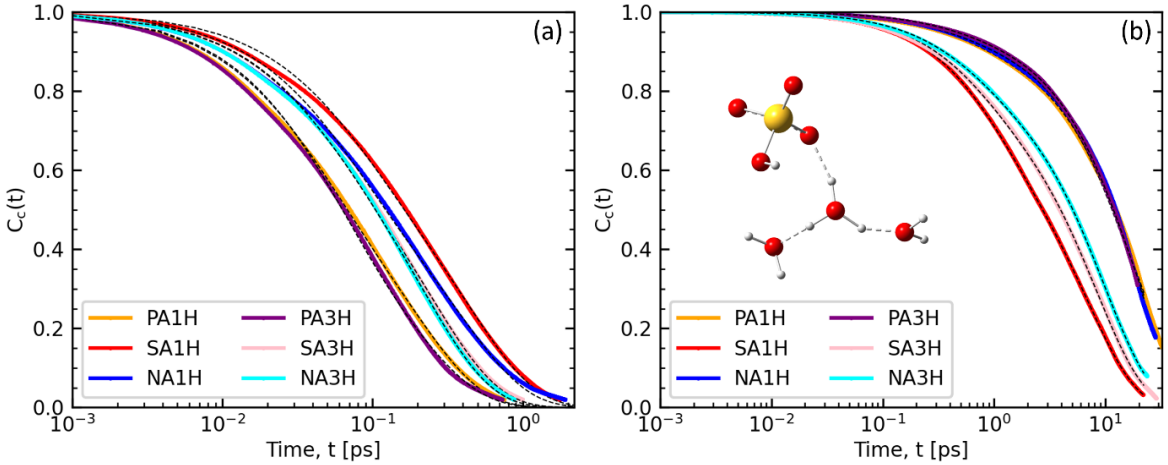

Figure 5.13. Continuous population correlation functions $C_c(t)$ for H_3O^+ at two conditions: (a) including proton rattling; and (b) excluding proton rattling.

Table 5.6. Calculated relaxation times (in ps) including and excluding rattling for hydronium ions in studied aqueous acid systems. The fitting results for the function excluding rattling are listed in parentheses.

	a_1	τ_1	τ_2	τ_{exch}
PA1H	0.37 (0.07)	0.034 (0.570)	0.198 (19.223)	0.138 (17.861)
PA3H	0.36 (0.04)	0.034 (0.458)	0.170 (18.139)	0.121 (17.396)
SA1H	0.33 (0.28)	0.068 (0.866)	0.455 (7.080)	0.328 (5.315)
SA3H	0.28 (0.20)	0.043 (0.655)	0.260 (8.309)	0.199 (6.809)
NA1H	0.39 (0.05)	0.059 (0.408)	0.401 (18.067)	0.268 (17.131)
NA3H	0.24 (0.15)	0.038 (0.587)	0.229 (9.690)	0.184 (8.288)

For the aqueous PA systems, the lifetime of H_3O^+ is the longest (around 17 ps) among the studied systems (see **Table** 5.6). It is surprising to note that the lifetime of H_3O^+ in NA1H is equally long as that in the aqueous PA systems. The reason for the long relaxation times in the three systems is likely different. In both aqueous PA systems, strong H-bonds trap the protons as H_3O^+, resulting in rapid rattling rather than effectively transferring to an adjacent molecule (~130 fs and ~17 ps for including and excluding rattling, respectively). Nevertheless, weak H-bonds and less coordinating water molecules give rise to the long lifetime of hydronium ions in NA1H when excluding rattling. This may lead to the dominant vehicular diffusion of protons in NA1H. An increase in the ratio of water to NA molecules significantly shortens the H_3O^+ lifetime, which may improve the structural diffusion of protons in NA3H. Interestingly, the opposite trend was observed in the aqueous SA systems. The relaxation time of H_3O^+ is very short in SA1H and the addition of water molecules slightly increases the relaxation time. This could be ascribed to a significant number of H_3O^+ in the aqueous SA systems and a further increase of dissociated protons may cause the "traffic jam" of proton in which there are less productive and forward proton transfers from the H_3O^+ to the water molecule.[122]

Based on the above discussion, we cannot clearly correlate the local environment and energy barriers for proton transfer around H_3O^+ to the long-range diffusion of the protons. It seems to be impossible for the aqueous PA systems to achieve high conductivity if protons are transported without the aid of PA molecules due to the long lifetime of H_3O^+ excluding rattling. To gain further insight into the dynamics of protons, we examine how an acid molecule plays a role in proton diffusion.

5.3.7 H^+ (aq.) Transport Mechanism

To glean the functionality of the acid molecules in the diffusion of the protons, we first verified the participation of the acid molecules in the actual diffusion. The RDFs of AO* are presented in **Figure** 5.14. The A represents the central acid atom in each system. Indeed, the first peaks are sharp and located at ~1.7 Å for the aqueous PA and SA systems, and ~1.4 Å for the aqueous NA systems, respectively. Such peaks correspond to A–H, in which the acid molecule accepts a proton from a neighboring H_3O^+, and their intensity indicates the relative time the proton

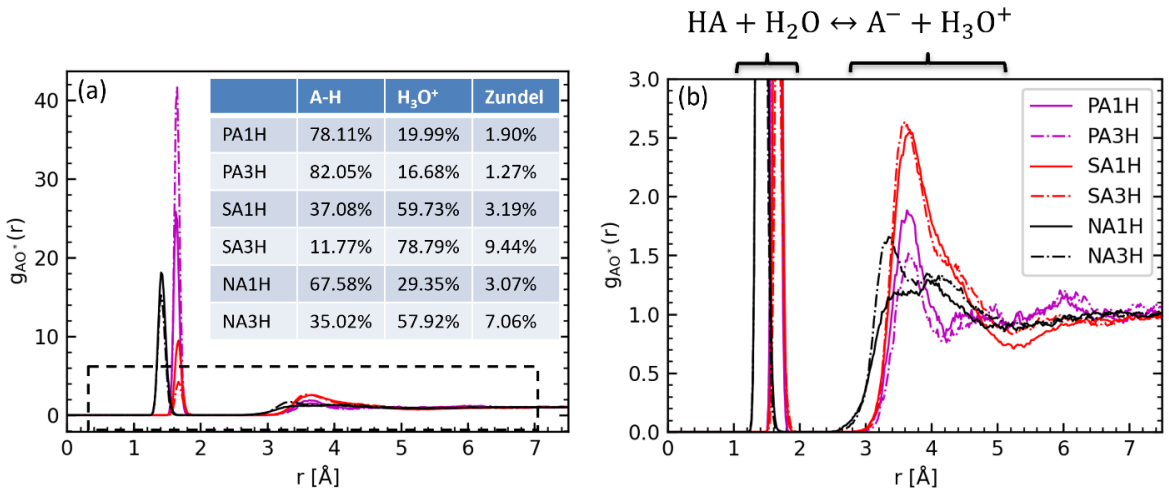

	A-H	H_3O^+	Zundel
PA1H	78.11%	19.99%	1.90%
PA3H	82.05%	16.68%	1.27%
SA1H	37.08%	59.73%	3.19%
SA3H	11.77%	78.79%	9.44%
NA1H	67.58%	29.35%	3.07%
NA3H	35.02%	57.92%	7.06%

Figure 5.14. (a) RDFs of the central atom of the acid with the oxygen of H_3O^+ for the aqueous acid systems. The inset lists the percentage time the proton spends as A-H, H_3O^+, or Zundel ions. (b) A close-up view of the second peak seen in (a).

remains with the acid molecule as shown in the inset of **Figure** 5.14(a). The second peak is broad, ranging from 3.0 to 4.0 Å, which refers to the state of A^- and H_3O^+ resulting in strong interaction between the ions. It is worth noting that the protonated states of the PA molecules are dynamic and exist more than $H_2PO_4^-$ anion (or neutral H_3PO_4), implying that the interaction between H_3O^+ and the acid molecule is different from that observed in the other two acids. These results suggest that the reaction: $HA + H_2O \leftrightarrow A^- + H_3O^+$ may play a key role in the diffusion of the protons. This phenomenon has been observed in AIMD simulations of a model PEM represented by graphane bilayers functionalized with SO_3^- at low hydration.[104, 124] Compared to the model PEM systems, the difference comes from the protonated states of the acid molecules. For example, in the aqueous PA systems, a neutral PA molecule accepts a proton from a neighboring H_3O^+ forming $H_4PO_4^+$ ion, thereby possessing four identical protons. This feature enriches the possibilities for a different proton (not the proton accepted from H_3O^+) to transfer to an adjacent water or another acid molecule. Obviously, these possibilities do not exist in the aqueous NA system because NA can have at most one proton.

Furthermore, we calculated the percentage of time the proton exists as A–H, H_3O^+, or $H_5O_2^+$. It is not surprising to observe that a proton appears in the A–H state for ~80% of the simulation time in the aqueous PA systems while this percentage decreases to ~37% in SA1H. Interestingly, the addition of water slightly increases the time percentage acting as A–H in aqueous PA systems, but significantly decreases the A–H time in the strong acid systems (~37 to ~12% for SA and ~68 to ~35% for NA, respectively).

These results motivated us to observe the protons in each system recording the coordinates of the H^+(aq), which can be readily used to calculate the mean squared displacement (MSD) of the proton. Note that for the transition state, the position of the shared proton as a Zundel ion is taken as the coordinate of the proton, and the central acid atom's position is recorded when the proton is covalently bonded to the acid molecule. The calculated MSDs of H_3O^+ and H_2O are presented in **Figure** A.7 and the diffusion coefficients are listed in **Table** 5.7. Water molecules diffuse only via a vehicular mechanism, which is governed by the hydrodynamics of the solution. The PA1H system has the lowest water diffusion coefficient but a very high H^+

Table 5.7. Diffusion coefficients of hydrated H^+ and H_2O (in $Å^2$/ps) and the computed conductivities of hydrated H^+ (in S/cm).

System	PA1H	PA3H	SA1H	SA3H	NA1H	NA3H	H_3O^+
$D_S^{O_W}$	0.030	0.109	0.042	0.068	0.153	0.165	0.134
$D_S^{O^*}$	1.40	2.18	0.31	0.29	0.22	0.28	0.77
$D_{\text{veh.}}^{O^*}$	0.043	0.089	0.054	0.119	0.145	0.159	0.177
$D_{\text{stru.}}^{O^*}$	1.408	1.908	0.291	0.303	0.112	0.249	0.586
$D_S^{O^*}/D_S^{O_W}$	46.7	20.0	7.4	4.3	1.4	1.7	4.9
$\sigma_{\text{NE}}^{O^*}$	0.426	0.823	0.790	0.840	0.143	0.504	0.102

diffusion coefficient. The increase in water content enhances the water diffusion by 3-fold (0.109 $Å^2/ps$ in PA3H vs. 0.03 $Å^2/ps$ in PA1H) but increases the proton diffusion by 50% (2.18 $Å^2/ps$ in PA3H vs. 1.4 $Å^2/ps$ in PA1H). These results suggest that structural diffusion dominates, and the water content has less influence on H^+ diffusion than on H_2O diffusion in aqueous PA. In aqueous SA, the diffusion of water increases with increasing water content while the diffusion of H^+ has the opposite trend. Aqueous NA has the highest water diffusion coefficient but the lowest H^+ diffusion coefficient, indicating that vehicular diffusion is the dominant contributor to the proton diffusion in aqueous NA. Compared to the proton diffusion in the slightly acidic water system, only the aqueous PA system has a higher H^+ diffusion. This clearly implies that PA enhances proton diffusion, but SA and NA impede the diffusion of protons.

To further glean insight into the mechanisms of proton transport, the MSDs were decomposed into continuous vehicular and discrete structural diffusion contributions as follows:

$$\Delta \boldsymbol{r}(t) = \Delta \boldsymbol{r}_{\mathrm{v}}(t) + \Delta \boldsymbol{r}_{\mathrm{s}}(t) \tag{5.10}$$

$$\langle |\Delta \boldsymbol{r}(t)|^2 \rangle = \langle |\Delta \boldsymbol{r}_{\mathrm{v}}(t)|^2 \rangle + \langle |\Delta \boldsymbol{r}_{\mathrm{s}}(t)|^2 \rangle + 2\langle \Delta \boldsymbol{r}_{\mathrm{v}}(t) \cdot \Delta \boldsymbol{r}_{\mathrm{s}}(t) \rangle \tag{5.11}$$

$$= \mathrm{MSD}_{\mathrm{v}} + \mathrm{MSD}_{\mathrm{s}} + 2\mathrm{Corr}\,, \tag{5.12}$$

where $\mathrm{MSD}_{\mathrm{v}}$ and $\mathrm{MSD}_{\mathrm{s}}$ are the vehicular and structural components, respectively. The term $\langle \Delta \boldsymbol{r}_{\mathrm{v}}(t) \cdot \Delta \boldsymbol{r}_{\mathrm{s}}(t) \rangle$ is the correlation between the two components in which the bracket denotes the ensemble average over all configurations. In the period from 0 to time *t*, all elementary displacements due to PT are accumulated in $\Delta \boldsymbol{r}_{\mathrm{s}}(t)$, and the remaining are accumulated in $\Delta \boldsymbol{r}_{\mathrm{v}}(t)$. The time window for the elementary displacement is set as the sampling time of 0.97 fs, which ensures that the structural component is not overestimated. We note that a large time window (i.e., 100 fs) was selected in prior studies.[33, 258]

Figure 5.15 and **Figure** A.8 display the decomposed MSDs including the vehicular and structural components along with the correlation term between these two components. As shown in **Figure** 5.15(a and d), the total diffusivity is mainly due to structural diffusion in the aqueous PA system. Interestingly, the correlation between the structural and vehicular components slightly fluctuates around 0, and this correlation becomes slightly positive after a

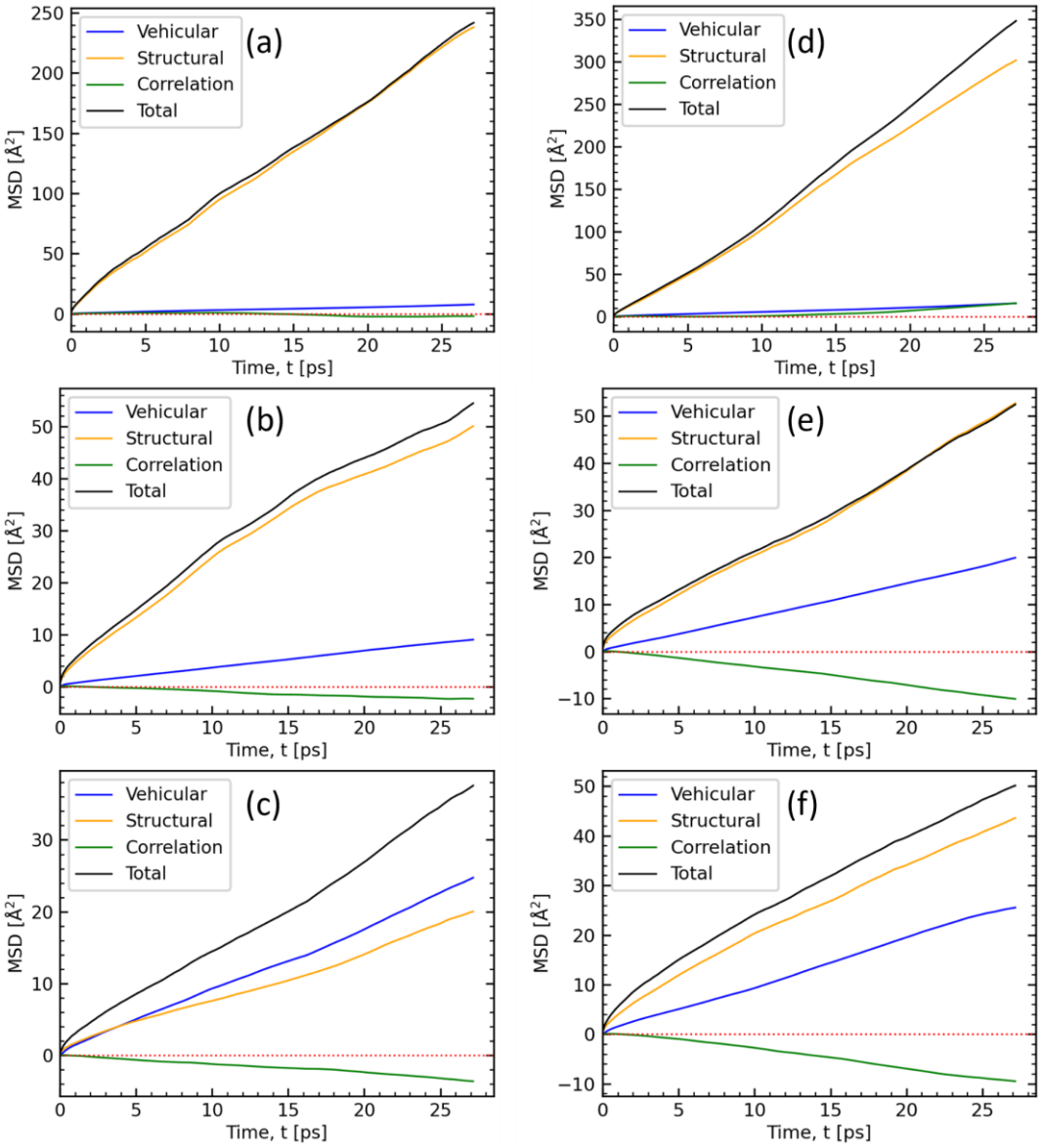

Figure 5.15. The mean squared displacement (MSD) of H_3O^+ decomposed into the continuous vehicular component; the discrete structural component; and the correlation between the two components in (a) PA1H; (b) SA1H; (c) NA1H; (d) PA3H; (e) SA3H; and (f) NA3H.

long time (> 15 ps) by increasing the water content (i.e., for PA3H). This may be ascribed to the participation of the PA molecule and the dynamic change of the protonated state of the neighboring PA molecules around the H_3O^+ although its state is generally as the neutral PA for most of the time. Meanwhile, the frustrated H-bond network facilitates the depolarization of the chain connecting two oppositely charged species. The conductivity of the PA1H system is mostly due to the displacement of protons, and may be calculated via the Nernst-Einstein (NE) relationship:

$$\sigma_{\mathrm{NE}}^{0^*} = \frac{\rho}{k_B T} z^2 D \,, \tag{5.13}$$

where ρ is the number density of H_3O^+, z the charge, and D the diffusion coefficient. The computed conductivity of PA1H is 0.426 S/cm in good agreement with the experimental conductivity, $\sigma_{\mathrm{exp}} = 0.43$ S/cm at 400 K.[94] Nevertheless, the estimated structural conductivity derived from experiments is lower than that due to vehicular transport,[94] in which the structural conductivity was approximately computed by subtracting the vehicular NE conductivity from the total measured conductivity. This trend is opposite to our results, which may arise from ignoring the distinct correlations between charge carriers in the vehicular diffusion. We note that the assumption of proton conductivity dominating the overall conductivity does not extend to the other aqueous acids.

However, the scenario is quite different in the strong acid solutions. In aqueous SA, there exists a theoretical possibility for the SA molecule to shuttle a proton for proton transport at a low ratio of water to acid, although the H_3O^+ prefers to transfer a proton to an adjacent water molecule rather than a strong acid molecule due to the lower energetic barrier for proton transfer from H_3O^+ to H_2O in comparison to H_3O^+ to an acid (**Figure** 5.12). This situation would be altered by adding additional water leading to less participation of SA molecules in the H^+(aq) transport since the water molecules form a connected H-bond network. That is one important reason for the observation that the structural diffusion slightly increases with increasing water content (from 0.291 $\text{Å}^2/\text{ps}$ in SA1H to 0.303 $\text{Å}^2/\text{ps}$ in SA3H). This analysis suggests that the maximum conductivity occurring as a function of the acid concentration may arise from a competition between the effective participation of acid molecules and the concentration of

dissociated protons. In addition, the structural and vehicular components are anticorrelated due to the interaction with the anion. As a proton moves away from the anion through proton transfer, vehicular diffusion has the potential to return it to the anion. Similarly, when the proton diffuses away from the anion via a vehicular mechanism, structural diffusion can counteract this movement by shuttling it back toward the anion. A similar anticorrelation between vehicular and structural diffusions was also observed in the AIMD and MS-EVB simulations of anion exchange membranes[33, 258] and the reactive MD and MS-EVB simulations of proton exchange membranes.[109, 125, 127] Nevertheless, this anticorrelation disappears in the slightly acidic water as shown in **Figure** A.9.

NA is of intermediate acidity (i.e., $pK_a = -1.4$) amongst these acids, and its molecular structure restricts its participation in proton transport. Indeed, vehicular diffusion is greater than structural diffusion in the NA1H system in part because the NA molecule appears to play a negative role in the transport of protons. This can be improved by increasing the water content to build up a connected H-bond network. As shown in **Figure** 5.15(c and f), the addition of water significantly enhances H^+ diffusion via structural diffusion over vehicular. Anticorrelation also occurs in the aqueous NA system and this anticorrelation is slightly stronger than that in the SA1H system although the anion concentration is lower in the NA1H system (see **Table** 5.3). This is because NA cannot as effectively participate in H^+ diffusion as SA does in the SA1H system to mitigate the interaction between H_3O^+ and the anions. This difference in the anticorrelation between aqueous NA and SA systems decreases as the water content increases see [**Figure** 5.15(e and f)].

Bearing that in mind, the acid molecule plays distinct roles in the diffusion of protons. Further insight into proton transport can be gained by accumulating the frequency of proton transfer events between the different species when following the H_3O^+. We classified proton transfer into three distinct types as follows: proton transfer from H_3O^+ to H_2O (Type 1), between H_3O^+ and an acid molecule (Type 2), and between acid molecules (Type 3). As shown in **Figure** 5.16, the frequency for Type 1 is about half of that for the other two types in the PA1H system, suggesting that the PA molecule accepting a proton from H_3O^+ may pass another proton to

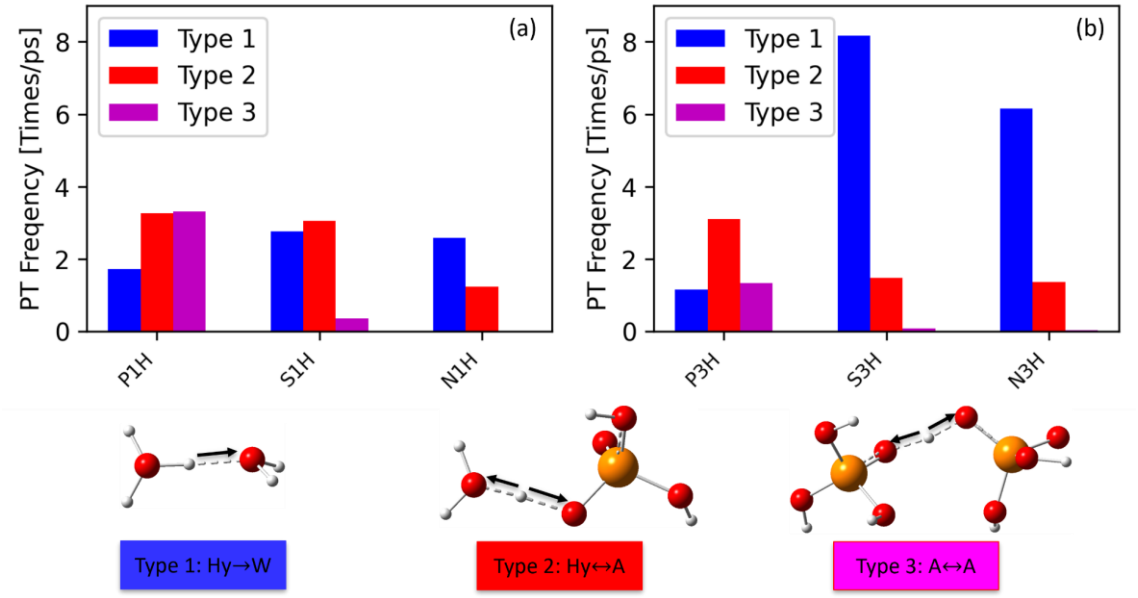

Figure 5.16. The average occurrence times per picosecond for three types of proton transfer as defined at the bottom: proton transfer from hydronium ion to water; from hydronium ion to acid molecule; and between acid molecules in the (a) 1:1 systems, and (b) 1:3 systems.

another water or a PA molecule due to the similar proton affinity between PA and H_2O. However, the frequency for Type 1 increases to that for Type 2 in the SA1H system in contrast to Type 3 events that rarely occur. This indicates that the SA molecule obtaining a proton from a H_3O^+ prefers to return the proton to the previous H_3O^+ rather than transfer a different proton to an SA molecule. In the NA1H system, Type 1 has an identical frequency as in the SA1H system, but the Type 2 has a relatively small frequency compared to the other two systems. This suggests that the NA molecule does not take an active part in the proton transport. The frequency for Type 1 significantly increases in the SA3H and NA3H systems but slightly decreases in the PA3H system when compared with the corresponding 1:1 systems leading to dominant structural diffusion through the H-bond formed by the water molecules. The addition of water molecules decreases the frequency for Type 2 in the aqueous SA system but has only a minimal effect on that for Type 2 in the aqueous NA system.

The frequency of these types of proton transfer events clearly indicates that the acid molecule plays a role in proton transport to varying extents. Remaining questions include: What roles does each acid molecule play in these aqueous systems? How do these acid molecules facilitate or impede proton transport? To shed light on these questions, we defined four functionalities of an acid molecule as shown in **Figure** 5.17. The first one is defined as rattling if the acid molecule accepting a H^+ from a H_3O^+ returns the proton to the H_3O^+; Type 2 is a relay event where the acid molecule obtaining a H^+ from a H_3O^+ and transfers it to another H_2O by rotating the covalent OH bond; Type 3 is a rotation event as the acid molecule accepting a H^+ from a H_3O^+ transfers a different H^+ to the water which was previously in the form of H_3O^+ by rotating its molecular structure; and Type 4 is the most efficient shuttling process in which the acid molecule receives a proton from H_3O^+ and transfers another proton to a different water molecule, resulting in a large charge displacement. Notice that Type 4 also includes the case where proton transfer events occur via a collective H-bonding formed by several acid molecules before transferring to form a new H_3O^+. This collective proton transfer over several PA molecules was observed in AIMD simulations of pure PA.[77] The occurrence probability for these functionalities was calculated and is shown in **Figure** 5.17. Obviously, most acid

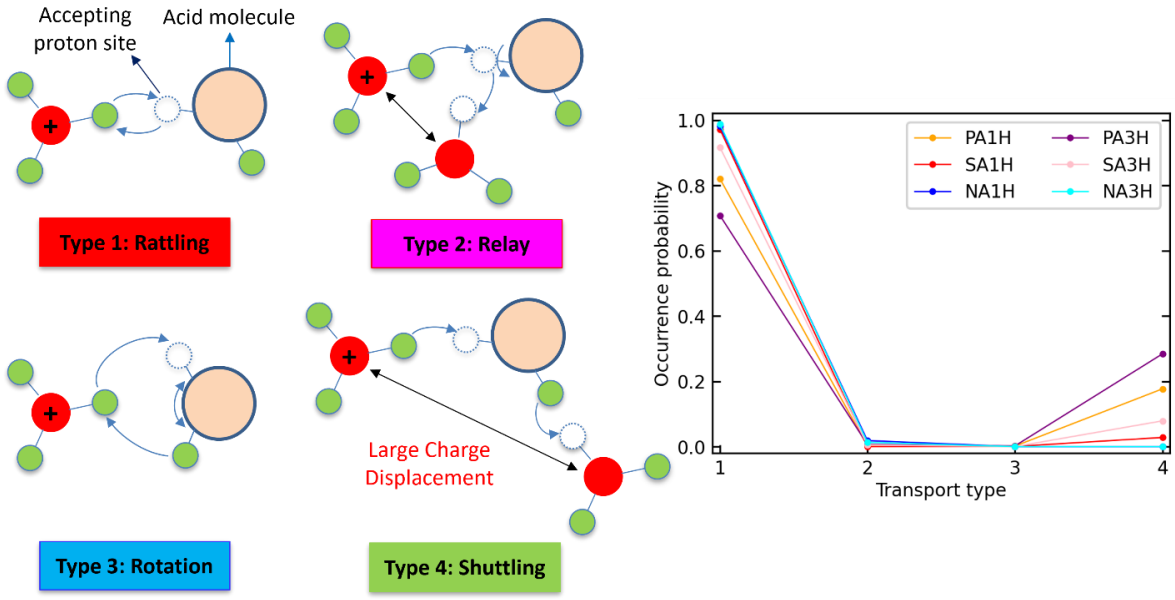

Figure 5.17. The occurrence probability for the distinct types of the acid functionality as defined on the left: Type 1: the acid molecule accepts the dissociated proton returns the proton; Type 2: the acid molecule accepts the dissociated proton and then passes the proton to a different water molecule; Type 3: the acid molecule accepts the dissociated proton and then passes another proton to the water molecule by rotating OH bond; and Type 4: the acid molecule accepts the dissociated proton and then passes a different proton to another water molecule.

molecules just accept a proton and transfer the proton back (above 70 %), which thereby does not contribute to proton diffusion. A very small fraction of the acid molecules plays a relay role for H^+ transport. The rotation functionality of the acid molecules is negligible since the molecular rotation happens on a large timescale that exceeds the length of the simulations. Efficient shuttling events occur in aqueous PA and SA systems. The order of the fraction of shuttling is as follows: PA3H > PA1H > SA3H > SA1H, which is consistent with the structural diffusion of protons in these systems (**Table** 5.7). Since NA is a monoprotic acid, the NA molecule does not act as a shuttle for H^+ transport.

Chapter 6 Ionic Correlations in Ionic Liquids

This chapter is adapted from portions of the following publication:[260]

- Ahmed, M. D; Zhu, Z; Khamzin, A; Paddison, S. J; Sokolov, A. P; Popov, I., Effect of Ion Mass on Dynamic Correlations in Ionic Liquids. *The Journal of Physical Chemistry B* **2023,** *127*, 10411-10421.

This chapter focuses on the dynamic correlations in ionic liquids (ILs), which significantly influence their ionic conductivity. Classical molecular dynamics (MD) simulations were performed on a series of IL systems composed of the same cation, 1-butyl-3-methylimidazolium [BMIM] ($M_+ \approx 139$ g/mol), but different anions: bis(trifluoromethane) sulfonimide ([TFSI], $M_- \approx 280$ g/mol), [PF_6] ($M_- \approx 145$ g/mol), [BF_4] ($M_- \approx 87$ g/mol), and [Br] ($M_- \approx 80$ g/mol). These simulations explored the impact of ion mass on ion-ion correlations. The results confirm the validity of the momentum conservation approach to evaluate the contributions of distinct ion-ion correlations from broadband dielectric spectroscopy (BDS) data. Furthermore, we extended the study to examine the effects of the alkyl tail length of the imidazolium ring on ion-ion correlations by modifying the two tails of imidazolium $[C_mC_nIM]^+$ (m = 1 and 2; n = 1 – 8).

6.1 Simulations

Classical MD simulations were performed for a variety of molecular BMIM-based ILs. Each system consisted of 500 pairs of ions, providing an optimal balance between statistical reliability and computational efficiency.[144, 145, 246, 247] The methodology was established by using the generalized AMBER force field (GAFF) utilizing a previously employed protocol.[162, 246, 247, 261] Partial charges on all atoms were determined with the Restrained Electrostatic Potential (RESP) algorithm[262] based on the optimized electronic structures of the isolated cation or anion. These calculations were carried out at the Hartree-Fock HF/6-31g(d) level of theory using the GAUSSIAN 09 package.[224] The computed atomic partial charges were scaled by a factor of 0.8 to account for polarization and charge transfer, which has been proven to be an efficient and reliable approach in ion-containing systems.[36, 247, 263] A cutoff distance of 14 Å was used for the electrostatic and Lennard-Jones interactions, with long-range corrections

handled by the particle mesh Ewald (PME) method and appropriate tail corrections, respectively. The initial systems were equilibrated for over 50 ns within the NPT ensemble, following a ~30 ns annealing process using the GROMACS code.[244, 245] Following an additional 30 ns equilibration under the NVT ensemble, a trajectory of 100 ns was collected every 1 ps. This length of trajectory ensured reliable ion-ion correlations in these IL systems.[4, 264] Temperature and pressure were controlled by the Bussi thermostat[265] and the Parrinello-Rahman barostat[266] with coupling times of 0.5 and 5 ps, respectively. The MD simulations for all the IL systems were conducted in a periodic cubic box with a time step of 2 fs. To assess the accuracy of the force fields applied to these systems, we compared the simulation and experimental densities as illustrated in **Figure** 6.1. The density of [BMIM][TFSI] closely matches the experimental data. While the densities of the other two systems are slightly lower than the experimental values,[267, 268] they still exhibit favorable agreement. Moreover, distinct correlations are susceptible to statistical uncertainty. All dynamic correlations were compiled from 4 – 6 trajectories to provide average values, along with their standard deviations.

6.2 Effect of Ion Mass Ratio

Atomistic MD simulations of several commonly used BMIM-based ILs provide the spatial and temporal correlations between ions. Radial distribution functions (RDFs) for the centers of mass of cations and anions were calculated at 360 K, as shown in **Figure** 6.2. The first peak of the cation-anion RDFs shifts to longer distances with increasing anion size, following the order: [Br] < [BF_4] < [PF_6] < [TFSI]. The first shell of cations surrounded by anions is located at 7.4 for [Br], 8.0 for [BF_4], 8.5 for [PF_6], and 9.0 Å for [TFSI]. The coordination number (CN), indicated by the dashed vertical lines, shows that the CN for [Br] is 6.2, smaller than that of the other three large anions (~ 6.5). This suggests a strong repulsive interaction between the small [Br] anions.

To further elucidate the distributions of anions around cations and cations around anions, spatial distribution functions (SDFs) are presented in **Figure** 6.3. The surface at the isovalue of 10 nm^{-3} demonstrates that anions preferentially occupy positions above and below the imidazolium ring, generally close to the top carbon, while the zone near the nonpolar alkyl tails

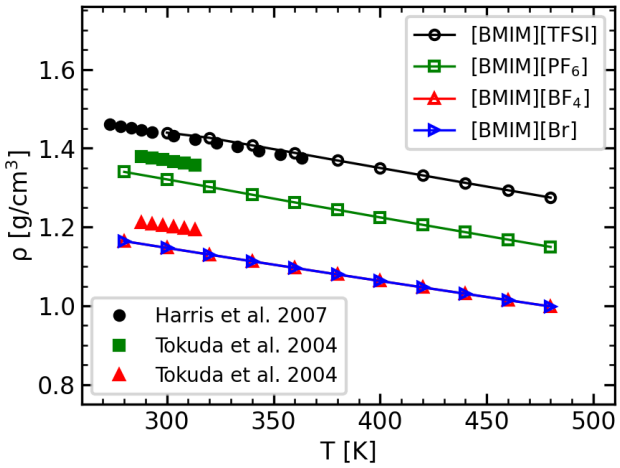

Figure 6.1. Comparison of simulated (open symbols) and experimental (filled symbols) (Refs.[267, 268]) densities of [BMIM] [TFSI], [BMIM][PF_6], [BMIM][BF_4], and [BMIM][Br] ILs as a function of temperature. The densities from our simulations are in good agreement with experimental ones over the entire temperature range.

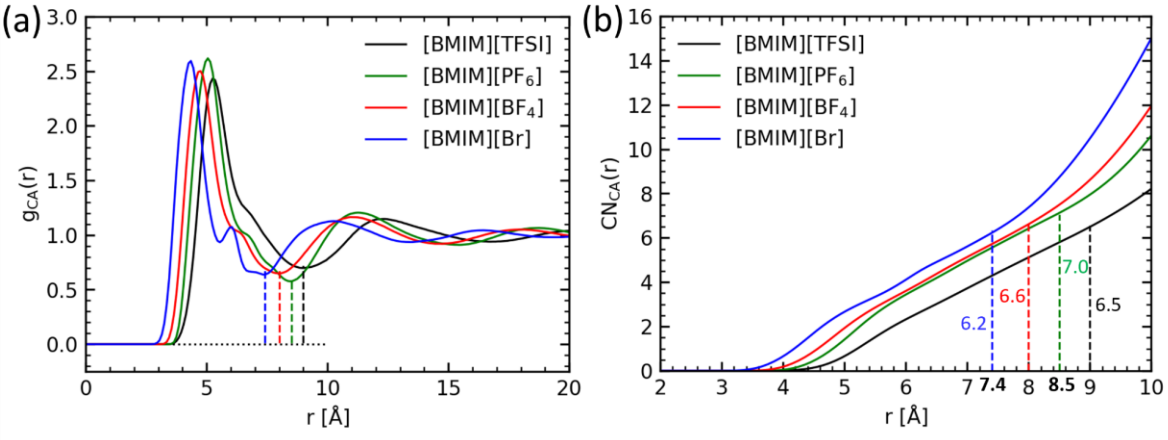

Figure 6.2. (a) Radial distribution functions of centers of mass of cations and anions in four BMIM-based ILs. (b) Coordination number functions of centers of mass of cations and anions in four BMIM-based ILs.

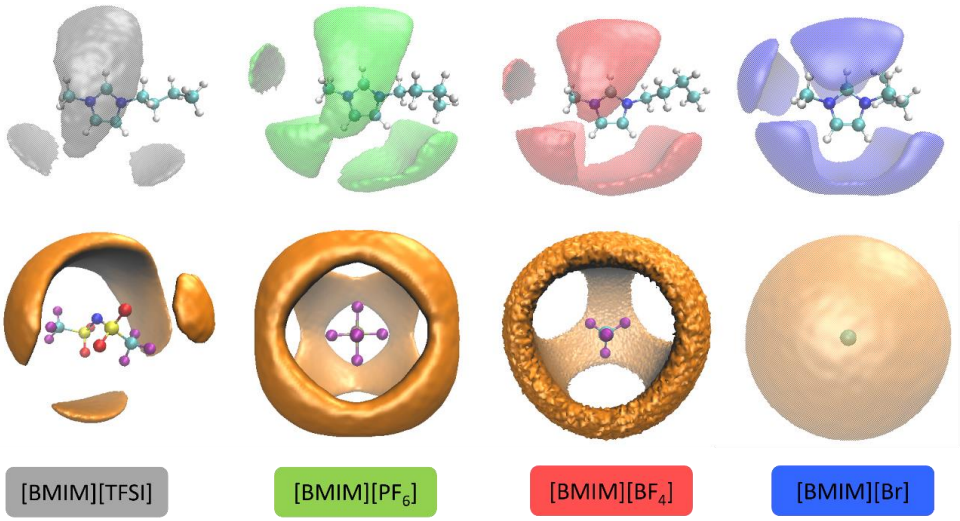

Figure 6.3. Spatial distribution functions of anions around the [BMIM] cation (top) and the [BMIM] cation around three anions (bottom). The SDFs were computed using TRAVIS program[269] and visualized by VMD program.[270] The contour surfaces are shown at the isovalues of 10 and 6 nm^{-3} for the top and bottom ones, respectively.

remains vacant (**Figure** 6.3 top). This creates a preferential direction for the movement of the cation. In addition, the surfaces become larger as the anion size decreases. On the contrary, the SDFs of the [BMIM] cation around the anions reveal that the cations distribute around the anions in a symmetric and well-ordered manner, especially noticeable for the [PF_6], [BF_4], and [Br] anions, forming an octahedron for [PF_6], a tetrahedron for [BF_4], and a sphere for [Br], respectively, as depicted in the bottom panel of **Figure** 6.3. The imbalance in the anion distribution around the methyl and butyl groups makes the diffusion of the imidazole ring directional, leading to a higher diffusion coefficient of the cations than for the anions in all these systems, as discussed below.

Our MD simulations also reveal heterogeneity of the nonpolar domains [**Figure** 6.4(a-f)], which can be quantified by RDFs of tail-tail. Indeed, **Figure** 6.4(g) shows that the first peaks of tail-tail RDFs are intense in all systems, indicating aggregation of the tail groups. Interestingly, the anion has minimal influence on the clustering of these nonpolar domains, represented by the tail groups of the imidazolium ring. However, increasing the tail length from C_4 to C_8 significantly promotes the aggregation of nonpolar domains [**Figure** 6.4(c and f)]. This trend was also observed in coarse-grained modeling of [C_xMIM][NO_3] (x = 1, 2, 3, 4, 6, and 8) systems.[271]

Of particular interest is the effect of anions on the dynamics in these systems. Self-diffusion coefficients were calculated using the Einstein relation for four IL systems at different temperatures, as shown in **Figure** 6.5. The results demonstrate that the cation has a higher self-diffusivity than its counterpart anion, despite the cation being larger than the anion. This behavior can be attributed to the preferential translational motion of the cation along the plane of the ring, as suggested by the SDFs. The self-diffusivity of the cation decreases as the anion size increases, except for [BMIM][Br], which exhibits the smallest diffusivity due to strong electrostatic interactions. However, this difference diminishes at lower temperatures, particularly for the [BMIM][BF_4] and [BMIM][PF_6] systems [**Figure** 6.5(a)]. A similar trend is observed for the anions in these IL systems, as shown in **Figure** 6.5(b). This phenomenon can be rationalized by considering momentum conservation. The diffusivities of both cations

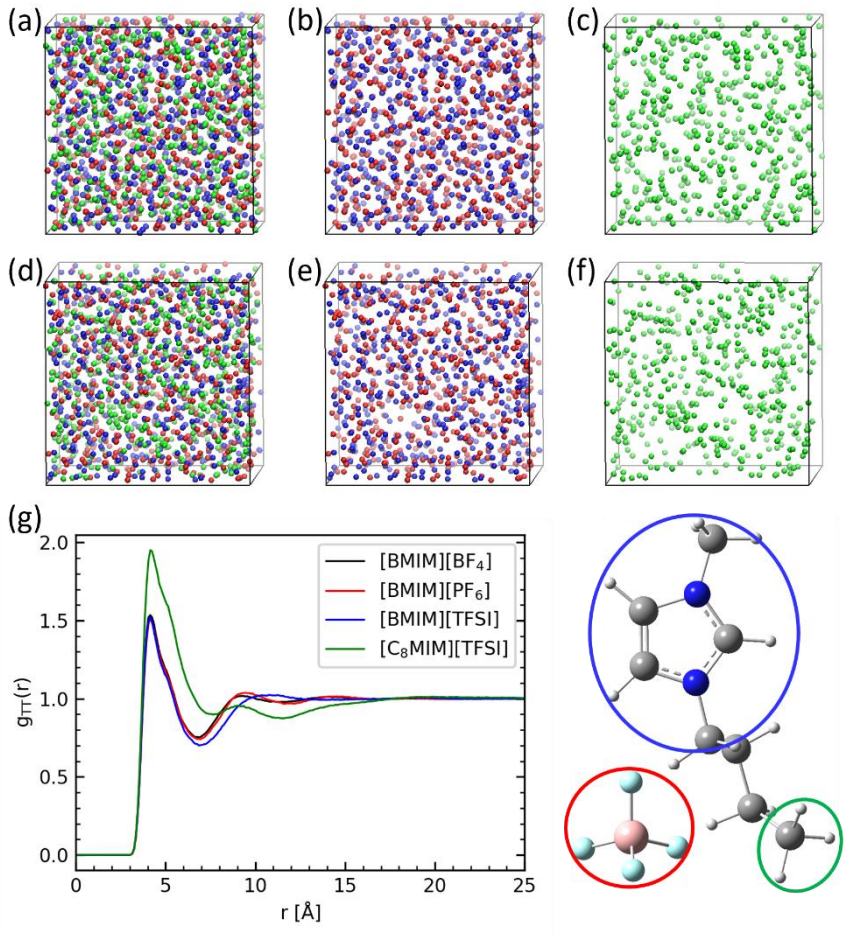

Figure 6.4. Snapshots of [BMIM][BF_4] at 400 K with (a) polar and nonpolar domains and tail groups; (b) polar domains only; and (c) tail groups only. The corresponding snapshots of [C_8MIM]][BF_4] at 400 K are illustrated in (d – f). The polar domain is composed of the imidazolium ring, the methyl and methylene groups and the anion. The tail groups represent the nonpolar domains. The center of mass of the heavy atoms in the circles is shown. (g) Radial distribution functions of tail-tail to quantitively charaterize the clustering of the tail groups. The anion has a minimal effect on the clustering of tail groups. However, the increase of the tail length significantly enhances the aggregation of tail groups.

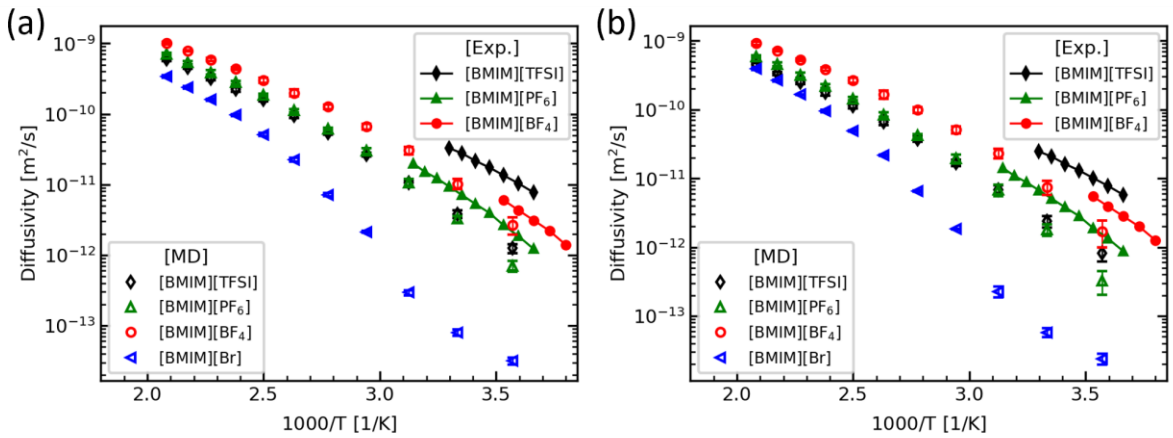

Figure 6.5. The self-diffusion coefficients of (a) cations and (b) anions of BMIM-based ILs as a function of temperature compared with the experimental data (closed symbols).

and anions increase with increasing temperature and their values align well with experimental data.

The conductivity of these IL systems is closely related to the self-diffusion coefficients of the ions and the distinct correlation contributions between them. These correlations play a crucial role in conductivity in ion-concentrated systems due to significant ion-ion interactions. **Figure** 6.6 presents the conductivity, including both self- and distinct- terms. Compared with experimental results, the conductivity obtained from MD simulations is slightly lower, especially for [TFSI], but overall, they exhibit a good agreement. Amongst the systems, [BMIM][Br] has the lowest conductivity, while [BMIM][BF_4] shows the highest.

In addition to conductivity, the inverse Haven ratio can be used to characterize the effect of distinct correlations between the ions. All ionic correlations were calculated, which allowed for the derivation of the inverse Haven ratio H^{-1} for these IL systems (**Figure** 6.7). The values of the inverse Haven ratio range from 0.5 to 0.8 with significant uncertainty, attributed to the negative distinct correlation contributions to the conductivity. Unexpectedly, the results do not show a strong temperature dependence. The average values of H^{-1} follow the order: [TFSI] > [BF_4] > [PF_6] > [Br].

The inverse Haven ratio $H^{-1} < 1$ in these ILs is a direct result of distinct ion-ion correlations. To elucidate the details of these correlations, we plotted the three distinct correlations (σ^{d}_{++}, σ^{d}_{--}, and σ_{+-}) normalized by σ_{NE} in **Figure** 6.8. The contribution of cation-anion correlation is positive, enhancing conductivity, while the movement of like-ions is anticorrelated, resulting in a negative contribution to conductivity. For $M_- > M_+$ ([BMIM][TFSI]), the magnitude of the distinct anion-anion correlation is larger than that of the distinct cation-cation correlation. However, when the molecular mass of the anion is less than that of cation ($M_- < M_+$) in [BMIM][BF_4] and [BMIM][Br], the magnitudes of distinct cation-cation and anion-anion correlations swap. Interestingly, in [BMIM][PF_6], where the cation and anion have similar masses, the cation-cation correlation is stronger than the anion-anion correlation. This phenomenon may be attributed to differences in the size and shape of the ions. The same trend was observed in experiments. This agreement justifies the use of simple momentum

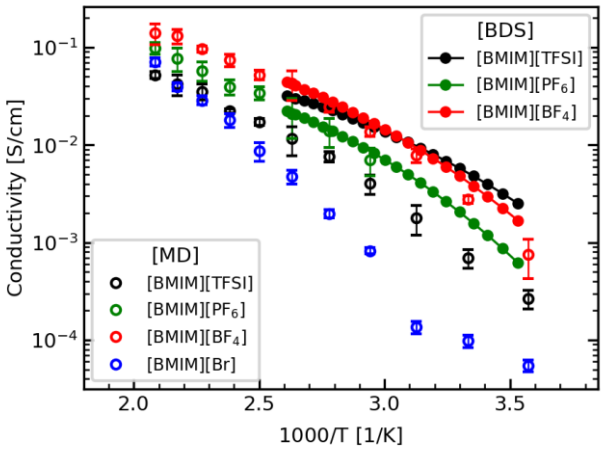

Figure 6.6. Temperature dependence of the DC conductivity obtained from the MD simulations and BDS experiments.

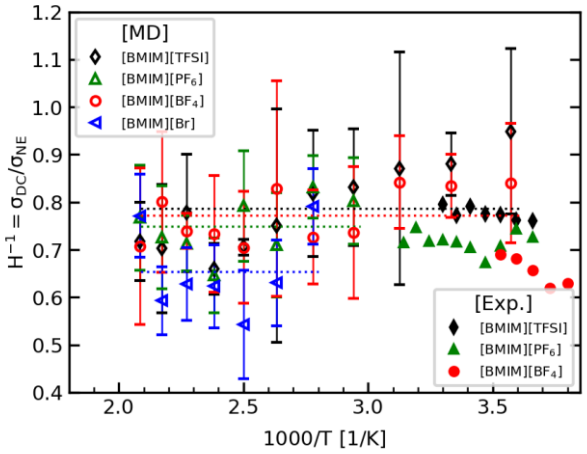

Figure 6.7. The inverse Haven ratio H^{-1} of [BMIM][TFSI], [BMIM][PF_6], [BMIM][BF_4], and [BMIM][Br] as a function of temperature compared with experimental data (closed symbols).

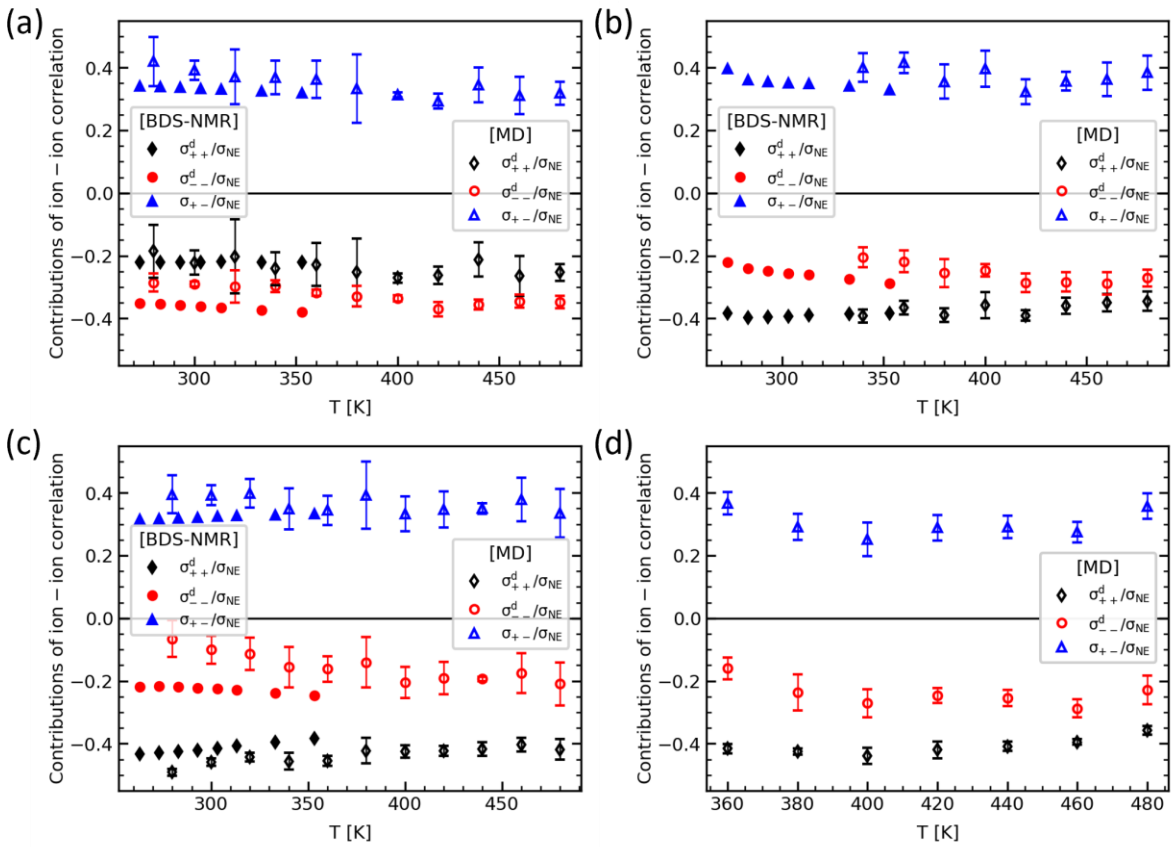

Figure 6.8. Contribution of distinct ion-ion correlations to conductivity normalized by σ_{NE} for: (a) [BMIM][TFSI]; (b) [BMIM][PF_6]; (c) [BMIM][BF_4]; and (d) [BMIM][Br] as a function of temperature compared with experimental data (closed symbols).

conservation to estimate distinct ion-ion correlations in IL systems.

To isolate the effect of the anion-to-cation ratio from other factors such as charge distribution and structure, we artificially varied the mass of [BF_4] in the MD simulations across a wide range of molecular weights, while retaining the same force field. As anticipated, the self-diffusivity of the anion decreases as the anion mass increases. A similar trend is observed for the cation [**Figure** 6.9(a)]. Notably, the self-diffusivity of the cation is consistently higher than that of the anion across all studied cases ($M_-/M_+ = 0.125 - 6.26$). This can be attributed to the geometry of the cation, which favors translational motion in the plane of the ring, which is shown in the SDFs of anions around the cation.[247, 272] This characteristic has been observed previously in both experimental and computational studies.[272-280] It is worth noting that the [BMIM] cation resides around the linear [TFSI] anion, contributing to the fast movement of the anion in [BMIM][TFSI] system, despite [TFSI] being heavier than the other two anions. However, this specific phenomenon was not captured in our simulations due to the limitations in the force field, which could not adequately represent the multiple conformations of the TFSI anion.[281] Not surprisingly, changes in anion mass have a negligible influence on the distribution of cations around anion and anions around cation as demonstrated in **Figure** 6.10, which implies that the changing of anion's mass does not affect the steric hindrance. This phenomenon elucidates why the [BMIM] cation exhibits faster diffusion than the anion across a wide range of anion-to-cation mass ratios [**Figure** 6.9(a)]. The relaxation time of ion-association increases with an increase in the mass of the anion (**Figure** 6.11). This suggests that heavier ions require more time to escape the cage formed by the oppositely charged ions.

We also examined the contributions of distinct ion-ion correlations, normalized by σ_{NE}, as a function of the anion-to-cation mass ratio [**Figure** 6.9(b)]. Our findings show that the movement of cations and anions is anticorrelated, leading to positively contribution to the conductivity, while the contributions of the distinct correlations between ions of the same charge are negative. Specifically, the negative contribution of distinct anion-anion correlation increases with the mass of the anion, whereas the distinct correlation of cation-cation shows the opposite trend. Additionally, all the distinct correlations change rapidly when the anion-to-

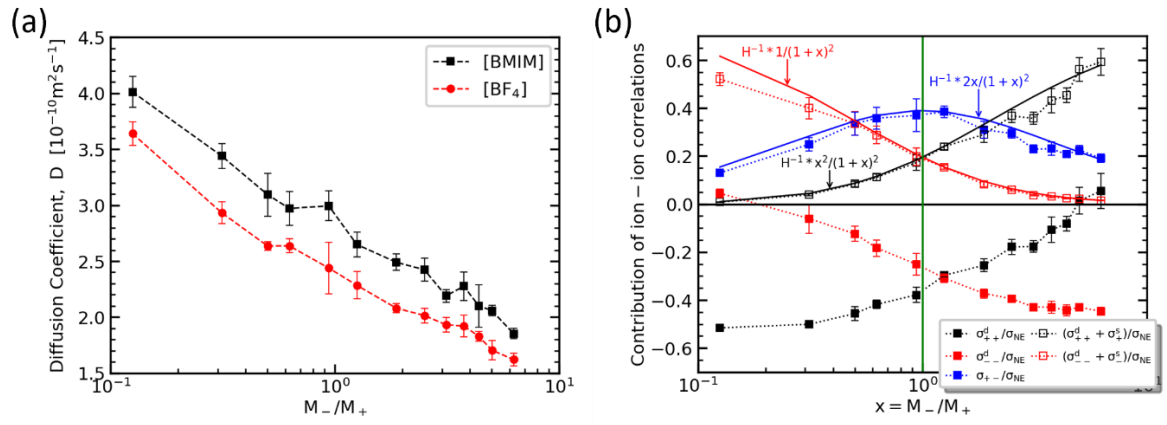

Figure 6.9. (a) The self-diffusion coefficient as a function of the anion-to-cation mass ratio, $x = M_-/M_+$, at 400 K obtained by MD simulations. (b) Contributions of distinct (closed symbols) and total (open symbols) ion-ion correlations to conductivity normalized by σ_{NE} of [BMIM][BF_4] ionic liquids as a function of the artificially changed anion-to-cation mass ratio, $x = M_-/M_+$, at 400 K. The green vertical line indicates the case in which the masses of anion and cation are equal. The solid lines present the theoretical prediction from the denoted equations, where we used $H^{-1} = 0.78$.

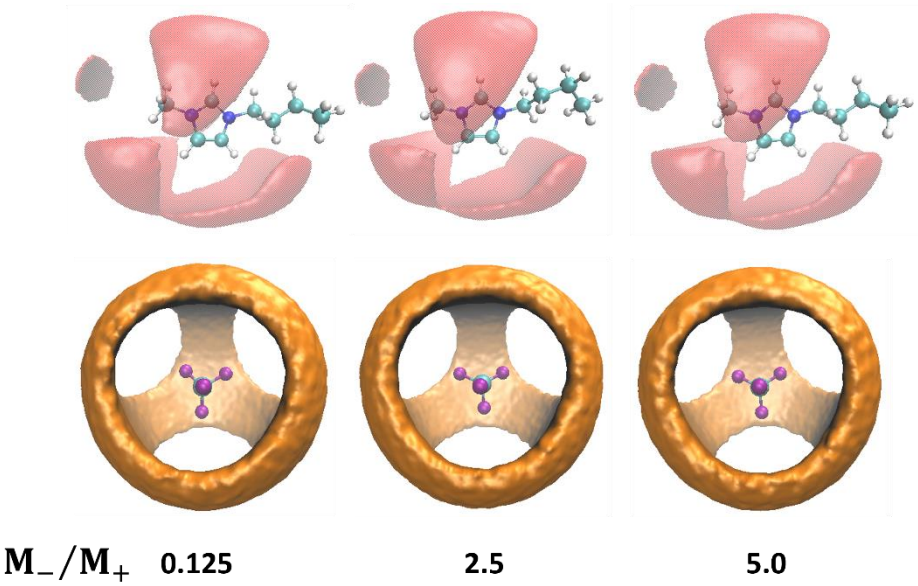

Figure 6.10. Spatial distribution functions of anions around the BMIM cation (top) and the BMIM cation around BF_4 anion (bottom) for [BMIM][BF_4] systems with artificially changed anion mass. The SDFs were computed using TRAVIS program[269] and visualized by VMD program.[270] The contour surfaces are shown at the isovalues of 10 nm^{-3} and 6 nm^{-3} for the top and bottom ones, respectively.

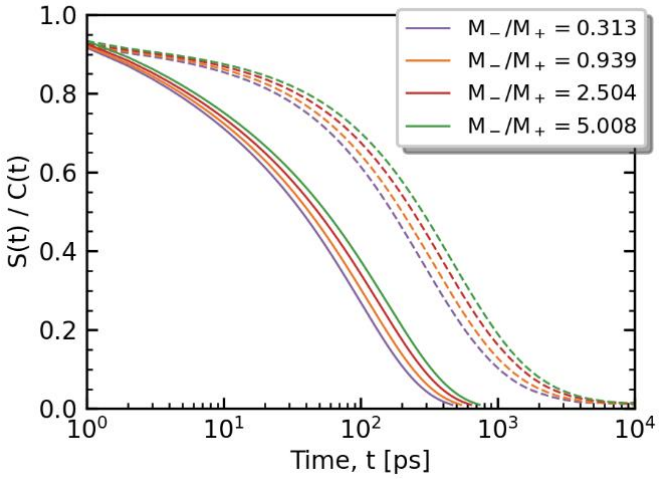

Figure 6.11. The continuous time correlation function, $S(t) = \langle H(t)h(0)\rangle/\langle h\rangle$, (solid), and the intermittent time correlation function, $C(t) = \langle h(t)h(0)\rangle/\langle h\rangle$, (dashed). $H(t)$ is assigned unity if an ion-association continuously retains from initial $t = 0$ to time t, while $h(t)$ is assigned unity if an ion-association occurs at time t. Ion-association is defined as the distance between cation and anion is within a cutoff of 8.0 Å that is the first local minimum of the cation and anion RDF. $S(t)$ provides insight into the average lifetime of the ion-association, while $C(t)$ reflects the relaxation behavior of all possible types of ion-associations including single ion-pairs, multiplets, and clusters.[144, 282]

cation mass ratio is very small or very large. This behavior aligns with the difference between the distinct like-charged ion correlations when the anion is lighter than the cation [**Figure** 6.8(c and d)] compared to the reverse situation [**Figure** 6.8(a)]. Notably, the distinct anion-anion correlation coincides with distinct cation-cation correlation when anion-to-cation mass ratio (M_-/M_+) equals 1.25, rather than when their masses are identical, as indicated by the green vertical line in **Figure** 6.9(b). This shift is consistent with the stronger negative σ^d_{++} than σ^d_{--} in [BMIM][PF_6] system with $M_+ \sim M_-$ [**Figure** 6.8(b)]. The shift in the crossing between the distinct ion correlations is related to the differences in the diffusivities of anion and cation, possibly due to the anisotropic movement of the cation compared to the isotropic diffusion of the anion as discussed above. When self-correlations are considered, we find that $\Delta_+^{total} = (\sigma_{++}^d + \sigma_+^s)/\sigma_{NE}$ and $\Delta_-^{total} = (\sigma_{--}^d + \sigma_-^s)/\sigma_{NE}$ switch exactly at $M_- = M_+$ [**Figure** 6.9(b)], in agreement with the Eqs.(2.35-37). Furthermore, these equations accurately predict how normalized cation-anion correlations $\sigma_{+-}^d/\sigma_{NE}$ and total contribution Δ_+^{total} and Δ_-^{total} depend on mass [solid lines in **Figure** 6.9(b)]. Interestingly, the distinct like-charged ion correlations shift from negative to slightly positive values as the anion-to-cation mass ratio is either sufficiently small or significantly large. The reason for this remains unclear. These findings conclusively demonstrate that disparities in anion and cation masses influence the magnitude of distinct correlations between ions. Remarkably, the sign of these contributions can change when the ion masses differ significantly. However, the results [**Figure** 6.9(b)] also suggest that the ion mass is not the sole factor influencing these correlations; the shape and/or size of the ion and their diffusion behavior also play significant roles.

6.3 Effect of Alkyl Tail Length of Imidazolium

The SDFs and dynamics of the [BMIM] cation present intriguing phenomena. One may pose the question: how the alkyl tails of the imidazolium ring affect dynamic correlations in IL systems. To shed light on this question, we adjusted the alkyl tail lengths of the imidazolium ring, denoted as [C_mC_nIM][TFSI] (m = 1 and 2; n = 1–8). **Figure** 6.12 illustrates the RDFs of the centers of mass of the cations and anions in these ILs at 400 K. The positions of the first peak range from 5.0 to 5.5 Å. The intensities of these peaks vary, with [C_1C_4IM] exhibiting the

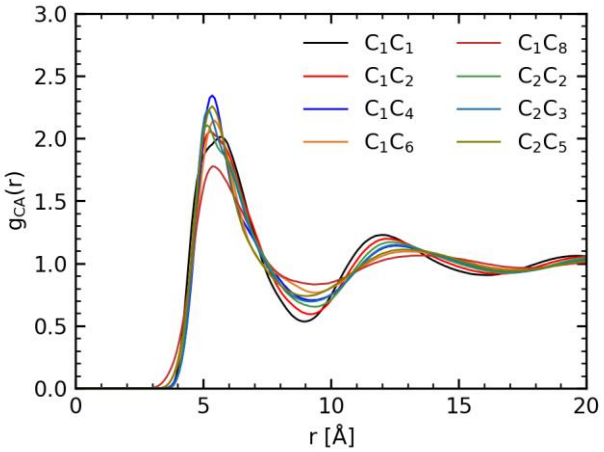

Figure 6.12. Radial distribution functions of center of mass of cations and anions in TFSI-based ILs at 400 K.

sharpest peak, indicating that alkyl tails moderately influence the interaction between the cations and anions. This is due to the steric hindrance and the decrease in total charge density of the cation with the addition of alkyl groups. These two factors are competitive: longer tails increase steric hindrance but also decrease the total charge density. This competition leads to a complex trend for the first peaks in these ILs. However, the second peak exhibits a consistent change: increasing the size of the cation ($m + n$) weakens the intensity but shifts the peak to a larger distance.

The computed diffusion coefficients of cations and anions in these ILs are presented in **Figure** 6.13(a). The cation consistently exhibits a larger diffusivity than the anion due to the preferentially directional motion of the imidazolium ring, although this difference diminishes as the cation size increases. For the [C_1C_nIM][TFSI] systems, the diffusivity of both the cation and the anion decreases with increasing tail length, except for the [C_1C_1IM][TFSI] system. A similar trend is observed in the [C_2C_nIM][TFSI] systems. Compared to [C_1C_2IM], the symmetrical [C_2C_2IM] has a greater diffusivity. This suggests that symmetrical shapes may facilitate the translational motion of the cation, but both tails need to be sufficiently long to make the motion directional. The conductivity of these systems follows the same trend as the diffusivity [**Figure** 6.13(b)].

The inverse Haven ration, H^{-1}, was also calculated and is shown in **Figure** 6.14. The values of H^{-1} lie in the range of 0.6 and 0.9 at 400 K. The largest value appears in the [C_2C_2IM][TFSI] system, followed by the [C_1C_2IM][TFSI] and [C_2C_3IM][TFSI] systems. The difference in the inverse Haven ration is small when the size of the cation is large ($m + n \geq 5$).

To reveal the mechanistic details of the distinct ion-ion correlations, the dynamic correlations between cations and anions (σ_{+-}), and like-ions (σ^{d}_{++} and σ^{d}_{--}) were evaluated directly from the MD simulations. The distinct contributions to conductivity, normalized by σ_{NE}, are plotted in **Figure** 6.15. In general, cation-anion correlations positively contribute to the conductivity, ranging from 0.25 to 0.4, while distinct like-ion correlations reduce the conductivity. Amongst the studied systems, the magnitude of the anion-anion correlations is consistently stronger than that of the cation-cation correlations. This difference, however, varies with changes in the tail

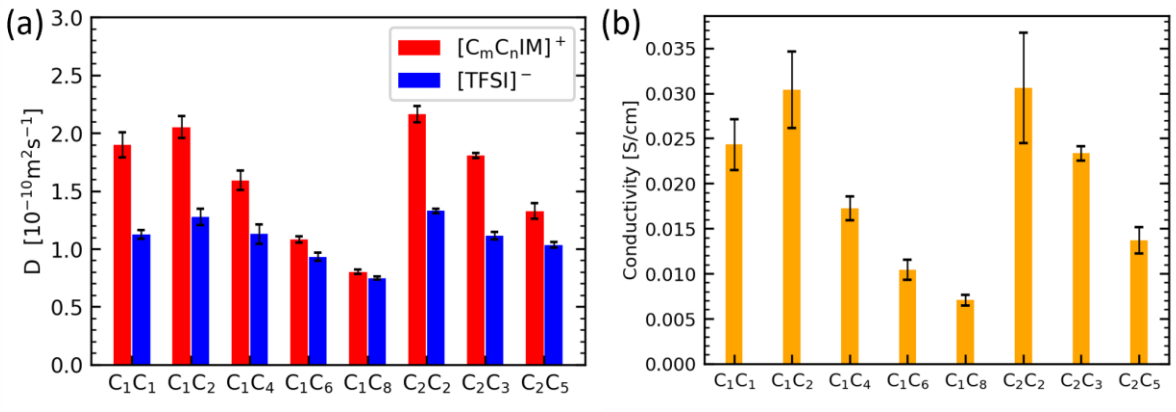

Figure 6.13. (a) Diffusion coefficient of cations and anions in TFSI-based ILs at 400 K. (b) Conductivity of TFSI-based ILs at 400 K.

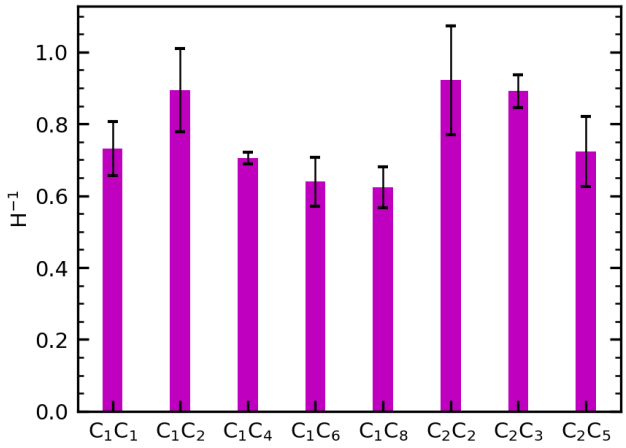

Figure 6.14. The inverse Haven ratio H^{-1} of TFSI-based ILs at 400 K.

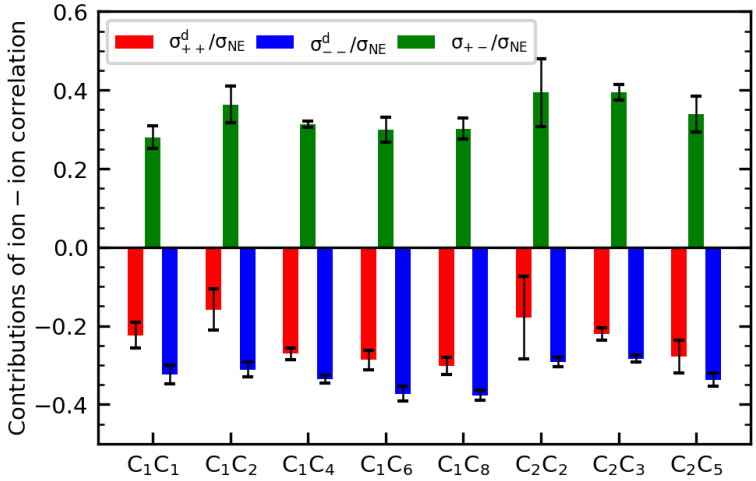

Figure 6.15. Contributions of distinct ion-ion correlations to conductivity normalized by σ_{NE} of TFSI-based ILs as a function of the alkyl tail lengths of the cation at 400 K.

lengths of the imidazolium ring. These results are consistent with the case where the cation is lighter than the anion ($M_+ < M_-$). Specifically, the contributions of cation-anion correlations in the $[C_2C_2IM][TFSI]$, $[C_1C_2IM][TFSI]$, and $[C_2C_3IM][TFSI]$ systems are similar and slightly larger than those in other systems. The negative contribution of anion-anion correlations varies slightly, with the largest magnitude in the $[C_1C_6IM][TFSI]$ and $[C_1C_8IM][TFSI]$ systems. However, the magnitudes of cation-cation correlations vary more strongly than those of anion-anion correlations, with the minimum amplitude appearing in $[C_2C_2IM][TFSI]$. Interestingly, comparisons between systems with the same cation mass ($[C_1C_4IM]$/ $[C_2C_3IM]$ and $[C_1C_6IM]$/ $[C_2C_5IM]$) show that systems with more symmetrical cations exhibit larger cation-anion correlations but smaller negative like-ion correlations, resulting in higher conductivity in the systems with more symmetrical cations. These findings highlight the interplay between different types of ionic correlations in determining the overall conductivity of the IL system, emphasizing the importance of considering both the mass and geometry of the ions in the design and optimization of the material for specific applications.

Chapter 7 Ion Transport in Polymerized Ionic Liquids

This chapter is based on the following manuscript:

- Zhu, Z; Sokolov, A. P; Paddison, S. J, Ion Transport in Polymerized Ionic Liquids: Effects of Sidechain Flexibility and Specific Interactions. *Advanced Energy Materials* **2024**, to be submitted.

This chapter focuses on ion transport mechanisms and dynamic correlations in polyILs. Atomistic MD simulations were undertaken on polyILs consisting of a polymethylmethacrylate (PMMA) based backbone with attached imidazolium cations through a series of linkers with different lengths (PMMA-C_x-IM (x = 2 – 8)) and the following anions: $TFSI^-$, PF_6^-, BF_4^-, and Br^-. Ionic correlations and the mechanisms of ion transport in these polyILs were systematically investigated to understand the effects of sidechain flexibility coupled with specific interactions.

7.1 Simulation Details

Molecular dynamics (MD) simulations were conducted using GROMACSS (2021.2)[244, 245] for various molecular PMMA-based polyILs. Each system was comprised of 10 polycation chains, each consisting of 40 monomers, and 400 anions, ensuring an optimal balance between statistical accuracy and computational efficiency.[144, 145, 149] The methodology followed a prior established protocol.[145, 149, 247, 260, 283] The generalized AMBER force field (GAFF) was utilized for bonded and nonbonded interactions.[162, 261] Partial charges on the atoms were calculated using the Restrained Electrostatic Potential (RESP) algorithm,[262] derived from optimized electronic structures of the repeating unit of the polycation or isolated anion at the Hartree-Fock HF/6-31g(d) level of theory using the GAUSSIAN 09 programs.[224] To accommodate polarization and charge transfer effects, the computed atomic partial charges on both polycations and anions were scaled by a factor of 0.8, known for its efficiency and reliability in ion-containing systems. This approach has been validated in prior studies.[36, 145, 247, 260, 263] Electrostatic and Lennard-Jones interactions were truncated at a distance of 14 Å, with long-range corrections handled by the particle mesh Ewald (PME) method and appropriate tail corrections, respectively. Initial configurations were generated by randomly packing the

polycation chains and associated anions in a cubic box using the PACKMOL software,[217] and force field assignments were made in the topology files with the aid of ACPYPE and antechamber tools.[284] Initial systems were equilibrated for over 50 ns in the NPT ensemble, preceded by an annealing process at high temperatures (750 – 950 K) and a pressure of 1.0 bar for approximately 55 ns. Subsequently, an additional 30 ns equilibration under the NVT ensemble was performed, followed by the collection of trajectories at 10 ps intervals for 50 ns, along with longer trajectories of 300 – 500 ns saved every 100 ps to ensure reliable ion-ion correlations in these polyIL systems.[4, 264] Temperature and pressure were controlled using the Bussi thermostat[265] and the Parrinello-Rahman barostat[266] with coupling times of 0.5 and 5 ps, respectively. The MD simulations for all polyIL systems were conducted in periodic cubic boxes with a time step of 2 fs. To mitigate statistical uncertainty, dynamic correlations were computed from 4 – 6 trajectories to provide average values and standard deviations.

7.2 Effects of Sidechain Flexibility and Specific Interactions

7.2.1 Structural and Ion Association Analysis

To assess the flexibility of the sidechain, we initially analyzed the distribution of the sidechain extension and projected distances as a function of the linker length (see **Figure** 7.1). For the shortest sidechain, two distinct peaks are evident, representing the two predominant configurations of the pendant imidazole ring. These configurations are influenced by interactions between the imidazole functional group and the acrylate group. As the alkyl linker length increases, these interactions weaken, leading to a transition from double peaks to a single peak with only minor shoulders. Consequently, both the extended and projected distances of the imidazole ring exhibit broad distributions, shifting towards longer distances with increasing linker length. This is indicative of enhanced flexibility with the longer linkers. **Figure** A.10 further elucidates this trend, depicting detailed distributions of the extension and angle between the sidechain and the backbone, underscoring that longer linkers afford increased flexibility in both extension and angle.

In **Figure** 7.2, we present the radial distribution function (RDF) of the center of mass of the cations and anions for a broad range of linker lengths as well as a function of the various mobile

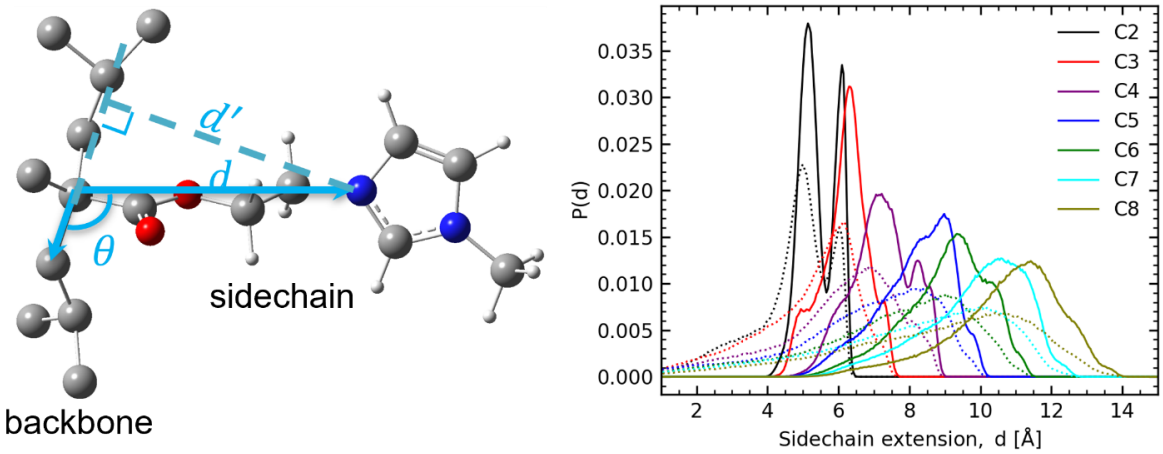

Figure 7.1. Distribution of the sidechain extended (solid lines) and projected (dotted lines) distances at 400 K.

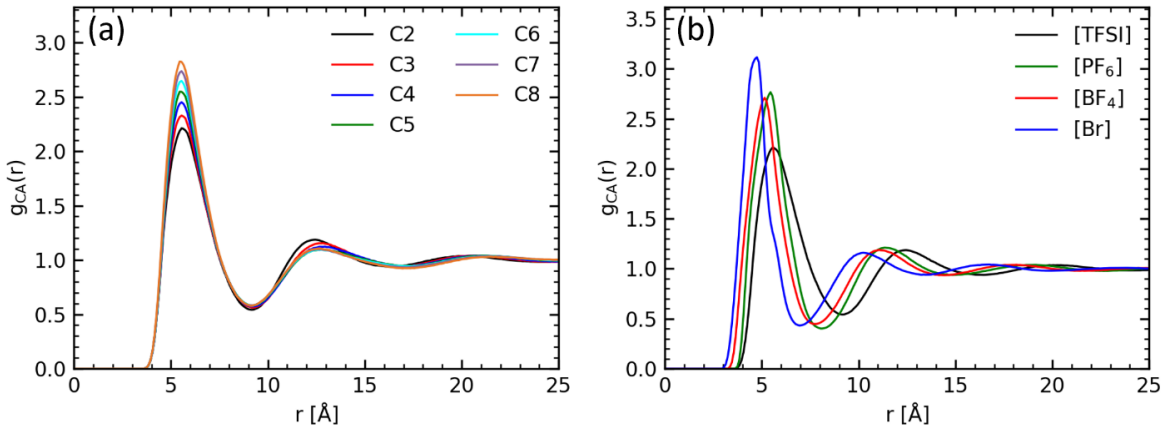

Figure 7.2. Radial distribution functions of the cation-anion at 580 K for (a) PMMA-C_x-IM[TFSI] (x = 2 – 8); and (b) PMMA-C_2-IM associated with various anions.

anions. **Figure** 7.2(a) illustrates that increasing the sidechain length does not alter the position of the primary peak, instead, it enhances the intensity of this peak. This suggests that the increase of sidechain flexibility better accommodates anions in the nearest shell due to reduced steric hindrance from the backbone, although it has a slight impact on the strong electrostatic interactions between the cation and anion. In contrast, the position of the first peak shifts to shorter distance as the size of the anion decreases and is depicted in **Figure** 7.2(b). Small spherical anions exhibit sharp peaks compared to the linear anion $TFSI^-$, owing to the strong electrostatic interactions for small anions with less delocalized charge. The first local minima of these cation-anion RDFs were used to define ion association in the subsequent discussion. The RDFs demonstrate that all anions strongly interact with the polymerized cations.

Furthermore, we examined the probabilities of the coordination numbers of the cations, $P(n)$, and of the polyIL chains, $P(N)$, with a given anion at 580 K (see **Figure** 7.3), which play an important role in the ion hopping mechanism. In **Figure** 7.3(a), the majority of the $TFSI^-$ anions associate with 4 – 7 cations. The maximum in $P(n)$ was observed at $n = 6$ for the shortest linker length and at $n = 5$ for longer sidechains ($x = 4 - 8$), with two comparable probabilities at $n = 5$ and 6 for the intermediate sidechain length ($x = 3$). However, linker length has little influence on the distribution of the coordinated chains, $P(N)$, especially when the linker is sufficiently long ($x \geq 5$) [**Figure** 7.3(c)]. An increase in the linker length slightly shifts $P(N)$ to the right with a maximum at $N = 3$. These results indicate that increased sidechain flexibility results in fewer cations associating with an anion but from more distinct chains, forming a loose "cage" around the anion. **Figure** 7.3(b and d) show the effect of the size of the anions on the coordination characteristics at 580 K. Interestingly, $TFSI^-$ and BF_4^- exhibit a similar distribution of associated cations, with peaks at $n = 6$, while PF_6^- displays a broad peak and the smaller Br^- associates with fewer cations, featuring a sharp peak at $n = 5$. Regarding the probability distribution of associated chains, $P(N)$, the three spherical anions exhibit similar distributions with a sharp peak at $N = 3$, whereas the linear $TFSI^-$ features a broad peak with the distribution shifted to the left. This implies that the ion association is influenced by the interplay between electrostatic interactions and steric hindrance arising from

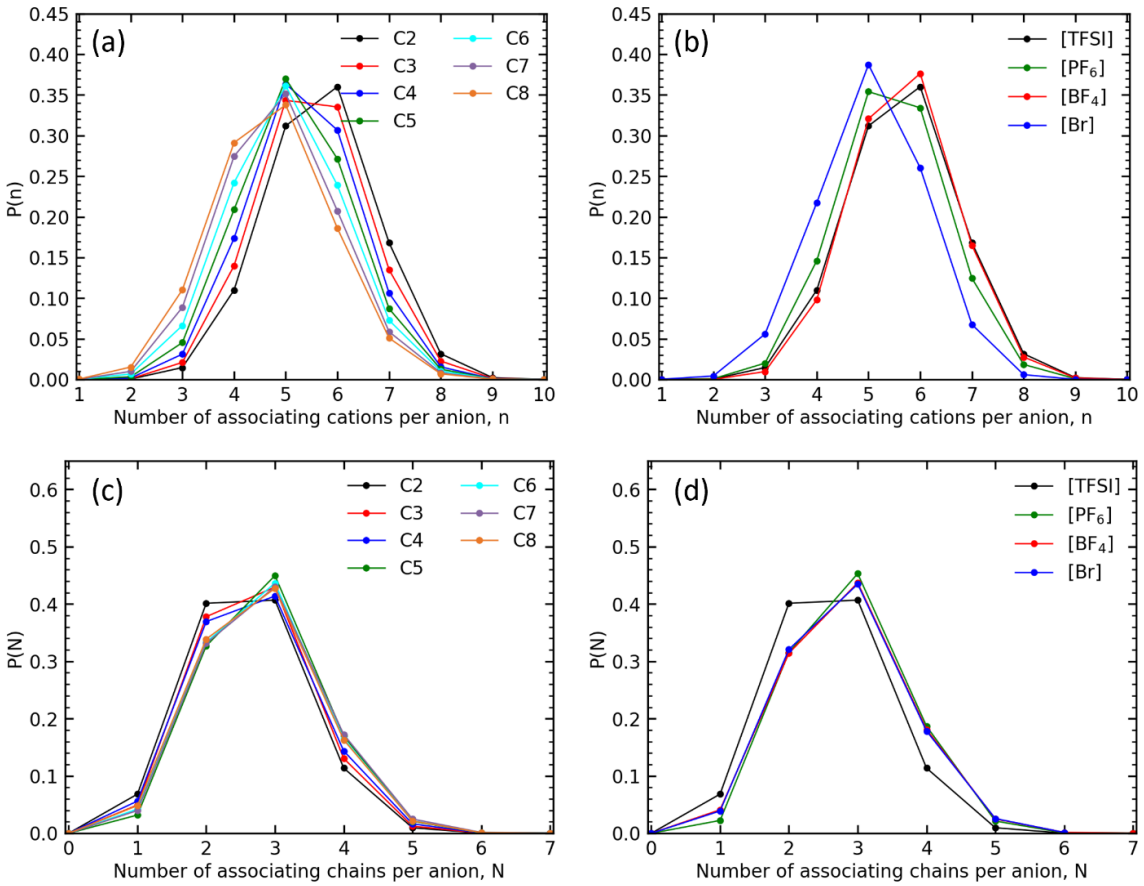

Figure 7.3. Probability of an anion coordinating with n cations, $P(n)$, for: (a) a broad range of linker lengths; and (b) four anions at 580 K. Probability of an anion associating with N cations, $P(N)$, for: (c) a broad range of linker lengths; and (d) four anions at 580 K.

both the shape of the anion and the backbone of the polycation.

7.2.2 Anion Dynamical Correlations

Our previous MD simulations revealed that anions associating with fewer cations from more coordinating polymers tend to exhibit higher mobility.[145] To explore the relationship between ion association and ion dynamics, the self-diffusivity of the anion was derived from the mean square displacement (MSD) using the Einstein relation:

$$D = \frac{1}{6}\lim_{t\to\infty}\frac{d}{dt}\langle\sum_{i=1}^{N}[\boldsymbol{r}_i(t_0+t)-\boldsymbol{r}_i(t_0)]^2\rangle, \tag{7.1}$$

where $\boldsymbol{r}_i(t_0+t)$ and $\boldsymbol{r}_i(t_0)$ represent the positions of the ith particle at time t_0+t and t_0, respectively. **Figure** 7.4 illustrates the self-diffusion coefficients of the anions as a function of linker length for the various anions. In general, the self-diffusivity increases to a varying extent with increasing linker length for the studied anions. Specifically, the diffusivity of the smallest anion, Br^-, increases significantly as the linker length is increased from C2 to that of C5, followed by a more gradual increase. This is the case for PF_6^-, although it has a larger volume than Br^-. Nevertheless, the increase in the linker length only marginally enhances the diffusion coefficients of BF_4^- and $TFSI^-$. As a result, the differences between these anions are substantial (exceeding one order of magnitude) in systems with short linkers, but diminish as the linker length increases. More interestingly, for the shortest linker, the diffusivity follows the order: $TFSI^- > BF_4^- > PF_6^- > Br^-$, consistent with observations in the poly(1-butyl-3-vinyl-imidazolium)[285] and poly(1-ethyl-3-vinyl-imidazolium)[149] systems where the imidazolium ring directly attaches to the backbone. However, the diffusivity of BF_4^- surpasses that of $TFSI^-$ with a sufficiently long linker.

In concentrated ionic systems, distinct correlations between the ions play a critical role in ion transport mechanisms due to the strong electrostatic interactions. The Onsager transport coefficients can be readily obtained from the following equation:

$$L^{ij} = \frac{1}{6k_BTV}\lim_{t\to\infty}\frac{d}{dt}\langle\sum_{i=0}^{N}[\boldsymbol{r}_i(t)-\boldsymbol{r}_i(0)]\cdot\sum_{j=0}^{N}[\boldsymbol{r}_j(t)-\boldsymbol{r}_j(0)]\rangle, \tag{7.2}$$

where k_B is the Boltzmann constant, T is the temperature, and V is the volume. The ionic

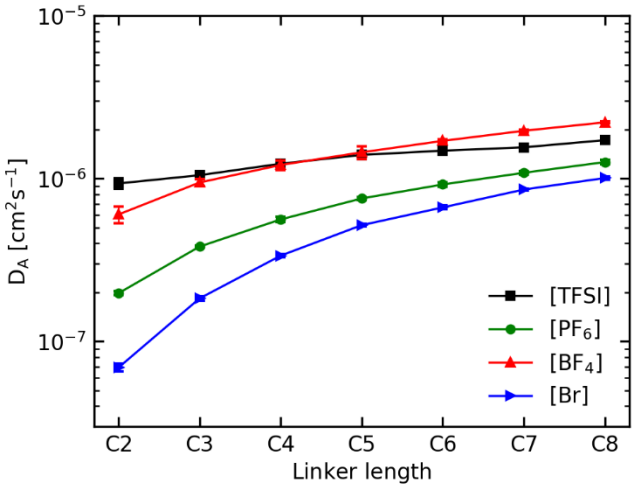

Figure 7.4. The diffusion coefficients of the four anions as a function of linker length at 580 K.

conductivity may then be related to L^{ij} with:

$$\sigma_{ij} = z_i z_j F^2 L^{ij}, \tag{7.3}$$

where z_i and z_j are the charge valences of species *i* and *j*, respectively; and *F* is the Faraday constant. First, we assume that the polymerized cations are fixed, and only the mobile anions contribute to the ionic conductivity.

Figure 7.5(a) shows the contributions of ionic correlations between $TFSI^-$ normalized by the self-component σ_{an}^{s}, representing ideal and uncorrelated particle movement as a function of linker length. It is observed that the distinct anion correlation is always negative, although the magnitude slightly decreases and then increases with the linker length. As a result, the total contribution seems to reach a maximum at a linker length of C5. This normalized total contribution is also interpreted as the inverse Haven ratio H^{-1}, which lies in the range between 0.3 and 0.5, consistent with experimental data.[135, 136] Note that these data were derived from Equation (7.3) using a barycentric reference frame (RF).

A recent study[286] reveals that the choice of the RF plays an important role in certain dynamical properties including the transference number that exhibits a negative value in PEO-LiTFSI under certain conditions. This negative transference number was reproduced in MD simulations by transforming the Onsager coefficients to the solvent-fixed RF from the barycentric RF.[286, 287] One may naturally ask the question: does the RF affect the distinct correlations and the inverse Haven ratio? To pursue an answer to this question, we calculated the distinct correlation between anions and cations and is shown with the blue upper triangles in **Figure** 7.5(a). Surprisingly, the magnitude of this anion-cation correlation is nontrivial, suggesting that the movement of polycations may also have an influence on the inverse Haven ratio. We chose the center of mass of all polycations in the systems as the RF. **Figure** 7.5(b) illustrates the corresponding contributions of ionic correlations with a polycation-fixed RF. Indeed, the anticorrelated motion between the anions become positive, indicating that the distinct anion-anion correlation positively contributes to the ionic conductivity under the polycation-fixed RF. Simultaneously, the distinct anion-cation correlation becomes negligible. This transformation leads to $H^{-1} > 1$ in these polyILs. Such a phenomenon was also observed

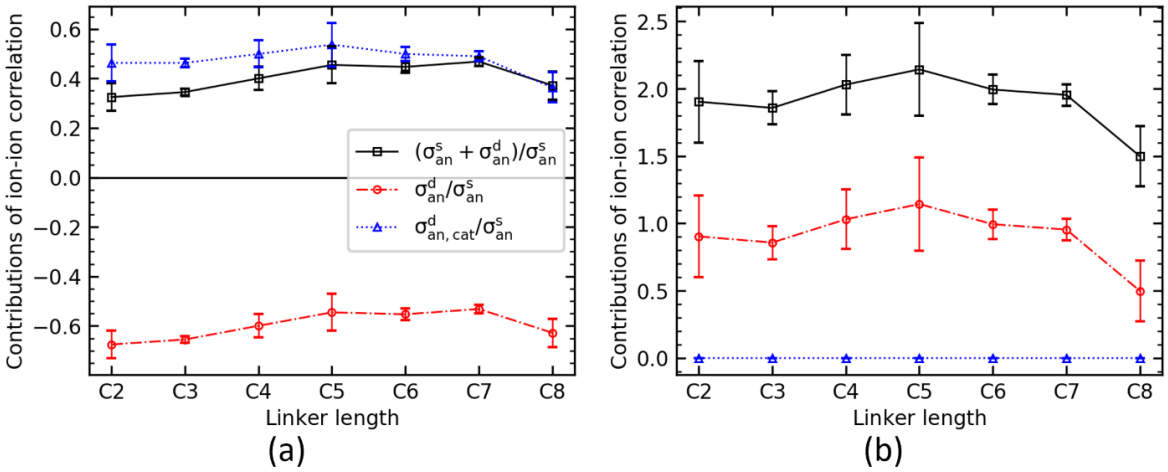

Figure 7.5. (a) Contribution of anion-anion correlations as a function of linker length under (a) barycentric reference frame and (b) polycation-fixed reference frame at 580 K.

in poly(1-butyl-3-vinyl-imidazolium) associated with various anions in which the distinct anion-anion correlation was obtained from the self-diffusivity and the true conductivity based on the equilibrium and non-equilibrium simulations, respectively.[285] Given the principle of momentum conservation, the momentum of the anions is dissipated by removing the movement of the polymerized cations, leading to an intriguing implication of constraining the poly-ion motion by crosslinking the polymer chains or introducing solvent in the design of polyILs with improved ionic conductivity.

Utilizing our prior categorization of ion hopping events,[145, 149] we classified four ion hopping types as depicted in **Figure** 7.6: Type 1 denotes instances where the anion changes its coordination of cationic groups from the same polymer chain during the hopping interval Δt; Type 2 occurs when the anion alters its coordination of cationic groups from the different polymers; Type 3 characterizes cases where the anion does not associate with any cations; and Type 4 is rattling events in which the anion gets trapped in a "cage" formed by the cationic groups. It has been suggested that the choice of Δt within the range of 10 – 100 ps for polyILs makes little difference, although the best option is around 2 ps or smaller corresponding to the fastest ion jumping rates.[144] Therefore, we chose a sampling interval of 10 ps to strike a balance between accuracy and computational expense.

Figure 7.7(a) shows the percentages of the four types of ion hopping for PMMA-C_x-IM[TFSI] (x = 2 – 8). Surprisingly, the occurrence of rattling events is only slightly affected by changes in the linker length with a minimum occurring at C5 and C6, although the self-diffusivity increases monotonically in **Figure** 7.4. It is observed that the rate of interchain hopping is consistently lower than that of intrachain hopping. However, as the linker length extends, the percentage of intrachain hopping decreases while the proportion of interchain hopping increases. Free anions are essentially not observed in these concentrated systems. These results indicate that intrachain and interchain hopping make different contributions to the diffusivity of the anions. In **Figure** 7.7(b), the occurrence probability of the hopping types across the various anions with the same C2 linker. The largest anion, $TFSI^-$, exhibits the lowest rattling percentage coupled with the highest percentage of intrachain and interchain hopping types,

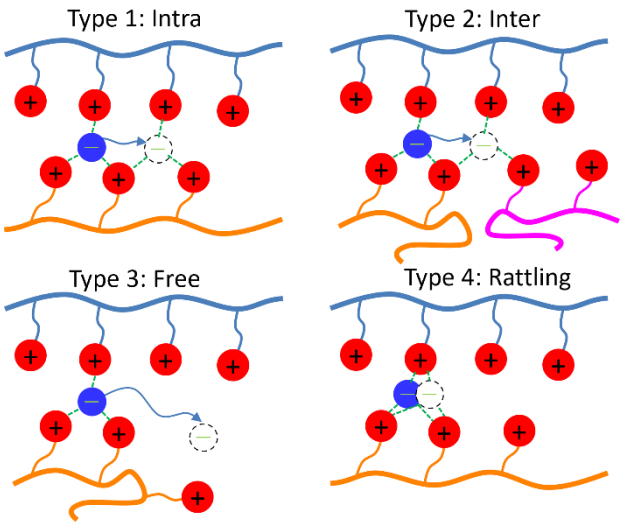

Figure 7.6. Categorization of the ion hopping types: Type 1 (intrachain); Type 2 (interchain); Type 3 (free ions without associated ions); and Type 4 (rattling).

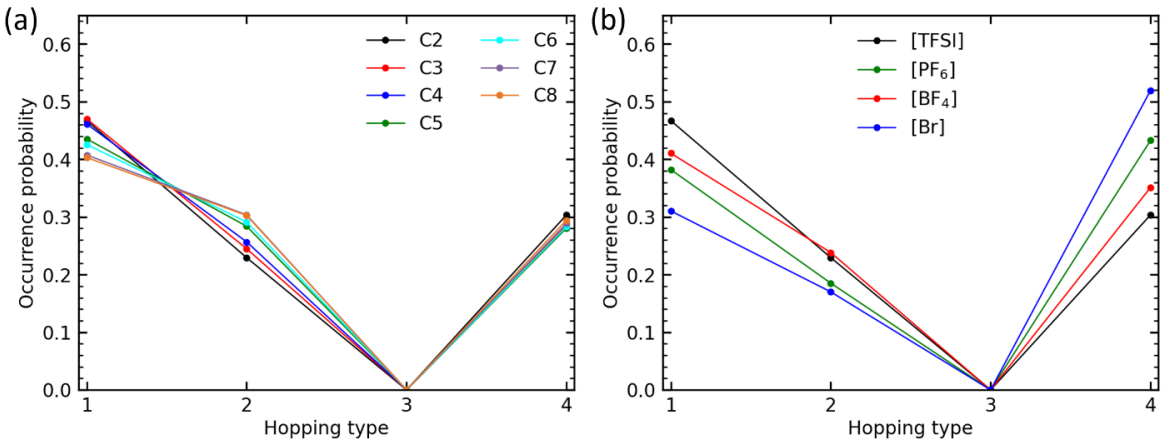

Figure 7.7. Occurrence probability of the hopping types for [TFSI] with: (a) different linker lengths; and (b) various anions with the linker length of C2 at 580 K.

while the smallest, Br^-, displays the highest rattling percentage along with the lowest percentage of intrachain and interchain hopping. Nevertheless, BF_4^- exhibits less rattling when compared to PF_6^- despite its smaller size, which underscores the competition between Coulomb interactions and the size of the mobile ion. These trends are similar at low temperature as shown in **Figure** A.11.

One may wonder what causes the variations in intrachain and interchain hopping types. Ganesan et al. suggested that the increase in the interchain hopping type is linked to a reduction in distance between the nearest cationic groups from distinct chains, as observed in their simulation study of three different linkers devoid of the acrylate group.[288] We surmised that the nearest cation from the same chain may potentially compete with one from a different chain to associate with the hopping anion. To investigate this hypothesis, we computed the minimum distance between the cations from the same chain as shown in **Figure** 7.8. Interestingly, the average distance between the cations from different chains in the closest proximity decreases slightly with increasing linker length from C2 to C5, followed by a small increase from C5 to C8, despite the monotonical increase of the interchain hopping type illustrated in **Figure** 7.7(a). However, the average distance between the nearest cations from the same chain exhibits a steady increase as the linker length is increased, resulting in a constant increase in the difference between these two average distances.

7.2.3 Anion Dynamical Heterogeneity

Dynamical heterogeneity of the ions is indicative of a deviation from ideal Gaussian behavior, which has been observed in supercooled liquids,[289] ionic liquids,[247, 290] and polyILs[145, 149, 283, 285] at intermediate time scales. This deviation can be quantified by the non-Gaussian parameter, α_2, defined as:

$$\alpha_2(t) = \frac{3\langle r^4(t)\rangle}{5\langle r^2(t)\rangle^2} - 1, \tag{7.4}$$

where $r(t)$ is the displacement of an ion at time t with respect to its position at time $t = 0$. Deviations from $\alpha_2(t) = 0$ provide insight into the degree and timescale of ion dynamical heterogeneity. The maximum of $\alpha_2(t)$ indicates the greatest dynamical heterogeneity of the anion at the intermediate timescale t^* as shown in the inset of **Figure** 7.9(a). The time at which

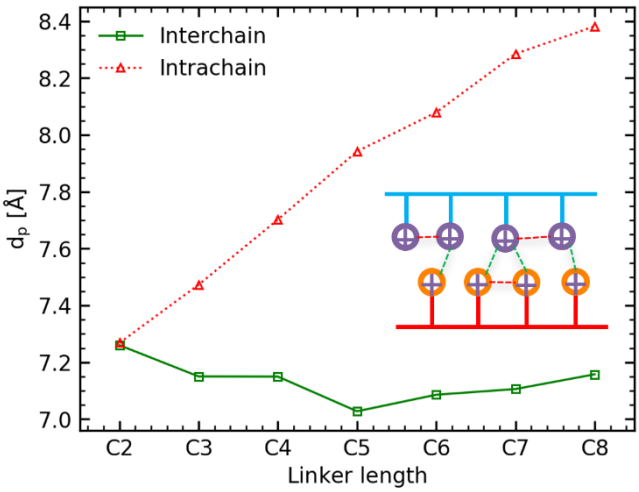

Figure 7.8. Average distance, d_p, between the nearest cationic groups from the same polymer chain and distinct polymers. Inset depicts the intermolecular distance (green dashed line) and the intramolecular distance (red dashed line) between the nearest cations, respectively.

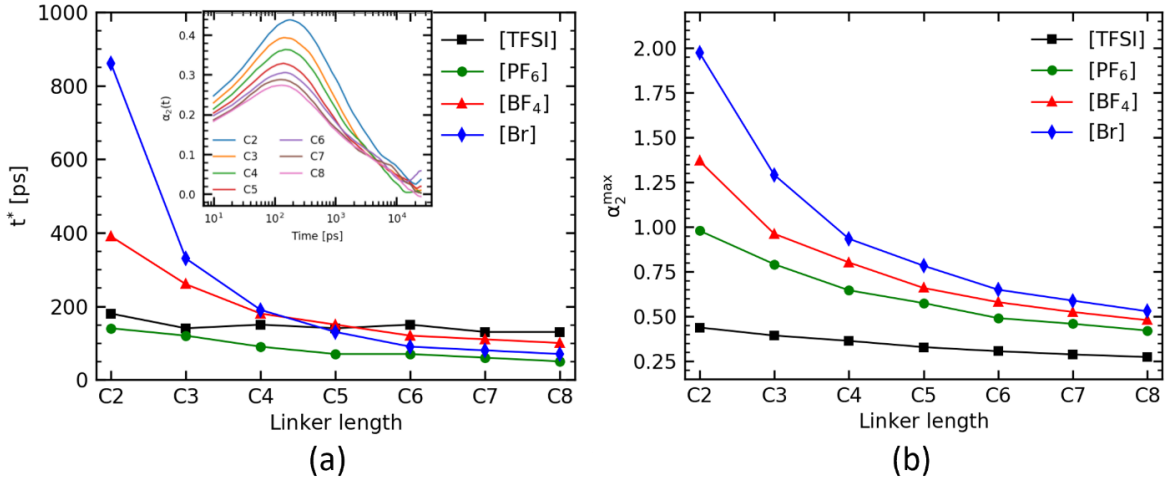

Figure 7.9. (a) The time scale (t^*) for the non-Gaussian parameter (α_2) reaching its maximum as a function of the linker length at 580 K. The inset shows the non-Gaussian parameters as a function of time for [TFSI] with different linker lengths at 580 K. (b) Maxima of α_2 as a function of the linker length at 580 K.

α_2 reaches its maximum value was extracted and plotted as a function of linker length for the four anions to define the characteristic time, t^*, for ion hopping in these systems [**Figure** 7.9(a)]. It is observed that the difference in t^* for different anions is large for the linker of C2, while this difference diminishes with increasing linker length. Moreover, it does not exhibit a consistent correlation between t^* and anion size along with varying linker lengths. In **Figure** 7.9(b), however, the maximum values, $\alpha_2^{\max}$, are inversely correlated to the size of the anion across all the linker lengths, although the difference decreases as the linker length increases. Specifically, the smallest anion (i.e., Br^-) possessing the largest $\alpha_2^{\max}$ exhibits the strongest heterogeneity by hopping from one Coulombic 'cage' to another formed by the polycations due to strong electrostatic interactions. The $\alpha_2^{\max}$ of Br^- sharply decreases with increasing linker length, while the linear and biggest anion, $TFSI^-$, consistently maintains the lowest $\alpha_2^{\max}$ values, typically below 0.5, which is only slightly influenced by changes in linker length.

To further demonstrate the motions of mobile anions with distinct extents of heterogeneities in terms of hopping types, we plotted trajectories of a typical anion from the system displaying the least heterogeneity, PMMA-C_8-IM[TFSI], and the system with the largest degree of heterogeneity, PMMA-C_2-IM[Br], respectively (**Figure** 7.10). Thin lines depict trajectories of the anion at intervals of 10 ps, while thick lines represent the trajectory of hopping anion at the characteristic time scale of t^*. Over a period of 50 ns, $TFSI^-$ is highly mobile with over 1500 interchain hops and over 2000 intrachain hops or jumps. The trajectory with a timestep of $t^* = 130$ ps exhibits diffusive motion resembling a random walk, consistent with its small $\alpha_2^{\max}$ value (< 0.5). In contrast, anion Br^- experiences only a few intrachain and interchain jumps compared to over 3000 rattling events [see **Figure** 7.10(b) and **Figure** A.12(b)]. For the majority of the time, Br^- remains trapped within a Columbic 'cage', with occasional effective hops from one "cage" to another, primarily contributing to long-range diffusion. The motion between the two "cages" are discrete, indicating strong heterogeneity in the system. Analysis of these hopping events at the interval of t^* provides the average hopping length of 2.22 Å for $TFSI^-$ and 1.13 Å for Br^-, respectively. The average hopping length for $TFSI^-$ and Br^- at the interval of 10 ps were plotted as a function of linker length in **Figure** A.12(c). The average

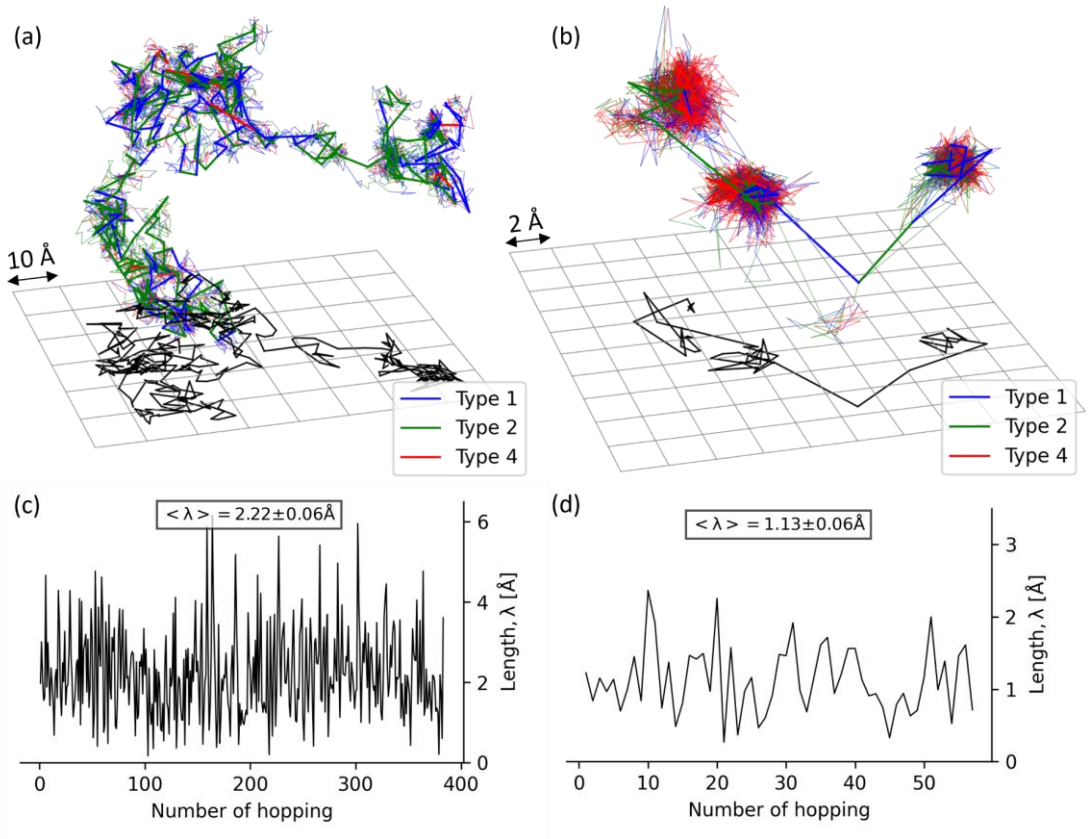

Figure 7.10. Trajectory lines of an individual anion in: (a) PMMA-C_8-IM[TFSI]; and (b) PMMA-C_2-IM[Br] at 580 K. Different color lines represent different types of ion hopping. Thin and thick lines refer to the trajectories with a timestep of 10 ps and the characteristic time, respectively (130 ps for (a) and 860 ps for (b), respectively). The length of each anion hopping from one "cage" to another at the interval of the characteristic time in (c) PMMA-C_8-IM[TFSI] and (d) PMMA-C_2-IM[Br] at 580 K.

jump length of $TFSI^-$ is consistently greater than that of Br^-. In addition, both anions exhibit a slight increase in the average jump length as the linker length increases.

To discern the correlations between mobile anions in terms of both time and space, we resorted to the van Hove correlation function, which can be split into two parts, self and distinct:

$$G(r,t) = G_s(r,t) + G_d(r,t) \tag{7.5}$$

$$G_s(r,t) = \frac{1}{N}\sum_{i=1}^{N}\langle\delta(r - |\boldsymbol{r}_i(t) - \boldsymbol{r}_i(0)|)\rangle \tag{7.6}$$

$$G_d(r,t) = \frac{1}{N}\sum_{i\neq j}^{N}\langle\delta\big(r - \big|\boldsymbol{r}_i(t) - \boldsymbol{r}_j(0)\big|\big)\rangle\,, \tag{7.7}$$

in which δ is the Dirac's delta function. Thus, the function $4\pi r^2 G_s(r,t)$ is the probability of finding a mobile ion at distance r provided that it was at the origin where $r = 0$ when $t = 0$. The distinct part, $G_d(r,t)$, evaluates the probability distribution of a mobile ion at time t at a distance of r away from another ion at $t = 0$. Meanwhile, ideal Gaussian behavior can be readily described by:

$$G_{s,0}(r,t) = \left(\frac{3}{2\pi\langle r^2(t)\rangle}\right)^{\frac{3}{2}}\exp\left(-\frac{3r^2}{2\langle r^2(t)\rangle}\right), \tag{7.8}$$

where $\langle r^2(t)\rangle$ is the MSD of a mobile ion at time t. **Figure** 7.11 shows the self-part and the distinct part of the van Hove function at the characteristic time, t^*, where $\alpha_2(t^*) = \alpha_2^{\max}$ for Br^-. Two peaks are evident when the linker is the shortest (i.e. C2), and this double-peak gradually disappears as the length of the linker is increased. Compared with the corresponding Gaussian distribution as shown by a dotted curve, the deviation remains, as seen by the tail at long distances. Therefore, anions that travel farther than the distance r^* within time t^*, for which $G_s(r^*,t^*) = G_{s,0}(r^*,t^*)$, are defined as fast "mobile" anions. Surprisingly, this distance criterion for distinguishing fast anions is not dictated by the linker length [**Figure** 7.11(a)]. However, **Figure** 7.11(c) reveals that the intersection between $G_s(r,t^*)$ and $G_{s,0}(r,t^*)$ varies with the associated anion and it seems to be correlated with the size of the anion. It is important to note that the crossing point coincides with the local minimum of $G_s(r,t^*)$ between two peaks in some systems, suggesting that this identification of fast anions is as effective as our

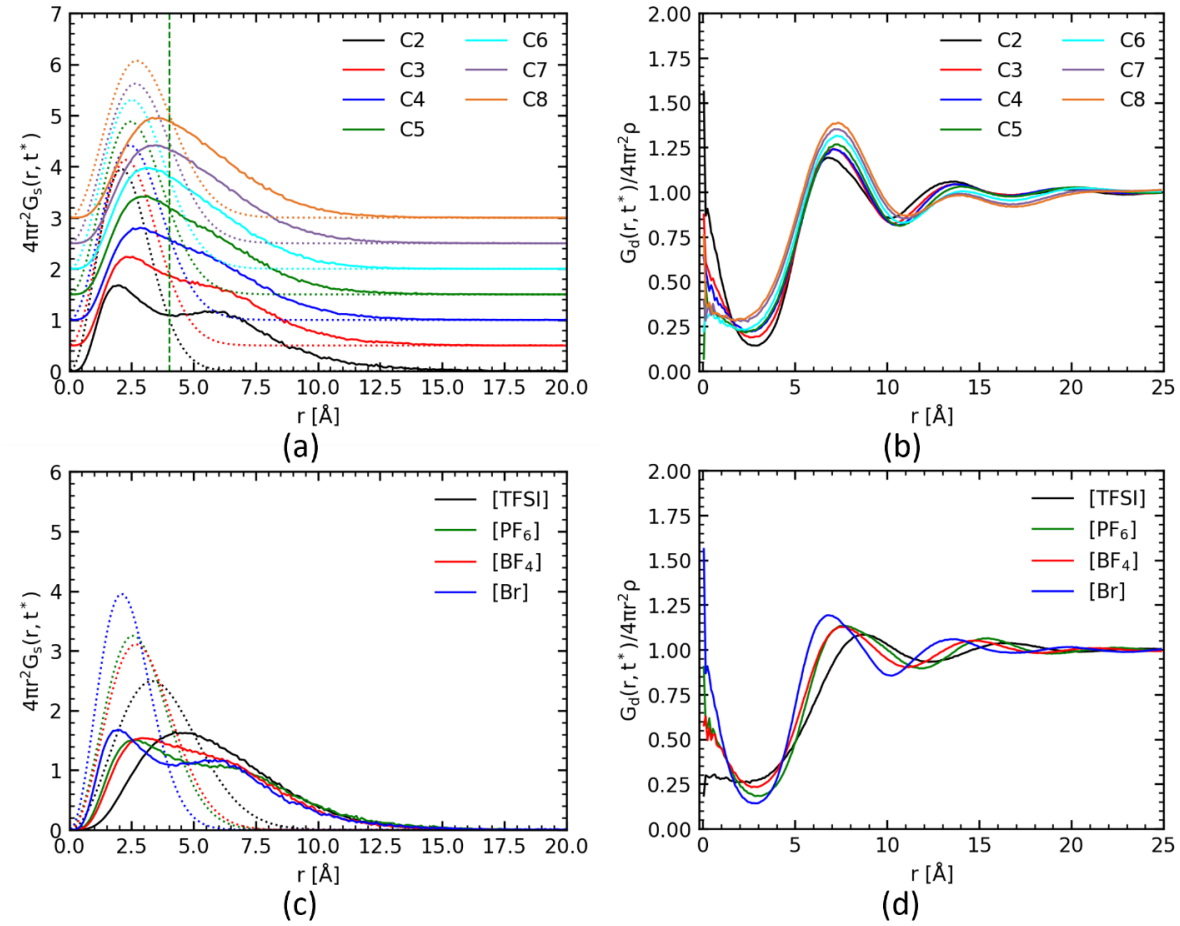

Figure 7.11. Self-part of the van Hove function, $G_s(r, t^*)$, for: (a) PMMA-C_x-IM[Br] systems and (c) four anions in PMMA-C_2-IM systems at 580K. Each curve in (a) is vertically shifted 0.5 for clarity. The vertical line represents the intersection of $G_s(r, t^*)$, (solid lines) and $G_{s,0}(r, t^*)$, (dotted lines), which is used as the r^* criterion to determine fast and slow anion populations. Distinct-part of the van Hove function, $G_d(r, t^*)$, for: (b) PMMA-C_x-IM[Br] systems and (d) four anions in PMMA-C_2-IM systems at 580K.

previous definition of a fast anion in which the local minimum was selected,[145, 149] especially for the case where there is a single peak in the self-part of the van Hove function due to weak heterogeneity ($\alpha_2^{\max} < 1.0$).[1] An alternative approach is to fit $G_s(r, t^*)$ with two separate Gaussian functions.[285]

Figure 7.11(b and d) illustrate the distinct part of the van Hove function, $G_d(r, t)$, for PMMA-C_x-IM[Br] and PMMA-C_2-IM systems, respectively. It is worth noting that a sharp peak at $r = 0$ reflects the replacement of the original anion by another anion at time t^*. The intensity of this peak becomes weak with increasing flexibility of the sidechain. This result indicates that a more flexible sidechain permits movement of the "cage" formed by the polycations, resulting in a less precise replacement of anions. **Figure** 7.11(d) shows that the distinct part of the van Hove function, $G_d(r, t)$, for different anions demonstrates that, compared to the smallest anion Br^-, the linear anion $TFSI^-$ exhibits a very low and flat peak when $r \cong 0$ Å, which arises from the loose "cage" due to the weak Coulombic interactions between the anion and polycations. These peaks at $r = 0$ also indicate concerted motion of the anions and is discussed in the following section.

To further elucidate the role of sidechain flexibility and specific interactions between the anions and polycations in ion hopping behavior, we defined the tail of $G_s(r, t^*)$ (i.e., the green area) that deviates from the ideal Gaussian distribution (i.e. the orange area) as the ion hopping contribution [**Figure** 7.12(a)]. The computed percentages of ion hopping contribution are presented in **Figure** 7.12(b). Generally, the hopping contribution decreases with increasing linker length, although the largest anion, $TFSI^-$ only exhibits a small reduction in the fraction of ion hopping. In terms of anion size, the ion hopping fractions follow the order: $Br^- > PF_6^- > BF_4^- > TFSI^-$, and this trend is consistent across all the linkers in this investigation while the difference diminishes as the linker length increases.

Combining these findings with the self-diffusivity results, we may conclude that enhanced sidechain flexibility significantly improves the diffusive motion of the anions but suppresses the ion hopping contribution to a lesser extent, resulting in an overall increase in the self-diffusivity constant. Moreover, a rigid Coulombic "cage" for less delocalized anions may be

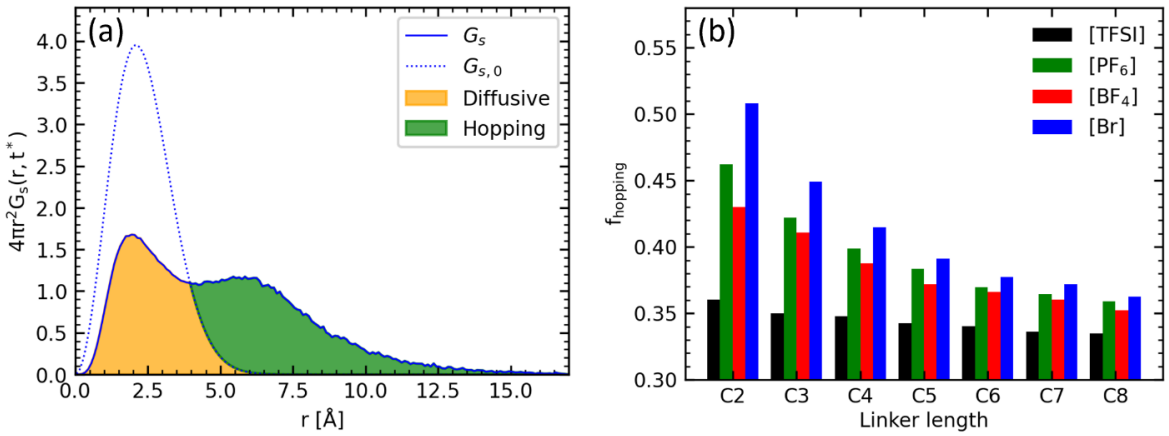

Figure 7.12. (a) Self-part of the van Hove function, $G_s(r, t^*)$, for PMMA-C_2-IM[Br] system to define the diffusive and hopping anions. (b) The fraction of hopping anions defined as the integral of the green area in (a) as a function of linker length for different anions.

softened by increasing sidechain flexibility. However, for a strongly delocalized anion (i.e., $TFSI^-$), the relatively weak electrostatic interactions form a loose "cage", indicated by the primary contribution to anion diffusivity from diffusive motion that is slightly affected by changes in linker length. Interestingly, for the intermediate-sized anions (i.e., BF_4^- and PF_6^-), the order of their diffusivities is not solely dictated by anion size. The higher intensity of $g_{CA}(r)$ for PF_6^- relative to BF_4^- seems to imply that Coulombic interaction predominates over size [see **Figure** 7.2(b)], consistent with the findings of Zhang et al.[285] These findings underscore the intricate interplay between anion mobility and various additional factors, including mobile ion size, electrostatic interactions between ions, and linker length.

7.2.4 Stringlike Cooperative Motion

The results from the self- and distinct- parts of the van Hove function indicate that an ion "replacement" mechanism via a series of correlated and concerted ion hopping at the characteristic time t^* of the strongest heterogeneity appears to underlie the mobile ion transport in these polyILs. These mobile ions may form a "string", indicating a stringlike cooperative motion. This behavior may be quantified by:

$$\min\left[\left|\boldsymbol{r}_i(t^*) - \boldsymbol{r}_j(0)\right|, \left|\boldsymbol{r}_j(t^*) - \boldsymbol{r}_i(0)\right|\right] < r_s, \tag{7.9}$$

where $\boldsymbol{r}_i(t)$ and $\boldsymbol{r}_j(t)$ are the coordinates of the ith and j^{th} mobile ion at time t, and r_s is the distance criterion for ion "replacement". For the linear anion $TFSI^-$, r_s is determined to be 2.5 Å, while for the spherical anions, it is set to 2.2 Å, based on their "hard core" radii.[145, 149] **Figure** 7.13(a and b) illustrate the probability distribution of string length, $P(n_s)$, that are greater than 10^{-4}. The string length $n_s = 0$ is referred to as the fraction of slow ions that travel less than r^* within time t^*. Only a small proportion of anions exhibit mobility sufficient to participate in stringlike motion. At 580 K, long strings containing over six anions are only observed in the PMMA-C_2-IM[Br] system. The probability distribution of string length shifts to the left as the linker length increases, suggesting that the flexibility of the sidechain impedes the formation of concerted string-like motion [**Figure** 7.13(a)]. In addition, larger anions are less likely to form long strings. The average string length $\langle n_s \rangle$, presented in Figure 14c, decreases with increasing linker length for all the studied anions. Interestingly, there is no significant

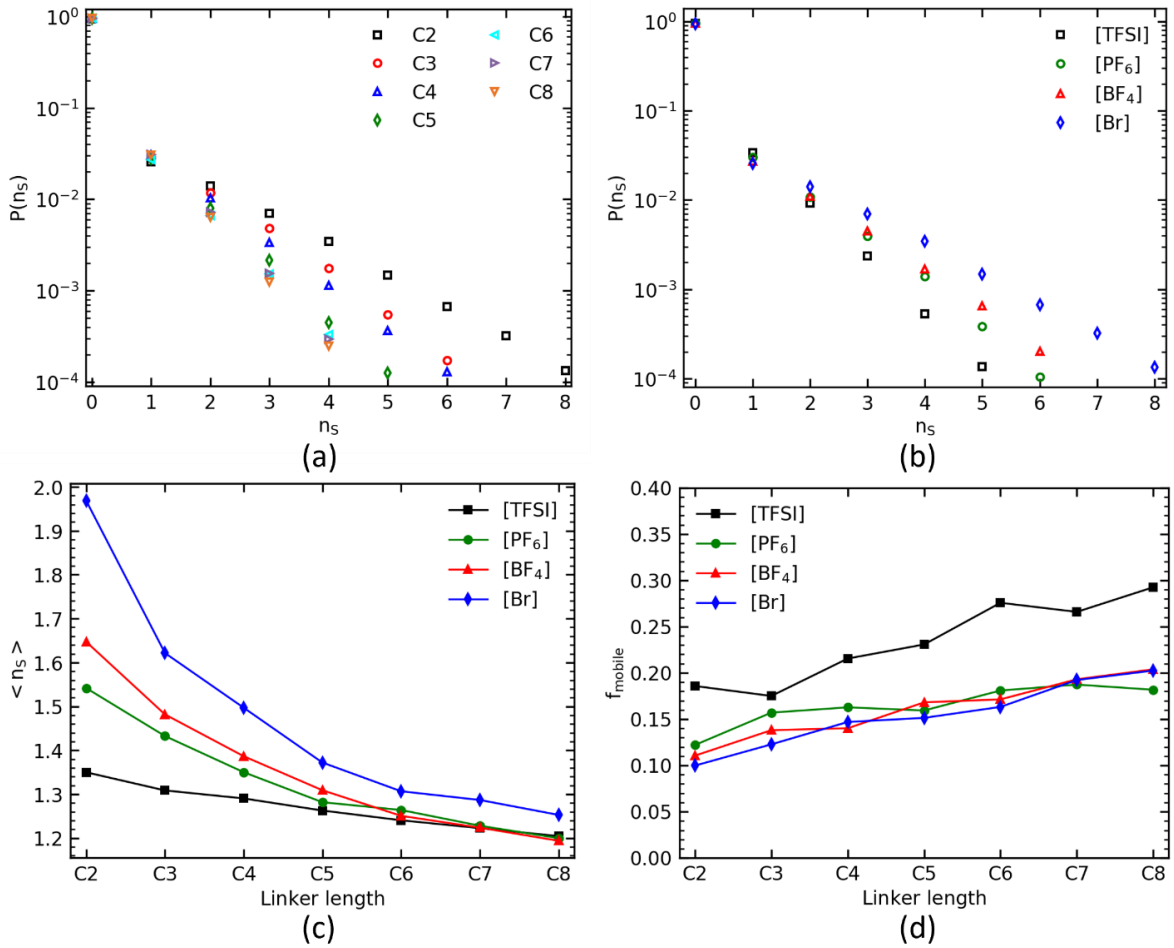

Figure 7.13. (a) The string length distribution for Br^- with different chain lengths in the linker at 580 K. (b) The string length distribution for various mobile anions. (c) The average string length $\langle n_s \rangle$ as a function of chain length for the four anions. (d) The fraction of mobile anions defined by both temporal and spatial scales (t^* and r^*).

difference in the average string length among the anions except for Br^- when the linker exceeds a certain length (> C6).

According to both the temporal and spatial criteria, the percentage of fast anions was accumulated in each system as shown in **Figure** 7.13(d). $TFSI^-$ consistently exhibits the highest fraction of fast anions ($15 - 30\%$), and this fraction generally increases with linker length. However, the three spherical anions do not show discernible differences or even a consistent order. Given that ion transport is primarily due to the fast anions, despite their limited numbers, it is worth comparing the characteristics of ion association and hoping types between the fast ions and slow ions.

Figure A.13 illustrates that the fast anions tend to associate with more cations from more coordinating chains compared with the slow anions, in contrast to the findings in poly(C2Vim)TFSI, where fast anions associate with fewer cations from more chains when the imidazole ring is directly attached to the backbone.[145] Moreover, interchain hopping predominates for fast anions, with only a slight influence from linker length. Conversely, linker length exerts a more pronounced effect on slow anions [see **Figure** A.13(c)].

7.2.5 Relaxation Time Underlying Anion Diffusivity

Ion diffusion has been correlated to the structural relaxation time, the ion association lifetime or ion cage lifetime in low molecular weight ILs[291] and polyILs.[144, 145, 148, 149, 283] To examine which relaxation process underlies ion diffusivity in these systems, we computed the intermittent correlation function, $C(t)$, and continuous time correlation function, $S(t)$, using the equations:

$$C(t) = \frac{\langle h(t)h(0)\rangle}{\langle h(0)\rangle} \tag{7.10}$$

$$S(t) = \frac{\langle H(t)h(0)\rangle}{\langle h(0)\rangle}, \tag{7.11}$$

where $h(t)$ is assigned unity if an ion association that was present at $t = 0$ will be present at time t independent of its occurrence in the interval $(0, t)$, and 0 otherwise, while $H(t)$ is unity if an ion association is retained up to time t, and 0 otherwise. The decay of $S(t)$ signifies the initial breaking of ion association, denoted by the ion association lifetime, τ_s, but the decay

of $C(t)$ indicates the ultimate dissociation of an ion pair without recovery, where the ion leaves the cage and does not return, denoted as a cage relaxation time τ_c. It is worth noting that this relaxation time, was also called the structural relaxation time in earlier papers,[144, 145, 149, 283] and can be confused with the structural relaxation time in liquid and polymer systems, which is obtained from the decay of intermediate scattering function. The fitting of $C(t)$ and $S(t)$ to a stretched exponential function is present in **Figure** A.14, and the corresponding relaxation times as a function of temperature are shown in **Figure** 7.14(a). Cage relaxation times are more than one order of magnitude larger than the average lifetime of ion association, and both decrease with temperature. An increase in the sidechain length gives rise to shorter τ_c and τ_s, particularly for the short linkers (C2 – C4). **Figure** 7.14(b) displays the correlation between anion self-diffusion coefficients and relaxation times for different linker lengths associated with four anions in the temperature range of 400 to 600 K. The fitting of the data to a power law $D_{\mathrm{A}} \sim \tau^{-\lambda}$ reveals that D_{A} exhibits a better linear correlation with τ_c^{-1} than τ_s^{-1} ($\lambda = 0.94$ for τ_c and $\lambda = 1.28$ for τ_s, respectively), which is consistent with our previous studies of other polyILs.[145, 149, 283] Notably, at low temperatures, the average lifetime of ion association significantly deviates from a power law. Such results confirm that the transient dissociation of an anion is necessary but not sufficient for the long-range diffusivity of the anions. It is worth mentioning that recent work has suggested that the time a mobile ion remains trapped inside a cage is associated with the mobility of the ion.[148]

7.3 Effect of Electrostatic Interactions

Another key factor in tuning ionic correlations in concentrated ionic systems is electrostatic interactions, whose role was investigated by changing the relative dielectric constant of the simulated systems.

7.3.1 Structural Highlights

We first examined how it influences the RDFs between the ions. **Figure** 7.15 depicts the cation-anion RDFs as a function of the relative permittivity at 500 K. The position of the first peak shifts to a larger distance when the relative dielectric constant is increased, and the peak becomes weaker and broader. However, the impact is small when the relative dielectric constant

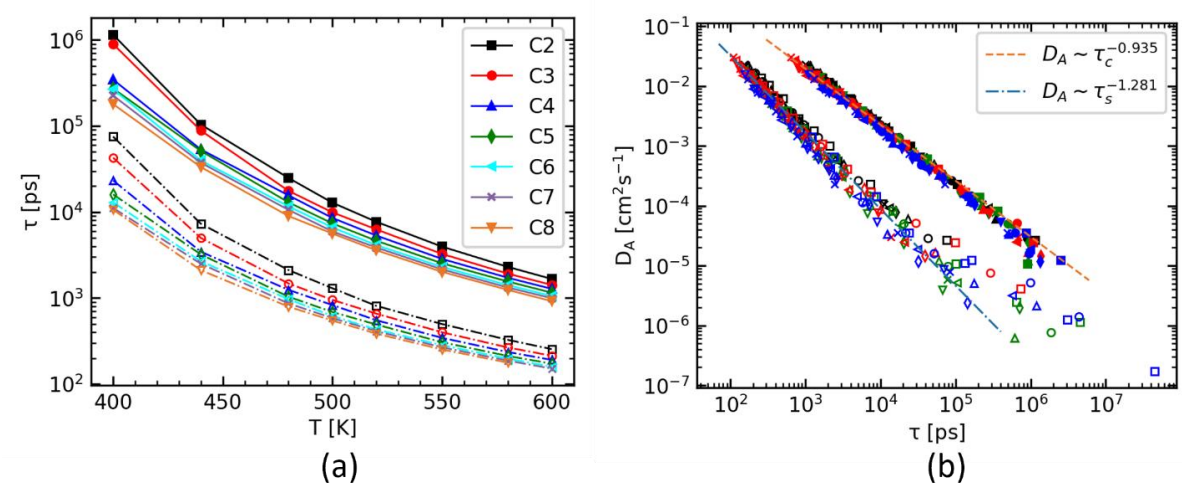

Figure 7.14. (a) Temperature dependence of cage time and average lifetime of ion association for various linker lengths. (b) Correlations of self-diffusivity and cage relaxation time or average lifetime of ion association for all studied systems.

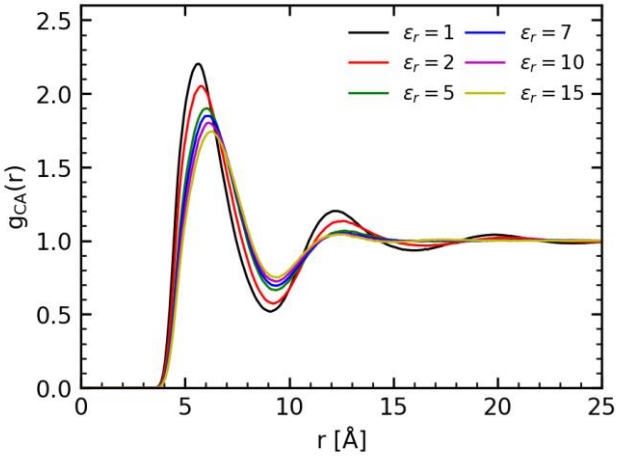

Figure 7.15. Radial distribution functions of cation-anion at 500 K for PMMA-C_2-IM[TFSI] as a function of the relative permittivity.

is sufficiently large ($\varepsilon_r > 5$). This trend is similar to that of the cation-anion RDFs for different anions, although the interactions between the cation with distinct anions are more complex due to multiple factors including the charge delocalization, size, and geometry. Interestingly, the positions of the first local minima remain unaffected by changes in the electrostatic interactions. To discern the effect of electrostatic interactions on the diffusion of anions, the diffusivities of $TFSI^-$, BF_4^-, and Br^- as a function of the relative permittivity in the PMMA-C_2-IM systems at 500 K were plotted in **Figure** 7.16. At low dielectric constants, the diffusivities of the smaller $BF4^-$ and Br^- are lower than that of the larger $TFSI^-$. However, at high dielectric constants, the smaller anions exhibit higher diffusivities. This shift occurs because, at high dielectric constants, the dominant factor changes from electrostatic interactions to the size/mass of the anion.

7.3.2 Dynamic Anion-Anion Correlations

Figure 7.17 shows the contribution of the anion-anion correlations as a function of the relative permittivity for three different anions. In general, the distinct anion-anion correlation is consistently negative, leading to a reduction in conductivity. Furthermore, electrostatic interactions influence these ionic correlations to varying extents. Specifically, changes in the dielectric constant have a more significant impact on the less delocalized anions (BF_4^- and Br^-) compared to the larger $TFSI^-$. Notably, when the relative permittivity is sufficiently large, Br^- exhibits similar correlation values to BF_4^-. This phenomenon may be due to the fact that at high relative permittivity, the mass of the anions becomes the dominant factor, and these two anions have similar mass. In contrast, the heavier $TFSI^-$ shows much smaller magnitudes for these correlations. This suggests that the increased mass and size of $TFSI^-$ result in weaker anion-anion correlations at high relative permittivity. Consequently, the impact of changes in the dielectric constant on $TFSI^-$ is less pronounced compared to BF_4^- and Br^-. This behavior highlights the importance of both the delocalization of charge and mass in determining the extent of anion-anion correlations and their influence on conductivity of the polyILs.

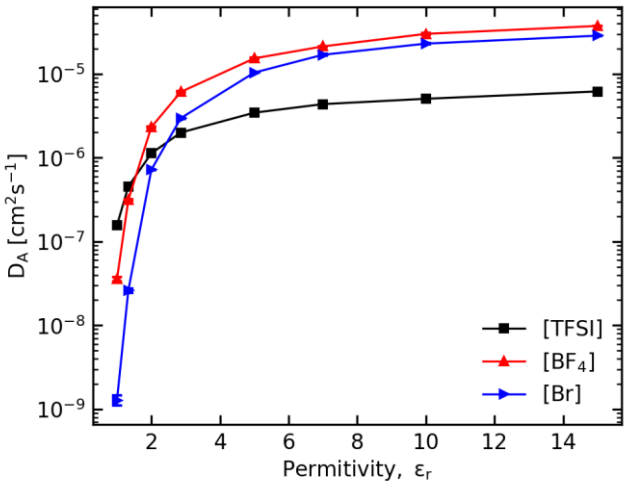

Figure 7.16. Diffusion coefficients of the three anions as a function of relative permittivity at 500 K.

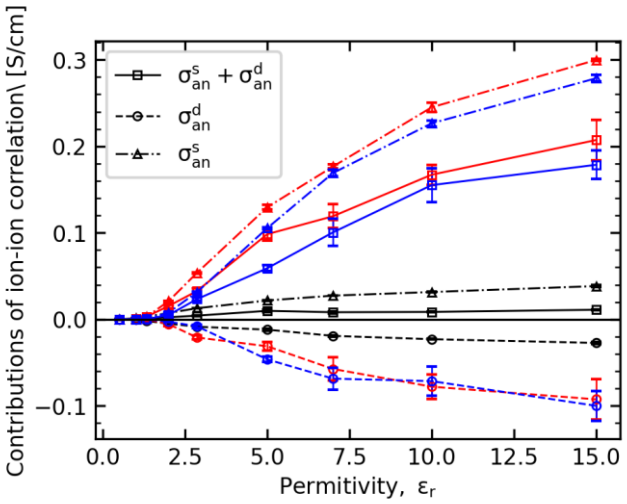

Figure 7.17. Contributions of anion-anion correlations as a function of relative permittivity for [TFSI] (black), [BF_4] (red), and [Br] (blue) at 500 K.

7.3.3 Dynamical Heterogeneity

The findings discussed above indicate that strong dynamical heterogeneity in the mobile anions results from strong interactions between the anions and polycations. To further verify if specific interactions between the ions are the dominant parameter, we examined the impact of electrostatic interactions on dynamical heterogeneity. In **Figure** 7.18(a), the MSD exhibits a plateau in the range of 1 – 10^3 ps before reaching the diffusive regime, indicating a ballistic motion when the anion is trapped in the "cage" formed by the strong specific interactions. As the electrostatic interactions decrease, the plateau gradually disappears, and the MSD increases. Meanwhile, the peak of α_2 weakens. Specifically, the maximum of α_2 decreases rapidly at lower relative permittivity and starts leveling off around 0.3 at higher relative permittivity [**Figure** 7.18(b)].

The corresponding time also decreases from ~10^3 to 10 ps as the dielectric constant increases. This behavior suggests that electrostatic interactions play a crucial role in modulating the dynamical heterogeneity of the system. As the dielectric constant increases, reducing the strength of the electrostatic interactions, the anions become less confined by the polycation "cage". Consequently, the anions exhibit more diffusive motion, as reflected by the disappearance of the plateau in the MSD and the decrease in the peak of α_2.

7.3.4 Stringlike Cooperative Motion

For fast anions, movement from one Coulombic cage to another, occupied by a different ion, can extend to a couple of anions, forming a dynamic string. When these Coulombic cages become loose due to the reduction in electrostatic interactions, the stringlike movement may be interrupted. Prior to examining the effects of electrostatic interactions on this stringlike cooperative motion, we determined the self-part and the distinct part of the van Hove function at the characteristic time, t^*, where $\alpha_2(t^*) = \alpha_2^{\max}$ for $TFSI^-$ as shown in **Figure** 7.19(a). The deviation from the corresponding Gaussian distribution decreases as the relative permittivity increases. Interestingly, if we define anions that travel farther than the distance r^* within time t^*, where $G_s(r^*, t^*) = G_{s,0}(r^*, t^*)$, as fast "mobile" anions, this distance criterion for distinguishing fast anions is only slightly affected by changes in the dielectric constant.

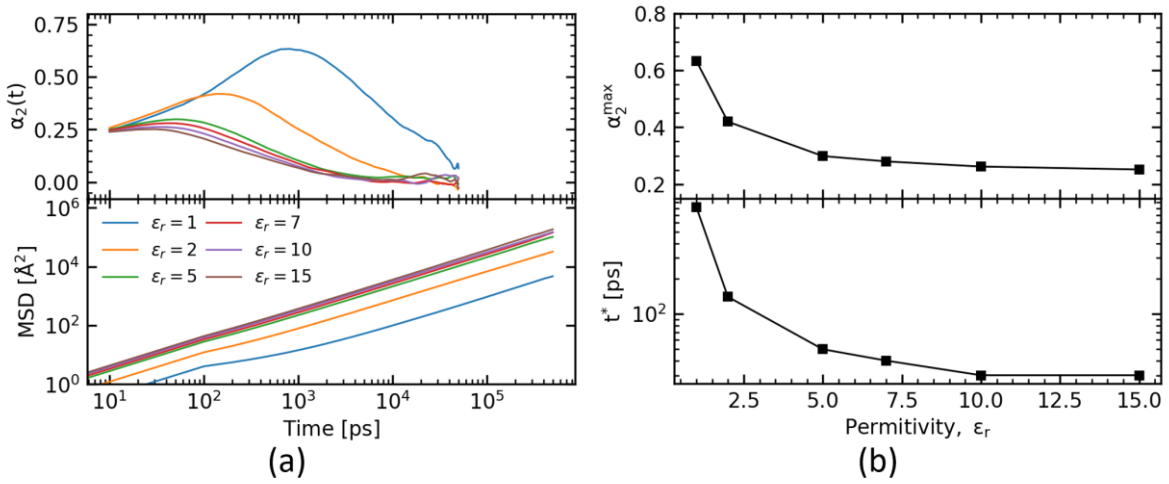

Figure 7.18. (a) Mean squared displacement (MSD) and the non-Gaussian parameters (α_2) for the anions as a function of the relative permittivity in PMMA-C_2-IM[TFSI] at 500 K. (b) Maxima of α_2 and the corresponding time when α_2 reaches the maximum as a function of the relative permittivity in PMMA-C_2-IM[TFSI] at 500 K.

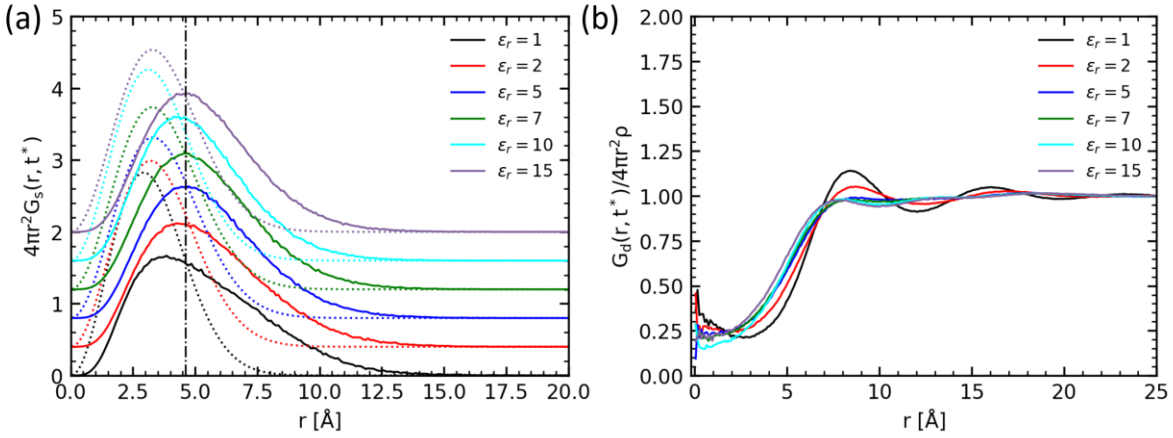

Figure 7.19. (a) Self-part of the van Hove function, $G_s(r, t^*)$, for PMMA-C_2-IM[TFSI] system as a function of the relative permittivity at 500K. Each curve in (a) is vertically shifted 0.5 for clarity. The vertical line represents the intersection of $G_s(r, t^*)$ (solid lines) and $G_{s,0}(r, t^*)$ (dotted lines), which is used as the r^* criterion to determine fast and slow anion populations. (b) Distinct-part of the van Hove function, $G_d(r, t^*)$, for PMMA-C_2-IM[TFSI] system as a function of the relative permittivity at 500 K.

Comparing the results for the different anions [**Figure** 7.12(c)], we may conclude that the size of the anion has a more significant impact on the distance criterion than electrostatic interactions.

Figure 7.19(b) shows the distinct part of the van Hove function as a function of the relative permittivity at 500 K. The peak at around $r = 0$ Å indicates the replacement of neighboring anions at the characteristic time, t^*. This peak decreases significantly when the relative dielectric constant increases from 1 to 5, and then does not exhibit a significant difference beyond that. Meanwhile, the dominant peak around $r = 9$ Å diminishes when the electrostatic interactions are sufficiently weak. Analysis of the stringlike motion for the fast anions demonstrates that the distribution of the string length generally shifts to the left as the relative permittivity increases (see **Figure** 7.20). The average string length decreases significantly at small values of permittivity while stabilizing at ~1.15 anions when $\varepsilon_r > 5$.

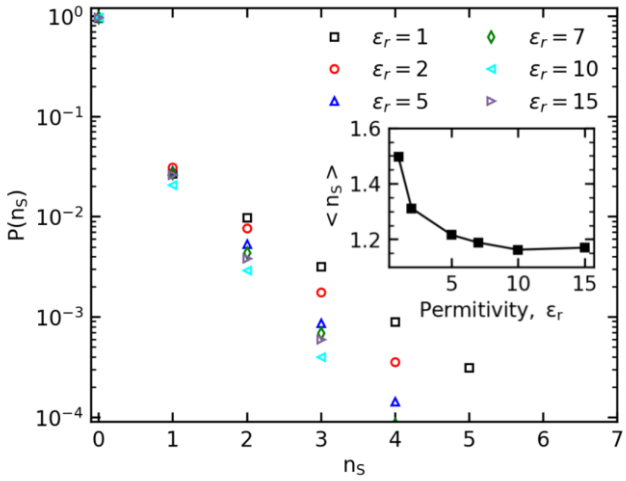

Figure 7.20. The string length distribution for PMMA-C_2-IM[TFSI] as a function of the relative permittivity at 500 K. Inset: average string length $\langle n_s \rangle$ as a function of the relative permittivity at 500 K.

Chapter 8 Conclusions

The exploration of novel electrolytes with high ionic conductivity is essential for advancing renewable and sustainable energy conversion and storage technologies. A fundamental understanding of the interplay between molecular structure, morphology, and proton/ion transport is critical for establishing design principles for high performance electrolytes. The research work reported in this dissertation focuses on applying and advancing multiscale modeling and simulations to study the morphology and proton/ion transport in various electrolytes, including: anion exchange membranes; protic ionic liquids; neat phosphoric acid; aqueous acid solutions; low molecular weight ionic liquids; and polymerized ionic liquids.

DPD simulations were performed to study the effect of pendant cationic groups and associated anions on the hydrated morphology and microstructure of SEBS-based AEMs. Microphase separation was observed in all simulations. It was determined that the functionalized polystyrene and polyethylene separate into a hydrophilic phase and a hydrophobic phase, respectively. Most water and the ionic species are only distributed throughout the hydrophilic phase, while some water is also present in the hydrophobic phase. The morphology transforms from perforated and interconnected lamellae to perfect lamellae and then to disordered bicontinuous domains as the hydration level increases from $\lambda = 4$ to 20. The perfect lamellae occur at $\lambda = 8$ for SEBS-TMP and $\lambda = 12$ for SEBS-TMA and SEBS-MIm. Exclusive water domains were observed at high hydration levels in all systems. However, the functional groups affect the distribution of water but have little influence on the backbone structure as observed through the analysis of the RDFs. The associated anion has greater impact on the size of the exclusive water domains when compared to the cationic groups. Large clusters of water and OH^- beads form when $\lambda \geq 8$ for SEBS-TMP, SEBS-TMA, and SEBS-MIm. Altering the anion leads to negligible changes in the W-W RDFs at $\lambda = 8$ and $\lambda = 12$, but the peaks increase significantly at $\lambda = 16$ and $\lambda = 20$. In addition, the effects of carbonation on the morphologies under different hydration levels were explored. At low water contents, CO_3^{2-} and HCO_3^- have a moderate influence on the morphologies. However, when the hydration level is sufficiently high, CO_3^{2-} exerts a more significant impact on the exclusive domains than HCO_3^-. This

phenomenon is likely due to the strong attraction between CO_3^{2-} and pendant cations, forming large hydrophilic domains. While HCO_3^- has minimal influence on the structure of water; it affects the shape of the hydrophilic region.

Ab initio molecular orbital calculations were performed to determine the fully optimized structures of TMA, IMI, LDC, and CRT with the addition of 1-3 PA molecules at the B3LYP/6-311G** level with inclusion of implicit solvation effects (i.e., $\varepsilon = 61$). Proton dissociation from PA occurs in all systems, resulting in the formation of ion pairs of the protonated base and negatively charged anion $H_2PO_4^-$ due to the relatively strong basicity of the bases and the effect of the high dielectric constant solvent on stabilizing the charge separation. The second and third PA molecules preferentially form 'ring-like' hydrogen bonds ranging from 2.48 to 2.73 Å in length with a PA molecule rather than with available hydrogen bond donor and acceptor sites of the base. Examination of the ZPE corrected binding energies of the PA molecules to various bases indicates that the first PA molecule is the most loosely bound to the IMI molecule compared to other systems. The binding energy per PA molecule increases with the addition of more PA molecules, as the second and third PA molecules form double hydrogen bonds with a PA molecule. The strongest binding energy was observed in the CRT systems.

PES scans were conducted to investigate the effects of the bases on the energetics of proton transfer between the PA molecules. The bases with stronger proton affinities exert a greater influence on the energetics for proton transfer between the PA molecules. However, the effects are minimal when the potential shifts from a double-well into a single-well. Barrierless proton transfer occurs in the CRT+3PA system, implying that the CRT may be a better potential candidate in the PA-based PILs. While these static electronic structure calculations provide some guidelines for understanding proton transfer in PILs, it is crucial to consider additional factors including quantum nuclear effects, dynamic bond length fluctuations, and effects of the extended hydrogen bond network.

The next section of this study investigated proton transport in pure PA and aqueous solutions of PA, sulfuric acid (SA), and nitric acid (NA) to elucidate proton transport mechanisms and

correlations using *ab initio* molecular dynamics (AIMD) simulations. Our findings reveal that protons move by surprisingly short jumps of only ~0.5-0.7 Å, which is much smaller than typical ion jump length in ILs and comparable to the distance of proton transfer between oxygen atoms. More importantly, AIMD results indicate that these proton jumps are anticorrelated, thereby suppressing conductivity. Consequently, we posit that a Grotthuss chain-like proton conductivity is impossible in a bulk liquid state.

On top of that, we extensively explored the similarities and differences in proton transport mechanisms in aqueous PA, SA, and NA at two acid-to-water ratios of 1:1 and 1:3. AIMD simulations systematically probe the solvation and transport of protons in these aqueous acids. Our observations highlight that self-dissociation between acid molecules occurs exclusively in aqueous PA systems, with higher water content reducing this phenomenon. PA solutions exhibit a small amount of H_3O^+ due to its weak acidity, while SA solutions have a notable population of hydrated protons alongside very few sulfate anions. The hydrogen bond structure is markedly influenced by the strength and character of the acid. In aqueous SA, strong hydrogen bonds form between water molecules due to the prevalence of H_3O^+, contrasting with the weak hydrogen bonds between SA molecules. In contrast, the strong hydrogen bonding between the PA molecules is only slightly affected by the presence of water. The hydronium ion exhibits a similar solvation structure as observed in slightly acidic water except for the donating hydrogen bond with an acid molecule that shows varying strengths in these systems.

Moreover, H_3O^+ population correlation functions indicate that proton rattling occurs on a very short time scale (~50 fs) in all these systems, enhanced by higher water contents. However, the lifetime of dissociated protons excluding rattling is much longer. This lifetime plays an important role in the structural diffusion of H^+, but it ignores the participation of the acid molecules in proton transport. Notably, acid molecules engage in proton diffusion by accepting a proton from H_3O^+, either facilitating the H^+ diffusion by shuttling the proton resulting in a large displacement via a collective proton hopping or impeding proton transport through rattling. Notable shuttling events occur in the aqueous PA systems, significantly contributing to proton transport. This is ascribed to the similar proton affinity of PA as water and its peculiar

proton donor and acceptor sites (3 OH proton donors and one unprotonated oxygen acceptor). Conversely, such shuttling rarely occurs in aqueous SA and is not observed in aqueous NA. Additionally, the decomposition of the proton diffusion into vehicular and structural components highlights that a significant contribution to H^+ transport occurs via structural diffusion facilitated by PA molecules. In aqueous NA systems, vehicular diffusion dominates at low water content. As hydration increases, structural diffusion improves due to more connected hydrogen bonds within the water molecules.

Dynamic correlations and the mechanism of ion transport in polyILs and their corresponding low molecular weight ILs were systematically studied using classical MD simulations by varying the molecular chemistry of the cation and anion. To validate the momentum conservation approach for assessing distinct ion-ion correlations from BDS data, we directly calculated dynamic correlations from the MD simulations using the Onsager transport coefficients. The excellent agreement between simulation and experimental data enables a detailed examination of how the anion-to-cation mass ratio and the tail length of the imidazolium ring impact ion-ion correlations. Our findings highlight that the behavior of the anion-anion and cation-cation correlations strongly depends on the anion-to-cation mass ratio, M_-/M_+. Specifically, when $M_-/M_+ > 1$, distinct anion-anion correlations exhibit a more pronounced suppression effect on the conductivity compared to distinct cation-cation correlations, where the opposite effect is observed, i.e., $M_-/M_+ < 1$. This switching effect was further confirmed by artificially varying the mass of [BF_4] in the MD simulations across a broad spectrum of molecular weight, while maintaining the same force field. Surprisingly, the distinct anion-anion correlation coincided with distinct cation-cation correlation when the ratio of the anion to cation mass (M_-/M_+) equals 1.25, rather than when the masses are identical. Experimental data also support this delay in the swapping, potentially due to the differences in ion shape and size. Moreover, simulations of a series of imidazolium-based ILs denoted as [C_mC_nIM][TFSI] (m = 1 and 2; n = 1-8) suggest that symmetrical shapes may facilitate the translational motion of the cation, but both tails need to be sufficiently long to make the motion directional.

Furthermore, classical MD simulations were performed for PMMA-C_x-IM with varying linker lengths (x = 2 – 8) and associated with various anions, including a linear $TFSI^-$, and three spherical anions: PF_6^-, BF_4^-, and Br^-. We systematically explored the effects of sidechain flexibility coupled with the specific interactions between anion and cation on ion transport. Initially, we verified that longer linkers afforded greater flexibility to the pendant cations, allowing them to extend over larger distances and explore wider angular ranges. This enhanced flexibility can potentially influence the interaction between the imidazole ring and the acrylate groups within the sidechain. However, the sidechain flexibility has minimal impact on the interactions between cations and anions compared to changes in the associated anion.

Importantly, our results show that the diffusion coefficients of smaller anions exhibit a more pronounced affect (i.e., increase) with increasing linker length compared to the larger ones. This enhancement of anion diffusivity may be ascribed to significant increases in diffusive motion, albeit with less pronounced reductions in ion hopping. To quantify the contribution of ion hopping to anion diffusion, we define the ion hopping as the deviated area of the self-part of the van Hove function from an ideal Gaussian distribution. The results demonstrate that the contribution of ion hopping is smaller than that of diffusive motion and this ion hopping fraction decreases as the linker length increases. Specifically, the smallest anion Br^- exhibits the largest portion of ion hopping from one "cage" to another amongst these anions due to the strongest specific interaction between the less charge delocalized Br^- and the cations.

Fortunately, the rigid "cage" can be significantly softened by increased sidechain flexibility. Dynamical heterogeneity in anion mobility further supports the softening effect of longer linkers, in which both the maximum of the non-Gaussian parameter and the time of the strongest heterogeneity swiftly decrease when the linker is varied from C2 to C4 followed by a much slower decrease when the linker is further increased. Moreover, our findings reveal that only a small fraction of anions travel beyond the characteristic distance determined by the distance at which the self-part of van Hove function at the characteristic time of the strongest heterogeneity intersected with its corresponding Gaussian distribution. Notably, the criteria for fast anions are not affected by the sidechain flexibility.

Regarding the ion hopping mechanism, fast mobile anions primarily engage in interchain hopping, with a higher involvement of cations from multiple chains compared to slow anions. A long linker promotes interchain hopping but reduces intrachain hopping. Our results also identify stringlike cooperative motion in the fast anions, with decreasing string length as the linker length is increased. Interestingly, distinct anion-anion correlations were observed to suppress conductivity in a barycentric reference frame but to enhance conductivity under a polycation-fixed reference frame. This highlights the importance of considering different reference frames when analyzing ion transport phenomena in polyILs. Ultimately, our findings underscore that cage escape plays a pivotal role as the primary mechanism governing anion transport in these systems.

In summary, this dissertation offers significant insight into the intricate interplay between molecular chemistry, morphology, and proton/ion transport in various specific electrolytes, including: AEMs; PILs; pure PA; aqueous acid; low molecular weight ILs; and polyILs. The findings from the multiscale simulations have improved our understanding of proton/ion transport mechanisms, which will pave the way for tailored design strategies aimed at optimizing the transport properties of these materials for diverse applications, ranging from energy storage devices to electrochemical sensors.

References

(1) Zhu, Z.; Paddison, S. J. Perspective: Morphology and Ion Transport in Ion-Containing Polymers from Multiscale Modeling and Simulations. *Front. Chem.* **2022,** *10*, 981508.

(2) Shen, K.-H.; Fan, M.; Hall, L. M. Molecular Dynamics Simulations of Ion-Containing Polymers Using Generic Coarse-Grained Models. *Macromolecules* **2021,** *54*, 2031-2052.

(3) Ma, B.; Olvera de la Cruz, M. A Perspective on the Design of Ion-Containing Polymers for Polymer Electrolyte Applications. *J. Phys. Chem. B* **2021,** *125*, 3015-3022.

(4) Fong, K. D.; Self, J.; McCloskey, B. D.; Persson, K. A. Ion Correlations and Their Impact on Transport in Polymer-Based Electrolytes. *Macromolecules* **2021,** *54*, 2575-2591.

(5) Wang, R.-Y.; Park, M. J. Self-Assembly of Block Copolymers with Tailored Functionality: From the Perspective of Intermolecular Interactions. *Annu. Rev. Mater. Res.* **2020,** *50*, 521-549.

(6) Bocharova, V.; Sokolov, A. P. Perspectives for Polymer Electrolytes: A View from Fundamentals of Ionic Conductivity. *Macromolecules* **2020,** *53*, 4141-4157.

(7) Elabd, Y. A. Ion Transport in Hydroxide Conducting Block Copolymers. *Mol. Syst. Des. Eng.* **2019,** *4*, 519-530.

(8) Gottesfeld, S.; Dekel, D. R.; Page, M.; Bae, C.; Yan, Y.; Zelenay, P.; Kim, Y. S. Anion Exchange Membrane Fuel Cells: Current Status and Remaining Challenges. *J. Power Sources* **2018,** *375*, 170-184.

(9) Dekel, D. R. Review of Cell Performance in Anion Exchange Membrane Fuel Cells. *J. Power Sources* **2018,** *375*, 158-169.

(10) Kusoglu, A.; Weber, A. Z. New Insights into Perfluorinated Sulfonic-Acid Ionomers. *Chem. Rev.* **2017,** *117*, 987-1104.

(11) Wojnarowska, Z.; Paluch, M. Recent Progress on Dielectric Properties of Protic Ionic Liquids. *J Phys. Condens. Matter.* **2015,** *27*, 073202.

(12) Greaves, T. L.; Drummond, C. J. Protic Ionic Liquids: Evolving Structure-Property Relationships and Expanding Applications. *Chem. Rev.* **2015,** *115*, 11379-11448.

(13) Sundmacher, K. Fuel Cell Engineering: Toward the Design of Efficient Electrochemical Power Plants. *Ind. Eng. Chem. Res.* **2010,** *49*, 10159-10182.

(14) Marx, D.; Chandra, A.; Tuckerman, M. E. Aqueous Basic Solutions: Hydroxide Solvation, Structural Diffusion, and Comparison to the Hydrated Proton. *Chem. Rev.* **2010,** *110*, 2174-2216.

(15) Armand, M.; Endres, F.; MacFarlane, D. R.; Ohno, H.; Scrosati, B. Ionic-liquid Materials for the Electrochemical Challenges of the Future. *Nat. Mater.* **2009,** *8*, 621-629.

(16) Belieres, J.-P.; Angell, C. A. Protic Ionic Liquids: Preparation, Characterization, and Proton Free Energy Level Representation. *J. Phys. Chem. B* **2007,** *111*, 4926-4937.

(17) Wraight, C. A. Chance and Design—Proton Transfer in Water, Channels and Bioenergetic Proteins. *Biochim. Biophys. Acta, Bioenerg.* **2006,** *1757*, 886-912.

(18) Marx, D. Proton Transfer 200 Years after von Grotthuss: Insights from Ab Initio Simulations. *ChemPhysChem* **2006,** *7*, 1848-1870.

(19) Sammes, N.; Bove, R.; Stahl, K. Phosphoric Acid Fuel Cells: Fundamentals and Applications. *Curr. Opin. Solid State Mater.* **2004,** *8*, 372-378.

(20) Kreuer, K.-D.; Paddison, S. J.; Spohr, E.; Schuster, M. Transport in Proton Conductors for Fuel-Cell Applications: Simulations, Elementary Reactions, and Phenomenology. *Chem. Rev.* **2004,** *104*, 4637-4678.
(21) Austen Angell, C.; Ansari, Y.; Zhao, Z. Ionic Liquids: Past, Present and Future. *Faraday Discuss.* **2012,** *154*, 9-27.
(22) Son, C. Y.; Wang, Z.-G. Ion Transport in Small-Molecule and Polymer Electrolytes. *J. Chem. Phys.* **2020,** *153*, 100903.
(23) Gebel, G.; Diat, O. Neutron and X-ray Scattering: Suitable Tools for Studying Ionomer Membranes. *Fuel Cells* **2005,** *5*, 261-276.
(24) Melchior, J.-P.; Jalarvo, N. H. A Quasielastic Neutron Scattering Study of Water Diffusion in Model Anion Exchange Membranes over Localized and Extended Volume Increments. *J. Phys. Chem. C* **2019,** *123*, 14195-14206.
(25) Perrin, J.-C.; Lyonnard, S.; Volino, F. Quasielastic Neutron Scattering Study of Water Dynamics in Hydrated Nafion Membranes. *J. Phys. Chem. C* **2007,** *111*, 3393-3404.
(26) Münchinger, A.; Kreuer, K.-D. Selective Ion Transport through Hydrated Cation and Anion Exchange Membranes I. The Effect of Specific Interactions. *J. Membr. Sci.* **2019,** *592*.
(27) Giffin, G. A.; Haugen, G. M.; Hamrock, S. J.; Di Noto, V. Interplay between Structure and Relaxations in Perfluorosulfonic Acid Proton Conducting Membranes. *J. Am. Chem. Soc.* **2013,** *135*, 822-834.
(28) Zimudzi, T. J.; Hickner, M. A. Signal Enhanced FTIR Analysis of Alignment in NAFION Thin Films at SiO_2 and Au Interfaces. *ACS Macro Lett.* **2016,** *5*, 83-87.
(29) Meek, K. M.; Reed, C. M.; Pivovar, B.; Kreuer, K.-D.; Varcoe, J. R.; Bance-Soualhi, R. The Alkali Degradation of LDPE-Based Radiation-Grafted Anion-Exchange Membranes Studied Using Different Ex Situ Methods. *RSC Adv.* **2020,** *10*, 36467-36477.
(30) Economou, N. J.; Barnes, A. M.; Wheat, A. J.; Schaberg, M. S.; Hamrock, S. J.; Buratto, S. K. Investigation of Humidity Dependent Surface Morphology and Proton Conduction in Multi-Acid Side Chain Membranes by Conductive Probe Atomic Force Microscopy. *J. Phys. Chem. B* **2015,** *119*, 14280-14287.
(31) Zhang, Z.; Cui, Y.; Vila, R.; Li, Y.; Zhang, W.; Zhou, W.; Chiu, W.; Cui, Y. Cryogenic Electron Microscopy for Energy Materials. *Acc. Chem. Res.* **2021,** *54*, 3505-3517.
(32) Allen, F. I.; Comolli, L. R.; Kusoglu, A.; Modestino, M. A.; Minor, A. M.; Weber, A. Z. Morphology of Hydrated As-Cast Nafion Revealed through Cryo Electron Tomography. *ACS Macro Lett.* **2015,** *4*, 1-5.
(33) Chen, C.; Tse, Y. L. S.; Lindberg, G. E.; Knight, C.; Voth, G. A. Hydroxide Solvation and Transport in Anion Exchange Membranes. *J. Am. Chem. Soc.* **2016,** *138*, 991-1000.
(34) Zhang, W.; van Duin, A. C. T. ReaxFF Reactive Molecular Dynamics Simulation of Functionalized Poly(phenylene oxide) Anion Exchange Membrane. *J. Phys. Chem. C* **2015,** *119*, 27727-27736.
(35) Bedrov, D.; Piquemal, J.-P.; Borodin, O.; MacKerell, A. D.; Roux, B.; Schröder, C. Molecular Dynamics Simulations of Ionic Liquids and Electrolytes Using Polarizable Force Fields. *Chem. Rev.* **2019,** *119*, 7940-7995.
(36) Zhang, Z.; Zofchak, E.; Krajniak, J.; Ganesan, V. Influence of Polarizability on the

Structure, Dynamic Characteristics, and Ion-Transport Mechanisms in Polymeric Ionic Liquids. *J. Phys. Chem. B* **2022,** *126*, 2583-2592.
(37) Zhu, Z.; Luo, X.; Paddison, S. J. Coarse-Grained Modeling of Ion-Containing Polymers. *Chem. Rev.* **2022,** *122*, 10710-10745.
(38) Peng, X.; Kashyap, V.; Ng, B.; Kurungot, S.; Wang, L.; Varcoe, J.; Mustain, W. High-Performing PGM-Free AEMFC Cathodes from Carbon-Supported Cobalt Ferrite Nanoparticles. *Catalysts* **2019,** *9*, 264.
(39) Chai, G. L.; Hou, Z.; Shu, D. J.; Ikeda, T.; Terakura, K. Active Sites and Mechanisms for Oxygen Reduction Reaction on Nitrogen-Doped Carbon Alloy Catalysts: Stone-Wales Defect and Curvature Effect. *J. Am. Chem. Soc.* **2014,** *136*, 13629-13640.
(40) Lee, M.-T. Designing Highly Conductive Block Copolymer-Based Anion Exchange Membranes by Mesoscale Simulations. *J. Phys. Chem. B* **2021,** *125*, 2729-2740.
(41) Luo, X.; Liu, H.; Bae, C.; Tuckerman, M. E.; Hickner, M. A.; Paddison, S. J. Mesoscale Simulations of Quaternary Ammonium-Tethered Triblock Copolymers: Effects of the Degree of Functionalization and Styrene Content. *J. Phys. Chem. C* **2020,** *124*, 16315-16323.
(42) Zhu, Z.; Luo, X.; Paddison, S. J. DPD Simulations of Anion Exchange Membranes Functionalized with Various Cationic Groups and Associated Anions. *Solid State Ion.* **2019,** *340*, 115011.
(43) Luo, X.; Paddison, S. J. DPD Simulations of Anion Exchange Membrane: The Effect of an Alkyl Spacer on the Hydrated Morphology. *Solid State Ion.* **2019,** *339*, 115012.
(44) Sepehr, F.; Liu, H.; Luo, X.; Bae, C.; Tuckerman, M. E.; Hickner, M. A.; Paddison, S. J. Mesoscale Simulations of Anion Exchange Membranes Based on Quaternary Ammonium Tethered Triblock Copolymers. *Macromolecules* **2017,** *50*, 4397-4405.
(45) Lee, M.-T. Designing Anion Exchange Membranes with Enhanced Hydroxide Ion Conductivity by Mesoscale Simulations. *J. Phys. Chem. C* **2020,** *124*, 4470-4482.
(46) Lee, M.-T. Exploring Side-Chain Designs for Enhanced Ion Conductivity of Anion-Exchange Membranes by Mesoscale Simulations. *J. Phys. Chem. C* **2019,** *123*, 10802-10815.
(47) Chen, S.; Wang, H.; Zhang, J.; Lu, S.; Xiang, Y. Effect of Side Chain on the Electrochemical Performance of Poly (ether ether ketone) Based Anion-Exchange Membrane: A Molecular Dynamics Study. *J. Membr. Sci.* **2020,** *605*, 118105.
(48) Li, L.; Wang, J.-A.; Ma, L.; Bai, L.; Zhang, A.; Qaisrani, N. A.; Yan, X.; Zhang, F.; He, G. Dual-Side-Chain-Grafted Poly(phenylene oxide) Anion Exchange Membranes for Fuel-Cell and Electrodialysis Applications. *ACS Sustain. Chem. Eng.* **2021,** *9*, 8611-8622.
(49) Zhu, L.; Pan, J.; Wang, Y.; Han, J.; Zhuang, L.; Hickner, M. A. Multication Side Chain Anion Exchange Membranes. *Macromolecules* **2016,** *49*, 815-824.
(50) Pan, J.; Li, Y.; Han, J.; Li, G.; Tan, L.; Chen, C.; Lu, J.; Zhuang, L. A Strategy for Disentangling the Conductivity–Stability Dilemma in Alkaline Polymer Electrolytes. *Energ. Environ. Sci.* **2013,** *6*.
(51) Dong, D.; Zhang, W.; van Duin, A. C. T.; Bedrov, D. Grotthuss versus Vehicular Transport of Hydroxide in Anion-Exchange Membranes: Insight from Combined Reactive and Nonreactive Molecular Simulations. *J. Phys. Chem. Lett.* **2018,** *9*, 825-829.
(52) Dong, D.; Wei, X.; Hooper, J. B.; Pan, H.; Bedrov, D. Role of Cationic Groups on

Structural and Dynamical Correlations in Hydrated Quaternary Ammonium-Functionalized Poly(p-phenylene oxide)-Based Anion Exchange Membranes. *Phys. Chem. Chem. Phys.* **2018,** *20*, 19350-19362.
(53) Ma, L.; Qaisrani, N. A.; Hussain, M.; Li, L.; Jia, Y.; Ma, S.; Zhou, R.; Bai, L.; He, G.; Zhang, F. Cyclodextrin Modified, Multication Cross-Linked High Performance Anion Exchange Membranes for Fuel Cell Application. *J. Membr. Sci.* **2020,** *607*, 118190.
(54) Chen, W.; Mandal, M.; Huang, G.; Wu, X.; He, G.; Kohl, P. A. Highly Conducting Anion-Exchange Membranes Based on Cross-Linked Poly(norbornene): Ring Opening Metathesis Polymerization. *ACS Appl. Energy Mater.* **2019,** *2*, 2458-2468.
(55) Jeon, J. Y.; Park, S.; Han, J.; Maurya, S.; Mohanty, A. D.; Tian, D.; Saikia, N.; Hickner, M. A.; Ryu, C. Y.; Tuckerman, M. E., et al. Synthesis of Aromatic Anion Exchange Membranes by Friedel–Crafts Bromoalkylation and Cross-Linking of Polystyrene Block Copolymers. *Macromolecules* **2019,** *52*, 2139-2147.
(56) Kacar, G.; Peters, E. A. J. F.; de With, G. Mesoscopic Simulations for the Molecular and Network Structure of a Thermoset Polymer. *Soft Matter* **2013,** *9*.
(57) Jorn, R.; Savage, J.; Voth, G. A. Proton Conduction in Exchange Membranes across Multiple Length Scales. *Acc. Chem. Res.* **2012,** *45*, 2002-2010.
(58) Tuckerman, M. E.; Chandra, A.; Marx, D. A Statistical Mechanical Theory of Proton Transport Kinetics in Hydrogen-Bonded Networks Based on Population Correlation Functions with Applications to Acids and Bases. *J. Chem. Phys.* **2010,** *133*, 124108.
(59) Tuckerman, M. E.; Marx, D.; Klein, M. L.; Parrinello, M. On the Quantum Nature of the Shared Proton in Hydrogen Bonds. *Science* **1997,** *275*, 817.
(60) Savage, J.; Tse, Y.-L. S.; Voth, G. A. Proton Transport Mechanism of Perfluorosulfonic Acid Membranes. *J. Phys. Chem. C* **2014,** *118*, 17436-17445.
(61) Devanathan, R.; Venkatnathan, A.; Rousseau, R.; Dupuis, M.; Frigato, T.; Gu, W.; Helms, V. Atomistic Simulation of Water Percolation and Proton Hopping in Nafion Fuel Cell Membrane. *J. Phys. Chem. B* **2010,** *114*, 13681-13690.
(62) Dong, D.; Zhang, W.; Barnett, A.; Lu, J.; van Duin, A. C. T.; Molinero, V.; Bedrov, D. Multiscale Modeling of Structure, Transport and Reactivity in Alkaline Fuel Cell Membranes: Combined Coarse-Grained, Atomistic and Reactive Molecular Dynamics Simulations. *Polymers* **2018,** *10*, 1289.
(63) Zelovich, T.; Long, Z.; Hickner, M.; Paddison, S. J.; Bae, C.; Tuckerman, M. E. Ab Initio Molecular Dynamics Study of Hydroxide Diffusion Mechanisms in Nanoconfined Structural Mimics of Anion Exchange Membranes. *J. Phys. Chem. C* **2019,** *123*, 4638-4653.
(64) Zelovich, T.; Vogt-Maranto, L.; Simari, C.; Nicotera, I.; Hickner, M. A.; Paddison, S. J.; Bae, C.; Dekel, D. R.; Tuckerman, M. E. Non-Monotonic Temperature Dependence of Hydroxide Ion Diffusion in Anion Exchange Membranes. *Chem. Mater.* **2022,** *34*, 2133-2145.
(65) Zelovich, T.; Tuckerman, M. E. Water Layering Affects Hydroxide Diffusion in Functionalized Nanoconfined Environments. *J. Phys. Chem. Lett.* **2020,** *11*, 5087-5091.
(66) Zelovich, T.; Vogt-Maranto, L.; Hickner, M. A.; Paddison, S. J.; Bae, C.; Dekel, D. R.; Tuckerman, M. E. Hydroxide Ion Diffusion in Anion-Exchange Membranes at Low Hydration: Insights from Ab Initio Molecular Dynamics. *Chem. Mater.* **2019,** *31*, 5778-5787.

(67) Kreuer, K.-D. Proton Conductivity: Materials and Applications. *Chem. Mater.* **1996,** *8*, 610-641.
(68) Arntsen, C.; Chen, C.; Calio, P. B.; Li, C.; Voth, G. A. The Hopping Mechanism of the Hydrated Excess Proton and its Contribution to Proton Diffusion in Water. *J. Chem. Phys.* **2021,** *154*, 194506.
(69) Berkelbach, T. C.; Lee, H.-S.; Tuckerman, M. E. Concerted Hydrogen-Bond Dynamics in the Transport Mechanism of the Hydrated Proton: A First-Principles Molecular Dynamics Study. *Phys. Rev. Lett.* **2009,** *103*, 238302.
(70) Tuckerman, M. E.; Marx, D.; Parrinello, M. The Nature and Transport Mechanism of Hydrated Hydroxide Ions in Aqueous Solution. *Nature* **2002,** *417*, 925-929.
(71) Agmon, N. The Grotthuss Mechanism. *Chem. Phys. Lett.* **1995,** *244*, 456-462.
(72) Kreuer, K.-D.; Rabenau, A.; Weppner, W. Vehicle Mechanism, A New Model for the Interpretation of the Conductivity of Fast Proton Conductors. *Angew. Chem., Int. Ed. Engl.* **1982,** *21*, 208-209.
(73) Greenwood, N. N.; Thompson, A. Proton-Switch as a Mechanism for Conduction in Anhydrous Phosphoric Acid. *P. Chem. Soc. London* **1958**, 352-353.
(74) Suwannakham, P.; Chaiwongwattana, S.; Sagarik, K. Proton Dissociation and Transfer in Hydrated Phosphoric Acid Clusters. *Int. J. Quantum Chem.* **2015,** *115*, 486-501.
(75) Clark, J. K., II; Paddison, S. J. Ab Initio Molecular Dynamics Simulations of Water and an Excess Proton in Water Confined in Carbon Nanotubes. *Phys. Chem. Chem. Phys.* **2014,** *16*, 17756-17769.
(76) Wang, Y.; Lane, N. A.; Sun, C. N.; Fan, F.; Zawodzinski, T. A.; Sokolov, A. P. Ionic Conductivity and Glass Transition of Phosphoric Acids. *J. Phys. Chem. B* **2013,** *117*, 8003-8009.
(77) Vilciauskas, L.; Tuckerman, M. E.; Bester, G.; Paddison, S. J.; Kreuer, K. D. The Mechanism of Proton Conduction in Phosphoric Acid. *Nat. Chem.* **2012,** *4*, 461-466.
(78) Habenicht, B. F.; Paddison, S. J. Ab Initio Simulations of the Effects of Nanoscale Confinement on Proton Transfer in Hydrophobic Environments. *J. Phys. Chem. B* **2011,** *115*, 10826-10835.
(79) Vilciauskas, L.; Paddison, S. J.; Kreuer, K.-D. Ab Initio Modeling of Proton Transfer in Phosphoric Acid Clusters. *J. Phys. Chem. A* **2009,** *113*, 9193–9201.
(80) Li, S. J.; Qian, W.; Tao, F. M. Ionic Dissociation of Methanesulfonic Acid in Small Water Clusters. *Chem. Phys. Lett.* **2007,** *438*, 190-195.
(81) Aihara, Y.; Sonai, A.; Hattori, M.; Hayamizu, K. Ion Conduction Mechanisms and Thermal Properties of Hydrated and Anhydrous Phosphoric Acids Studied With1H, 2H, And31P NMR. *J. Phys. Chem. B* **2006,** *110*, 24999–25006.
(82) Dippel, T.; Kreuer, K. D.; Lassègues, J. C.; Rodriguez, D. Proton Conductivity in Fused Phosphoric Acid; A $^{1}H/^{31}P$ PFG-NMR and QNS Study. *Solid State Ion.* **1993,** *61*, 41-46.
(83) Hoarfrost, M. L.; Tyagi, M.; Segalman, R. A.; Reimer, J. A. Proton Hopping and Long-Range Transport in the Protic Ionic Liquid [Im][TFSI], Probed by Pulsed-Field Gradient NMR and Quasi-Elastic Neutron Scattering. *J. Phys. Chem. B* **2012,** *116*, 8201-8209.
(84) Kreuer, K. D.; Fuchs, A.; Ise, M.; Spaeth, M.; Maier, J. Imidazole and Pyrazole-based

Proton Conducting Polymers and Liquids. *Electrochim. Acta* **1998,** *43*, 1281-1288.
(85) Wojnarowska, Z.; Paluch, K. J.; Shoifet, E.; Schick, C.; Tajber, L.; Knapik, J.; Wlodarczyk, P.; Grzybowska, K.; Hensel-Bielowka, S.; Verevkin, S. P., et al. Molecular Origin of Enhanced Proton Conductivity in Anhydrous Ionic Systems. *J Am. Chem. Soc.* **2015,** *137*, 1157-1164.
(86) Wojnarowska, Z.; Grzybowska, K.; Hawelek, L.; Swiety-Pospiech, A.; Masiewicz, E.; Paluch, M.; Sawicki, W.; Chmielewska, A.; Bujak, P.; Markowski, J. Molecular Dynamics Studies on the Water Mixtures of Pharmaceutically Important Ionic Liquid Lidocaine HCl. *Mol. Pharm.* **2012,** *9*, 1250-1261.
(87) Wojnarowska, Z.; Wang, Y.; Paluch, K. J.; Sokolov, A. P.; Paluch, M. Observation of Highly Decoupled Conductivity in Protic Ionic Conductors. *Phys. Chem. Chem. Phys.* **2014,** *16*, 9123-9127.
(88) Elm, J.; Myllys, N.; Kurtén, T. Phosphoric Acid – A Potentially Elusive Participant in Atmospheric New Particle Formation. *Mol. Phys.* **2017,** *115*, 2168-2179.
(89) Sipilä, M.; Berndt, T.; Petäjä, T.; Brus, D.; Vanhanen, J.; Stratmann, F.; Patokoski, J.; Mauldin, R. L.; Hyvärinen, A.-P.; Lihavainen, H., et al. The Role of Sulfuric Acid in Atmospheric Nucleation. *Science* **2010,** *327*, 1243-1246.
(90) Turco, R. P.; Whitten, R. C.; Toon, O. B. Stratospheric Aerosols: Observation and Theory. *Rev. Geophys.* **1982,** *20*, 233-279.
(91) Galloway, J. N.; Likens, G. E. Acid Precipitation: The Importance of Nitric Acid. *Atmos. Environ. (1967)* **1981,** *15*, 1081-1085.
(92) Mikalčiūtė, A.; Vilčiauskas, L. Insights into the Hydrogen Bond Network Topology of Phosphoric Acid and Water Systems. *Phys. Chem. Chem. Phys.* **2021,** *23*, 6213-6224.
(93) Ahlmann, S.; Münzner, P.; Moch, K.; Sokolov, A. P.; Böhmer, R.; Gainaru, C. The Relationship between Charge and Molecular Dynamics in Viscous Acid Hydrates. *J. Chem. Phys.* **2021,** *155*, 014505.
(94) Melchior, J.-P.; Kreuer, K.-D.; Maier, J. Proton Conduction Mechanisms in the Phosphoric Acid–Water System ($H_4P_2O_7$–$H_3PO_4 \cdot 2H_2O$): a ^{1}H, ^{31}P and ^{17}O PFG-NMR and Conductivity Study. *Phys. Chem. Chem. Phys.* **2017,** *19*, 587-600.
(95) Frick, B.; Vilčiauskas, L.; Deen, P. P.; Lyonnard, S. The Nanosecond Proton Dynamics of Phosphoric Acid – from the Solid to the Melt – Investigated by Neutron Backscattering. *Solid State Ion.* **2013,** *252*, 26-33.
(96) Tromp, R. H.; Spieser, S. H.; Neilson, G. W. A Neutron Diffraction and Computer Modeling Study of the Interatomic Structure of Phosphoric Acid. *J. Chem. Phys.* **1999,** *110*, 2145-2150.
(97) Choe, Y.-K.; Tsuchida, E.; Ikeshoji, T. First-Principles Molecular Dynamics Study on Aqueous Sulfuric Acid Solutions. *J. Chem. Phys.* **2007,** *126*, 154510.
(98) Wang, J. T.; Savinell, R. F.; Wainright, J.; Litt, M.; Yu, H. A H_2O_2 Fuel Cell Using Acid Doped Polybenzimidazole as Polymer Electrolyte. *Electrochim. Acta* **1996,** *41*, 193-197.
(99) Wainright, J. S.; Wang, J. T.; Weng, D.; Savinell, R. F.; Litt, M. Acid-Doped Polybenzimidazoles: A New Polymer Electrolyte. *J. Electrochem. Soc.* **1995,** *142*, L121.
(100) Kreuer, K. D. On the Development of Proton Conducting Materials for Technological Applications. *Solid State Ion.* **1997,** *97*, 1-15.

(101) Cukierman, S. Et tu, Grotthuss! and Other Unfinished Stories. *Biochim. Biophys. Acta, Bioenerg.* **2006,** *1757*, 876-885.
(102) von Grotthuss, C. J. T. Sur la Décomposition de L'eau et des Corps Qu'elle Tient en Dissolution à L'aide de L'électricité Galvanique. *Ann. Chim.* **1806,** *58*, 54– 73.
(103) Zelovich, T.; Tuckerman, M. E. Controlling Hydronium Diffusivity in Model Proton Exchange Membranes. *J. Phys. Chem. Lett.* **2022,** *13*, 2245-2253.
(104) Zelovich, T.; Winey, K. I.; Tuckerman, M. E. Hydronium Ion Diffusion in Model Proton Exchange Membranes at Low Hydration: Insights from Ab Initio Molecular Dynamics. *J. Mater. Chem. A* **2021,** *9*, 2448-2458.
(105) Calio, P. B.; Li, C.; Voth, G. A. Resolving the Structural Debate for the Hydrated Excess Proton in Water. *J. Am. Chem. Soc.* **2021,** *143*, 18672-18683.
(106) Long, Z.; Atsango, A. O.; Napoli, J. A.; Markland, T. E.; Tuckerman, M. E. Elucidating the Proton Transport Pathways in Liquid Imidazole with First-Principles Molecular Dynamics. *J. Phys. Chem. Lett.* **2020,** *11*, 6156-6163.
(107) Peng, Y.; Swanson, J. M. J.; Kang, S.-g.; Zhou, R.; Voth, G. A. Hydrated Excess Protons Can Create Their Own Water Wires. *J. Phys. Chem. B* **2015,** *119*, 9212-9218.
(108) Knight, C.; Voth, G. A. The Curious Case of the Hydrated Proton. *Acc. Chem. Res.* **2012,** *45*, 101-109.
(109) Feng, S.; Voth, G. A. Proton Solvation and Transport in Hydrated Nafion. *J. Phys. Chem. B* **2011,** *115*, 5903-5912.
(110) Cao, Z.; Peng, Y.; Yan, T.; Li, S.; Li, A.; Voth, G. A. Mechanism of Fast Proton Transport along One-Dimensional Water Chains Confined in Carbon Nanotubes. *J. Am. Chem. Soc.* **2010,** *132*, 11395-11397.
(111) Swanson, J. M. J.; Simons, J. Role of Charge Transfer in the Structure and Dynamics of the Hydrated Proton. *J. Phys. Chem. B* **2009,** *113*, 5149-5161.
(112) Hayes, R. L.; Paddison, S. J.; Tuckerman, M. E. Proton Transport in Triflic Acid Hydrates Studied via Path Integral Car-Parrinello Molecular Dynamics. *J. Phys. Chem. B* **2009,** *113*, 16574–16589.
(113) Marx, D.; Tuckerman, M. E.; Hutter, J.; Parrinello, M. The Nature of the Hydrated Excess Proton in Water. *Nature* **1999,** *397*, 601-604.
(114) Tuckerman, M.; Laasonen, K.; Sprik, M.; Parrinello, M. Ab Initio Molecular Dynamics Simulation of the Solvation and Transport of Hydronium and Hydroxyl Ions in Water. *J. Chem. Phys.* **1995,** *103*, 150-161.
(115) Tuckerman, M.; Laasonen, K.; Sprik, M.; Parrinello, M. Ab Initio Molecular Dynamics Simulation of the Solvation and Transport of H_3O^+ and OH^- Ions in Water. *J. Phys. Chem.* **1995,** *99*, 5749-5752.
(116) Chen, M.; Zheng, L.; Santra, B.; Ko, H.-Y.; DiStasio Jr, R. A.; Klein, M. L.; Car, R.; Wu, X. Hydroxide Diffuses Slower than Hydronium in Water because its Solvated Structure Inhibits Correlated Proton Transfer. *Nat. Chem.* **2018,** *10*, 413-419.
(117) Zundel, G.; Metzger, H. Energiebänder der tunnelnden Überschuß-Protonen in flüssigen Säuren. Eine IR-spektroskopische Untersuchung der Natur der Gruppierungen $H_5O_2^+$. *Z. für Phys. Chem.* **1968,** *58*, 225-245.

(118) Markovitch, O.; Chen, H.; Izvekov, S.; Paesani, F.; Voth, G. A.; Agmon, N. Special Pair Dance and Partner Selection: Elementary Steps in Proton Transport in Liquid Water. *J. Phys. Chem. B* **2008,** *112*, 9456-9466.
(119) Lapid, H.; Agmon, N.; Petersen, M. K.; Voth, G. A. A Bond-Order Analysis of the Mechanism for Hydrated Proton Mobility in Liquid Water. *J. Chem. Phys.* **2004,** *122*, 014506.
(120) Schmitt, U. W.; Voth, G. A. The Computer Simulation of Proton Transport in Water. *J. Chem. Phys.* **1999,** *111*, 9361-9381.
(121) Liu, R.; Zhang, C.; Liang, X.; Liu, J.; Wu, X.; Chen, M. Structural and Dynamic Properties of Solvated Hydroxide and Hydronium Ions in Water from Ab Initio Modeling. *J. Chem. Phys.* **2022,** *157*, 024503.
(122) Adams, E. M.; Hao, H.; Leven, I.; Rüttermann, M.; Wirtz, H.; Havenith, M.; Head-Gordon, T. Proton Traffic Jam: Effect of Nanoconfinement and Acid Concentration on Proton Hopping Mechanism. *Angew. Chem.* **2021,** *133*, 25623-25631.
(123) Clark, J. K., II; Habenicht, B. F.; Paddison, S. J. Ab Initio Molecular Dynamics Simulations of Aqueous Triflic Acid Confined in Carbon Nanotubes. *Phys. Chem. Chem. Phys.* **2014,** *16*, 16465-16479.
(124) Zelovich, T.; Tuckerman, M. E. OH(-) and $H_3O(+)$ Diffusion in Model AEMs and PEMs at Low Hydration: Insights from Ab Initio Molecular Dynamics. *Membranes (Basel)* **2021,** *11*.
(125) Tse, Y.-L. S.; Herring, A. M.; Kim, K.; Voth, G. A. Molecular Dynamics Simulations of Proton Transport in 3M and Nafion Perfluorosulfonic Acid Membranes. *J. Phys. Chem. C* **2013,** *117*, 8079-8091.
(126) Park, K.; Lin, W.; Paesani, F. A Refined MS-EVB Model for Proton Transport in Aqueous Environments. *J. Phys. Chem. B* **2012,** *116*, 343-352.
(127) Petersen, M. K.; Voth, G. A. Characterization of the Solvation and Transport of the Hydrated Proton in the Perfluorosulfonic Acid Membrane Nafion. *J. Phys. Chem. B* **2006,** *110*, 18594-18600.
(128) Vuilleumier, R.; Borgis, D. Proton Conduction: Hopping Along Hydrogen Bonds. *Nat. Chem.* **2012,** *4*, 432-433.
(129) Vilčiauskas, L.; Tuckerman, M. E.; Melchior, J. P.; Bester, G.; Kreuer, K.-D. First Principles Molecular Dynamics Study of Proton Dynamics and Transport in Phosphoric Acid/Imidazole (2:1) System. *Solid State Ion.* **2013,** *252*, 34-39.
(130) Ingenmey, J.; Gehrke, S.; Kirchner, B. How to Harvest Grotthuss Diffusion in Protic Ionic Liquid Electrolyte Systems. *ChemSusChem* **2018,** *11*, 1900-1910.
(131) Li, Q.; Yan, F.; Texter, J. Polymerized and Colloidal Ionic Liquids─Syntheses and Applications. *Chem. Rev.* **2024,** *124*, 3813-3931.
(132) Popov, I.; Biernacka, K.; Zhu, H.; Nti, F.; Porcarelli, L.; Wang, X.; Khamzin, A.; Gainaru, C.; Forsyth, M.; Sokolov, A. P. Strongly Correlated Ion Dynamics in Plastic Ionic Crystals and Polymerized Ionic Liquids. *J. Phys. Chem. C* **2020,** *124*, 17889-17896.
(133) Ganesan, V. Ion Transport in Polymeric Ionic Liquids: Recent Developments and Open Questions. *Mol. Syst. Des. Eng.* **2019,** *4*, 280-293.
(134) Mogurampelly, S.; Borodin, O.; Ganesan, V. Computer Simulations of Ion Transport in Polymer Electrolyte Membranes. *Annu. Rev. Chem. Biomol. Eng.* **2016,** *7*, 349-371.

(135) Kisliuk, A.; Bocharova, V.; Popov, I.; Gainaru, C.; Sokolov, A. P. Fundamental Parameters Governing Ion Conductivity in Polymer Electrolytes. *Electrochim. Acta* **2019,** *299*, 191-196.
(136) Stacy, E. W.; Gainaru, C. P.; Gobet, M.; Wojnarowska, Z.; Bocharova, V.; Greenbaum, S. G.; Sokolov, A. P. Fundamental Limitations of Ionic Conductivity in Polymerized Ionic Liquids. *Macromolecules* **2018,** *51*, 8637-8645.
(137) Iacob, C.; Matsumoto, A.; Brennan, M.; Liu, H.; Paddison, S. J.; Urakawa, O.; Inoue, T.; Sangoro, J.; Runt, J. Polymerized Ionic Liquids: Correlation of Ionic Conductivity with Nanoscale Morphology and Counterion Volume. *ACS Macro Lett.* **2017,** *6*, 941-946.
(138) Fu, Y.; Bocharova, V.; Ma, M.; Sokolov, A. P.; Sumpter, B. G.; Kumar, R. Effects of Counterion Size and Backbone Rigidity on the Dynamics of Ionic Polymer Melts and Glasses. *Phys. Chem. Chem. Phys.* **2017,** *19*, 27442-27451.
(139) Bocharova, V.; Wojnarowska, Z.; Cao, P.-F.; Fu, Y.; Kumar, R.; Li, B.; Novikov, V. N.; Zhao, S.; Kisliuk, A.; Saito, T., et al. Influence of Chain Rigidity and Dielectric Constant on the Glass Transition Temperature in Polymerized Ionic Liquids. *J. Phys. Chem. B* **2017,** *121*, 11511-11519.
(140) Wojnarowska, Z.; Feng, H.; Fu, Y.; Cheng, S.; Carroll, B.; Kumar, R.; Novikov, V. N.; Kisliuk, A. M.; Saito, T.; Kang, N.-G., et al. Effect of Chain Rigidity on the Decoupling of Ion Motion from Segmental Relaxation in Polymerized Ionic Liquids: Ambient and Elevated Pressure Studies. *Macromolecules* **2017,** *50*, 6710-6721.
(141) Fan, F.; Wang, W.; Holt, A. P.; Feng, H.; Uhrig, D.; Lu, X.; Hong, T.; Wang, Y.; Kang, N.-G.; Mays, J., et al. Effect of Molecular Weight on the Ion Transport Mechanism in Polymerized Ionic Liquids. *Macromolecules* **2016,** *49*, 4557-4570.
(142) Fan, F.; Wang, Y.; Hong, T.; Heres, M. F.; Saito, T.; Sokolov, A. P. Ion Conduction in Polymerized Ionic Liquids with Different Pendant Groups. *Macromolecules* **2015,** *48*, 4461-4470.
(143) Sangoro, J. R.; Iacob, C.; Agapov, A. L.; Wang, Y.; Berdzinski, S.; Rexhausen, H.; Strehmel, V.; Friedrich, C.; Sokolov, A. P.; Kremer, F. Decoupling of Ionic Conductivity from Structural Dynamics in Polymerized Ionic Liquids. *Soft Matter* **2014,** *10*, 3536-3540.
(144) Mogurampelly, S.; Keith, J. R.; Ganesan, V. Mechanisms Underlying Ion Transport in Polymerized Ionic Liquids. *J. Am. Chem. Soc.* **2017,** *139*, 9511-9514.
(145) Liu, H.; Luo, X.; Sokolov, A. P.; Paddison, S. J. Quantitative Evidence of Mobile Ion Hopping in Polymerized Ionic Liquids. *J. Phys. Chem. B* **2021,** *125*, 372-381.
(146) Wang, Y.; Fan, F.; Agapov, A. L.; Yu, X.; Hong, K.; Mays, J.; Sokolov, A. P. Design of Superionic Polymers—New Insights from Walden Plot Analysis. *Solid State Ion.* **2014,** *262*, 782-784.
(147) Yoshida, K.; Manabe, H.; Takahashi, Y.; Furukawa, T. Correlation between Ionic and Molecular Dynamics in the Liquid State of Polyethylene Oxide/Lithium Perchlorate Complexes. *Electrochim. Acta* **2011,** *57*, 139-146.
(148) Xiao, W.; Yang, Q.; Zhu, S. Comparing Ion Transport in Ionic Liquids and Polymerized Ionic Liquids. *Sci. Rep.* **2020,** *10*, 7825.
(149) Luo, X.; Liu, H.; Paddison, S. J. Molecular Dynamics Simulations of Polymerized Ionic

Liquids: Mechanism of Ion Transport with Different Anions. *ACS Appl. Polym. Mater.* **2020,** *3*, 141-152.
(150) Gainaru, C.; Stacy, E. W.; Bocharova, V.; Gobet, M.; Holt, A. P.; Saito, T.; Greenbaum, S.; Sokolov, A. P. Mechanism of Conductivity Relaxation in Liquid and Polymeric Electrolytes: Direct Link between Conductivity and Diffusivity. *J Phys. Chem. B* **2016,** *120*, 11074-11083.
(151) Dyre, J. C.; Maass, P.; Roling, B.; Sidebottom, D. L. Fundamental Questions Relating to Ion Conduction in Disordered Solids. *Rep. Prog. Phys.* **2009,** *72*, 046501.
(152) Roling, B.; Martiny, C.; Brückner, S. Ion Transport in Glass: Influence of Glassy Structure on Spatial Extent of Nonrandom Ion Hopping. *Phys. Rev. B* **2001,** *63* 214203.
(153) Maass, P.; Meyer, M.; Bunde, A. Nonstandard Relaxation Behavior in Ionically Conducting Materials. *Phys. Rev. B* **1995,** *51*, 8164.
(154) Kashyap, H. K.; Annapureddy, H. V.; Raineri, F. O.; Margulis, C. J. How is Charge Transport Different in Ionic Liquids and Electrolyte Solutions? *J. Phys. Chem. B* **2011,** *115*, 13212-13221.
(155) Zhang, Z.; Wheatle, B. K.; Krajniak, J.; Keith, J. R.; Ganesan, V. Ion Mobilities, Transference Numbers, and Inverse Haven Ratios of Polymeric Ionic Liquids. *ACS Macro Lett.* **2020,** *9*, 84-89.
(156) Shen, K.-H.; Hall, L. M. Ion Conductivity and Correlations in Model Salt-Doped Polymers: Effects of Interaction Strength and Concentration. *Macromolecules* **2020,** *53*, 3655-3668.
(157) Nürnberg, P.; Atik, J.; Borodin, O.; Winter, M.; Paillard, E.; Schönhoff, M. Superionicity in Ionic-Liquid-Based Electrolytes Induced by Positive Ion–Ion Correlations. *J. Am. Chem. Soc.* **2022,** *144*, 4657-4666.
(158) Hohenberg, P.; Kohn, W. Inhomogeneous Electron Gas. *Phys. Rev.* **1964,** *136*, B864-B871.
(159) Becke, A. D. Density-functional Thermochemistry. III. The Role of Exact Exchange. *J. Chem. Phys.* **1993,** *98*, 5648-5652.
(160) Marx, D.; Hutter, J., *Ab Initio Molecular Dynamics: Basic Theory and Advanced Methods*; Cambridge University Press: Cambridge: 2009.
(161) Car, R.; Parrinello, M. Unified Approach for Molecular Dynamics and Density Functional Theory. *Phys. Rev. Lett.* **1985,** *55*, 2471−2474.
(162) Sprenger, K. G.; Jaeger, V. W.; Pfaendtner, J. The General AMBER Force Field (GAFF) Can Accurately Predict Thermodynamic and Transport Properties of Many Ionic Liquids. *J. Phys. Chem. B* **2015,** *119*, 5882-5895.
(163) Hoogerbrugge, P. J.; Koelman, J. M. V. A. Simulating Microscopic Hydrodynamic Phenomena with Dissipative Particle Dynamics. *Europhys. Lett.* **1992,** *19*, 155-160.
(164) Español, P. Dissipative Particle Dynamics with Energy Conservation. *Europhys. Lett.* **1997,** *40*, 631-636.
(165) Español, P.; Warren, P. B. Statistical Mechanics of Dissipative Particle Dynamics. *Europhys. Lett.* **1995,** *30*, 191-196.
(166) Español, P. Hydrodynamics from Dissipative Particle Dynamics. *Phys. Rev. E* **1995,** *52*, 1734-1742.

(167) Avalos, J. B.; Mackie, A. D. Dissipative Particle Dynamics with Energy Conservation. *Europhys. Lett.* **1997,** *40*, 141-146.
(168) Groot, R. D.; Warren, P. B. Dissipative Particle Dynamics: Bridging the Gap between Atomistic and Mesoscopic Simulation. *J. Chem. Phys.* **1997,** *107*, 4423-4435.
(169) Sliozberg, Y. R.; Strawhecker, K. E.; Andzelm, J. W.; Lenhart, J. L. Computational and Experimental Investigation of Morphology in Thermoplastic Elastomer gels Composed of AB/ABA Blends in B-Selective Solvent. *Soft Matter* **2011,** *7*, 7539-7551.
(170) Sliozberg, Y. R.; Andzelm, J. W.; Brennan, J. K.; Vanlandingham, M. R.; Pryamitsyn, V.; Ganesan, V. Modeling Viscoelastic Properties of Triblock Copolymers: A DPD Simulation Study. *J. Polym. Sci. B: Polym. Phys.* **2010,** *48*, 15-25.
(171) Soto-Figueroa, C. s.; Rodríguez-Idalgo, M. a.-D.-R.; Martínez-Magadán, J.-M.; Vicente, L. Dissipative Particle Dynamics Study of Order−Order Phase Transition of BCC, HPC, OBDD, and LAM Structures of the Poly(styrene)−Poly(isoprene) Diblock Copolymer. *Macromolecules* **2008,** *41*, 3297-3304.
(172) Soto-Figueroa, C.; Vicente, L.; Martínez-Magadán, J. M.; Rodríguez-Hidalgo, M. D. R. Mesoscopic Simulation of Asymmetric-Copolymer/Homopolymer Blends: Microphase Morphological Modification by Homopolymer Chains Solubilization. *Polymer* **2007,** *48*, 3902-3911.
(173) Soto-Figueroa, C.; Vicente, L.; Martínez-Magadán, J. M.; Rodríguez-Hidalgo, M. D. R. Self-Organization Process of Ordered Structures in Linear and Star Poly (styrene)-Poly(isoprene) Block Copolymers: Gaussian Models and Mesoscopic Parameters of Polymeric Systems. *J. Phys. Chem. B* **2007,** *111*, 11756-11764.
(174) Abu-Sharkh, B.; Alsunaidi, A. Morphology and Conformation Analysis of Self-Assembled Triblock Copolymer Melts. *Macromol. Theor. Simul.* **2006,** *15*, 507-515.
(175) Soto-Figueroa, C.; Rodríguez-Hidalgo, M. D. R.; Martínez-Magadán, J. M. Molecular Simulation of Diblock Copolymers; Morphology and Mechanical Properties. *Polymer* **2005,** *46*, 7485-7493.
(176) Groot, R. D.; Rabone, K. L. Mesoscopic Simulation of Cell Membrane Damage, Morphology Change and Rupture by Nonionic Surfactants. *Biophys. J.* **2001,** *81*, 725-736.
(177) Matsen, M. W.; Tompson, R. B. Equilibrium Behavior of Asymmetric ABA Triblock Copolymer Melts. *J. Chem. Phys.* **2000,** *113*, 5539.
(178) Groot, R. D.; Madden, T. J.; Tildesley, D. J. On the Role of Hydrodynamic Interactions in Block Copolymer Microphase Separation. *J. Chem. Phys.* **1999,** *110*, 9739-9749.
(179) Español, P.; Warren, P. B. Perspective: Dissipative Particle Dynamics. *J. Chem. Phys.* **2017,** *146*, 16.
(180) Santo, K. P.; Neimark, A. V. Dissipative Particle Dynamics Simulations in Colloid and Interface Science: A Review. *Adv. Colloid Interface Sci.* **2021,** *298*, 102545.
(181) Mao, R.; Lee, M.-T.; Vishnyakov, A.; Neimark, A. V. Modeling Aggregation of Ionic Surfactants Using a Smeared Charge Approximation in Dissipative Particle Dynamics Simulations. *J. Phys. Chem. B* **2015,** *119*, 11673-11683.
(182) Vishnyakov, A.; Neimark, A. V. Self-Assembly in Nafion Membranes upon Hydration: Water Mobility and Adsorption Isotherms. *J. Phys. Chem. B* **2014,** *118*, 11353-11364.

(183) Groot, R. D. Electrostatic Interactions in Dissipative Particle Dynamics-Simulation of Polyelectrolytes and Anionic Surfactants. *J. Chem. Phys.* **2003,** *118*, 11265-11277.
(184) Lee, M.-T.; Vishnyakov, A.; Neimark, A. V. Coarse-Grained Model of Water Diffusion and Proton Conductivity in Hydrated Polyelectrolyte Membrane. *J. Chem. Phys.* **2016,** *144*, 12.
(185) Lee, M.-T.; Vishnyakov, A.; Neimark, A. V. Modeling Proton Dissociation and Transfer Using Dissipative Particle Dynamics Simulation. *J. Chem. Theory Comput.* **2015,** *11*, 4395-4403.
(186) Chantawansri, T. L.; Sirk, T. W.; Mrozek, R.; Lenhart, J. L.; Kröger, M.; Sliozberg, Y. R. The Effect of Polymer Chain Length on the Mechanical Properties of Triblock Copolymer Gels. *Chem. Phys. Lett.* **2014,** *612*, 157-161.
(187) Chantawansri, T. L.; Sirk, T. W.; Sliozberg, Y. R. Entangled Triblock Copolymer Gel: Morphological and Mechanical Properties. *J. Chem. Phys.* **2013,** *138*, 024908
(188) Sirk, T. W.; Slizoberg, Y. R.; Brennan, J. K.; Lisal, M.; Andzelm, J. W. An Enhanced Entangled Polymer Model for Dissipative Particle Dynamics. *J. Chem. Phys.* **2012,** *136*, 134903.
(189) Vishnyakov, A.; Talaga, D. S.; Neimark, A. V. DPD Simulation of Protein Conformations: From α-Helices to β-Structures. *J. Phys. Chem. Lett.* **2012,** *3*, 3081-3087.
(190) Roy, S.; Markova, D.; Kumar, A.; Klapper, M.; Mu, F. Morphology of Phosphonic Acid-Functionalized Block Copolymers Studied by Dissipative Particle Dynamics Morphology of Phosphonic Acid-Functionalized Block Copolymers Studied by Dissipative Particle Dynamics. *Macromolecules* **2009,** *42*, 841-848.
(191) Lindvig, T.; Michelsen, M. L.; Kontogeorgis, G. M. A Flory-Huggins Model Based on the Hansen Solubility Parameters. *Fluid Phase Equilib.* **2002,** *203*, 247-260.
(192) Hansen, C. M., *Hansen Solubility Parameters: A User's Handbook*; CRC press: 2002; p 544.
(193) Mayoral, E.; Goicochea, A. G. Modeling the Temperature Dependent Interfacial Tension between Organic Solvents and Water Using Dissipative Particle Dynamics. *J. Chem. Phys.* **2013,** *138*, 094703.
(194) Maiti, A.; McGrother, S. Bead-Bead Interaction Parameters in Dissipative Particle Dynamics: Relation to Bead-Size, Solubility Parameter, and Surface Tension. *J. Chem. Phys.* **2004,** *120*, 1594-1601.
(195) Fan, C.; Olafson, B. D.; Blanco, M. Application of Molecular Simulation to Derive Phase Diagrams of Binary Mixtures. *Macromolecules* **1992,** *25*, 3667-3676.
(196) Metropolis, N.; Rosenbluth, A. W.; Rosenbluth, M. N.; Teller, A. H.; Teller, E. Equation of State Calculations by Fast Computing Machines. *J. Chem. Phys.* **1953,** *21*, 1087-1092.
(197) Yamamoto, S.; Hyodo, S.-A. A Computer Simulation Study of the Mesoscopic Structure of the Polyelectrolyte Membrane Nafion. *Polym. J.* **2003,** *35*, 519-527.
(198) Vishnyakov, A.; Lee, M.-T.; Neimark, A. V. Prediction of the Critical Micelle Concentration of Nonionic Surfactants by Dissipative Particle Dynamics Simulations. *J. Phys. Chem. Lett.* **2013,** *4*, 797-802.
(199) Widom, B. Some Topics in the Theory of Fluids. *J. Chem. Phys.* **1963,** *39*, 2808-2812.
(200) Eckert, F.; Klamt, A. Cosmotherm, Version C3.0, Release 12.01. *Cosmologic Gmbh &*

Co. Kg: Leverkusen, Germany **2012**.
(201) Klamt, A. Conductor-Like Screening Model for Real Solvents: A New Approach to the Quantitative Calculation of Solvation Phenomena. *J. Phys. Chem.* **1995,** *99*, 2224-2235.
(202) Vishnyakov, A.; Mao, R.; Lee, M.-T.; Neimark, A. V. Coarse-Grained Model of Nanoscale Segregation, Water Diffusion, and Proton Transport in Nafion Membranes. *J. Chem. Phys.* **2018,** *148*, 024108.
(203) Sepehr, F.; Paddison, S. J. Dissipative Particle Dynamics Interaction Parameters from Ab Initio Calculations. *Chem. Phys. Lett.* **2016,** *645*, 20-26.
(204) Okuwaki, K.; Mochizuki, Y.; Doi, H.; Ozawa, T. Fragment Molecular Orbital Based Parametrization Procedure for Mesoscopic Structure Prediction of Polymeric Materials. *J. Phys. Chem. B* **2018,** *122*, 338-347.
(205) Fedorov, D. G.; Kitaura, K.; eds, *The Fragment Molecular Orbital Method: Practical Applications to Large Molecular Systems*; CRC press, Boca Raton: 2009; p 288.
(206) Okuwaki, K.; Mochizuki, Y.; Doi, H.; Kawada, S.; Ozawa, T.; Yasuoka, K. Theoretical Analyses on Water Cluster Structures in Polymer Electrolyte Membrane by Using Dissipative Particle Dynamics Simulations with Fragment Molecular Orbital Based Effective Parameters. *RSC Adv.* **2018,** *8*, 34582-34595.
(207) J-OCTA Website. https://www.j-octa.com.
(208) Mochizuki, Y.; Koikegami, S.; Nakano, T.; Amari, S.; Kitaura, K. Large Scale MP2 Calculations with Fragment Molecular Orbital Scheme. *Chem. Phys. Lett.* **2004,** *396*, 473-479.
(209) Schoenert, H. J. Evaluation of Velocity Correlation Coefficients from Experimental Transport Data in Electrolytic Systems. *J. Phys. Chem.* **1984,** *88*, 3359-3363.
(210) Dyre, J. C.; Maass, P.; Roling, B.; Sidebottom, D. L. Fundamental Questions Relating to Ion Conduction in Disordered Solids. *Rep. Prog. Phys.* **2009,** *72*, 046501.
(211) Popov, I.; Khamzin, A.; Matsumoto, R. A.; Zhao, W.; Lin, X.; Cummings, P. T.; Sokolov, A. P. Controlling the Ion Transport Number in Solvent-in-Salt Solutions. *J. Phys. Chem. B* **2022,** *126*, 4572-4583.
(212) Zadok, I.; Long, H.; Pivovar, B.; Roznowska, A.; Michalak, A.; Dekel, D. R.; Srebnik, S. Unexpected Hydroxide Ion Structure and Properties at Low Hydration. *J. Mol. Liq.* **2018,** *313*, 113485.
(213) Zhu, Z.; Tuckerman, M. E. Ab Initio Molecular Dynamics Investigation of the Concentration Dependence of Charged Defect Transport in Basic Solutions via Calculation of the Infrared Spectrum†. *J. Phys. Chem. B* **2002,** *106*, 8009-8018.
(214) Bajaj, P.; Riera, M.; Lin, J. K.; Mendoza Montijo, Y. E.; Gazca, J.; Paesani, F. Halide Ion Microhydration: Structure, Energetics, and Spectroscopy of Small Halide–Water Clusters. *J. Phys. Chem. A* **2019,** *123*, 2843-2852.
(215) Ge, L.; Bernasconi, L.; Hunt, P. Linking Electronic and Molecular Structure: Insight into Aqueous Chloride Solvation. *Phys. Chem. Chem. Phys.* **2013,** *15*, 13169-13183.
(216) Plimpton, S. Fast Parallel Algorithms for Short-Range Molecular Dynamics. *J. Comput. Phys.* **1995,** *117*, 1-19.
(217) Martinez, L.; Andrade, R.; Birgin, E. G.; Martinez, J. M. PACKMOL: A Package for Building Initial Configurations for Molecular Dynamics Simulations. *J. Comput. Chem.* **2009,**

30, 2157-2164.
(218) Dekel, D. R.; Rasin, I. G.; Brandon, S. Predicting Performance Stability of Anion Exchange Membrane Fuel Cells. *J. Power Sources.* **2019,** *420*, 118-123.
(219) Omasta, T.; Wang, L.; Peng, X.; Lewis, C. A.; Varcoe, J.; Mustain, W. Importance of Balancing Membrane and Electrode Water in Anion Exchange Membrane Fuel Cells. *J. Power Sources* **2018,** *375*, 205-213.
(220) Ziv, N.; Mondal, A. N.; Weissbach, T.; Holdcroft, S.; Dekel, D. R. Effect of CO_2 on the Properties of Anion Exchange Membranes for Fuel Cell Applications. *J. Membr. Sci.* **2019,** *586*, 140-150.
(221) Ziv, N.; Mustain, W. E.; Dekel, D. R. The Effect of Ambient Carbon Dioxide on Anion-Exchange Membrane Fuel Cells. *ChemSusChem* **2018,** *11*, 1136-1150.
(222) Krewer, U.; Weinzierl, C.; Ziv, N.; Dekel, D. R. Impact of Carbonation Processes in Anion Exchange Membrane Fuel Cells. *Electrochim. Acta* **2018,** *263*, 433-446.
(223) Zhu, Z.; Luo, X.; Sokolov, A. P.; Paddison, S. J. Proton Transfer in Phosphoric Acid-Based Protic Ionic Liquids: Effects of the Base. *J. Phys. Chem. A* **2020,** *124*, 4141-4149.
(224) Frisch, M. J.; Trucks, G. W.; Schlegel, H. B.; Scuseria, G. E.; Robb, M. A.; Cheeseman, J. R.; Scalmani, G.; Barone, V.; Mennucci, B.; Petersson, G. A., et al. *Gaussian 09*, Revision E.01; Gaussian, Inc.: Wallingford, CT, 2013.
(225) Becke, A. D. A New Mixing of Hartree-Fock and Local Density-Functional Theories. *J. Chem. Phys.* **1993,** *98*, 1372-1377.
(226) Hariharan, P. C.; Pople, J. A. The Influence of Polarization Functions on Molecular Orbital Hydrogenation Energies. *Theor. Chim. Acta.* **1973,** *28*, 213-222.
(227) Schlegel, H. B. Optimization of Equilibrium Geometries and Transition Structures. *J. Comput. Chem.* **1982,** *3*, 214-218.
(228) Becke, A. D. Density-functional Thermochemistry. I. The Effect of the Exchange-only Gradient Correction. *J. Chem. Phys.* **1992,** *96*, 2155-2160.
(229) Becke, A. D. Density-functional Thermochemistry. II. The Effect of the Perdew–Wang Generalized-gradient Correlation Correction. *J. Chem. Phys.* **1992,** *97*, 9173-9177.
(230) Lee, C.; Yang, W.; Parr, R. G. Development of the Colle-Salvetti Correlation-energy Formula into a Functional of the Electron Density. *Phys. Rev. B* **1988,** *37*, 785-789.
(231) McLean, A. D.; Chandler, G. S. Contracted Gaussian Basis Sets for Molecular Calculations. I. Second Row Atoms, Z = 11--18. *J. Chem. Phys.* **1980,** *72*, 5639–5648.
(232) Clark, J. K., II; Paddison, S. J.; Hamrock, S. J. The Effect of Hydrogen Bond Reorganization and Equivalent Weight on Proton Transfer in 3M Perfluorosulfonic Acid Ionomers. *Phys. Chem. Chem. Phys.* **2012,** *14*, 16349-16359.
(233) Grimme, S. Semiempirical GGA-type Density Functional Constructed with a Long-range Dispersion Correction. *J. Comput. Chem.* **2006,** *2715*, 1787-1799.
(234) Marenich, A. V.; Cramer, C. J.; Truhlar, D. G. Universal Solvation Model Based on Solute Electron Density and on A Continuum Model of the Solvent Defined by the Bulk Dielectric Constant and Atomic Surface Tensions. *J. Phys. Chem. B* **2009,** *113*, 6378–6396.
(235) Munson, R. A. Dielectric Constant of Phosphoric Acid. *J. Chem. Phys.* **1964,** *40*, 2044-2046.

(236) Sepehr, F.; Paddison, S. J. Primary Hydration and Proton Transfer of Electrolyte Acids: An Ab Initio Study. *Solid State Ion.* **2017,** *306*, 2-12.
(237) Sepehr, F.; Paddison, S. J. Effect of Sulfuric and Triflic Acids on the Hydration of Vanadium Cations: An ab Initio Study. *J. Phys. Chem. A* **2015,** *119*, 5749-5761.
(238) Sepehr, F.; Paddison, S. J. The Solvation Structure and Thermodynamics of Aqueous Vanadium Cations. *Chem. Phys. Lett.* **2013,** *585*, 53-58.
(239) Krakowiak, J.; Lundberg, D.; Persson, I. A Coordination Chemistry Study of Hydrated and Solvated Cationic Vanadium Ions in Oxidation States +III, +IV, and +V in Solution and Solid State. *Inorg. Chem.* **2012,** *51*, 9598-9609.
(240) Wang, C.; Clark II, J. K.; Kumar, M.; Paddison, S. J. An Ab Initio Study of the Primary Hydration and Proton Transfer of CF_3SO_3H and $CF_3O(CF_2)_2SO_3H$: Effects of the Hybrid Functional and Inclusion of Diffuse Functions. *Solid State Ion.* **2011,** *199-200*, 6-13.
(241) Li, X.; Frisch, M. J. Energy-Represented Direct Inversion in the Iterative Subspace within a Hybrid Geometry Optimization Method. *J. Chem. Theory Comput.* **2006,** *2*, 835-839.
(242) Hunter, E. P.; Lias, S. G. Evaluated Gas Phase Basicities and Proton Affinities of Molecules: An Update. *J. Phys. Chem. Ref. Data* **1998,** *27*, 413-656.
(243) Popov, I.; Zhu, Z.; Young-Gonzales, A. R.; Sacci, R. L.; Mamontov, E.; Gainaru, C.; Paddison, S. J.; Sokolov, A. P. Search for a Grotthuss Mechanism through the Observation of Proton Transfer. *Commun. Chem.* **2023,** *6*, 77.
(244) Abraham, M. J.; Murtola, T.; Schulz, R.; Páll, S.; Smith, J. C.; Hess, B.; Lindahl, E. GROMACS: High Performance Molecular Simulations through Multi-Level Parallelism from Laptops to Supercomputers. *SoftwareX* **2015,** *1-2*, 19-25.
(245) Pronk, S.; Páll, S.; Schulz, R.; Larsson, P.; Bjelkmar, P.; Apostolov, R.; Shirts, M. R.; Smith, J. C.; Kasson, P. M.; van der Spoel, D., et al. GROMACS 4.5: A High-Throughput and Highly Parallel Open Source Molecular Simulation Toolkit. *Bioinformatics* **2013,** *29*, 845-854.
(246) Liu, H.; Maginn, E.; Visser, A. E.; Bridges, N. J.; Fox, E. B. Thermal and Transport Properties of Six Ionic Liquids: An Experimental and Molecular Dynamics Study. *Ind. Eng. Chem. Res.* **2012,** *51*, 7242–7254.
(247) Liu, H.; Maginn, E. A Molecular Dynamics Investigation of the Structural and Dynamic Properties of the Ionic Liquid 1-n-Butyl-3-Methylimidazolium Bis(trifluoromethanesulfonyl) Imide. *J. Chem. Phys.* **2011,** *135*, 124507.
(248) Hutter, D. M. J.; Alavi, A.; Deutsch, T.; Bernasconi, M.; Goedecker, S.; Parrinello, M. T. M. *CPMD*, IBM Corporation 1990− 2009 and MPI für Festkörperforschung 1997−2001: 2009.
(249) Marx, D.; Hutter, J., *Ab Initio Molecular Dynamics: Theory and Implementation. In Modern Methods and Algorithms of Quantum Chemistry*; Forschungszentrum: Juelich: 2000; Vol. Vol. 1.
(250) Aeberhard, P. C.; Arey, J. S.; Lin, I.-C.; Rothlisberger, U. Accurate DFT Descriptions for Weak Interactions of Molecules Containing Sulfur. *J. Chem. Theory Comput.* **2009,** *5*, 23−28.
(251) Lin, I.-C.; Coutinho-Neto, M. D.; Felsenheimer, C.; von Lilienfeld, O. A.; Tavernelli, I.; Rothlisberger, U. Library of Dispersion-Corrected Atom-Centered Potentials for Generalized Gradient Approximation Functionals: Elements H, C, N, O, He, Ne, Ar, and Kr. *Phys. Rev. B* **2007,** *75*, 205131.

(252) Becke, A. D. Density-Functional Exchange-Energy Approximation with Correct Asymptotic Behavior. *Phys. Rev. A* **1988,** *38*, 3098−3100.
(253) Martyna, G. J.; Tuckerman, M. E.; Klein, M. L. Nose-Hoover Chains: The Canonical Ensemble via Continuous Dynamics. *J. Chem. Phys.* **1992,** *97*, 2635−2643.
(254) Persson, I.; Trublet, M.; Klysubun, W. Structure Determination of Phosphoric Acid and Phosphate Ions in Aqueous Solution Using EXAFS Spectroscopy and Large Angle X-ray Scattering. *J. Phys. Chem. A* **2018,** *122*, 7413-7420.
(255) Caminiti, R. Sulphate-H_2O Interactions in a Concentrated Aqueous H_2SO_4 Solution. *Chem. Phys. Lett.* **1983,** *96*, 390-394.
(256) Newton, M. D. Ab Initio Studies of the Hydrated H_3O^+ Ion. II. The Energetics of Proton Motion in Higher Hydrates (n=3–5). *J. Chem. Phys.* **1977,** *67*, 5535-5546.
(257) Triolo, R.; Narten, A. H. Diffraction Pattern and Structure of Aqueous Hydrochloric Acid Solutions at 20 °C. *J. Chem. Phys.* **1975,** *63*, 3624-3631.
(258) Long, Z.; Tuckerman, M. E. Hydroxide Diffusion in Functionalized Cylindrical Nanopores as Idealized Models of Anion Exchange Membrane Environments: An Ab Initio Molecular Dynamics Study. *J. Phys. Chem. C* **2023,** *127*, 2792-2804.
(259) Chandra, A.; Tuckerman, M. E.; Marx, D. Connecting Solvation Shell Structure to Proton Transport Kinetics in Hydrogen-Bonded Networks via Population Correlation Functions. *Phys. Rev. Lett.* **2007,** *99*, 145901.
(260) Ahmed, M. D.; Zhu, Z.; Khamzin, A.; Paddison, S. J.; Sokolov, A. P.; Popov, I. Effect of Ion Mass on Dynamic Correlations in Ionic Liquids. *J. Phys. Chem. B* **2023,** *127*, 10411-10421.
(261) Slingsby, J. G.; Vyas, S.; Maupin, C. M. A Charge-Modified General Amber Force Field for Phospholipids: Improved Structural Properties in the Tensionless Ensemble. *Mol. Simulat.* **2015,** *41*, 1449-1458.
(262) Bayly, C. I.; Cieplak, P.; Cornell, W.; Kollman, P. A. A Well-behaved Electrostatic Potential Based Method Using Charge Restraints for Deriving Atomic Charges: the RESP Model. *J. Phys. Chem.* **1993,** *97*, 10269-10280.
(263) Barbosa, G. D.; Liu, X.; O'Harra, K. E.; Bara, J. E.; Turner, C. H. Charge Scaling Parameter Evaluation for Multivalent Ionic Liquids with Fixed Point Charge Force Fields. *J. Ion. Liq.* **2022,** *2*, 100020.
(264) Vargas-Barbosa, N. M.; Roling, B. Dynamic Ion Correlations in Solid and Liquid Electrolytes: How Do They Affect Charge and Mass Transport? *ChemElectroChem* **2020,** *7*, 367-385.
(265) Bussi, G.; Donadio, D.; Parrinello, M. Canonical Sampling through Velocity Rescaling. *J. Chem. Phys.* **2007,** *126*.
(266) Parrinello, M.; Rahman, A. Crystal Structure and Pair Potentials: A Molecular-Dynamics Study. *Phys. Rev. Lett.* **1980,** *45*, 1196-1199.
(267) Harris, K. R.; Kanakubo, M.; Woolf, L. A. Temperature and Pressure Dependence of the Viscosity of the Ionic Liquids 1-Hexyl-3-Methylimidazolium Hexafluorophosphate and 1-Butyl-3-Methylimidazolium Bis(trifluoromethylsulfonyl)imide. *J. Chem. Eng. Data* **2007,** *52*, 1080-1085.
(268) Tokuda, H.; Hayamizu, K.; Ishii, K.; Susan, M. A. B. H.; Watanabe, M. Physicochemical

Properties and Structures of Room Temperature Ionic Liquids. 1. Variation of Anionic Species. *J. Phys. Chem. B* **2004,** *108*, 16593-16600.
(269) Brehm, M.; Thomas, M.; Gehrke, S.; Kirchner, B. TRAVIS—A Free Analyzer for Trajectories from Molecular Simulation. *J. Chem. Phys.* **2020,** *152*, 164105.
(270) Humphrey, W.; Dalke, A.; Schulten, K. VMD: Visual Molecular Dynamics. *J. Mol. Graph.* **1996,** *14*, 33-38.
(271) Wang, Y.; Voth, G. A. Unique Spatial Heterogeneity in Ionic Liquids. *J. Am. Chem. Soc.* **2005,** *127*, 12192-12193.
(272) Urahata, S. M.; Ribeiro, M. C. C. Single Particle Dynamics in Ionic Liquids of 1-Alkyl-3-Methylimidazolium Cations. *J. Chem. Phys.* **2004,** *122*.
(273) Sarangi, S. S.; Zhao, W.; Müller-Plathe, F.; Balasubramanian, S. Correlation between Dynamic Heterogeneity and Local Structure in a Room-Temperature Ionic Liquid: A Molecular Dynamics Study of [BMIm][PF_6]. *ChemPhysChem* **2010,** *11*, 2001-2010.
(274) Kanakubo, M.; Harris, K. R.; Tsuchihashi, N.; Ibuki, K.; Ueno, M. Effect of Pressure on Transport Properties of the Ionic Liquid 1-Butyl-3-Methylimidazolium Hexafluorophosphate. *J. Phys. Chem. B* **2007,** *111*, 2062-2069.
(275) Bhargava, B. L.; Balasubramanian, S. Refined Potential Model for Atomistic Simulations of Ionic Liquid [BMIm][PF_6]. *J. Chem. Phys.* **2007,** *127*.
(276) Rey-Castro, C.; Vega, L. F. Transport Properties of the Ionic Liquid 1-Ethyl-3-Methylimidazolium Chloride from Equilibrium Molecular Dynamics Simulation. The Effect of Temperature. *J. Phys. Chem. B* **2006,** *110*, 14426-14435.
(277) Cadena, C.; Zhao, Q.; Snurr, R. Q.; Maginn, E. J. Molecular Modeling and Experimental Studies of the Thermodynamic and Transport Properties of Pyridinium-Based Ionic Liquids. *J. Phys. Chem. B* **2006,** *110*, 2821-2832.
(278) Tokuda, H.; Hayamizu, K.; Ishii, K.; Susan, M. A. B. H.; Watanabe, M. Physicochemical Properties and Structures of Room Temperature Ionic Liquids. 2. Variation of Alkyl Chain Length in Imidazolium Cation. *J. Phys. Chem. B* **2005,** *109*, 6103-6110.
(279) Liu, Z.; Huang, S.; Wang, W. A Refined Force Field for Molecular Simulation of Imidazolium-Based Ionic Liquids. *J. Phys. Chem. B* **2004,** *108*, 12978-12989.
(280) Morrow, T. I.; Maginn, E. J. Molecular Dynamics Study of the Ionic Liquid 1-n-Butyl-3-Methylimidazolium Hexafluorophosphate. *J. Phys. Chem. B* **2002,** *106*, 12807-12813.
(281) Fujii, K.; Fujimori, T.; Takamuku, T.; Kanzaki, R.; Umebayashi, Y.; Ishiguro, S.-i. Conformational Equilibrium of Bis(trifluoromethanesulfonyl) Imide Anion of a Room-Temperature Ionic Liquid: Raman Spectroscopic Study and DFT Calculations. *J. Phys. Chem. B* **2006,** *110*, 8179-8183.
(282) Zhao, W.; Leroy, F.; Heggen, B.; Zahn, S.; Kirchner, B.; Balasubramanian, S.; MUeller-Plathe, F. Are There Stable Ion-Pairs in Room-Temperature Ionic Liquids? Molecular Dynamics Simulations of 1-n-Butyl-3-Methylimidazolium Hexafluorophosphate. *J. Am. Chem. Soc.* **2009,** *131*, 15825-15833.
(283) Luo, X.; Paddison, S. J. Molecular Dynamics Simulations of Ammonium-Based Acrylate Polymerized Ionic Liquids. *J. Electrochem. Soc.* **2023,** *170*, 106502.
(284) Sousa da Silva, A. W.; Vranken, W. F. ACPYPE - AnteChamber PYthon Parser interfacE.

BMC Res. Notes **2012,** *5*, 367.
(285) Zhang, Z.; Krishna, R.; Zofchak, E. S.; Marioni, N.; Sachar, H. S.; Ganesan, V. The Influence of Counterion Structure Identity on Conductivity, Dynamical Correlations, and Ion Transport Mechanisms in Polymerized Ionic Liquids. *J. Chem. Phys.* **2023,** *159*, 084902.
(286) Shao, Y.; Gudla, H.; Brandell, D.; Zhang, C. Transference Number in Polymer Electrolytes: Mind the Reference-Frame Gap. *J. Am. Chem. Soc.* **2022,** *144*, 7583-7587.
(287) Wheatle, B. K.; Lynd, N. A.; Ganesan, V. Effect of Polymer Polarity on Ion Transport: A Competition between Ion Aggregation and Polymer Segmental Dynamics. *ACS Macro Lett.* **2018,** *7*, 1149-1154.
(288) Keith, J. R.; Mogurampelly, S.; Wheatle, B. K.; Ganesan, V. Influence of Side Chain Linker Length on Ion-Transport Properties of Polymeric Ionic Liquids. *J. Polym. Sci. B: Polym. Phys.* **2017,** *55*, 1718-1723.
(289) Kob, W.; Donati, C.; Plimpton, S. J.; Poole, P. H.; Glotzer, S. C. Dynamical Heterogeneities in a Supercooled Lennard-Jones Liquid. *Phys. Rev. Lett.* **1997,** *79*, 2827-2830.
(290) Del Pópolo, M. G.; Voth, G. A. On the Structure and Dynamics of Ionic Liquids. *J. Phys. Chem. B* **2004,** *108*, 1744-1752.
(291) Zhang, Y.; Maginn, E. J. Direct Correlation between Ionic Liquid Transport Properties and Ion Pair Lifetimes: A Molecular Dynamics Study. *J. Phys. Chem. Lett.* **2015,** *6*, 700-705.

Appendices

Appendix A. Tables

Table A.1. Bonded parameters in DPD simulations.

Bond	K_b	R_b^0	Angle	K_a	θ_a^0
Bs-Bs	30	0.7	Bs-Bs-Bs	15	150
Bs-Ph	30	0.7	Bs-Bs-Bm	10	150
Bs-Bm	30	0.7	Bs-Bm-Bm	1	90
Bm-Bm	20	0.7	Bm-Bm-Bm	1	90
Ph-TMM	20	0.7	Bs-Ph-TMM	1	90
TMM-TMA^+	20	0.7	Ph-TMM- TMA^+	1	90
TMM- TMP^+	20	0.7	Ph-TMM- TMP^+	1	90
TMM- MIm^+	20	0.7	Ph-TMM- MIm^+	1	90

Table A.2. Calculated conservative interaction parameters in DPD simulations.

α_{ij}	Butane	Benzene	TMM	TMA^+	MIm^+	TMP^+	W	$OH^-(H_2O)_4$	$OH^-(H_2O)_3$	Cl^-	Br^-	HCO_3^-	CO_3^{2-}
Butane	30.28												
Benzene	35.02	30.53											
TMM	29.24	27.74	26.03										
TMA^+	27.52	27.31	25.59	65.79									
MIm^+	32.59	34.42	26.70	68.41	71.97								
TMP^+	30.30	29.65	27.55	-	-	71.37							
W	35.57	33.44	27.46	26.61	31.27	27.34	25.01						
$OH^-(H_2O)_4$	34.80	30.05	27.88	-15.02	-12.12	-13.52	27.34	65.68					
$OH^-(H_2O)_3$	27.55	26.90	25.94	-16.91	-15.89	-15.64	26.45	-	65.93				
Cl^-	32.22	30.50	29.34	-16.65	-12.53	-15.85	28.17	-	-	73.99			
Br^-	28.50	28.51	26.79	-17.33	-16.32	-14.78	27.96	-	-	-	71.57		
HCO_3^-	33.06	31.24	30.55	-16.75	-	-12.91	29.31	-	69.84	-	-	76.28	
CO_3^{2-}	27.25	26.16	23.90	-65.64	-	-	26.81	-	-	-	-		181.97

Table A.3. Relaxation times obtained by fitting the self-intermediate scattering function with $ISF_s = a_1\exp(-t/\tau_1) + a_2\exp(-t/\tau_2) + a_3\exp[-(t/\tau_3)^\beta]$ for pure PA at 400 K.

Q[Å^{-1}]	a_1	τ_1[ps]	a_2	τ_2[ps]	a_3	τ_3[ps]	β	τ_R[ps]	E_3	error
1.600	0.008	0.013	0.102	0.150	0.504	14.029	0.745	16.794	39.192	0.038
2.200	0.011	0.011	0.155	0.121	0.438	7.736	0.673	10.189	64.597	0.141
3.000	0.026	0.012	0.198	0.110	0.292	4.843	0.644	6.686	98.450	0.563

Table A.4. Relaxation times obtained by fitting the self-intermediate scattering function with $ISF_s = a_2\exp(-t/\tau_2) + a_3\exp[-(t/\tau_3)^\beta]$ for pure PA at 383 K.

Q[Å^{-1}]	a_2	τ_2[ps]	a_3	τ_3[ps]	β	τ_R[ps]	E_3	error
0.800	0.042	0.169	0.787	54.923	0.827	60.834	10.820	0.005
1.000	0.069	0.166	0.827	34.383	0.824	38.175	17.242	0.007
1.200	0.099	0.162	0.818	24.066	0.816	26.890	24.478	0.017
1.400	0.127	0.155	0.769	18.146	0.803	20.510	32.093	0.039
1.600	0.157	0.147	0.735	14.380	0.784	16.529	39.823	0.070
1.800	0.182	0.138	0.684	11.785	0.764	13.829	47.595	0.106
2.000	0.206	0.131	0.638	9.898	0.744	11.868	55.462	0.141
2.200	0.227	0.124	0.582	8.480	0.727	10.364	63.510	0.164
2.400	0.252	0.119	0.541	7.392	0.716	9.167	71.802	0.206
2.600	0.278	0.114	0.501	6.534	0.707	8.191	80.355	0.260
2.800	0.304	0.110	0.464	5.835	0.701	7.381	89.178	0.372
3.000	0.322	0.105	0.421	5.250	0.695	6.695	98.308	0.470

Table A.5. Relaxation times obtained by fitting the self-intermediate scattering function with $ISF_s = a_2\exp(-t/\tau_2) + a_3\exp[-(t/\tau_3)^\beta]$ for pure PA at 400 K.

Q [Å^{-1}]	a_2	τ_2[ps]	a_3	τ_3[ps]	β	τ_R[ps]	E_3	error
0.800	0.028	0.194	0.439	56.930	0.841	62.341	10.558	0.011
1.000	0.042	0.178	0.444	35.936	0.818	40.097	16.415	0.011
1.200	0.064	0.164	0.483	24.769	0.795	28.197	23.344	0.023
1.400	0.081	0.150	0.470	18.181	0.770	21.198	31.050	0.045
1.600	0.099	0.138	0.462	13.975	0.742	16.780	39.226	0.075
1.800	0.120	0.128	0.462	11.131	0.715	13.818	47.636	0.125
2.000	0.138	0.121	0.440	9.136	0.690	11.724	56.144	0.170
2.200	0.156	0.115	0.416	7.706	0.671	10.174	64.693	0.251
2.400	0.180	0.110	0.401	6.662	0.658	8.984	73.262	0.359
2.600	0.201	0.106	0.374	5.876	0.649	8.042	81.849	0.507
2.800	0.221	0.103	0.347	5.257	0.643	7.273	90.497	0.810
3.000	0.242	0.099	0.322	4.745	0.638	6.626	99.333	0.910

Table A.6. Relaxation times obtained by fitting the self-intermediate scattering function with $ISF_s = a_2\exp(-t/\tau_2) + a_3\exp[-(t/\tau_3)^\beta]$ for aqueous PA85 at 390 K.

Q[Å^{-1}]	a_2	τ_2[ps]	a_3	τ_3[ps]	β	τ_R[ps]	E_3	error
0.800	0.063	0.274	0.692	49.644	0.864	53.477	12.308	0.024
1.000	0.084	0.227	0.672	31.759	0.812	35.597	18.491	0.042
1.200	0.108	0.192	0.673	21.622	0.767	25.288	26.029	0.096
1.400	0.134	0.169	0.665	15.467	0.734	18.763	35.080	0.177
1.600	0.163	0.154	0.642	11.616	0.713	14.448	45.556	0.280
1.800	0.190	0.145	0.590	9.158	0.704	11.526	57.105	0.412
2.000	0.223	0.139	0.546	7.552	0.704	9.511	69.204	0.594
2.200	0.255	0.133	0.497	6.459	0.708	8.090	81.361	0.850
2.400	0.284	0.127	0.448	5.661	0.712	7.053	93.327	1.157
2.600	0.310	0.121	0.404	5.036	0.713	6.262	105.116	1.648
2.800	0.330	0.115	0.360	4.524	0.712	5.633	116.840	1.716
3.000	0.348	0.110	0.323	4.087	0.708	5.116	128.662	2.152

Table A.7. Relaxation times obtained by fitting the self-intermediate scattering function with $ISF_s = a_2\exp(-t/\tau_2) + a_3\exp[-(t/\tau_3)^\beta]$ for aqueous PA85 at 420 K.

Q[Å^{-1}]	a_2	τ_2[ps]	a_3	τ_3[ps]	β	τ_R[ps]	E_3	error
0.800	0.048	0.197	0.623	22.769	0.847	24.833	26.505	0.028
1.000	0.074	0.178	0.654	14.061	0.825	15.595	42.207	0.113
1.200	0.100	0.168	0.615	9.496	0.819	10.588	62.164	0.300
1.400	0.132	0.166	0.554	6.982	0.839	7.659	85.940	0.473
1.600	0.178	0.169	0.506	5.570	0.886	5.914	111.306	0.585
1.800	0.222	0.167	0.452	4.680	0.934	4.830	136.271	0.774
2.000	0.255	0.157	0.409	3.977	0.949	4.072	161.648	1.161
2.200	0.277	0.143	0.376	3.370	0.929	3.487	188.760	1.500
2.400	0.294	0.130	0.347	2.870	0.896	3.027	217.450	1.694
2.600	0.311	0.121	0.319	2.482	0.868	2.666	246.851	2.112
2.800	0.328	0.113	0.290	2.190	0.850	2.383	276.157	2.817
3.000	0.345	0.107	0.262	1.966	0.839	2.156	305.308	3.435

Table A.8. Computed fractions (%) of special pair acid molecules in their different states of protonation in the studied aqueous acid systems.

System	A^{2-}	A^-	A	A^+
PA1H	0.24	33.59	65.69	0.48
PA3H	0.42	43.39	56.05	0.14
SA1H	0.58	76.9	22.51	0
SA3H	2.44	95.22	2.34	0
NA1H	0	76.78	23.22	0
NA3H	0	94.65	5.35	0
δ_{min} < 0.1 Å				
PA1H	0.46	37.46	61.52	0.56
PA3H	0.94	52.06	46.93	0.07
SA1H	0.86	72.6	26.53	0.01
SA3H	3.01	93.86	3.14	0
NA1H	0	75.04	24.96	0
NA3H	0	94.91	5.09	0

Appendix B. Figures

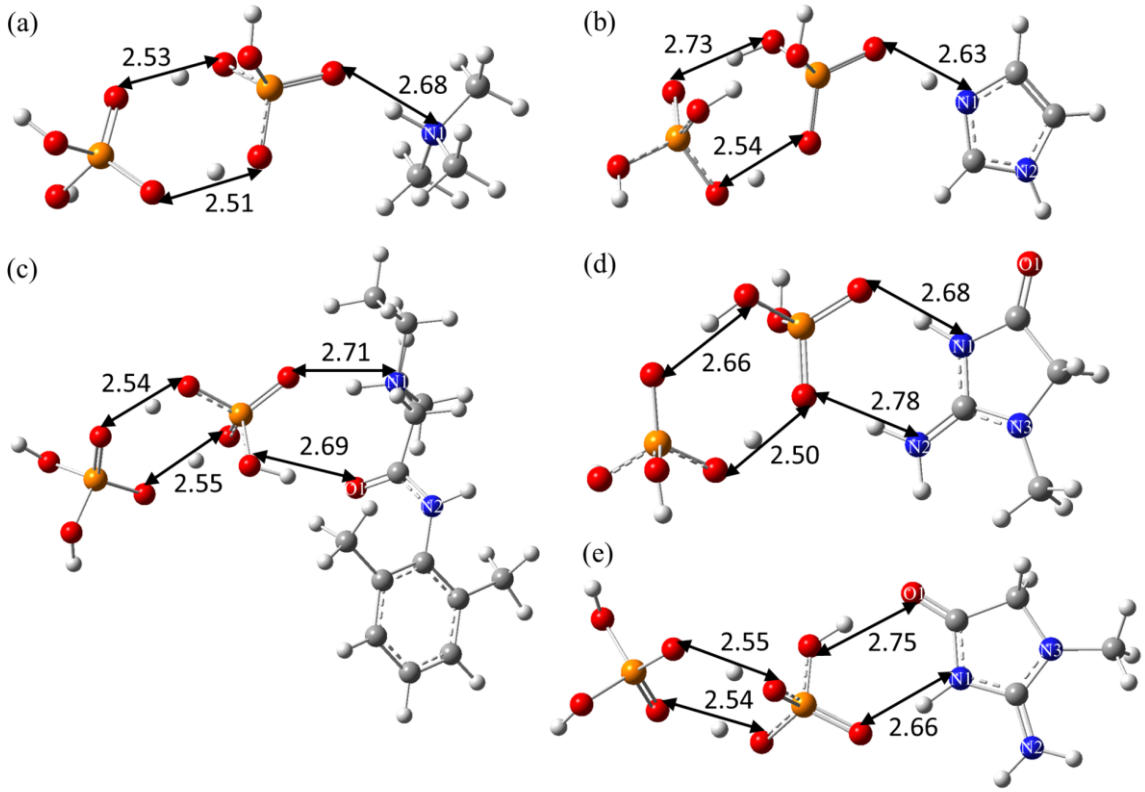

Figure A.1. Fully optimized configurations of cluster of two PA molecules with (a) TMA, (b) IMI, (c) LDC, (d) CRT, and (e) CRT* at the B3LYP/6-311G**/SMD level of theory. All values are reported in Å. CRT*+2PA is more energetic favorable than the structure of CRT+2PA by 0.16 kcal/mol.

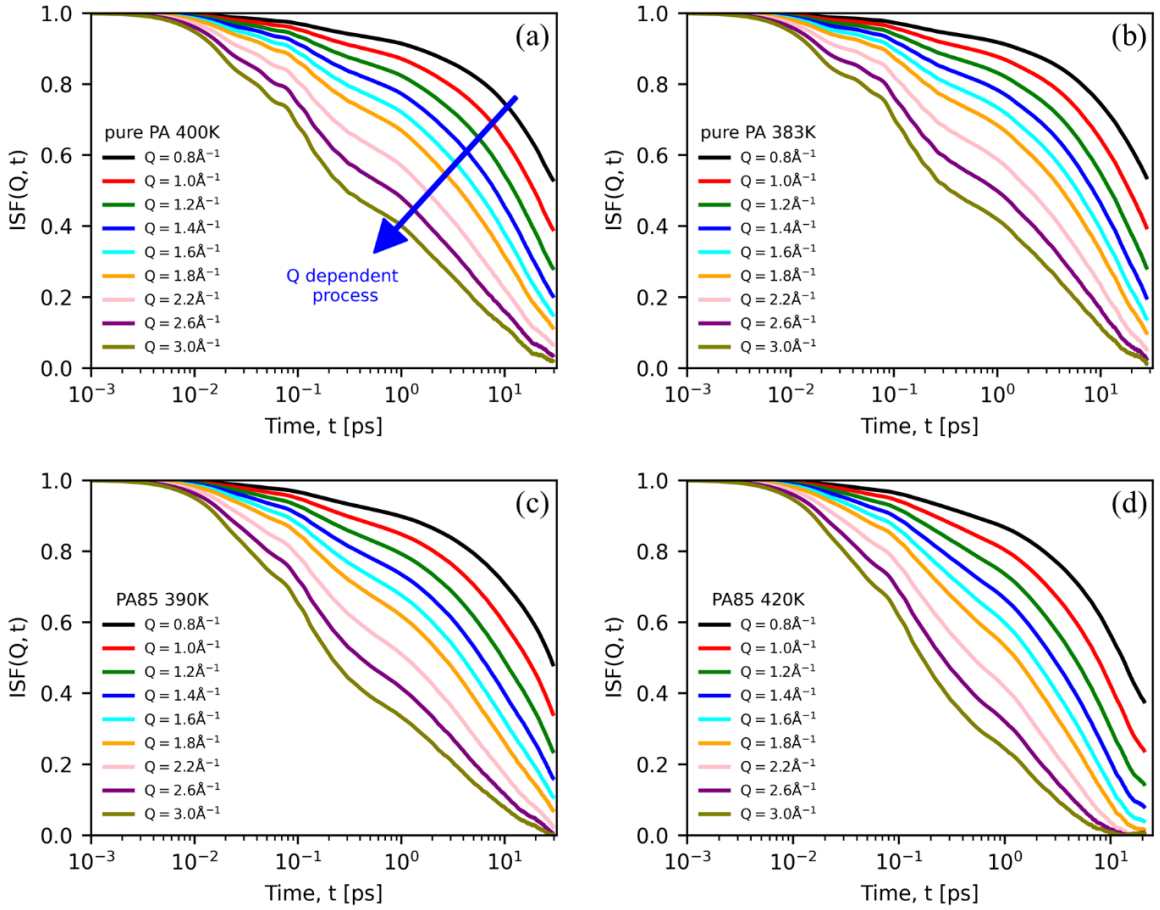

Figure A.2. Self-intermediate scattering function $ISF_s(Q, t)$ of protons for different Q values probed at 400 K for pure PA (a), at 383 K for pure PA (b), at 390 K for aqueous PA85 (c), and at 420K for aqueous PA85.

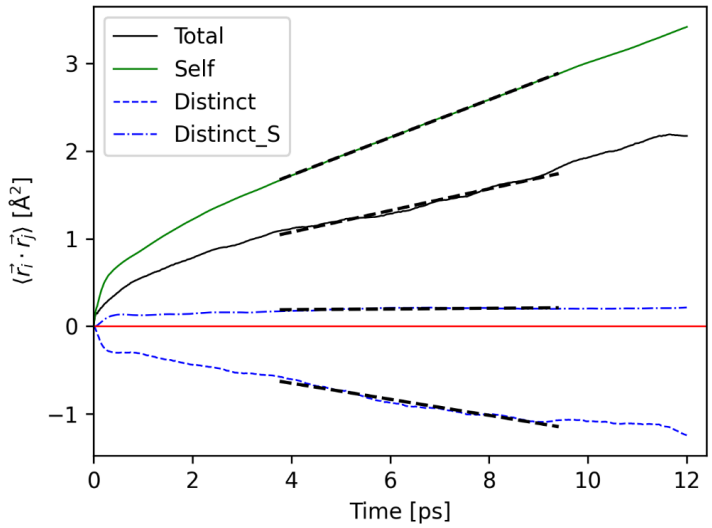

Figure A.3. Correlation functions of proton displacement vectors excluding the protons from the same PA molecule. We obtained the inverse Haven ratio as $H^{-1} = 0.56$, that was slightly smaller than that computed by including all protons ($H^{-1} = 0.58$).

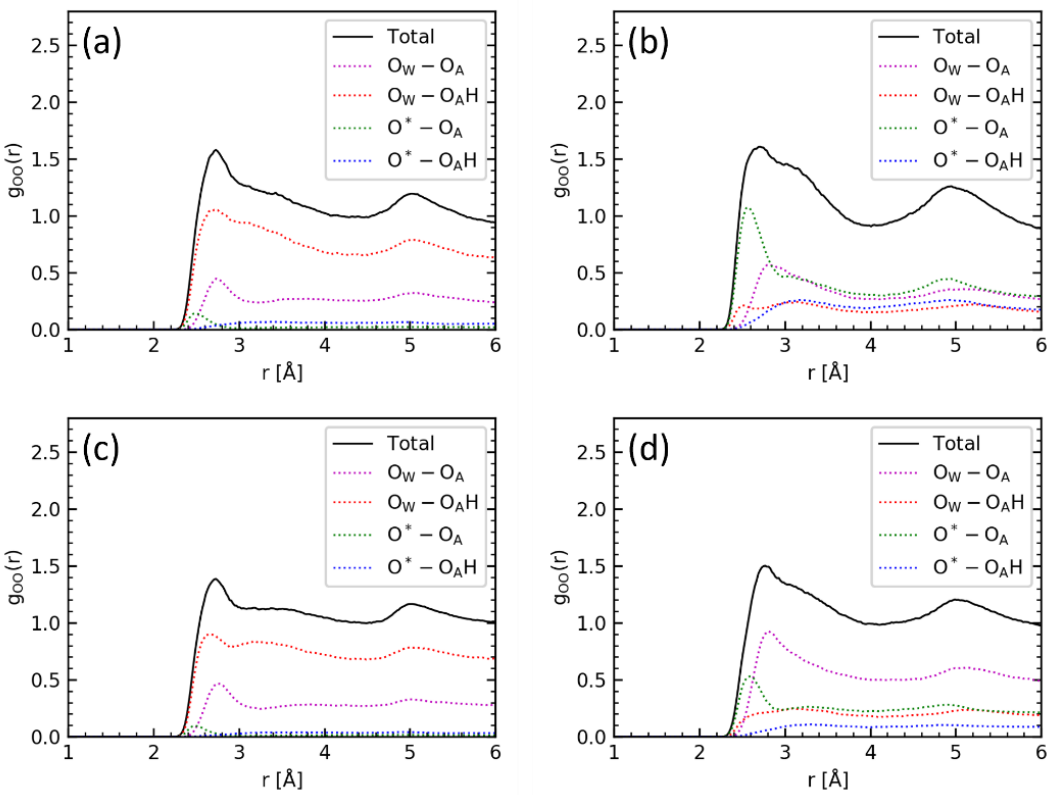

Figure A.4. The total RDFs of OO pairs of water and acid molecules and the split OO RDFs between 4 pairs: oxygen of H_2O (O_W) and unprotonated oxygen of acid molecules (O_A); oxygen of H_2O (O_W) and protonated oxygen of acid molecules (O_AH); oxygen of H_3O^+ (O^*) and unprotonated oxygen of acid molecules (O_A); oxygen of H_3O^+ (O^*) and protonated oxygen of acid molecules (O_AH) in (a) PA1H; (b) SA1H; (c) PA3H; and (d) SA3H. In PA1H, strong H-bonds mainly form between H_2O molecules and protonated/unprotonated O atoms of PA molecules. The addition of water molecules slightly affects this composition due to the similar proton affinity. In SA1H, however, the strongest H-bond forms between H_3O^+ and the unprotonated O atoms of the SA molecules significantly contributing to the first peak of the OO RDF between water and SA molecules and the shoulder on the right of the peak comes from the weaker H-bonds between H_2O and the unprotonated O of SA. Increasing the water content switches the intensities of these two peaks.

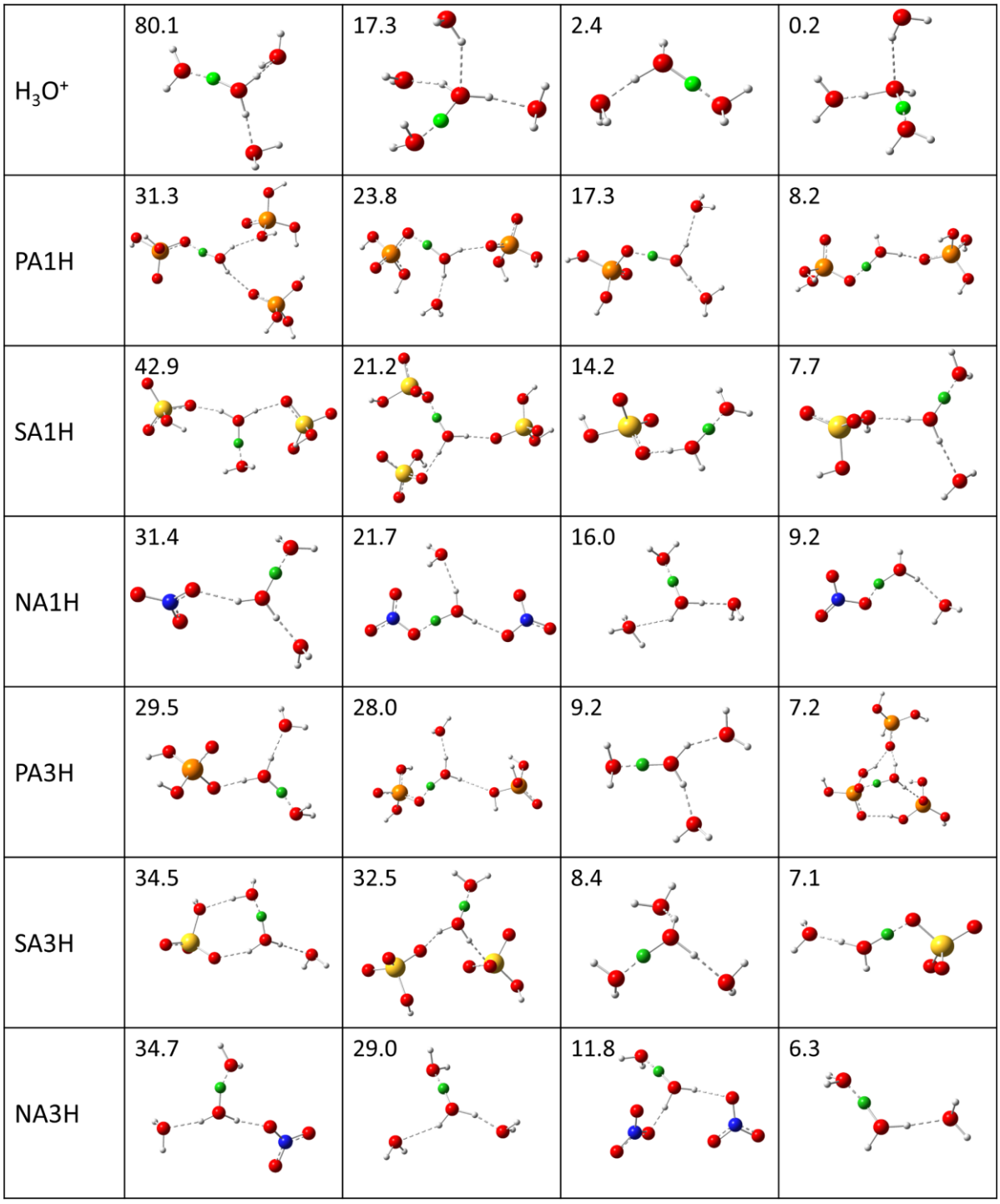

Figure A.5. Representative solvation patterns for active H_3O^+ ($\delta_{min} < 0.1$ Å) in the studied aqueous acid systems. The numbers displayed in the top-left corner represent the population percentages (%) of these solvation patterns. The green ball represents the transferring proton of the active H_3O^+.

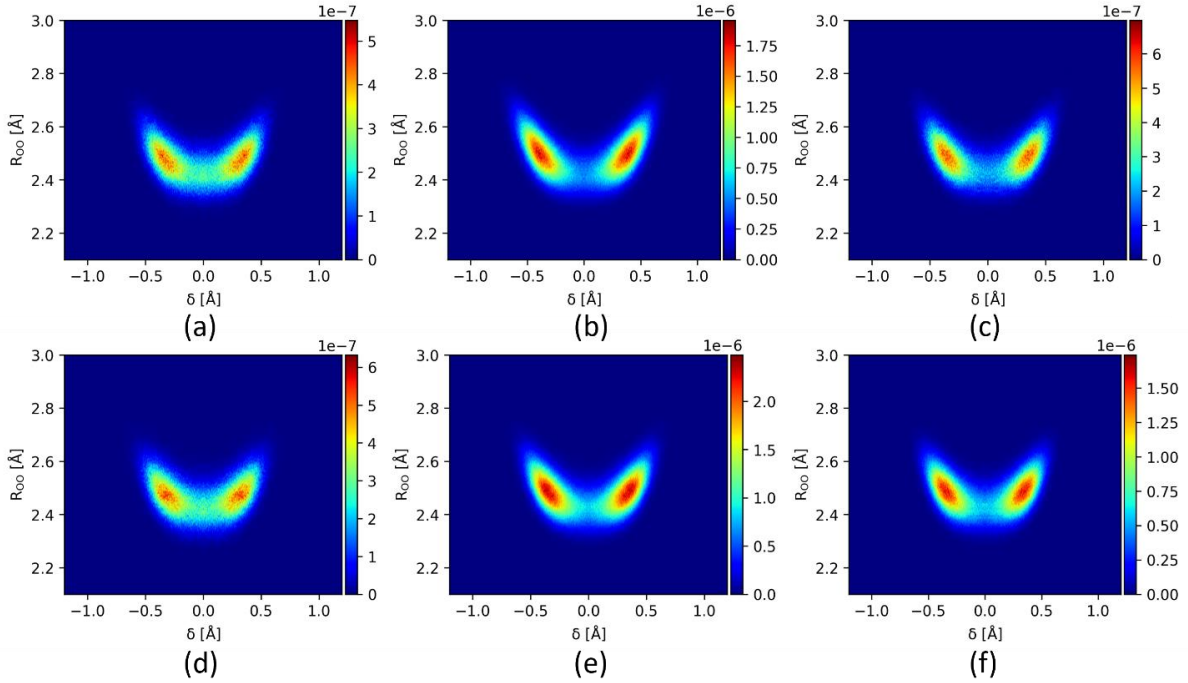

Figure A.6. $P(R_{OO}, \delta)$ probability distribution for proton transfer between H_3O^+ and other species in (a) PA1H, (b) SA1H, (c) NA1H, (d) PA3H, (e) SA3H, and (f) NA3H.

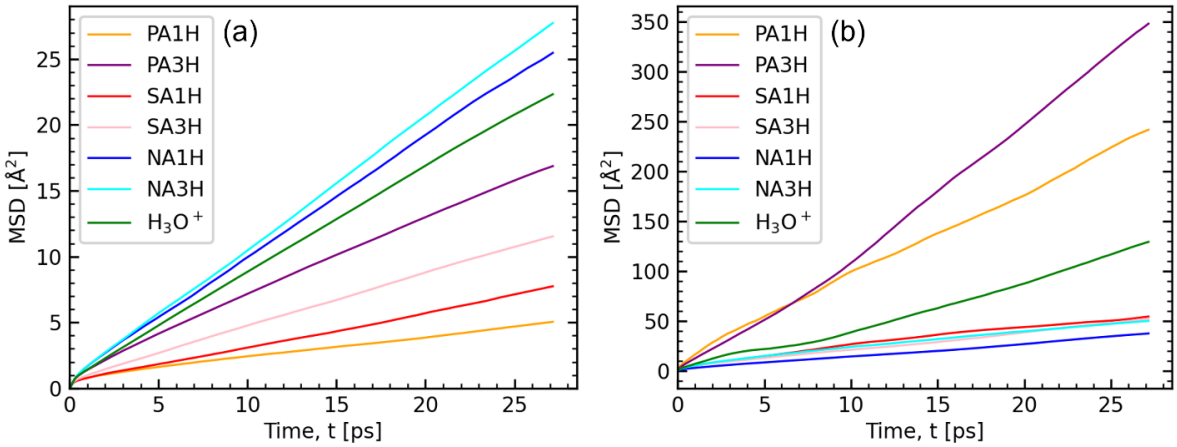

Figure A.7. The mean squared displacement (MSD) for the: (a) water oxygen atoms; and (b) hydronium oxygen atoms.

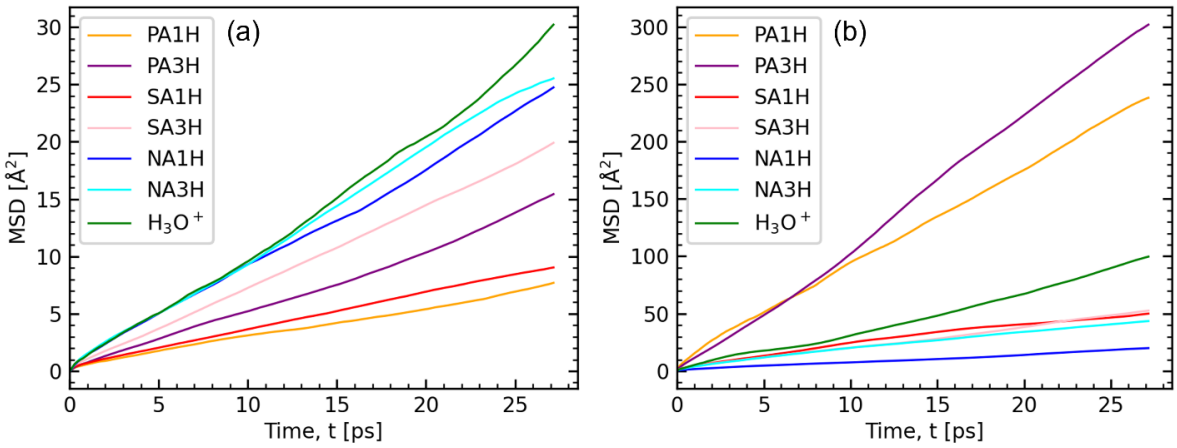

Figure A.8. The MSD of the hydronium ion decomposed into: (a) continuous vehicular component; and (b) discrete structural component.

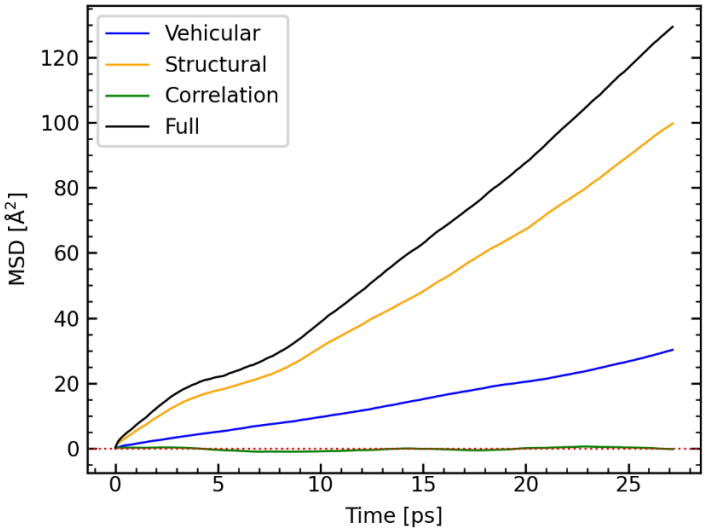

Figure A.9. The MSD of the hydronium ion decomposed into a continuous vehicular component; a discrete structural component; and the correlation between the vehicular and structural components in the slightly acidic water.

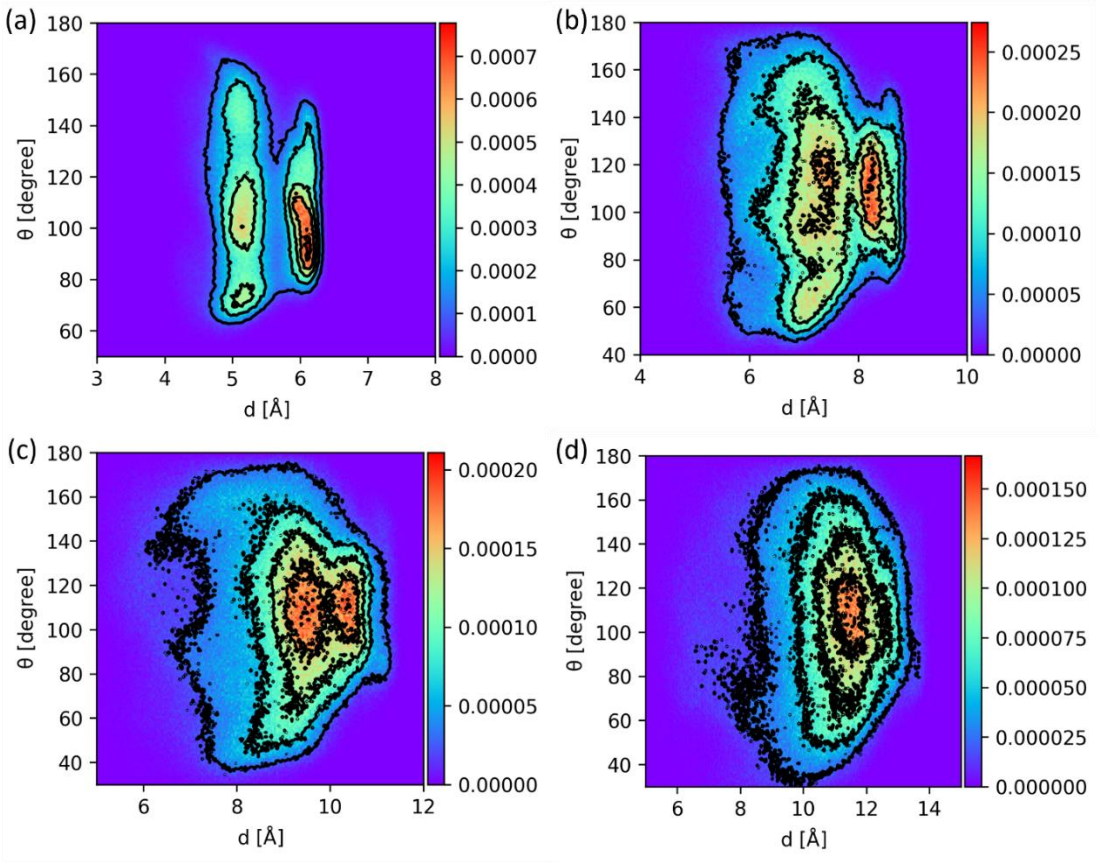

Figure A.10. Contour plots of sidechain conformation as a function of both distance and angle from polymer backbone at 480 K for (a) PMMA-C_2-IM[TFSI]; (b) PMMA-C_4-IM[TFSI]; (c) PMMA-C_6-IM[TFSI]; and (d) PMMA-C_8-IM[TFSI].

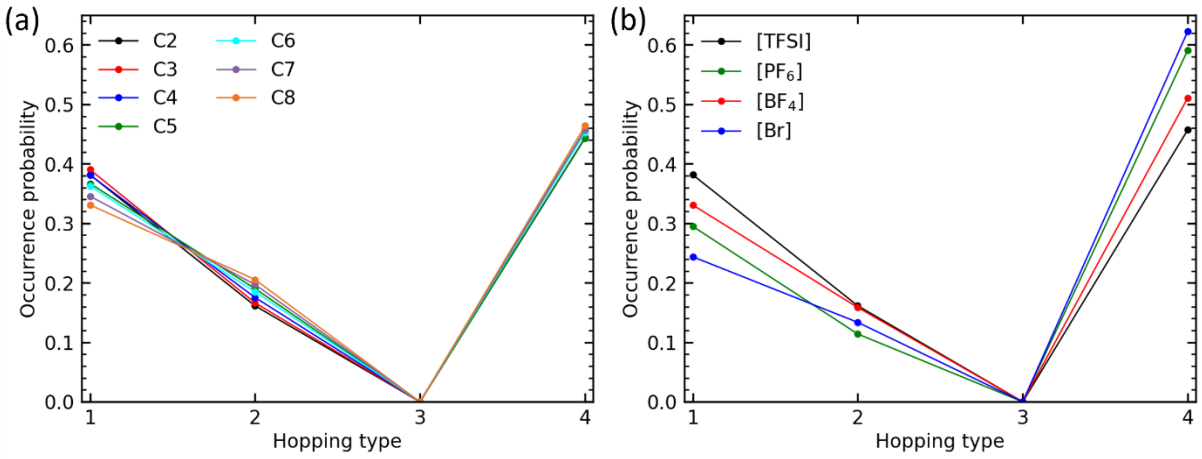

Figure A.11. Occurrence probability of the hopping types for TFSI with (a) different linker lengths; and (b) various anions with the linker length of C2 at 480 K.

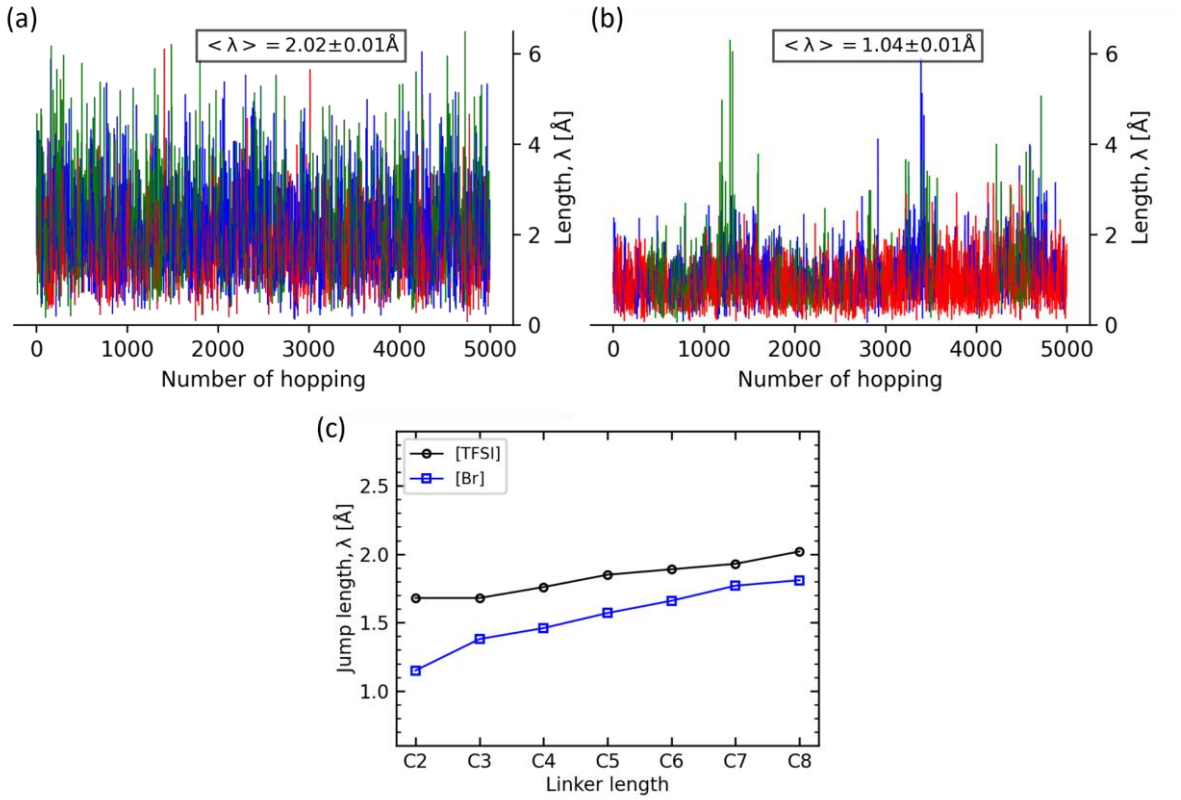

Figure A.12. The length of each anion hopping from one "cage" to another at the interval of 10 ps in (a) PMMA-C_8-IM[TFSI] and (b) PMMA-C_2-IM[Br] at 580 K. Color codes: blue: Type 1; green: Type 2; and red: Type 3. (c) The average jump length of $TFSI^-$ and Br^- as a function of linker length at 580 K.

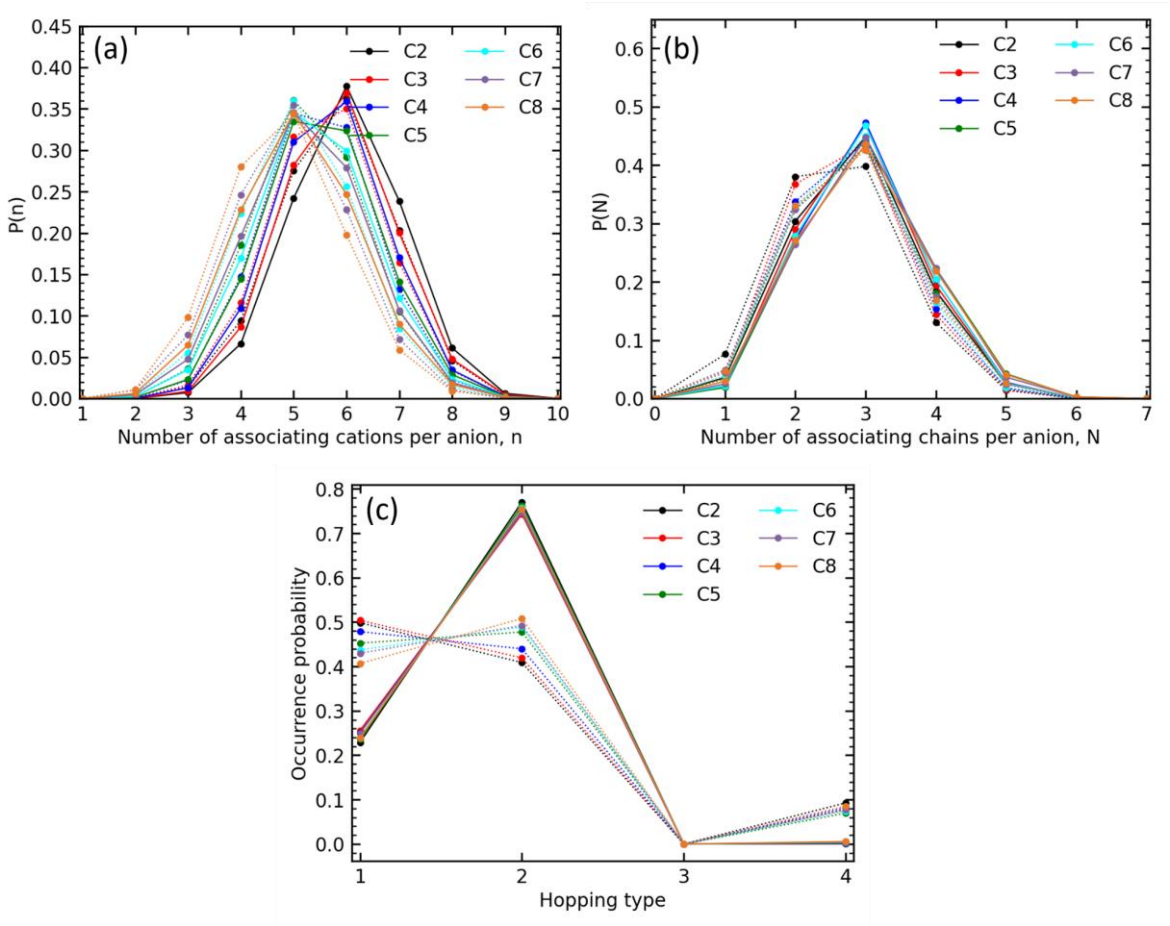

Figure A.13. (a) Probability of a fast anion (solid lines) compared to a slow anion (dotted lines) (a) coordinating with *n* cations $P(n)$ and (b) associating with *N* cations $P(N)$for a broad range of linker lengths for the PMMA-C_x-IM[TFSI] systems at 580 K. (c) Occurrence probability of the hopping types for fast anions (solid lines) compared with slow anions (dotted lines) for the PMMA-C_x-IM[TFSI] systems at 580 K.

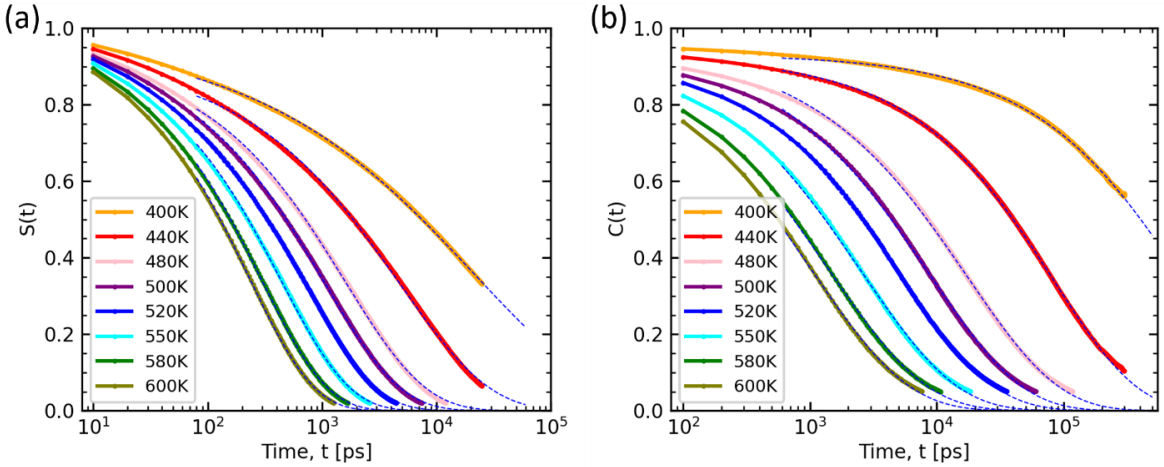

Figure A.14. (a) Continuous time correlation function, $S(t)$, and (b) intermittent time correlation function, $C(t)$, at various temperatures for the PMMA-C_2-IM[TFSI] system. $S(t)$ was computed from trajectories sampled every 10 ps, while $C(t)$ was derived from trajectories sampled every 100 ps. Both functions are fitted to a stretched exponential function as shown in blue dotted lines.

Appendix C. List of Presentations and Publications

Publications:

1. Ahmed, M. D.; **Zhu, Z.**; Khamzin, A.; Paddison, S. J.; Sokolov, A. P.; Popov, I., Effect of Ion Mass on Dynamic Correlations in Ionic Liquids. *Journal of Physical Chemistry B* **2023**, *127*, 10411-10421.
2. Popov, I.; **Zhu, Z.**; Young-Gonzales, A. R.; Sacci, R. L.; Mamontov, E.; Gainaru, C.; Paddison, S. J.; Sokolov, A. P., Search for a Grotthuss Mechanism through the Observation of Proton Transfer. *Communications Chemistry* **2023**, *6*, 77.
3. **Zhu, Z.**; Paddison, S. J., Perspective: Morphology and Ion Transport in Ion-Containing Polymers from Multiscale Modeling and Simulations. *Frontiers in Chemistry* **2022**, *10*, 981508.
4. **Zhu, Z.**; Luo, X.; Paddison, S. J., Coarse-Grained Modeling of Ion-Containing Polymers. *Chemical Reviews* **2022**, *122,* 10710-10745.
5. **Zhu, Z.**; Luo, X.; Sokolov, A. P.; Paddison, S. J., Proton Transfer in Phosphoric Acid-based Protic Ionic Liquids: Effects of the Base. *Journal of Physical Chemistry A* **2020**, *124*, 4141-4149.
6. **Zhu, Z.;** Luo, X.; Paddison, S. J.**,** DPD Simulations of Anion Exchange Membranes Functionalized with Various Cationic Groups and Associated Anions. *Solid State Ionics* **2019**, *340*, 115011.

Manuscripts Submitted:

1. **Zhu, Z.;** Sokolov, A. P.; Paddison, S. J., Ion Transport in Polymerized Ionic Liquids: Effects of Sidechain Flexibility and Specific Interactions. *Advanced Energy Materials* **2024**, to be submitted.
2. Popov, I.; **Zhu, Z.**; Singh, H.; Abdullah, M.; Sacci, R. L.; Mamontov, E.; Damron, J. T.; Gainaru, C.; Paddison, S. J.; Sokolov, A. P., Mechanisms of Proton Transport in Aqueous Acid Solutions. *Cell Reports Physical Science* **2024**, CR-PHYS-SCI-D-24-00474, submitted.

3. **Zhu, Z.;** Sokolov, A. P.; Paddison, S. J., Proton Transport Mechanisms in Aqueous Acids: Insight from Ab Initio Molecular Dynamics Simulations. *Journal of Chemical Physics,* **2024**, JCP24-AR-MD602024-02497, submitted.

Presentations:

1. **Zhu, Z.**; Popov, I.; Sokolov, A. P.; Paddison, S. J., (2024). Proton Transport in Aqueous Phosphoric, Sulfuric, and Nitric Acids: An *Ab Initio* Study. The Electrochemical Society. 245th ECS Meeting, San Francisco, CA, USA.
2. **Zhu, Z.**, (2024). Multiscale Modeling of Morphology and Proton/Ion Transport in Electrolytes. Seminar. Department of Chemical & Biomolecular Engineering, UTK, USA.
3. **Zhu, Z.**; Popov, I.; Sokolov, A. P.; Paddison, S. J., (2023). Mechanistic Insights into Ion Transport in Polymerized Ionic Liquids. The Electrochemical Society. 243rd ECS Meeting, Boston, MA, USA.
4. **Zhu, Z.**; Popov I.; Sokolov, A. P.; Paddison, S. J., (2022). Mechanistic Insights into Proton Transport in Pure and Aqueous Phosphoric Acid. The Electrochemical Society. 242nd ECS Meeting, Atlanta, GA, USA.
5. **Zhu, Z.**; Luo, X.; Paddison, S. J., (2019). Proton Dissociation and Transfer in Protic Ionic Liquids (PILs). The Electrochemical Society. 236th ECS Meeting, Atlanta, GA, USA.
6. Paddison, S. J.; Luo, X.; **Zhu Z.,** (2019). Effects of an Alkyl Spacer and the Cationic Group on the Hydrated Morphology of Anion Exchange Membranes. The Electrochemical Society. 235th ECS Meeting, Dallas, TX, USA.
7. **Zhu, Z.**; Luo, X.; Paddison, S. J., (2019). Proton Dissociation and Transfer in Protic Ionic Liquids (PILs). Southeastern Theoretical Chemistry Association (SETCA) Meeting, Knoxville, TN, USA.
8. **Zhu, Z.**; Luo, X.; Paddison, S. J., (2018). DPD Simulation of Anion Exchange Membrane Functionalized with Various Cationic Groups and Anions. 19th Solid State Protonic Conductors (SSPC), Stowe, VT, USA.

Appendix D. Reprints and Preprints of Publications

Reprinted with permission from Elsevier
Copyright 2019 Elsevier

Solid State Ionics 340 (2019) 115011

Contents lists available at ScienceDirect

Solid State Ionics

journal homepage: www.elsevier.com/locate/ssi

DPD simulations of anion exchange membranes functionalized with various cationic groups and associated anions

Zhenghao Zhu, Xubo Luo, Stephen J. Paddison*

Department of Chemical and Biomolecular Engineering, University of Tennessee, 1512 Middle Drive, Knoxville, TN 37996, USA

ARTICLE INFO

Keywords:
SEBS membranes
Cationic groups
Morphology
Dissipative particle dynamics

ABSTRACT

Anion exchange membranes (AEMs) continue to provoke interest as electrolytes in low temperature fuel cells. AEMs based on the triblock copolymer and polystyrene-b-poly(ethylene-*co*-butylene)-b-polystyrene (SEBS) can be functionalized with different cationic groups. The coexisting anion, due to the possibility of different routes of synthesis, can also be varied. The hydrated morphology of SEBS functionalized with various cationic groups provides a suitable platform for understanding the mechanism of anion transport and the route to preparing highly conductive and stable membranes. In this work, mesoscale dissipative particle dynamics (DPD) simulations were utilized to study the morphology of various SEBS-based ionomers: SEBS-trimethylammonium (SEBS-TMA), SEBS- methylimidazolium SEBS-MIm and SEBS-trimethylphosphonium (SEBS-TMP) as a function of hydration levels. The morphology was transformed to perfect lamellae followed by disordered bicontiuous domains from perforated and interconnected lamellae as the hydration was increased from 4 to 20 H_2O/head group. Perfect lamellae occur at $\lambda = 8$ for SEBS-TMP and at $\lambda = 12$ for SEBS-TMA and SEBS-MIm. Moreover, exclusive water domains were observed at high hydration levels for all systems. Large clusters of the water and hydrated OH^- are formed when $\lambda \geq 8$ for SEBS-TMP, SEBS-TMA, and SEBS-MIm. The choice of the functional group was found to moderately affect the distribution of water but have little influence on the structure of the backbone. The associated anion seemed to have a greater impact on the size of the exclusive water domains rather than the cationic groups.

1. Introduction

The anion exchange membrane (AEM) is a key component in anion exchange membrane fuel cells (AEMFCs) and facilitates the transport of hydroxide ions and the separation of fuels from oxidants. They provide a potential alternative to proton exchange membrane fuel cells (PEMFCs) whose limitation is the need of expensive noble metal catalyst in the acidic environments [1,2]. Although the facile oxygen reduction reaction under alkaline condition enables AEMFCs to utilize non-noble metal catalysts with high stability [3,4], there are still challenges of possessing mechanical and chemical stability under high pH conditions. Recent studies have achieved high hydroxide ion conductivity [2], the means of designing membranes with high OH^- conductivities is still not fully understood.

In order to overcome the lower mobility of hydroxide ions in comparison to protons, extensive efforts have been made to improve the OH^- conductivity of AEMs. Weiber et al. [5] found that optimizing the nanophase separation and the local concentration and distribution of the cationic groups of an AEM instead of merely increasing the ion exchange capacity (IEC) enhances the hydroxide ion conductivity. Recently, comb-shaped AEMs were reported to have excellent OH^- conductivity due to enhanced nanophase separation [6–10]. The construction of ion clusters and well-defined OH^- channels was investigated to enhance the conductivity [11,12]. Chemical stability is another key challenge, which has also attracted significant research. Functional cationic groups such as ammonium, phosphonium, and imidazolium have been widely studied as the degradation of AEMs is generally initiated around the functional groups [13–16]. Recent studies revealed that chemical degradation of pendant cationic groups significantly increases under a combination of alkaline and low

Abbreviations: AEM, anion exchange membrane; SEBS, polystyrene-b-poly(ethylene-*co*-butylene)-b-polystyrene; DPD, dissipative particle dynamics; TMA, trimethylammonium head group; MIm, methylimidazolium head group; TMP, trimethylphosphonium head group; AEMFC, anion exchange membrane fuel cell; PEMFC, proton exchange membrane fuel cell; IEC, ion exchange capacity; DFT, density functional theory; AIMD, ab initio molecular dynamics; RDF, radial distribution function; CN, coordination number

* Corresponding author.
E-mail address: spaddison@utk.edu (S.J. Paddison).

https://doi.org/10.1016/j.ssi.2019.115011
Received 10 May 2019; Received in revised form 17 June 2019; Accepted 24 June 2019
Available online 02 July 2019
0167-2738/ © 2019 Elsevier B.V. All rights reserved.

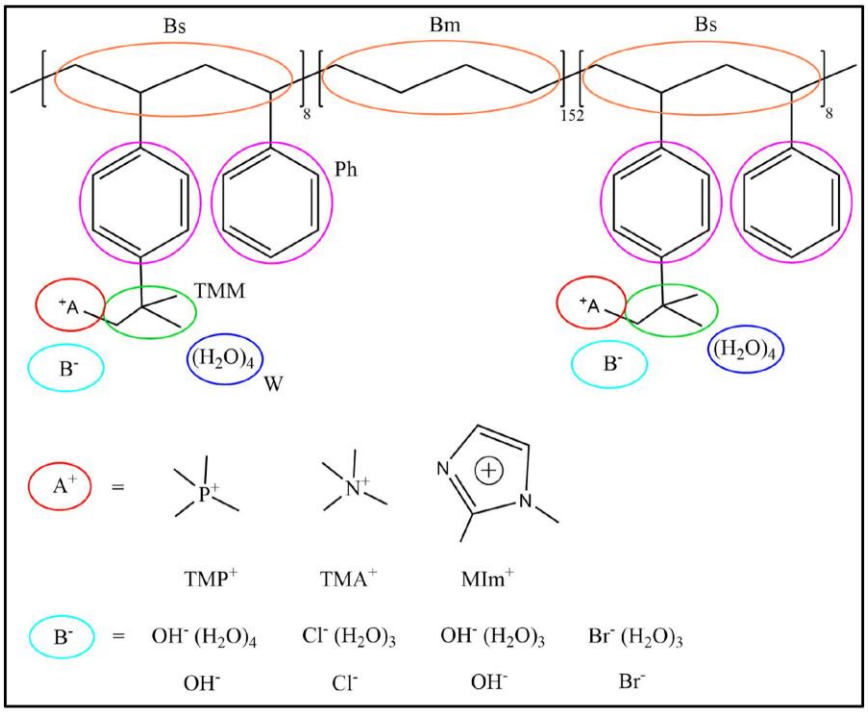

Fig. 1. Coarse-grained model of hydrated SEBS-based AEM in various forms. Each circle represents the specific bead/particle of the selected chemical group or collection of atoms.

Table 1
Bead type, chemical structure, and volume.

Bead type	Structure	Volume[a] (Å^3)
Bs, Bm	$[H](CH_2CH_2)_2[H]$	125.5
Ph	$C_6H_4[H_2]$	129.7
TMM	$[H]C(CH_3)_2CH_2[H]$	124.8
TMA^+	$[H]N(CH_3)_3$	121.8
TMP^+	$[H]P(CH_3)_3$	136.8
MIm^+	$[H]C_3N_2H_3CH_3$	130.9
W	$(H_2O)_4$	120.1
OH^-	$OH^-(H_2O)_4$	134.6
Cl^-	$Cl^-(H_2O)_3$	125.0
OH^-	$OH^-(H_2O)_3$	118.8
Br^-	$Br^-(H_2O)_3$	132.3

[a] Volumes were referred to or obtained using the same approach in our previous work [26].

hydration conditions in AEMs [17–19]. Bae's group systematically investigated the alkaline stability of the backbones of AEMs and suggested that the less expensive all-carbon-based polymers are promising backbones of the durable AEMs, such as the triblock copolymer polystyrene-b-poly(ethylene-*co*-butylene)-b-polystyrene (SEBS) [20,21].

Multiscale simulations may provide further insight into the nanophase separation, transport mechanisms, formation of ion and water clusters and extended domains (e.g. channels), the structure of solvated hydroxide ions, correlation between ions/molecules, and the stability of AEMs. Several quantum density functional theory (DFT) based studies of the pathways of attack by hydroxide ions have elucidated possible directions for improving the stability of the backbones and the functional groups [20,22,23]. Recently, ab initio molecular dynamics (AIMD) simulations were undertaken to elucidate the mechanisms of the hydroxide ion transport in the hydrated AEMs [24]. van Duin et al. [25] investigated the effect of the hydration level on membrane swelling, structure, and hydroxide ion transport of AEMs with different pendant side chains to the functional group utilizing reactive force-field (ReaxFF) molecular dynamics. Here we continue our studies of the nanophase separation (hydrophilic/hydrophobic) and hydrated morphology of AEMs with dissipative particle dynamics (DPD) simulations because of the computational efficiency and relatively long accessible length and time scales [26–32].

In the present study, the impact of the choice of the cationic group on the morphology and the microstructures of SEBS-based AEMs over a broad range of hydration level is investigated with a similar parametrization utilized in our previous work [26]. In addition, the effect of associated anions (OH^-, Cl^-, and Br^-) was investigated.

2. Simulation method

DPD [33–35] simulations have been successfully utilized into the investigation of the morphology of PEMs and AEMs [26,27,36–40].

2.1. Coarse-grained model

Particles of analogous volume but of dissimilar chemical structure are selected and coarse-grained to a bead, ignoring the detailed atomic information which is not deemed necessary for studying the morphological features of the hydrated materials. The selected structure of our

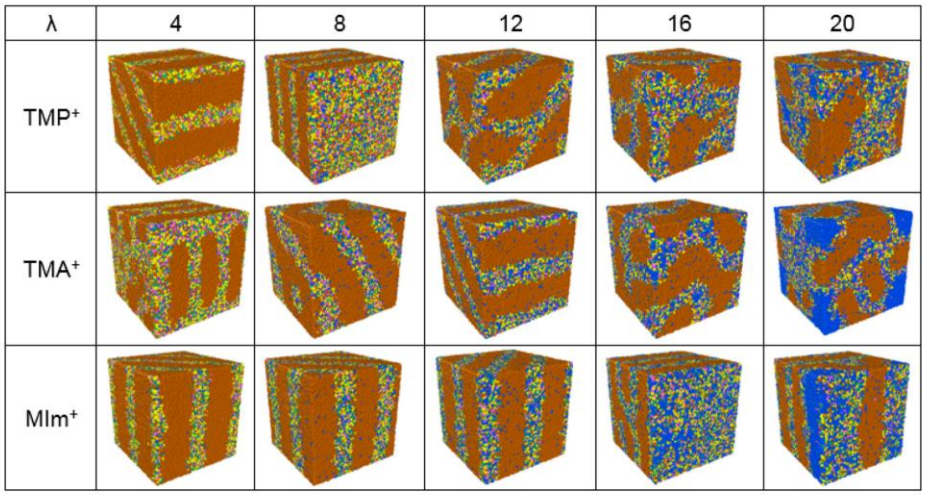

Fig. 2. Morphologies of the SEBS functionalized with different cationic groups in the alkaline form. There are two phases: hydrophilic and hydrophobic phases occurring at all hydration levels. For low λ, perforated and interconnected lamellae are formed; for high λ, disordered bicontinuous lamellas are formed and water droplets (blue regions) can be found. Color code: Bs and Bm (orange); Ph (mauve); TMM (green); TMA^+ (purple); TMP^+ (light orange); MIm^+ (dark blue); OH^- (cyan); and W (blue). (For interpretation of the references to color in this figure legend, the reader is referred to the web version of this article.)

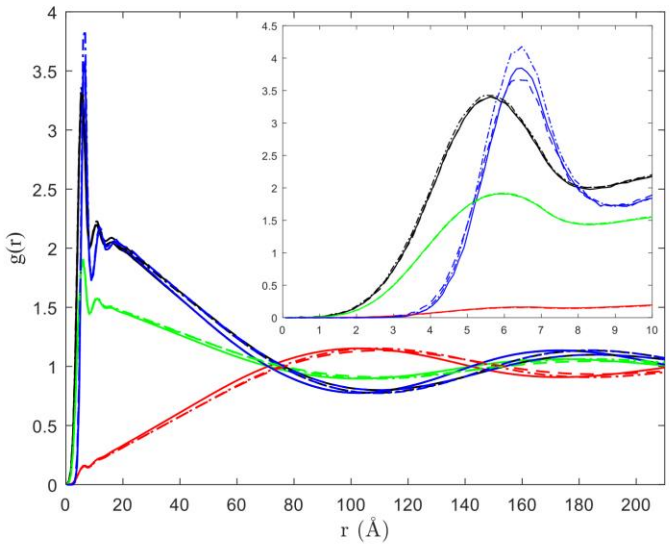

Fig. 3. RDFs of the hydrated AEM in the alkaline form at λ = 8. The inset shows a magnification at short distances. Color code: BsPh-BsPh (black); BsPh-Bm (red); Bm-Bm (green); and Cation-Cation (blue). Line scheme: SEBS-TMP (solid line); SEBS-MIm (dash-dotted line); SEBS-TMA (dashed line). (For interpretation of the references to color in this figure legend, the reader is referred to the web version of this article.)

coarse-grained model is shown in Fig. 1. The SEBS-based backbone consists of polystyrene blocks and poly(ethylene-*co*-butylene) blocks which were modelled with two distinct bead types: the Bs ($(CH_2CH_2)_2$) bead and the Ph (phenyl group) bead. The middle blocks, however, are treated as polyethylene represented by a Bm bead. For the AEM ionomers, one end of the TMM (Trimethylenemethane) beads is attached with Ph whereas the other end is linked to different cationic groups including trimethylammonium (TMA^+), methyl Imidazolium (MIm^+), and trimethylphosphonium (TMP^+) to compare the impact of the functional groups on the ionomers. To compare the effect of associated anion on the hydrated AEMs, three associated anions are introduced: an OH^- bead for alkaline form, a Cl^- bead and a Br^- for the chloride and bromide precursor form, respectively. The OH^- bead is comprised of an hydroxide ion and three or four water molecules, the latter based on its primary hydrated structure [41–43]. The Cl^- and Br^- beads consist of three water molecules along with a chloride or bromide anion, respectively. A water bead includes four water molecules. The hydrated OH^-, Cl^-, and Br^- structures were referred to previous literature [26,42–45] which meet the criteria of similar volume (see Table 1). The bonded interactions and the DPD conservative interaction parameters

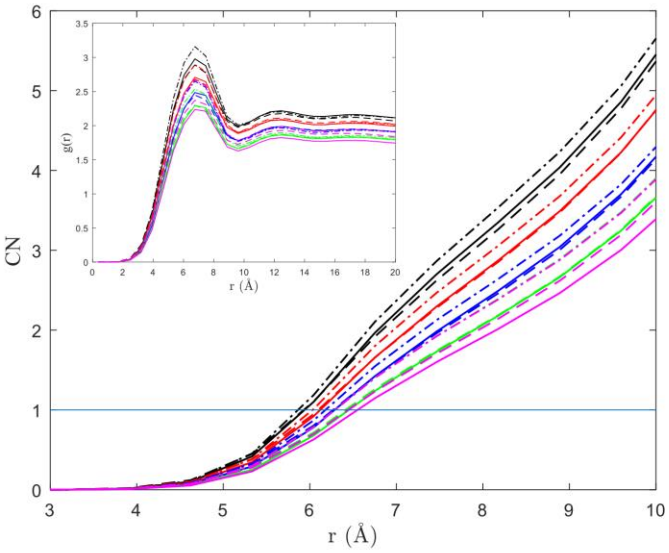

Fig. 4. The coordination number (CN) of the cations as a function of cation distance across the various hydration levels: λ = 4 (black); λ = 8 (red); λ = 12 (blue); λ = 16 (green); and λ = 20 (pink). Line scheme: SEBS-TMP (solid line); SEBS-MIm (dash-dotted line); and SEBS-TMA (dashed line). The inset shows the cation-cation RDFs over the regions from 0 to 20 Å. The first minima of the RDFs lie around 9.5 Å. (For interpretation of the references to color in this figure legend, the reader is referred to the web version of this article.)

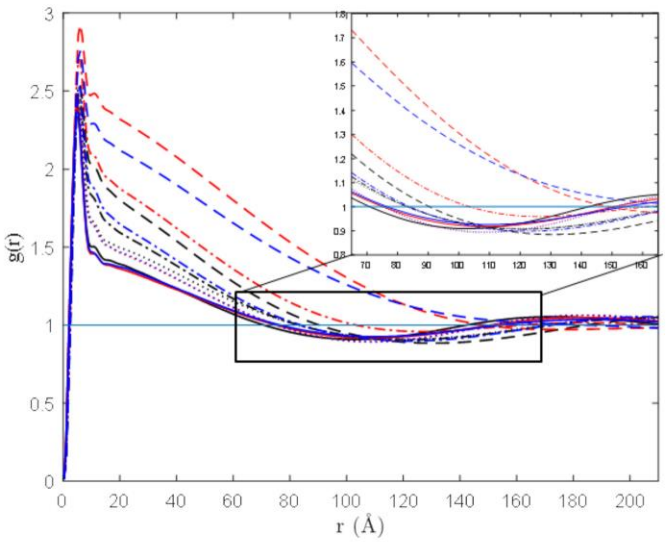

Fig. 5. W–W RDFs for the AEMs functionalized with different cationic group in the alkaline form at various water contents. Color scheme: SEBS-TMP (black); SEBS-MIm (red); SEBS-TMA (blue). Line scheme: λ = 8 (solid line); λ = 12 (dotted line); λ = 16 (dash-dotted line); and λ = 20 (dashed). Zoom up shows the minimal radial distance where $g(r) = 1$. (For interpretation of the references to color in this figure legend, the reader is referred to the web version of this article.)

were obtained from reference [26] or calculated by the parameterization method [46] (see Tables S1 and S2).

2.2. Simulations

The LAMMPS (large scale atomic/molecular massively parallel simulator) was employed to perform all DPD simulations undertaken in this investigation on Stampede2 at the Texas Advanced Computing Center (TACC). Generation of random initial configurations was performed with the PACKMOL package [47]. In a typical simulation box, there were 648,000 beads in a 3-dimensional periodic unit cell of 60 DPD length units (42.7 nm) and a density of 3. The time step was fixed at 0.01 DPD time units, i.e., 38 fs, and the overall number of steps was typically 70,000,000 (i.e., a total of 2.68 μs of simulation time) to ensure each system reached equilibrium.

The AEM ionomers were constructed with a molecular weight (MW) of 11,830 g/mol with 29.63% composition of polystyrene end-blocks and 50% of the styrene being functionalized with the TMM and cationic groups as described above. All chains were built to have a similar MW. The impact of water content on the morphology was assessed by simulating a broad range of hydration levels. Hence, the water content in the systems ranged from λ = 4 to 20, where λ is the number of water

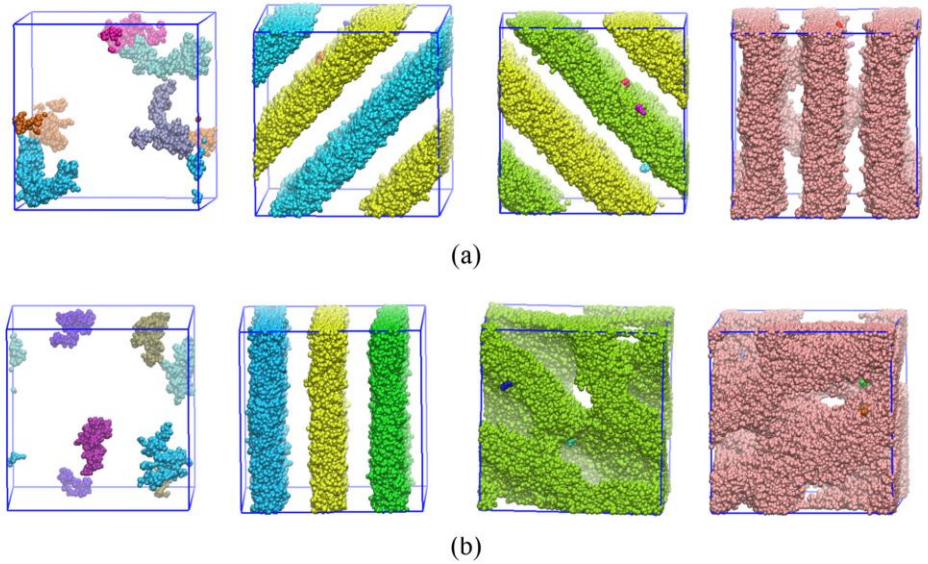

Fig. 6. Five largest clusters of water and OH^- beads at $\lambda = 4, 8, 12, 16$. (a) SEBS-MIm; (b) SEBS-TMP.

molecules per cationic functional group. Although it is not the focus of the present study, it would be worthwhile to extend the hydration to extreme since ultra-low hydration gives rise to serious OH^--derived AEM degradation [48] and excessively high water content causes electrode flooding and ionomer swelling that leads to the great decrease of the mechanical integrity of AEMs [49]. Each system consists of water, anions, and more than two thousand macromolecules; the latter is determined by the degree of hydration. The numbers of positively and negatively charged beads were constrained to be equal to ensure electroneutrality of each system.

3. Results and discussion

3.1. The effect of cationic group

Fig. 2 illustrates the simulated morphologies of an SEBS ionomer functionalized with different cationic groups in the alkaline form over a broad range of hydration ($\lambda = 4$, 8, 12, 16, and 20). Generally, there are two clearly defined phases: hydrophilic and hydrophobic phases, which occurred at all hydration levels. The hydrophilic domains consist of the functionalized polystyrene end-blocks (Bs, Ph, TMM, cationic groups, anions and water beads) whereas the other phase forms backbone of AEMs. For the SEBS-TMP and SEBS-MIm, the interconnected lamellae occur at very low hydration ($\lambda = 4$). The morphology gradually transformed into organized lamellae from interconnected lamellae, and then into disordered bicontinuous regions as the hydration level was increased. The SEBS-TMP reaches a perfect lamellae morphology at $\lambda = 8$, while the SEBS-MIm does not until $\lambda = 12$. With increased water content, the disordered bicontinuous domains are observed in both SEBS-TMP and SEBS-MIm, and the exclusive water clusters (blue regions) form at the same time. Moreover, the water clusters in the SEBS-MIm are larger than that in the SEBS-TMP, which seems to suggest that the water is more uniformly distributed in SEBS-TMP. Compared these results with our previous work [26], we note that perforated lamellae do not seem to form at low hydration levels.

The RDFs of the hydrated SEBS-based polymers functionalized with three different cationic groups in the alkaline form at $\lambda = 8$ are depicted in Fig. 3. The black lines are the BsPh-BsPh RDFs with solid, dash-dotted, and dashed lines corresponding to the SEBS-TMP, SEBS-MIm, and SEBS-TMA, respectively. The RDFs of cation-cation shown with the blue lines are similar to that of the end-blocks at distances > 15 Å, which is expected as the cationic groups are attached to the end-blocks. The green lines correspond to the hydrophobic mid-blocks. The red lines correspond to the RDFs of the hydrophobic blocks and illustrate that the two phases are, as expected, repulsive to each other. The RDFs of the same pair with different cationic groups have a similar pattern, meaning these pendant functionalized groups appear to have little influence on the morphologies of the backbone. It is noticeable from the inset of Fig. 3 that the first peaks of the cation-cation RDFs shift to the right with shorter distance compared to the RDFs of the hydrophilic phase because of the repulsive coulombic force between them. Furthermore, the first peaks have different intensities for SEBS-based functionalized with different cationic groups: the SEBS-MIm has the highest while the SEBS-TMA has the lowest one.

Fig. 4 shows a plot of the coordination number (CN) of the cationic groups as a function of the distance from the cation group over a range of water contents. The CN of the cation-cation shown in Fig. 4 indicates that there is one other cationic group with the sphere radius of 5.5–6.5 Å, which can be treated as a characteristic length that the hydroxide ion needs to overcome if its motion trajectory is between two cationic groups [50]. For all cases, at the CN = 1, the separations between the immediate vicinity expand when the hydration levels increase. The SEBS-MIm always has the smallest distance at CN = 1 at various hydration levels in comparison with the SEBS-TMP and the SEBS-TMA whose separations are similar. It is clear that the cationic groups are separated by at least 4.0 Å.

Fig. 5 shows the W—W RDFs of ionomers with different pendant cationic groups at hydration levels where $\lambda = 8$, 12, 16, and 20. The intensity of the peaks increases with increasing hydration for these three AEMs, indicating that the water is more structured at high hydration levels. At low levels of hydration ($\lambda = 8$ and 12), the effect of the cationic group is somewhat smaller. However, the affect becomes

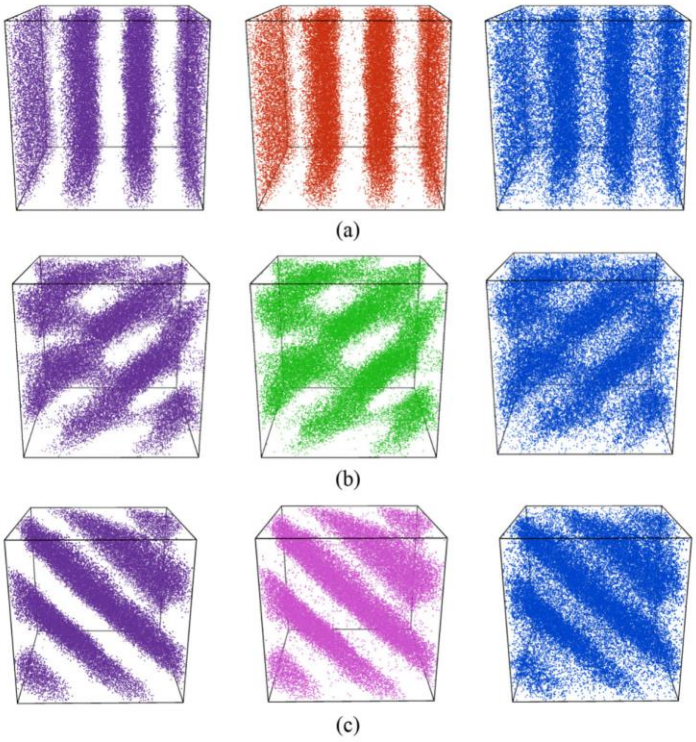

Fig. 7. Simulated morphology of the hydrated AEM in different forms at λ = 8. (a) TMA^+ in $Br^-(H_2O)_3$; (b) TMA^+ in $Cl^-(H_2O)_3$; (c) TMA^+ in $OH^-(H_2O)_3$. Color code: TMA^+ (purple); Br^- (red); Cl^- (light green); OH^- (pink); and W (blue). (For interpretation of the references to color in this figure legend, the reader is referred to the web version of this article.)

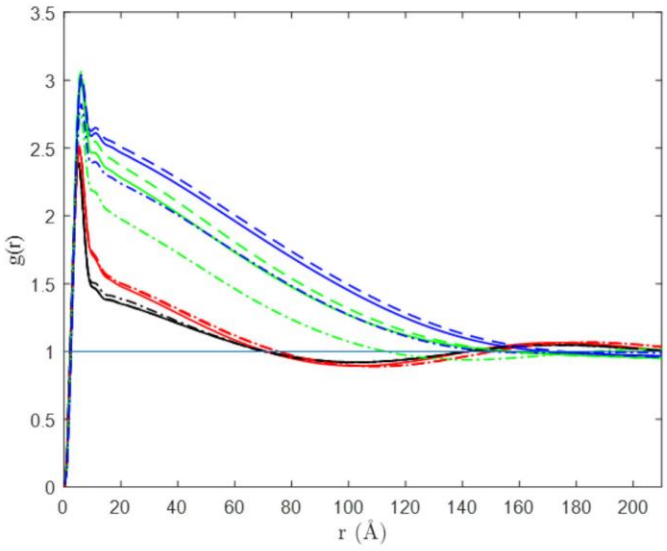

Fig. 8. W−W RDFs for the hydrated AEM in the alkaline (solid line), chloride (dash-dotted line), and bromide (dash line) forms at various levels of hydrations. Color scheme: λ = 8 (black); λ = 12 (red); λ = 16 (green); λ = 20 (blue). (For interpretation of the references to color in this figure legend, the reader is referred to the web version of this article.)

significant at the highest water contents: λ = 16 and 20, of which the water in the SEBS-MIm is the most structured. The point where $g(r)$ first becomes 1 varies little for the three AEMs at the lowest water content, in contrast to what occurs at the highest water contents where there is substantial differences. It suggests that the cationic group affects the distribution of water but has little impact on the size of the exclusive water domains.

Fig. S1 reveals that the distribution in water cluster size at the different water contents. In general, the left side of the cluster size distribution shifts to the left, while the right branch shifts to the right with increasing water content, suggesting there are increasing number of water beads contributing to the clusters. The snapshots of the five largest clusters at various hydration levels are shown in Fig. 6. In the case of SEBS-MIm, the largest cluster consists of 823 beads at λ = 4. It is evident that no percolating domains emerge. The percolating domains begin to appear at λ = 8 and the size expands with increasing water content: 32,225 beads at λ = 8; 49,330 beads at λ = 12; and 127,412 beads at λ = 16. The structure of the clusters become bicontinuous at λ = 12 in the SEBS-TMP, but do not occur until the water content reaches 16 for SEBS-MIm. Clearly the more polar head group (TMP) facilitates a more connected network of water. The largest water clusters for the SEBS-TMP at different hydration levels are 532 beads for λ = 4, 21,803 beads for λ = 8, 97,875 beads for λ = 12, and 128,036 beads for λ = 16.

3.2. The effect of the associated anion

To investigate the effect of the associated anions, the hydroxide ion bead containing three water molecules was introduced instead of $OH^-(H_2O)_4$ to match the systems of $Cl^-(H_2O)_3$ and $Br^-(H_2O)_3$. The simulated morphology of the SEBS-TMA in the three different forms (hydroxide, chloride, and bromide) are shown in Fig. S2. It is clear that phase separation occurred in all systems and perfect lamellae were observed at λ = 8 for the three different associated anions. At the lowest hydration level, perforated lamellae appeared in the cases of $OH^-(H_2O)_3$ and $Cl^-(H_2O)_3$, while perforated lamellae were not observed in the bromide form. This would seem to imply that it is easier to form the interconnected lamellae in the bromide form than in the other two forms. It is important to be aware of the lack of connectivity between isolated tiny hydrophilic clusters and the occurrence of the water-bridged double-hydroxide structures in the OH^- form when the hydration levels are extremely low (λ < 4) as shown in the recent study [41]. In Fig. 7, the morphology of a specific bead type at λ = 8 was presented for clarity. It is evident that the ionic species have the similar distributions in all systems since there is strong coulombic attraction between the cationic groups and the associated anions. Most of the water is distributed within the same phase (i.e., all ionic species), while some isolated water appears in the polyethylene phase. In the case of the Cl^- form, the perforated and interconnected morphology is shown, which does not emerge in the other two forms at λ = 8. This implies that different anion forms can result in qualitative differences in the hydrated morphology.

The RDFs of the alkaline, the chloride, and the bromide forms as a function of water content are shown in Fig. 8. Generally, the intensity of peaks in three forms rises as the water content increases. The associated anion has little impact on the W−W RDFs at low hydrations (λ = 8 and 12). However, the effect becomes noticeable when the level of hydration is > 12. The distance the RDF reaches a value of one increases considerably at λ = 16 with the largest water domains occurring in the bromide form, in sharp contrast to the chloride form. It is interesting to note that the associated anion has more impact on the size of the exclusive water domains at the highest water contents in comparison to the somewhat minimal effect of the choice of the cationic group.

It is worth noting that carbonate anions are also important to study in order to better understand the adverse impact of ambient air feed (i.e., CO_2) on the performance of AEMFCs [51,52]. As CO_2 can react with OH^- to form HCO_3^- and CO_3^{2-}, the effective anion conductivity in the AEM would be significantly decreased through the carbonation process. Future work may focus on simulations of AEM properties under the impact of carbon dioxide and carbonation products (carbonate and bicarbonate anions) to better understand the AEM behavior during operation of AEMFCs under ambient air.

4. Conclusions

We have performed DPD simulations to study the effect of pendant cationic groups and associated anions on the hydrated morphology and microstructure of SEBS-based AEMs. Microphase separation was observed in all simulations. The functionalized polystyrene and the polyethylene separated into a hydrophilic phase and a hydrophobic phase, respectively. Most water and the ionic species were only distributed throughout the hydrophilic phase, while some water was also in the hydrophobic phase. The morphology was transformed from perforated and interconnected lamellae to perfect lamellae and then to disordered bicontinuous domains by increasing the hydration level from λ = 4 to 20. The perfect lamellae occur at λ = 8 for SEBS-TMP and λ = 12 for SEBS-TMA and SEBS-MIm. The exclusive water domains were observed at the high hydration levels for all systems. However, the functional groups affect the distribution of water but have few influences on the structure of the backbone via analysing the RDFs. The associated anion has greater impact on the size of exclusive water domains compared to the cationic groups. Large clusters of the water and OH^- beads are formed when λ ≥ 8 for SEBS-TMP, SEBS-TMA, and SEBS-MIm. Changing the anion leads to negligible changes in W−W RDFs at λ = 8 and λ = 12, but the peaks are significantly increased at λ = 16 and λ = 20.

Acknowledgements

Financial support was provided by the National Science Foundation under CHE 1534355: “DMREF: Collaborative Research: Development of Design Rules for High Hydroxide Transport in Polymer Architectures”. Computing resource was provided through an XSEDE allocation: DMR130078.

Appendix A. Supplementary data

Supplementary data to this article can be found online at https://doi.org/10.1016/j.ssi.2019.115011.

References

[1] S. Gottesfeld, D.R. Dekel, M. Page, C. Bae, Y. Yan, P. Zelenay, Y.S. Kim, Anion exchange membrane fuel cells: current status and remaining challenges, J. Power Sources 375 (2018) 170–184, https://doi.org/10.1016/j.jpowsour.2017.08.010.
[2] D.R. Dekel, Review of cell performance in anion exchange membrane fuel cells, J. Power Sources 375 (2018) 158–169, https://doi.org/10.1016/j.jpowsour.2017.07.117.
[3] X. Peng, V. Kashyap, B. Ng, S. Kurungot, L. Wang, J. Varcoe, W. Mustain, High-performing PGM-free AEMFC cathodes from carbon-supported cobalt ferrite nanoparticles, Catalysts 9 (2019) 264, https://doi.org/10.3390/catal9030264.
[4] G.L. Chai, Z. Hou, D.J. Shu, T. Ikeda, K. Terakura, Active sites and mechanisms for oxygen reduction reaction on nitrogen-doped carbon alloy catalysts: stone-wales defect and curvature effect, J. Am. Chem. Soc. 136 (2014) 13629–13640, https://doi.org/10.1021/ja502646c.
[5] E.A. Weiber, D. Meis, P. Jannasch, Anion conducting multiblock poly(arylene ether sulfone)s containing hydrophilic segments densely functionalized with quaternary ammonium groups, Polym. Chem. 6 (2015) 1986–1996, https://doi.org/10.1039/C4PY01588F.
[6] Y. He, J. Si, L. Wu, S. Chen, Y. Zhu, J. Pan, X. Ge, Z. Yang, T. Xu, Dual-cation comb-shaped anion exchange membranes: structure, morphology and properties, J. Membr. Sci. 515 (2016) 189–195, https://doi.org/10.1016/j.memsci.2016.05.058.
[7] A.H.N. Rao, S. Nam, T.-H. Kim, Comb-shaped alkyl imidazolium-functionalized poly(arylene ether sulfone)s as high performance anion-exchange membranes, J. Mater. Chem. A 3 (2015) 8571–8580, https://doi.org/10.1039/C5TA01123J.
[8] J. Pan, C. Chen, Y. Li, L. Wang, L. Tan, G. Li, X. Tang, L. Xiao, J. Lu, L. Zhuang, Constructing ionic highway in alkaline polymer electrolytes, Energy Environ. Sci. 7

(2014) 354–360, https://doi.org/10.1039/C3EE43275K.
[9] N. Li, L. Wang, M. Hickner, Cross-linked comb-shaped anion exchange membranes with high base stability, Chem. Commun. 50 (2014) 4092–4095, https://doi.org/10.1039/C3CC49027K.
[10] N. Li, Y. Leng, M.A. Hickner, C.-Y. Wang, Highly stable, anion conductive, comb-shaped copolymers for alkaline fuel cells, J. Am. Chem. Soc. 135 (2013) 10124–10133, https://doi.org/10.1021/ja403671u.
[11] N. Li, M.D. Guiver, Ion transport by nanochannels in ion-containing aromatic copolymers, Macromolecules 47 (2014) 2175–2198, https://doi.org/10.1021/ma402254h.
[12] D. Chen, M.A. Hickner, Ion clustering in quaternary ammonium functionalized benzylmethyl containing poly(arylene ether ketone)s, Macromolecules 46 (2013) 9270–9278, https://doi.org/10.1021/ma401620m.
[13] J. Yang, C. Liu, Y. Hao, X. He, R. He, Preparation and investigation of various imidazolium-functionalized poly(2,6-dimethyl-1,4-phenylene oxide) anion exchange membranes, Electrochim. Acta 207 (2016) 112–119, https://doi.org/10.1016/j.electacta.2016.04.176.
[14] J. Schauer, J. Hnát, L. Brožová, J. Žitka, K. Bouzek, Anionic catalyst binders based on trimethylamine-quaternized poly(2,6-dimethyl-1,4-phenylene oxide) for alkaline electrolyzers, J. Membr. Sci. 473 (2015) 267–273, https://doi.org/10.1016/j.memsci.2014.09.011.
[15] A.M. Park, F.E. Turley, R.J. Wycisk, P.N. Pintauro, Electrospun and cross-linked nanofiber composite anion exchange membranes, Macromolecules 47 (2014) 227–235, https://doi.org/10.1021/ma401932h.
[16] B. Zhang, S. Gu, J. Wang, Y. Liu, A.M. Herring, Y. Yan, Tertiary sulfonium as a cationic functional group for hydroxide exchange membranes, RSC Adv. 2 (2012) 12683–12685, https://doi.org/10.1039/C2RA21402D.
[17] C.E. Diesendruck, D.R. Dekel, Water – a key parameter in the stability of anion exchange membrane fuel cells, Curr. Opin. Electrochem. 9 (2018) 173–178, https://doi.org/10.1016/j.coelec.2018.03.019.
[18] D.R. Dekel, S. Willdorf, U. Ash, M. Amar, S. Pusara, S. Dhara, S. Srebnik, C.E. Diesendruck, The critical relation between chemical stability of cations and water in anion exchange membrane fuel cells environment, J. Power Sources 375 (2018) 351–360, https://doi.org/10.1016/j.jpowsour.2017.08.026.
[19] D.R. Dekel, M. Amar, S. Willdorf, M. Kosa, S. Dhara, C.E. Diesendruck, Effect of water on the stability of quaternary ammonium groups for anion exchange membrane fuel cell applications, Chem. Mater. 29 (2017) 4425–4431, https://doi.org/10.1021/acs.chemmater.7b00958.
[20] A.D. Mohanty, S.E. Tignor, J.A. Krause, Y.-K. Choe, C. Bae, Systematic alkaline stability study of polymer backbones for anion exchange membrane applications, Macromolecules 49 (2016) 3361–3372, https://doi.org/10.1021/acs.macromol.5b02550.
[21] A.D. Mohanty, C.Y. Ryu, Y.S. Kim, C. Bae, Stable elastomeric anion exchange membranes based on quaternary ammonium-tethered polystyrene-b-poly(ethylene-co-butylene)-b-polystyrene triblock copolymers, Macromolecules 48 (2015) 7085–7095, https://doi.org/10.1021/acs.macromol.5b01382.
[22] H. Long, B.S. Pivovar, Hydroxide degradation pathways for substituted benzyltrimethyl ammonium: a DFT study, ECS Electrochem. Lett. 4 (2015) F13–F16, https://doi.org/10.1149/2.0041501eel.
[23] S. Chempath, J.M. Boncella, L.R. Pratt, N. Henson, B.S. Pivovar, Density functional theory study of degradation of tetraalkylammonium hydroxides, J. Phys. Chem. C 114 (2010) 11977–11983, https://doi.org/10.1021/jp9122198.
[24] T. Zelovich, Z. Long, M. Hickner, S.J. Paddison, C. Bae, M.E. Tuckerman, Ab initio molecular dynamics study of hydroxide diffusion mechanisms in nanoconfined structural mimics of anion exchange membranes, J. Phys. Chem. C 123 (2019) 4638–4653, https://doi.org/10.1021/acs.jpcc.8b10298.
[25] W.W. Zhang, A.C.T. van Duin, ReaxFF reactive molecular dynamics simulation of functionalized poly(phenylene oxide) anion exchange membrane, J. Phys. Chem. C 119 (2015) 27727–27736, https://doi.org/10.1021/acs.jpcc.5b07271.
[26] F. Sepehr, H. Liu, X. Luo, C. Bae, M.E. Tuckerman, M.A. Hickner, S.J. Paddison, Mesoscale simulations of anion exchange membranes based on quaternary ammonium tethered triblock copolymers, Macromolecules 50 (2017) 4397–4405, https://doi.org/10.1021/acs.macromol.7b00082.
[27] S.S. Tallury, R.J. Spontak, M.A. Pasquinelli, Dissipative particle dynamics of triblock copolymer melts: a midblock conformational study at moderate segregation, J. Chem. Phys. 141 (2014), https://doi.org/10.1063/1.4904388.
[28] T.L. Chantawansri, T.W. Sirk, R. Mrozek, J.L. Lenhart, M. Kroger, Y.R. Sliozberg, The effect of polymer chain length on the mechanical properties of triblock copolymer gels, Chem. Phys. Lett. 612 (2014) 157–161, https://doi.org/10.1016/j.cplett.2014.08.013.
[29] T.L. Chantawansri, T.W. Sirk, Y.R. Sliozberg, Entangled triblock copolymer gel: morphological and mechanical properties, J. Chem. Phys. 138 (2013), https://doi.org/10.1063/1.4774373.
[30] Y.R. Sliozberg, K.E. Strawhecker, J.W. Andzelm, J.L. Lenhart, Computational and experimental investigation of morphology in thermoplastic elastomer gels composed of AB/ABA blends in b-selective solvent, Soft Matter 7 (2011) 7539–7551, https://doi.org/10.1039/c1sm05820g.
[31] C. Soto-Figueroa, M.D.R. Rodríguez-Hidalgo, J.M. Martínez-Magadan, L. Vicente, Dissipative particle dynamics study of order-order phase transition of BCC, HPC, OBDD, and LAM structures of the poly(styrene)-poly(isoprene) diblock copolymer, Macromolecules 41 (2008) 3297–3304, https://doi.org/10.1021/ma7028264.
[32] B. Abu-Sharkh, A. AlSunaidi, Morphology and conformation analysis of self-assembled triblock copolymer melts, Macromol. Theory Simul. 15 (2006) 507–515, https://doi.org/10.1002/mats.200600014.
[33] R.D. Groot, P.B. Warren, Dissipative particle dynamics: bridging the gap between atomistic and mesoscopic simulation, J. Chem. Phys. 107 (1997) 4423–4435, https://doi.org/10.1063/1.474784.
[34] P. Español, Dissipative particle dynamics with energy conservation, Europhys. Lett. 40 (1997) 631–636, https://doi.org/10.1209/epl/i1997-00515-8.
[35] P.J. Hoogerbrugge, J.M.V.A. Koelman, Simulating microscopic hydrodynamic phenomena with dissipative particle dynamics, Europhys. Lett. 19 (1992) 155–160, https://doi.org/10.1209/0295-5075/19/3/001.
[36] C. Wang, S.J. Paddison, Mesoscale modeling of hydrated morphologies of sulfonated polysulfone ionomers, Soft Matter 10 (2014) 819–830, https://doi.org/10.1039/C3sm52330f.
[37] D.S. Wu, S.J. Paddison, J.A. Elliott, S.J. Hamrock, Mesoscale modeling of hydrated morphologies of 3m perfluorosulfonic acid-based fuel cell electrolytes, Langmuir 26 (2010) 14308–14315, https://doi.org/10.1021/La102358y.
[38] D.S. Wu, S.J. Paddison, J.A. Elliott, Effect of molecular weight on hydrated morphologies of the short-side-chain perfluorosulfonic acid membrane, Macromolecules 42 (2009) 3358–3367, https://doi.org/10.1021/Ma900016w.
[39] D.S. Wu, S.J. Paddison, J.A. Elliott, A comparative study of the hydrated morphologies of perfluorosulfonic acid fuel cell membranes with mesoscopic simulations, Energy Environ. Sci. 1 (2008) 284–293, https://doi.org/10.1039/B809600g.
[40] S. Yamamoto, S.-A. Hyodo, A computer simulation study of the mesoscopic structure of the polyelectrolyte membrane Nafion, Polym. J. 35 (2003) 519–527, https://doi.org/10.1295/polymj.35.519.
[41] I. Zadok, D.R. Dekel, S. Srebnik, Unexpected Water-Hydroxide Ion Structure and Diffusion Behavior in Low Hydration Media, (2018) (1812.06961 [cond-mat.soft).
[42] Z. Zhu, M.E. Tuckerman, Ab initio molecular dynamics investigation of the concentration dependence of charged defect transport in basic solutions via calculation of the infrared spectrum, J. Phys. Chem. B 106 (2002) 8009–8018, https://doi.org/10.1021/jp020866m.
[43] M.E. Tuckerman, D. Marx, M. Parrinello, The nature and transport mechanism of hydrated hydroxide ions in aqueous solution, Nature 417 (2002) 925–929, https://doi.org/10.1038/nature00797.
[44] P. Bajaj, M. Riera, J.K. Lin, Y.E. Mendoza Montijo, J. Gazca, F. Paesani, Halide ion microhydration: structure, energetics, and spectroscopy of small halide–water clusters, J. Phys. Chem. A 123 (2019) 2843–2852, https://doi.org/10.1021/acs.jpca.9b00816.
[45] L. Ge, L. Bernasconi, P. Hunt, Linking electronic and molecular structure: insight into aqueous chloride solvation, Phys. Chem. Chem. Phys. 15 (2013) 13169–13183, https://doi.org/10.1039/c3cp50652e.
[46] F. Sepehr, S.J. Paddison, Dissipative particle dynamics interaction parameters from ab initio calculations, Chem. Phys. Lett. 645 (2016) 20–26, https://doi.org/10.1016/j.cplett.2015.12.032.
[47] L. Martinez, R. Andrade, E.G. Birgin, J.M. Martinez, Packmol: a package for building initial configurations for molecular dynamics simulations, J. Comput. Chem. 30 (2009) 2157–2164, https://doi.org/10.1002/jcc.21224.
[48] D.R. Dekel, I.G. Rasin, S. Brandon, Predicting performance stability of anion exchange membrane fuel cells, J. Power Sources 420 (2019) 118–123, https://doi.org/10.1016/j.jpowsour.2019.02.069.
[49] T. Omasta, L. Wang, X. Peng, C.A. Lewis, J. Varcoe, W. Mustain, Importance of balancing membrane and electrode water in anion exchange membrane fuel cells, J. Power Sources 375 (2018) 205–213, https://doi.org/10.1016/j.jpowsour.2017.05.006.
[50] D. Dong, X. Wei, J.B. Hooper, H. Pan, D. Bedrov, Role of cationic groups on structural and dynamical correlations in hydrated quaternary ammonium-functionalized poly(p-phenylene oxide)-based anion exchange membranes, Phys. Chem. Chem. Phys. 20 (2018) 19350–19362, https://doi.org/10.1039/C8CP02211A.
[51] N. Ziv, A.N. Mondal, T. Weissbach, S. Holdcroft, D.R. Dekel, Effect of CO_2 on the properties of anion exchange membranes for fuel cell applications, J. Membr. Sci. 586 (2019) 140–150, https://doi.org/10.1016/j.memsci.2019.05.053.
[52] N. Ziv, W.E. Mustain, D.R. Dekel, The effect of ambient carbon dioxide on anion-exchange membrane fuel cells, ChemSusChem 11 (2018) 1136–1150, https://doi.org/10.1002/cssc.201702330.

Reprinted with permission from American Chemical Society
Copyright 2020 American Chemical Society

THE JOURNAL OF PHYSICAL CHEMISTRY A

pubs.acs.org/JPCA Article

Proton Transfer in Phosphoric Acid-Based Protic Ionic Liquids: Effects of the Base

Zhenghao Zhu, Xubo Luo, Alexei P. Sokolov, and Stephen J. Paddison*

Cite This: J. Phys. Chem. A 2020, 124, 4141−4149 Read Online

ACCESS | Metrics & More | Article Recommendations | Supporting Information

ABSTRACT: Electronic structure calculations were performed to understand highly decoupled conductivities recently reported in protic ionic liquids (PILs). To develop a molecular-level understanding of the mechanisms of proton conductivity in PILs, minimum-energy structures of trimethylamine, imidazole, lidocaine, and creatinine (CRT) with the addition of one to three phosphoric acid (PA) molecules were determined at the B3LYP/6-311G** level of theory with the inclusion of an implicit solvation model (SMD with $\varepsilon = 61$). The proton affinity of the bases and zero-point energy corrected binding energies were computed at a similar level of theory. Proton dissociation from PA occurs in all systems, resulting in the formation of ion pairs due to the relatively strong basicity of the bases (proton acceptors) and the effect of the high dielectric constant solvent in stabilizing the charge separation. The second and third PA molecules preferentially form "ring-like" hydrogen bonds with one another instead of forming hydrogen bonds at the donor and acceptor sites of the bases. Potential energy scans reveal that the bases with stronger proton affinity exert greater influence on the energetics of proton transfer between the individual PA molecules. However, the effects are minimal when shifted into a single-well from a double-well potential. Barrierless proton transfer was observed to occur in the CRT system with several PA molecules present, implying that the CRT may be a promising PA-based PIL.

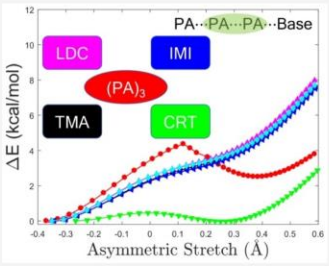

INTRODUCTION

Ionic liquids may be aprotic, zwitterionic, or protic in their chemical compositions.[1] Protic ionic liquids (PILs) are typically the combinations of Brønsted−Lowry acids and bases. Their promising properties, including high thermal and electrochemical stability, low vapor pressure, and high open circuit voltage and efficiency, have driven PILs to become favorable anhydrous electrolytes used in the fuel cells.[2,3] Thus, PILs have attracted significant attention for the investigation of their perspective properties and potential use in various applications.[2−4] Recent studies[5,6] revealed exceptionally strong decoupling of proton conductivity from viscosity in a mixture of lidocaine (LDC) with phosphoric acid (PA). Proton conductivity in this mixture even exceeds that of PA at a similar viscosity. Both LDC and PA possess proton donor and acceptor sites, which is deemed to be of central importance to build up hydrogen bond networks with an efficient proton transport mechanism. For comparison, trimethylammonium has only one proton acceptor site, and its mixture with $H_2PO_4^-$ has significantly lower conductivity than LDC with PA at the same viscosity.[6] Hence, it is necessary to develop a fundamental molecular-level understanding of the chemical and structural aspects that control proton transfer in these PILs.

The two main types of proton transport mechanisms are (1) vehicular in which a molecular entity "carries" the excess positive charge and (2) structural diffusion where protons move by being transferred through the connected hydrogen bond network with a change of the proton identity.[7−12] The high efficiency of the latter is generally viewed to be the principal reason for the high proton conductivity in neat PA and high diffusivity in slightly acidic water.[13−18] Generally, it is expected that the chemical structure and orientation of the Brønsted−Lowry acid−base pair is responsible for the formation of hydrogen bond networks that facilitates fast proton diffusivity in a PIL.[9,19] Several experimental investigations have been performed to elucidate the mechanisms of proton transport in PILs. Hoarfrost and co-workers[20] found that the proton conductivity was enhanced by the proton hopping as well as the long-range transport in the PIL imidazolium bis(trifluoromethylsulfonyl)imide through pulsed-field gradient NMR and quasi-elastic neutron scattering techniques. Kreuer *et al.*[21] compared the experimentally measured self-diffusion coefficient of proton with that obtained by using the Nernst−Einstein relation in three imidazole (IMI)-doped systems. They attributed the greatest contribu-

Received: March 31, 2020
Revised: April 20, 2020
Published: April 21, 2020



ACS Publications © 2020 American Chemical Society

https://dx.doi.org/10.1021/acs.jpca.0c02863
J. Phys. Chem. A 2020, 124, 4141−4149

tion to structural diffusion of the proton. It is impossible to have a fundamental molecular-level understanding of the chemical and structure aspects that control the proton conductivity in PILs from only experimental studies.

Quantum mechanical calculations have been successfully performed to study the mechanisms of proton transfer in many different systems.[8,10,11,22−29] For example, Scheiner and Yi[30−36] systematically investigated the effects of external ions and molecular charge and methyl substitution as well as stretches and bends of the hydrogen bond on energetics for proton transfer in a number of different systems. In the work of Clark *et al.*,[26] three pairs of ionomers (fully fluorinated sulfonyl imides, partially fluorinated sulfonyl imides, and aromatic sulfonic acid-based materials) were investigated to compare the role of the neighboring group substitutions on the proton dissociation of hydrated acidic moieties. Wang and Paddison[37] examined the hydrogen bonding and energetics related to proton transport of substituted phosphonic acid molecules and their self-condensation products and found that the fluorinated molecules show stronger binding to water than the non-fluorinated molecules. Recently, Sepehr and Paddison[22,23] investigated the effects of sulfuric and triflic acids on the hydration of vanadium species within a highly acidic environment and studied the primary hydration and proton transfer of 10 acid molecules including CF_3SO_3H, FSO_3H, CH_3SO_3H, H_2SO_4, and so forth. Kumar and Venkatnathan studied the mechanism of proton transport in several systems including ionic liquid-doped perfluorosulfonic acid membranes,[38] imidazolium methanesulfonate ionic liquid,[39] and IMI chains.[40] Additionally, *ab initio* molecular dynamics (AIMD) simulations have been extensively applied into various systems[9,10,14−16,41] and provided insightful interpretation of the proton-transfer mechanisms.

The present work focuses on the influence of the chemical composition and molecular geometry of several bases on proton dissociation and transfer in the PA-based PILs. These results will form the basis for simulations of extended systems using AIMD. Specially, in the reported studies here, quantum chemical calculations were performed on systems of PA paired with trimethylamine (TMA), IMI, LDC, and creatinine (CRT). The computational details are briefly described in the following section followed by the results and discussion. Finally, the major findings are concluded in the last section.

■ COMPUTATIONAL DETAILS

We carried out all electronic structure calculations with the GAUSSIAN 09 suite of programs.[42] The molecular geometry optimizations of bases and acids were initially performed with Hartree−Fock theory and the 6-31G** split valence basis set[43,44] with conjugate gradient methods[45] without symmetry constraints. Hybrid density functional theory with Beck's 3 parameter functional (B3LYP)[46−49] using the same basis set was employed to further optimize electronic structures, followed by the final refinement of structures at the B3LYP/6-311G** level.[50] This procedure was found to be the most efficient approach for obtaining the fully optimized global minimum-energy structure. The effect of the dispersion interactions has been tested in previous work[25] by comparing the results of the B3LYP functional to the dispersion-corrected B97D functional,[51] and only minor differences in the optimized structures and energetics for proton transfer were observed. Subsequently, the density-based solvation model (SMD)[52] was implemented to all the optimized structures considering the effect of the environment of PA (at a high dielectric constant, $\varepsilon = 61$)[53] on the global minimum-energy structures and proton transfer. It is worth emphasizing that there is a minimal effect of the numerical value of the dielectric constant on the energetics for the proton transfer (see Figure S1). The choice of B3LYP/6-311G** with the SMD model is due to its success and reliability when applying into many systems previously.[22,23,54,55] The calculation of frequency at the same level of theory were undertaken to confirm local minima without imaginary frequency and zero-point energies (ZPEs) for each of the systems. Proton affinities of bases and molecular binding energies of PA molecules to different bases were calculated from the ZPE-corrected total electronic energies.

In the present study, from 1 to 3 PA molecules were added to the fully optimized structures of each base starting from different initial positions. We selected the lowest energy structure for each system as the "ground state" structure. The potential energy surface (PES) scan at the B3LYP/6-311G**/SMD level of theory was employed on the optimized structures of pairs and clusters of the PA molecules with the bases to determine the relative energetics (*i.e.*, energetic barrier) associated with proton transfer from a proton donor to an acceptor site. The profiles of the energy associated with the proton transfer were obtained by incrementally changing the length of the OH or NH between the transferring proton and the oxygen or nitrogen accepting the proton with steps of 0.02 Å where this bond length is the only fixed parameter and the optimization was carried out over all other degrees of freedom without symmetry constraints at each step of the scan. A reverse set of scans was also implemented by decreasing the bond length of the OH or NH in the same step starting from the geometry obtained at the last step of the original scan. The energetic profiles were plotted *via* selecting the configuration with the lower energy at the same OH or NH bond length from the forward and the reverse scans. A transition state (TS) structure was further optimized *via* the Berny algorithm[56] and confirmed by the determination of one imaginary frequency.

■ RESULTS AND DISCUSSION

Optimized Structures of Base + *n*PA (*n* = 1−3). The fully optimized configurations of one PA molecule paired with (a) TMA; (b) IMI; (c) LDC; and (d) CRT were obtained, and the minimum energy structures at the B3LYP/6-311G** level with inclusion of the implicit solvation effect are illustrated in Figure 1. The hydrogen bond lengths between the molecules (*i.e.*, the O···O or O···N separation) are denoted by double arrow lines along with the corresponding lengths in Å because this is an important feature of proton transfer in PILs. The proton affinity is an important parameter indicating the entity's capability of intrinsically attracting a proton.[57] Computed affinities in the gas phase and with the continuum solvation model are reported in Table 1. The results demonstrate that the inclusion of an implicit solvent noticeably raises the proton affinity of the four investigated bases to various extents as the positively charged base molecules are stabilized by the high dielectric constant solvent. Comparison with the experimental values of TMA and IMI in the gas phase shows that our computed affinities are in good agreement at the B3LYP/6-311G** level of theory. The order of the proton affinities calculated with the SMD model is as follows: LDC > TMA > CRT > IMI. Generally, the proton dissociation from PA occurs in four systems, resulting in the formation of ion

https://dx.doi.org/10.1021/acs.jpca.0c02863
J. Phys. Chem. A 2020, 124, 4141−4149

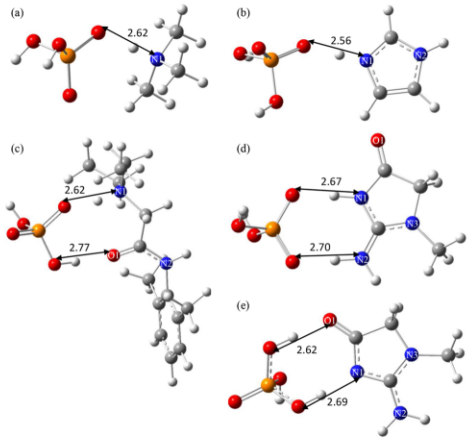

Figure 1. Fully optimized configurations of one PA molecule with (a) TMA, (b) IMI, (c) LDC, (d) CRT, and (e) CRT* (congener of CRT cluster) at the B3LYP/6-311G**/SMD level of theory. All values are reported in Å. The atomic color schemes in Figures 1 and 2 are hydrogen (white), carbon (gray), nitrogen (blue), oxygen (red), and phosphor (orange). Although there is one more hydrogen bond between O1 and PA in system LDC + 1PA, the distances between O···N1 in both TMA + 1PA system and LDC + 1PA system are the same. In the CRT + 1PA system, there are two hydrogen bonds, while the N2···PA hydrogen bond is formed between the acceptor site of the PA molecule and the donor site of the CRT compared to the O1···PA hydrogen bond built between the donor site of PA and the acceptor site of the LDC. CRT* + 1PA is less energetic favorable than the structure of CRT + 1PA by 1.1 kcal/mol.

Table 1. Proton Affinities for the Bases

	proton affinities/kcal mol^{-1}		
	gas phase[a]	SMD[b]	Exp.
TMA	226.12	289.36	231.44[c]
IMI	227.46	283.97	229.95[c]
LDC (N1 site)	240.85	290.15	
LDC (O1 site)	222.45	264.11	
CRT (N1 site)	234.47	286.04	
CRT (O1 site)	230.63	273.09	

[a]ZPE-corrected proton affinities at the B3LYP/6-311G** level of theory in the gas phase. [b]ZPE-corrected proton affinities at the B3LYP/6-311G** level of theory with the SMD model. [c]From ref S7.

pairs consisting of the positively charged base and negatively charged anion $H_2PO_4^-$ due to the relatively strong basicity of the bases and the effect of the high dielectric constant solvent on stabilizing the charge separation. In Figure 1a, there is only one hydrogen bond of 2.62 Å in the open structure of TMA + 1PA as the TMA molecule possesses only one proton accepting site. Although IMI has both proton donor and acceptor sites, only one hydrogen bond of 2.56 Å exists in the system of IMI + 1PA shown in Figure 1b because of the coplanar heterocycle of the IMI molecule. In Figure 1c,d, the equilibrium structures show that the PA molecule adopts a similar orientation paired with LDC and CRT leading to a "ring-like" hydrogen bonding network, though these two bases have different geometries. The critical differences in their configurations are that the PA molecule in the CRT + 1PA cluster acts as both a hydrogen bond donor and acceptor with two hydrogen bonds of intermediate length (2.67 and 2.70 Å) while the PA molecule in the LDC + 1PA system plays the role of an hydrogen bond donor forming a short hydrogen bond of 2.62 Å and a weak hydrogen bond of 2.77 Å, demonstrating the characteristics of PA molecules: three proton donor sites and one proton acceptor site contributing to the configurational frustration in pure PA.[15] It is worth noting that there is a congener of CRT* + 1PA (distinguished by *) shown in Figure 1e. In this case, two hydrogen bonds were formed with O1 and N1 of the CRT molecule instead of N1 and N2 atoms in the CRT + 1PA pair, showing similar hydrogen bond networks with the LDC + 1PA system, except that the proton is still associated with PA in CRT* + 1PA due to the interaction between O1 and N1 of the CRT molecule. This geometric isomer is less favorable in energy by 1.1 kcal/mol.

The fully optimized structures of TMA, IMI, LDC, CRT, and CRT* with the addition of two PA molecules are shown in Figure S2. There is little difference in the hydrogen bonding networks between the bases and PA molecules except for the observed increase in hydrogen bond length. It was noted that the second PA molecule preferentially forms "ring-like" hydrogen bonds ranging from 2.50 to 2.73 Å with the first PA molecule rather than with available hydrogen bond donor and acceptor sites of the base (based on the minimum energy structure at the B3LYP/6-311G**/SMD level of theory), as were the cases for the complexes of bases with subsequently adding the third PA molecule (see Figure 2); the hydrogen bond lengths continuously increase to some extent, resulting in slight shortening of the covalent bond between the dissociated

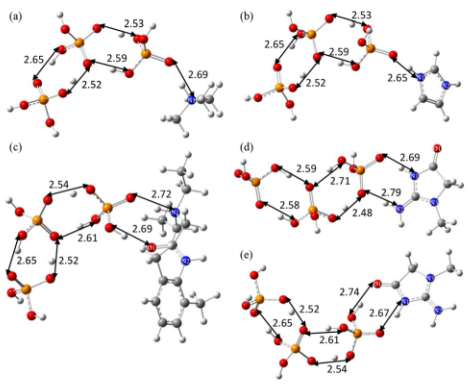

Figure 2. Fully optimized configurations of cluster of three PA molecules with (a) TMA, (b) IMI, (c) LDC, (d) CRT, and (e) CRT* (congener of CRT cluster) at the B3LYP/6-311G**/SMD level of theory. All values are reported in Å. The second and third PA molecules energetic preferentially form "ring-like" hydrogen bonds ranging from 2.48 to 2.73 Å with the PA molecule rather than with available hydrogen bond donor and acceptor sites of the base. Compared with systems of base + 1PA, the hydrogen bond distances between N1 and PA in all systems increase to various extents (the most for IMI and LDC systems), while the structures of the clusters of PA molecules formed through hydrogen bonding are similar. CRT* + 3PA is more energetic favorable than the structure of CRT + 3PA by 1.1 kcal/mol.

https://dx.doi.org/10.1021/acs.jpca.0c02863
J. Phys. Chem. A 2020, 124, 4141−4149

Table 2. Structural Parameters[a] of PA-Based PILs at the Level of B3LYP/6-311G**/SMD

	r(N1···O)	r(N2/O1···O)	r(O···O)(1st and 2nd PA)		r(O···O)(2nd and 3rd PA)	
TMA−1PA	2.62 (1.07)[b]					
IMI−1PA	2.56 (1.09)					
LDC−1PA	2.62 (1.08)	2.77 (0.98)				
CRT−1PA	2.67 (1.06)	2.70 (1.05)				
CRT*−1PA	2.69 (1.01)	2.62 (1.01)				
TMA−2PA	2.68 (1.05)		2.51 (1.04)	2.53 (1.03)		
IMI−2PA	2.63 (1.06)		2.54 (1.02)	2.73 (0.99)		
LDC−2PA	2.71 (1.06)	2.69 (0.98)	2.54 (1.02)	2.55 (1.02)		
CRT−2PA	2.68 (1.05)	2.78 (1.04)	2.50 (1.04)	2.66 (0.99)		
CRT*−2PA	2.66 (1.06)	2.75 (0.98)	2.54 (1.03)	2.55 (1.02)		
TMA−3PA	2.69 (1.05)		2.53 (1.02)	2.59 (1.01)	2.52 (1.03)	2.65 (0.99)
IMI−3PA	2.65 (1.05)		2.53 (1.02)	2.59 (1.01)	2.52 (1.03)	2.65 (0.99)
LDC−3PA	2.72 (1.05)	2.69 (0.98)	2.54 (1.02)	2.61 (1.01)	2.52 (1.03)	2.65 (0.99)
CRT−3PA	2.69 (1.05)	2.79 (1.03)	2.48 (1.05)	2.63 (0.99)	2.58 (1.01)	2.59 (1.01)
CRT*−3PA	2.67 (1.05)	2.74 (0.99)	2.54 (1.02)	2.61 (1.01)	2.52 (1.03)	2.65 (0.99)

[a]All reported values are in the unit of Å. [b]Values in parenthesis are the distances of covalent bond N−H or O−H.

H atom and protonated N1 atom of the bases from various distances to the same final value of 1.05 Å (see Table 2). It is interesting to note that the distances of the hydrogen bonds formed between the second and third PA molecules are the same (2.65 and 2.52 Å) for all of the base + 3PA systems (shown in Figure 2a−c,e) except for the CRT + 3PA complex in Figure 2d with two comparable hydrogen bonds (2.58 and 2.59 Å), which implies that the hydrogen bonding networks between the second and third PA molecules are influenced by the base molecules even separated by another PA molecule. In most of the studied systems, the charged ions were separated by a neutral PA molecule forming the complex: base−H^+···PA···PA^-···PA, in which the excess charge is delocalized over the PA molecules through the hydrogen bonding network. Specifically, the contact ion pairs were only observed in the system of CRT + 3PA (see Figure 2d) in the form of CRT−H^+···PA^-···PA···PA because the original proton accepting oxygen of a PA in the proximity of $CRTH^+$ not only forms a hydrogen bond with the N2 atom of the CRT molecule but also with the neighboring PA molecule.

Examination of the ZPE-corrected binding energies of the PA molecules to the various bases (shown in Table 3) indicates that the first PA molecule is most loosely bound to IMI in comparison with the other systems, while the binding energy per PA molecule increases with the addition of more PA molecules because the second and third PA molecules form double hydrogen bonds with the first PA. Although only one hydrogen bond is formed in the TMA + 1PA complex, a much larger ZPE-corrected binding energy of 18.26 kcal/mol is observed, meaning that the basicity of TMA is stronger than IMI, which is confirmed by the greater proton affinity of TMA (see Table 1). It is also noted that the ZP-corrected binding energies of PA to LDC increase followed by the slight decrease with adding PA molecules, which implies that the PA molecule is more strongly bound to another PA molecule than to LDC. Similar magnitude in the binding energy per PA is observed in both systems of CRT + nPA and CRT* + nPA (n = 1−3), revealing that there is a small difference in binding energies between the PA molecules and PA and CRT. It is important to recognize that the shorter the hydrogen bond, the stronger the binding energy when there is no accompanying covalent bond breaking and formation. However, the equilibrium structures show that the proton initially covalently bonded to PA has been transferred to the base molecule except in the complex of CRT* + 1PA. Specifically, the smallest binding energy of the first PA molecule paired with IMI through the shortest hydrogen bond O···N1 results from the partial covalent bond between the proton and N1 of the IMI molecule; that is, the proton in closest proximity to IMI is shared by the proton donor oxygen and the proton acceptor nitrogen.

Table 3. Energetics of PA-Based PILs at the Level of B3LYP/6-311G**/SMD

	E_{elec} + ZPE[a]	ΔE_{ZPE}[b] /kcal mol^{-1}	ΔE^c /kcal mol^{-1}
PA	−644.239902		
TMA	−174.413899		
LDC	−731.370596		
IMI	−226.229286		
CRT	−396.153573		
TMA−1PA	−818.682904	−18.26	−18.26
IMI−1PA	−870.491277	−13.86	−13.86
LDC−1PA	−1375.639985	−18.50	−18.50
CRT−1PA	−1040.427675	−21.46	−21.46
CRT*−1PA	−1040.425845	−20.31	−20.31
TMA−2PA	−1462.960320	−41.80	−20.90
IMI−2PA	−1514.765266	−35.26	−17.63
LDC−2PA	−2019.919933	−43.64	−21.82
CRT−2PA	−1684.699093	−41.24	−20.62
CRT*−2PA	−1684.699342	−41.39	−20.69
TMA−3PA	−2107.229423	−60.12	−20.04
IMI−3PA	−2159.036694	−55.02	−18.34
LDC−3PA	−2664.189472	−62.22	−20.74
CRT−3PA	−2328.966906	−58.74	−19.58
CRT*−3PA	−2328.968909	−60.01	−20.00

[a]Total electronic energy corrected for ZPE in Hartrees. [b]Energy difference based on ZPE-corrected electronic energies (*i.e.* ΔE_b = $E[\mathbf{base}(\mathbf{H_3PO_4})_n] - n \times E[\mathbf{H_3PO_4}] - E[\mathbf{base}]$). [c]Binding energy per PA molecule.

Energetics of Proton Transfer. The PES scans for proton transfer were performed with respect to the fully optimized structures. The relative energy profiles shown in Figures 3−5 are plotted as a function of the asymmetric stretch coordinate, $q_{asym} = 1/2(r_{D\cdots H} - r_{H\cdots A})$, where D indicates the nitrogen or oxygen atom initially covalently bonded to the proton and A represents the nitrogen or oxygen atom acting as the proton

https://dx.doi.org/10.1021/acs.jpca.0c02863
J. Phys. Chem. A 2020, 124, 4141−4149

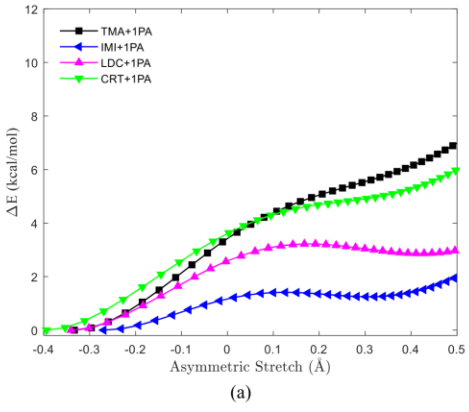

Figure 3. Energetics for proton transfer from protonated base to PA in systems of cluster of (a) one PA molecules with TMA, IMI, LDC, and CRT and (b) three PA molecules with TMA, IMI, LDC, and CRT at the B3LYP/6-311G**/SMD level of theory. The energetics for transfer of a proton from protonated TMA or CRT to PA is monotonically increasing in both base + 1PA and base + 3PA systems, demonstrating that the ionic pairs are energetically preferable and stable in these systems. Although there is a relatively tiny second well in IMI + 1PA and LDC + 1PA systems, the second well would disappear as the number of PA molecules in the cluster increases.

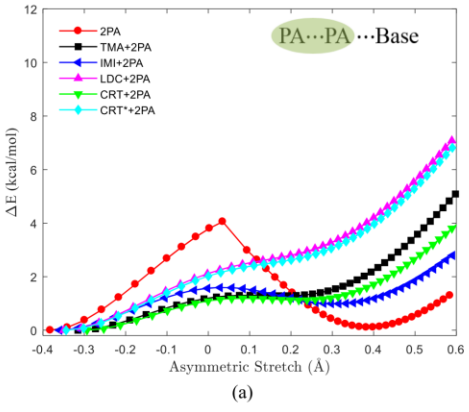

Figure 4. Energetics for proton transfer between the PA molecules in systems of (a) cluster of two PA molecules with TMA, IMI, LDC, CRT, and CRT* and (b) cluster of two PA subunits flanked by two base molecules at the B3LYP/6-311G**/SMD level of theory. Note that the bases with stronger proton affinity exert greater influence on the energetics for proton transfer between individual PA molecules. However, the effects are minimal when the potentials are shifted into the single-well from the double-well. The double-well potential recovers with deformations in various manners when one additional base molecule is added to the other side of these complexes forming (base···PA···PA···base) clusters.

acceptor. As indicated previously, the PA molecule has dissociated one proton to the base in all systems excepting the CRT* + 1PA complex. Thus, it is necessary to investigate the proton transfer from the base to PA molecule. The relative energy profiles for proton transfer from the protonated N1 atom of the base to the PA molecule through the hydrogen bond between them in systems of base + 1PA and base + 3PA were determined at the B3LYP/6-311G** level of theory with the inclusion of the implicit SMD continuum solvation model, as shown in Figure 3. All curves demonstrate that the bridging proton between the PA and the base has a marked propensity of remaining associated with the base. In both systems of TMA + 1PA and CRT + 1PA shown in Figure 3a, the relative energy profiles reveal a monotonically increasing trend, indicating that there is only one minimum energy structure, that is the contact ion pair, base−H^+···PA^-, which attributes its stability to the effect of the implicit continuum solvation and the strong basicity of the base. There is a very shallow minimum in the clusters of LDC + 1PA and IMI + 1PA. This is because in the LDC + 1PA complex another hydrogen bond between the proton donor oxygen of the PA molecule and O1 atom of LDC stabilizes the charge distribution accompanying the proton transfer event, which can be confirmed by the contraction of the hydrogen bond O···O1 (from 2.77 to 2.61 Å) and the slight elongation of the O−H bond length (from 0.98 to 1.00

https://dx.doi.org/10.1021/acs.jpca.0c02863
J. Phys. Chem. A 2020, 124, 4141−4149

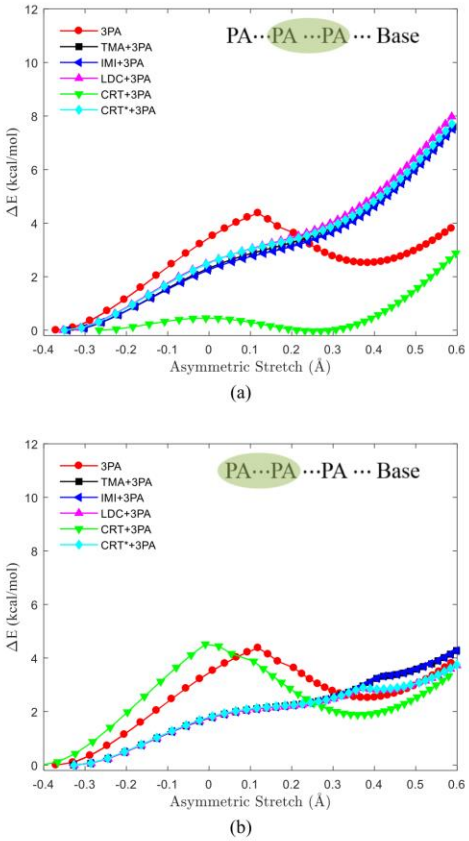

Figure 5. Energetics for proton transfer between (a) first and second PA and (b) second and third PA in systems of cluster consisting of three PA molecules with TMA, IMI, LDC, CRT, and CRT* at the B3LYP/6-311G**/SMD level of theory. Note that the neighboring cation base−H^+ results in either a negligible energetic barrier or a single minimum between the first and second PA molecules. The energetics for proton transfer in systems of base + 3PA (base = TMA, IMI, CRT*, and LDC) have similar trends in which the energies are monotonically increasing without the formation of a TS. Barrierless proton transfer occurs in the system of CRT with several PA molecules.

Å). It is important to note that the second hydrogen bond in the CRT + 1PA pair strengthens the dissociation of the PA molecule because the N2 atom donates a hydrogen bond to PA, which causes higher endothermicity for proton transport in CRT + 1PA than LDC + 1PA. However, in the IMI + 1PA system, the lowest endothermicity for transferring of the proton results from the weakening covalent bond between the proton and the N1 atom of IMI. On the other hand, these small wells may disappear when the ZPE-corrected energies are included as the ground vibrational energy is probably higher than this tiny barrier.

Figure 3b illustrates the higher energetics for proton transfer from protonated base to the PA molecule upon the addition of three PA molecules to various bases in comparison to those shown in Figure 3a. This means that the extra PA molecules act to retain the proton on the bases. This observation is consistent with the AIMD results that there is no proton back-transfer from IMI−H^+ to PA or PA^- occurring in the PA/IMI (2:1) system.[41] It is interesting to note that the low energetics with a second well for proton transfer is observed in the congener of CRT* + 3PA because there is proton transfer simultaneously occurring from the first PA to the second PA (see Figure S3) and the reorientation of the hydrogen bonding, while this phenomenon is not shown in the cluster of LDC + 3PA that possesses the analogous hydrogen bond network to the CRT* + 3PA system. These differences may be caused in part by two different situations in proton affinity for LDC and CRT: one site of LDC with strong proton affinity and another site with considerably weak proton affinity (*i.e.*, 290.15 kcal/mol *vs* 264.11 kcal/mol); both sites of the CRT molecule have medium proton affinities (*i.e.* 286.04 kcal/mol *vs* 273.09 kcal/mol), as reported in Table 1. Another crucial factor is the huge difference in the geometries of LDC and CRT. It may be concluded that the ionicity of these PILs is reasonably high based on these calculations.

Of particular interest is the influence of the protonated bases (*i.e.* base−H^+) on the energetics for proton transfer from one PA molecule to another. The relative proton-transfer energy profiles for both clusters of $(H_3PO_4)_2$ and $(H_3PO_4)_3$ are illustrated with a red line as a reference for comparison in Figures 4 and 5. Compared with the energetics for proton transfer within PA clusters in the gas phase,[17] the trends are similar to each other, but the energetic barrier is almost equivalent for the $(H_3PO_4)_2$ cluster while much lower in the solvation SMD model than in the gas phase for the cluster of $(H_3PO_4)_3$. It should be pointed out that the proton transfer exactly occurs in the cluster of $(H_3PO_4{\cdot}H_2PO_4)^-$ or $(H_3PO_4{\cdot}H_3PO_4{\cdot}H_2PO_4)^-$ in the proximity of a positively charged base molecule instead of the pure PA clusters. To some extent, the cationic base−H^+ may be treated as a substituent hydrogen bonded to the PA molecules, but it is more complex because the bases have different proton affinities and possess various proton acceptor and/or donor sites.

The energetics for transferring a proton between two PA molecules in the systems with two added PA molecules are shown in Figure 4a. The curves indicate that the symmetric double-well potential for proton transfer are distorted to various extents, leading to a considerable weakening of the barriers with small secondary wells in the systems of base + 2PA (base = IMI, CRT, and TMA) and the single minimum potential in the complexes of base + 2PA (base = LDC and CRT*). These changes may be ascribed to the different proton affinities of these bases: IMI < CRT < TMA < LDC (reported in Table 1). Although the proton affinity of a single site of CRT is somewhat smaller than TMA, the cooperative effects of the two proton acceptor sites rather than one acceptor and one donor strengthen the ability of attracting a proton. Interestingly, when the single-well potential appears, the differences are not discernible in comparison to the curves of LDC + 2PA and CRT* + 2PA, which will be further borne out by examining the energetic profiles for proton transfer between PA molecules in the systems of base + 3PA (see below).

To aid in understanding the effects of the base molecules, one additional base molecule was added to the "other side" of

https://dx.doi.org/10.1021/acs.jpca.0c02863
J. Phys. Chem. A 2020, 124, 4141−4149

these complexes forming (base···PA···PA···base) clusters (base = TMA, IMI, CRT, and CRT*) including (CRT···PA···PA···CRT*). Note that the LDC was not included due to the enormous computational cost. It is not surprising to observe that the double-well potential recovers with deformations in various degrees. First, the curves of the proton-transfer energetics coincide with the reference in the systems of (base···PA···PA···base) (base = TMA and CRT*), which implies that the influence of the initial base molecule is exactly counterbalanced by the additional identical base. It should be noted that the energetic barrier is dramatically higher in the CRT···PA···PA···CRT system. This may be because the electron density of proton-accepting oxygen atoms of PA molecules is shared by the proton-donating N2 atoms, leading to the attenuation of attracting the proton. In addition, the symmetry was distorted upon adding the CRT to CRT* + 2PA complex, consequently giving rise to a slight decrease in the energetic barrier to proton transfer with a less energetically favorable configuration after transferring the proton. The relatively small penalty for proton transfer occurs in the system (IMI···PA···PA···IMI) due to the feasible movement of the bridging proton between the base and the PA molecule to stabilize the system during the proton transfer. The adjustment of the bridging proton is due to the moderate proton affinity of IMI.

Figure 5 displays the energetics for transferring a proton between the first and second PA molecules as well as between the second and third PA molecules in the complexes of a base paired with three PA molecules. It is worthy of noting that the neighboring cation base−H^+ results in either a negligible energetic barrier or a single minimum for the proton-transfer energetics between the first and second PA molecules, as shown in Figure 5a. More specifically, the monotonically increasing curves are nearly coincident with each other in the base + 3PA complexes (base = TMA, IMI, LDC, and CRT*). The similarity in these systems is that the base is hydrogen bonded to a PA *via* only one proton accepting site or two proton accepting sites. It may be concluded that the involvement of only proton accepting sites of the base molecule could lead to the analogous energetic situation on the proton transfer between the central PA subunits flanked by a cation and a neutral PA molecule. The endothermicity for proton transfer is roughly 4 kcal/mol, a similar value to the barrier to transfer a proton in the cluster of $(H_3PO_4)_3$, if the asymmetric stretch coordinate where the second well resides in the pure cluster of $(H_3PO_4)_3$ are treated as the final (or end) position in the transfer. Nevertheless, the occurrence of a negligible barrier to proton transfer in the system of CRT + 3PA does not mean that the small barrier would appear as long as there is a proton-donating site of the base molecule involved in the neighboring hydrogen bonding networks. In terms of dynamics, the proton transfer in PA clusters could facilely happen when protonated base molecule approaches this cluster and forms such a hydrogen bonding network at the cost of 2 kcal/mol (the difference in energy between the second minimum and endothermicity). Again, the monotonically increasing curves (*i.e.*, in the cases with a single-well potential) of the proton-transfer energetics between the second and third PA molecules in Figure 5b that nearly coincide indicate that the effects of the protonated bases are quite insensitive to the specific molecular geometries and the proton affinities except for the case in which the proton-donating site of the base molecule is involved. This pattern is further underscored by comparing the results of the CRT + 3PA and CRT* + 3PA systems in which the differences are the hydrogen bonds formed through different pairs of proton donor and acceptor sites. It is surprising to observe that the endothermicities decrease in comparison to the energetics for proton transfer between PA molecules in the vicinity of the cationic ions (shown in Figure 5a). The flattening of these curves may be the result of the better stabilization of charge by the neighboring PA molecule when in proximity to the bases. However, the curve of the proton-transfer energetics in the CRT + 3PA complex resembles that in a pure (or neat) PA cluster but shifts to the left with a lower well. The formation of a contact ion pair in CRT + 3PA may be responsible for the weakening influence of the base molecule on the energetics for proton transfer between the second and third PA molecules.

Assuming that the computed energetics in these small clusters reflect the behavior in the bulk systems and that the entropic effects would not qualitatively change the observed trends, we can speculate about the behavior of the proton transport in mixtures of PA with the bases. According to the analysis in the present study, the proton transferred from a PA molecule to any of the bases examined here remains with the base (*i.e.*, protonating the base) and might not contribute significantly to the proton conductivity of the bulk system. At the same time, the presence of a protonated base and the existence of the deprotonated PA molecules polarize the network of the hydrogen-bonded PA molecules. As a result, the energy barrier for proton transfer between the neighboring PA molecules is decreased. Thus, changes of the proton conductivity in PA with specific bases might be caused by the changes in the energy barrier for the proton transfer between the PA molecules, rather than due to the proton transfer between the base and PA molecules. AIMD simulations on larger and extended systems should provide verification of this proposed idea.

■ CONCLUSIONS

Ab initio molecular orbital calculations were performed to determine the fully optimized structures of TMA, IMI, LDC, and CRT with the addition of 1−3 PA molecules at the B3LYP/6-311G** level with the inclusion of implicit solvation effects ($\varepsilon = 61$). It was found that the proton dissociation from the PA molecule occurs in all systems, resulting in the formation of ion pairs of the protonated base and negatively charged anion $H_2PO_4^-$ due to the relatively strong basicity of the bases and the effect of the high dielectric constant solvent on stabilizing the charge separation. The second and third PA molecules preferentially form "ring-like" hydrogen bonds ranging from 2.48 to 2.73 Å with a PA molecule rather than with available hydrogen bond donor and acceptor sites of the base. Examination of the ZPE-corrected binding energies of the PA molecules to various bases indicates that the first PA molecule is the most loosely bound to the IMI molecule in comparison with other systems. The binding energy per PA molecule increases with the addition of more PA molecules because the second and third PA molecules form double hydrogen bonds with a PA molecule. The strongest binding energy was observed in the CRT systems.

PES scans were carried out with respect to the optimized configurations to investigate the effects of the bases on the energetics for proton transfer between the PA molecules. It was found that the bases with stronger proton affinities exert greater influence on the energetics for proton transfer between

https://dx.doi.org/10.1021/acs.jpca.0c02863
J. Phys. Chem. A 2020, 124, 4141−4149

the PA molecules. However, the effects are minimal when the potentials are shifted into the single-well from the double-well. There is energetic barrierless proton transfer occurring in the system of CRT + 3PA, implying that the CRT may be a better potential candidate in the PA-based PILs. Although these static electronic structure calculations provide some guidelines in understanding proton transfer in PILs, it is crucial to consider additional factors including quantum nuclear effects, dynamic bond length fluctuations, and effects of the extended hydrogen bond network. Hence, AIMD simulations will be carried out on these systems in our future work.

■ ASSOCIATED CONTENT

Supporting Information

The Supporting Information is available free of charge at https://pubs.acs.org/doi/10.1021/acs.jpca.0c02863.

> Energetics for proton transfer between first and second PA molecules in the system of CRT + 3PA with various dielectric constants at the B3LYP/6-311G**/SMD level of theory; fully optimized configurations of cluster of two PA molecules with TMA, IMI, LDC, CRT, and CRT*; and configurations of cluster CRT* + 3PA shown correspond to the structure of the maximum and the structure of the second minimum during the proton transfer from N1 of CRT* to PA (PDF)

■ AUTHOR INFORMATION

Corresponding Author

Stephen J. Paddison − *Department of Chemical and Biomolecular Engineering, University of Tennessee, Knoxville, Tennessee 37996, United States;* orcid.org/0000-0003-1064-8233; Email: spaddison@utk.edu; Fax: +1 865 974 2026

Authors

Zhenghao Zhu − *Department of Chemical and Biomolecular Engineering, University of Tennessee, Knoxville, Tennessee 37996, United States*

Xubo Luo − *Department of Chemical and Biomolecular Engineering, University of Tennessee, Knoxville, Tennessee 37996, United States;* orcid.org/0000-0002-1591-7466

Alexei P. Sokolov − *Department of Chemistry, University of Tennessee, Knoxville, Tennessee 37996; Chemical Sciences Division, Oak Ridge National Laboratory, Oak Ridge, Tennessee 37831, United States;* orcid.org/0000-0002-8187-9445

Complete contact information is available at: https://pubs.acs.org/10.1021/acs.jpca.0c02863

Notes

The authors declare no competing financial interest.

■ ACKNOWLEDGMENTS

This work was supported by the National Science Foundation under CHE 1764409: "Mechanisms of Proton Transport in Ionic Liquids: Grotthuss *versus* Vehicular". Computing resource was provided through an XSEDE allocation award: DMR130078.

■ REFERENCES

(1) Greaves, T. L.; Drummond, C. J. Protic Ionic Liquids: Evolving Structure-Property Relationships and Expanding Applications. *Chem. Rev.* **2015**, *115*, 11379−11448.

(2) Wojnarowska, Z.; Grzybowska, K.; Hawelek, L.; Swiety-Pospiech, A.; Masiewicz, E.; Paluch, M.; Sawicki, W.; Chmielewska, A.; Bujak, P.; Markowski, J. Molecular Dynamics Studies on the Water Mixtures of Pharmaceutically Important Ionic Liquid Lidocaine HCl. *Mol. Pharm.* **2012**, *9*, 1250−1261.

(3) Austen Angell, C.; Ansari, Y.; Zhao, Z. Ionic Liquids: Past, Present and Future. *Faraday Discuss.* **2012**, *154*, 9−27.

(4) Adrjanowicz, K.; Kaminski, K.; Paluch, M.; Wlodarczyk, P.; Grzybowska, K.; Wojnarowska, Z.; Hawelek, L.; Sawicki, W.; Lepek, P.; Lunio, R. Dielectric Relaxation Studies and Dissolution Behavior of Amorphous Verapamil Hydrochloride. *J. Pharm. Sci.* **2010**, *99*, 828−839.

(5) Wojnarowska, Z.; Paluch, K. J.; Shoifet, E.; Schick, C.; Tajber, L.; Knapik, J.; Wlodarczyk, P.; Grzybowska, K.; Hensel-Bielowka, S.; Verevkin, S. P.; et al. Molecular Origin of Enhanced Proton Conductivity in Anhydrous Ionic Systems. *J. Am. Chem. Soc.* **2015**, *137*, 1157−1164.

(6) Wojnarowska, Z.; Wang, Y.; Paluch, K. J.; Sokolov, A. P.; Paluch, M. Observation of Highly Decoupled Conductivity in Protic Ionic Conductors. *Phys. Chem. Chem. Phys.* **2014**, *16*, 9123−9127.

(7) Mogurampelly, S.; Keith, J. R.; Ganesan, V. Mechanisms Underlying Ion Transport in Polymerized Ionic Liquids. *J. Am. Chem. Soc.* **2017**, *139*, 9511−9514.

(8) Wang, C.; Clark, J. K., II; Kumar, M.; Paddison, S. J. An ab initio Study of the Primary Hydration and Proton Transfer of CF3SO3H and CF3O(CF2)2SO3H: Effects of the Hybrid Functional and Inclusion of Diffuse Functions. *Solid State Ionics* **2011**, *199-200*, 6−13.

(9) Tuckerman, M. E.; Chandra, A.; Marx, D. A Statistical Mechanical Theory of Proton Transport Kinetics in Hydrogen-Bonded Networks Based on Population Correlation Functions with Applications to Acids and Bases. *J. Chem. Phys.* **2010**, *133*, 124108.

(10) Hayes, R. L.; Paddison, S. J.; Tuckerman, M. E. Proton Transport in Triflic Acid Hydrates Studied via Path Integral Car−Parrinello Molecular Dynamics. *J. Phys. Chem. B* **2009**, *113*, 16574−16589.

(11) Elliott, J. A.; Paddison, S. J. Modelling of Morphology and Proton Transport in PFSA Membranes. *Phys. Chem. Chem. Phys.* **2007**, *9*, 2602−2618.

(12) Greenwood, N. N.; Thompson, A. Proton-Switch as a Mechanism for Conduction in Anhydrous Phosphoric Acid. *Proc. Chem. Soc., London* **1958**, 352−353.

(13) Suwannakham, P.; Chaiwongwattana, S.; Sagarik, K. Proton Dissociation and Transfer in Hydrated Phosphoric Acid Clusters. *Int. J. Quantum Chem.* **2015**, *115*, 486−501.

(14) Clark, J. K., II; Paddison, S. J. Ab initio Molecular Dynamics Simulations of Water and an Excess Proton in Water Confined in Carbon nanotubes. *Phys. Chem. Chem. Phys.* **2014**, *16*, 17756.

(15) Vilčiauskas, L.; Tuckerman, M. E.; Bester, G.; Paddison, S. J.; Kreuer, K. D. The Mechanism of Proton Conduction in Phosphoric Acid. *Nat. Chem.* **2012**, *4*, 461−466.

(16) Habenicht, B. F.; Paddison, S. J. Ab initio Simulations of the Effects of Nanoscale Confinement on Proton Transfer in Hydrophobic Environments. *J. Phys. Chem. B* **2011**, *115*, 10826−10835.

(17) Vilciauskas, L.; Paddison, S. J.; Kreuer, K.-D. Ab Initio Modeling of Proton Transfer in Phosphoric Acid Clusters. *J. Phys. Chem. A* **2009**, *113*, 9193−9201.

(18) Li, S.; Qian, W.; Tao, F.-M. Ionic Dissociation of Methanesulfonic Acid in Small Water Clusters. *Chem. Phys. Lett.* **2007**, *438*, 190−195.

(19) Vuilleumier, R.; Borgis, D. Proton Conduction: Hopping Along Hydrogen Bonds. *Nat. Chem.* **2012**, *4*, 432−433.

(20) Hoarfrost, M. L.; Tyagi, M.; Segalman, R. A.; Reimer, J. A. Proton Hopping and Long-Range Transport in the Protic Ionic Liquid [Im][TFSI], Probed by Pulsed-Field Gradient NMR and

Quasi-Elastic Neutron Scattering. *J. Phys. Chem. B* **2012**, *116*, 8201−8209.
(21) Kreuer, K. D.; Fuchs, A.; Ise, M.; Spaeth, M.; Maier, J. Imidazole and Pyrazole-based Proton Conducting Polymers and Liquids. *Electrochim. Acta* **1998**, *43*, 1281−1288.
(22) Sepehr, F.; Paddison, S. J. Primary Hydration and Proton Transfer of Electrolyte Acids: An ab initio Study. *Solid State Ionics* **2017**, *306*, 2−12.
(23) Sepehr, F.; Paddison, S. J. Effect of Sulfuric and Triflic Acids on the Hydration of Vanadium Cations: An ab Initio Study. *J. Phys. Chem. A* **2015**, *119*, 5749−5761.
(24) Clark, J. K., II; Paddison, S. J. Side Chain Flexibility in Perfluorosulfonic Acid Ionomers: an ab initio Study. *J. Phys. Chem. A* **2013**, *117*, 10534−10543.
(25) Clark, J. K., II; Paddison, S. J.; Hamrock, S. J. The Effect of Hydrogen Bond Reorganization and Equivalent Weight on Proton Transfer in 3M Perfluorosulfonic Acid Ionomers. *Phys. Chem. Chem. Phys.* **2012**, *14*, 16349−16359.
(26) Clark, J. K., II; Paddison, S. J.; Eikerling, M.; Dupuis, M.; Zawodzinski, T. A. A Comparative Ab Initio Study of the Primary Hydration and Proton Dissociation of Various Imide and Sulfonic Acid Ionomers. *J. Phys. Chem. A* **2012**, *116*, 1801−1813.
(27) Feng, S.; Voth, G. A. Proton Solvation and Transport in Hydrated Nafion. *J. Phys. Chem. B* **2011**, *115*, 5903−5912.
(28) Paddison, S. J.; Kreuer, K.-D.; Maier, J. About the Choice of the Protogenic Group in Polymer Electrolyte Membranes: Ab initio Modelling of Sulfonic Acid, Phosphonic Acid, and Imidazole Functionalized Alkanes. *Phys. Chem. Chem. Phys.* **2006**, *8*, 4530−4542.
(29) Escribano, R.; Couceiro, M.; Gómez, P. C.; Carrasco, E.; Moreno, M. A.; Herrero, V. J. The Nitric Acid Hydrates: Ab Initio Molecular Study, and RAIR Spectra of the Solids. *J. Phys. Chem. A* **2003**, *107*, 651−661.
(30) Scheiner, S.; Yi, M. Proton Transfer Properties of Imidazole. *J. Phys. Chem.* **1996**, *100*, 9235−9241.
(31) Scheiner, S. Bent Hydrogen Bonds and Proton Transfers. *Acc. Chem. Res.* **1994**, *27*, 402−408.
(32) Scheiner, S. Theoretical Studies of Proton Transfers. *Acc. Chem. Res.* **1985**, *18*, 174−180.
(33) Scheiner, S. Proton Transfers in Hydrogen-bonded Systems. 4. Cationic Dimers of Ammonia and OH2. *J. Phys. Chem.* **1982**, *86*, 376−382.
(34) Scheiner, S. Comparison of Proton Transfers in Teterodimers and Homodimers of NH3 and OH2. *J. Chem. Phys.* **1982**, *77*, 4039−4050.
(35) Scheiner, S.; Harding, L. B. Proton Transfers in Hydrogen-bonded Systems. 2. Electron Correlation Effects in Diamminehydrogen(1+). *J. Am. Chem. Soc.* **1981**, *103*, 2169−2173.
(36) Scheiner, S. Proton Transfers in Hydrogen-bonded Systems. Cationic Oligomers of Water. *J. Am. Chem. Soc.* **1981**, *103*, 315−320.
(37) Wang, C.; Paddison, S. J. Proton Transfer in Functionalized Phosphonic Acid Molecules. *Phys. Chem. Chem. Phys.* **2010**, *12*, 970−981.
(38) Kumar, M.; Venkatnathan, A. Mechanism of Proton Transport in Ionic-Liquid-Doped Perfluorosulfonic Acid Membranes. *J. Phys. Chem. B* **2013**, *117*, 14449−14456.
(39) Pant, R.; Kumar, M.; Venkatnathan, A. Quantum Mechanical Investigation of Proton Transport in Imidazolium Methanesulfonate Ionic liquid. *J. Phys. Chem. C* **2017**, *121*, 7069−7080.
(40) Kumar, M.; Venkatnathan, A. Quantum Chemistry Study of Proton Transport in Imidazole Chains. *J. Phys. Chem. B* **2015**, *119*, 3213−3222.
(41) Vilčiauskas, L.; Tuckerman, M. E.; Melchior, J. P.; Bester, G.; Kreuer, K.-D. First Principles Molecular Dynamics Study of Proton Dynamics and Transport in Phosphoric Acid/Imidazole (2:1) System. *Solid State Ionics* **2013**, *252*, 34−39.
(42) Frisch, M. J.; Trucks, G. W.; Schlegel, H. B.; Scuseria, G. E.; Robb, M. A.; Cheeseman, J. R.; Scalmani, G.; Barone, V.; Mennucci, B.; Petersson, G. A.; et al. *Gaussian 09*, Revision E.01; Gaussian, Inc.: Wallingford, CT, 2013.
(43) Becke, A. D. A New Mixing of Hartree-Fock and Local Density-Functional Theories. *J. Chem. Phys.* **1993**, *98*, 1372−1377.
(44) Hariharan, P. C.; Pople, J. A. The Influence of Polarization Functions on Molecular Orbital Hydrogenation Energies. *Theor. Chim. Acta* **1973**, *28*, 213−222.
(45) Schlegel, H. B. Optimization of Equilibrium Geometries and Transition Structures. *J. Comput. Chem.* **1982**, *3*, 214−218.
(46) Becke, A. D. Density-functional Thermochemistry. III. The Role of Exact Exchange. *J. Chem. Phys.* **1993**, *98*, 5648−5652.
(47) Becke, A. D. Density-functional Thermochemistry. II. The Effect of the Perdew−Wang Generalized-gradient Correlation Correction. *J. Chem. Phys.* **1992**, *97*, 9173−9177.
(48) Becke, A. D. Density-functional Thermochemistry. I. The Effect of the Exchange-only Gradient Correction. *J. Chem. Phys.* **1992**, *96*, 2155−2160.
(49) Lee, C.; Yang, W.; Parr, R. G. Development of the Colle-Salvetti Correlation-energy Formula into a Functional of the Electron Density. *Phys. Rev. B* **1988**, *37*, 785−789.
(50) McLean, A. D.; Chandler, G. S. Contracted Gaussian Basis Sets for Molecular Calculations. I. Second Row Atoms, Z= 11−18. *J. Chem. Phys.* **1980**, *72*, 5639−5648.
(51) Grimme, S. Semiempirical GGA-type Density Functional Constructed with a Long-range Dispersion Correction. *J. Comput. Chem.* **2006**, *27*, 1787−1799.
(52) Marenich, A. V.; Cramer, C. J.; Truhlar, D. G. Universal Solvation Model Based on Solute Electron Density and on A Continuum Model of the Solvent Defined by the Bulk Dielectric Constant and Atomic Surface Tensions. *J. Phys. Chem. B* **2009**, *113*, 6378−6396.
(53) Munson, R. A. Dielectric Constant of Phosphoric Acid. *J. Chem. Phys.* **1964**, *40*, 2044−2046.
(54) Sepehr, F.; Paddison, S. J. The Solvation Structure and Thermodynamics of Aqueous Vanadium Cations. *Chem. Phys. Lett.* **2013**, *585*, 53−58.
(55) Krakowiak, J.; Lundberg, D.; Persson, I. A Coordination Chemistry Study of Hydrated and Solvated Cationic Vanadium Ions in Oxidation States +III, +IV, and +V in Solution and Solid State. *Inorg. Chem.* **2012**, *51*, 9598−9609.
(56) Li, X.; Frisch, M. J. Energy-represented Direct Inversion in the Iterative Subspace within a Hybrid Geometry Optimization Method. *J. Chem. Theory Comput.* **2006**, *2*, 835−839.
(57) Hunter, E. P. L.; Lias, S. G. Evaluated Gas Phase Basicities and Proton Affinities of Molecules: An Update. *J. Phys. Chem. Ref. Data* **1998**, *27*, 413−656.

https://dx.doi.org/10.1021/acs.jpca.0c02863
J. Phys. Chem. A 2020, 124, 4141−4149

Reprinted with permission from American Chemical Society
Copyright 2022 American Chemical Society

CHEMICAL REVIEWS

pubs.acs.org/CR Review

Coarse-Grained Modeling of Ion-Containing Polymers

Zhenghao Zhu, Xubo Luo, and Stephen J. Paddison*

Cite This: *Chem. Rev.* 2022, 122, 10710−10745 Read Online

ACCESS | Metrics & More | Article Recommendations

ABSTRACT: Ion-containing polymers have continued to be an important research focus for several decades due to their use as an electrolyte in energy storage and conversion devices. Elucidation of connections between the mesoscopic structure and multiscale dynamics of the ions and solvent remains incompletely understood. Coarse-grained modeling provides an efficient approach for exploring the structural and dynamical properties of these soft materials. The unique physicochemical properties of such polymers are of broad interest. In this review, we summarize the current development and understanding of the structure−property relationship of ion-containing polymers and provide insights into the design of such materials determined from coarse-grained modeling and simulations accompanying significant advances in experimental strategies. We specifically concentrate on three types of ion-containing polymers: proton exchange membranes (PEMs), anion exchange membranes (AEMs), and polymerized ionic liquids (polyILs). We posit that insight into the similarities and differences in these materials will lead to guidance in the rational design of high-performance novel materials with improved properties for various power source technologies.

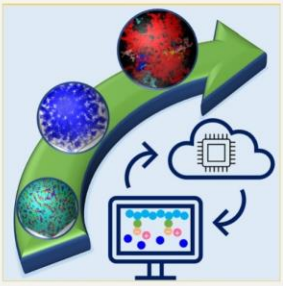

CONTENTS

1. Introduction 10710
2. Methodologies 10712
  2.1. Coarse-Grained Monte Carlo (CGMC) 10712
  2.2. Coarse-Grained Molecular Dynamics (CGMD) 10713
  2.3. Langevin Dynamics (LD) 10713
  2.4. Force Fields for CGMC, CGMD, and LD 10713
  2.5. Dissipative Particle Dynamics (DPD) 10715
  2.6. Continuum Models 10717
  2.7. Reverse Mapping 10719
3. Proton Exchange Membranes 10719
  3.1. PFSA-based PEMs 10719
  3.2. Alternatives to PFSA-based PEMs 10727
4. Anion Exchange Polymers 10732
  4.1. Anion Exchange Membranes 10732
  4.2. Polymerized Ionic Liquids 10734
  4.3. Other Systems 10734
5. Polyion (Mixture of Polyanion and Polycation) 10735
  5.1. Adsorption of PEC to Membrane/Surface 10735
  5.2. Isolated Assembly 10735
6. Salt-Doped Polymers 10737
7. Conclusions and Outlooks 10738
Author Information 10739
  Corresponding Author 10739
  Authors 10739
  Notes 10739
  Biographies 10739
Acknowledgments 10739
References 10739

1. INTRODUCTION

Ion-containing polymers are an important emerging class of functional polymer materials, which consist of a polymer matrix and a relatively high concentration of mobile and fixed ions.[1−17] This class of polymers has drawn increasing attention during the past several decades due to the rapidly increasing demand for the development of renewable energy technology. The requirements for the application in energy storage and conversion include chemical and mechanical stability, fast and highly selective ionic transport, low reactant permeability, long lifetime, improved safety, and low cost.[8−17] Ion-containing polymers combine the amazing advantages of the robust mechanical strength of a polymer matrix with high ionic conductivity. However, this also brings about a complex interplay of membrane morphology and the dynamic behavior of the ions and solvent molecules as well as polymer chains over a broad range of time and length scales, which makes it challenging to fundamentally understand the structural

Special Issue: Computational Electrochemistry

Received: October 29, 2021
Published: May 20, 2022



ACS Publications © 2022 American Chemical Society

https://doi.org/10.1021/acs.chemrev.1c00913
Chem. Rev. 2022, 122, 10710−10745

characteristics and the transport mechanisms in these materials.[6,13]

Typically, ion-containing polymers are divided into three main classes of materials in terms of the mobile ions along with the presence of a solvent in the membrane. These include proton exchange membranes (PEMs), anion exchange membranes (AEMs), and polymerized ionic liquids (polyILs). Nafion is the benchmark PEM and has been extensively and systematically investigated. Two main aspects have been studied: the reasons why Nafion functions well as a PEM and modifications and alternatives to Nafion-type polymers.[12,15] The AEMs are cationic polymers that conducts anions. When synthesized in the hydroxide form, they may be used as the electrolyte in a fuel cell under high pH conditions where the oxygen reduction electrokinetics are facile. PolyILs find use in batteries as a solid polymeric electrolyte. They typically exhibit favorable properties including high mechanical strength, low vapor pressure, and nonflammability compared with conventional liquid electrolytes that have safety issues including short-circuit of the electrodes, explosion risk, and battery failure.

Water plays a significant role in the performance of both PEMs and AEMs. The hydration of these membranes, typically defined as the number of water molecules per functional group, facilitates mesophase separation into hydrophobic domains which provide good dimensional integrity and a hydrophilic phase that consists of water, ions, and pendant head groups. The management of the transport and distribution of water through the membrane is critical and often challenging. Water typically accumulates in the cathode region due to electro-osmosis drag and the production of water from the oxygen reduction reaction (ORR) in PEMs. This results in flooding of the cathode and drying out at the anode side. Nevertheless, water is not permitted in polyILs due to the reactive materials in the battery electrodes. The low ionic conductivity and transference number of polyILs strongly limit their application in batteries.[1,4]

Substantial and continuing efforts have been made to secure fundamental insight into the structural and dynamical properties of ion-containing polymers. However, a significant number of problems remain unresolved. Taking the structural characteristics of Nafion as an example, several models were proposed based on both small-angle X-ray scattering (SAXS) and small-angle neutron scattering (SANS) measurements. Gierke et al.[18] proposed a model of spherical water clusters linked by small channels. Schmidt-Rohr and Chen[19] utilized an algorithm in a quantitative analysis method to describe the morphology of Nafion as parallel cylindrical water nanochannels. Although this model is widely accepted and supported by other studies, Kreuer et al.[20] pointed out that this parallel cylinder model was only able to reproduce the experimental data at a low degree of hydration (20 vol %), while several models could match the high q-region of the experimental data at high water contents (∼40 vol %). They proposed a morphology with locally flat and narrow water structures sandwiched by the polymer backbones, demonstrating that this is more energetically favorable.[20] It is obvious that these interpretations of the experimental data are model dependent to some extent and therefore remain under debate, suggesting that it is difficult to secure a clear understanding of the mesoscopic properties through only traditional experimental approaches.

The morphological properties and dynamical behavior of ions are influenced by a variety of factors, including the architecture of the backbones and side chains, chemistry of the functional groups, distribution (i.e., spacing) of the headgroups, ion exchange capacity, and presence of plasticizers. Understanding how these tunable parameters affect the structure and the ion transport of the material is critically important in developing optimal or high-performance polymers with superior ionic conductivity as well as high mechanical and chemical stability. To explore the underlying mechanisms governing nanophase separation, the formation of percolating networks, and the transport of ions, experimental techniques are not sufficient to address the role of these factors for a specific application. Therefore, modeling and simulations are promising complementary strategies in the discovery of novel avenues that may guide the development of functional materials for electrochemical applications.

In view of the complexity of ion-containing polymer systems, there exist important molecular-level features regarding the structure and transport properties. Nanophase separation is important in providing the mechanical strength of the material and the formation of ion conducting pores as a result of the interactions between the polymer and solvent. Importantly, the interplay of ionic species with the polymer chains strongly influences ion association, segmental movement (i.e., of side chains), and correlative dynamics of the ionic species, which continues to be an interesting direction in connecting ionic conductivity with diffusivity of the ions.[1,4,21] In addition, electrostatic interactions also play a large role in the self-assembly and formation of ionic aggregates. Through the addition of solvents with different polarities, the behavior can be tailored through distinctions in the screening effects of the solvent. In most cases, the performance of a polymeric system is determined by all of these parameters to some extent, but how these interactions govern the properties in a synergistic or uncooperative manner and which are dominant are critical but unresolved.

To explore structural and dynamical features in ion-containing polymers, multiscale investigations are necessary to extract information in various time and length scales considering the balance between computational efficiency and required accuracy. Static electronic structure calculations were extensively utilized to investigate the dissociation and transfer of a proton from an acid group and the solvation behavior of the dissociated proton.[22−25] Ab initio molecular dynamics simulations, a powerful tool, were undertaken to describe the dynamic behavior of hydrated protons under nanoconfinement, where "on the fly" force fields (i.e., force fields updated at each time step) enable one to simulate the breaking and formation of covalent bonds.[26−34] Although these high-fidelity calculations and simulations provide molecular-level insight into structure/function relationships of these polymeric materials, the accessible length and time scales are limited.

Given these limitations, coarse-grained modeling and simulations are an effective tool to search for the optimal combination of factors by ignoring or averaging over the atomistic details.[35−38] Compared with atomistic MD simulations, coarse-grained approaches can reduce the complexity of the physical representatives and allow one to gain insight into multiple ranges or types of phenomena. In view of the scale of the hydrated morphology of these ionomers, dissipative particle dynamics (DPD) simulations have proven to be a suitable methodology for determining the morpho-

https://doi.org/10.1021/acs.chemrev.1c00913
Chem. Rev. 2022, 122, 10710−10745

logical characteristics of ion-containing polymers even for cases where electrostatic interactions are not explicitly included. The soft beads and simple bead−spring chains allow one to simulate large systems on a relatively long-time scale and thereby secure an equilibrium microphase separation morphology for the system. There are drawbacks, however, in the inability of these methods to estimate dynamical properties.[35,37−42] To make up for this deficit, significant effort has been undertaken to compute the diffusivity of ions and solvent by introducing novel strategies. For example, Dorenbos et al.[43−48] developed grid-based Monte Carlo trajectory calculations to estimate the water diffusivity in equilibrated water-containing pores embedded in a backbone matrix. Neimark et al.[49,50] employed a dissociative Morse potential to describe the "Grotthuss mechanism" of proton hopping between acidic groups, which was also applied to model hydroxide ion transport in AEMs by Lee et al.[51−53] Smoothed particle hydrodynamics was used to capture qualitative morphology and proton transport properties by Voth et al.[54]

Hence, coarse-grained modeling and simulations play an important role in the molecular-level understanding of morphological and dynamical properties of ion-containing polymers. Given the computational efficiency of coarse-grained models, one promising route for the development of novel ion-containing membranes may be to first conduct fast screening of potential candidates through modeling and simulations prior to their synthesis and experimental testing and then to obtain feedback from experimental studies to validate and improve the theoretical approaches. This strategy will facilitate exploring for more advanced ion-containing polymeric materials and gain time and competitive advantages for future electrochemical technologies. In this review, we focus on the application and implementation of coarse-grained modeling of ion-containing polymers, including the hydrated/anhydrous morphologies, ionic aggregation (shape, size, and connectivity), water cluster analysis, and the influences of various molecular features on structural and dynamical properties.

Furthermore, we discuss recent progress in ion-containing polymers as well as the advances in coarse-graining strategies. The interplay between morphology and transport properties in these materials is highlighted, with a focus on the insight obtained from theoretical and simulation studies. The remainder of the review is organized as follows. In section 2, we briefly describe a variety of coarse-grained modeling and simulation methods, including coarse-grained Monte Carlo, MD, Langevin Dynamics, DPD simulations along with a summary of strategies for the development of force fields, and continuum modeling. Section 3 presents the influences of the various factors on the morphology and the transport of protons and water in PEMs, along with emerging directions for improving membrane performance. Section 4 describes the significant developments of AEMs and the insights into the design of high-performance polyILs based on multiscale coarse-grained modeling and simulations. Following this discussion, some interesting phenomena within polyion systems and salt-doped polymers are shown in Sections 5 and 6, respectively. Finally, we summarize the advances in both the development of coarse graining methodologies and the rational design of ion-containing polymers followed by an outlook into the applications of ion-containing polymers in the field of energy storage and conversion.

2. METHODOLOGIES

The structure−property relationships of polymeric materials require scrutiny over a range of various time and length scales. Multiscale methods have been utilized to understand these phenomena, which span from the quantum mechanical scale to the macroscopic realm.[55] For polymeric materials, properties including the morphology and distribution of the solvent do not require an atomistic description but rather involve large spatial and temporal scales.[56] Therefore, using coarse-grained models is essential to being able to reproduce the desired properties at a reasonable (computational) cost.

Multiscale simulations have been extensively utilized in the study of polymers as these methods are capable of probing properties over a range of distinct length and time scales.[55] Before briefly summarizing the various models, it is necessary to first define what is generally understood by the term: coarse graining. We recognize that united-atom molecular dynamics or Monte Carlo simulations may be classified as a type of coarse graining, where the hydrogen atoms are grouped with heavy atom(s).[57−59] For ion containing polymers, the coarse-grained models generally used include coarse grained Monte Carlo (CGMC), coarse grained molecular dynamics (CGMD), Langevin dynamics (LD), dissipative particle dynamics (DPD), and continuum models. In general, CGMC and CGMD have the finest resolution among these models. A small group of heavy atoms are generally lumped into a single entity typically referred to as a bead. The potential, or force field, typically has a form comparable to all-atom models, where the nonbonded interactions consist of Coulombic and dispersion forces, and the bonded forces consist of length, angle, and dihedral angle constraints. The relatively detailed topology and force field are conceptually more applicable for the atomistic scale. Unlike CGMD, coarse-gained Langevin dynamics uses random forces as an implicit model for the solvent molecules, thereby enabling longer simulation times. LD uses a similar force field as in CGMC and CGMD simulations, which retains the detailed interactions for the explicitly modeled solute molecules. Dissipative particle dynamics has a greater degree of coarse graining that omits even more of the atomistic information. In principle, one DPD bead can represent significantly more atoms, especially for linear polymer chains,[60−63] although the topology of the real material may limit this. DPD has random and dissipation forces, and its force field has a linear expression, which is sufficiently simple to enable faster computing to achieve simulations at the mesoscopic scale. Continuum models, which may even reach the a macroscale, consist of differential equations. Generally, continuum models do not contain particle dynamics, but the model can be developed to consider the interactions of atom groups. Hence, it may be regarded as a coarse graining method. The following sections summarize the methodologies beginning from the finest resolution and progressing to the most coarse-grained, i.e., Monte Carlo, molecular dynamics, and Langevin dynamics, the introduction of CG force field, dissipative particle dynamics, and finally, continuum modeling.

2.1. Coarse-Grained Monte Carlo (CGMC)

A full description of Monte Carlo theory may be found in the standard texts, such as Allen and Tildesley[64,65] and Leach.[66] Briefly, an MC simulation conducts many stochastic computer experiments to sample the phase space, and the ensemble averages are computed from the generated trajectories. The sampling procedure utilizes a weighted sampling algorithm that

https://doi.org/10.1021/acs.chemrev.1c00913
Chem. Rev. 2022, 122, 10710−10745

different configurations are obtained, and the standard Metropolis method is used to sample important contributions.[67] The idea of the method is briefly summarized here: The new configuration of the system is generated by randomly or systematically moving a particle from its original position i to the temporary trial position j, i.e., the initial state of Γ_i is changed to the trial state Γ_j. It is worth noting that the new trial state can also be obtained by changing certain parameters in the molecular structure, e.g., the dihedral conformation. Then, the corresponding potential energies of the initial state and the new trial state, V_i and V_j, are evaluated and the change in the potential energy is calculated:

$$\Delta V = V_j - V_i \tag{1}$$

If the change of state results in a lower potential energy, i.e., $\Delta V < 0$, the new configuration is accepted. If $\Delta V > 0$, the new state is accepted with a probability proportional to the Boltzmann factor in the energy difference:

$$p_{i\to j} \propto \exp\left(-\frac{\Delta V}{k_B T}\right) \tag{2}$$

where k_B is Boltzmann's constant and T the temperature. The Boltzmann factor $\exp(-\Delta V/k_B T)$ is then compared with a random number, ζ, which has an even distribution in the range of (0,1). If $\zeta < \exp(-\Delta V/k_B T)$, the trial configuration is accepted, and the displaced particle is in a new position. Otherwise, the displacement is rejected, and the system is backstepped to the initial configuration for the next iteration.

2.2. Coarse-Grained Molecular Dynamics (CGMD)

Unlike Monte Carlo theory, molecular dynamics is a deterministic method where the motions of the particles obey Newton's second law:

$$\frac{d^2 \boldsymbol{r}_i}{dt^2} = \frac{\boldsymbol{F}_i(t)}{m_i} \tag{3}$$

where $\boldsymbol{r}_i$, $\boldsymbol{F}_i$, m, t are the position, total force, mass of the ith particle, and time. In MD simulations, the evolution of particle positions is achieved by integrating over discrete time steps. The position and velocity of each particle at the current time step are dependent on the previous step, and an integrator is used for the evolution of the trajectory. One commonly employed integrator is the leapfrog integrator:[68]

$$\boldsymbol{v}_i\left(t + \frac{1}{2}\Delta t\right) = \boldsymbol{v}_i\left(t - \frac{1}{2}\Delta t\right) + \Delta t \frac{\boldsymbol{F}_i(t)}{m_i} \tag{4}$$

$$\boldsymbol{r}_i(t + \Delta t) = \boldsymbol{r}_i(t) + \Delta t \boldsymbol{v}_i(t + \Delta t) \tag{5}$$

where $\boldsymbol{r}_i$, $\boldsymbol{v}_i$, $\boldsymbol{F}_i$, m_i, and Δt are the position, velocity, total force, mass of the ith particle, and the time step size, respectively. The force, $\boldsymbol{F}_i$, is calculated from the potential, V:

$$\boldsymbol{F}_i = -\nabla_i V = -\left(\frac{\partial V}{\partial x_i}\boldsymbol{i} + \frac{\partial V}{\partial y_i}\boldsymbol{j} + \frac{\partial V}{\partial z_i}\boldsymbol{k}\right) \tag{6}$$

where $\boldsymbol{i}$, $\boldsymbol{j}$, and $\boldsymbol{k}$ are the unit vectors in the x, y, and z directions.

2.3. Langevin Dynamics (LD)

Langevin dynamics is utilized for the motions of colloidal particles in dilute dispersions, where the solvent molecules are negligibly small and the motions of the solvent molecules are seemingly quiescent. LD models the effect of solvent in MD with an implicit continuum medium, and the dissipative and random forces are introduced:

$$\boldsymbol{F}_i = \boldsymbol{F}_c - \zeta \boldsymbol{v}_i + \boldsymbol{F}_i^B = -\nabla_i V - \zeta \boldsymbol{v}_i + \boldsymbol{F}_i^B \tag{7}$$

where $\boldsymbol{F}_c$ is the conservative force evaluated from the potential, similar to the CGMD method, ζ_i is the friction coefficient that is related to the collision frequency γ_i by $\gamma_i = \zeta_i/m_i$, and $\boldsymbol{F}_i^B$ is the random force. The random force induces Brownian motion due to collision with the implicit solvent molecules, and must satisfy the following:

$$\langle \boldsymbol{F}_i^B(t) \rangle = 0 \tag{8}$$

$$\langle \boldsymbol{F}_i^B(t) \cdot \boldsymbol{F}_i^B(t + s) \rangle = 2 m_i \gamma_i k_B T \delta(s) \tag{9}$$

where t and s are the time and time step, and δ is the Dirac delta function. The evolution of particle positions is in the same framework as discussed earlier for MD, i.e., a leapfrog integrator can be used to obtain the trajectory. The friction and random force can be regarded as a special thermostat with a random number. This treatment of the solvent as an implicit continuum medium enables a large time scale, but it still maintains the force field as in CGMC and CGMD for the explicitly modeled molecules.

2.4. Force Fields for CGMC, CGMD, and LD

Unlike all-atom simulations, the particles/beads in CGMC, CGMD, and LD represent a group of atoms, and all of these methods involve the evaluation of the potential energy. Thus, the coarse-grained force field is one of the key components of a successful simulation. For molecular systems, the potential usually consists of intermolecular (nonbonded) and intramolecular (bonded) interactions. The coarse graining of the real materials may lead to versatile force fields and simplification of the interactions. Clearly, a coarse-grained (CG) force field is dependent on the coarse-grain mapping. An initial approach in the parametrization is to map the atomistic structure into the CG representation with a well-established force field. In this section, the popular Martini force field is briefly described as an example. The Martini force field is continuously under development, and the latest version (version 3.0) has shown success in modeling biomolecules and ionic liquids.[69] The nonbonded interactions have the form:

$$V_{LJ} + V_{Coul} = \sum_{i<j} 4\varepsilon_{ij}\left[\left(\frac{\sigma_{ij}}{r_{ij}}\right)^{12} - \left(\frac{\sigma_{ij}}{r_{ij}}\right)^{6}\right] + \sum_{i<j} \frac{q_i q_j}{4\pi\epsilon_0\epsilon_r r_{ij}} \tag{10}$$

where V_{LJ} and V_{Coul} are the Lennard-Jones and Coulombic interactions. The bonded interactions are described by

$$V_b + V_a + V_{id} = \sum_b \frac{1}{2}k_b(r - r_0)^2 + \sum_a \frac{1}{2}k_\theta(\cos\theta - \cos\theta_0)^2 + \sum_{id} k_{id}(\theta_{id} - \theta_{id,0})^2 \tag{11}$$

where V_b, V_a, and V_{id} are the bond, angle, and improper or dihedral constraints, respectively. The parameters are determined according to the topology of the center of mass of the

https://doi.org/10.1021/acs.chemrev.1c00913
Chem. Rev. 2022, 122, 10710−10745

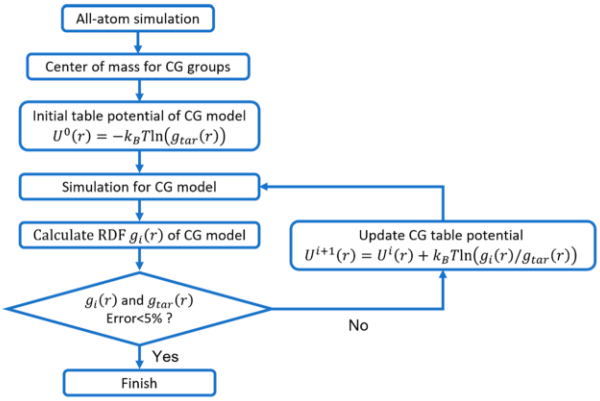

Figure 1. Diagram of the iterative Boltzmann inversion (IBI) scheme. Adapted with permission from ref 72. Copyright 2020 Elsevier.

coarse-grained groups. The Martini 3 force field is elaborately designed with seven chemical bead types according to the polarity and the charge, and each type has a finer denotation of polarity at up to six levels. Further, there is the option of the bead size from regular to tiny for each bead, where the regular bead typically consists of four heavy atoms (i.e., a 4 to 1 mapping), while the small and tiny beads consist of three (3 to 1 mapping) and two heavy atoms (2 to 1 mapping), respectively. This very refined set of bead types, along with its matrices for the selection and refining of the force field parameters, enables a more accurate prediction of molecular interactions and structures. It also balances coarse-graining and the inclusion of the details of a wide range of molecules. A full description may be found in a recent publication.[69] The advantage of using the existing CG force field is obvious. One can perform CG simulations efficiently after properly mapping from the atomistic to the CG model without additional all-atom simulations for the parametrization. However, the shortcoming is the lack of the fine-tuning of the parameters because the CG beads of the real materials can only be fitted into the predefined beads in the database.

Alternatively, the iterative Boltzmann inversion (IBI) scheme has become a popular method for CG force field parametrization.[70] This method uses the structural properties from all-atom simulations to construct the CG force field, hence this is a bottom-up approach. Fortunately, the Versatile Object-Oriented Toolkit for Coarse-Graining Applications software package (VOTCA) can facilitate this procedure.[71] In this section, the basic idea of the IBI procedure is briefly introduced. Like all-atom force fields for molecular systems, the CG force field consists of both bonded and nonbonded potentials. The parametrization of the bonded interactions is usually conducted prior to the parametrization for the nonbonded interactions. It is worth noting that the Boltzmann inversion is typically sufficient for bonded parameters, i.e., iteration is not necessary in practice. Assuming the independence of the coarse-grained degrees of freedom for the bonded interactions, the distribution functions for the bonded variables may be written as

$$P(r, \theta, \varphi) = P_r(r)P_\theta(\theta)P_\varphi(\varphi) \tag{12}$$

$$P_r(r) = \frac{H_r(r)}{4\pi r^2}, \quad P_\theta(\theta) = \frac{H_\theta(\theta)}{\sin\theta}, \quad H_\varphi(\varphi) = H_\varphi(\varphi) \tag{13}$$

where P_q with $q = r, \theta, \varphi$ denotes the volume normalized distribution functions for the bond, angle, and torsion angles, and H_q with $q = r, \theta, \varphi$ is the corresponding histogram of the distribution. In the canonical ensemble, the independent degrees of freedom obey a Boltzmann distribution:

$$P(r, \theta, \varphi) = \exp\left[-\frac{U(r, \theta, \varphi)}{k_BT}\right] \tag{14}$$

where the potential of the bonded interactions, $U(r, \theta, \varphi)$, satisfies:

$$U(r, \theta, \varphi) = U_r(r) + U_\theta(\theta) + U_\varphi(\varphi) \tag{15}$$

and hence, for each freedom q

$$U_q(q) = -k_BT\ln(P_q(q)), \qquad q = r, \theta, \varphi \tag{16}$$

In eq 16, P_q can be obtained from atomistic simulations with the calculation of the centers of mass according to the coarse-graining, and consequently the tabulated CG potential U_q. In practice, these discrete data points are typically fitted to analytical equations. Unlike the bonded potential, the iterative scheme is utilized for the nonbonded parameters. An initial guess for the nonbonded potential of the CG force field, U^0, can be adopted as

$$U^0(r) = -k_BT\ln(g_{tar}(r)) \tag{17}$$

where $g_{tar}(r)$ is the target radial distribution function obtained from atomistic simulations after lumping the atoms into CG beads. In fact, $g(r)$ is equivalent to the $P_r(r)$ in eq 13. This initial potential is then used to perform a coarse-grained simulation in order to obtain the radial distribution function, and the nonbonded potential is updated iteratively with the following equation:

$$U^{i+1}(r) = U^i(r) + k_BT\ln\left(\frac{g_i(r)}{g_{tar}(r)}\right) \tag{18}$$

https://doi.org/10.1021/acs.chemrev.1c00913
Chem. Rev. 2022, 122, 10710−10745

where $U^i(r)$ and $g_i(r)$ are the nonbonded potential and the radial distribution function obtained from the ith CG simulation, respectively. The iteration finishes when the difference between $g_i(r)$ and $g_{tar}(r)$ is sufficiently small, which is evaluated with the following function:

$$\text{Error}(r) = \int_{r=1}^{r_{cut}} \exp\left(-\frac{r}{r_{cut}}\right)((g_i(r) - g_{tar}(r))^2 \, dr \tag{19}$$

The IBI scheme is illustrated in Figure 1. Different from using the well-established database, IBI provides a protocol to refine the CG force field for the exact material being simulated. A CG force field can be obtained for almost any material, and the reproduction of the structural properties, e.g., $g(r)$, is guaranteed. However, it is costly because of the extra all-atom simulations and multiple runs of the CG simulations.

2.5. Dissipative Particle Dynamics (DPD)

The development of DPD can be traced back to the 1990s, when Hoogerbrugge,[42] Espanol[73−75] and Avalos[76] first introduced the methodology. In 1997, Groot and Warren summarized the DPD method with an applicable algorithm and a case study of water, making DPD an applicable technique for simulations.[77] DPD has been successfully utilized for polymers and membranes.[60−63,78−83] This review briefly summarizes the original DPD method. A complete description of the theory can be found in Groot and Warren,[77] Espanol and Warren,[38] and Santo and Neimark.[84]

The DPD model groups several atoms into a particle or "bead". The dynamics of the DPD particles are governed by Newton's law, but the mass of all particles is treated as unity because the coarse graining in a DPD simulation requires the particles have similar sizes and masses:

$$\frac{d\boldsymbol{r}_i}{dt} = \boldsymbol{v}_i \text{ and } \frac{d\boldsymbol{v}_i}{dt} = \boldsymbol{f}_i \tag{20}$$

where $\boldsymbol{r}_i$, $\boldsymbol{v}_i$, and $\boldsymbol{f}_i$ are the position, velocity, and net force of the ith particle, respectively. The net force consists of three nonbonded pairwise interactions of conservative ($\boldsymbol{F}_{ij}^C$), dissipative ($\boldsymbol{F}_{ij}^D$), and random ($\boldsymbol{F}_{ij}^R$) forces, and additional bonded interaction $\boldsymbol{f}_i^{bonded}$:

$$\boldsymbol{f}_i = \sum_{j \neq i} (\boldsymbol{F}_{ij}^C + \boldsymbol{F}_{ij}^D + \boldsymbol{F}_{ij}^R) + \boldsymbol{f}_i^{bonded} \tag{21}$$

$$\boldsymbol{F}_{ij}^C = \begin{cases} a_{ij}(1 - r_{ij})\boldsymbol{e}_{ij} & r_{ij} < r_c \\ 0 & r_{ij} \geq r_c \end{cases} \tag{22}$$

$$\boldsymbol{F}_{ij}^D = -\gamma_{ij}(1 - r_{ij})^2(\boldsymbol{e}_{ij} \cdot \boldsymbol{v}_{ij})\boldsymbol{e}_{ij} \tag{23}$$

$$\boldsymbol{F}_{ij}^R = \sigma_{ij}(1 - r_{ij})\xi_{ij}\frac{1}{\sqrt{\Delta t}}\boldsymbol{e}_{ij} \tag{24}$$

The forces are unitless (i.e., in LJ units), where the conservative force has a cutoff $r_c = 1$ that F_{ij}^C is linear to the distance of the two beads inside r_c but vanishes if the two beads are farther apart. The parameter a_{ij} denotes the interaction of the two beads, which is material specific and is typically determined for each pair of beads. $r_{ij} = |\boldsymbol{r}_i - \boldsymbol{r}_j|$ is the distance between each pair of beads. The unit vector $\boldsymbol{e}_{ij}$ points toward the centers of the ith and jth beads and the relative velocity $\boldsymbol{v}_{ij}$ are defined as $\boldsymbol{e}_{ij} = \frac{\boldsymbol{r}_i - \boldsymbol{r}_j}{|\boldsymbol{r}_i - \boldsymbol{r}_j|}$ and $\boldsymbol{v}_{ij} = \boldsymbol{v}_i - \boldsymbol{v}_j$, respectively. In the dissipative and random forces $\boldsymbol{F}_{ij}^D$ and $\boldsymbol{F}_{ij}^R$, the dissipation constant, γ_{ij}, and the noise amplitude, σ_{ij}, are related by $\sigma_{ij} = \sqrt{2\gamma_{ij}k_BT}$ which functions as a thermostat dictated by the fluctuation−dissipation theorem.[74] Practically, the dissipation constant and the noise amplitude typically have values of 4.5 and 3, respectively, with the dimensionless temperature $k_BT = 1$, and ξ_{ij} is a uniform random number with zero mean and unit variance. The bonded force, $\boldsymbol{f}_i^{bonded}$, describes the polymer chains in which the particles or beads are connected by covalent bonds, and the angle constraints are applied to the consecutive bonds in order to control chain flexibility.[85,86] To reproduce specific properties, a DPD model can be further modified to include additional interactions, such as explicit Coulombic interactions,[85,87] proton and hydroxide ion transport,[50,52,88] and the entanglement of polymer chains.[89−91]

A DPD simulation requires a reasonable estimation of the conservative a_{ij} parameters. A certain type of bead is chosen as the reference and its self-interaction, a_{RR}, is initially determined to guarantee adequate fluctuation. Typically, water is used to obtain the a_{RR} so that the compressibility of water is reproduced when a water molecule is coarse-grained into a single bead, i.e., $a_{RR} = 25$. It is acknowledged that the more water molecules grouped into one DPD bead, a higher a_{RR} should be chosen to reproduce the physical property in real units.[53,92] However, this is only a numerical preference if the simulations are aimed at structural properties. The system might be too stiff if the a_{RR} is too high. For other species, a_{ij} can be arbitrarily assigned from guessing,[86,92,93] which is highly dependent on the intuition of chemistry. Another widely used approach is assigning $a_{ii} = a_{RR}$ for all the particles and mapping the a_{ij} $(i \neq j)$ to the Flory−Huggins χ-parameter. For a numerical density of 3, it was determined by Warren and Groot that the χ and a_{ij} obey the relation: $0.286(a_{ij} - a_{ii}) = \chi$. The χ-parameter may be calculated from the solubility parameter available in a handbook of experimental data for common solvents and equivalent polymer segments.[94,95] The χ-parameter is most directly calculated with

$$\chi = \frac{V_{bead}}{RT}(\delta_A - \delta_B)^2 \tag{25}$$

where δ_A and δ_B are the solubility parameters of the chemicals corresponding to bead A and B, respectively, R is the gas constant, and V_{bead} is the molar volume of the DPD bead, which is the same for all beads. The shortcoming of the handbook method is obvious because the number of available chemicals is limited. If an accurate match cannot be found, one must search for a similar material in the handbook as a substitute for the desired DPD bead.

The χ-parameter may also be estimated from atomistic simulations with classical force fields. An early methodology used the cohesive energy or heat of vaporization.[60−63,96,97] From the heat of vaporization, the solubility parameter is calculated with

$$\delta_i = \sqrt{\frac{\Delta E_{coh,i}}{V_i}} = \sqrt{\frac{\Delta H_i^{vap} - RT}{V_i}} \tag{26}$$

where $\Delta E_{coh,i}$, ΔH_i^{vap}, and V_i are the cohesive energy, heat of vaporization, and molar volume of the ith species (bead type i), respectively. The $\Delta E_{coh,i}$ may be obtained from atomistic simulations of the pure ith species:

https://doi.org/10.1021/acs.chemrev.1c00913
Chem. Rev. 2022, 122, 10710−10745

$$\Delta E_{\mathrm{coh},i} = E_{\mathrm{liquid},i} - nE_{\mathrm{gas},i} \tag{27}$$

where $E_{\mathrm{liquid},i}$ is the potential energy of i in the liquid state, n is the number of molecules in this liquid system, and $E_{\mathrm{gas},i}$ is the potential energy of an isolated molecule. Alternatively, the χ-parameter can also be calculated from the mixing energy using the atomic MC calculations:[98]

$$\chi = Z\left(\frac{\Delta E_{12}}{RT}\right) \tag{28}$$

$$\Delta E_{12} = E_{12} - \frac{1}{2}(E_{11} + E_{22}) \tag{29}$$

where Z is the coordination number, i.e., the number of possible interaction partners, ΔE_{12} is the heat of mixing of components 1 and 2, and E_{12} and $E_{11(12)}$ are the energies of the mixture and pure systems, respectively. Z can be estimated by placing the nearest neighbors around the center molecule, and E_{ij} is evaluated with an all-atom MC calculation for a pair consisting of i and j. To obtain E_{ij}, a large number of orientations are sampled, and the distance of i and j is kept constant to satisfy the contact of their van der Waals surfaces. Before averaging the obtained energies, the Metropolis algorithm is used to determine acceptance.[67] This method has been used for copolymers and proton exchange membranes.[60−63,99] The χ-parameter from either the cohesive energy or the mixing energy is conceptually a more precise way than searching for similarity in a handbook of materials. However, the extra cost of performing the atomistic simulations can be considerable, especially when there are many different beads.

Vishnyakov et al.[100] suggested a methodology whereby the DPD repulsion parameters could be matched with infinite dilution activity coefficients (IDAC). Lee and coauthors further developed the IDAC method to polymer chains and polymeric electrolytes for insoluble bead pairs.[50−53] To find the calibration between $\Delta a_{ij} = (a_{ij} - a_{\mathrm{RR}})$ and the infinite dilution activity coefficient, a series of hybrid DPD−Monte Carlo simulations were performed, with the Widom test particle insertion methodology.[101] For example, a water bead was inserted into the pure 4-mer melt. The activity coefficient of the inserted species was calculated with

$$\ln(\gamma_i^{\infty}) = \ln\left\langle \exp\left(-\frac{E_{i\to j}^{\mathrm{ins}}}{k_{\mathrm{B}}T}\right)\right\rangle - \ln\left\langle \exp\left(-\frac{E_{i\to i}^{\mathrm{ins}}}{k_{\mathrm{B}}T}\right)\right\rangle - \ln\left(\frac{n_j b_j \rho_{ij}}{n_i b_j \rho_{ii}}\right) \tag{30}$$

where γ_i^{∞} is the activity coefficient of dilute i in the solvent of j, $E_{i\to j}^{\mathrm{ins}}$ is the energy of random insertion of one i bead to a bath of j molecules, n_j is the number of atomistic molecules that a coarse-grained molecule represents, b_i is the number of beads in a coarse-grained molecule, and ρ_{ij} is the numerical density of the simulation box after insertion (approximately 3). The insertion energies are calculated by running trial DPD simulations with different values of Δa_{ij}, and a series of ln (γ_i^{∞}) can be obtained from eq 30. Usually, a linear correlation of ln $(\gamma_i^{\infty}) \sim \Delta a_{ij}$ is found. Finally, if γ_i^{∞} is known from either experimental data or the COSMO-RS model,[102,103] it is used to calculate the ln (γ_i^{∞}), and the exact Δa_{ij} is obtained from a calibration curve.

The above approaches for parametrization prove the versatility of various methodologies but are not suitable for charged beads. For DPD simulations of ion containing polymers, the solution is either combining the oppositely charged moieties into a single bead or introducing extra forces into a standard DPD model. The former will lack an adequate description of ion transport, while the latter with removing the simplicity of the DPD model and possibly be too computationally expensive. To reconcile this problem, Fatemeh and Paddison introduced an ab initio-based method for treating beads that carry a charge, where electrostatic interaction is implicitly included and the a_{ij}s retain some chemical specificity of the ion containing polymers.[104] The basic philosophy involves sampling various orientations of the two rigid clusters of atoms, which have the identical structures to the DPD beads. Density functional theory calculations are conducted for the energy. The a_{ij} is then estimated by fitting the excess energies with the distances between the two beads using

$$U_{ij}^{\mathrm{ex}} = U_{(i+j)} - U_{(i)} - U_{(j)} = \frac{a_{ij}^{\mathrm{int}}}{2}(1 - r_{ij})^2 + b_{ij}^{\mathrm{int}} \tag{31}$$

where $U_{(i+j)}$ and $U_{(i)}$ are the energies of the cluster of $i + j$ beads and the isolated i bead, respectively, and a_{ij}^{int} and b_{ij}^{int} are fitting parameters. These parameters are further scaled to obtain the Δa_{ij} with

$$\Delta a_{ij} = \frac{a_{ij}^{\mathrm{int}}}{r_c^2 s} + \frac{b_{ij}^{\mathrm{int}}}{s} \tag{32}$$

where r_c is a value comparable to the cutoff distance in real units and s is an arbitrary scaling factor. This method requires the fine-tuning and careful scaling of the energy curves, but it provides an all-in-one solution that allows the utilization of charged beads within the standard DPD model.

The fragmental molecular orbital (FMO) method also estimates the a_{ij} parameters from ab initio calculations,[105,106] and has been successfully applied in DPD simulations of ion conducting membranes by Okuwaki et al.[107] Their original work only contained neutral DPD beads, but the FMO method is in principle capable of treating charged beads. This method shares a similar philosophy with eqs 28 and 29. However, it invokes a modified relation for the χ-parameter and mixing energy:

$$\chi = \frac{(E_{12}Z_{12}S_{12} + E_{21}Z_{21}S_{21}) - (E_{11}Z_{11}S_{11} + E_{22}Z_{22}S_{22})}{RT} \tag{33}$$

where Z_{ij}, E_{ij}, and S_{ij} are the coordination number, energy of the bead pair, and the scaling factor of bead i and j. Z_{ij} is estimated from the configuration setup with the J-OCTA program.[108] The energy of the bead pair, E_{ij}, is calculated from ab initio calculations for a fragment of the polymer and cluster of small molecules. This is done with a large number of FMO calculations, for example, using the ABINIT-MP program.[109] S_{ij} reflects the anisotropy of the orientations for the two approaching fragments i and j, which is evaluated by MC sampling. S_{ij} is equal to unity when the interactions between two fragments are uniform in all directions, otherwise, S_{ij} is smaller than one. It is worth noting that for the same material (Nafion), the FMO method yielded a different set of a_{ij} parameters from classical MC calculations.[99,107] This indicates the various applicable strategies of parametrization and that the derived DPD parameter set may not need to be unique. To

https://doi.org/10.1021/acs.chemrev.1c00913
Chem. Rev. 2022, 122, 10710−10745

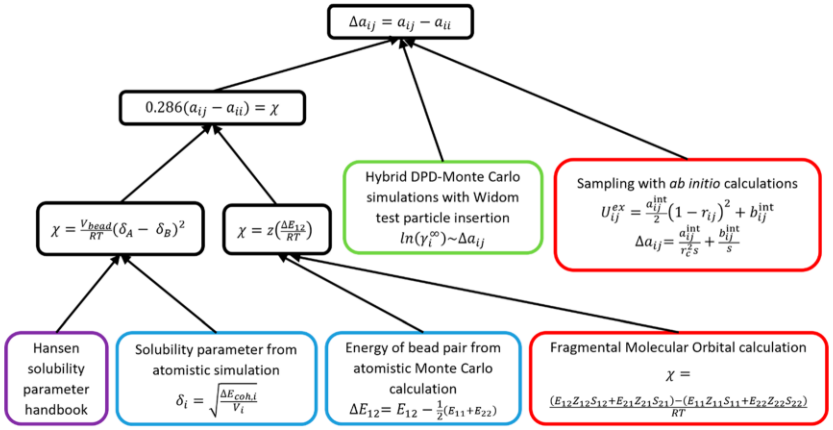

Figure 2. Various pathways to obtain the Δa_{ij} for DPD simulations. Color codes: purple, handbook data; blue, atomic simulation with classical force field; red, ab initio calculation; green, trial DPD simulation.

sum up all the aforementioned methods, Figure 2 demonstrates the different pathways to computing or estimating the a_{ij} parameters.

To model the transport of protons or hydroxide ions in hydrated membranes, the mobile charged bead is modeled as a special one, and it interacts with the oppositely charged beads and water beads via an attractive short-range Morse potential $\mathbf{F}_{ij}^{(M)}$ in DPD simulations:[49−53]

$$\mathbf{F}_{ij}^{(M)}(r_{ij}) = -2\alpha_{IJ}K_{IJ}e^{\alpha_{IJ}r_{ij}}(1 - e^{\alpha_{IJ}r_{ij}})\frac{\boldsymbol{r}_{ij}}{r_{ij}}, \quad \text{at } r_{ij} < r_{ij}^{M} \tag{34}$$

where K_{IJ}, α_{IJ}, and r_{ij}^{M} are the effective strength parameter, the effective steepness of the Morse potential, and the cutoff distance for a Morse bond, respectively. These parameters are obtained by fitting the mobility of the simulated bead in bulk water and degree of dissociation in dilute reference solutions with the experimental values. In these simulations, the electrostatic interactions between the charged species are explicitly treated using a smeared charge approach, which increases the computational cost and causes unphysical clustering phenomena in some systems.[50] An alternative may be to incorporate the electrostatic interactions into the repulsion component via ab initio parametrization approaches.

2.6. Continuum Models

Continuum models have been developed for transport phenomena in proton exchange membranes.[6,110,111] The macroscopic governing equations can be written in differential form as a conservation equation for property Ω:

$$\frac{\partial \Omega}{\partial t} + \nabla \cdot N_{\Omega} = S_{\Omega} \tag{35}$$

where the first term is a time-dependent property that can be neglected for steady-state problems, N_{Ω}, the second term, is the flux of Ω into or out of the control unit, and S_{Ω}, the third term is the source of generation or consumption of the property. The variable Ω can be any property, such as heat, charge, mass of ion species and water content, etc., and the above equation is a universal governing equation not only valid for a polymeric electrolyte, but also for all the components of electrochemical devices. A complete review of the continuum models for fuel cells can be found in a recent article by Weber et al.[110]

Because this review only focuses on the coarse-grained models, this section is limited to mass transport in a membrane. Dilute solution theory may be initially adopted for a simple illustration.[112] In this case, the flux of the ion may be described by the Nernst−Planck equation:

$$\boldsymbol{N}_i = -z_i u_i F c_i \nabla \Phi - D_i \nabla c_i + c_i \boldsymbol{v}_0 \tag{36}$$

where F is the Faraday constant, Φ is the potential experienced by the ion of charge number z_i, concentration c_i, the mobility of u_i, D_i is the diffusion coefficient, and $\boldsymbol{v}_0$ is the velocity of the solvent, respectively. The first term is a migration term, and the second is the diffusive flux. Because a hydrated polymeric electrolyte is static, the solvent is assumed to be static and thus the velocity $\boldsymbol{v}_0$ is zero and may be neglected.[111] The diffusion coefficient may be calculated by the Stokes−Einstein relation:

$$D_i = k_B T u_i = \frac{k_B T}{\zeta} \tag{37}$$

From the above, the mobility, u_i, or the friction coefficient $\zeta = 1/u_i$ appears in both the migration term and the diffusive flux term, and hence, the total flux is available with the successful derivation of the friction coefficient.

Albeit for the simplicity, the dilute solution approach does not account for the interactions between solute molecules, and thus, the more rigorous concentrated solution approach is adopted for an electrolyte membrane.[110,111,113] This approach may be introduced with the Stefan−Maxwell−Onsager theory for multicomponent transport:[114−116]

$$\boldsymbol{d}_i = \sum_{j \neq i} K_{ij}(\boldsymbol{v}_j - \boldsymbol{v}_i) \tag{38}$$

where $\boldsymbol{d}_i$ is the driving force of species i balanced against the drag forces between i and all j species. K_{ij} is the friction between i and j. The driving force for transport may be expressed as[116]

https://doi.org/10.1021/acs.chemrev.1c00913
Chem. Rev. 2022, 122, 10710−10745

$$\boldsymbol{d}_i = c_i\left(\nabla\mu_i - \frac{M_i}{\rho}\nabla p - X_i + \frac{M_i}{\rho}\sum_j X_j c_j\right) \tag{39}$$

where c_i, μ_i, M_i, and X_i are the concentration, electrochemical potential, molar mass, and external body force on species i, respectively; p is the pressure, and ρ is the mass density, respectively. The electrostatic forces are accounted in the electrochemical potential. The membrane is fixed to a support and the pinning force, X_M, is balanced with the gradient of the pressure in the membrane (i.e., $\nabla p = X_M c_M$) and satisfies the isothermal Gibbs−Duhem equation:

$$c_M\nabla\mu_M - \nabla p = \sum_{i\neq M} K_{iM}\boldsymbol{v}_i \tag{40}$$

For mobile species (ions and water), the force $\boldsymbol{d}_i$ can be substituted to yield:

$$c_i\nabla\mu_i = K_{iM}(-\boldsymbol{v}_i) + \sum_{j\neq i,M} K_{ij}(\boldsymbol{v}_j - \boldsymbol{v}_i) \tag{41}$$

where the subscript M denotes the membrane and $\boldsymbol{v}_M = 0$. Hence, the above equations for N − 1 nonmembrane species can be written in matrix form:

$$\boldsymbol{\Delta} = \boldsymbol{M}^M\boldsymbol{V} \tag{42}$$

where $\boldsymbol{\Delta}$ and $\boldsymbol{V}$ are N − 1 by 3 matrices for the driving force ($\Delta_{i*} = c_i\nabla\mu_i$) and velocity $V_{i*} = \boldsymbol{v}_i$ (* denotes a row), and $\boldsymbol{M}_{ij}^M = K_{ij}$ for $i \neq j$ and $\boldsymbol{M}_{ii}^M = -\sum_{j\neq i,M} K_{ij}$. It is worth noting that $K_{ij} = K_{ji}$ and the friction coefficient are related to a binary diffusion coefficient:[117]

$$D_{ij} = \frac{RTc_ic_j}{K_{ij}c_T} \tag{43}$$

where c_T is the total molar concentration of all species. For membranes, friction exist between each pair of ions, ion−solvent, ion−membrane, and solvent−membrane.[114,118,119] The first two types are the same as in bulk solutions, which can be further scaled by the tortuosity, τ, and volume fraction of the hydrophilic domain, $1 - \varphi_M$.[119] Archie's law gives that $\tau = (1 - \varphi_M) - \chi$, where χ is the tortuosity scaling parameter, an intrinsic parameter of the membrane, and φ_M is the volume of the backbone.[120]

For ion−solvent friction, the Stokes−Einstein equation gives the following:

$$D_{i0} = \left(\frac{1-\varphi_M}{\tau}\right)\frac{\eta^\infty}{\eta}D_{i0}^\infty \tag{44}$$

where η is the solution viscosity and the superscript ∞ denotes infinite dilute. Equation 44 gives the difference of the viscosity, η, at finite concentration and dilute solution, which is available from Einstein's viscosity equation.[121] Thus, the diffusion coefficient and the friction coefficient maybe computed for associating electrolytes. For ion−ion friction, on the other hand, Debye−Hückel−Onsager theory indicates that for oppositely charged ions:

$$D_{ij} \propto \left(\frac{1-\varphi_M}{\tau}\right)\sqrt{I} \tag{45}$$

where the ionic strength is given by $I = \frac{1}{2}\sum_{i\neq 0,M}^{N} c_i z_i^2$. Therefore, it relates the diffusion coefficient with a certain ionic strength in the membrane to the bulk solution.

For the ion−membrane and solvent−membrane, both the hydrodynamic and frictional interactions are considered at the microscopic scale, and the overall friction coefficient is given by[113]

$$K_{iM} = w_iH_i + \sum_{i\neq M} K_{ij}\left(\frac{H_i}{H_j} - 1\right) \tag{46}$$

where the first term on the right is the hydrodynamic interactions caused by the membrane on i, the second term is the hydrodynamic friction by the membrane on j and in turn, acts on i, and H_i is

$$H_i = \frac{4G\eta}{R_{pore}{}^2\theta_i}\left(\frac{\tau}{1-\varphi_M}\right) \tag{47}$$

where R_{pore} is the radius of the pore related to the polymer volume fraction φ_M, $R_{pore} = d_0\varphi_M^{-m}(1-\varphi_M)^{1/2}/2$, with the dry membrane domain spacing d_0 and swelling parameter m for a particular membrane. G is the semiempirical geometric factor independent of hydration and ion concentration. The parameter θ_i accounts for how species i distributes across the channel. It is equal to unity when i is uniformly distributed but requires a more elaborate treatment for real membranes. The reader is referred to Crothers et al.[113] for values of θ_i for fully hydrated cation exchange membranes.

Briefly, concentrated solution theory considers the interaction of each pair of species: ion−ion, ion−solvent, solvent−membrane, and ion−membrane. Hence, the macroscopic model comparable to eq 36 in matrix form may be written:

$$\boldsymbol{N}_i = -\sum_{j\neq M} L_{ij}c_ic_j\nabla\mu_j \tag{48}$$

where N_i is the molar flux for nonmembrane species and L_{ij} is the element in the symmetric matrix $\boldsymbol{L} = -(\boldsymbol{M}^M)^{-1}$ as defined in eq 42. The molar flux can be further written as

$$\boldsymbol{N}_i = -\sum_{j\neq M}\alpha_{ij}\nabla\mu_{j,n} = -\sum_{j\neq M}\left(L_{ij}c_ic_j - \frac{t_it_j\kappa}{z_iz_jF^2}\right)\nabla\mu_{j,n} \tag{49}$$

for the conditions with zero current in the membrane, where F is the Faraday constant, t_i and z_i are the transference number and charge number of species i, κ is ion conductivity, $\mu_{j,n}$ is the chemical potential of species j relative to that of species n. The introduction of $\mu_{j,n}$, which is defined by $\mu_{j,n} = \mu_j - \frac{z_j}{z_n}\mu_n$, brings convenience for measurements where μ_n is a controlled chemical potential.[114,117]

The friction coefficient and the molar flux include multiple parameters with interactions of a species pair indicated by the subscripts i and j. Other than explicitly keeping the terms of pair interactions, Paddison and co-workers developed a continuum model for hydrated proton exchange membranes,[122,123] which considers the pair interactions but avoids the matrix terms in the friction coefficient of a mobile ion. The model assumes that the ion conducting pore has cylindrical shape with a periodic array of fixed anionic groups, and the pore is filled with water molecules and a targeted hydronium ion. Four types of interactions are considered: H_3O^+−water, H_3O^+−water-pendant ionic group (the interaction of hydronium with an anionic headgroup via water), water-pendant ionic group−H_3O^+, and water−H_3O^+-pendant ionic group. The friction coefficient for H_3O^+ is written as

https://doi.org/10.1021/acs.chemrev.1c00913
Chem. Rev. 2022, 122, 10710−10745

$$\zeta = \zeta^{(0)} + \zeta_2^{(c)} + \zeta_3^{(c)} + \zeta_4^{(c)} \quad (50)$$

where the superscript (0) denotes the traditional friction coefficient due to the mobility in bulk water, i.e., the interaction between H_3O^+ and water. $\zeta^{(0)}$ follows the Stokes' law that $\zeta^{(0)} = 6\pi\eta\alpha$ (i.e., 2.7×10^{-12} kg s^{-1}). The superscript (c) denotes a "correction" to the first or bulk term due to the interactions described above. These correction terms are computed within a statistical mechanical framework and, when compared among themselves as a function of membrane specific parameters including the length and the radius of the pore, density, and protrusion of the pendant anionic groups, may be used to distinguish causes for low diffusivities of the hydronium ions.[123]

2.7. Reverse Mapping

The coarse graining for CGMD, CGMC, and DPD extends the time and length scales of the simulation but obscures many of the details of the chemical structure. Reverse mapping, which restores much of the atomistic details, is necessary when this information is important. Aimed at a near-optimal reconstruction or a short all-atom simulation for relaxation afterward, the two typical reverse mapping approaches are the predetermined fragment database approach[124] and the fragment rotation approach.[125,126] Kuo et al. suggested using a combination of the two for PEMs.[127] Their procedure is briefly described here: a fragment database is initially established from a preliminary all-atom simulation, where multiple conformations are extracted for each CG bead. When the CG simulation is completed, each CG bead is then replaced by a randomly chosen all-atom fragment corresponding to its type, using the center of mass of the fragment. All of the fragments are treated as rigid structures with only the freedom to rotate. For the polymer beads, this mapping procedure starts from the head to the end of the chain, and each all-atom fragment is subsequently rotated by an optimization algorithm until the distance between the connecting atoms of the neighboring fragments falls within 0.9−2.1 Å. The fragment may then be replaced by another fragment from the database if this criterion cannot be matched, and sometimes neighboring fragments are also replaced. Finally, an energy minimization and a short atomistic simulation are performed to further relax the all-atom structure before commencing with production runs.

3. PROTON EXCHANGE MEMBRANES

3.1. PFSA-based PEMs

Perfluorosulfonic acid (PFSA) based PEMs (Figure 3) are an important class of ion-containing polymers, which can be dated back to the 1970s when DuPont first commercialized PFSA ionomers as the trademark polymer Nafion.[13] These types of materials have been known for their significant ion conductivity and chemical/mechanical stability. Hence, PFSA-based membranes have been widely utilized as a solid electrolyte in electrochemical technologies including energy storage and conversion.[6,7] Nafion is composed of a highly hydrophobic polymer backbone (polytetrafluoroethylene (PTFE)) and a randomly pendant functionalized side chain (polysulfonyl fluoride vinyl ether) terminating with a sulfonic acid group, $-SO_3H$, that readily dissociates when hydrated via: $-SO_3H + H_2O \leftrightarrow -SO_3^- + H_3O^+$. This amphiphilicity facilitates nanoscale phase separation, leading to high mobility of the protons and water molecules. It is well understood that there is an underlying interplay of the phase-separated morphology and the mobility of H_3O^+ and H_2O.[14,16,17] However, the exploration of the microstructure of Nafion membranes is still ongoing because some ambiguity exists in the various interpretations of scattering experiments or phenomenological considerations.[20] Apart from the efforts of experimentalists, theoretical studies and simulations have to some extent improved the understanding of the microstructure of Nafion assisted by the advances in computing.[40,48,49,99,128−132]

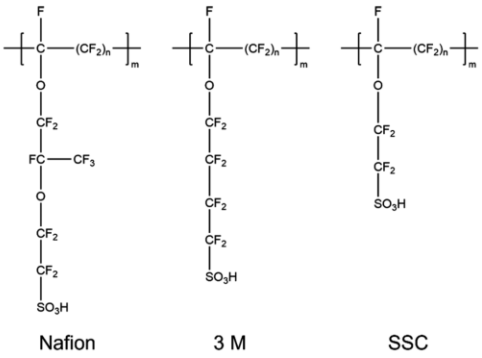

Figure 3. Molecule structures of PFSA-type membranes.

Yamamoto and Hyodo[99] first applied DPD simulations to the study of the mesoscopic structure of hydrated Nafion. These results underscored that nanophase separation spontaneously occurred in the hydrated material into a hydrophilic phase containing water and the hydrophilic side chains and a hydrophobic phase consisting of the backbones. A bicontinuous pathway of Nafion and water regions was embedded in the hydrophobic domain of the Nafion backbone, showing a percolated pore for proton conduction in any direction. This morphology seemingly contributes to the high proton conductivity. The shape of the water clusters was irregular rather than spherical as proposed by early experimental studies.[133,134] Although the water cluster size increased with hydration level, the water clusters were indistinguishable from water channels, which was not the case for the proposed cluster-network model.[134]

A coarse-grained mesoscale model of hydrated PFSA membranes (EW of 1100) comprised of backbone, side chain, and water components was used to investigate the morphology as a function of hydration with a dynamic self-consistent mean field theory.[132] According to the simulated morphology, there exists water-filled micelles surrounded by side chains containing sulfonic acid groups and embedded in the fluorocarbon backbones upon nanophase separation. When the water content is low ($\lambda < 6$), the isolated domains are roughly spherical, while the domains deform into elliptical and barbell shapes as they merge at higher water levels ($\lambda < 8$). Compared with experimental results, the simulated morphology as well as ionic pore size and shape is in good agreement, implying the reliability of these mesoscale modeling and simulations.

The interplay of morphology with mechanical properties is important in many technological applications of ion-containing polymers. The 3D hydrothermomechanical finite element methods (FEM) were applied for the prediction of mechanical

https://doi.org/10.1021/acs.chemrev.1c00913
Chem. Rev. 2022, 122, 10710−10745

properties of PFSA membranes based on simulated microstructures.[135] Spherical and cylindrical ionic domain morphologies as two representatives were selected to predict mechanical performance. Although the overall Young's moduli of both morphologies are similar and the results are consistent with those derived from experiments, the peak stress of the cylindrical morphology is relatively lower than that of the isotropic spherical morphology under the same conditions. The water/PFSA interface endures the highest local stress due to nanoscale phase separation. These results reveal that an extruded cylindrical microstructure has a higher durability than cast spherical membranes consistent with experiments.[135] The mechanical strength of hydrated PFSA membranes was also investigated by Morohoshi et al. using DPD simulations.[136] Their analysis shows that hydrated membranes with narrow water channels have a high mechanical strength but low proton diffusivity, indicating that improving both membrane mechanical strength and proton transport synergistically remains a challenge.[136]

Inspired by the successful application of DPD simulations in Nafion membranes, Paddison et al. performed an extensive investigation of the morphology of PFSA-based PEMs as a function of hydration, molecular weight, equivalent weight, and side chain modification.[40,129,131,137−140] It was pointed out that parametrization using classical atomistic MD simulations and a DFT-based structural optimization was necessary for PFSA-based systems because protons dissociate from the sulfonic acid groups.[131,137,138] Recently, a DFT-based parametrization scheme was developed to effectively treat the charged beads in the DPD simulations, along with a quantitative method to analyze cluster characteristics, the latter to clarify the connectivity of the ion containing and conducting domains.[104,141,142]

The hydrated morphology of Nafion, the short side chain (SSC) membrane, and the 3 M PFSA membrane were examined by systematically varying ionomer equivalent weight (EW), molecular weight (MW), and degree of hydration.[131,137,138] The results show that a significantly greater dispersion of the water domains occurs in high EW ionomers. At similar EW, the local and extended distribution of water changes as a function of the side chain length. Specifically, the size of the water domains appears to increase with an increase in side chain length due to the larger aggregation of the sulfonate groups linked to the longer side chains. Meanwhile, hydration clearly plays a crucial role in the formation of elongated and connected water domains. The water appears in isolated clusters at the lower water contents, and these individual water regions gradually become connected and percolated as the water content is increased. The fully percolated domains clearly serve as ion transport channels or pores. Comparison of the SSC and 3 M PFSA ionomers at the same EW and at a water content above $\lambda = 9H_2O/SO_3H$ indicates that the slightly longer side chains in the 3 M membrane promote the formation of much larger clusters of water. The average size of the water clusters estimated from water−water radial distribution functions (RDFs) range from about 2 nm at $\lambda = 5$ to nearly 13 nm for $\lambda = 16$.[131]

To gain a better understanding of these PFSA-based ionomers, additional DPD simulations were carried out to investigate the morphological differences in terms of the size and connectivity of the water clusters. For the SSC PFSA membranes, an increase in polymer MW facilitates the formation of the fluorocarbon backbone aggregates so as to minimize the energy associated with the chain bending, consequently resulting in elongated and large water channels, especially at high EWs.[137] Similarly, the water clusters transform from being isolated at lower hydration levels to being percolated at higher water contents. The Bragg spacing between water domains shows minimal difference at lower hydration levels, while the spacing significantly increases as the hydration level increases particularly for higher MW ionomers at high hydration.[137] For the 3 M PFSA membrane, the DPD simulations reveal stronger aggregation of the water clusters and lower water uptake with increasing EW (corresponding to a lower ion exchange capacity (IEC)), which is attributed to the increased flexibility of the sulfonate-terminated side chains provided by the longer side chain and higher hydrophobicity of the longer PTFE backbones.[138] It is worth noting that the fluorocarbon crystallinity cannot be examined directly with DPD simulations, in contrast to experiments where estimates may be made of the size and extent of the crystalline PTFE regions. Recently, Sengupta and Lyulin[143] found that Aciplex, which has longer side chains than Nafion, exhibits faster water uptake and a higher rate of water cluster formation preserving the shape of the clusters. The results suggest that the longer side chain Aciplex may be promising for use in fuel cells and flow batteries.[143]

A combination of a model-independent procedure for obtaining structural information from SAXS patterns based on a maximum entropy approach in conjunction with coarse-grained DPD simulations of the morphology of hydrated Nafion was utilized to secure an understanding of the nanophase separated morphology of PFSA-based membranes.[129] It was found that the relationship between nanoscale ionic clustering in PFSAs and the larger scale organization of the fluorocarbon backbone is intimately related but spatially separate. The results obtained from this statistical maximum entropy approach and mesoscale simulations are in quantitative agreement and favor the formation of percolated ionic channel pores embedded in a polymer matrix comprised of fluorocarbon chains.

Although SAXS experiments have provided, at least to some extent, a description of the microstructure of hydrated PFSA-based membranes, complete information remains ambiguous because the interpretation of these results is dependent on the particular model implemented. Wang et al. applied another combination of TEM/STEM equipped with EELS detector and DPD simulations into examining the morphology of dry and hydrated PFSA ionomers at cryo and room temperature.[139] The directly observed morphologies from *Z*-contrast images are in good agreement with those obtained from DPD simulation results. Specifically, the microstructural evolution of 3 M and Aquivion membranes was observed with increasing water content. It was observed that the microstructure in the dry state was generally retained in a partially hydrated state, but reorganization occurred while fully hydrating the membrane. Compared with previous SAXS measurements,[144] the structural inversion of the ionic clusters from a reverse micellar structure to a connected network of polymer rod-like entities occurs when fully hydrated along with the presence of "web-like" ionic channels.[139]

These results indicate that DPD simulations are useful in elucidating the microstructure of polymeric membranes. However, the parametrization of the conservative interactions is still challenging, especially for the systems containing charged beads. Therefore, development of a broadly applicable

https://doi.org/10.1021/acs.chemrev.1c00913
Chem. Rev. 2022, 122, 10710−10745

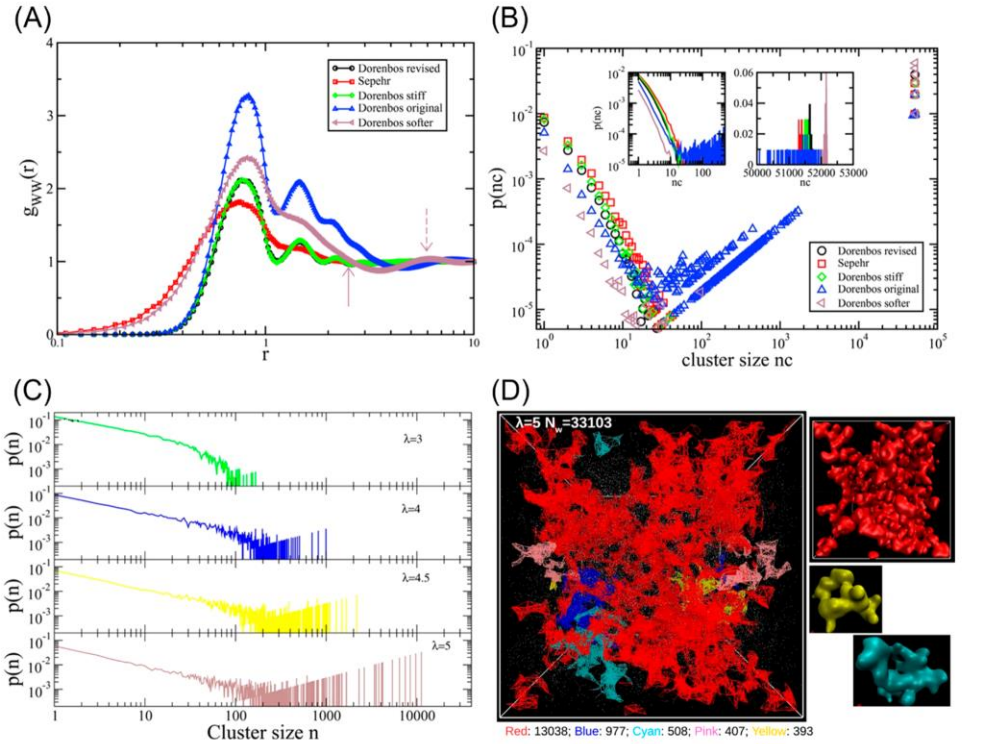

Figure 4. (A) Radial distribution functions (RDFs) of water−water in hydrated Nafion at $\lambda = 9$ for five different DPD parametrizations. As a demo for derivation of the cluster information from $g_{ww}(r)$ of the Dorenbos softer potential: the solid arrow denotes the cluster size, and the dashed arrow refers to the cluster separation. (B) Water cluster size distribution. Chain stiffness and repulsion parameters affect the water structure in a complex manner. All parametrizations show a percolating water domain at $\lambda = 9$. (C) Quantitative cluster size distributions from a cluster analysis algorithm with emphasis on approaching the percolation threshold at $\lambda = 5$. (D) Representative snapshots of color-coded water clusters by the unique cluster IDs at the percolation threshold of $\lambda = 5$. The largest cluster (red) percolates in all three dimensions. Reproduced with permission from ref 141. Copyright 2018 Wiley-VCH. Adapted with permission from ref 142. Copyright 2018 American Chemical Society.

parametrization scheme is an important aspect of these simulations. Sepehr and Paddison[104] developed a DFT-based parametrization method to calculate the DPD pairwise interaction parameters in which the electrostatic interactions for charged beads were treated implicitly without sacrificing computational efficiency. This pragmatic approach has been successfully applied to derive the parameters for hydrated PFSA PEMs[104,141,142] and SEBS (polystyrene-*b*-poly(ethylene-*co*-butylene)-*b*-polystyrene)-based AEMs.[145−148]

The scaling behavior of the polymer chain structure and dynamics of dry and hydrated Nafion membranes were also examined with mesoscale DPD simulations.[142] The results indicate that Rouse theory generally governs the scaling behavior of both dry and hydrated Nafion with various parametrizations for the repulsion parameters. The increase in chain stiffness moderately causes a shrink in the polymer chain and gives rise to slower dynamics (i.e., longer polymer end-to-end relaxation times) for the polymer melt and Nafion. This was explained by the longer residence time of the polymer chain inside the first coordination shell of its neighbors and the stronger back scattering (i.e., longer time to escape from the cage). In contrast, both the polymer and water have faster dynamics in softer repulsion systems, and improved water diffusion occurs for systems containing stiff chains. It was suggested that sufficiently long polymer chains are necessary to mimic the relatively immobile Nafion backbones and proton conducting water domains. The authors pointed out that a direct cluster analysis was more appropriate than the conventional method of measuring water cluster sizes and the separation between the clusters (Figure 4A,B) from water−water RDFs. Additionally, the water cluster distribution results suggest that a connective ionic pore can be successfully demonstrated from all five DPD parametrizations of Nafion, although a threshold of hydration level of $9H_2O/SO_3H$ was corrected to $\lambda = 5$ further study.[141] To gain precise insight into the ion conducting channels in Nafion, the authors[141] developed a quantitative cluster analysis along with realistic microscopic images colored by unique IDs to study the evolution of the hydrated morphology of Nafion over a range of water contents. This analysis shows a wealth of information on water domain size, shape, and connectivity, which is considered as fundamental and challenging for a mechanistic

https://doi.org/10.1021/acs.chemrev.1c00913
Chem. Rev. 2022, 122, 10710−10745

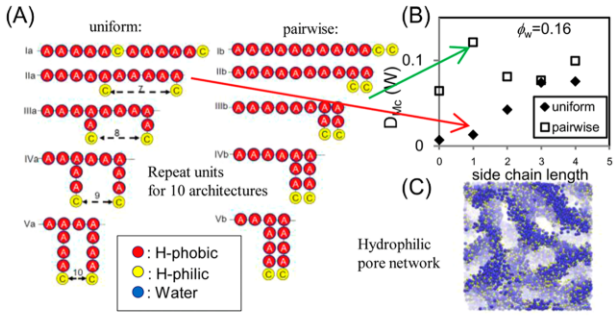

Figure 5. (A) Repeat units of the various simulated polymer types. For the block type I architectures, the hydrophilic C beads are arranged uniformly (Ia) and pairwise (Ib) along the backbone. For the grafted architectures (II–V), the numbers of beads per side chain are 1, 2, 3, and 4 for architectures of types II, III, IV, and V, respectively. For architectures IIa, IIIa, IVa, and Va, the number of bonds or topological distance, $D_{topol,1}$, between nearest C beads are indicated. (B) Time averages of D_{MC} (W) obtained at φ_w = 0.16 plotted against side chain length for uniform architectures and pairwise architectures. (C) Representative pore morphology obtained for the membrane type IIb at φ_w = 0.25. Color codes: yellow, C beads; blue, W beads. Reproduced and adapted with permission from ref 152. Copyright 2014 Elsevier.

understanding of proton transport. A hydration level of λ = 5 was determined as the percolation threshold for the water domains in hydrated Nafion (Figure 4C,D).[141]

To systematically aid in elucidating general design rules in terms of the architecture of the backbones and side chains and also the chemistry of the pendant acidic or basic groups, Dorenbos and co-workers performed extensive studies on the hydrated morphology and the size and shape of ionic channels as a function of EW, hydrophilic site distribution, hydrophilic/hydrophobic side chain length and distribution, doping proton transport channels, and amphiphilic block architecture.[43−48,149−153]

Among the various studies, hydrated Nafion membranes were simulated to determine the effects of branching density by tuning equivalent weights between ∼800 and 1400 g/mol and water contents ranging from 10 to 30%.[48] In all cases, microphase separation was observed to occur, forming hydrophilic pores containing sulfonic acidic groups and water surrounded by the hydrophobic Teflon phase. It was found that both branching density and hydration control the pore morphologies in which ions and water transport across the polymer. Specifically, low branching density corresponding to high EW facilitates the formation of spherical pores connected with severe bottlenecks. This leads to restrictions on the mobility over large length scales. It was reasoned that water molecules can move freely within the larger spherical clusters but are not able to enter and traverse the small bottlenecks into a neighboring larger cluster. Although DPD simulations cannot provide a reliable estimate of the water diffusion constant, the pore morphologies derived from DPD simulations may be used to compute water diffusion by employing Monte Carlo trajectory calculations, in which water is assumed to transport only in the hydrophilic domain. A linear relation between water diffusion constants and branching density was obtained based on these DPD-MC calculations. It was suggested that this approach may be extended to simulate the proton transport within the hydrophilic pores if electrostatic interactions and screening effects between the various ions can be considered properly.[48] Further investigation[47] showed that an increase in side chain length improves the connectivity of the hydrophilic clusters, consequently leading to high long-range water transport for grafted polymers with similar IEC. Nevertheless, increasing the side-chain length in block copolymers (i.e., polymers that consist of hydrophobic monomers and hydrophilic acid-containing monomers) also results in better water transport due to larger water domains rather than better connection.[47]

Another architecture design approach was proposed to improve the long-range water mobility by alternating long and short blocks in the copolymer membranes with hydrophilic acid-containing entities sandwiched between the blocks.[46] The results reveal that the greater the difference in the length of the long and short blocks, the higher the water diffusion is through the hydrophilic phase for polymers with equal IEC, which was ascribed to an increase in the distance between the water clusters.[46] When a hydrophilic acid group was attached to the end of a fixed side chain, tailoring the separation distance between neighboring branching points alters the uniformity in the distribution of side chains and the asymmetry ratio of shorter and longer blocks.[45,153] They observed that a highly nonuniform distribution of side chains and large asymmetry ratio facilitate long-range water diffusion, while increasing the side chain density facilitates the formation of small water domains as well as a shorter distance between the water domains. Examination of the resulting morphologies demonstrates that close adjacent terminal acidic groups distribute along the hydrophilic phase boundaries in pairwise fashion, resulting in larger water-containing pores.[45,153]

In view of the movement of water within the mesoscale morphology, another scheme was proposed by Yuan et al.[154] DPD simulations were used to obtain the equilibrium membrane structure followed by a simulation in which only water beads were allowed to move randomly in the pore morphology of the membrane (i.e., beads belonging to the polymer were fixed). The mean square displacement as well as diffusivity of the water beads was calculated from the simulation trajectories. The results reveal that the water diffusivity increases with hydration, in agreement with experimental data. In addition to the water diffusivity, the tortuosity of the membrane was estimated by comparing the diffusivities of the water beads in the simulated pores with those in ideal cylindrical pores of a similar radius.[154]

https://doi.org/10.1021/acs.chemrev.1c00913
Chem. Rev. 2022, 122, 10710−10745

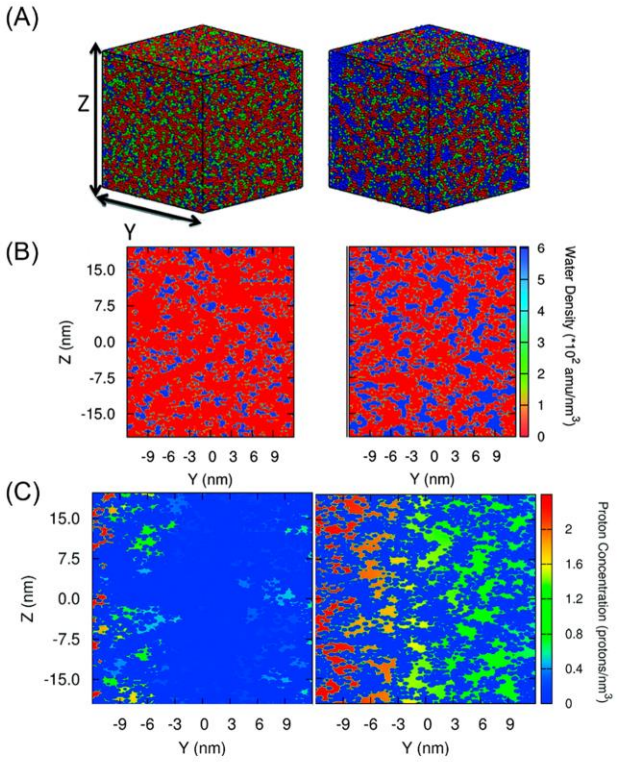

Figure 6. (A) Snapshots of the equilibrated DPD structures for hydrated Nafion at hydration levels of λ = 5 (left panel) and 15 (right panel). (B) Water density distribution for the slice through the middle of each structure using SPH summation. (C) Concentration profiles for slices through the middle of the equilibrated DPD structures shown in (A). Color codes: turquoise, carbon atoms; white, fluorine atoms; red, oxygen atoms; yellow, sulfur atoms. Reproduced and adapted with permission from ref 54. Copyright 2012 American Chemical Society.

To gain additional insight into design rules of high-performance PEMs based on these findings, long side chains with a highly nonuniform distribution of side chains were hypothesized to enhance long-range water diffusion. To this end, the pore size, distance between the pores and the connectivity between domains were examined. DPD simulations were performed on two block-type and eight grafted architectures with similar IEC, in which the hydrophilic acid-containing beads or side chains were distributed uniformly or in a pairwise fashion (Figure 5A).[152] Through an analysis of the water-containing pore networks, it was determined that the smallest pores occur in the block-type membranes (1a of Figure 5A), and the size of pores gradually increases with increasing side chain length in the grafted architectures, while the observed trend is reversed in the pairwise architectures. With regards to water diffusion obtained from DPD-MC approach, the optimal architectures are the one with short side chains for the grafted pairwise architecture and the one with long side chains for uniform architectures, respectively (Figure 5B). These interesting results suggested that the length of side chain and the distribution of the side chains clearly play an important role in governing pore morphology.[152]

Voth et al. pointed out that several challenges must be addressed, including a proper description of the proton hopping mechanism among the functionalized groups and the conformation of water networks due to nanophase separation.[54,155] Both classical MD and coarse-grained descriptions replacing the atomistic representations with collective coordinates were used to study proton transport in polymers as a function of hydration level. Nanophase separation appears to promote the formation of nanometer-sized torturous pathways. Hence, the combination of a coarse-grained description of the membrane structure and novel multiscale methods appears to be a promising approach in resolving proton mobility at the mesoscale in these complex materials.[155] A new multiscale approach that combined coarse-grained modeling with smoothed particle hydrodynamics (SPH) was developed to obtain a qualitative description of morphology with a quantitative description of proton transport in a PEM at the length scale of tens of nanometers.[54] The foundation of SPH is a Lagrangian discretization of the Navier−Stokes equations with a prespecified weight function implemented, which provides a particle-based description of a field variable as an integral over a set of interpolation points connected by smoothing functions. Information including the

https://doi.org/10.1021/acs.chemrev.1c00913
Chem. Rev. 2022, 122, 10710−10745

Table 1. Summary of the Advantages and Disadvantages of Each CG Model[159]

CG model	density	thermodynamic property	$G(r)$	morphology	transferability
SDK	excellent	excellent	poor	good	excellent
IBI	good	poor	excellent	excellent	poor
hybrid	excellent	good	good	excellent	excellent

flux and chemical potential within the membrane was utilized to calculate the macroscopic conductivity by volume averaging. In this scheme, proton transport was effectively coarse-grained by introducing a composition variable that carries the field information with respect to each interacting site. This method was properly validated with hydrated Nafion. An important finding revealed that it is necessary to consider local electrostatics within the polymer in order to accurately estimate the conductivity of the membrane as a function of water content. These results with Nafion underscore the complex interplay of morphology, proton distribution, and transport properties at larger length scales than can be achieved by atomistic MD simulations, consequently leading to a better understanding of the structure−property relations between mesoscopic morphology and proton conductivity (Figure 6). Specifically, isolated hydrophilic regions form at a hydration level of five, consequently leading to significant proton depletion in the middle region (left panel of Figure 6C). Increasing the water content facilitates the expansion of the water clusters to build up percolating networks (Figure 6A,B), in which the protons move through the entire system to form a concentration gradient of protons in the Y direction (right panel of Figure 6C). In addition, this work also revealed the effects of double layer formation within the water pores and the influence of the proximity of sulfonate groups on transport properties.[54]

This SPH-based mesoscale approach was further extended to examine proton transport in polymers with specific morphologies including lamellar, cylindrical, and cluster.[156] The results indicate that the proton conductivity in a cluster morphology is inferior to that for the other two morphologies, suggesting that a potential route to improving the proton conductivity would be to reduce the porosity and tortuosity within the PEM. A position-dependent diffusion constant (PDDC) was found to be determined by the local environment. This was proven to be crucial for proton transport in anisotropic systems based on a comparison of the results obtained by introducing the PDDC and using a uniform diffusion constant. These findings highlight the necessity of considering the inhomogeneity in ion transport, heat conductivity, viscosity, and other dynamical properties.[156]

Another proposed direction was to incorporate protonation/deprotonation processes into mesoscale simulations to account for proton hopping in the materials. Neimark and co-workers introduced dissociable Morse bonds between the protons and the base and water beads into DPD simulations to mimic "Grotthuss" hopping of the protons.[49,50] This technique resolves the larger length scale of nanometer-size phase separation and the transport properties of water and proton simultaneously. Models of Nafion were simulated by explicitly considering proton transport in which the association between the proton and water beads is described by dissociable Morse bonds.[49] The simulated systems demonstrated a percolation transition of the hydrophilic subphase from a collection of isolated water clusters to a water network surrounded by the hydrophobic backbone in all directions at increasing hydration levels. The pore size was observed to vary from ∼1 to 4 nm with increasing water content. In terms of diffusion of the water and protons, the trend in proton diffusivity with changing hydration levels was qualitatively reproduced in light of the diverse experimental data. Specifically, a sharp decrease around the percolation threshold was observed. Comparison of the calculated water diffusivity and the experimental data revealed that there was good agreement at moderate and high hydration but significantly different at low hydration. This was attributed to the dynamic formation and cleaving of temporary junctions between the water clusters when below the percolation threshold. The interplay of hydrophilic subphase connectivity and water diffusion suggests the importance of including a hopping mechanism to correctly predict proton transport behavior.[49]

Application of an external electric field is an effective method to induce morphological changes in ion-containing polymers. However, there are limited modeling and simulation studies on the impact of electric fields on morphology. Allahyarov and Taylor[157] carried out CGMD simulations of Nafion-type membranes to investigate structural changes in the presence of a strong electric field. The applied field invokes the formation of a hexatic array with its axis parallel to the direction of the field, which is comprised of rod-like aggregates of the acidic functional groups. Among these clusters, there was observed to be a variety of shapes including five-wire structures and spiral three-wire shapes. Importantly, these hexatic structures remained after removal of the electric field, their viability being confirmed by a lower computed free energy.[157] The authors also explored the role of structural orientation induced by stretching the polymer backbone of Nafion-type ionomers on proton transport.[158] The applied stretching force gives rise to the ordering of the backbone chain and side chain in different directions. The backbone is aligned along the stretching direction while the side chain tends to be perpendicular to the applied force. This results in enhanced proton conductivity parallel to the stretching direction but reduced proton conductivity perpendicular to the stretching force. It was emphasized that stretching membranes in an effort to enhance proton conductivity is difficult to produce in practice.[158]

Shinoda et al. constructed a predictive CG model for the structure and morphology of PFSA membranes compatible with the Sinoda−DeVane−Klein (SDK) CG water model to describe nonbonded interactions. They extended the parameter set for the force field to examine a hydrated PFSA membrane from thermodynamic and structural data from experiments and all-atom molecular dynamics simulations, improving the structural properties by using an IBI approach.[159] In this work, three approaches including SDK, IBI, and the hybrid SDK/IBI were adopted to construct a CG model of a PFSA ionomer. The SDK-CG model gives a good prediction of density and thermodynamic properties but only marginally acceptable RDFs and morphology. In contrast, the IBI-CG model gives excellent results for morphology and RDFs but only fair description of density and thermodynamic

https://doi.org/10.1021/acs.chemrev.1c00913
Chem. Rev. 2022, 122, 10710−10745

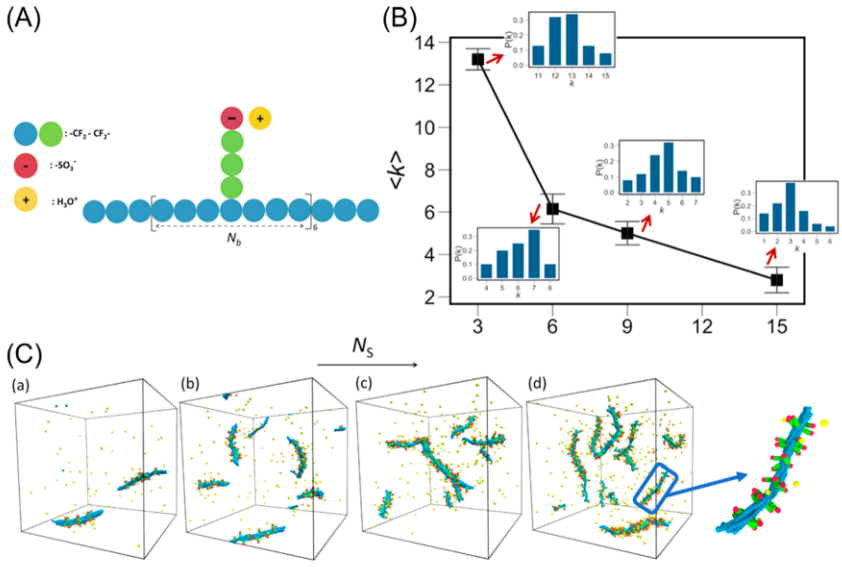

Figure 7. (A) Coarse-grained representation of a Nafion ionomer mapped from atomistic structure. Color codes: blue, apolar beads (backbone); green, apolar beads (side chain); red, anionic; yellow, counterion beads. (B) Effect of the pendant side chain number N_S on equilibrium aggregate size (inset plots show the distribution function of the bundle number vs bundle size k). (C) Snapshots showing the ionomer bundles at different values of N_S: (a) N_S = 3, (b) N_S = 6, (c) N_S = 9, (d) N_S = 15. Reproduced and adapted with permission from ref 163. Copyright 2016 American Chemical Society.

properties. However, the hybrid model is capable of reproducing reasonable structural and thermodynamic properties of PFSAs with either longer polymer chains or longer side chains over a range of hydration levels as well as offering good transferability. Thus, the hybrid model of SDK/IBI-CG was suggested for potential application in realistic PFSA membranes as shown in Table 1.[159]

To extract molecular-level insight from larger length scale simulations, reverse mapping is a considerably potential tool to extend the dimensional and temporal scales without sacrificing the efficiency of CG modeling and simulations. Combination of two reverse mapping methods (predetermined fragment database and fragment rotation) together with molecular dynamic simulations were applied to simulate PFSA membranes with large length scales and to investigate the origin of fracture under a uniaxial tensile loading.[127] The finding shows that the interface regions between hydrophobic and hydrophilic domains are the location where the void growth with tensile loading occurs based on the analysis of voids in the deformed membrane.

Not only do the mechanical integrity and transport properties of the water and ions play a critical role in the operation of a fuel cell, but chemical stability is also required for versatility of application.[8,10,11] It is a significant challenge to model and simulate the chemical degradation of ionomers because of the requirement of multiscale strategies and understanding the specifics of the degradation mechanisms. Eikerling et al.[160] developed a coarse-grained kinetic model for PFSA-based ionomers matched with experimental findings. The authors introduced three types of beads to represent a backbone segment, a trunk part, and a functional group, for which there are inactive and active states. Head groups are assumed to be always in an active state, while trunk units are activated as losing the pendant functional group. This coarse-grained kinetic model provides detailed information on IEC variations and fluorine loss in PFSA-type ionomers. The results indicate that the degradation of functional groups facilitates the backbone scission as well as the subsequent nascent defective head groups, implying that improving the stability of the functional groups is important. Interestingly, an increase in the backbone segment length and side chain length enhances the chemical integrity by reducing the indirect side chain loss and backbone scission, respectively.[160] Franco et al.[161] introduced a multiparadigm model of membrane chemical degradation by combining CGMD simulations and a multiscale cell performance model. The mesoscale membrane morphology is generated by the CGMD simulations followed by the multiscale cell performance model in which the electrochemical reactions and species transport are described with kinetic Monte Carlo simulations coupled with continuum models. The instantaneous PEM conductivity and side chain content are calculated at each time step, allowing a description of the feedback between cell performance and membrane degradation. The results with Nafion membranes obtained from this multiparadigm model show that when a high current density is applied the degradation of the sulfonate groups increases, consequently leading to a decrease in the tortuosity of the pore morphology, in qualitative agreement with experiments. This suggests that this model may be utilized to optimize the operation conditions as well as the chemistry of polymer backbones and side chains for the electrochemical

https://doi.org/10.1021/acs.chemrev.1c00913
Chem. Rev. 2022, 122, 10710−10745

applications in terms of materials degradation and durability.[161]

The self-assembly behavior of ionomer molecules has a vital impact on proton and water transport, water uptake, and chemical durability.[162] Coarse-grained Langevin MD simulations were performed to explain the formation of cylindrical bundle-like aggregates of ionomer chains in dilute solution through the self-assembly of semiflexible ionomer molecules (see Figure 7).[163] In these simulations, ionomer chains were modeled as hydrophobic backbones grafted with functional headgroups bound with side chains. The results illustrate that the interplay of the hydrophobicity of the backbone, chemistry of the side chains and counterions and strength of the electrostatic interactions govern the properties of bundle-like ionomer aggregates. Specifically, strong backbone hydrophobicity of the polymers results in larger bundle sizes, while increasing the grafting density of acid terminated side chains gives rise to a monotonic decrease in bundle size due to the strong repulsive Coulombic interactions between neighboring pendant anionic groups (Figure 7B,C). Regarding the effects of electrostatic interactions, the size of aggregations decreases with the strength of the Coulombic forces for a range of weak interactions but increases as increasing the strength of interaction for a regime of large Coulombic interactions. These findings suggest possible strategies to enhance the stability and performance of PFSA-based membranes by tailoring the architecture of the backbones, the distribution and length of the side chains, and the selection of the solvents.[163] Recently, all atom MD simulations were utilized to develop force fields for a novel coarse-grained model of short and long side chain PFSA-based ionomers.[164] Examination of the structure and dynamics of these systems at various hydration levels and different proportions of 2-propanol mixed solvents elucidate the effects of the chemistry of the side chain on the aggregation of ionomer molecules and their transport properties. Compared with long side chain Nafion membranes, the distribution of water clusters is more dispersed in the short side chain Aquivion when the water content is low. Increasing hydration level improves the connection between the water domains, while adding 2-propanol solvent reduces the water network connectivity, leading to 4−5 times smaller diffusivity of hydronium ions rather than that of water molecules. Strong electrostatic interactions retard the movement of hydronium ions, which may be mitigated by adding more water molecules due to the solvation stabilization of the hydronium ions.[164]

The flooding on the cathode side and drying out on the anode side are still a challenge to resolve in operating PEM fuel cells. The electro-osmotic drag coefficient can be used to measure the ratio between the fluxes of solvent molecules and ions in the presence of an external electric field. Nevertheless, electro-osmotic drag coefficients have been estimated with theoretical modeling and simulations.[165,166] Molinero et al.[167] developed a coarse-grained scheme with an efficient model of water and ions to study the effect of membrane structural parameters, operational conditions, and ion concentration on the electro-osmotic drag. Significant findings from their studies reveal that electro-osmotic drag decreases with decreasing pore size in the membrane but increases with the ion concentration. Stronger Na^+−water interactions results in larger electro-osmotic drag than Cl^-−water interactions, which is confirmed by longer lifetime of the water molecules in the first solvation shell of Na^+. Interestingly, electro-osmotic drag in PEMs is larger than that in AEMs.[167]

Although united atom MD simulations cannot access the length and temporal scales of coarse-grained DPD simulations, they are still capable of modeling larger systems without compromising much of the detailed atomic-level information. Allahyarov et al.[168−170] applied united-atom MD simulations to investigate the effects of the lengths of the backbone segment and side chain in different confinements on the hydrophilic cluster morphology and proton transport in Nafion-type ionomers. The authors modeled the variations of Nafion under low hydration levels in which the lengths of the backbone segments and side chains are up to 2- and 3-fold higher than in original Nafion, respectively.[170] The results show that increasing the EW of homologous ionomers enlarges the hydrophilic sulfonic acid-containing cluster size accompanied by the sulfonate density decline, resulting in a lower contribution to proton diffusion from the proton hopping between sulfonate groups with or without water molecules involved. One approach to mitigate this unfavorable effect is to increase the side chain length without changing the EW of the membranes. The longer side chains facilitate the formation of larger clusters with higher sulfonate density, which to some extent improves proton transport.[170] Another study investigated the morphological changes induced by a cylindrical pore confinement in Nafion-type ionomers.[168,169] They found that the pore diameter and sulfonate density play an important role in ionic cluster shape and transport properties. Specifically, a branched wire-like network was observed along with the pore axis in the larger pores, while sulfonate head groups tend to form smooth clusters in the center part of the pores as the pore diameter is decreased. Interestingly, decreasing the length of the backbone segments enhances the smoothness of the ionic cluster distribution in the center of the small pores due to the increased sulfonate density. This results in larger ionic diffusivity along the pore axis. Additionally, ballistic ionic motion was observed in the narrow pores, seemingly due to the collective motion of the ions in such a limited space.[169] Their simulation results indicate that the optimal conditions for enhanced ion transport are pores with medium length side chains under moderate hydration levels, for which the sulfonate ions have sufficient flexibility but do not reach the center of the pore, leading to a distribution of less structured water around both the ions.[168]

The porous catalyst layers (CLs) are important components in PEMFCs, in which a PEM is sandwiched between Pt nanoparticles and carbon substrates to provide proton pathways during operation of a fuel cell. Because of the complex microstructure of these building blocks, it is crucial but challenging to investigate the microscopic structure and transport properties as well as electrochemical phenomena in the CLs. Keffer et al. used united atom MD simulations to study the structural and transport properties at the electrode/electrolyte interface in hydrogen-based PEMFCs.[171] A mixture of Nafion, water, and hydronium ions in the simulations were observed to reach the catalyst surface of small gaps (7.4 Å) in the graphite, suggesting that proton transport could occur from the catalyst to the membrane through ionic channels, while no wetting of the graphite or the catalyst surface was observed for gaps of 14.8 Å. Additionally, the diffusivity of water in systems with a graphite gap of 7.4 Å width decreased by at least an order of magnitude compared to systems with no gap. The results from these simulations suggest that there may not exist

https://doi.org/10.1021/acs.chemrev.1c00913
Chem. Rev. 2022, 122, 10710−10745

a pathway for efficient proton transport from the catalyst surfaces to the PEM when the gaps between them are larger than 1 nm in the electrodes.[171]

Yuan and co-workers[172−174] applied large-scale MD simulations to understand the mesoscale morphology formation of CLs to gain a better understanding of the interplay of microstructure and ion transport in the complex and multiphase porous structure. Following the step-by-step experimental fabrication process, the authors first added a Pt/C catalyst by randomly dispersing it in the simulation box, then added Nafion chains, and finally followed by evaporating the residual solvent.[174] The equilibrium morphology, confirmed by the pair correlation functions, revealed that the ionomer backbones exhibit good contact with the Pt/C agglomerates by covering the Pt/C surface with side chains located at the interface of water-containing pores. Several methods were used to estimate that the size of the primary pores was 2−10 nm.[173] In addition, the size distribution of Pt nanoparticles was found similar to the Feret's diameters in the range of 2−6 nm, which was in reasonable agreement with TEM images. The distribution of primary pore size as computed with a rolling probe method reveals that weak polar solvents facilitate the formation of more complex and larger pore structures, suggesting that the CLs fabricated with nonpolar solvents have larger agglomerates with well-developed pores (i.e., better performance).[174] By introducing smoothed particle hydrodynamics (SPH) coupled with a finite element modeling (FEM) method incorporating elementary kinetic reaction schemes, the authors proposed an approach to secure detailed information on the meso- and macroscopic transport properties in the complex structures of the CLs.[172]

In addition to coarse-grained modeling and simulations, continuum models have been developed to examine the transport of water and ions in these polymeric membranes. Paddison et al.[122,123] derived a mathematical method to compute the effective friction coefficient of hydronium ions in assumed cylindrical pores of a PEM, in which sulfonate groups are attached on the wall and water molecules added inside the pore. The transport of the mobile species (i.e., hydronium ions) was described based on the interactions among the H_3O^+, H_2O, and SO_3^-. Friction and diffusion coefficients were calculated as a function of the distribution of the functional groups, length of side chains, and structural parameters of the cylindrical pores. The results indicate that long side chain intrusion and high local density of the sulfonate groups generally reduce the H_3O^+ diffusion coefficient in pores with a constant number of sulfonate groups and fixed volume. It also suggests that enhanced proton transport occurs in the pores with larger radii and shorter lengths.[122]

Weber and Newman[175,176] used a continuum model based on concentrated solution theory to determine the transport properties of PEMs. The model was utilized for both vapor- and liquid-equilibrated transport. Hydration and membrane properties were selected as important parameters in the modeling. They found that the vapor-equilibrated transport coefficient increased with increasing hydration but reached a plateau when the water content was at $\lambda = 14$. The model also showed that the transport coefficient increases with temperature for both vapor- and liquid-equilibrated membranes.

Delacourt and Newman studied the multicomponent transport in cation exchange membrane for both H^+ and K^+.[114] The authors derived the macroscopic parameters including conductivity, transference number, and the water electro-osmotic coefficient. These were characterized as functions of binary interaction parameters at zero current. The two-cation model was then used to model the CO_2/H_2O electrolysis cell, where the cell was a Nafion membrane with aqueous solution of potassium and proton on one side and an electrode with oxygen on the other side. Proton fraction and hydration level were predicted through the electrolyzer, and the membrane thickness, anode potential, and net water flux per cation flux were also modeled as a function of the current density.

An analytical model for water and charge transport in highly acidic and highly confined systems was developed in which three factors, including acidity, confinement, and connectivity, were considered.[177] The results show that both MD simulation and confined random walk theory are capable of quantitatively reproducing experimentally measured self-diffusivities of water in PFSA membranes.

More recently, the multicomponent phenomena in cation exchange membranes were investigated by Crothers et al. using the model of concentrated-solution transport.[113] It considered the porous medium theories as the scaling factor for the tortuosity. This research first modeled the multicomponent of mixed cation from membrane in water, which predicted the water volume fraction and the binary interaction parameters. Then, the transport in concentrated electrolytes was under investigation. The results showed that macroscale ionomer properties including conductivity, permeability, and transference numbers were controlled by the ion type and concentration in the external solution, which altered the solvent volume fraction and viscosity in the hydrophilic pathways of the membrane. The authors developed a physicochemical scheme to evaluate ion exchange membrane performance in multicomponent systems with coupled transport considered.

3.2. Alternatives to PFSA-based PEMs

Despite the high performance of PFSA-based membranes, there remain several challenges in terms of techniques and economics.[6,178] Water management is demanding because there are a variety of water transport under the complex environment of PEMFCs. Water moves from anode to cathode because of the electro-osmotic drag caused by the proton transport, which results in a dry anode side and a flooding cathode side. Meanwhile, the reaction at the cathode side generates more water. These processes would lead to a high concentration gradient of water, which consequently gives rise to water back diffusion from the cathode side to the anode side. The nonuniform water distribution in turn results in the reduction of proton conductivity as sufficient water content facilitates proton dissociation and transport. This requirement of hydration restricts the operational temperature in the range of ∼0 to ∼100 °C, while high temperature can enhance the cathode reactions and reduce the catalyst poisoning. In view of commercialization, the high costs of Pt-based catalysts and PFSA-based membranes hinder the wide application for fuel cells in everyday life.[178]

Therefore, alternatives to PFSA-based membranes have attracted increasing efforts to search for low cost and high-performance materials. Several potential candidates have been proposed such as sulfonated poly(ether−ether−ketone) (sPEEK), sulfonated poly(phenylene) sulfone ($sPSO_2$), polybenzimidazole (PBI), disulfonated poly(arylene ether sulfone) (BPSH), sulfonated polyimide (sPI), and poly-

https://doi.org/10.1021/acs.chemrev.1c00913
Chem. Rev. 2022, 122, 10710−10745

(arylene thioether sulfone) (PATS).[12,15] These materials also exhibit promising performance in terms of microphase separation, water cluster networks, and water and proton transport. Thus, the combination of experimental techniques and multiscale modeling and simulations has gained to some extent fundamental understanding of how the chemical and structural parameters govern the performance of these membranes.

Among these potential alternatives, the sPEEK ionomers possess advantages of simple preparation, tunable architecture, and high chemical and dimensional integrity as well as low cost. In addition, the sPEEK membranes show lower methanol permeability and smaller electro-osmotic drag in comparison to the benchmark Nafion membranes.[179] Thus, extensive research work has been undertaken to understand the structure−property relationships for these membranes.

Khalatur et al.[130,180] utilized both particle-based classical MD simulation and a field-based mesoscale dynamic density functional theory (DDFT) approach to investigate the influence of chemical composition, backbone architecture, and hydration level on the morphology of hydrated sPEEK ionomers. Both methods simulated the self-organization process leading to nanophase separated morphologies that are consistent with each other.[180] In their findings, the hydrated sPEEK morphology features irregular shapes without long-range order due to microphase separation. With regard to the order parameter (defined as the volume average of the ratio of local density squared to overall density squared), there exists an optimal degree of sulfonation at a value of 0.6, which suggests one strategy to balance the microphase segregation of hydrophobic and hydrophilic domains may be by tuning the degree of sulfonation. Although longer block segments enhance the proton conductivity, significant membrane swelling occurs, and this decreases the mechanical strength. High water contents facilitate the formation of a percolating tricontinuous morphology, in which the water-containing pores demonstrate irregular sponge-like networks with bottlenecks. Compared to Nafion membranes, the water channels are narrower but have comparable average cross-sectional areas. The estimated percolation threshold in sPEEK is lower than in Nafion. Surprisingly, the sPEEK chains were determined to be more flexible than anticipated.[130,180]

Recently, a nonempirical fragment molecular orbital (FMO) method[105] was developed to calculate the repulsive parameters between DPD beads, and this was successfully applied to PEM systems by Okuwaki et al.[107] The reliability of this FMO−DPD scheme was confirmed by comparing simulation results of Nafion and sPEEK membranes with experimental data. Their findings demonstrate the difference in the water-containing pore morphology between Nafion and sPEEK ionomers. Specifically, the hydrated sPEEK cluster analysis indicates less connectivity among the water domains in comparison to hydrated Nafion membranes.[107]

To enhance the phase separation in PEEK-type ionomers, multiblock copolymers grafted with pendant sulfoalkoxyl side chains were studied experimentally along with a dynamic mean-field DFT method.[181] Indeed, the nanophase separation can be significantly improved by high density of sulfonic acid groups as well as the flexibility of side chains, consequently giving rise to high proton conductivity and good mechanical stability. Specifically, the increase in block length enhances the water retention capacity and facilitates the formation of percolating ion channels. The results suggest that these types of copolymers can be potential alternatives to PFSA-based membranes for fuel cell applications.[181] Another direction for improving microphase separation is to blend sPEEK-type ionomers with other polymers. Wang et al. performed DPD simulations to investigate the effects of adding poly(ether sulfone) (PES) to sPEEK.[182] Their results demonstrate that the addition of PES facilitates the nanophase separation and the formation of larger water-containing clusters. The optimal ratio of sPEEK/PES was found to be 4:6, for which the largest water channels form to improve the transport of water and protons.[182] Recently, Ma et al.[183] performed DPD simulations to study the compatibility between sPEEK and PVDF polymers. The results show that the compatibility of sPEEK/PVDF is poor, which can be significantly improved by grafting PVDF with PSSA (PVDF-*g*-PSSA). The optimal degree of sulfonation and grafting rate were determined to be 50% and 10%, respectively. The blend of sPEEK/PVDF-*g*-PSSA shows preferable compatibility with the blend proportions of PVDF-*g*-PSSA in the range of 10−20%, in which a channel network was observed. Importantly, the addition of PVDF-*g*-PSSA is a key factor in enhancing proton conductivity along with mechanical stability.[183]

To capitalize on a coarse-graining strategy, Kumar et al.[184] systematically study a variety of structural distributions including bonded and nonbonded pairs of hydrated sPEEK, with a 50% degree of sulfonation. A single chain system was initially undertaken with atomistic MD simulations, which was subsequently used to develop CG potentials via an iterative Boltzmann inversion approach. These CG potentials were extended to multichain systems as well as longer single-chain polymers. Various structural distributions were collected by back mapping the systems with efficient CG simulations. The results show that the maximum possible coarse-graining level for this system is 71:3 CG mapping (i.e., representing a 71-atom repeat unit with 3 CG beads) without sacrificing the chemical specificity of the polymer. The water-containing clusters were observed to be distributed in the polymer matrix with the back-mapped system. It is worth noting that the developed CG potentials are not transferable between systems with different conditions including the temperature, degree of sulfonation, and hydration level.[184]

Sulfonated Diels−Alder poly(phenylene) (SDAPP) has been explored as a potential candidate for fuel cell applications because it possesses a rigid aromatic backbone with sulfonic acid groups directly attached to aromatic rings. Frischknecht et al.[128,185] undertook significant efforts to understand the interplay of microscale morphology and the transport of water and protons in SDAPP membranes using both experimental and theoretical techniques. The effects of hydration and degree of sulfonation along with temperature were examined using multiple computational and experimental strategies.[185] Both methods confirmed microphase separation. The isolated water-containing clusters occur at relatively low water contents, and the addition of water facilitates the formation of percolated water networks. The difference between diffusivity calculated with electrical impedance spectroscopy and those determined from PFG-NMR measurements indicates that the vehicular transport of proton dominates at low sulfonation and hydration levels while structural diffusion of protons contributes more to the conductivity at higher degrees of hydration and sulfonation.[185] On the basis of the atomistic MD simulations, a modified DPD model of SDAPP polymers was used to study the morphology

https://doi.org/10.1021/acs.chemrev.1c00913
Chem. Rev. 2022, 122, 10710−10745

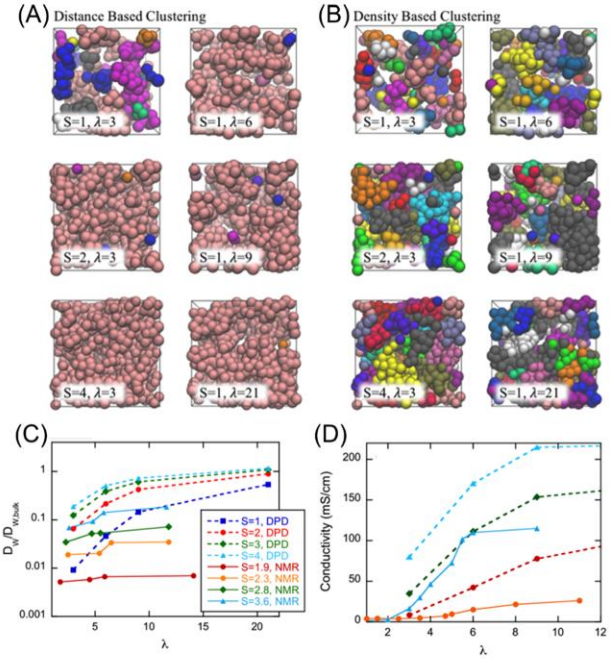

Figure 8. Representative snapshots showing results from (A) the distance-based clustering algorithm and (B) the density-based clustering algorithm, for various degrees of sulfonation, S, and degrees of hydration, λ. Only S and W beads are shown. Each cluster has a unique color. (C) Water diffusion constant relative to the bulk for DPD simulations and NMR measurements. (D) Conductivity calculated from the DPD proton diffusion constant for $S = 2$ (red circles), $S = 3$ (green diamonds), and $S = 4$ (blue triangles), and measured by impedance spectroscopy at 30 °C, for $S = 2.3$ (orange circles) and for $S = 3.6$ (blue triangles). Reproduced and adapted with permission from ref 128. Copyright 2019 American Institute of Physics.

and proton diffusion mechanism, in which the intramolecular parameters were derived from an iterative Boltzmann inversion and a Morse potential between the proton and water beads as well as proton and sulfonic acid groups, was introduced to mimic the proton hopping mechanism.[128] In addition to a distance-based cluster analysis (see Figure 8A), a density-based cluster analysis was conducted from the simulation trajectories to provide detailed information about the percolated clusters especially for the overlapped clusters (shown in Figure 8B). The clustering results obtained with these two methods indicate that there are some clusters that are bridged by narrow regions. With regard to transport of water and protons, the water diffusivity increases with hydration and sulfonation (Figure 8C), which is in good agreement with NMR data in terms of the trends. In addition, when fully percolated water-containing clusters appear through increasing the hydration and sulfonation, proton hopping becomes dominant, leading to a high proton conductivity (Figure 8D). This combination of experimental and simulation results confirms that pore morphology plays a crucial role in proton conductivity in SDAPP membranes.[128]

The $sPSO_2$ ionomers are comprised of phenyl rings linked by electron-accepting sulfone groups ($-SO_2-$) and functionalized with sulfonic acid groups.[186] To obtain molecular level insight into the characteristics of hydrated morphology of this type of membranes, DPD simulations were utilized to investigate the influences of EW, MW, and hydration level on the morphology, water domain connection, and water cluster distribution.[140] The findings show that water molecules tend to evenly disperse within the hydrophilic phase of the membrane compared to typical PFSA ionomers at the same hydration level, which indicates weak microphase separation, especially for low water contents. The increase of sulfonation degree enhances the phase separation and consequently leads to percolating water pores. Interestingly, the effect of MW is smaller on $sPSO_2$ ionomers than PFSA-based membranes. It suggested that the well-connected hydrophilic channels contribute to the high proton conductivity in the $sPSO_2$ ionomers.[140]

The cross-linked sulfonated poly(1,3-cyclohexadiene) (xsPCHD) is another alternative ionomer to PFSA-type membranes because its six-atom ring-like structure provides high chemical and mechanical stability and superior proton conductivity at high temperatures.[187] Keffer et al.[188] developed a new coarse-grained model of sulfonated xsPCHD membranes based on atomistic MD simulation results using a simple inversion of the probability distribution functions and an iterative Boltzmann inversion approach for bonded and nonbonded CG potentials, respectively. After the validation of these CG potentials through CGMD simulation of various architectures of xsPCHD, the authors extended the model to simulate hydrated membranes.[189] It was found that the

https://doi.org/10.1021/acs.chemrev.1c00913
Chem. Rev. 2022, 122, 10710−10745

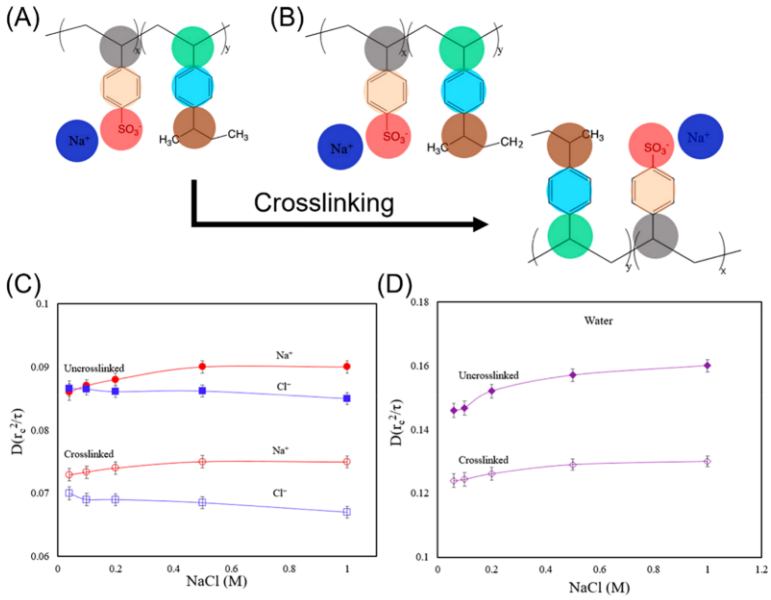

Figure 9. Chemical structure of sulfonate polystyrene-*co*-divinylbenzene with the corresponding DPD model for (A) non-cross-linked and (B) cross-linked polymers. (C) Diffusion coefficient of Na^+ and $\overline{Cl}$ ions and (D) diffusivity of water in non-cross-linked membrane (closed symbols) and in the cross-linked membrane (open symbols) as a function of NaCl concentration. Reproduced and adapted with permission from ref 192. Copyright 2019 American Institute of Physics.

transferability of the CG potentials at different hydration levels was limited without considering the solvent effects explicitly. The results still provide molecular level understanding of the interplay of the structure and the transport of water and hydronium ions.[189]

Sulfonated polyimides (sPIs) have proven to be a promising alternative for fuel cell applications because of their high performance at elevated temperatures. The sequence distributions of hydrophobic and hydrophilic units in sPI copolymer chains play an important role in nanophase separation and in the shape and size of the water pores over a range of hydration levels. Hu et al.[190] carried out DPD simulations of diblock copolymers, alt-copolymers, and multiblock copolymers. The simulated morphologies demonstrate that the multiblock copolymer has more dispersed water channels than the diblock copolymer and the alt-copolymer, which generally means that water diffusivity is higher in the multiblock copolymer. With regard to mechanical stability, decreasing the block length gives rise to large Yong's modulus, and high hydration levels mitigate this effect of sequence distributions. The authors proposed that the multiblock sPI copolymer has tremendous potential due to the high diffusive coefficient of water, good swelling resistance, and favorable mechanical properties.[190]

Disulfonated poly(arylene ether sulfone) (BPSH) and the well-known PFSA ionomers were simulated by using a DPD scheme with greater time and length scales.[191] Among the hydrated microphase segregations, the cluster network model proposed by Gierke[18] was observed at very low hydration levels. When the water content was increased to 30 vol %, the water clusters were observed to form continuous microphase segregations, similar to the cluster channel network model by Kreuer.[14] The configurations show the characteristics of the modified cluster network model by Newman[176] at moderate water contents. The authors concluded that PFSA-based membranes show clearer characteristic features of the physical models than BPSH-type membranes. In addition, the radial distribution functions of the water beads indicate that the BPSH ionomer has a higher water uptake and tends to form water clusters at lower hydration levels in comparison to PFSA ionomers. The simulated morphologies were found to be in good agreement with experimental AFM data.[191]

An efficient approach to strengthen the dimensional integrity of hydrated membranes and reduce the swelling of the membrane is by cross-linking the polymer chains. However, the influence of cross-linking on the transport properties of water and ions has not been fully understood. Aryal and Ganesan[192] used coarse-grained DPD simulations to investigate the effect of the degree of cross-linking in sulfonate polystyrene-*co*-divinylbenzen on the water and ion transport. Comparison between the DPD simulations results and atomistic MD results[193] confirmed the validity of this mesoscale scheme based on non-cross-linked membranes. The cross-link formation was simulated by attaching bonds between the aliphatic carbon beads when the distance between them satisfied the criteria (Figure 9A,B). The major findings reveal that the diffusivities of water and ions decrease with increasing the degree of cross-linking of polymer chains (shown in Figure 9C,D), which are ascribed to the structural changes due to the cross-linking, leading to slower dynamics of polymer chains. Importantly, Figure 9C demonstrates that

https://doi.org/10.1021/acs.chemrev.1c00913
Chem. Rev. 2022, 122, 10710−10745

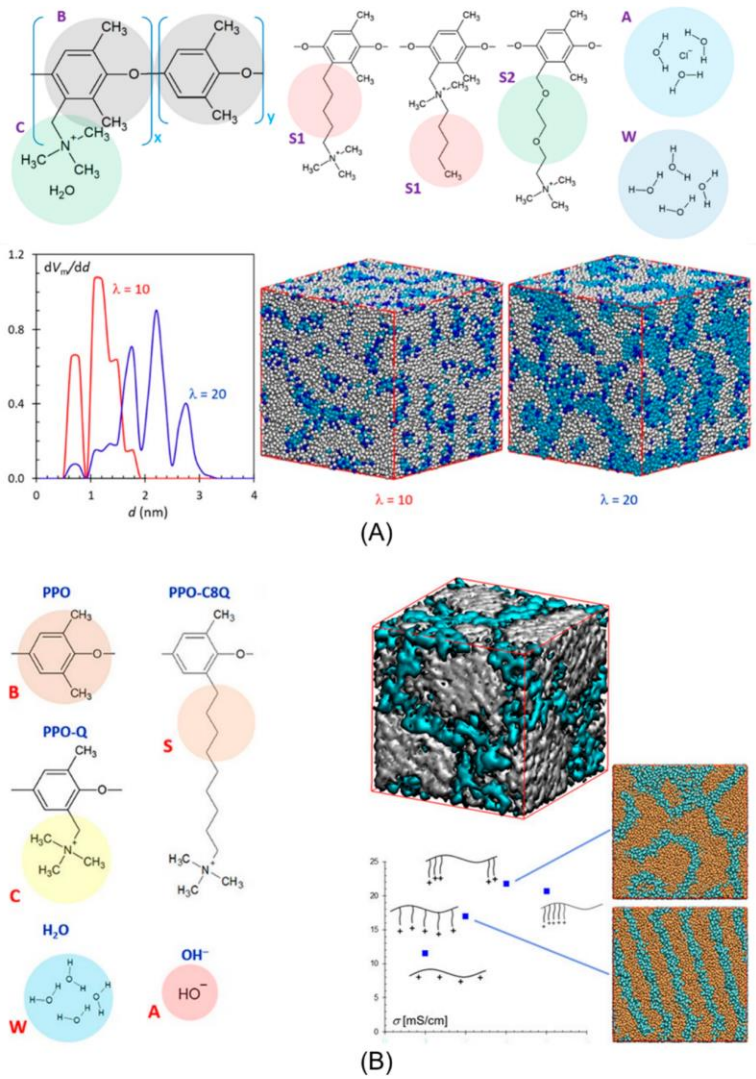

Figure 10. (A) DPD simulations of PPO-TMA in Cl^- form.[53] (upper) Coarse-grain model where a chloride ion is grouped with four water molecules. (lower) Pore size distribution and phase separation for PPO-C8-TMA (B) a DPD simulation of PPO-TMA in OH^- form.[52] (left) DPD bead definitions. (right) Phase separation for the different topologies. The hydroxide ion was modeled as a special bead experiencing a Morse potential. Reproduced and adapted with permission from ref 52. Copyright 2019 American Chemical Society. Reproduced and adapted with permission from ref 53. Copyright 2020 American Chemical Society.

increasing the concentration of NaCl moderately enhances the diffusivity of Na^+ and enlarges the difference between Na^+ and Cl^- diffusivities as the Cl diffusivity is nearly insensitive to NaCl concentration. These results are in good agreement with experiment results.[192,194]

Addition of a salt into a polymer solution can also induce various cross-linking due to metal coordination, which gives rise to changes in membrane morphology, cluster formation, and rheological properties. Neimark et al.[195−197] used DPD simulations of polymer solutions to gain mechanistic insight into the morphological and rheological changes due to metal coordination in the presence of multivalent cations. The coordinating metal was modeled as a 3D complex of planar, tetrahedral, or octahedral geometry, in which the metal cation

https://doi.org/10.1021/acs.chemrev.1c00913
Chem. Rev. 2022, 122, 10710−10745

was surrounded by either four or six dummy beads that correspond to coordination sites. A Morse potential was introduced to simulate the dynamic coordination states where dissociation and formation of a link between the vacant coordination site and a ligand of the polymer chain occur. Simulation results of polyvinylpyrrolidone−dimethylformamide solutions reveal that coordination-induced interchain and intrachain cross-links lead to a sol−gel transition into a weak gel phase with increasing of the metal concentration. The metal grafted polymer chains were also observed when there was only one link to them. Different cross-links were found to have various effects on the morphology and viscosity. Specifically, the interchain cross-link changes the viscosity of a polymer solution as a power law function of the metal concentration with an exponent of 1.18, while the grafted metal atoms and intrachain cross-link have minimal effect on the viscosity.[195]

Recently, Neimark et al. extended this strategy to metal-substituted polyelectrolyte membranes with charged metal ions.[196] Their findings reveal that the increase of valency and coordination strength of the metal ions gives rise to more spherical and larger water pores. This is due to the formation of the interfacial cross-links between the hydrophobic and the hydrophilic phases that strengthen the interfacial tension and reduce the interfacial area. The size of water clusters increases with the hydration level and water clusters as large as 6.5 nm in diameter appear in the system of trivalent ions with strong metal−sulfonate interactions at high hydration levels. In addition, water diffusion coefficients were obtained from both the dynamic mean-square displacement and the static DPD-MC approach. These results demonstrate that the increase in the ion valency and metal−sulfonate coordination strength hinders water mobility and transport in the membranes. Comparison of the diffusivities calculated with both methods confirms that it is crucial to account for thermal fluctuations of the polymer matrix at low hydration and the collisions of water beads with metal ions at high hydration levels. It is worth noting that it is necessary to allow for the metal−sulfonate coordination effects rather than a purely electrostatic interaction in terms of the dynamics of the ions.[196]

4. ANION EXCHANGE POLYMERS

In this section, anion exchange polymers refer to solid-state materials where the polymers contain the covalently bonded cationic groups, and the system achieves a neutral charge due to the existence of low-molecular-weight anionic counterions, the latter of which are mobile. Common materials include anion exchange membranes (AEMs), which may be hydroxide ion conducting, as well as conducting other types of small anions. Polymerized ionic liquids (polyILs) are another type of material that will be discussed in this section. In polyILs, only one component of the ionic liquid counterpart is polymerized, and the other component is a free or mobile counterion. In addition, other systems, including polyanions with nanoparticles or substrates, will also be discussed.

4.1. Anion Exchange Membranes

Functionalized poly(phenylene oxide), or PPO-based AEMs, are widely simulated AEMs with coarse-grained methods. The phenylene ring of the PPO is typically functionalized by a cationic side chain, as shown in Figure 10. Molinero et al. performed extensive multiscale simulations of various AEMs.[198−200] Their work focused on PPO functionalized by quaternary ammonium groups with chloride serving as the counteranion. They chose a "partially" coarse-grained model: the PPO backbone was represented at the united atom level, with all heavy atoms. However, water, chloride ions, and the quaternary ammonium groups were coarse-grained and represented by a single bead. Despite the various degrees of coarse graining, the model successfully reproduced many structural properties similar to all-atom simulations. Phase separation was observed, along with the formation of water channels. The simulated morphology was used for the finer models, including all-atom MD and reactive force field MD to study hydroxide ion transport and the degradation of the membrane. Furthermore, the established CG model was utilized to study the AEMs consisting of block copolymers. The blocks included pure PPO, PPO with alkyl side chains, PPO-QA, PPO-C_n-QA, and PPO-QA-C_n. These blocks, in different arrangements, enable a variety of block copolymers. The CG simulations revealed that the transport properties were sensitive to the water content, but robust against the molecular structure of a polymer electrolyte, which was attributed to the similar structures of the hydrophilic domains under a similar hydration level.

Yang et al.[201] performed CGMD simulations in addition to their experimental studies of PPO-QAPc AEMs. These consisted of a PPO backbone functionalized with quaternary ammonium phthalocyanine. The degree of coarse graining consists of lumping three to six heavy atoms into a single bead, except for the metal atom in the phthalocyanine. The Martini Force field was employed, and the simulated morphology showed a microphase separation where hydroxide ion containing channels were observed, consistent with experimental TEM images.

Lee[52,53] conducted DPD simulations of mesoscale structures of the hydrated AEMs: poly(phenylene oxide) (PPO) functionalized with tetramethylamine (TMA) [PPO-C_n-QA], in either Cl^- or OH^- form. These DPD simulations included explicit electrostatic interactions to the standard DPD model. To avoid the divergence when the charged beads overlapped, a charge smearing technique was adopted such that the point charge was distributed in an electronic cloud by a Slater-type function.[87,202] The coarse graining consisted of grouping four water molecules into one water bead. However, for the chloride and hydroxide ion forms, they chose two different strategies for the counterion. In the simulations of Cl^- form, the anion was lumped with four water molecules. For the polymer chains, one PPO monomer was represented by a single bead, and the same strategy was adopted for the quaternary ammonium headgroup. Phase separation was observed especially for the materials with side chain linkers. A pore size distribution (PSD) analysis was conducted using Poreblazer 3.0.2,[203] which provided useful information concerning the size and distribution of ion conducting channels. As anticipated, higher hydration promoted an increase in the size of these channels (Figure 10A). Ion conductivity was computed with the Nernst equation, but the calculated values were distinctly different from those available from experiments, indicating the limitation of the DPD method from quantitative determination of transport coefficients. In the case of OH^- form, the author chose to model the counterion as a small bead without inclusion of any primary hydration water, probably due to the hypothesized dominant mechanism of structural diffusion for OH^- transport.

https://doi.org/10.1021/acs.chemrev.1c00913
Chem. Rev. 2022, 122, 10710−10745

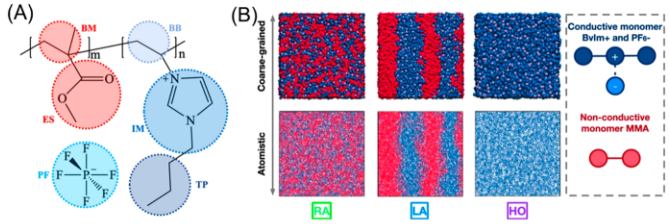

Figure 11. (A) Coase-graining map of the polyILs in Ganesen et al.[207] (B) Simulated morphologies: RA, random copolymer; LA, lamellar block copolymer; HO, homopolymer. Reproduced and adapted with permission from ref 207. Copyright 2019 American Chemical Society.

The OH^- bead was modeled with a Morse potential, as an addition to the DPD model, in a similar manner as the author used for PEMs.[49,50] The author simulated materials with different lengths of the alkyl linker or tail and investigated the different topologies of the side chain, including the comb topology, diblock and triblock functionalization, and multicationic side chains. Significant phase separation was observed with an alkyl spacer, along with increased diameter of water-rich pores. The Nernst equation was used, which was the first semiquantitative prediction based on mean square displacements from DPD simulations, to compute the OH^- conductivity, although it was still an overestimation. Despite this limitation, the quantitative comparison of different chemistries showed that the existence of a long linker promoted an increase in OH^- conductivity as shown in Figure 10B, which may be due to a more flexible headgroup.

AEMs based on functionalized polystyrene are another group of materials that have been investigated. A number of studies with SEBS-QA have been undertaken by the Paddison group.[145−148] These membranes have three different blocks but only two are functionalized, i.e., grafted with ionic head groups. A model was selected with a water bead consisting of four water molecules and the macromolecules and hydrated anion mapped into DPD beads of similar size. Equilibrium morphologies were obtained for the hydrated membranes and microphase separation was observed under all hydration conditions. The functionalized blocks formed a hydrophilic phase, where the majority of the water was found to reside. This microphase separation was observed to be the structural basis of ion conducting channels where both ions and water were concentrated and evidently controlling water uptake but also ion conduction. Cluster analysis was carried out to explore the connectivity of the water domains, which showed the beneficial effect of higher hydration levels for the percolation of water. They also investigated the impact of different molecular structures, including the addition of alkyl spacers, alternating the ionic species, tuning the percentage of functionalized monomers, and changing the molar ratio of the three blocks. These different chemical structures, in combination with the varied hydration conditions, formed the basis of a systematic study of design criteria for membranes with specific morphology and water distribution. It was found that the hydration level, the percentage of functionalized monomers, and the molar ratio of the three blocks were more influential on the morphology and water percolation. This led to a general but not strict rule, that the relative size of the hydrophilic block to the hydrophobic block of the triblock polymer is the more dominant factor in controlling the morphology.

In addition to the above, several other AEMs have been investigated using coarse-grained simulations. Pan et al. undertook both CGMD simulations and experimental studies of quaternary ammonia polysulfones.[204] The impact of the alkyl side chain was examined. In the simulations, the hydrated materials were coarse-grained into five types of beads: backbone segment, side chain segment, quaternary ammonia ion, hydrated hydroxide ion, and water cluster. Martini force field was used for the interactions of beads, and the time step of 20 fs was chosen. The simulation successfully demonstrated the morphology and the aggregation of ionic species. The incorporation of a hydrophobic side chain was confirmed to change the aggregation behavior of the hydrophilic species to a varying extent. This promoted interconnection between the ionic clusters when the material was fully hydrated. The experimental counterpart found that the alkyl spacer between the backbone and headgroup also increased the ion conductivity, which demonstrated the applicability and promise of simulations in the development of novel materials.

Ran et al. conducted both CGMD and experimental studies aiming at identifying routes for enhancing OH^- conductivity in AEMs.[205] Different configurations of alkyl chains were proposed in poly(arylene ether phosphine oxide) functionalized with quaternary ammonium to promote aggregation of the cationic groups. In these CGMD simulations, the backbone monomer was modeled with three CG beads, and a typical side chain contained two CG beads. Quaternary ammonium and the hydrated OH^- were coarse grained into beads carrying opposite charges. Using the Martini force field with a time step of 20 fs, the simulations yielded structure factors and confirmed phase separation and formation of ionic clusters. Dense and long side chain structures were observed to enhance and promote the formation of large ionic clusters. These simulation results were used to guide the design and synthesis of novel AEMs for OH^- transport.

Chen et al. conducted CGMD simulations to investigate hydrated AEMs based on PEEK (poly(ether ether ketone)).[206] The side chains contained one or two QA groups. A coarse-graining scheme based on the Martini force field was implemented, where two to four heavy atoms were mapped into one bead, and the hydroxide ion modeled as a single bead. A time step of 20 fs was used in the production runs. Microphase separation and connected water channels were observed from the CGMD simulations. They found no significant difference in self-diffusion coefficients with AEMs containing one or two QA groups per side chain. However, the simulations indicated that more water molecules hydrated the hydroxide ions in polymers where 2 QA groups were attached to each side chain.

https://doi.org/10.1021/acs.chemrev.1c00913
Chem. Rev. 2022, 122, 10710−10745

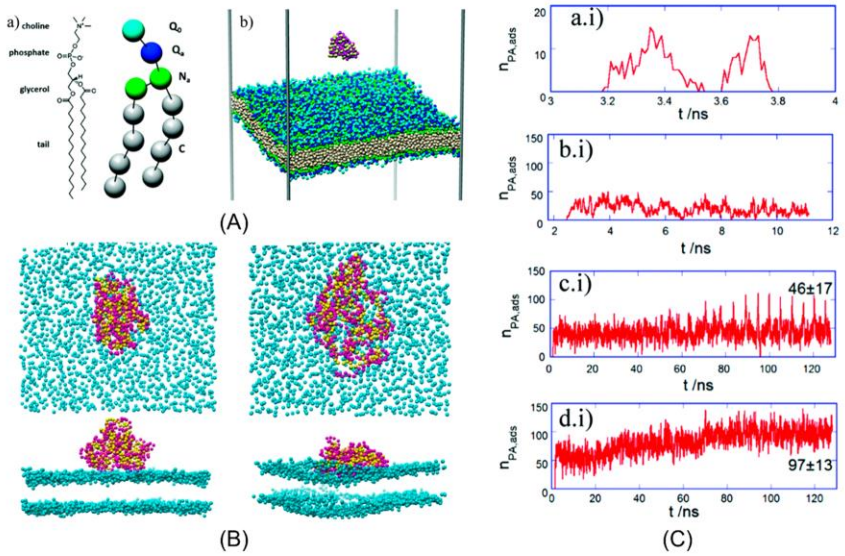

Figure 12. Coarse-grained MD simulations of the adsorption of PECs onto a zwitterionic lipid bilayer of dipalmitoylphosphatidylcholine (DPPC).[210] (A) Coarse-grained DPPC molecule and initial configuration of the simulation are shown, where the polyelectrolyte is placed above the lipid bilayer. (B) Top and side view snapshots of the final configuration of PEC with different polyanion to polycation charge ratios β = 1.2 (left) and polyion 1.4 (right). (C) Time dependence of the number of bound polyanion beads with a Q_0 of DPPC β = 0.8, 1.0, 1.2, and 1.4 (a–d). Averaged values over the last 40 ns are given. Reproduced and adapted with permission from ref 210. Copyright 2019 the Owner Societies.

4.2. Polymerized Ionic Liquids

Ganesan et al. investigated block copolymers containing polymerized ionic liquids (polyIL-BCPs)[207] as these materials are of interest in lithium-ion batteries. It was hypothesized that an understanding of the factors controlling the morphology of polyIL-BCPs could resolve the trade-offs between mechanical strength and ion conductivity. Simulations were performed on a copolymer consisting of two different monomers: 1-*n*-butyl,3-methylimidazolium hexafluorophosphate ($[BvIm]^+[PF_6^-]$) and methyl methacrylate (MMA). Random and diblock copolymers, as well as homogeneous poly-($[BvIm]^+[PF_6^-]$) were studied as three representative molecular structures. In the coarse-grained model, the beads of the alkyl chains had two or three heavy atoms. The methacrylate, imidazolium, and PF_6^- were each represented by a single bead. The CG force field was optimized from all-atom MD simulations with an iterative Boltzmann inversion method with a time step set to 2 fs. These CGMD simulations yielded morphologies where only the diblock copolymers exhibited a lamellar structure, as seen in Figure 11. Ion association was examined, and the random copolymers had fewer cations per anion, however, the ionic rich domains in the diblock copolymers had a similar number of cations per anion to the pure polymerized ionic liquids. Ion hopping events were also investigated. The counterion was considered in a hopping event when the cation–anion association was formed or broken. The block copolymers showed more hopping events than the random copolymers, but slightly fewer hopping events than pure poly($[BvIm]^+[PF_6]^-$). This work is one of the very few that specifically reports on ion transport mechanisms in copolymer ionic liquids.

Qifeng Li et al. developed a CGMD model of poly(1-vinyl-3-ethylimidazolium) tetrafluoroborate ($[PolyC_2VIm][BF_4]$) with a force field mapped from benchmark all-atom MD simulations.[72] An iterative Boltzmann inversion method was used for the nonbonded potential, which resulted in a tabulated force field.[71] The imidazolium ring, C_2 chain, and BF_4 were modeled as three coarse-grained beads and a time step of 2 fs was chosen. Their CGMD results accurately described the structural characteristics and reproduced the thermodynamic properties in agreement with an all-atom model. The deviation of the densities obtained from the CG model and the experiments was within 5% at 298 K. This work provokes additional large-scale modeling of PolyILs.

4.3. Other Systems

In addition to AEMs and polyILs, additional work has been undertaken with coarse-grained simulations of cationic polymers. Although these materials may not be suitable as ion exchange membranes in electrochemical devices, they do, however, feature similar components including polycations and low molecular-weight anions as counterions. Chong and Hernandez simulated the deposition of the polycation: poly(allylamine hydrochloride) onto 4 nm citrate-coated gold nanoparticles.[208] In these coarse-grained simulations, three carbon atoms were simplified into one hydrophobic bead and an ammonium group was modeled as a single charged bead. The results of these simulations revealed that the polymerized cationic groups formed a bilayer-like motif on the nanoparticle surface. Washizu et al. modeled a polyelectrolyte brush, where the ionomers were grafted onto a plane.[209] The effects of adding salt ions to the system and altering the charge density were investigated. In salt-free solutions, the structures of the

https://doi.org/10.1021/acs.chemrev.1c00913
Chem. Rev. 2022, 122, 10710–10745

polyelectrolyte brush with low linear charge density ξ were well described by the scaling theories of Pincus in the form of $h \approx Na\xi^{\alpha}$, where h, N, a, and α are the brush height, the number of monomers, the monomer size, and the fitting parameter, respectively. However, the height of polyelectrolyte brushes with high linear charge density was overestimated by the scaling theories due to the additional shrinkage caused by the counterion condensation. The addition of salt gave rise to a decrease in the heights of the polyelectrolyte brush because of the screening of local charge by the added salt.

5. POLYION (MIXTURE OF POLYANION AND POLYCATION)

Polyions, or polyelectrolyte complexes (PECs), are materials consisting of both a polyanion and a polycation. Much of the computational studies of coexisting polyanions and polycations concern materials for biological applications, i.e., the behavior of DNA-like materials. Unlike the materials in sections 3 and 4, where the simulation box is usually packed with particles, simulations of these systems typically involve isolated molecules. The effect of a solvent (e.g., water) is modeled implicitly by choosing a corresponding dielectric constant, and sometimes using Langevin dynamics. These materials, described below, are sorted into two categories: adsorption of PEC to a membrane/surface and isolated assembly.

5.1. Adsorption of PEC to Membrane/Surface

Angelescu explored the adsorption of PECs onto a zwitterionic lipid bilayer of dipalmitoylphosphatidylcholine (DPPC).[210] The coarse-grained model grouped 3−5 heavy atoms into a single bead and implicitly included the effect of water. A LJ form force field was used that included Coulombic forces for the charged beads. A time step of 20 fs at a temperature of 323 K was used for production runs. The adsorption began with the polyelectrolyte complex located 3 nm above the bilayer DPPC, displayed in Figure 12A. The charged groups (choline) in the bilayers faced outward, and the ratio of negative to positive beads, β, in the polyelectrolyte complex was tuned from 0.83 to 1.4 to investigate these effects. The PECs with $\beta \leq 1.0$ were defined as undercharged, otherwise overcharged. Dynamic results revealed that the charge neutral and undercharged complexes contacted closely with the choline group of the lipid. The complex only bound sporadically to the membrane with no internalization into the core, and subsequent desorption occurred, shown as Figure 12B. Overcharging of the complex is a requisite for irreversible adsorption, and the binding was found to be in two phases: fast extension of the complex parallel to the membrane followed by slow relaxation which included spreading along the membrane, net charge gathering, and increased intrusion into the bilayer core, as shown in Figure 12C.

Duan et al. undertook a series of studies simulating the adsorption of a single polyelectrolyte molecule to an ionic lipid membrane,[211−213] which contained neutral (phosphatidylcholine, PC), multivalent (phosphatidylinositol, PIP_2), and monovalent (phosphatidylserine, PS) anionic lipids. The lipid membrane was modeled as a hexagonal array of closed packed disks, and the polyelectrolyte as a freely jointed chain with hard spheres. A systematic study was performed for the effects of chain length and charge density of the polyelectrolyte, solution ionic strength, and membrane composition. Polyelectrolytes with longer chain length and higher charge density were observed to adsorb on the membrane with increased anionic lipid density when under a higher critical ionic concentration. This group also investigated the influence on the lateral rearrangement and mobility restriction of multivalent anionic lipids in the membrane. A complex hierarchical mobility behavior was observed for the lipid. In addition, the total charge of the polyelectrolyte, in comparison with the local charges of the lipid, was found to play an important role. The polymer would either drag the multivalent lipid or further bind monovalent liquid to achieve local electrical neutrality.

Brettmann et al. conducted experiments and simulations of a PEC coacervate assembly with cellulose nanofibers (CNF).[214] Poly(allylamine hydrochloride) (PAH) was chosen as the positively charged polyelectrolyte represented by one bead for the backbone monomer and one bead for the NH_3^+ headgroup, and poly(acrylic acid) sodium salt (PAA) was selected as the anionic polyelectrolyte modeled by the same coarse-graining in which one bead was used for the monomer in the backbone and one bead for the COO^- headgroup. The 60-mers were used as the chains. Small counterions of Na^+ and Cl^- were incorporated as single beads. CNF was modeled by one type of negatively charged bead for simplicity, and water was considered implicitly as is common in Langevin Dynamics. The CG model was a dimensionless toy model. The addition of polycations and polyanions to the CNF was investigated by optionally switching off the interactions of either polyanion-CNF or polycation-CNF to mimic the experiments. When the polycation was initially added to CNF, the polycations were strongly attracted to the CNFs because of the opposite charges. Successive addition of polyanions formed larger coacervates with the residual positive charges of the polycations on the CNF surface. In contrast, large PEC coacervates were formed with very few polycations attached to the CNF surface when the polyanion was first added followed by the polycation.

Sethuraman et al. used coarse-grained Langevin dynamics to model the adsorption of polyelectrolytes to oppositely charged polyelectrolyte brushes.[215] In their CG model, the polycation was selected as a copolymer with 15 charged beads out of the total 40 beads. One end of the polycation was grafted to the substrate (brush). Polyanions (free chains) had 30 beads, and half of them were charged. The force field was a toy model including LJ and Coulombic forces. Umbrella sampling simulations were also performed to determine free energy, internal energy, and entropy of adsorption. The polyanions and polycations were varied to have a topology of block copolymers as well as alternating copolymers. It was demonstrated that free chains adsorb most strongly when both free and tethered chains had a block charge sequence but weaker when both species had alternating sequences. Adsorption was stronger when the free polyanion was in a block sequence and the polycation of the brush was alternating than the reverse case of alternating free polymer and tethered block copolymer. From a quantitative analysis, this group concluded that the sequence-dependent effects were largely energetic, rather than entropic, in origin.

5.2. Isolated Assembly

Dias and Pais recently summarized important findings from coarse-grained simulations of aqueous solutions of polyelectrolytes.[216] This review discussed the condensation of polyanion (100 monomers) representing DNA in bulk solution. It was found that increasing the concentration of opposite charges by adding more salt promoted the globule

https://doi.org/10.1021/acs.chemrev.1c00913
Chem. Rev. 2022, 122, 10710−10745

conformation of polyanion.[217] The same effect was also found by adding longer polycation chains to the system, or adding more polycation chains, by examining the radius of gyration.[218,219]

Narambuena et al. simulated polyelectrolyte complexes with CGMC simulations.[220] The system consisted of several polycations, polyanions, neutral polymer chains and small ions, and a toy model was adopted. CGMC simulations were performed to understand the effect of chain stiffness on the morphology, as well as changing the chain length of the polyanion component. The simulations resulted in different morphologies, such as globules, toroids, and rods, seemingly dependent on the stiffness. The effect of chain length revealed that longer chains tended to have more toroids than rods, but the size of the toroids did not depend entirely on the chain length. From these observations, it was concluded that chain stiffness, rather than electrostatic contributions, was more important in determining the morphology.

Angelescu and Caragheorgeopol studied polyion copolymers with CGMC simulations in an investigation of the condensation and phase stability of charged biomacromolecules.[221] The complexes consisted of a linear charged homopolymer and oppositely charged copolymers. A toy model was utilized which included both the Lennard-Jones and electrostatic interactions, and the solvent was only considered implicitly as a dielectric continuum. They conducted a systematic study by simulating three different architectures of the copolymer: branched, multiblock, and random, as well as altering the bead charge. Core−shell, structureless spherical, and globular structures were found when the electrostatic coupling was set to a high level, while there was no segregation when the electrostatic coupling was reduced.

Torres et al. studied the complexation and aggregation of protein-polyelectrolyte by using CGMD simulations.[222] The simulation box had two protein chains and one polyanion or polycation chain, with some explicit small ions. The researchers investigated the β-lactoglobulin protein, with some of the simulation parameters estimated. It is worth noting that this study employed a Monte Carlo trial for titration of the protein beads, where the charge of a chosen titratable protein bead could be removed or recovered during the simulation to mimic protonation and deprotonation. Meanwhile, one small ion was created or deleted to maintain a neutral net charge of the system, but the charge of the protein chains was allowed to change dynamically. Using an established model, the acid−base equilibrium of titratable groups of the protein was investigated. The isoelectric point value was predicted for the protein, and the absorption of the polyanion or polycation to the protein chain was observed under certain pH conditions.

Elder and Jayaraman performed coarse-grained Langevin dynamics to understand how lysine-based polycations affect their complexation with DNA-like polyanions.[223] The coarse graining was performed by grouping about three heavy atoms into one bead for the polycation. The force field was of the LJ form with the Coulombic interactions in the CG simulation. The polyplex was formed by a linear polyanion entangled with the polycation. Poly(L-lysine), poly(cyclopentene-*g*-oligolysine), and grafted poly(cyclooctene-*g*-oligolysine) were simulated to combine the effects of architecture and charge on the structure and flexibility of these lysine-based polycations. Increasing oligolysine graft length and decreasing graft spacing both increased the size and rigidity of the grafted oligolysines. Increasing ionic strength or counterion valency reduced the polycation size and most architecture-dependent effects. The effects of polycation architecture on polyplex size and flexibility were found to depend on the charge ratio in the system. The polyplex surface charge increased with increasing graft length or decreasing graft spacing of the polycation.

Peng and Muthukumar modeled the competitive substitution of a PEC with Langevin dynamics.[224] The PEC consisted of a polycation chain and a polyanion chain was invaded by another longer polyanion chain (i.e., the polyanion chain of the PEC was substituted by another longer polyanion chain). A united atom model was employed for the chains and the Langevin dynamics was performed. They calculated the potential of mean force (PMF) along with the center-of-mass distance reaction coordinate and reported a constant force of attraction (linear PMF) for a large range of distances in comparison to the PE contour length. The invading chain was required to be longer to substitute the chain being displaced. Adding salt to the system reduced the substitution time. Their analysis showed that the dominant driving force for substitution was the release of counterion from the polyelectrolyte.

Zhan et al. simulated polycation block copolymer/DNA-like polyanion complexes, which can potentially be used as gene delivery vehicles.[225] The system had a single polyanion chain mimicking DNA represented by 100 beads, each with a negative charge. Several short polycations, either diblock (20 beads) or triblock (30 beads), were added. There was only one block consisting of charged beads, and the other block(s) was either hydrophobic or hydrophilic. A sufficient number of small counterions was added to neutralize the system. A Lennard-Jones type potential and columbic charge were used to model the interactions, and Langevin dynamics simulations were performed. The results revealed aggregation of the chains carrying opposite charges. Core−corona and tadpole-like morphologies were observed, and the radius of gyration of the aggregate was observed to be affected by the noncharged blocks. In this work, a triblock polycation with a hydrophobic middle block and a hydrophilic tail block displayed distinct advantages as a potential gene carrier and suggested that careful design of the hydrophobic block would probably reduce the zeta potential.

Xu et al. systematically studied the pair association of two polyelectrolytes of similar size but opposite charge in terms of the PMF along their center-of-mass reaction coordinate via coarse-grained simulations.[226] Each polycation and polyanion had 25 charged beads, and the counterions were considered via the bare charge density (monomer charge). The simulations were conducted at room temperature using Langevin dynamics. A "pull code" was implemented to investigate the transition states along with the reaction coordination between the two chains. With the high bare charge density, the two isolated chains were found in a coil shape, but the coils were stretched and aligned in a parallel fashion when the distance of their centers of mass was reduced. This sliding mechanism was interpreted from the PMFs along the reaction coordinate to indicate that the higher bare charge density significantly reduced the free energy when the two chains approached each other.

Saha et al. conducted experimental study for PECs consisting of poly(alanine methacryloyloxyethyl ester-*co*-styrene) and poly(acrylic acid-*co*-methyl acrylate).[227] CGMD simulations were performed as a tool assisting the rational

https://doi.org/10.1021/acs.chemrev.1c00913
Chem. Rev. 2022, 122, 10710−10745

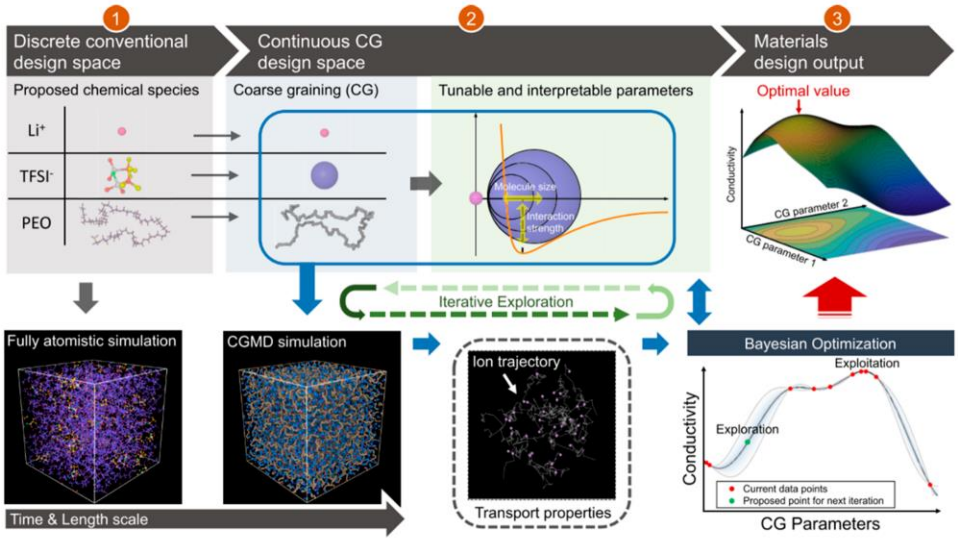

Figure 13. Illustration of a coarse-grained molecular dynamics−Bayesian optimization (CGMD-BO) framework. Materials design starts with the coarse-graining process to transform the conventional chemical species space to a continuous space composed of CG parameters (1 → 2). This space is then explored by BO-guided CGMD simulations in iterations to predict the relationships between the transport properties and the associated CG parameters (2 → 3). Reproduced and adapted with permission from ref 233. Copyright 2020 American Chemical Society.

design of these materials. The polymers were represented by the linear bead−spring chains (FENE) without the details of the side chains. Hence, each monomer was represented by a single bead. The polycation had positively charged beads and neutral hydrophobic beads with the ratio of 512:512, while the polyanion had 512 negatively charged beads and 512−1536 neutral hydrophilic beads. LJ and long-range Coulombic potentials were included, as well as the Yukawa-type potential for the beads in polycation. Langevin thermostat was used to maintain constant temperature. The morphology of the PEC was found dependent on the strength of the electrostatic interactions, the fraction of charged groups on the polyanion, and the characteristic energy of hydrophobic−hydrophobic interactions. Spherical core−shell structure, vesicular, toroidal, and necklace-like complexes were found, and the phase segregation was always observed. It was concluded that a variety of morphologies were obtained as the tuning of incompatibility of nonionic segments of oppositely charged polyelectrolytes, together with the strength of electrostatic interactions.

Wang et al. examined the impact of chain length and stiffness on the formation and aggregation of polyelectrolyte complexes.[228] A toy model in dimensionless form was chosen, and a Langevin thermostat was used. For PECs consisting of a single polyanion chain, the simulation results showed three structural regimes depending on the polyanion stiffness: a collapsed complex for flexible polyanions, various morphologies including toroids and hairpins for semiflexible polyanions, and rod-like structures for stiff polyanions. In simulations of multiple polyanions, aggregation was observed with the semiflexible and stiff polyanions, promoted by shorter polycation lengths. Simulations of short and stiff polyanions with long polycations showed that polyanions were spaced along the polycation, which were used as a model for siRNA gene delivery complexes. These structures differed from aggregates of longer polyanions in which the polyanions were packed together in parallel bundles.

6. SALT-DOPED POLYMERS

Salt-doped polymers are neutral polymer chains doped with an equal number of anions and cations of the salt. Different from the aforementioned materials described in sections 3−5, the polymer chains do not carry a net charge, and thus the chains themselves are merely considered as ion-containing polymers. Salt-doped polymers are considered as possible polymer electrolyte candidates, and as there are a few reports of coarse graining simulations, they are included in this review.

Shen and co-workers undertook a number of studies using a generic model to understand the relationship between physical characteristics and ion conductivity.[229−232] Toy models were adopted for both the homopolymers and diblock copolymers doped with a salt. They pointed out that their model was not mapped to a particular chemical system but was still able to reproduce the features of the salt doped polymer systems, including poly(ethylene oxide) and poly(ethylene oxide)-polystyrene, both doped with LiTFSI. These researchers also applied an additional ion−monomer potential to represent the dielectric and size-dependent ion solvation. They investigated the effects of various physical properties, including ion−ion and ion−solvent interactions, ion size, dielectric constant, etc. In the salt-doped block copolymer systems, phase separation was observed. Moreover, nonequilibrium MD simulations with an applied external electric field were undertaken and were observed to yield results that were more accurate than equilibrium MD simulations. Other interesting observations include: (1) High MW resulted in more uniformly distributed

https://doi.org/10.1021/acs.chemrev.1c00913
Chem. Rev. 2022, 122, 10710−10745

and faster diffusing ions. (2) Strong ion−polymer and ion−ion interactions along with more correlated motion of cation−anion pairs were observed at lower concentrations. (3) Systems with low or little disparity in ion size where the dielectric constant was increased enhanced cation conduction. However, in systems with high ion size disparity, a high dielectric constant resulted in strong preferential solvation of cations and reduced cation mobility and transference number. It was, however, noted that some of these findings were in contrast to expectations. They attributed them to the ion aggregation and the rate of ion cluster relaxation, which seemed to attest to the insight gained by simulations toward the development of novel materials.

Finally, it is worth noting that Wang et al. proposed a framework of machine learning assisted CGMD for the design of highly conductive polymer electrolytes and as a starting point studied PEO doped with LiTFSI.[233] In this framework, the coarse graining did not only reduce the computational cost by lumping the atoms into beads but also converted the discrete chemical species space to a continuous space of coarse-grained parameters. Put another way, the chemistry-specified properties, with some loss of atomistic details, were expressed purely by a finite set of continuous variables facile for optimization. As shown in Figure 13, a Bayesian optimization (BO) algorithm was then employed to efficiently explore this high-dimensional continuous space via autonomous CGMD simulations. This CGMD-BO approach enabled a comprehensive description of the relationships between lithium-ion conductivity and intrinsic material properties in terms of coarse-grained parameters, which may further enlighten a pathway to promising polymeric electrolytes.

7. CONCLUSIONS AND OUTLOOKS

In this review, we have summarized the development and current understanding of structure−property relationships in ion-containing polymers. Insight is provided into the design of such materials based on findings from coarse-grained modeling and simulations accompanied by the significant advances in experimental strategies. Specifically, we concentrate on three types of ion-containing polymers: PEMs, AEMs, and polyILs, which provide guidance in the rational design of high-performance materials with improved properties for novel power source technologies. In addition, we highlight coarse-grained modeling as a powerful tool that provides structural and dynamical information including hydrated/anhydrous morphologies, ionic aggregation (shape, size, and connectivity), water cluster distributions, and the influence of various molecular features on structural and dynamical properties. Importantly, future directions for the development and improvement of ion-containing polymeric material are discussed.

Although PFSA-based membranes and their alternatives have been the subject of a significant number of theoretical and experimental studies, general design rules for high-performance PEMs remain unresolved as there are many factors governing the mesoscale phase separation and the associated transport properties. Therefore, there is a need to continue exploring the correlations between chemistry, phase-separated morphology, and the dynamics of ions, solvent molecules, and polymer chains. As discussed in section 3, a good management of water transport and distribution is crucial as this facilitates microphase separation, which generally enhances both ion transport and mechanical strength but also prevents flooding and swelling of the membranes. One novel strategy to mitigate such issues is the modification of side chain chemistry, including cross-linking of the side chains and the inclusion of multiple functionalized side chains. In contrast to PEMs, AEMs can be used in fuel cells to produce high power densities at similar temperatures but with nonprecious metal catalysts, which have the obvious advantage of low cost. Recently, advances in synthesis have significantly improved AEMs performance. These appealing properties continue to suggest an avenue to synergistically combine multiple orthogonal properties. To this end, a more thorough fundamental understanding of how various chemistries and chain architectures control the morphology and transport properties should be pursued.

Recent analyses of polyILs reveal that there are at least two prominent strategies: decoupling the ion dynamics from segmental relaxation and reversing negative ion−ion correlations by constructing ionic channels. Understanding fundamental correlations among the multiscale dynamics of ions, doped plasticizers, and polymer chains may pave the way to design solid polyILs for the application for solid-state batteries. As repeatedly highlighted, the combination of theoretical and experimental strategies would be an efficient route to explore for appealing ion-containing soft materials.

However, it remains a demanding process to develop a force field for coarse-grained modeling and simulations, especially considering the effects of multibody interactions, polarizability, and delocalization of charge. To date, there are DFT-based parametrization schemes, a fragment molecular orbital approach, the MARTINI, and the conventional mapping method from Flory−Huggins χ-parameter obtained from experimental data or MD/MC simulations. These methods have been successfully applied to various ion-containing polymers, but it would be insightful to further improve and expand their application to more complex materials, especially the interfacial properties of the phases.

In an effort to elucidate the interplay of the transport behavior of ions and solvent molecules and mesoscopic structure, grid-based Monte Carlo trajectory calculations are capable of estimating the water diffusivity based on equilibrated phase-separated morphology but fail to mimic the proton transport due to the lack of the local environment information for protons. Still, this approach may not be suitable given that water clusters are dynamically connected by "temporal bridges" that appear and disappear. Smoothed particle hydrodynamics simulations were able to capture a qualitative description of the morphology and proton transport properties based on information derived from DPD simulations. To incorporate the interactions between protons and water as well as the acidic groups in a DPD simulations, a dissociative Morse potential was developed to describe the behavior of proton hopping from one headgroup to another such that the dynamical and morphological properties could be evaluated consistently and simultaneously in the mesoscale framework of these materials, which included the dynamic percolation effect of formation and breakup of temporary junctions between the clusters. These emerging theoretical approaches demonstrate the need to validate predictive capability for more extensive ion-containing materials and improvement of the efficiency of modeling schemes to even larger systems and for longer time frames.

One direction is to develop a multiscale simulation scheme, which, on the one hand, provides potentials to predict various

https://doi.org/10.1021/acs.chemrev.1c00913
Chem. Rev. 2022, 122, 10710−10745

highly coupled phenomena such as phase separation, ion dissociation, and ion transport, and on the other hand, hierarchically and rigorously maps/back-maps from one simulation scale (e.g., a molecular or atomistic scale) to disparate length and time scales in a coupled and cohesive manner. The latter is certainly a fundamental challenge. Another emerging approach is to capitalize on the high efficiency of machine learning algorithms, which have proven to be promising for exploring high-performance materials with synergistic conjoining of multiple orthogonal properties.

AUTHOR INFORMATION

Corresponding Author

Stephen J. Paddison − *Department of Chemical & Biomolecular Engineering, University of Tennessee, Knoxville, Tennessee 37996, United States;* orcid.org/0000-0003-1064-8233; Email: spaddison@utk.edu

Authors

Zhenghao Zhu − *Department of Chemical & Biomolecular Engineering, University of Tennessee, Knoxville, Tennessee 37996, United States*

Xubo Luo − *Department of Chemical & Biomolecular Engineering, University of Tennessee, Knoxville, Tennessee 37996, United States*

Complete contact information is available at: https://pubs.acs.org/10.1021/acs.chemrev.1c00913

Notes

The authors declare no competing financial interest.

Biographies

Zhenghao Zhu received his B.S. and M.S. degrees in Chemical Engineering from East China University of Science and Technology. His M.S. research mainly focused on investigating thermodynamic properties of polymer solutions based on the COSMO-SAC model and the Lattice model, which indicated significant guidance in the preparation of membranes. After working as an engineer dealing with wastewater treatment in Shanghai Sep-Bio Engineering Co., Ltd., he is currently a Ph.D. student at the University of Tennessee under the supervision of Prof. Stephen Paddison. His research focuses on understanding the interplay of morphology and ion transport in electrolyte membranes for clean energy applications through multi-scale modeling and simulations.

Xubo Luo was born in Tianjin, China. He received his B.Eng. and M.S. from Tianjin University. In 2020, he completed his Ph.D. in chemical engineering at the University of Tennessee, Knoxville. His Ph.D. research concentrated on the mesoscale and atomic simulations of polymeric materials as electrolytes. He is now a postdoctoral fellow at Lawrence Berkeley National Lab. His current research focuses on the modeling and simulation of the nanostructures for biomimetic polymers.

Stephen J. Paddison is currently the Gibson Endowed Professor of Engineering at the University of Tennessee, Knoxville. He received a B.Sc. (Honours) in Chemical Physics and a Ph.D. in Physical/Theoretical Chemistry (1996) from the University of Calgary, Canada. He was, subsequently, a postdoctoral fellow and staff member in the Materials Science Division at Los Alamos National Laboratory. He joined the Department of Chemical & Biomolecular Engineering at the University of Tennessee in 2007. His research work has focused on elucidating fundamental molecular-level understanding of polymer electrolyte membranes and electrocatalysts. He employs a multiscale approach to materials modeling with methodologies including high level (DFT) electronic structure calculations, ab initio molecular dynamics (AIMD), classical molecular dynamics, quantum mechanics/molecular mechanics (QM/MM), dissipative particle dynamics, and equilibrium and nonequilibrium statistical mechanics.

ACKNOWLEDGMENTS

Financial support of the U.S. Army Research Office under contracts W911NF-15-1-0501 and W911NF-16-1-0402 is gratefully acknowledged.

REFERENCES

(1) Bocharova, V.; Sokolov, A. P. Perspectives for Polymer Electrolytes: A View from Fundamentals of Ionic Conductivity. *Macromolecules* **2020**, *53*, 4141−4157.
(2) Di Noto, V.; Lavina, S.; Giffin, G. A.; Negro, E.; Scrosati, B. Polymer Electrolytes: Present, Past and Future. *Electrochim. Acta* **2011**, *57*, 4−13.
(3) Hickner, M. A. Ion-Containing Polymers: New Energy and Clean Water. *Mater. Today* **2010**, *13*, 34−41.
(4) Ganesan, V. Ion Transport in Polymeric Ionic Liquids: Recent Developments and Open Questions. *Mol. Syst. Des. Eng.* **2019**, *4*, 280−293.
(5) Elabd, Y. A. Ion Transport in Hydroxide Conducting Block Copolymers. *Mol. Syst. Des. Eng.* **2019**, *4*, 519−530.
(6) Kusoglu, A.; Weber, A. Z. New Insights into Perfluorinated Sulfonic-Acid Ionomers. *Chem. Rev.* **2017**, *117*, 987−1104.
(7) Kreuer, K.-D. Ion Conducting Membranes for Fuel Cells and other Electrochemical Devices. *Chem. Mater.* **2014**, *26*, 361−380.
(8) Wang, Y.; Chen, K. S.; Mishler, J.; Cho, S. C.; Adroher, X. C. A Review of Polymer Electrolyte Membrane Fuel Cells: Technology, Applications, and Needs on Fundamental Research. *Appl. Energy* **2011**, *88*, 981−1007.
(9) Kornyshev, A. A.; Spohr, E. *Proton Transport in Polymer Electrolyte Membranes Using Theory and Classical Molecular Dynamics*; Springer: New York, 2009; pp 349−363.
(10) Wu, J.; Yuan, X. Z.; Martin, J. J.; Wang, H.; Zhang, J.; Shen, J.; Wu, S.; Merida, W. A Review of PEM Fuel Cell Durability: Degradation Mechanisms and Mitigation Strategies. *J. Power Sources* **2008**, *184*, 104−119.
(11) de Bruijn, F. A.; Dam, V. A. T.; Janssen, G. J. M. Review: Durability and Degradation Issues of PEM Fuel Cell Components. *Fuel Cells* **2008**, *8*, 3−22.
(12) Hickner, M. A.; Pivovar, B. S. The Chemical and Structural Nature of Proton Exchange Membrane Fuel Cell Properties. *Fuel Cells* **2005**, *5*, 213−229.
(13) Mauritz, K. A.; Moore, R. B. State of Understanding of Nafion. *Chem. Rev.* **2004**, *104*, 4535−4585.
(14) Kreuer, K.-D.; Paddison, S. J.; Spohr, E.; Schuster, M. Transport in Proton Conductors for Fuel-Cell Applications: Simulations, Elementary Reactions, and Phenomenology. *Chem. Rev.* **2004**, *104*, 4637−4678.
(15) Hickner, M. A.; Ghassemi, H.; Kim, Y. S.; Einsla, B. R.; McGrath, J. E. Alternative Polymer Systems for Proton Exchange Membranes (PEMs). *Chem. Rev.* **2004**, *104*, 4587−4612.
(16) Kreuer, K. D. On the Development of Proton Conducting Polymer Membranes for Hdyrogen and Methonal Fuel Cells. *J. Membr. Sci.* **2001**, *185*, 29−39.
(17) Kreuer, K. D. On the Development of Proton Conducting Materials for Technological Applications. *Solid State Ion.* **1997**, *97*, 1−15.
(18) Hsu, W. Y.; Gierke, T. D. Ion Transport and Clustering in Nafion Perfluorinated Membranes. *J. Membr. Sci.* **1983**, *13*, 307−326.

(19) Schmidt-Rohr, K.; Chen, Q. Parallel Cylindrical Water Nanochannels in Nafion Fuel-Cell Membranes. *Nat. Mater.* **2008**, *7*, 75−83.
(20) Kreuer, K.-D.; Portale, G. A Critical Revision of the Nano-Morphology of Proton Conducting Ionomers and Polyelectrolytes for Fuel Cell Applications. *Adv. Funct. Mater.* **2013**, *23*, 5390−5397.
(21) Middleton, L. R.; Winey, K. I. Nanoscale Aggregation in Acid- and Ion-Containing Polymers. *Annu. Rev. Chem. Biomol. Eng.* **2017**, *8*, 499−523.
(22) Kumar, M.; Paddison, S. J. Side-Chain Degradation of Perfluorosulfonic Acid Membranes: An Ab Initio Study. *J. Mater. Res.* **2012**, *27*, 1982−1991.
(23) Wang, C.; Clark, J. K.; Kumar, M.; Paddison, S. J. An Ab Initio Study of the Primary Hydration and Proton Transfer of CF(3)SO(3) H and CF(3)O (CF(2))(2)SO(3)H: Effects of the Hybrid Functional and Inclusion of Diffuse Functions. *Solid State Ion.* **2011**, *199*, 6−13.
(24) Paddison, S. J.; Kreuer, K. D.; Maier, J. About the Choice of the Protogenic Group in Polymer Electrolyte Membranes: Ab Initio Modelling of Sulfonic Acid, Phosphonic Acid, and Imidazole Functionalized Alkanes. *Phys. Chem. Chem. Phys.* **2006**, *8*, 4530−4542.
(25) Paddison, S. J.; Elliott, J. A. On the Consequences of Side Chain Flexibility and Backbone Conformation on Hydration and Proton Dissociation in Perfluorosulfonic Acid Membranes. *Phys. Chem. Chem. Phys.* **2006**, *8*, 2193−2203.
(26) Zelovich, T.; Vogt-Maranto, L.; Hickner, M. A.; Paddison, S. J.; Bae, C.; Dekel, D. R.; Tuckerman, M. E. Hydroxide Ion Diffusion in Anion-Exchange Membranes at Low Hydration: Insights from Ab Initio Molecular Dynamics. *Chem. Mater.* **2019**, *31*, 5778−5787.
(27) Zelovich, T.; Long, Z.; Hickner, M.; Paddison, S. J.; Bae, C.; Tuckerman, M. E. Ab Initio Molecular Dynamics Study of Hydroxide Diffusion Mechanisms in Nanoconfined Structural Mimics of Anion Exchange Membranes. *J. Phys. Chem. C* **2019**, *123*, 4638−4653.
(28) Clark, J. K., 2nd; Habenicht, B. F.; Paddison, S. J. Ab Initio Molecular Dynamics Simulations of Aqueous Triflic Acid Confined in Carbon Nanotubes. *Phys. Chem. Chem. Phys.* **2014**, *16*, 16465−16479.
(29) Hayes, R. L.; Paddison, S. J.; Tuckerman, M. E. Proton Transport in Triflic Acid Pentahydrate Studied via Ab Initio Path Integral Molecular Dynamics. *J. Phys. Chem. A* **2011**, *115*, 6112−6124.
(30) Habenicht, B. F.; Paddison, S. J.; Tuckerman, M. E. The Effects of the Hydrophobic Environment on Proton Mobility in Perfluorosulfonic Acid Systems: An Ab Initio Molecular Dynamics Study. *J. Mater. Chem.* **2010**, *20*, 6342.
(31) Habenicht, B. F.; Paddison, S. J.; Tuckerman, M. E. Ab Initio Molecular Dynamics Simulations Investigating Proton Transfer in Perfluorosulfonic Acid Functionalized Carbon Nanotubes. *Phys. Chem. Chem. Phys.* **2010**, *12*, 8728−8732.
(32) Zelovich, T.; Winey, K. I.; Tuckerman, M. E. Hydronium Ion Diffusion in Model Proton Exchange Membranes at Low Hydration: Insights from Ab Initio Molecular Dynamics. *J. Mater. Chem. A* **2021**, *9*, 2448−2458.
(33) Zelovich, T.; Tuckerman, M. E. OH(−) and $H_3O(+)$ Diffusion in Model AEMs and PEMs at Low Hydration: Insights from ab Initio Molecular Dynamics. *Membranes (Basel)* **2021**, *11*, 355.
(34) Zelovich, T.; Tuckerman, M. E. Water Layering Affects Hydroxide Diffusion in Functionalized Nanoconfined Environments. *J. Phys. Chem. Lett.* **2020**, *11*, 5087−5091.
(35) Wang, J.; Han, Y.; Xu, Z.; Yang, X.; Ramakrishna, S.; Liu, Y. Dissipative Particle Dynamics Simulation: A Review on Investigating Mesoscale Properties of Polymer Systems. *Macromol. Mater. Eng.* **2021**, *306*, 2000724.
(36) Shen, K.-H.; Fan, M.; Hall, L. M. Molecular Dynamics Simulations of Ion-Containing Polymers Using Generic Coarse-Grained Models. *Macromolecules* **2021**, *54*, 2031−2052.
(37) Li, Z.; Bian, X.; Li, X.; Deng, M.; Tang, Y.-H.; Caswell, B.; Karniadakis, G. E., Dissipative Particle Dynamics: Foundation, Evolution, Implementation, and Applications. In *Particles in Flows*; Bodnár, T., Galdi, G. P., Nečasová, Š., Eds.; Springer International: Cham, 2017; pp 255−326.
(38) Español, P.; Warren, P. B. Perspective: Dissipative Particle Dynamics. *J. Chem. Phys.* **2017**, *146*, 160901.
(39) Solano Canchaya, J. G.; Dequidt, A.; Goujon, F.; Malfreyt, P. Development of DPD Coarse-Grained Models: From Bulk to Interfacial Properties. *J. Chem. Phys.* **2016**, *145*, 054107.
(40) Elliott, J. A.; Paddison, S. J. Modelling of Morphology and Proton Transport in PFSA Membranes. *Phys. Chem. Chem. Phys.* **2007**, *9*, 2602−2618.
(41) Avalos, J. B.; Mackie, A. D. Dissipative Particle Dynamics with Energy Conservation. *Europhys. Lett.* **1997**, *40*, 141−146.
(42) Hoogerbrugge, P. J.; Koelman, J. M. V. A. Simulating Microscopic Hydrodynamic Phenomena with Dissipative Particle Dynamics. *Europhys. Lett.* **1992**, *19*, 155−160.
(43) Dorenbos, G. Water Diffusion Dependence on Amphiphilic Block Design in (Amphiphilic-Hydrophobic) Diblock Copolymer Membranes. *J. Phys. Chem. B* **2016**, *120*, 5634−5645.
(44) Dorenbos, G. Morphology and Diffusion within Model Membranes: Application of Bond Counting Method to Architectures with Bimodal Side Chain Length Distributions. *Eur. Polym. J.* **2015**, *69*, 64−84.
(45) Dorenbos, G.; Morohoshi, K. Pore Morphologies and Diffusion within Hydrated Polyelectrolyte Membranes: Homogeneous vs Heterogeneous and Random Side Chain Attachment. *J. Chem. Phys.* **2013**, *138*, 064902.
(46) Dorenbos, G. Dependence of Pore Morphology and Diffusion on Hydrophilic Site Distribution within Hydrated Amphiphilic Multi Block Co-Polymer Membranes. *Polymer* **2013**, *54*, 5024−5034.
(47) Dorenbos, G.; Morohoshi, K. Chain Architecture Dependence of Pore Morphologies and Water Diffusion in Grafted and Block Polymer Electrolyte Fuel Cell Membranes. *Energy Environ. Sci.* **2010**, *3*, 1326−1338.
(48) Dorenbos, G.; Suga, Y. Simulation of Equivalent Weight Dependence of Nafion Morphologies and Predicted Trends Regarding Water Diffusion. *J. Membr. Sci.* **2009**, *330*, 5−20.
(49) Vishnyakov, A.; Mao, R.; Lee, M.-T.; Neimark, A. V. Coarse-Grained Model of Nanoscale Segregation, Water Diffusion, and Proton Transport in Nafion Membranes. *J. Chem. Phys.* **2018**, *148*, 024108.
(50) Lee, M. T.; Vishnyakov, A.; Neimark, A. V. Coarse-Grained Model of Water Diffusion and Proton Conductivity in Hydrated Polyelectrolyte Membrane. *J. Chem. Phys.* **2016**, *144*, 014902.
(51) Lee, M. T. Designing Highly Conductive Block Copolymer-Based Anion Exchange Membranes by Mesoscale Simulations. *J. Phys. Chem. B* **2021**, *125*, 2729−2740.
(52) Lee, M.-T. Designing Anion Exchange Membranes with Enhanced Hydroxide Ion Conductivity by Mesoscale Simulations. *J. Phys. Chem. C* **2020**, *124*, 4470−4482.
(53) Lee, M.-T. Exploring Side-Chain Designs for Enhanced Ion Conductivity of Anion-Exchange Membranes by Mesoscale Simulations. *J. Phys. Chem. C* **2019**, *123*, 10802−10815.
(54) Jorn, R.; Voth, G. A. Mesoscale Simulation of Proton Transport in Proton Exchange Membranes. *J. Phys. Chem. C* **2012**, *116*, 10476−10489.
(55) Gooneie, A.; Schuschnigg, S.; Holzer, C. A Review of Multiscale Computational Methods in Polymeric Materials. *Polymers (Basel)* **2017**, *9*, 16.
(56) Praprotnik, M.; Site, L. D.; Kremer, K. Multiscale Simulation of Soft Matter: From Scale Bridging to Adaptive Resolution. *Annu. Rev. Chem. Biomol. Eng.* **2008**, *59*, 545−571.
(57) Lee, S.; Tran, A.; Allsopp, M.; Lim, J. B.; Hénin, J.; Klauda, J. B. CHARMM36 United Atom Chain Model for Lipids and Surfactants. *J. Phys. Chem. B* **2014**, *118*, 547−556.
(58) Yang, L.; Tan, C.-h.; Hsieh, M.-J.; Wang, J.; Duan, Y.; Cieplak, P.; Caldwell, J.; Kollman, P. A.; Luo, R. New-Generation Amber United-Atom Force Field. *J. Phys. Chem. B* **2006**, *110*, 13166−13176.
(59) Jorgensen, W. L.; Tirado-Rives, J. The OPLS [Optimized Potentials for Liquid Simulations] Potential Functions for Proteins,

Energy Minimizations for Crystals of Cyclic Peptides and Crambin. *J. Am. Chem. Soc.* **1988**, *110*, 1657−1666.
(60) Soto-Figueroa, C. s.; Rodríguez-Hidalgo, M. a.-d.-R.; Martínez-Magadán, J.-M.; Vicente, L. Dissipative Particle Dynamics Study of Order-Order Phase Transition of BCC, HPC, OBDD, and LAM Structures of the Poly(styrene)-Poly(isoprene) Diblock Copolymer. *Macromolecules* **2008**, *41*, 3297−3304.
(61) Soto-Figueroa, C.; Vicente, L.; Martínez-Magadán, J. M.; Rodríguez-Hidalgo, M. D. R. Self-Organization Process of Ordered Structures in Linear and Star Poly (styrene)-Poly(isoprene) Block Copolymers: Gaussian Models and Mesoscopic Parameters of Polymeric Systems. *J. Phys. Chem. B* **2007**, *111*, 11756−11764.
(62) Soto-Figueroa, C.; Vicente, L.; Martínez-Magadán, J. M.; Rodríguez-Hidalgo, M. d. R. Mesoscopic Simulation of Asymmetric-Copolymer/Homopolymer Blends: Microphase Morphological Modification by Homopolymer Chains Solubilization. *Polymer* **2007**, *48*, 3902−3911.
(63) Soto-Figueroa, C.; Rodríguez-Hidalgo, M. D. R.; Martínez-Magadán, J. M. Molecular Simulation of Diblock Copolymers; Morphology and Mechanical Properties. *Polymer* **2005**, *46*, 7485−7493.
(64) Allen, M. P.; Tildesley, D. J. *Computer Simulation of Liquids*, 2nd ed.; Oxford University Press, 2017; p 640.
(65) Allen, M. P.; Tildesley, D. J. *Computer Simulation of Liquids*; Oxford University Press, 1987; p 408.
(66) Leach, A. R. *Molecular Modelling: Principles and Applications*; Pearson Education Limited, 2001; p 768.
(67) Metropolis, N.; Rosenbluth, A. W.; Rosenbluth, M. N.; Teller, A. H.; Teller, E. Equation of State Calculations by Fast Computing Machines. *J. Chem. Phys.* **1953**, *21*, 1087−1092.
(68) Hockney, R. W.; Goel, S.; Eastwood, J. Quiet High-Resolution Computer Models of a Plasma. *J. Comput. Phys.* **1974**, *14*, 148−158.
(69) Souza, P. C.; Alessandri, R.; Barnoud, J.; Thallmair, S.; Faustino, I.; Grünewald, F.; Patmanidis, I.; Abdizadeh, H.; Bruininks, B. M.; Wassenaar, T. A.; et al. Martini 3: A General Purpose Force Field for Coarse-Grained Molecular Dynamics. *Nat. Methods* **2021**, *18*, 382−388.
(70) Reith, D.; Pütz, M.; Müller-Plathe, F. Deriving Effective Mesoscale Potentials from Atomistic Simulations. *J. Comput. Chem.* **2003**, *24*, 1624−1636.
(71) Rühle, V.; Junghans, C.; Lukyanov, A.; Kremer, K.; Andrienko, D. Versatile Object-Oriented Toolkit for Coarse-Graining Applications. *J. Chem. Theory Comput.* **2009**, *5*, 3211−3223.
(72) Li, Q.; Guo, Y.; Tong, J.; He, H.; Zhang, X.; Huo, F. Development of a Coarse-Grained Force Field Model of Polymeric 1-Vinyl-3-Ethylimidazolium Tetrafluoroborate Ionic Liquids. *Chem. Phys. Lett.* **2020**, *754*, 137656.
(73) Español, P. Dissipative Particle Dynamics with Energy Conservation. *Europhys. Lett.* **1997**, *40*, 631−636.
(74) Español, P.; Warren, P. B. Statistical Mechanics of Dissipative Particle Dynamics. *Europhys. Lett.* **1995**, *30*, 191−196.
(75) Español, P. Hydrodynamics from Dissipative Particle Dynamics. *Phys. Rev. E* **1995**, *52*, 1734−1742.
(76) Español, P. Dissipative Particle Dynamics with Energy Conservation. *Europhys. Lett.* **1997**, *40*, 631.
(77) Groot, R. D.; Warren, P. B. Dissipative Particle Dynamics: Bridging the Gap between Atomistic and Mesoscopic Simulation. *J. Chem. Phys.* **1997**, *107*, 4423−4435.
(78) Sliozberg, Y. R.; Strawhecker, K. E.; Andzelm, J. W.; Lenhart, J. L. Computational and Experimental Investigation of Morphology in Thermoplastic Elastomer gels Composed of AB/ABA Blends in B-Selective Solvent. *Soft Matter* **2011**, *7*, 7539−7551.
(79) Sliozberg, Y. R.; Andzelm, J. W.; Brennan, J. K.; Vanlandingham, M. R.; Pryamitsyn, V.; Ganesan, V. Modeling Viscoelastic Properties of Triblock Copolymers: A DPD Simulation Study. *J. Polym. Sci. B: Polym. Phys.* **2010**, *48*, 15−25.
(80) Matsen, M. W.; Tompson, R. B. Equilibrium Behavior of Asymmetric ABA Triblock Copolymer Melts. *J. Chem. Phys.* **2000**, *113*, 5539.
(81) Groot, R. D.; Madden, T. J.; Tildesley, D. J. On the Role of Hydrodynamic Interactions in Block Copolymer Microphase Separation. *J. Chem. Phys.* **1999**, *110*, 9739−9749.
(82) Abu-Sharkh, B.; Alsunaidi, A. Morphology and Conformation Analysis of Self-Assembled Triblock Copolymer Melts. *Macromol. Theor. Simul.* **2006**, *15*, 507−515.
(83) Groot, R. D.; Rabone, K. L. Mesoscopic Simulation of Cell Membrane Damage, Morphology Change and Rupture by Nonionic Surfactants. *Biophys. J.* **2001**, *81*, 725−736.
(84) Santo, K. P.; Neimark, A. V. Dissipative Particle Dynamics Simulations in Colloid and Interface Science: A Review. *Adv. Colloid Interface Sci.* **2021**, *298*, 102545.
(85) Mao, R.; Lee, M. T.; Vishnyakov, A.; Neimark, A. V. Modeling Aggregation of Ionic Surfactants Using a Smeared Charge Approximation in Dissipative Particle Dynamics Simulations. *J. Phys. Chem. B* **2015**, *119*, 11673−11683.
(86) Vishnyakov, A.; Neimark, A. V. Self-Assembly in Nafion Membranes upon Hydration: Water Mobility and Adsorption Isotherms. *J. Phys. Chem. B* **2014**, *118*, 11353−11364.
(87) Groot, R. D. Electrostatic Interactions in Dissipative Particle Dynamics-Simulation of Polyelectrolytes and Anionic Surfactants. *J. Chem. Phys.* **2003**, *118*, 11265−11277.
(88) Lee, M. T.; Vishnyakov, A.; Neimark, A. V. Modeling Proton Dissociation and Transfer Using Dissipative Particle Dynamics Simulation. *J. Chem. Theory Comput.* **2015**, *11*, 4395−4403.
(89) Chantawansri, T. L.; Sirk, T. W.; Mrozek, R.; Lenhart, J. L.; Kröger, M.; Sliozberg, Y. R. The Effect of Polymer Chain Length on the Mechanical Properties of Triblock Copolymer Gels. *Chem. Phys. Lett.* **2014**, *612*, 157−161.
(90) Chantawansri, T. L.; Sirk, T. W.; Sliozberg, Y. R. Entangled Triblock Copolymer Gel: Morphological and Mechanical Properties. *J. Chem. Phys.* **2013**, *138*, 024908.
(91) Sirk, T. W.; Slizoberg, Y. R.; Brennan, J. K.; Lisal, M.; Andzelm, J. W. An Enhanced Entangled Polymer Model for Dissipative Particle Dynamics. *J. Chem. Phys.* **2012**, *136*, 134903.
(92) Vishnyakov, A.; Talaga, D. S.; Neimark, A. V. DPD Simulation of Protein Conformations: From α-Helices to β-Structures. *J. Phys. Chem. Lett.* **2012**, *3*, 3081−3087.
(93) Roy, S.; Markova, D.; Kumar, A.; Klapper, M.; Müller-Plathe, F. Morphology of Phosphonic Acid-Functionalized Block Copolymers Studied by Dissipative Particle Dynamics Morphology of Phosphonic Acid-Functionalized Block Copolymers Studied by Dissipative Particle Dynamics. *Macromolecules* **2009**, *42*, 841−848.
(94) Lindvig, T.; Michelsen, M. L.; Kontogeorgis, G. M. A Flory-Huggins Model Based on the Hansen Solubility Parameters. *Fluid Phase Equilib.* **2002**, *203*, 247−260.
(95) Hansen, C. M. *Hansen Solubility Parameters: A User's Handbook*; CRC, 2002; p 544.
(96) Mayoral, E.; Goicochea, A. G. Modeling the Temperature Dependent Interfacial Tension between Organic Solvents and Water Using Dissipative Particle Dynamics. *J. Chem. Phys.* **2013**, *138*, 094703.
(97) Maiti, A.; McGrother, S. Bead-Bead Interaction Parameters in Dissipative Particle Dynamics: Relation to Bead-Size, Solubility Parameter, and Surface Tension. *J. Chem. Phys.* **2004**, *120*, 1594−1601.
(98) Fan, C.; Olafson, B. D.; Blanco, M.; Hsu, S. L. Application of Molecular Simulation to Derive Phase Diagrams of Binary Mixtures. *Macromolecules* **1992**, *25*, 3667−3676.
(99) Yamamoto, S.; Hyodo, S.-A. A Computer Simulation Study of the Mesoscopic Structure of the Polyelectrolyte Membrane Nafion. *Polym. J.* **2003**, *35*, 519−527.
(100) Vishnyakov, A.; Lee, M.-T.; Neimark, A. V. Prediction of the Critical Micelle Concentration of Nonionic Surfactants by Dissipative Particle Dynamics Simulations. *J. Phys. Chem. Lett.* **2013**, *4*, 797−802.
(101) Widom, B. Some Topics in the Theory of Fluids. *J. Chem. Phys.* **1963**, *39*, 2808−2812.
(102) Eckert, F.; Klamt, A. *Cosmotherm*, version C3.0, release 12.01; Cosmologic: Leverkusen, Germany, 2012.

https://doi.org/10.1021/acs.chemrev.1c00913
Chem. Rev. 2022, 122, 10710−10745

(103) Klamt, A. Conductor-Like Screening Model for Real Solvents: A New Approach to the Quantitative Calculation of Solvation Phenomena. *J. Phys. Chem.* **1995**, *99*, 2224−2235.
(104) Sepehr, F.; Paddison, S. J. Dissipative Particle Dynamics Interaction Parameters from Ab Initio Calculations. *Chem. Phys. Lett.* **2016**, *645*, 20−26.
(105) Okuwaki, K.; Mochizuki, Y.; Doi, H.; Ozawa, T. Fragment Molecular Orbital Based Parametrization Procedure for Mesoscopic Structure Prediction of Polymeric Materials. *J. Phys. Chem. B* **2018**, *122*, 338−347.
(106) Fedorov, D. G.; Kitaura, K., Eds.; *The Fragment Molecular Orbital Method: Practical Applications to Large Molecular Systems*; CRC: Boca Raton, FL, 2009; p 288.
(107) Okuwaki, K.; Mochizuki, Y.; Doi, H.; Kawada, S.; Ozawa, T.; Yasuoka, K. Theoretical Analyses on Water Cluster Structures in Polymer Electrolyte Membrane by Using Dissipative Particle Dynamics Simulations with Fragment Molecular Orbital Based Effective Parameters. *RSC Adv.* **2018**, *8*, 34582−34595.
(108) *J-OCTA*; NTT Data Group, 2022; https://www.j-octa.com.
(109) Mochizuki, Y.; Koikegami, S.; Nakano, T.; Amari, S.; Kitaura, K. Large Scale MP2 Calculations with Fragment Molecular Orbital Scheme. *Chem. Phys. Lett.* **2004**, *396*, 473−479.
(110) Weber, A. Z.; Borup, R. L.; Darling, R. M.; Das, P. K.; Dursch, T. J.; Gu, W.; Harvey, D.; Kusoglu, A.; Litster, S.; Mench, M. M.; et al. A Critical Review of Modeling Transport Phenomena in Polymer-Electrolyte Fuel Cells. *J. Electrochem. Soc.* **2014**, *161*, F1254−F1299.
(111) Weber, A. Z.; Newman, J. Modeling Transport in Polymer-Electrolyte Fuel Cells. *Chem. Rev.* **2004**, *104*, 4679−4726.
(112) Newman, J. S. *Electrochemical Systems*; Prentice Hall: Englewood Cliffs, NJ, 1991; p 560.
(113) Crothers, A. R.; Darling, R. M.; Kusoglu, A.; Radke, C. J.; Weber, A. Z. Theory of Multicomponent Phenomena in Cation-Exchange Membranes: Part II. Transport Model and Validation. *J. Electrochem. Soc.* **2020**, *167*, 013548.
(114) Delacourt, C.; Newman, J. Mathematical Modeling of a Cation-Exchange Membrane Containing Two Cations. *J. Electrochem. Soc.* **2008**, *155*, B1210.
(115) Pintauro, P. N.; Bennion, D. N. Mass Transport of Electrolytes in Membranes. 1. Development of Mathematical Transport Model. *Ind. Eng. Chem. Fundam.* **1984**, *23*, 230−234.
(116) Hirschfelder, J. O.; Curtiss, C. F.; Bird, R. B. *Molecular Theory of Gases and Liquids*; Wiley: New York, 1964; Vol. *165*, p 1280.
(117) Newman, J. S.; Thomas-Alyea, K. E. *Electrochemical Systems*, 3rd ed.; John Wiley & Sons, 2012; p 672.
(118) Krishna, R.; Wesselingh, J. A. The Maxwell-Stefan Approach to Mass Transfer. *Chem. Eng. Sci.* **1997**, *52*, 861−911.
(119) Wesselingh, J. A.; Vonk, P.; Kraaijeveld, G. Exploring the Maxwell-Stefan Description of Ion Exchange. *Chem. Eng. J. Biochem. Eng. J.* **1995**, *57*, 75−89.
(120) Ghanbarian, B.; Hunt, A. G.; Ewing, R. P.; Sahimi, M. Tortuosity in Porous Media: A Critical Review. *Soil Sci. Soc. Am. J.* **2013**, *77*, 1461−1477.
(121) Heimenz, P. C. *Principles of Colloid and Surface Chemistry*; M. Dekker: New York, 1986; p 672.
(122) Paddison, S. J.; Paul, R.; Zawodzinski, T. A. Proton Friction and Diffusion Coefficients in Hydrated Polymer Electrolyte Membranes: Computations with a Non-Equilibrium Statistical Mechanical Model. *J. Chem. Phys.* **2001**, *115*, 7753−7761.
(123) Paddison, S. J.; Paul, R.; Zawodzinski, T. A. A Statistical Mechanical Model of Proton and Water Transport in a Proton Exchange Membrane. *J. Electrochem. Soc.* **2000**, *147*, 617−626.
(124) Stansfeld, P. J.; Sansom, M. S. P. From Coarse Grained to Atomistic: A Serial Multiscale Approach to Membrane Protein Simulations. *J. Chem. Theory Comput.* **2011**, *7*, 1157−1166.
(125) Ensing, B.; Nielsen, S. O., Multiscale Molecular Dynamics and the Reverse Mapping Problem. In *Trends in Computational Nanomechanics: Transcending Length and Time Scales*; Dumitrica, T., Ed.; Springer: Dordrecht, 2010; pp 25−59.
(126) Hess, B.; León, S.; van der Vegt, N.; Kremer, K. Long Time Atomistic Polymer Trajectories from Coarse Grained Simulations: Bisphenol-A Polycarbonate. *Soft Matter* **2006**, *2*, 409−414.
(127) Kuo, A. T.; Miyazaki, Y.; Jang, C.; Miyajima, T.; Urata, S.; Nielsen, S. O.; Okazaki, S.; Shinoda, W. Large-Scale Molecular Dynamics Simulation of Perfluorosulfonic Acid Membranes: Remapping Coarse-Grained to All-Atomistic Simulations. *Polymer* **2019**, *181*, 121766.
(128) Clark, J. A.; Santiso, E. E.; Frischknecht, A. L. Morphology and Proton Diffusion in a Coarse-Grained Model of Sulfonated Poly(phenylenes). *J. Chem. Phys.* **2019**, *151*, 104901.
(129) Elliott, J. A.; Wu, D.; Paddison, S. J.; Moore, R. B. A Unified Morphological Description of Nafion Membranes from SAXS and Mesoscale Simulations. *Soft Matter* **2011**, *7*, 6820−6827.
(130) Komarov, P. V.; Veselov, I. N.; Chu, P. P.; Khalatur, P. G. Mesoscale Simulation of Polymer Electrolyte Membranes Based on Sulfonated Poly(ether ether ketone) and Nafion. *Soft Matter* **2010**, *6*, 3939−3956.
(131) Wu, D.; Paddison, S. J.; Elliott, J. A. A Comparative Study of the Hydrated Morphologies of Perfluorosulfonic Acid Fuel Cell Membranes with Mesoscopic Simulations. *Energy Environ. Sci.* **2008**, *1*, 284−293.
(132) Wescott, J. T.; Qi, Y.; Subramanian, L.; Weston Capehart, T. Mesoscale Simulation of Morphology in Hydrated Perfluorosulfonic Acid Membranes. *J. Chem. Phys.* **2006**, *124*, 134702.
(133) Eikerling, M.; Kornyshev, A. A.; Stimming, U. Electrophysical Properties of Polymer Electrolyte Membranes: A Random Network Model. *J. Phys. Chem. B* **1997**, *101*, 10807−10820.
(134) Gierke, T. D.; Munn, G. E.; Wilson, F. C. The Morphology in Nafion Perfluorinated Membrane Products, as Determined by Wide- and Small-Angle X-Ray Studies. *J. Polym. Sci., Polym. Phys.* **1981**, *19*, 1687−1704.
(135) Qi, Y.; Lai, Y. H. Mesoscale Modeling of the Influence of Morphology on the Mechanical Properties of Proton Exchange Membranes. *Polymer* **2011**, *52*, 201−210.
(136) Morohoshi, K.; Hayashi, T. Modeling and Simulation for Fuel Cell Polymer Electrolyte Membrane. *Polymers (Basel)* **2013**, *5*, 56−76.
(137) Wu, D. S.; Paddison, S. J.; Elliott, J. A. Effect of Molecular Weight on Hydrated Morphologies of the Short-Side-Chain Perfluorosulfonic Acid Membrane. *Macromolecules* **2009**, *42*, 3358−3367.
(138) Wu, D.; Paddison, S. J.; Elliott, J. A.; Hamrock, S. J. Mesoscale Modeling of Hydrated Morphologies of 3M Perfluorosulfonic Acid-Based Fuel Cell Electrolytes. *Langmuir* **2010**, *26*, 14308−14315.
(139) Wang, C.; Krishnan, V.; Wu, D. S.; Bledsoe, R.; Paddison, S. J.; Duscher, G. Evaluation of the Microstructure of Dry and Hydrated Perfluorosulfonic Acid Ionomers: Microscopy and Simulations. *J. Mater. Chem. A* **2013**, *1*, 938−944.
(140) Wang, C.; Paddison, S. J. Mesoscale Modeling of Hydrated Morphologies of Sulfonated Polysulfone Ionomers. *Soft Matter* **2014**, *10*, 819−830.
(141) Liu, H.; Cavaliere, S.; Jones, D. J.; Rozière, J.; Paddison, S. J. Morphology of Hydrated Nafion through a Quantitative Cluster Analysis: A Case Study Based on Dissipative Particle Dynamics Simulations. *J. Phys. Chem. C* **2018**, *122*, 13130−13139.
(142) Liu, H.; Cavaliere, S.; Jones, D. J.; Rozière, J.; Paddison, S. J. Scaling Behavior of Nafion with Different Model Parameterizations in Dissipative Particle Dynamics Simulations. *Macromol. Theor. Simul.* **2018**, *27*, 1800003.
(143) Sengupta, S.; Lyulin, A. Dissipative Particle Dynamics Modeling of Polyelectrolyte Membrane-Water Interfaces. *Polymers (Basel)* **2020**, *12*, 907.
(144) Gebel, G. Structural Evolution of Water Swollen Perfluorosulfonated Ionomers from Dry Membrane to Solution. *Polymer* **2000**, *41*, 5829−5838.
(145) Luo, X.; Liu, H.; Bae, C.; Tuckerman, M. E.; Hickner, M. A.; Paddison, S. J. Mesoscale Simulations of Quaternary Ammonium-Tethered Triblock Copolymers: Effects of the Degree of Function-

alization and Styrene Content. *J. Phys. Chem. C* **2020**, *124*, 16315−16323.
(146) Zhu, Z.; Luo, X.; Paddison, S. J. DPD Simulations of Anion Exchange Membranes Functionalized with Various Cationic Groups and Associated Anions. *Solid State Ion.* **2019**, *340*, 115011.
(147) Luo, X.; Paddison, S. J. DPD Simulations of Anion Exchange Membrane: The Effect of an Alkyl Spacer on the Hydrated Morphology. *Solid State Ion.* **2019**, *339*, 115012.
(148) Sepehr, F.; Liu, H.; Luo, X.; Bae, C.; Tuckerman, M. E.; Hickner, M. A.; Paddison, S. J. Mesoscale Simulations of Anion Exchange Membranes Based on Quaternary Ammonium Tethered Triblock Copolymers. *Macromolecules* **2017**, *50*, 4397−4405.
(149) Dorenbos, G. How Hydrophobic Side Chain Design Affects Water Cluster Connectivity In Model Polymer Electrolyte Membranes: Linear Versus Y-Shaped Side Chains. *Int. J. Hydrogen Energy* **2020**, *45*, 33906−33924.
(150) Dorenbos, G. Coarse-Grained Study of the Effect of Hydrophobic Side Chain Length on Cluster Size Distributions and Water Diffusion in (Amphiphilic-Hydrophobic) Multi-Block Co-Polymer Membranes. *Polymer* **2019**, *173*, 43−57.
(151) Dorenbos, G. Doping Proton Transport Channels in Poly-Electrolyte Membranes with High Acidic Site Density Polymers. *Eur. Polym. J.* **2017**, *97*, 14−25.
(152) Dorenbos, G. Competition between Side Chain Length and Side Chain Distribution: Searching for Optimal Polymeric Architectures for Application in Fuel Cell Membranes. *J. Power Sources* **2015**, *276*, 328−339.
(153) Dorenbos, G. Dependence of Percolation Threshold on Side Chain Distribution within Amphiphilic Polyelectrolyte Membranes. *RSC Adv.* **2013**, *3*, 18630−18642.
(154) Johansson, E. O.; Yamada, T.; Sunden, B.; Yuan, J. L. Dissipative Particle Dynamics Approach for Nano-Scale Membrane Structure Reconstruction and Water Diffusion Coefficient Estimation. *Int. J. Hydrogen Energy* **2015**, *40*, 1800−1808.
(155) Jorn, R.; Savage, J.; Voth, G. A. Proton Conduction in Exchange Membranes across Multiple Length Scales. *Acc. Chem. Res.* **2012**, *45*, 2002−2010.
(156) Liu, S.; Savage, J.; Voth, G. A. Mesoscale Study of Proton Transport in Proton Exchange Membranes: Role of Morphology. *J. Phys. Chem. C* **2015**, *119*, 1753−1762.
(157) Allahyarov, E.; Taylor, P. L. Predicted Electric-Field-Induced Hexatic Structure in an Ionomer Membrane. *Phys. Rev. E* **2009**, *80*, 020801.
(158) Allahyarov, E.; Taylor, P. L. Simulation Study of the Correlation between Structure and Conductivity in Stretched Nafion. *J. Phys. Chem. B* **2009**, *113*, 610−617.
(159) Kuo, A. T.; Okazaki, S.; Shinoda, W. Transferable Coarse-Grained Model for Perfluorosulfonic Acid Polymer Membranes. *J. Chem. Phys.* **2017**, *147*, 094904.
(160) Ghelichi, M.; Melchy, P. E. A.; Eikerling, M. H. Radically Coarse-Grained Approach to the Modeling of Chemical Degradation in Fuel Cell Ionomers. *J. Phys. Chem. B* **2014**, *118*, 11375−11386.
(161) Quiroga, M. A.; Malek, K.; Franco, A. A. A Multiparadigm Modeling Investigation of Membrane Chemical Degradation in PEM Fuel Cells. *J. Electrochem. Soc.* **2016**, *163*, F59−F70.
(162) Rodgers, M. P.; Bonville, L. J.; Kunz, H. R.; Slattery, D. K.; Fenton, J. M. Fuel Cell Perfluorinated Sulfonic Acid Membrane Degradation Correlating Accelerated Stress Testing and Lifetime. *Chem. Rev.* **2012**, *112*, 6075−6103.
(163) Ghelichi, M.; Malek, K.; Eikerling, M. H. Ionomer Self-Assembly in Dilute Solution Studied by Coarse-Grained Molecular Dynamics. *Macromolecules* **2016**, *49*, 1479−1489.
(164) Malek, A.; Sadeghi, E.; Jankovic, J.; Eikerling, M.; Malek, K. Aquivion Ionomer in Mixed Alcohol-Water Solution: Insights from Multiscale Molecular Modeling. *J. Phys. Chem. C* **2020**, *124*, 3429−3438.
(165) Yan, L.; Shao, C.; Ji, X. Evaluation of Electroosmotic Drag Coefficient of Water in Hydrated Sodium Perfluorosulfonate Electrolyte Polymer. *J. Comput. Chem.* **2009**, *30*, 1361−1370.
(166) Choe, Y.-K.; Tsuchida, E.; Ikeshoji, T.; Yamakawa, S.; Hyodo, S.-a. Nature of Water Transport and Electro-Osmosis in Nafion: Insights from First-Principles Molecular Dynamics Simulations under an Electric Field. *J. Phys. Chem. B* **2008**, *112*, 11586−11594.
(167) Jacobson, L. C.; Ren, X. M.; Molinero, V. Assessing the Effects of Crowding, Pore Size, and Interactions on Electro-Osmotic Drag Coefficients. *J. Phys. Chem. C* **2014**, *118*, 2093−2103.
(168) Allahyarov, E.; Lowen, H.; Taylor, P. L. Simulation Study of Ion Diffusion in Charged Nanopores with Anchored Terminal Groups. *Electrochim. Acta* **2017**, *242*, 73−85.
(169) Allahyarov, E.; Taylor, P. L.; Lowen, H. Enhanced Ionic Diffusion in Ionomer-Filled Nanopores. *J. Chem. Phys.* **2015**, *143*, 243126.
(170) Allahyarov, E.; Taylor, P. L. Simulation Study of the Equilibrium Morphology in Ionomers with Different Architectures. *J. Polym. Sci. B: Polym. Phys.* **2011**, *49*, 368−376.
(171) Liu, J.; Cui, S.; Keffer, D. J. Molecular-Level Investigation of Critical Gap Size between Catalyst Particles and Electrolyte in Hydrogen Proton Exchange Membrane Fuel Cells. *Fuel Cells* **2008**, *8*, 422−428.
(172) Yuan, J. L.; Xiao, Y. Modeling Development on the Meso-Scale Reacting Transport Phenomena in Proton Exchange Membrane Fuel Cells. *Acta Mech. Sin.* **2013**, *29*, 370−378.
(173) Xiao, Y.; Yuan, J. L.; Sunden, B. Process Based Large Scale Molecular Dynamic Simulation of a Fuel Cell Catalyst Layer. *J. Electrochem. Soc.* **2012**, *159*, B251−B258.
(174) Xiao, Y.; Dou, M. L.; Yuan, J. L.; Hou, M.; Song, W.; Sunden, B. Fabrication Process Simulation of a PEM Fuel Cell Catalyst Layer and Its Microscopic Structure Characteristics. *J. Electrochem. Soc.* **2012**, *159*, B308−B314.
(175) Weber, A. Z.; Newman, J. Transport in Polymer-Electrolyte Membranes: II. Mathematical Model. *J. Electrochem. Soc.* **2004**, *151*, A311.
(176) Weber, A. Z.; Newman, J. Transport in Polymer-Electrolyte Membranes: I. Physical Model. *J. Electrochem. Soc.* **2003**, *150*, A1008.
(177) Esai Selvan, M.; Calvo-Munoz, E.; Keffer, D. J. Toward a Predictive Understanding of Water and Charge Transport in Proton Exchange Membranes. *J. Phys. Chem. B* **2011**, *115*, 3052−3061.
(178) Kraytsberg, A.; Ein-Eli, Y. Review of Advanced Materials for Proton Exchange Membrane Fuel Cells. *Energy Fuels* **2014**, *28*, 7303−7330.
(179) Drioli, E.; Regina, A.; Casciola, M.; Oliveti, A.; Trotta, F.; Massari, T. Sulfonated PEEK-WC Membranes for Possible Fuel Cell Applications. *J. Membr. Sci.* **2004**, *228*, 139−148.
(180) Komarov, P. V.; Veselov, I. N.; Chu, P. P.; Khalatur, P. G.; Khokhlov, A. R. Atomistic and Mesoscale Simulation of Polymer Electrolyte Membranes Based on Sulfonated Poly(ether ether ketone). *Chem. Phys. Lett.* **2010**, *487*, 291−296.
(181) Dong, T. D.; Hu, J. H.; Ueda, M.; Wu, Y. M.; Zhang, X.; Wang, L. J. Enhanced Proton Conductivity of Multiblock Poly-(phenylene ether ketone)s via Pendant Sulfoalkoxyl Side Chains with Excellent H2 /Air Fuel Cell Performance. *J. Mater. Chem. A* **2016**, *4*, 2321−2331.
(182) Wang, J.; Xu, Z.; Chen, J.; Yang, X.; Ramakrishna, S.; Liu, Y. Mesoscale Simulation on the Hydrated Morphologies of SPEEK Membrane. *Macromol. Theor. Simul.* **2021**, *30*, 2100006.
(183) Ma, Y.; Wang, Y.; Deng, X.; Zhou, G.; Khalid, S.; Sun, X.; Sun, W.; Zhou, Q.; Lu, G. Dissipative Particle Dynamics and Molecular Dynamics Simulations on Mesoscale Structure and Proton Conduction in a SPEEK/PVDF-g-PSSA Membrane. *RSC Adv.* **2017**, *7*, 39676−39684.
(184) Tripathy, M.; Deshpande, A. P.; Kumar, P. B. S. How Much Can We Coarse-Grain while Retaining the Chemical Specificity? A Study of Sulfonated Poly(ether ether ketone). *Macromol. Theor. Simul.* **2016**, *25*, 155−169.
(185) Sorte, E. G.; Paren, B. A.; Rodriguez, C. G.; Fujimoto, C.; Poirier, C.; Abbott, L. J.; Lynd, N. A.; Winey, K. I.; Frischknecht, A. L.; Alam, T. M. Impact of Hydration and Sulfonation on the

https://doi.org/10.1021/acs.chemrev.1c00913
Chem. Rev. 2022, 122, 10710−10745

Morphology and Ionic Conductivity of Sulfonated Poly(phenylene) Proton Exchange Membranes. *Macromolecules* **2019**, *52*, 857−876.
(186) Schuster, M.; Kreuer, K.-D.; Andersen, H. T.; Maier, J. Sulfonated Poly(phenylene sulfone) Polymers as Hydrolytically and Thermooxidatively Stable Proton Conducting Ionomers. *Macromolecules* **2007**, *40*, 598−607.
(187) Deng, S.; Hassan, M. K.; Nalawade, A.; Perry, K. A.; More, K. L.; Mauritz, K. A.; McDonnell, M. T.; Keffer, D. J.; Mays, J. W. High Temperature Proton Exchange Membranes with Enhanced Proton Conductivities at Low Humidity and High Temperature Based on Polymer Blends and Block Copolymers of Poly(1,3-Cyclohexadiene) and Poly(ethylene Glycol). *Polymer* **2015**, *77*, 208−217.
(188) Wang, Q. F.; Keffer, D. J.; Deng, S. X.; Mays, J. Multi-Scale Models for Cross-Linked Sulfonated Poly (1, 3-Cyclohexadiene) Polymer. *Polymer* **2012**, *53*, 1517−1528.
(189) Wang, Q. F.; Suraweera, N. S.; Keffer, D. J.; Deng, S. X.; Mays, J. Atomistic and Coarse-Grained Molecular Dynamics Simulation of a Cross-Linked Sulfonated Poly(1,3-cyclohexadiene)-Based Proton Exchange Membrane. *Macromolecules* **2012**, *45*, 6669−6685.
(190) Hu, C. C.; Lu, T.; Guo, H. X. Mesoscale Modeling of Sulfonated Polyimides Copolymer Membranes: Effect of Sequence Distributions. *J. Membr. Sci.* **2018**, *564*, 146−158.
(191) Kim, Y. G.; Bae, Y. C. A Particle Dynamic Simulation for Morphological Aspects of Proton Exchange Membranes. *Macromol. Res.* **2013**, *21*, 502−510.
(192) Aryal, D.; Ganesan, V. Impact of Cross-Linking of Polymers on Transport of Salt and Wwater in Polyelectrolyte Membranes: A Mesoscopic Simulation Study. *J. Chem. Phys.* **2018**, *149*, 224902.
(193) Aryal, D.; Ganesan, V. Reversal of Salt Concentration Dependencies of Salt and Water Diffusivities in Polymer Electrolyte Membranes. *ACS Macro Lett.* **2018**, *7*, 739−744.
(194) Kamcev, J.; Paul, D. R.; Manning, G. S.; Freeman, B. D. Ion Diffusion Coefficients in Ion Exchange Membranes: Significance of Counterion Condensation. *Macromolecules* **2018**, *51*, 5519−5529.
(195) Santo, K. P.; Vishnyakov, A.; Kumar, R.; Neimark, A. V. Elucidating the Effects of Metal Complexation on Morphological and Rheological Properties of Polymer Solutions by a Dissipative Particle Dynamics Model. *Macromolecules* **2018**, *51*, 4987−5000.
(196) Santo, K. P.; Neimark, A. V. Effects of Metal-Polymer Complexation on Structure and Transport Properties of Metal-Substituted Polyelectrolyte Membranes. *J. Colloid Interface Sci.* **2021**, *602*, 654−668.
(197) Santo, K. P.; Fabijanic, K. I.; Cheng, C.-Y.; Potanin, A.; Neimark, A. V. Modeling of the Effects of Metal Complexation on the Morphology and Rheology of Xanthan Gum Polysaccharide Solutions. *Macromolecules* **2021**, *54*, 8675−8692.
(198) Lu, J.; Barnett, A.; Molinero, V. Effect of Polymer Architecture on the Nanophase Segregation, Ionic Conductivity, and Electro-Osmotic Drag of Anion Exchange Membranes. *J. Phys. Chem. C* **2019**, *123*, 8717−8726.
(199) Dong, D.; Zhang, W.; Barnett, A.; Lu, J.; van Duin, A. C. T.; Molinero, V.; Bedrov, D. Multiscale Modeling of Structure, Transport and Reactivity in Alkaline Fuel Cell Membranes: Combined Coarse-Grained, Atomistic and Reactive Molecular Dynamics Simulations. *Polymers (Basel)* **2018**, *10*, 1289.
(200) Lu, J.; Jacobson, L. C.; Perez Sirkin, Y. A.; Molinero, V. High-Resolution Coarse-Grained Model of Hydrated Anion-Exchange Membranes that Accounts for Hydrophobic and Ionic Interactions through Short-Ranged Potentials. *J. Chem. Theory Comput.* **2017**, *13*, 245−264.
(201) Yang, Y.; Fu, N.; Dong, Q.; Li, M.; Li, J.; Li, C.; Wei, Z. Self-Aggregation to Construct Hydroxide Highways in Anion Exchange Membranes. *Adv. Mater. Interfaces* **2020**, *7*, 1902143.
(202) González-Melchor, M.; Mayoral, E.; Velázquez, M. E.; Alejandre, J. Electrostatic Interactions in Dissipative Particle Dynamics Using the Ewald Sums. *J. Chem. Phys.* **2006**, *125*, 224107.
(203) Sarkisov, L.; Harrison, A. Computational Structure Characterisation Tools in Application to Ordered and Disordered Porous Materials. *Mol. Simul.* **2011**, *37*, 1248−1257.
(204) Pan, J.; Chen, C.; Li, Y.; Wang, L.; Tan, L.; Li, G.; Tang, X.; Xiao, L.; Lu, J.; Zhuang, L. Constructing Ionic Highway in Alkaline Polymer Electrolytes. *Energy Environ. Sci.* **2014**, *7*, 354−360.
(205) Ran, J.; Ding, L.; Chu, C.; Liang, X.; Pan, T.; Yu, D.; Xu, T. Highly Conductive and Stabilized Side-Chain-Type Anion Exchange Membranes: Ideal Alternatives for Alkaline Fuel Cell Applications. *J. Mater. Chem. A* **2018**, *6*, 17101−17110.
(206) Chen, S.; Wang, H.; Zhang, J.; Lu, S.; Xiang, Y. Effect of Side Chain on the Electrochemical Performance of Poly (ether ether ketone) Based Anion-Exchange Membrane: A Molecular Dynamics Study. *J. Membr. Sci.* **2020**, *605*, 118105.
(207) Zhang, Z.; Krajniak, J.; Keith, J. R.; Ganesan, V. Mechanisms of Ion Transport in Block Copolymeric Polymerized Ionic Liquids. *ACS Macro Lett.* **2019**, *8*, 1096−1101.
(208) Chong, G.; Hernandez, R. Adsorption Dynamics and Structure of Polycations on Citrate-Coated Gold Nanoparticles. *J. Phys. Chem. C* **2018**, *122*, 19962−19969.
(209) Washizu, H.; Kinjo, T.; Yoshida, H. Structure of Polyelectrolyte Brushes Studied by Coarse Grain Simulations. *Friction* **2014**, *2*, 73−81.
(210) Angelescu, D. G. Coarse-Grained Simulation Studies on the Adsorption of Polyelectrolyte Complexes upon Lipid Mmembranes. *Phys. Chem. Chem. Phys.* **2019**, *21*, 12446−12459.
(211) Duan, X.; Zhang, R.; Li, Y.; Yang, Y.; Shi, T.; An, L.; Huang, Q. Effect of Polyelectrolyte Adsorption on Lateral Distribution and Dynamics of Anionic Lipids: A Monte Carlo Study of a Coarse-Grain Model. *Eur. Biophys. J.* **2014**, *43*, 377−391.
(212) Duan, X.; Zhang, R.; Li, Y.; Shi, T.; An, L.; Huang, Q. Monte Carlo Study of Polyelectrolyte Adsorption on Mixed Lipid Membrane. *J. Phys. Chem. B* **2013**, *117*, 989−1002.
(213) Duan, X.; Li, Y.; Zhang, R.; Shi, T.; An, L.; Huang, Q. Regulation of Anionic Lipids in Binary Membrane upon the Adsorption of Polyelectrolyte: A Monte Carlo Simulation. *AIP Adv.* **2013**, *3*, 062128.
(214) Khan, N.; Zaragoza, N. Z.; Travis, C. E.; Goswami, M.; Brettmann, B. K. Polyelectrolyte Complex Coacervate Assembly with Cellulose Nanofibers. *ACS Omega* **2020**, *5*, 17129−17140.
(215) Sethuraman, V.; McGovern, M.; Morse, D. C.; Dorfman, K. D. Influence of Charge Sequence on the Adsorption of Polyelectrolytes to Oppositely-Charged Polyelectrolyte Brushes. *Soft Matter* **2019**, *15*, 5431−5442.
(216) Dias, R. S.; Pais, A. A. C. C. Polyelectrolyte Condensation in Bulk, at Surfaces, and under Confinement. *Adv. Colloid Interface Sci.* **2010**, *158*, 48−62.
(217) Sarraguça, J. M. G.; Skepö, M.; Pais, A. A. C. C.; Linse, P. Structure of Polyelectrolytes in 3:1 Salt Solutions. *J. Chem. Phys.* **2003**, *119*, 12621−12628.
(218) Dias, R. S.; Linse, P.; Pais, A. A. C. C. Stepwise Disproportionation in Polyelectrolyte Complexes. *J. Comput. Chem.* **2011**, *32*, 2697−2707.
(219) Dias, R. S.; Pais, A. A. C. C.; Miguel, M. G.; Lindman, B. Modeling of DNA Compaction by Polycations. *J. Chem. Phys.* **2003**, *119*, 8150−8157.
(220) Narambuena, C. F.; Leiva, E. P. M.; Chávez-Páez, M.; Pérez, E. Effect of Chain Stiffness on the Morphology of Polyelectrolyte Complexes. A Monte Carlo Simulation Study. *Polymer* **2010**, *51*, 3293−3302.
(221) Angelescu, D. G.; Caragheorgheopol, D. Investigating the Effects of the Copolymer Architecture on the Properties of the Polyion Complexes by Monte Carlo Simulations. *Colloid Polym. Sci.* **2016**, *294*, 965−979.
(222) Torres, P.; Bojanich, L.; Sanchez-Varretti, F.; Ramirez-Pastor, A. J.; Quiroga, E.; Boeris, V.; Narambuena, C. F. Protonation of β-Lactoglobulin in the Presence of Strong Polyelectrolyte Chains: A Study Using Monte Carlo Simulation. *Colloid Surface B* **2017**, *160*, 161−168.
(223) Elder, R. M.; Jayaraman, A. Coarse-Grained Simulation Studies of Effects of Polycation Architecture on Structure of the

Polycation and Polycation-Polyanion Complexes. *Macromolecules* **2012**, *45*, 8083−8096.
(224) Peng, B.; Muthukumar, M. Modeling Competitive Substitution in a Polyelectrolyte Complex. *J. Chem. Phys.* **2015**, *143*, 243133.
(225) Zhan, B.; Shi, K.; Dong, Z.; Lv, W.; Zhao, S.; Han, X.; Wang, H.; Liu, H. Coarse-Grained Simulation of Polycation/DNA-Like Complexes: Role of Neutral Block. *Mol. Pharmaceutics* **2015**, *12*, 2834−2844.
(226) Xu, X.; Kanduč, M.; Wu, J.; Dzubiella, J. Potential of Mean Force and Transient States in Polyelectrolyte Pair Complexation. *J. Chem. Phys.* **2016**, *145*, 034901.
(227) Saha, B.; Gordievskaya, Y. D.; De, P.; Kramarenko, E. Y. Unusual Nanostructured Morphologies Enabled by Interpolyelectrolyte Complexation of Polyions Bearing Incompatible Nonionic Segments. *Macromolecules* **2020**, *53*, 10754−10764.
(228) Gallops, C. E.; Ziebarth, J. D.; Wang, Y. Coarse-Grained Simulations of the Impact of Chain Length and Stiffness on the Formation and Aggregation of Polyelectrolyte Complexes. *Macromol. Theor. Simul.* **2020**, *29*, 2000015.
(229) Shen, K.-H.; Hall, L. M. Effects of Ion Size and Dielectric Constant on Ion Transport and Transference Number in Polymer Electrolytes. *Macromolecules* **2020**, *53*, 10086−10096.
(230) Shen, K.-H.; Hall, L. M. Ion Conductivity and Correlations in Model Salt-Doped Polymers: Effects of Interaction Strength and Concentration. *Macromolecules* **2020**, *53*, 3655−3668.
(231) Seo, Y.; Shen, K.-H.; Brown, J. R.; Hall, L. M. Role of Solvation on Diffusion of Ions in Diblock Copolymers: Understanding the Molecular Weight Effect through Modeling. *J. Am. Chem. Soc.* **2019**, *141*, 18455−18466.
(232) Brown, J. R.; Seo, Y.; Hall, L. M. Ion Correlation Effects in Salt-Doped Block Copolymers. *Phys. Rev. Lett.* **2018**, *120*, 127801.
(233) Wang, Y.; Xie, T.; France-Lanord, A.; Berkley, A.; Johnson, J. A.; Shao-Horn, Y.; Grossman, J. C. Toward Designing Highly Conductive Polymer Electrolytes by Machine Learning Assisted Coarse-Grained Molecular Dynamics. *Chem. Mater.* **2020**, *32*, 4144−4151.

Recommended by ACS

Combined Simulation and Experimental Study of Polyampholyte Solution Properties: Effects of Charge Ratio, Hydrophobic Groups, and Polymer Concentration
Wengang Zhang, Jack F. Douglas, *et al.*
JULY 14, 2022
MACROMOLECULES
READ

Molecular Simulations to Elucidate Transport Phenomena in Polymeric Membranes
Mohammad Heiranian, Menachem Elimelech, *et al.*
MARCH 02, 2022
ENVIRONMENTAL SCIENCE & TECHNOLOGY
READ

Unclonable Features via Electrospraying of Bulk Polymers
Abidin Esidir, M. Serdar Onses, *et al.*
JUNE 30, 2022
ACS APPLIED POLYMER MATERIALS
READ

Charged Block Copolymers: From Fundamentals to Electromechanical Applications
Jaemin Min, Moon Jeong Park, *et al.*
SEPTEMBER 24, 2021
ACCOUNTS OF CHEMICAL RESEARCH
READ

Get More Suggestions >

https://doi.org/10.1021/acs.chemrev.1c00913
Chem. Rev. 2022, 122, 10710−10745

frontiers | Frontiers in Chemistry

TYPE Review
PUBLISHED 19 August 2022
DOI 10.3389/fchem.2022.981508

Check for updates

OPEN ACCESS

EDITED BY
Siddhartha Das,
University of Maryland, College Park,
United States

REVIEWED BY
Zidan Zhang,
University of Texas at Austin,
United States
Rajarshi Chakrabarti,
Indian Institute of Technology Bombay,
India

*CORRESPONDENCE
Stephen J. Paddison,
spaddison@utk.edu

SPECIALTY SECTION
This article was submitted to Theoretical and Computational Chemistry, a section of the journal Frontiers in Chemistry

RECEIVED 29 June 2022
ACCEPTED 14 July 2022
PUBLISHED 19 August 2022

CITATION
Zhu Z and Paddison SJ (2022), Perspective: Morphology and ion transport in ion-containing polymers from multiscale modeling and simulations.
Front. Chem. 10:981508.
doi: 10.3389/fchem.2022.981508

COPYRIGHT
© 2022 Zhu and Paddison. This is an open-access article distributed under the terms of the Creative Commons Attribution License (CC BY). The use, distribution or reproduction in other forums is permitted, provided the original author(s) and the copyright owner(s) are credited and that the original publication in this journal is cited, in accordance with accepted academic practice. No use, distribution or reproduction is permitted which does not comply with these terms.

Perspective: Morphology and ion transport in ion-containing polymers from multiscale modeling and simulations

Zhenghao Zhu and Stephen J. Paddison*

Department of Chemical and Biomolecular Engineering, University of Tennessee, Knoxville, TN, United States

Ion-containing polymers are soft materials composed of polymeric chains and mobile ions. Over the past several decades they have been the focus of considerable research and development for their use as the electrolyte in energy conversion and storage devices. Recent and significant results obtained from multiscale simulations and modeling for proton exchange membranes (PEMs), anion exchange membranes (AEMs), and polymerized ionic liquids (polyILs) are reviewed. The interplay of morphology and ion transport is emphasized. We discuss the influences of polymer architecture, tethered ionic groups, rigidity of the backbone, solvents, and additives on both morphology and ion transport in terms of specific interactions. Novel design strategies are highlighted including precisely controlling molecular conformations to design highly ordered morphologies; tuning the solvation structure of hydronium or hydroxide ions in hydrated ion exchange membranes; turning negative ion-ion correlations to positive correlations to improve ionic conductivity in polyILs; and balancing the strength of noncovalent interactions. The design of single-ion conductors, well-defined supramolecular architectures with enhanced one-dimensional ion transport, and the understanding of the hierarchy of the specific interactions continue as challenges but promising goals for future research.

KEYWORDS

ion-containing polymers, specific interactions, morphology, ion transport, multiscale modeling, simulations

Introduction

Ion-containing polymers are an emerging class of materials including ionic polymers with counter ions and nonionic/neutral polymers doping with ionic material of low molecular weight, combining the advantages of a polymer matrix with mobile ions. They exhibit versatile and attractive properties and have attracted considerable interest as solid electrolytes for a variety of applications. They selectively conduct ions but not electrons. They are broadly used in energy conversion and storage devices, electrodialysis for water treatment, and solar-driven desalination. Next-generation ion-conducting polymeric materials are being developed for fuel cells, lithium batteries, electrolyzers, and other

electrochemical devices. In fuel cells, a fuel such as: hydrogen, methane, or methanol is efficiently converted into electrical energy with the aid of catalysts with the typical byproduct being only water. This contrasts with solid-state Li-ion battery electrolytes where there must be no water present because of the reactive materials used in the electrodes. Thus, the presence of water is a crucial parameter in distinguishing the electrolytes suitable for fuel cells from those employed in some batteries. Differences in these materials including the coupled dynamics of the mobile ions and the chains naturally lead to different ion transport mechanisms and consequently design principles.

Over the past several decades, three main types of polymeric electrolytes: proton exchange membranes (PEMs), anion exchange membranes (AEMs), and polymerized ionic liquids (polyILs) have gained fundamental understanding and hence improvement from experimental work and theoretical studies (Kusoglu and Weber, 2017; Elabd, 2019; Wang and Park, 2020; Ma and Olvera de la Cruz, 2021; Shen et al., 2021). PEMs were commercialized to some extent because of their high proton conductivity and first use in the Gemini space program in the early 1960s (Kusoglu and Weber, 2017). However, the requirement of expensive noble metal catalysts impedes the application in the real world and provokes additional research into alternative PEMs. AEMs have also attracted significant attention as an alternative to PEMs in fuel cells due to the use of non-noble transition metals as electrocatalysts under the high OH^- environment even though their conductivity is typically much lower (Dekel, 2018; Elabd, 2019). Thus, substantial effort has been expended to investigate the mechanisms underlying ion transport and improve the performance of AEMs. In view of the use of polymer electrolytes in batteries, polyILs, in which each repeating unit may be charged as opposed to ionomers that contain a relatively small percentage of charged units, are promising alternatives to organic liquid-based electrolytes that are toxic, flammable, and have a limited electrochemical stability window, due to their generally good mechanical stability, flexibility, improved safety, and durability. However, it remains challenging to enhance the ion conductivity of polyILs to a sufficient degree for electrochemical applications due to the sluggish local dynamics of the polymer chains, low dielectric constant, and small fraction of mobile ions in this class of materials (Bocharova and Sokolov, 2020; Son and Wang, 2020).

The performance of ion-containing materials is influenced by a variety of tunable factors, including: the functionalized end-groups; composition of block copolymers; polarity and rigidity of polymer backbones; molecular weight; conformational asymmetry; etc. Such factors provide an opportunity to tailor the structural and dynamical properties of the materials, although they bring challenges to identifying broadly applicable design rules. We hypothesize that the origins of how these factors affect the molecular packing and the dynamics of ions are mainly from the relatively weak specific interactions in comparison to covalent bonds as they play a key role in block copolymers (Wang and Park, 2020). This provokes several important but as of yet unanswered questions: How do these specific interactions affect the properties of an ion-containing polymer? Do the specific interactions have synergistic or uncooperative effects? Which interactions are the most dominant or important? Hence, the development of more advanced ion-containing polymers depends on a better understanding of specific interactions of polymer/polymer, polymer/solvent, acidic or basic group/solvent, and fixed-/counter-ions. These interactions including hydrogen bonding, ion-dipole interactions, Coulombic, and acid-base interactions may govern molecular arrangements, selectivity of ion uptake and transport, and ion transference.

In determining the role of the specific interactions on the performance of a material, experimental techniques have been employed to study the structural and dynamical properties of ion-containing polymers at various length and time scales. For example, small angle x-ray scattering (SAXS), wide angle x-ray scattering (WAXS), small angle neutron scattering (SANS) have been widely applied to deduce hydrated morphology (Gebel and Diat, 2005), and quasi-elastic neutron scattering (QENS) (Perrin et al., 2007; Melchior and Jalarvo, 2019) and pulsed field gradient NMR (PFG-NMR) (Münchinger and Kreuer, 2019) to measure the self-diffusion coefficient of the ions and water molecules, and broadband dielectric spectroscopy (BDS) (Giffin et al., 2013) to compute the ion conductivity. Other techniques have been brought to bear including infrared (IR) spectroscopy (Zimudzi and Hickner, 2016), Raman spectroscopy (Meek et al., 2020), atomic force microscopy (AFM) (Economou et al., 2015), and transmission electron microscopy (TEM) (Allen et al., 2015; Zhang et al., 2021a), with which one can obtain a description of the molecular interactions, direct images of the surface and 3-D morphology.

Although advances in technology provide powerful and robust tools to elucidate important information on these materials, modeling and simulations are clearly necessary to complement experiment findings and guide further experimental directions with the purpose of enhancing our understanding of morphology formation and ion transport mechanisms as well as the development of improved materials for electrochemical applications. Given the complex morphological and dynamic behavior of ion-containing polymers, multiscale theoretical approaches are required to describe characteristics over a wide range of temporal and spatial scales. Quantum mechanical calculations and *ab initio* molecular dynamics (AIMD) simulations are regarded as highly accurate methods to gain information on the static and dynamic properties allowing for both the electronic and nuclear degrees of freedom, which are critical when studying proton/hydroxide ion diffusion since the associated proton transfer involves the breaking and forming of covalent bonds. However, the use of AIMD is limited to access small time and length scales. To

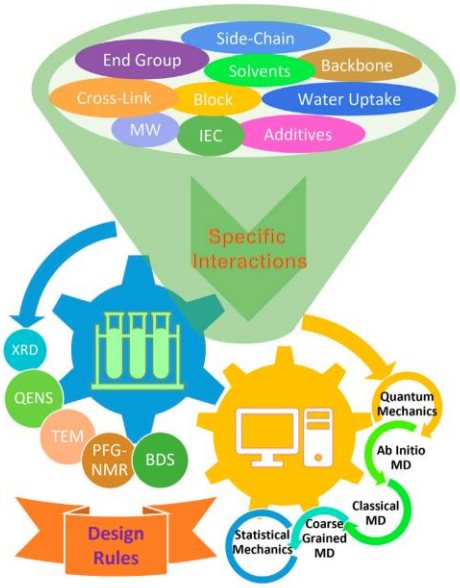

FIGURE 1
Schematic summary of experimental and theoretical approaches used to study the effects of various chemical factors in pursuit of rational design strategies. Although the understanding of non-bonded specific interactions is in its infancy, it is recognized that they may play a key role in the dynamic properties within the local environment and structural formation due to long-range effects. Many techniques have been widely utilized to study the effects of various chemical and structural factors with the aid of theoretical modeling and simulations in an effort to discover general design rules for advanced ion-containing polymeric materials.

expand the systems up to the size of a hydrophilic pore or domain, multistate empirical valence bond (MS-EVB) (Chen et al., 2016) and reactive ReaxFF (Zhang and Van Duin, 2015) methodologies may be employed to study both vehicular diffusion and structural diffusion in hydrated ion exchange membranes, but it is still challenging to capture the solvation structures of proton/hydroxide ions and to transfer the force fields to different chemical structures. When dealing with nonreactive systems such as polyILs, classical molecular dynamics (MD) simulations are suitable in investigating the structure and ion transport at time scales up to microseconds. The deficiency is the difficulty in allowing for polarization effects, which is resolved by either developing a computationally expensive polarizable force field (Bedrov et al., 2019) or simply scaling the full charges by some fraction. The latter was recently proven to be capable of capturing polarizability effects on both structural and dynamic properties of polyILs based on the comparison of the results obtained from the scaled partial charge force field and the Drude oscillator polarizable force field (Zhang et al., 2022). Although classical MD simulations are capable of predicting transport phenomena and structures within a small region, due to the limitations of time (<1 μs) and length (<10 nm) scales, coarse-grained MD and dissipative particle dynamics (DPD) simulations are widely utilized in modeling phase separations within membranes that typically require large length scale of 10–200 nm (Zhu et al., 2022). To capitalize on both experimental and theoretical strategies, a tight feedback loop of modeling and simulations with a broad spectrum of experimental techniques will serve as a protocol for the rational design of functional materials with optimal properties (Figure 1).

This Perspective describes recent and significant results regarding the specific interactions, morphology, and ion transport within ion-containing polymers. Emphasis is put on the interplay of morphology and ion transport. Specifically, we discuss the influences of polymer architecture, choice of the tethered ionic group, the rigidity of the polymer backbone, presence of a solvent, and additives on the morphology and ion transport. Finally, we highlight the challenges and prospects in advancing the performance of ion-containing materials, including the effects of specific interactions, the design of single-ion conductors, and well-defined supramolecular architectures with one dimensional enhanced ion transport channels.

Specific interactions

Through decades of research into ion-containing polymers, important fundamental understanding of structure-property relationships has been elucidated. However, challenges remain, including addressing the following issues: how to retain water at high temperatures to improve water-mediated ion transport; how to synergistically achieve mechanical stability and fast ion transport; how to facilitate decoupling of the ion transport from segmental dynamics or viscosity; and how to organize tethered ionic groups to facilitate efficient transport of ions. To resolve these issues, the specific interactions have been thought to play a crucial role in governing the microstructure and dynamics of the ions in such materials, which is a promising perspective for future research and development.

These interactions include hydrogen bonding, acid-base interactions, Coulombic interactions, ionic interactions, and π-π stacking (which may govern molecular arrangements). In view of the need to devise rational design rules, a hierarchy of intermolecular interactions should be fundamentally investigated through theoretical computations and simulations tightly coupled with advanced experimental strategies. This information should lead to insight into tailoring properties by

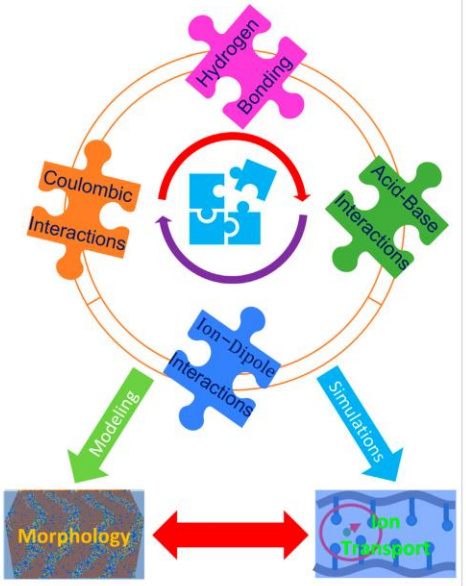

FIGURE 2
Schematic illustration of the pieces of "the puzzle" including specific interactions that need to be resolved to control morphology and dynamical properties. Coulombic, hydrogen bonding, acid-base, and ion-dipole interactions all play a crucial role in the performance of ion-containing polymers. Tuning these interactions with innovative strategies, though challenging, is an important direction in the design of high-performance materials.

balancing the specific interactions between fragments or molecules. It is a challenging but promising target to resolve this "puzzle" of the various specific interactions within ion-containing polymers in order to guide the design of high-performance materials (Figure 2).

Hydrogen bonding is the most well known and thoroughly investigated interaction and has led to an adequate understanding of the nature of bonding and functionality. It plays a crucial role in determining the water uptake in ion exchange polymer systems and the miscibility of polymer chains. The combination of *in situ* FTIR spectroscopy, molecular dynamics simulations, and statistical thermodynamics methods has been employed to investigate the effects of these interactions on the local structures of a hydrated poly(ether imide)(PEI) system (De Nicola et al., 2017). The authors (De Nicola et al., 2017) concluded that water molecules tended to form "bridges" connecting two successive intrachain carbonyl groups of PEI through hydrogen bonding and water-water interactions led to a "second shell" hydration layer.

The impact of acid-base interactions between sulfonic acid groups in a PEM and incorporated basic groups on the physicochemical properties of a membrane was investigated by synthesizing novel multi-block PEMs with three different basic groups (i.e. benzoxazolium, benzotriazolium, and propylamino groups) (Sui et al., 2019). The results reveal that a PEM with benzotriazolium (with an intermediate pK_a) had the highest proton conductivity although the excessive water absorption and the membrane swelling were suppressed in all three membranes. It was reasoned that the moderate basicity forms a "protonation-deprotonation" loop between the hydrophobic and hydrophilic moieties reducing the proton transfer barrier. Strong basicity was thought to neutralize the membrane acidity thereby lowering the concentration of dissociated (i.e., mobile) protons.

Ionic interactions between fixed ionic groups and mobile ions have an influence on the ionomer's local structure, hydration, ion transport within the ionic domain, and even the polymer chain segmental motion/dynamics. This type of interaction is strongly dependent on the hydration level since their effect is shielded and diminished as the water content is increased. The micromorphology of block copolymers was tailored by casting with various counter-cations (i.e. H^+, Li^+, K^+, Cs^+, TEA^+, and Ca^{2+}), which acted as either a block compatibilizer or a block separator by tuning the ionic interactions (Nguyen et al., 2020). The choice of counter-cations can vary the phase-separated morphologies from disordered to highly ordered, and thereby the conductivity of the membrane. Shi et al. (Shi et al., 2020) studied the role of ionic interactions in the deformation and fracture behavior in model perfluorosulfonic acid (PFSA) membranes. They determined that the ionic crosslinks formed between the cations and the sulfonate anions of the polymer enhance the alignment and stretching of the polymer matrix and the effect decreases with the cation radius. Another theoretical study (Ghosh and Chakrabarti, 2016) showed that small sodium ions favorably reside around the sulfonate groups due to electrostatic interactions while bulky tetramethylammonium ions tend to stay near the hydrophobic backbones because of strong hydrophobic interactions in Nafion membranes.

Recently, these specific interactions between fixed-ions and counter-ions were also confirmed in Nafion, Aquivion, sulfonated polystyrene, sulfonated polyether ketone, sulfonated poly(phenylene sulfone), poly(acrylic acid) and ammonium functionalized poly(phenylene oxide) ionomers (Münchinger and Kreuer, 2019). The experimental observation of the different degrees of localizing Li^+ and Cs^+ by the dissolved ionomers suggests that the ion partitioning seems to be controlled by the acidity of the fixed ionic groups but not electrostatics. Explicitly, the ratio of $[Li^+]/[Cs^+]$ decreases with increasing acidity, which ascribes to stronger stabilization of Cs^+ in comparison to Li^+. The diffusivity of Cs^+ decreases as the

acidity of the fixed ionic group increases, while the trend is inversed for Li^+ before the onset of counter-ion binding, similar to the behavior of H^+. It was concluded that the strongest specific interaction exists between the most acidic fixed functional groups and cations with the highest polarizability and lowest electronegativity.

In summary, there exists several interactions between the various molecules and ions in these materials. It is worth noting that π-π stacking interactions play a crucial role in promoting micro- or nano-phase separation and stabilizing porous structures. However, it is still at nascent stage especially in ion-containing materials since these interactions require delicate description of π systems allowing for electron density. It is crucial to elucidate how the interactions affect the morphology and dynamics, which are discussed in the following sections. To develop the desired properties, we have to balance the interactions *via* various approaches. For instance, the addition of nanoparticles into polymeric materials can reduce the hydrogen bonding between the cations and anions, improving the dissociation of ions by balancing the interaction of nanoparticles with cations and anions, which has been proven by the FTIR and the Raman spectroscopy (Pundir et al., 2018).

Morphology

Understanding nanophase separation (i.e., characteristics of the hydrophobic domain in comparison to the ion conducting phase) in ion-containing polymeric systems is fundamentally important in the rational design of highly conducting electrolytes with mechanically and chemically stable integrity under diverse operating conditions. Generally, these polymers possess hydrophobic and hydrophilic components, which provoke phase separation of ionic domains from the polymeric matrix when exposed to polar solvents. Morphological differences are governed by various factors, such as the dissimilarity between pendant acidic or basic groups and the backbone, equivalent weight, side-chain chemistry, degree of hydration, *etc*. The underlying fundamentals of how these factors affect morphology are of significant interest.

Hydrated PEM morphology

Phase separation upon hydration enhances the formation of pore networks that provide pathways for the movement of water and ions. The hydrophobic polymer matrix provides dimensional strength. The connectivity of the pore network is key to promoting long-range ion transport, which ultimately determines conductivity. An increase in hydration may improve phase separation by establishing percolating pore networks, but high-water content may also cause the swelling of membranes resulting in the reduction of mechanical stability and constraint in the operating temperature below the boiling point of water. It is recognized that an increase in temperature enhances reaction kinetics and reduces the poisoning of the catalysts (Kusoglu and Weber, 2017). Therefore, it is desired, on one side, to form well-connected channels in membranes at low relative humidity; on the other side, to retain water in the ionic domains of membranes at higher operating temperatures. Nevertheless, there are various factors including polymeric architecture, degree of functionalization, pendant ionic groups, counterions, and hydration level, which play a complex role in the hydrated morphology of ion-containing membranes. It is impractical to conduct a case-by-case study to elucidate the interplay of the multitude of these factors. Moreover, the model-dependent interpretation of scattering data cannot provide precise geometries of the multiscale domains, which has been extensively discussed for perfluorosulfonic acid ionomers (Kusoglu and Weber, 2017).

Given these challenges of unambiguously determining the morphology, theoretical approaches have been resorted to providing insight into the quantification of morphology for ion-containing membranes. Coarse grained MD and DPD simulations are widely utilized in modeling phase separations within membranes that typically requires long-time relaxation and a large length scale of 10–200 nm (Dorenbos, 2017a; Dorenbos, 2017b; Sepehr et al., 2017; Liu et al., 2018a; Dong et al., 2018b; Liu et al., 2018b; Wang R. et al., 2019; Clark et al., 2019; Dorenbos, 2019; Lee, 2019; Luo and Paddison, 2019; Zhu et al., 2019; Chen C. et al., 2020; Luo et al., 2020a; Dorenbos, 2020; Lee, 2020; Sevinis Ozbulut et al., 2020; Zhu et al., 2022). To further quantify the morphology including the size, shape, and connectivity of the ionic domains, which cannot be extracted from the peaks obtained by scattering methods, cluster analysis including distance-based and density-based algorithms is a powerful tool to provide a plethora of information on water domain size, shape, and connectivity from the trajectory of a MD or DPD simulation, which will be described in this section. The latter is capable of characterizing the local regions of high density and isolating clusters that have some overlap (Clark et al., 2019; Sorte et al., 2019).

Nafion is the prototypical perfluorosulfonic acid (PFSA) ionomer and has been subject to extensive investigation (Yandrasits et al., 2019). Recently, Liu and coworkers examined the scaling behavior of the conformations and dynamics of mesoscopic models of hydrated Nafion membranes as well as a polymer melt. The authors compared the results obtained from five distinct DPD parameterizations of hydrated Nafion including one based on electronic structure calculations and others mapped from Flory-Huggins parameters along with varying harmonic spring bonded interactions (Liu et al., 2018b). The effect of the chain stiffness was also investigated in the dry and hydrated Nafion systems. The increase in chain stiffness gives rise to larger polymer end-to-

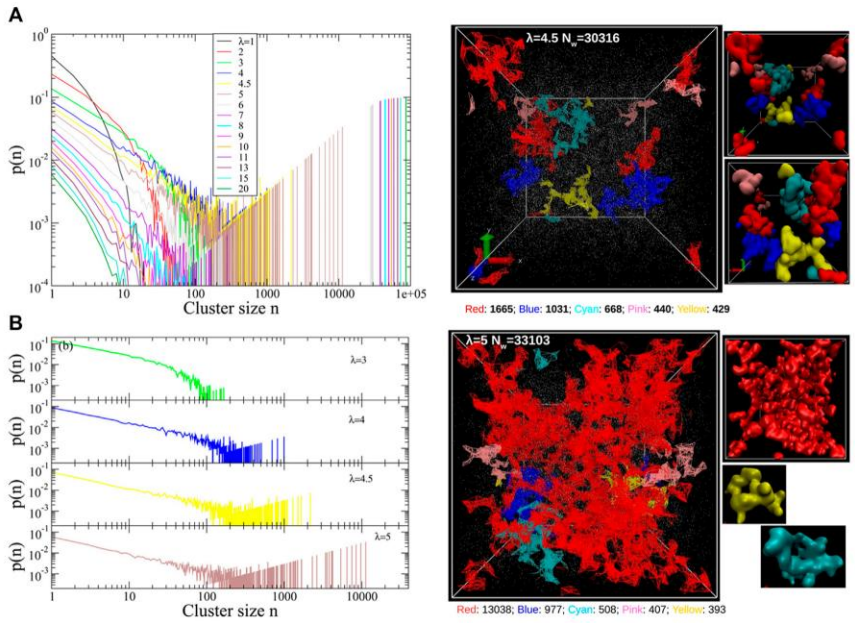

FIGURE 3
(A) Quantitative cluster size distribution from a distance-based cluster analysis algorithm for various hydration levels. **(B)** Cluster size distributions underlining the percolation threshold at λ = 5. Snapshots of water clusters for λ = 4.5 (no percolating clusters) and λ = 5 (percolating clusters) color-coded by the unique cluster IDs on the right panel. Reprinted and adapted with permission from ref. (Liu et al., 2018a). Copyright 2018 American Chemical Society.

end relaxation time along with slow segmental dynamics due to the stronger back scattering in the velocity autocorrelation function and larger residence time within the "cage" formed by the nearest neighbors. To demonstrate detailed information concerning the ionic aggregates, quantitative distance-based cluster analysis with realistic microscopic images colored by unique IDs was further developed to provide a wealth of information on water-filled ionic channel size, shape, and connectivity (Liu et al., 2018a). The water cluster size distribution suggests that all five DPD parameterizations of Nafion correctly show a percolating network after a certain degree of hydration (Liu et al., 2018b). The percolation threshold of the water domains in Nafion was determined to occur at a hydration level of 5 H_2O/SO_3H through direct cluster analysis in contrast to a methodology that derived from radial distribution functions and the Connolly surface analysis (Liu et al., 2018a). Agglomerate of the small water domains is clearly demonstrated *via* this cluster analysis method (shown in Figure 3). These results further demonstrated the validity of a density functional theory (DFT) based parameterization (Sepehr and Paddison, 2016) to compute the interaction parameters needed for the repulsion interaction in the simulations. This scheme addresses the challenge for the charged beads without reducing the efficiency of the DPD methodology by implicitly considering electrostatic interactions for the charged beads. A non-empirical fragment molecular orbital (FMO) method (Okuwaki et al., 2018a; Okuwaki et al., 2018b) was also developed as a novel scheme to consider polarization and charge transfer between beads. It is interesting to note that DPD is flexible for hydrated ion exchange membranes in terms of parameterization and coupling with smoothed particle hydrodynamics (SPH) (Jorn and Voth, 2012) or a dissociable Morse potential between the protons and the base and/or water beads (Lee et al., 2016; Vishnyakov et al., 2018).

Based on the successful application of DPD simulation on PFSA-type PEMs, there have been several attempts to control the architecture of the backbones and side-chains. Dorenbos (Dorenbos, 2017b) recently constructed three different parent architectures of a backbone by covalently bonding hydrophobic beads ([A]) to: short hydrophilic beads ([C]); long ($[A_3C]$) beads;

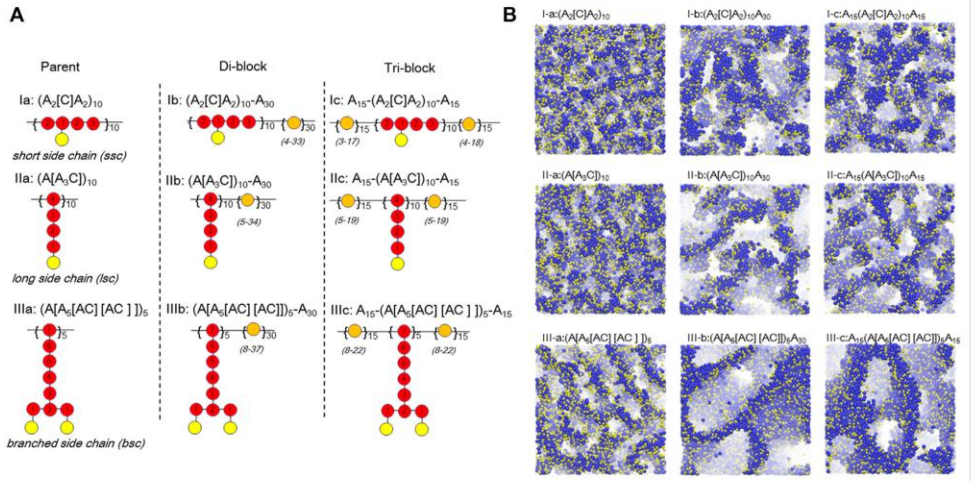

FIGURE 4
(A) The architectures of polymer chains including: amphiphilic parent (I-a; II-a; III-a), amphiphilic-hydrophobic di-block (I-b; II-b; III-b), and hydrophobic-amphiphilic-hydrophobic tri-block (I-c; II-c; III-c) functionalized with short side chain, long side chain, and branched side chain, respectively. Color codes: red, amphiphilic block beads; orange, hydrophobic block beads; yellow, C beads. Number of bonds, N_{bond}, towards the nearest C bead Numbers is indicated within A beads. The range of N_{bond} for A beads within the hydrophobic block(s) is shown in parenthesis. **(B)** Simulated pore morphologies for corresponding architectures in **(A)**. Only hydrophilic beads are displayed. Color codes: blue, W beads; yellow, C beads. Reprinted and adapted from ref. (Dorenbos, 2017b). Copyright 2017 American Institute of Physics.

or symmetrically branched $A_5[AC][AC]$ side-chains. Subsequently, three di-block copolymers and three tri-block derivatives were modeled by connecting an A_{30} block (30 hydrophobic A beads) or an A_{15} block with three different parent architectures as shown in Figure 4A. The results demonstrated that the increase in side-chain length enlarges the pore size for polymers of similar ion exchange capacity (IEC) and that the largest pore size appears in the systems with branched side-chains (Figure 4B). Meanwhile, the author investigated the effects of doping $(A_2[C])_{10}$ polymers with high IEC into a host polymer of $A_{30}(A[A_5[AC][AC]])_5$ with a low IEC (Dorenbos, 2017a). These results show that the clearly distinguished pore networks disappear as the ratio of dopant is increased. This suggests that for a low dopant content the small amount of high IEC dopants is situated near well-connected pores formed by the low IEC host polymers, implying that one can increase the overall IEC of the blended membrane without sacrificing the percolated networks by adding a dopant. To further study the influence of designs with hydrophobic side-chains on the connectivity of the water containing domains, Dorenbos correlated the pore connectivity to the average number of bonds separating A from the nearest C (N_{bond}^{A-C}) and between nearest C beads (N_{bond}^{C-C}) (Dorenbos, 2019; Dorenbos, 2020). It was determined that the connectivity of the water domains generally increases with increasing N_{bond}^{C-C} for the cases where $N_{bond}^{C-C} > N_{bond\,(\max)}^{A-C}$ and fixed IEC, while the opposite trend occurs for the cases where $N_{bond}^{C-C} < N_{bond\,(\max)}^{A-C}$.

These results show a larger pore size for branched side-chain membranes than single side-chain membranes. Another potential strategy is to utilize multi-acid side-chains to improve the conductivity while retaining the good mechanical properties of the perfluorinated backbone, such as perfluorosulfonic imide side-chain perfluorinated polymers (PFIA) (Kusoglu et al., 2020) and perfluoroalkyl ionene chain-extended ionomers (PFICE) (Su et al., 2019). Compared with the PFSA material, the PFIA demonstrates higher proton conductivity at low hydrations due to both inter- and intra-side-chain interactions. The experimental and simulation results indicate highly ordered backbone configuration and better-dispersed smaller water clusters in PFIA than in PFSA (Kusoglu et al., 2020). Similarly, phase-separated morphology with enhanced local order was revealed by resonant X-ray scattering in both dry and hydrated PFICE ionomers, which improves proton dissociation at low hydration that can be discerned by the DFT-computed spectra of the PFICE side-chain (Su et al., 2019).

In addition to these modifications of the polymeric chemistry, the interactions between polymer segments and solvent molecules also have a strong influence on the aggregate structures. For instance, the aggregate structure of PFSA ionomers can be tuned with different solvents or mixtures of solvents (Welch et al., 2012; Doo et al., 2018). Fully atomistic MD simulations instead of coarse-grained approaches were used to study the effects of solvents (i.e., with dielectric constants, ε_r = 2.38–109) in PFSA ionomer dispersions (Tarokh et al., 2020). The authors introduced a new aggregation phase diagram for Nafion in the various solvents. The ionomer chains are physically cross-linked through strong electrostatic interaction between ionic clusters in low dielectric solvents (i.e., $\varepsilon_r = 1.41 - 42.5$), self-assembled into lamella-like aggregates *via* weak hydrophobic interactions in the solvents with intermediate dielectric constant (i.e., $\varepsilon_r = 42.5–78$), and formed elongated aggregates because of strong hydrophobic interactions in high dielectric solvents (i.e., $\varepsilon_r \geq 78$). Simultaneously, the major deficiencies of a coarse-grained approach were revealed in that the aggregate structure in all solvents obtained from a coarse-grained model is unrealistic due to the fact that the solvent atoms are not explicitly modeled (Doo et al., 2018). More recently, experimental results show that the decrease in the polarity of the solvent increases the swelling of the fluoropolymer resulting in low proton mobility. Alkanes do not change the Nafion structure from its dry state due to the minimal interaction with fluoropolymer backbone and ionic groups (Katzenberg et al., 2021; Shi et al., 2021).

Compared to the pronounced hydrophobic/hydrophilic interactions in PFSA-based membranes, polymers with sulfonated aromatic rings have been explored as promising alternatives for fuel cell applications because they possess a wide variety of tunable chemical structures such as different degrees of sulfonation, various linkers between aromatic rings and fluorinated components of the macromolecules. Specifically, sulfonated Diels-Alder poly(phenylene) (SDAPP) (Abbott and Frischknecht, 2017; Clark et al., 2019; Sorte et al., 2019) and sulfonated poly(ether ether ketone) (sPEEK)(Chen S. et al., 2020) are the focus of many studies aiming at the elucidation of structure-property relationships. Frischknecht et al. (Abbott and Frischknecht, 2017; Clark et al., 2019; Sorte et al., 2019) undertook experimental and theoretical studies to investigate the influence of the degrees of sulfonation and hydration level as well as temperature on the morphology and the dynamic properties of water molecules and protons within SDAPP membranes (Sorte et al., 2019). The isolated hydrophilic clusters were observed at relatively low degrees of hydration and sulfonation and the increase of hydration and/or sulfonation improved the connectivity of the water (Clark et al., 2019). Besides the distance-based cluster analysis, the density-based clustering algorithm was applied to distinguish the local size and shape of the percolated water-containing clusters in particular for overlapped clusters. The clustering results obtained from these two algorithms demonstrated that the densest clusters were bridged by narrow regions. Furthermore, the relative anisotropy of the shape in these clusters quantitatively showed that the clusters became more spherical with increasing degree of hydration and sulfonation (Abbott and Frischknecht, 2017; Clark et al., 2019).

MD simulations show that sPEEK membranes possess stronger electrostatic interactions between the sulfonate oxygen atoms and hydrated protons leading to much lower hydronium ion diffusivity and lower delocalization of free H_3O^+ when compared to Nafion (Wang R. et al., 2019). The structure of hydrated hydronium ions deforms to adapt to the narrow regions of hydrophilic pores. The confinement effect on the diffusion of H_2O and H_3O^+ is affected by the hydration level and the formation of conductive channels. It was concluded that weak nanophase separation and poor connected ionic domains in sPEEK membrane contribute to lower proton conductivity in comparison to Nafion. Okuwaki et al.(Okuwaki et al., 2018a) drew the same conclusion from FMO-DPD simulations of sPEEK and Nafion membranes.

As mentioned above, one conventional strategy is the blending of different types of polymers to enhance the chemical and physical properties of the materials. However, additional intermolecular interactions within the blends make the prediction of properties challenging. Recently, Ozbulut et al. studied the morphology of polymer blends of highly branched poly(arylene ether sulfone) (HBPAES) and linear poly(arylene ether sulfone) (LPAES) *via* both experiments and DPD simulations (Sevinis Ozbulut et al., 2020). The branched topology of HBPAES was tuned by changing the distance between the branch positions. The results revealed the miscibility of highly branched and linear polymers that was not influenced by the separation between the branch positions, which was further confirmed by the distribution of the radii of gyration for the pure polymers and the blend systems. It is also interesting to note that the increased strain at the break values is attributed to the anchoring regions rather than the strength of the non-bonded interactions in the blend.

Another promising route to advance the performance of non-PFSA membranes is to design highly ordered morphologies for efficient proton transport. This requires a fundamental understanding of how to balance the specific interactions within these materials. Recently, well-controlled chain folding has been achieved by Trigg and coworkers (Trigg et al., 2018) through precisely tethering sulfonic acid groups into the linear polyethylene backbone every twenty-first carbon atom to obtain highly ordered conductive layers for fast proton diffusion. The classical MD simulations further demonstrated that the diffusivities of water and hydronium ions were enhanced in the well-ordered water channels compared to that in the amorphous morphology. It was

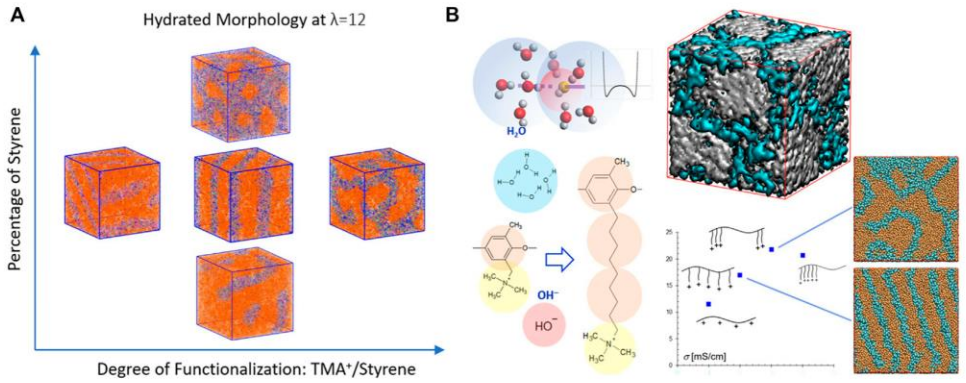

FIGURE 5
(A) Effects of the degree of functionalization and the content of polystyrene on the hydrated morphology of SEBS-based AEMs at λ = 12. Color scheme: orange, beads representing two polymerized vinyl groups; mauve, phenyl group; green, trimethylmethane group; purple, TMA; cyan, OH; and blue, water. **(B)** The hydroxide ion model and the Morse potential-based associative forces between hydroxide ion and water bead; molecular structures of the species and their coarse-grained models as well as the side-chain modifications of PPO-TMA; Simulated morphology of the hydrated PPO-C8Q-comb and PPO-C8Q-triblock at λ = 11. Color scheme: orange: polymer; and cyan: water. Isosurface of PPO-C8QC8Q-C16-triblock in which polymer domain and water domain are shown in white and cyan, respectively. Figure A reprinted with permission from ref. (Luo et al., 2020a) and figure B reprinted and adapted with permission from ref. (Lee, 2020). Copyrights 2020 and 2020 American Chemical Society.

suggested that this state-of-the-art strategy may be applied for cation/anion transport as well as anhydrous proton transport by modifying the chemistry of functional groups.

Hydrated AEM morphology

In addition to PEMs, extensive investigations were performed on the hydrated morphology of polystyrene-b-poly(ethylene-co-butylene)-b-polystyrene (SEBS)-based AEMs (Sepehr et al., 2017; Luo and Paddison, 2019; Zhu et al., 2019; Luo et al., 2020a). The results indicated that the quaternary ammonium-functionalized SEBS AEMs phase separates into a functionalized polystyrene-rich phase and a hydrophobic phase. The water content clearly controls the morphology which evolves from perforated and interconnected lamella to perfect lamellae and then to disordered bicontinuous structures as the water content is increased (Sepehr et al., 2017). Reducing the functionalization and/or the percentage of styrene delays the formation of largely interconnected water networks (Figure 5A), but the increase in the styrene content facilitates the percolation to occur at a lower hydration level (Luo et al., 2020a). An alkyl spacer (C_4H_8) grafted between the backbone and functional QA group as the linker, tail, and as both a linker and a tail strongly affect the morphology, the domain spacing of the hydrophilic phase, the distribution of the backbone-TMA^+ distance, and the water clusters. Specifically, additional spacers may postpone the occurrence of a percolated water domain and thereby evenly distribute the water (Luo and Paddison, 2019). The choice of the functional group (trimethylammonium, methylimidazolium, or trimethylphosphonium) was found to have minimum effect on the backbone structures while moderately affecting water distribution. Compared to the cationic groups, the associated anion seemed to have a greater impact on the size of the exclusive water domains (Zhu et al., 2019).

The influences of alkyl chain length, side-chain structure, hydrophilic and hydrophobic spacers, and distribution and aggregation of the side-chains on the microstructure of polyphenylene oxide tetramethylammonium (PPO-TMA) as well as SEBS-based AEMs were systematically explored with DPD simulations by Lee and coworkers (Lee, 2019; Lee, 2020; Lee, 2021). The comparison of PPO-based and SEBS-based triblock copolymers shows that the latter possesses more hydrophobic and flexible backbones, in which nano-segregation occurs even without any side-chain modifications. The comb-like structure distribution of the side-chains contributed to the formation of a lamellar structure. Short side-chains acting as spacers helped to break the percolated water domain into smaller domains as the cationic groups were close to PPO backbones, indicating the larger impact of an alkyl spacer than an alkyl extender. A lamellar morphology may be transformed into an interconnected water network by tailoring the pendant length or composition of the side-chains as shown in Figure 5B (Lee, 2020). Adding hydrophobic alkyl

spacers was observed to enhance the phase separation and promote the formation of large water clusters. However, the strong hydrophobicity of the side-chains (either alkyl spacers or alkyl extenders) resulted in substantial protrusion into the water phase, which formed bottlenecks within the transport pathways retarding anion mobility. These results suggested that the less hydrophobic alkoxy spacers may help to form narrower but more connected channels (Lee, 2019). In contrast, adding hydrophilic spacers impedes the transport of hydroxide ions as well as water, ascribing to the stretched side-chains dispersing in the hydrophilic phase (Lee, 2021). This drawback may be resolved by altering multi-cation side-chain designs, which facilitate the formation of largely connected ion-conducting pathways. Coarse-grained MD simulations of two poly(ether ether ketone) (PEEK) membranes (Chen S. et al., 2020), in which the side-chains consist of either one or two quaternary ammonium (QA) groups, indicate that slightly smaller and better interconnected hydrophilic clusters occur in two QA than in single QA membranes and that the increase of grafting degree results in the decrease of cluster sizes for both membranes. In addition, the coordination number of OH^- is greater in two QA systems than in single QA membranes, which probably improves the alkaline stability of two QA polymers (Chen S. et al., 2020). Furthermore, Li and coworkers (Li et al., 2021) found that both OH^- conductivity and chemical/mechanical stability of the PPO-based AEM can be significantly improved by grafting a tri-cation side-chain with a long hydrophobic extender and an additional hydrophilic side-chain. These results further demonstrate the success of the strategy of multi-cations on each grafted functional group to balance the ionic conductivity and the chemical stability (Pan et al., 2013; Zhu et al., 2016; Li et al., 2021).

Alternatively, a delicate balance of hydrophilic and hydrophobic features in functional groups can mitigate the bottleneck issue (Zhang and Van Duin, 2015; Dong et al., 2018a; Dong et al., 2018c). Reactive force-field MD simulations were conducted on hydrated PPO-based homopolymers with five distinct quaternary ammonium cationic groups (R_1: $-CH_3$, R_2: $-C_2H_5$, R_3: $-C_3H_7$, R_4: $-C_6H_{13}$ and R_5: $-C_4H_8OCH_3$) (Dong et al., 2018a). The hydrated morphology indicated that the nanoscale water domains were connected by narrow channels and the size of the water channels increased dramatically with increasing water content. For the systems with symmetrically modified cation groups, long alkyl tails (i.e., $3R_3$) enhanced phase segregation, giving rise to the formation of large water clusters with fewer connections between those clusters. For the systems with asymmetric cationic groups, the distribution of pore sizes was narrower in the $2R_1R_4$ and $2R_1R_5$ than in $3R_3$ at a hydration level of 5. Enhancement in the hydrophilicity for $2R_1R_5$ by introducing an ether group resulted in a more uniform distribution of the size of the water channels when compared with $2R_1R_4$, indicating the formation of narrow connections between the water domains. These findings show that the hydrophobicity of the functional groups should be strong enough to provide the desired nanophase segregation but not so strong as to provoke the formation of narrow bottlenecks between the water domains, e.g. $2R_1R_4$ (Dong et al., 2018a).

Although a high IEC improves the ionic conductivity of an AEM, it also causes swelling of the membrane giving rise to low dimensional stability. One potential approach is to utilize cross-linking to manage excess swelling in AEMs. Experimental results have shown that cross-linking significantly reduces the water uptake and swelling without sacrificing the anion conductivity and the interdomain spacing of the AEMs decreases with the degree of cross-linking for the poly(bromopropyl norbornene)-b-poly(butyl norbornene) copolymers (Chen et al., 2019) and the TMA-functionalized SEBS membranes (Jeon et al., 2019) both by using *N,N,N′,N′*-tetramethyl-1,6-hexanediamine (TMHDA) as cross-linker, and the multiple quaternary ammonium-functionalized polysulfone AEMs modified with rigid β-cyclodextrin (Ma et al., 2020). However, few simulations have been undertaken to probe the influences of cross-linking on the morphology of AEMs despite the availability of the cross-link formation algorithm (Kacar et al., 2013).

To date, a significant effort has been devoted to determining rational design rules. Nevertheless, general conclusions have not been obtained since there is a complex interplay of a number of factors. To this end, we suggest that machine learning may be a promising approach to resolving the complexity of effects on the hydrated morphology of ionomers.

Anhydrous morphology

In anhydrous ion-containing polymers, ionic aggregates form due to specific interactions including strong electrostatic, metal/ion-dipole, etc. The influence of polymer architecture, the dielectric constant, and the specific mobile ions on the morphology of the ionic aggregates are of significant interest. Similar to hydrated ionomers, only percolating ionic domains may serve as ion conducting channels thereby providing high ionic conductivity. Although experiments can provide microscopic images of the ionomer such as those obtained from scanning transmission electron microscopy (STEM), and the approximate ionic aggregate size distribution from X-ray scattering, the details of the morphology such as the shape, size, and the percolation of the ionic domains are incompletely understood (Ketkar et al., 2019). Thus, MD simulations have been undertaken to resolve this problem.

Recently, Liu and Paddison performed atomistic MD simulations to study the structural properties of a homologous series of poly(n-alkyl-vinylimidzolium bistrifluoromethylsulfonylimide) (poly(nVim Tf2N)) ionic liquids (Liu and Paddison, 2016). The computed structure factors were observed to be in excellent agreement with X-ray scattering results in terms of peak position and shape. Three

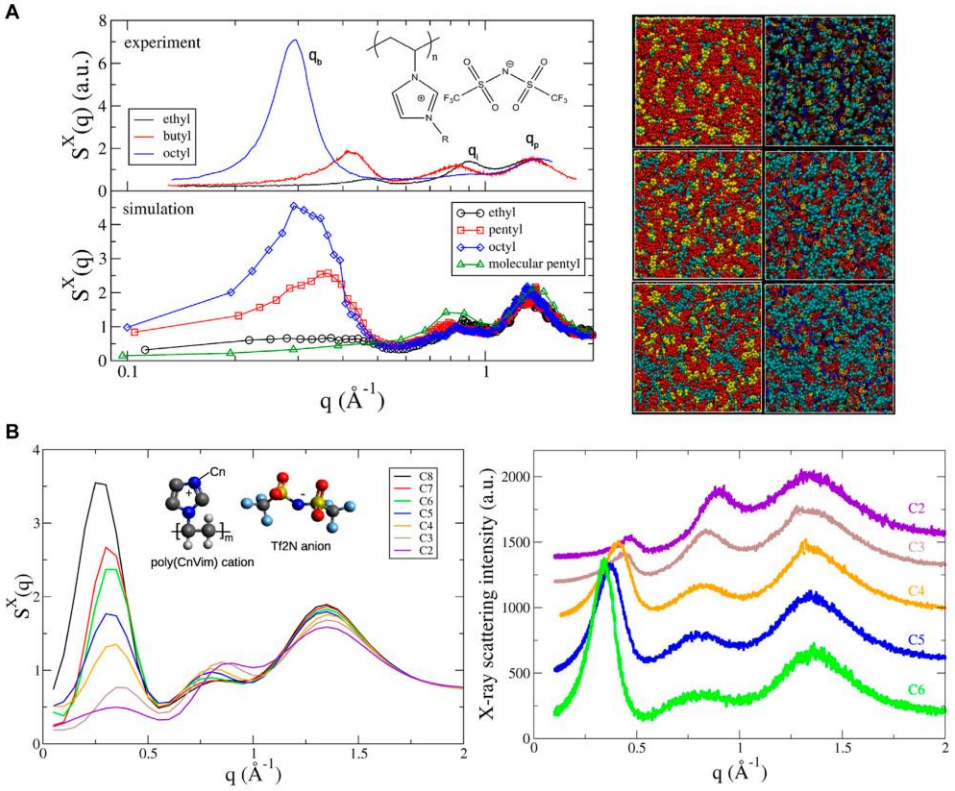

FIGURE 6
(A) Simulated X-ray scattering profiles of poly(CnVim Tf2N) as a function of alkyl side chain length (n = 2–8) compared with experimental data (left); morphologies shown with space-filling models as well as snapshots of poly(CnVim Tf2N) (n = 2, 5, and 8 from top to bottom) (right). Color scheme: red, anions; yellow, imidazolium rings; cyan, cationic tails; red bonds, anions; cyan sphere, cationic side-chains; yellow line, imidazolium rings; blue bonds, cationic backbones. **(B)** Simulated total X-ray structure factors with an inset of the molecular structure of poly(CnVim Tf2N) and experimental X-ray scattering profiles of poly(CnVim Tf2N). Figure A reprinted and adapted with permission from ref. (Liu and Paddison, 2016) and figure B reprinted with permission from ref. (Liu and Paddison, 2017). Copyrights 2016 and 2017 American Chemical Society.

distinct peaks were characterized as the low-q peaks at 0.2–0.6 Å^{-1} according to the backbone-to-backbone correlations (q_b), the intermediated-q peaks in the range of 0.8–1.0 Å^{-1} corresponding to the ionic interactions (q_i), and the high-q peaks at 1.0–2.0 Å^{-1} representing the pendant-to-pendant peak (q_p) as shown in Figure 6A. The simulated nanostructures of poly(nVim Tf2N) (n = ethyl, pentyl, and octyl) on the right side of Figure 6A illustrated the dramatic growth of the nonpolar aggregates with increasing the length of alkyl chain along with the homologous series and was quantified by the distribution of the nonpolar cluster size. It is worth noting that the rational choice of the criterion for the connectivity in the distance-based cluster analysis algorithm is critical to correctly predicting the cluster size distribution. One strategy is to deconvolve the first peak of the radial distribution function by fitting it to a series of Gaussian functions and choosing the limit of the strongest Gaussian peak as the cutoff for the connectivity. Furthermore, a systematic increase in the alkyl chain length leads to the growth of nonpolar domain size (i.e., the backbone-to-backbone correlation length) and a slight increase in the ionic domains, despite a negligible shift of the pendant-to-pendant peak (Liu and Paddison, 2017). These results reveal a satisfactory

agreement between simulation and experiment as shown in Figure 6B. The complex interplay between morphology and ionic conductivity is discussed in the following section.

Analogous to the hydrated morphology, nanophase separation has been observed in block copolymers containing polyILs experimentally by Elabd and coworkers (Ye et al., 2012; Choi et al., 2013) and by Ganesan group with simulations (Zhang et al., 2019; Zhang et al., 2021b). The results show that the lamellar block copolymer has a similar anion concentration in the center to that of the homopolymers while the random copolymer displays the lowest local ion concentration. Moreover, the strength of cation-anion coordination is influenced by introducing nonconducting monomers, in which frustrated coordination behavior occurs in the interfacial area of the lamellar block copolymer and the bulk regions of the random copolymer. This was rationalized to be responsible for the low anion mobility in comparison to the homopolymer (Zhang et al., 2019). It should be noted that a multiscale simulation framework consisting of CG modeling and reverse mapping of the CG morphology was developed to extend the length and time scales of the simulated systems (Zhang et al., 2021b).

Ionomers are another essential type of single-ion conducting polymers, in which only the mobile ions contribute to the conductivity. Ion transport is governed by the morphology of the ionic aggregates. In an effort to reveal the distinct morphologies consisting of these ionic aggregates that are included in the single ionomer peaks of X-ray scattering, Frischknecht and Winey (Frischknecht and Winey, 2019) performed microsecond-long, all-atom classical MD simulations on a series of precise poly(ethylene-co-acrylic acid) ionomers with mobile lithium ions at 423 and 600 K. The spacer lengths between the backbone and acid groups were varied and tuned. The percolated ionic aggregates were found in three spacer length systems that were totally neutralized with lithium ions. For partially lithium neutralized systems, the acidic groups prefer to stay on the sides or ends of the lithium ion aggregates with some coexisting acid aggregates formed *via* hydrogen bonding. The evolution of the ionic domains revealed that the morphology reached steady state over hundreds of nanoseconds at a higher temperature while it cannot within the microsecond-long simulation at a lower temperature.

In contrast, Agrawal and coworkers (Agrawal et al., 2016) demonstrated that the ionic clusters formed in PSS melts with both Na^+ and Mg^{2+} did not percolate across the sample according to the definition of the cluster that consists of SO_3^- groups that are within the distance criterion of 6 Å. Specifically, the majority of the clusters in a PSS/Na^+ system are highly ordered and ladder-like in shape, while the clusters in PSS with Mg^{2+} are irregular and elongated. The cluster size distributions for both melts illustrate that charge-neutral clusters with an even number of SO_3^- groups are dominant over charged ones. Although both melts have a broad distribution of cluster size, the PSS/Mg^{2+} has a larger average cluster size than that of PSS/Na^+ even under shearing.

Ion transport

Transport phenomena in ion-containing polymers comprise multiple mechanisms at different time and length scales. In hydrated ionomers, the rapid dynamical hydrogen bonding of the water facilitates the transport of ions in a vehicular (i.e., as a carrier) and/or in a structural way (i.e., typically in the case of proton transfer). Typically, ion diffusivity increases with hydration level, but a high degree of hydration generally causes swelling of the polymer matrix and may limit the operating conditions. In anhydrous polymeric systems, the ion conductivity is generally controlled by the slow segmental dynamics of the polymer. Thus, one strategy is to reduce the glass transition temperature (T_g) or add liquid plasticizers, leading to the enhancement of the ion and segmental dynamics (Bocharova et al., 2017). In contrast, another method is to enhance the decoupling of ion transport from segmental dynamics (Wojnarowska et al., 2017), which would probably be achieved by the morphological confinement and/or tuning of specific interactions within ion-containing membranes.

In hydrated systems

Hydrated membranes illustrate various hydrophilic ionic domains due to nanophase separation, in which various proton transport phenomena occur according to distinctions in the chemical structures of the ionomers. The formed hydrophilic ionic domains and in some cases, channels are composed of pendant functional groups, water molecules, and dissociated protons, giving rise to a complex confined environment for proton carrier transport.

Given the disparate range in the time and length scales of the phase-separated hydrated morphology and proton transport within a local environment, it is challenging with only a single model to properly describe proton transport (*via* structural diffusion) within a polymeric system and the conformation of a water network due to nanophase separation (Jorn et al., 2012). More importantly, the transport of H^+ or OH^- occurs through the migration of a charged defect in the hydrogen bond network through a sequence of elementary proton transfer reactions/events, which requires a quantum mechanical description of covalent and hydrogen bond breaking and forming (Tuckerman et al., 1997; Tuckerman et al., 2010). Thus, significant effort has been devoted to addressing these challenges. There are two major directions: simulating the diffusion of ions and/or water in an equilibrium morphology

obtained from DPD simulations; and incorporating local interactions into coarse-grained MD/DPD simulations.

Dorenbos (Dorenbos, 2019; Dorenbos, 2020) performed grid-based Monte Carlo tracer diffusion calculations, which are capable of evaluating the diffusivity of water molecules based on equilibrium DPD morphologies but fails to describe proton transport behavior due to the lack of local interactions between the protons and the functional groups and solvent molecules. Another drawback is that the fixed pore networks cannot accurately represent the dynamical percolated water-containing domains (i.e., "channels"). A similar strategy was developed to simulate the transport of water in the fixed channels of the membrane (Johansson et al., 2015). The results obtained from both methods show that an increase in hydration improves the water diffusivity within the system (Johansson et al., 2015; Dorenbos, 2017a). It is interesting to note that the diffusivity of hydronium ions was also obtained from DPD simulations by modeling the hydronium ion bead with the proton associated with one to four water molecules (Xiao et al., 2018). The results indicate that the increase in the size of solvated hydronium complexes retards the hydronium transport.

Another approach is to map the coordinate of the coarse-grained water beads to the interpolation quasi-particles within the theory of SPH to describe proton transport in a mesoscopic structure of a PEM (tens of nanometers) (Jorn and Voth, 2012). This method combines the dynamic behavior of the protons from atomistic MD simulations and the mesoscopic structure of PEMs driven by the hydrophilic/hydrophobic interactions among the polymer matrix, functionalized side-chains, water, and protons. This scheme was applied to hydrated Nafion. To properly include double layer effects and the local strong interaction between the functional groups and protons, electrostatics and position dependent diffusivity were introduced. The computed conductivities showed good agreement with experimental data (Jorn and Voth, 2012). Moreover, proton transport behavior within various morphologies including lamellar, cylindrical, and cluster were also investigated using this SPH-based mesoscale method (Liu et al., 2015). The proton conductivity within the cluster morphology was found to be lower than that within the other two morphologies due to the higher porosity and tortuosity in the cluster morphology.

Apparently, these methods consider the proton/water transport indirectly based on the static equilibrated morphology. The dynamic dissociation and association of protons from the acidic groups cannot be simulated. An elegant way to incorporate protonation/deprotonation processes is to introduce a dissociative Morse potential into mesoscale DPD simulations. Neimark and coworkers (Lee et al., 2016; Vishnyakov et al., 2018) performed DPD simulations in synergy with dissociable Morse bonds between the protons and the conjugate bases and/or water beads to model proton hopping occurring in PEMs. This strategy successfully achieves the goal of simultaneously simulating the explicit proton/water transport and the nanophase separation in hydrated PEMs. Model Nafion membranes were simulated using this method and the resulting proton diffusivities at moderate and high hydration levels agreed well with the diverse experimental data. Nevertheless, there was a significant discrepancy at low hydration, which was ascribed to the dynamic narrow bridges between water domains that required a higher fidelity in the simulations than achievable in DPD simulations (Vishnyakov et al., 2018). Importantly, the results showed a sharp increase around the percolation threshold. This phenomenon was directly observed using PFG-NMR by Vasenkov et al. (Berens et al., 2020). It is worth noting that the dynamic hydrophilic subphase connectivity plays a critical role in water diffusion, suggesting that it is still challenging to accurately estimate proton diffusivity at low hydration through coarse-grained modeling.

In an effort to mimic the structural diffusion of protons, various techniques have been implemented into classical MD simulations including multistate empirical valence bond models (e.g. MS-EVB) (Savage et al., 2014), bond order-based reactive force fields (e.g. ReaxFF) (Zhang and Van Duin, 2015), and quantum hopping (Q-HOP) (Devanathan et al., 2010). Recently, a combination of reactive and nonreactive polarizable MD simulations was used to study transport mechanisms of OH^- in hydrated PPO-QA AEMs (Dong et al., 2018c). The morphology of these non-blocky AEMs at a hydration of 10 exhibited narrow percolating channels connecting the water domains. It was found that the vehicular mechanism made the dominant contribution to the conductivity in water-rich domains, while structural diffusion played a significant role in crossing the bottlenecks between large water domains under the confined environment of a channel (Dong et al., 2018a; Dong et al., 2018c). Their findings demonstrate that structural diffusion of OH^- facilitates the diffusion through these bottlenecks without loss of anion hydration structure, while the vehicular diffusion of OH^- through the bottlenecks requires a change in the hydration structure giving rise to a high kinetic barrier for such events. Notably, the decomposition of the total diffusivity into vehicular motion and discrete structural diffusion revealed that the structural diffusion is dominant and the structural diffusion is anticorrelated with the vehicular diffusion (Dong et al., 2018b).

To capture the delicate interplay of proton transfer and solvation structure, AIMD simulations are utilized, in which "on the fly" force fields obtained from DFT-based electronic structure calculations enable one to accurately simulate the breaking and formation of covalent bonds. However, the extremely high computational cost of AIMD simulations limits the accessible length and time scales. Thus, it is important to make careful selection in the simulated systems. Recent AIMD simulations of a model PEM functionalized with sulfonate end groups (SO_3^-) using graphane bilayers were undertaken to study the hydronium ion diffusion mechanism (Zelovich et al., 2021; Zelovich and Tuckerman, 2021).

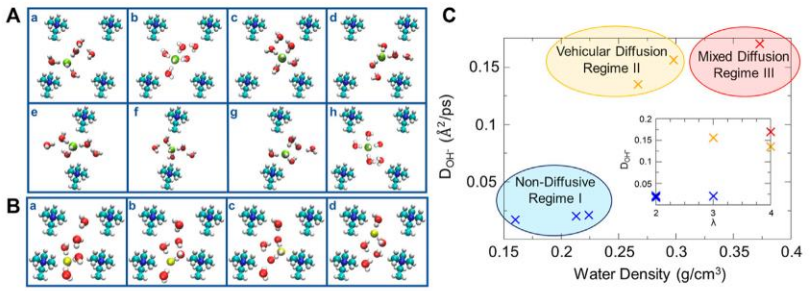

FIGURE 7
(A) Vehicular diffusion mechanism of OH^- in system a4 from a z-perspective. **(B)** Structural diffusion mechanism of OH^- in system b4 from a z-perspective. **(C)** Relationship between average diffusivity of OH^- and water density, inset: OH^- diffusivity vs. the hydration level. Reprinted and adapted with permission from ref. (Zelovich et al., 2019b). Copyright 2019 American Chemical Society.

Surprisingly, low coordination of the hydronium ions at a hydration level of $3H_2O/SO_3H$ promotes the participation of the pendant SO_3^- groups in the structural diffusion process of the hydronium ions with the reaction: $SO_3^- + H_3O^+ \leftrightarrow SO_3H + H_2O$. It was reasoned that the non-uniform water distribution at a low hydration level facilitates the reaction between the hydronium ion and the anion group as the oxygen located next to SO_3^- obtains a coordination number of approximately one from surrounding H_2O and H_3O^+ (Zelovich et al., 2021). Furthermore, the sulfonate functional group with the linker of $(CH_2)_2$ possesses weaker acidity than with the linker of $(CF_2)_2$, resulting in more active participation in the SO_3^-/H_3O^+ reaction and thereby improving instead of impeding the hydronium transport (Zelovich and Tuckerman, 2022).

Zelovich and coworkers (Zelovich et al., 2019a, Zelovich et al., 2019b) also employed graphane bilayers or carbon nanotubes with selected cationic groups attached with added water molecules and hydroxide ions to model the complex nanoconfined environment of an AEM. The effects of the hydration level, cation spacing, and cell geometry were studied to explore the mechanisms of OH^- transport. Structurally similar water layers exhibit a symmetrical distribution of oxygen atoms between the graphane layers while structurally dissimilar water layers enable the flow of water molecules. These exist in different systems under various structural confinement. The structural similarity in the water layers reduces the hydroxide ion diffusion, while structural dissimilarity improves the hydroxide ion transport. In regard to enhancing OH^- diffusion, various solvated OH^- structures were considered to be active/inactive complexes. The active 3-fold and inactive 4-fold structures (i.e., hydroxide ion coordinated by three or four water molecules) correlate with fast and slow time scale processes, respectively, based on the fitting of results from proton transfer correlation functions. In systems of low hydration, the cation stabilizes the 3-fold complex acting as a fourth neighbor (shown in subplot a of Figure 7A), followed by the drift of this 3-fold complex toward the water molecules in the center of the cell forming a 4-fold planar structure (shown in subplot c of Figure 7A). This complex continues to move toward the nearby cation forming a stable 3-fold structure in the vicinity of the cation. An insufficient number of water molecules around the hydroxide ions leads to vehicular movement of the 3-fold complex between cationic groups. Increasing hydration helps build up a wire between the cation groups by rearranging the hydrogen bonds, which consequently invokes a series of proton transfer events *via* structural diffusion (shown in Figure 7B). Three distinct diffusion regimes were identified under low-hydration conditions: a non-diffusive regime at very low effective water density, a vehicular diffusion regime at intermediate water density, and a mixed diffusion regime with higher water density (Figure 7C). In contrast to PEMs, the cationic groups in AEMs form a bottleneck-like region for hydroxide ion transport at low water contents, consequently giving rise to the suppression of the diffusion of hydroxide ions (Zelovich et al., 2019a; Zelovich et al., 2019b; Zelovich and Tuckerman, 2021). Moreover, it is surprising to observe the non-monotonic temperature dependence of hydroxide diffusivity in both theoretical and experimental studies (Zelovich et al., 2022). This unexpected phenomenon was rationalized by examining the transport mechanisms of hydroxide ions at different hydration levels. Specifically, the vehicular diffusion is dominant at extremely low hydration ($\lambda = 2$) and high temperature is required to break the hydrogen bonds of the stable solvated hydroxide clusters. At low hydration ($2 < \lambda < 5$), moderate temperatures enhance trivial proton rattling but the hydroxide ions are still trapped in the cell center, which requires high temperatures to overcome the bottleneck between cations. Layered water structures occur at

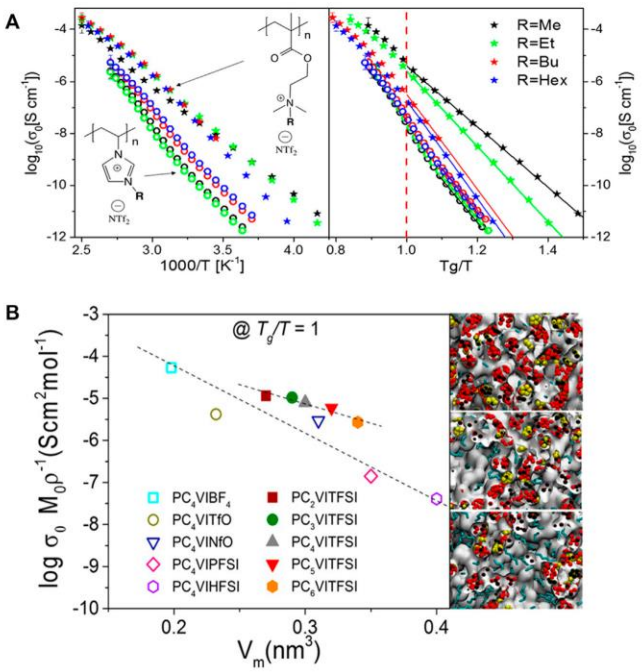

FIGURE 8
(A) Left: dc ionic conductivity vs. inverse temperature; right: T_g-independent ionic conductivity for ammonium (stars) and imidazolium (open circles) based polyILs. **(B)** Anion concentration-normalized dc conductivity at T_g/T = 1 as a function of repeat unit molecular volume, V_m, (including the counterion) for imidazolium-based polyILs with different side chains and counterions. Figure A reprinted with permission from ref. (Heres et al., 2018) and figure B reprinted with permission from ref. (Iacob et al., 2017). Copyright 2018 and 2017 American Chemical Society.

high hydration ($\lambda > 5$), leading to higher hydroxide diffusivity in the upper layer than in the cation-containing layer. Therefore, the temperature threshold for high hydroxide diffusivity occurs when the hydroxide ions can move to the upper layer where efficient structural diffusion is predominant (Zelovich et al., 2022). It may be concluded that the water distribution and the solvation structure of OH^- play a key role in determining the proton transport mechanisms. Obviously, the combination of water density, the space between cationic groups, and confinement conditions results in complex local environments.

Recognizing the important role of the solvation structure of OH^- under functionalized nanoconfined conditions, further study of the interplay of solvation patterns and diffusion mechanisms was undertaken by Zelovich and Tuckerman (Zelovich and Tuckerman, 2020). Five layers were defined and distinguished as outer water layers (i.e., the water in immediate proximity to the graphane bilayer L1 and L5), and inner water layers between the outer ones based on the distribution of the oxygen atoms. Planar 3-fold and 4-fold solvation structures were observed in L1 and L5, respectively. This leads to a less preferable environment for enhancing hydroxide diffusion due to the relatively stable planar structures. The inner water layers exhibit the solvation characteristics similar to that in bulk aqueous hydroxide. Specifically, in the L2 water layer located on top of the cationic groups, a series of successive proton transfer events occur followed by a quiescent period, while the frequency of proton transfer in the L3 and L4 layers is higher than in the L2 layer. These interesting results show a novel avenue to design high-performance AEMs by engineering the water within a nanoconfined environment.

The transport mechanisms of hydroxide ions within poly(arylene ether sulfone ketone)s functionalized by quaternized ammonio-substituted fluorenyl groups (QPE) AEMs were investigated *via* classical and first-principles MD simulations (Takaba et al., 2017). The impact of the number of

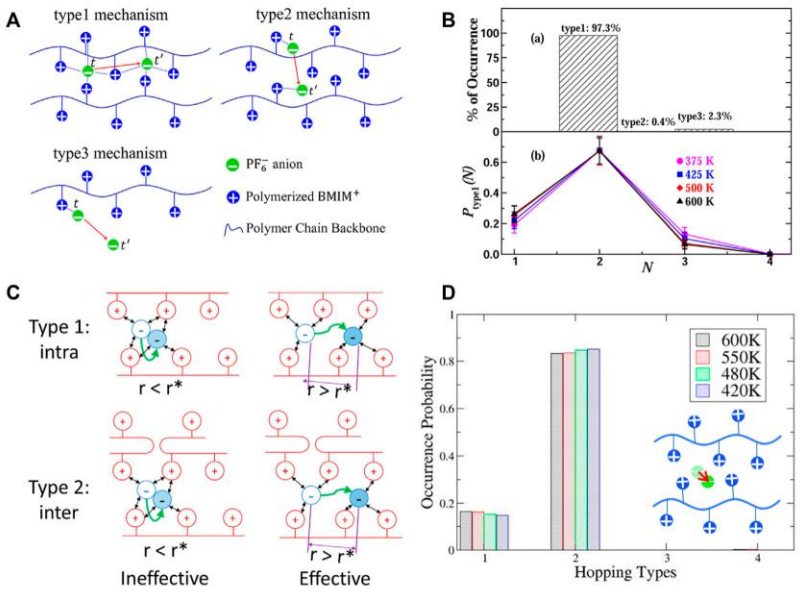

FIGURE 9
(A) Illustration of ion hopping types in polyIL electrolytes. **(B)** Percentage of hopping events in polyIL electrolytes (top); and decomposition of intrachain hopping events (type 1) assisted by N number of polymer chains (bottom). **(C)** Definition of effective hopping contributing to the long-range diffusion. **(D)** Probability of occurrence as a function of hopping type at four different temperatures when the ineffective ions were excluded. The inset is the definition of type 4: remaining intact (i.e. rattling). Figures A and B reprinted with permission from ref. (Mogurampelly et al., 2017) and Figures C and D reprinted and adapted with permission from ref. (Liu et al., 2021). Copyrights 2017 and 2021 American Chemical Society.

repeating units in QPE on the ion conductivity of OH^- is minimal and OH^- transport in hydrated QPE occurs through structural diffusion (i.e. hopping between the ammonium groups of QPE) accompanied by vehicular transport based on the classical MD results. The first principles MD simulations show that the transport of OH^- occurs through the formation of $H_3O_2^-$ *via* the hydrogen bond network of the water molecules. AIMD simulations of the quaternary ammonium functionalized polystyrene-block-poly(ethylene-ran-butylene)-block-polystyrene (QSEBS) AEMs systems demonstrate that hydration increases structural diffusion, which contributes to OH^- conductivity, and hydroxide ions have the longest lifetime when the system is dry (Castañeda and Ribadeneira, 2020).

In anhydrous systems

In addition to extensive investigations of proton transport in aqueous polymeric electrolytes, the mechanisms underlying ion transport in polyILs because of their application in batteries have attracted attention. Significant effort has been undertaken to address the low conductivity in polyILs which may be promising materials due to their long lifetime and safety advantages. Thus far, many factors have been studied to promote a better understanding of ion transport mechanisms and formulate design rules for high-performance polyILs (Aziz et al., 2018; Bocharova and Sokolov, 2020; Son and Wang, 2020).

Early studies (Iacob et al., 2017; Heres et al., 2018) revealed that the length and rigidity of the side-chains play a crucial role in transporting ions along the polymer chains. It was found that ammonium-based polyILs show higher dc ionic conductivity than imidazolium systems at their respective glass transition temperatures based on the results from BDS, WAXS, and classical MD simulations (shown in the left panel of Figure 8A) (Heres et al., 2018). Additionally, the alkyl spacer length has a strong influence on the ionic conductivity at comparable time scales of the segmental dynamics for imidazolium polyILs (shown in the right panel of Figure 8A). Specifically, in the imidazolium polyILs, the T_g-independent ionic conductivity experiences one decade decrease as the alkyl side-chain length is systematically increased, which is correlated with an increase in the characteristic backbone-to-

backbone distance (Iacob et al., 2017). In contrast, the reduction of anion molecular volume leads to ~3 orders of magnitude increase in the T_g-independent ionic conductivity. Complemented by atomistic MD simulations, the morphologies were transformed from isolated apolar clusters within a continuous polar matrix for shorter alkyl groups to bicontinuous sponge-like morphologies for longer alkyl chains, which is shown in Figure 8B. Variation in the molecular structure results in greater effects on ion mobility than the effective number density of the mobile ions (Heres et al., 2018).

Ganesan et al. used atomistic MD simulations based on quantum-mechanically parametrized force fields to obtain a molecular-level understanding of the time scale and mechanisms underlying ion transport in model systems of poly(1-butyl-3-vinylimidazolium-hexafluorophosphate) polyILs (Mogurampelly et al., 2017). The intermittent and continuous correlation functions were used to probe the structural relaxation behavior of the association of anions and cations, and the average lifetime of the associations. The former was calculated with $C(t) = h(t)h(0)/h$, where $h(t)$ is unity if one ion remains associated with another according to the first minima of the cation-anion radial distribution function at a given time t. The structural relaxation time was extracted by fitting the function to a stretched exponential. Alternatively, the structural relaxation processes can be captured from the intermediate scattering function at a characteristic wave vector, corresponding to the first peak of the anion-anion radial distribution function. Based on these detailed analyses, their results show that anion transport in polyILs is mainly governed by a mechanism involving intra- and inter-chain ion hopping that is facilitated through the breaking and formation of ion associations involving four polymerized cationic groups that belong to two polymer chains (*see* Figures 9A,B). This finding was confirmed by atomistic simulations that included polarizability effects (Zhang et al., 2022). More interestingly, the authors found that the mobile ions tend to associate with three polycations from two polymer chains when refining the ion hopping mechanism by excluding the rattling ions (Zhang et al., 2022). They determined that ion mobilities in these imidazolium-based polyILs are directly correlated to the average lifetimes of the ion associations while the ion mobilities in pure ILs are correlated to the structural relaxation time; indicating that anion hopping along the cation monomer chains underlies the transport of ions in polyILs (Mogurampelly et al., 2017). These results conclusively imply that anion transport is decoupled from the slow segmental relaxations in imidazolium-based polyILs, which is different from what has been observed in poly(ethylene oxide) and poly(propylene glycol) systems (Yoshida et al., 2011; Wang et al., 2014). The difference may be ascribed to the rigid polymer matrix that facilitates decoupling of ion transport from segmental dynamics.

However, it was subsequently argued that the breaking and forming of ion association probably do not contribute to long-range ion transport because most ions merely "rattle" amongst the polymerized cationic monomers within a cage (Xiao et al., 2020; Liu et al., 2021). No long-range transport may occur unless the ion escapes from its cage. Based on the MD simulations performed on both 1-butyl-3-methylimidazolium tetrafluoroborate ([BMIM]-[BF4]) IL and poly(1-butyl-3-vinylimidazolium-tetrafluoroborate) (poly([BVIM]-[BF4])) polyIL, the comparison between ion transport in ILs and that in polyILs confirmed that the anion diffusivity in polyIL is directly correlated with the anion hopping among cages formed by the cationic branch chains. Hence, the trap time in which an anion is trapped inside a cage determines the time scale of the anion transport rather than the ion association lifetime (Xiao et al., 2020). Nevertheless, the coupled motion of an anion and the surrounding ions governs the diffusivities of ions in the IL, i.e., the ion transport is correlated with the ion association lifetime. These phenomena were observed in additional all-atom MD simulations (Luo et al., 2020b; Liu et al., 2021), which improved the understanding of ion hopping mechanisms in polyILs. Specifically, the ion transport mechanism in polyIL poly(C2Vim)Tf_2N was investigated by defining an additional ion transport mode, i.e., an intact type that corresponds to the rattling of an ion when trapped in a cage. As expected, there is a significant portion of intact anions (35–50%), implying that a considerable amount of mobile anions are trapped in the cages and do not contribute to long-range transport. Examination of the self-part of the van Hove function of the anions at the characteristic time of the greatest dynamical heterogeneity illustrates the occurrence of a secondary peak, which is a quantitative indication of diffusion *via* hopping (Liu et al., 2021). Note that the dynamical heterogeneity can be quantified with a non-Gaussian parameter (α_2) to indicate the deviation from purely Gaussian behavior and is required to be large enough ($\alpha_2 > 1$) to distinguish the double peaks in the self-part of the van Hove function. If the effective mobile anions are distinguished from slow "immobile" ones according to the distance criterion of the local minimum between the two peaks in the self-part of the van Hove function of the anions, the categorization for only these effective mobile anions shows negligible intact anions and dominant inter-chain hopping over intra-chain events. This is in contrast to the classification with a short interval of sampling (Figures 9C,D). Indeed, these results conclusively show that the instant ion dissociation is necessary but not sufficient for effective hopping transport. Furthermore, the stringlike cooperative motion of the mobile ions was quantified according to the criterion: $min[|r_i(t) - r_j(0)|, |r_i(0) - r_j(t)|] < r_s$, in which $r_i(t)$ and $r_j(t)$ are the coordinates of ith and jth anions at time t, and r_s is the cutoff distance for the string collection. The average string length for the polyILs is in the range of 1.6–2.2 anions, but close loops in the anion transport were not observed, which were

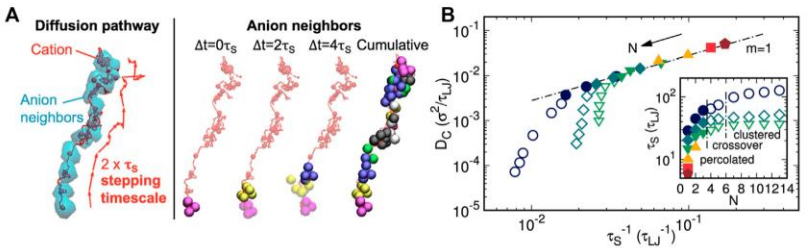

FIGURE 10
(A) Instant anion neighbor positions at the first three successive Δt = 0 τ_S, 2 τ_S, and 4 τ_S increments, where transparent and opaque beads are previous and present neighbors, respectively. The three sets of anion neighbors (magenta, yellow, and purple) comprise no shared anion identities. **(B)** Cation diffusivity D_C vs. inverse characteristic ion-association lifetime τ_S^{-1} for all spacer lengths N and dielectric constants ε_R. Reprinted with permission from ref. (Bollinger et al., 2020). Copyright 2020 American Chemical Society.

hypothesized to be the consequence of the low ionic conductivity in polyILs (Stacy et al., 2018).

A subsequent study (Luo et al., 2020b) provides some understanding of the ion transport mechanism in the polyILs with various counterions (Br^-, BF_4^-, PF_6^-, and Tf_2N). It was further confirmed that only a small fraction of the anions contributes to effective hopping transport. Although the relationship between the diffusivity of anions and the lifetime of ion association is also close to unity based on the power law fitting, it was suggested that the linear correlation is more possible between the diffusivity of the anions and the structural relaxation rather than the lifetime of ion association. Additionally, these findings show that both the stronger interaction between cationic groups and Br^- and the flexibility of Tf_2N^- hinder effective hopping, which implies the significance of specific interactions in polyILs governing transport mechanisms. Notably, the analysis methods employed in these studies including the categorization of hopping types, the definitions of dynamic heterogeneity and stringlike cooperative motion, can be extended to other ion-containing polymer systems.

In view of the role of ionic aggregate morphology in the mechanisms of ion transport, coarse-grained MD simulations were performed on single-ion conducting polymers to obtain an understanding of how the nanoscale aggregation of the cations and anions covalently bonded to the polymer affect the rates and mechanism of cation transport (Bollinger et al., 2020). The authors suggested that cations diffused *via* stepping motions along with the ionic aggregates and correlated the diffusivity of cations to the lifetimes of continuous association between oppositely charged ions in percolated ionic aggregate formed systems (shown in Figure 10). It was emphasized that this correlation did not hold for systems with isolated ionic clusters. Additionally, a strategy was proposed to enhance ion transport based on the strength of the Coulombic interactions: sufficiently strong to support percolated aggregates but weak enough to facilitate ion dissociation (Bollinger et al., 2020).

The mechanisms of ion transport are more complex in salt-doped polymeric ionic liquids due to a variety of interactions between the polymer and ions and between the ions themselves. It was found that an increase in salt concentration reduces the movement of ion species attributing to the increased viscosity upon the addition of a salt (Haskins et al., 2014). However, recent experimental and simulation results (Wang X. et al., 2019; Zhang et al., 2020a) have shown that in lithium salt-doped poly(1-butyl-3methyl-imidazolium bistrifluoroimide) systems, the addition of salt increases the dynamics of both lithium and the anions. It was also observed that there is a stronger coupling between lithium-ion transport and polymer segmental dynamics as well as the decoupling of the anion mobility from polymer segmental dynamics. The lithium ions show stronger dependence on salt concentration than the anions, which leads to higher lithium-ion transference numbers (Zhang et al., 2020a). Another surprising trend was recently deduced by Seo et al. (Seo et al., 2019). They determined that the increase in molecular weight enhances the ionic conduction in di-block copolymers using coarse-grained MD simulations, introducing an extra $1/r^4$ solvation potential. They suggested that the solvation strength dominantly controls the relationship between ion diffusion and ion concentration. This counterintuitive trend can be best explained by local ion agglomeration caused by the strong ion-ion interactions rather than interfacial width. Furthermore, the increase in molecular weight mitigates the ion agglomeration effect, consequently leading to high ion diffusivity due to a more even distribution of ions in salt-doped block copolymers.

To achieve high lithium selectivity (indicated by transport number and transference number) in polymer electrolytes, one potential approach is to incorporate nanoparticles into ion-conducting solid polymers or liquids; although the mechanisms underlying ion transport in such materials

remain poorly understood (Diederichsen et al., 2017). Recently, coarse-grained multiscale simulations were performed on this type of polymer (Kadulkar et al., 2020). Their results suggest that the ionic conductivity is mainly due to Li^+ transport along nanoparticle surfaces, in the vicinity of tethered anions. The increase in nanoparticle loading improves the connectivity of the cationic surface transport pathways at low nanoparticle concentrations. High nanoparticle loadings were observed to suppress ion mobility because of the strong cation-anion interaction and steric hindrance effects. It was further observed that high dielectric constant solvents facilitate the dissociation of cations, leading to higher ionic conductivity.

Another novel strategy is to develop locally ordered and rigid channels for ion transport with semicrystalline poly-zwitterionic (polyZI) materials, in which the Li^+ transport number achieves up to 0.67 (Jones et al., 2022). This recent study demonstrated that formation of a nanoscale crystal phase occurs in the polyZI tethered with the zwitterion imidazolium-trifluoromethanesulfonamide (Im-TFSI), which is ascribed to the weak Coulombic interactions that prevent the pendant zwitterions from noncovalent cross-linking. The disparity in size between Li^+ and the tethered anions promotes sufficient free volume for Li^+ transport but not for the much larger $TFSI^-$, resulting in large selectivity for Li^+ transport. These special confined conditions enable the decoupling of Li^+ from the slow segmental relaxation in crystalline conductive pathways, although the transport of Li^+ in the amorphous phase was also observed in these systems. Dating back to earlier studies, the influences of polyZI chemistry (Lind et al., 2016; Taylor et al., 2021) and ionic organization (Keith and Ganesan, 2020) on Li^+ transport were investigated in theoretical and experimental studies. The experimental results showed improved room temperature ionic conductivities and elastic modulus. This was explained by the enhanced cation/anion dissociation and physical cross-linking within the polymers due to the strong interactions between zwitterions and the mobile ions (Lind et al., 2016; Taylor et al., 2021). Classical MD simulations of polyZIs with distinct organizations indicated that the counterion of the terminal moiety of the zwitterions possesses higher diffusivity than the counterion of the moiety adjacent to the backbone (Keith and Ganesan, 2020). Interestingly, the mobility of the former was found to be correlated with the ion-association behavior, while the latter transported coupling with a cage relaxation. These findings provide crucial insights into this emerging class of ion-containing materials.

In concluding this section, it is important to mention the origin of the difference between charge diffusivity computed from conductivity measurements and that determined by NMR. This is typically quantified with the Haven ratio, $H = D_i/D_\sigma$, in which D_i is the self-diffusivity measured by NMR without including all the ionic correlation terms, whereas D_σ the diffusivity derived from impedance spectroscopy using the Nernst-Einstein equation. The interested reader is referred to the excellent perspective (Fong et al., 2021). In ionic liquids that are salts having a melting point below 100°C, an $H > 1$ is explained by the movement of the cation-anion pairs that contribute to ion diffusion, but not to conductivity. However, this explanation was challenged by results from atomistic MD simulations (Kashyap et al., 2011). Further experimental studies of polyILs revealed that the major mechanism suppressing ionic conductivity is due to the strongly correlated movement of mobile ions with a like charge (Popov et al., 2020). Recently, simulations of ILs and polymerized ionic liquids with various degrees of polymerization (N) revealed that the strong distinct correlations between neighboring cations in the backbone of polyILs lead to distinct cation-cation diffusivity that is larger than the self-diffusivity of cations in magnitude and independent of N at larger N (Zhang et al., 2020b). Hence, the inverse Haven ratio shows a maximum at N = 3. Moreover, the authors demonstrated that the ideal transference numbers decrease with increasing N for large N due to the cationic contribution to the conductivity, which challenges the notion that pure polyILs are single-ion conductors. Shen and Hall studied the effects of ion-polymer and ion-ion interactions on the correlation of anion and cation motions by modeling salt-doped homopolymers and block copolymers (Shen and Hall, 2020). The authors found that the increase of ion-monomer interactions gave rise to competing diffusion and ion correlation effects at low salt concentrations and progressively suppressed the conductivity with increasing salt concentration. The stronger ion-ion interactions reduce ion conductivity without being affected by ion concentration (Shen and Hall, 2020). It is worth noting that ion-ion correlations reduce the ionic conductivity in these systems, but enhance the conductivity in superionic ceramics. We would emphasize that one potential strategy is to turn negative ion-ion correlation into positive by tailoring the structure of ion channels and the specific interactions between the ions and lattice. For example, Kumar and coworkers developed one-dimensional ionic channels for anhydrous proton conduction by self-assembly of functionalized organic phosphonic acid and aromatic heterocyclic 1,2,4-triazole molecules (Kumar et al., 2019). The results demonstrate that the one-dimensional conductivity is improved compared with the 3-dimensional channels in Nafion.

Summary and outlook

Recent significant findings are summarized including the morphology and the ion transport as well as underdeveloped specific interactions within the ion-containing membranes, emphasizing the interplay of morphology and ion transport. We discussed the influences of polymer architectures, tethered ionic groups, the rigidity of the backbone, the solvents, and the additives on the morphology and ion transport of the membranes from a multiscale perspective. Importantly, some novel design strategies were highlighted such as tuning the solvation structures

of hydronium/hydroxide ion in hydrated ion exchange membranes, turning negative ion-ion correlation to positive to improve the ionic conductivity in polyILs, etc. In addition, a variety of analytical approaches were reviewed including quantitative cluster analysis, categorization of hopping type, the definitions of dynamic heterogeneity, stringlike cooperative motion, *etc.*, for the purpose of gaining mechanistic insight. The remaining challenges include, but not limit to, the design of single-ion conductors, well-defined supramolecular architectures with one-dimensional enhanced ion transport channels, and the understanding of the specific interactions.

To further resolve fundamental issues in theoretically exploring the design rules for advancing the performance of ion-containing materials, we would like to propose several promising directions. First of all, the force field development for atomistic molecular dynamics and coarse-grained models would provide the possibility to gain accurate morphology and dynamical properties from simulations. Specifically, the novel machine learning technique could be extensively applied to the improvement of force fields considering the effects of multi-body interactions, polarizability, and delocalization of charge. New developed force fields for coarse-grained models such as the DFT-based parameterization method (Sepehr and Paddison, 2016), the fragment molecular orbital method (Okuwaki et al., 2018b), the MARTINI (Marrink et al., 2007), and the SPICA (Griffiths and Shinoda, 2019; Miyazaki et al., 2020) could be modified and extended to model ion-containing materials, especially the interfacial phenomena of bipolar membranes. Additionally, machine learning assisted backmapping coarse-grained models to atomistic represented models offers an opportunity to restore details at the atomistic level, leading to an increase in the spatial and temporal scales (Zhang et al., 2019; Li et al., 2020). In view of the temporal limitation of *ab initio* molecular dynamics simulations, it would be potentially promising to develop multi-timestep algorithms to investigate large time scale dynamic properties. To this end, the incorporation of proton transport behaviors into mesoscopic heterogeneity of phase-separated hydrated ionomers is still challenging. It would be promising to introduce various levels of theory into the systems of interest, although the bridging between different levels of theory including coarse-grained approach has yet to be addressed. In addition, an energy decomposition analysis would be a powerful tool for a quantitative interpretation of the specific interactions between fragments/molecules to provide detailed insight into the interactions in terms of chemically meaningful components including: electrostatic, repulsive exchange, induction, and dispersion terms (Zhao et al., 2017).

Author contributions

ZZ reviewed the literature and wrote the initial draft. SP proposed an article outline, revised the draft, and made editorial suggestions for the draft. Both ZZ and SP discussed the conceptual issues and themes for the review article.

Funding

This work was supported by the U.S. Army Research Office under contracts W911NF-15-1-0501 and W911NF-16-1-0402.

Conflict of interest

The authors declare that the research was conducted in the absence of any commercial or financial relationships that could be construed as a potential conflict of interest.

Publisher's note

All claims expressed in this article are solely those of the authors and do not necessarily represent those of their affiliated organizations, or those of the publisher, the editors and the reviewers. Any product that may be evaluated in this article, or claim that may be made by its manufacturer, is not guaranteed or endorsed by the publisher.

References

Abbott, L. J., and Frischknecht, A. L. (2017). Nanoscale structure and morphology of sulfonated polyphenylenes via atomistic simulations. *Macromolecules* 50 (3), 1184–1192. doi:10.1021/acs.macromol.6b02232

Agrawal, A., Perahia, D., and Grest, G. S. (2016). Cluster morphology-polymer dynamics correlations in sulfonated polystyrene melts: Computational study. *Phys. Rev. Lett.* 116 (15), 158001. doi:10.1103/PhysRevLett.116.158001

Allen, F. I., Comolli, L. R., Kusoglu, A., Modestino, M. A., Minor, A. M., Weber, A. Z., et al. (2015). Morphology of hydrated as-cast nafion revealed through cryo electron tomography. *ACS Macro Lett.* 4 (1), 1–5. doi:10.1021/mz500606h

Aziz, S. B., Woo, T. J., Kadir, M. F. Z., and Ahmed, H. M. (2018). A conceptual review on polymer electrolytes and ion transport models. *J. Sci. Adv. Mater. Devices* 3 (1), 1–17. doi:10.1016/j.jsamd.2018.01.002

Bedrov, D., Piquemal, J.-P., Borodin, O., Mackerell, A. D., Roux, B., Schröder, C., et al. (2019). Molecular dynamics simulations of ionic liquids and electrolytes using polarizable force fields. *Chem. Rev.* 119 (13), 7940–7995. doi:10.1021/acs.chemrev.8b00763

Berens, S. J., Yahya, A., Fang, J., Angelopoulos, A., Nickels, J. D., Vasenkov, S., et al. (2020). Transition between different diffusion regimes and its relationship with structural properties in nafion by high field diffusion NMR in combination with small-angle X-ray and neutron scattering. *J. Phys. Chem. B* 124 (40), 8943–8950. doi:10.1021/acs.jpcb.0c07249

Bocharova, V., and Sokolov, A. P. (2020). Perspectives for polymer electrolytes: A view from fundamentals of ionic conductivity. *Macromolecules* 53 (11), 4141–4157. doi:10.1021/acs.macromol.9b02742

Bocharova, V., Wojnarowska, Z., Cao, P.-F., Fu, Y., Kumar, R., Li, B., et al. (2017). Influence of chain rigidity and dielectric constant on the glass transition temperature in polymerized ionic liquids. *J. Phys. Chem. B* 121 (51), 11511–11519. doi:10.1021/acs.jpcb.7b09423

Bollinger, J. A., Stevens, M. J., and Frischknecht, A. L. (2020). Quantifying single-ion transport in percolated ionic aggregates of polymer melts. *ACS Macro Lett.* 9 (4), 583–587. doi:10.1021/acsmacrolett.0c00139

Castañeda, S., and Ribadeneira, R. (2020). Description of hydroxide ion structural diffusion in a quaternized SEBS anion exchange membrane using ab initio molecular dynamics. *J. Phys. Chem. C* 124 (18), 9834–9851. doi:10.1021/acs.jpcc.9b10018

Chen, C., Arntsen, C., and Tse, Y.-L. S. (2020a). Simulation study of the effects of phase separation on hydroxide solvation and transport in anion exchange membranes. *J. Chem. Phys.* 152, 094903. doi:10.1063/1.5143168

Chen, C., Tse, Y. L. S., Lindberg, G. E., Knight, C., and Voth, G. A. (2016). Hydroxide solvation and transport in anion exchange membranes. *J. Am. Chem. Soc.* 138 (3), 991–1000. doi:10.1021/jacs.5b11951

Chen, S., Wang, H., Zhang, J., Lu, S., and Xiang, Y. (2020b). Effect of side chain on the electrochemical performance of poly (ether ether ketone) based anion-exchange membrane: A molecular dynamics study. *J. Memb. Sci.* 605, 118105. doi:10.1016/j.memsci.2020.118105

Chen, W., Mandal, M., Huang, G., Wu, X., He, G., Kohl, P. A., et al. (2019). Highly conducting anion-exchange membranes based on cross-linked poly(norbornene): Ring opening metathesis polymerization. *ACS Appl. Energy Mat.* 2 (4), 2458–2468. doi:10.1021/acsaem.8b02052

Choi, J.-H., Ye, Y., Elabd, Y. A., and Winey, K. I. (2013). Network structure and strong microphase separation for high ion conductivity in polymerized ionic liquid block copolymers. *Macromolecules* 46 (13), 5290–5300. doi:10.1021/ma400562a

Clark, J. A., Santiso, E. E., and Frischknecht, A. L. (2019). Morphology and proton diffusion in a coarse-grained model of sulfonated poly(phenylenes). *J. Chem. Phys.* 151 (10), 104901. doi:10.1063/1.5116684

De Nicola, A., Correa, A., Milano, G., La Manna, P., Musto, P., Mensitieri, G., et al. (2017). Local structure and dynamics of water absorbed in poly(ether imide): A hydrogen bonding anatomy. *J. Phys. Chem. B* 121 (14), 3162–3176. doi:10.1021/acs.jpcb.7b00992

Dekel, D. R. (2018). Review of cell performance in anion exchange membrane fuel cells. *J. Power Sources* 375, 158–169. doi:10.1016/j.jpowsour.2017.07.117

Devanathan, R., Venkatnathan, A., Rousseau, R., Dupuis, M., Frigato, T., Gu, W., et al. (2010). Atomistic simulation of water percolation and proton hopping in nafion fuel cell membrane. *J. Phys. Chem. B* 114 (43), 13681–13690. doi:10.1021/jp103398b

Diederichsen, K. M., Mcshane, E. J., and Mccloskey, B. D. (2017). Promising routes to a high Li+ transference number electrolyte for lithium ion batteries. *ACS Energy Lett.* 2 (11), 2563–2575. doi:10.1021/acsenergylett.7b00792

Dong, D., Wei, X., Hooper, J. B., Pan, H., and Bedrov, D. (2018a). Role of cationic groups on structural and dynamical correlations in hydrated quaternary ammonium-functionalized poly(p-phenylene oxide)-based anion exchange membranes. *Phys. Chem. Chem. Phys.* 20 (29), 19350–19362. doi:10.1039/C8CP02211A

Dong, D., Zhang, W., Barnett, A., Lu, J., Van Duin, A. C. T., Molinero, V., et al. (2018b). Multiscale modeling of structure, transport and reactivity in alkaline fuel cell membranes: Combined coarse-grained, atomistic and reactive molecular dynamics simulations. *Polymers* 10, 1289. doi:10.3390/polym10111289

Dong, D., Zhang, W., Van Duin, A. C. T., and Bedrov, D. (2018c). Grotthuss versus vehicular transport of hydroxide in anion-exchange membranes: Insight from combined reactive and nonreactive molecular simulations. *J. Phys. Chem. Lett.* 9 (4), 825–829. doi:10.1021/acs.jpclett.8b00004

Doo, G., Lee, J. H., Yuk, S., Choi, S., Lee, D.-H., Lee, D. W., et al. (2018). Tuning the ionomer distribution in the fuel cell catalyst layer with scaling the ionomer aggregate size in dispersion. *ACS Appl. Mat. Interfaces* 10 (21), 17835–17841. doi:10.1021/acsami.8b01751

Dorenbos, G. (2020). How hydrophobic side chain design affects water cluster connectivity in model polymer electrolyte membranes: Linear versus Y-shaped side chains. *Int. J. Hydrogen Energy* 45 (58), 33906–33924. doi:10.1016/j.ijhydene.2020.09.010

Dorenbos, G. (2019). Coarse-grained study of the effect of hydrophobic side chain length on cluster size distributions and water diffusion in (Amphiphilic-Hydrophobic) multi-block co-polymer membranes. *Polymer* 173, 43–57. doi:10.1016/j.polymer.2019.04.025

Dorenbos, G. (2017a). Doping proton transport channels in poly-electrolyte membranes with high acidic site density polymers. *Eur. Polym. J.* 97, 14–25. doi:10.1016/j.eurpolymj.2017.09.040

Dorenbos, G. (2017b). Improving proton conduction pathways in di- and triblock copolymer membranes: Branched versus linear side chains. *J. Chem. Phys.* 146, 244909. doi:10.1063/1.4989487

Economou, N. J., Barnes, A. M., Wheat, A. J., Schaberg, M. S., Hamrock, S. J., Buratto, S. K., et al. (2015). Investigation of humidity dependent surface morphology and proton conduction in multi-acid side chain membranes by conductive probe atomic force microscopy. *J. Phys. Chem. B* 119 (44), 14280–14287. doi:10.1021/acs.jpcb.5b07255

Elabd, Y. A. (2019). Ion transport in hydroxide conducting block copolymers. *Mol. Syst. Des. Eng.* 4 (3), 519–530. doi:10.1039/c9me00022d

Fong, K. D., Self, J., Mccloskey, B. D., and Persson, K. A. (2021). Ion correlations and their impact on transport in polymer-based electrolytes. *Macromolecules* 54 (6), 2575–2591. doi:10.1021/acs.macromol.0c02545

Frischknecht, A. L., and Winey, K. I. (2019). The evolution of acidic and ionic aggregates in ionomers during microsecond simulations. *J. Chem. Phys.* 150 (6), 064901. doi:10.1063/1.5085069

Gebel, G., and Diat, O. (2005). Neutron and X-ray scattering: Suitable tools for studying ionomer membranes. *Fuel Cells* 5 (2), 261–276. doi:10.1002/fuce.200400080

Ghosh, S., and Chakrabarti, R. (2016). Molecular dynamics simulation elucidates the preferential binding affinity of sodium and tetramethylammonium ions for tetrameric nafion unit under aqueous conditions. *RSC Adv.* 6 (100), 97961–97968. doi:10.1039/C6RA21845H

Giffin, G. A., Haugen, G. M., Hamrock, S. J., and Di Noto, V. (2013). Interplay between structure and relaxations in perfluorosulfonic acid proton conducting membranes. *J. Am. Chem. Soc.* 135 (2), 822–834. doi:10.1021/ja3099799

Griffiths, M. Z., and Shinoda, W. (2019). tSPICA: Temperature- and pressure-dependent coarse-grained force field for organic molecules. *J. Chem. Inf. Model.* 59 (9), 3829–3838. doi:10.1021/acs.jcim.9b00480

Haskins, J. B., Bennett, W. R., Wu, J. J., Hernández, D. M., Borodin, O., Monk, J. D., et al. (2014). Computational and experimental investigation of Li-doped ionic liquid electrolytes: [pyr14] [TFSI], [pyr13] [FSI], and [EMIM] [BF4]. *J. Phys. Chem. B* 118 (38), 11295–11309. doi:10.1021/jp5061705

Heres, M., Cosby, T., Mapesa, E. U., Liu, H., Berdzinski, S., Strehmel, V., et al. (2018). Ion transport in glassy polymerized ionic liquids: Unraveling the impact of the molecular structure. *Macromolecules* 52 (1), 88–95. doi:10.1021/acs.macromol.8b01273

Iacob, C., Matsumoto, A., Brennan, M., Liu, H., Paddison, S. J., Urakawa, O., et al. (2017). Polymerized ionic liquids: Correlation of ionic conductivity with nanoscale morphology and counterion volume. *ACS Macro Lett.* 6 (9), 941–946. doi:10.1021/acsmacrolett.7b00335

Jeon, J. Y., Park, S., Han, J., Maurya, S., Mohanty, A. D., Tian, D., et al. (2019). Synthesis of aromatic anion exchange membranes by friedel–crafts bromoalkylation and cross-linking of polystyrene block copolymers. *Macromolecules* 52 (5), 2139–2147. doi:10.1021/acs.macromol.8b02355

Johansson, E. O., Yamada, T., Sundén, B., and Yuan, J. (2015). Dissipative particle dynamics approach for nano-scale membrane structure reconstruction and water diffusion coefficient estimation. *Int. J. Hydrogen Energy* 40 (4), 1800–1808. doi:10.1016/j.ijhydene.2014.11.030

Jones, S. D., Nguyen, H., Richardson, P. M., Chen, Y.-Q., Wyckoff, K. E., Hawker, C. J., et al. (2022). Design of polymeric zwitterionic solid electrolytes with superionic lithium transport. *ACS Cent. Sci.* 8 (2), 169–175. doi:10.1021/acscentsci.1c01260

Jorn, R., Savage, J., and Voth, G. A. (2012). Proton conduction in exchange membranes across multiple length scales. *Acc. Chem. Res.* 45 (11), 2002–2010. doi:10.1021/ar200323q

Jorn, R., and Voth, G. A. (2012). Mesoscale simulation of proton transport in proton exchange membranes. *J. Phys. Chem. C* 116 (19), 10476–10489. doi:10.1021/jp300040w

Kacar, G., Peters, E. a. J. F., and De With, G. (2013). Mesoscopic simulations for the molecular and network structure of a thermoset polymer. *Soft Matter* 9, 5785. doi:10.1039/c3sm50304f

Kadulkar, S., Milliron, D. J., Truskett, T. M., and Ganesan, V. (2020). Transport mechanisms underlying ionic conductivity in nanoparticle-based single-ion electrolytes. *J. Phys. Chem. Lett.* 11 (17), 6970–6975. doi:10.1021/acs.jpclett.0c01937

Kashyap, H. K., Annapureddy, H. V., Raineri, F. O., and Margulis, C. J. (2011). How is charge transport different in ionic liquids and electrolyte solutions? *J. Phys. Chem. B* 115 (45), 13212–13221. doi:10.1021/jp204182c

Katzenberg, A., Angulo, A., Kusoglu, A., and Modestino, M. A. (2021). Impacts of organic sorbates on the ionic conductivity and nanostructure of perfluorinated sulfonic-acid ionomers. *Macromolecules* 54 (11), 5187–5195. doi:10.1021/acs.macromol.1c00494

Keith, J. R., and Ganesan, V. (2020). Ion transport mechanisms in salt-doped polymerized zwitterionic electrolytes. *J. Polym. Sci.* 58 (4), 578–588. doi:10.1002/pol.20190099

Ketkar, P. M., Shen, K.-H., Hall, L. M., and Epps, T. H. (2019). Charging toward improved lithium-ion polymer electrolytes: Exploiting synergistic experimental and computational approaches to facilitate materials design. *Mol. Syst. Des. Eng.* 4 (2), 223–238. doi:10.1039/c8me00105g

Kumar, A., Pisula, W., and Mullen, K. (2019). One dimensional enhanced anhydrous proton conduction in well defined molecular columns induced by non-covalent interactions. *ChemPhysChem* 20 (5), 651–654. doi:10.1002/cphc.201801017

Kusoglu, A., Vezzù, K., Hegde, G. A., Nawn, G., Motz, A. R., Sarode, H. N., et al. (2020). Transport and morphology of a proton exchange membrane based on a doubly functionalized perfluorosulfonic imide side chain perflourinated polymer. *Chem. Mat.* 32 (1), 38–59. doi:10.1021/acs.chemmater.8b05012

Kusoglu, A., and Weber, A. Z. (2017). New insights into perfluorinated sulfonic-acid ionomers. *Chem. Rev.* 117 (3), 987–1104. doi:10.1021/acs.chemrev.6b00159

Lee, M.-T. (2020). Designing anion exchange membranes with enhanced hydroxide ion conductivity by mesoscale simulations. *J. Phys. Chem. C* 124 (8), 4470–4482. doi:10.1021/acs.jpcc.9b11566

Lee, M.-T. (2019). Exploring side-chain designs for enhanced ion conductivity of anion-exchange membranes by mesoscale simulations. *J. Phys. Chem. C* 123 (17), 10802–10815. doi:10.1021/acs.jpcc.9b01815

Lee, M. T. (2021). Designing highly conductive block copolymer-based anion exchange membranes by mesoscale simulations. *J. Phys. Chem. B* 125 (10), 2729–2740. doi:10.1021/acs.jpcb.0c10909

Lee, M. T., Vishnyakov, A., and Neimark, A. V. (2016). Coarse-grained model of water diffusion and proton conductivity in hydrated polyelectrolyte membrane. *J. Chem. Phys.* 144, 014902. doi:10.1063/1.4938271

Li, L., Wang, J.-A., Ma, L., Bai, L., Zhang, A., Qaisrani, N. A., et al. (2021). Dual-side-chain-grafted poly(phenylene oxide) anion exchange membranes for fuel-cell and electrodialysis applications. *ACS Sustain. Chem. Eng.* 9 (25), 8611–8622. doi:10.1021/acssuschemeng.1c02189

Li, W., Burkhart, C., Polinska, P., Harmandaris, V., and Doxastakis, M. (2020). Backmapping coarse-grained macromolecules: An efficient and versatile machine learning approach. *J. Chem. Phys.* 153 (4), 041101. doi:10.1063/5.0012320

Lind, F., Rebollar, L., Bengani-Lutz, P., Asatekin, A., and Panzer, M. J. (2016). Zwitterion-containing ionogel electrolytes. *Chem. Mat.* 28 (23), 8480–8483. doi:10.1021/acs.chemmater.6b04456

Liu, H., Cavaliere, S., Jones, D. J., Rozière, J., and Paddison, S. J. (2018a). Morphology of hydrated nafion through a quantitative cluster Analysis: A case study based on dissipative particle dynamics simulations. *J. Phys. Chem. C* 122 (24), 13130–13139. doi:10.1021/acs.jpcc.8b01842

Liu, H., Cavaliere, S., Jones, D. J., Rozière, J., and Paddison, S. J. (2018b). Scaling behavior of nafion with different model parameterizations in dissipative particle dynamics simulations. *Macromol. Theory Simul.* 27, 1800003. doi:10.1002/mats.201800003

Liu, H., Luo, X., Sokolov, A. P., and Paddison, S. J. (2021). Quantitative evidence of mobile ion hopping in polymerized ionic liquids. *J. Phys. Chem. B* 125 (1), 372–381. doi:10.1021/acs.jpcb.0c06916

Liu, H., and Paddison, S. J. (2017). Alkyl chain length dependence of backbone-to-backbone distance in polymerized ionic liquids: An atomistic simulation perspective on scattering. *Macromolecules* 50 (7), 2889–2895. doi:10.1021/acs.macromol.6b02708

Liu, H., and Paddison, S. J. (2016). Direct comparison of atomistic molecular dynamics simulations and X-ray scattering of polymerized ionic liquids. *ACS Macro Lett.* 5 (4), 537–543. doi:10.1021/acsmacrolett.6b00061

Liu, S., Savage, J., and Voth, G. A. (2015). Mesoscale study of proton transport in proton exchange membranes: Role of morphology. *J. Phys. Chem. C* 119 (4), 1753–1762. doi:10.1021/jp511830f

Luo, X., Liu, H., Bae, C., Tuckerman, M. E., Hickner, M. A., Paddison, S. J., et al. (2020a). Mesoscale simulations of quaternary ammonium-tethered triblock copolymers: Effects of the degree of functionalization and styrene content. *J. Phys. Chem. C* 124, 16315–16323. doi:10.1021/acs.jpcc.0c03903

Luo, X., Liu, H., and Paddison, S. J. (2020b). Molecular dynamics simulations of polymerized ionic liquids: Mechanism of ion transport with different anions. *ACS Appl. Polym. Mat.* 3 (1), 141–152. doi:10.1021/acsapm.0c00834

Luo, X., and Paddison, S. J. (2019). DPD simulations of anion exchange membrane: The effect of an alkyl spacer on the hydrated morphology. *Solid State Ion.* 339, 115012. doi:10.1016/j.ssi.2019.115012

Ma, B., and Olvera De La Cruz, M. (2021). A perspective on the design of ion-containing polymers for polymer electrolyte applications. *J. Phys. Chem. B* 125 (12), 3015–3022. doi:10.1021/acs.jpcb.0c08707

Ma, L., Qaisrani, N. A., Hussain, M., Li, L., Jia, Y., Ma, S., et al. (2020). Cyclodextrin modified, multication cross-linked high performance anion exchange membranes for fuel cell application. *J. Memb. Sci.* 607, 118190. doi:10.1016/j.memsci.2020.118190

Marrink, S. J., Risselada, H. J., Yefimov, S., Tieleman, D. P., and Vries, A. H. D. (2007). The MARTINI force field: Coarse grained model for biomolecular simulations. *J. Phys. Chem. B* 111, 7812–7824. doi:10.1021/jp071097f

Meek, K. M., Reed, C. M., Pivovar, B., Kreuer, K.-D., Varcoe, J. R., Bance-Soualhi, R., et al. (2020). The alkali degradation of LDPE-based radiation-grafted anion-exchange membranes studied using different *ex situ* methods. *RSC Adv.* 10 (60), 36467–36477. doi:10.1039/d0ra06484j

Melchior, J.-P., and Jalarvo, N. H. (2019). A quasielastic neutron scattering study of water diffusion in model anion exchange membranes over localized and extended volume increments. *J. Phys. Chem. C* 123 (23), 14195–14206. doi:10.1021/acs.jpcc.9b01873

Miyazaki, Y., Okazaki, S., and Shinoda, W. (2020). pSPICA: A coarse-grained force field for lipid membranes based on a polar water model. *J. Chem. Theory Comput.* 16 (1), 782–793. doi:10.1021/acs.jctc.9b00946

Mogurampelly, S., Keith, J. R., and Ganesan, V. (2017). Mechanisms underlying ion transport in polymerized ionic liquids. *J. Am. Chem. Soc.* 139 (28), 9511–9514. doi:10.1021/jacs.7b05579

Münchinger, A., and Kreuer, K.-D. (2019). Selective ion transport through hydrated cation and anion exchange membranes I. The effect of specific interactions. *J. Memb. Sci.* 592, 117372. doi:10.1016/j.memsci.2019.117372

Nguyen, H.-D., Nguyen, T. K. L., Planes, E., Jestin, J., Porcar, L., Lyonnard, S., et al. (2020). Tailoring the proton conductivity and microstructure of block copolymers by countercation-selective membrane fabrication. *J. Phys. Chem. C* 124 (24), 13071–13081. doi:10.1021/acs.jpcc.0c04682

Okuwaki, K., Mochizuki, Y., Doi, H., Kawada, S., Ozawa, T., Yasuoka, K., et al. (2018a). Theoretical analyses on water cluster structures in polymer electrolyte membrane by using dissipative particle dynamics simulations with fragment molecular orbital based effective parameters. *RSC Adv.* 8 (60), 34582–34595. doi:10.1039/c8ra07428c

Okuwaki, K., Mochizuki, Y., Doi, H., and Ozawa, T. (2018b). Fragment molecular orbital based parametrization procedure for mesoscopic structure prediction of polymeric materials. *J. Phys. Chem. B* 122 (1), 338–347. doi:10.1021/acs.jpcb.7b08461

Pan, J., Li, Y., Han, J., Li, G., Tan, L., Chen, C., et al. (2013). A strategy for disentangling the conductivity–stability dilemma in alkaline polymer electrolytes. *Energy Environ. Sci.* 6, 2912. doi:10.1039/c3ee41968a

Perrin, J.-C., Lyonnard, S., and Volino, F. (2007). Quasielastic neutron scattering study of water dynamics in hydrated nafion membranes. *J. Phys. Chem. C* 111 (8), 3393–3404. doi:10.1021/jp065039q

Popov, I., Biernacka, K., Zhu, H., Nti, F., Porcarelli, L., Wang, X., et al. (2020). Strongly correlated ion dynamics in plastic ionic crystals and polymerized ionic liquids. *J. Phys. Chem. C* 124 (33), 17889–17896. doi:10.1021/acs.jpcc.0c03297

Pundir, S. S., Mishra, K., and Rai, D. K. (2018). Ion transport studies in nanocomposite polymer electrolyte membrane of pva–[C4C1Im] [HSO4]–SiO2. *J. Solid State Electrochem.* 22 (6), 1801–1815. doi:10.1007/s10008-018-3881-7

Savage, J., Tse, Y.-L. S., and Voth, G. A. (2014). Proton transport mechanism of perfluorosulfonic acid membranes. *J. Phys. Chem. C* 118 (31), 17436–17445. doi:10.1021/jp504714d

Seo, Y., Shen, K. H., Brown, J. R., and Hall, L. M. (2019). Role of solvation on diffusion of ions in diblock copolymers: Understanding the molecular weight effect through modeling. *J. Am. Chem. Soc.* 141 (46), 18455–18466. doi:10.1021/jacs.9b07227

Sepehr, F., Liu, H., Luo, X., Bae, C., Tuckerman, M. E., Hickner, M. A., et al. (2017). Mesoscale simulations of anion exchange membranes based on quaternary ammonium tethered triblock copolymers. *Macromolecules* 50 (11), 4397–4405. doi:10.1021/acs.macromol.7b00082

Sepehr, F., and Paddison, S. J. (2016). Dissipative particle dynamics interaction parameters from *ab initio* calculations. *Chem. Phys. Lett.* 645, 20–26. doi:10.1016/j.cplett.2015.12.032

Sevinis Ozbulut, E. B., Seven, S., Bilge, K., Akkas, T., Tas, C. E., Yildiz, B., et al. (2020). Blends of highly branched and linear poly(arylene ether Sulfone)s: Multiscale effect of the degree of branching on the morphology and mechanical properties. *Polymer* 188, 122114. doi:10.1016/j.polymer.2019.122114

Shen, K.-H., Fan, M., and Hall, L. M. (2021). Molecular dynamics simulations of ion-containing polymers using generic coarse-grained models. *Macromolecules* 54 (5), 2031–2052. doi:10.1021/acs.macromol.0c02557

Shen, K.-H., and Hall, L. M. (2020). Ion conductivity and correlations in model salt-doped polymers: Effects of interaction strength and concentration. *Macromolecules* 53 (10), 3655–3668. doi:10.1021/acs.macromol.0c00216

Shi, C., Liu, T., Chen, W., Cui, F., Liu, L., Cai, Y., et al. (2021). Interaction, structure and tensile property of swollen Nafion® membranes. *Polymer* 213, 123224. doi:10.1016/j.polymer.2020.123224

Shi, S., Liu, Z., Lin, Q., Chen, X., and Kusoglu, A. (2020). Role of ionic interactions in the deformation and fracture behavior of perfluorosulfonic-acid membranes. *Soft Matter* 16 (6), 1653–1667. doi:10.1039/c9sm01964b

Son, C. Y., and Wang, Z.-G. (2020). Ion transport in small-molecule and polymer electrolytes. *J. Chem. Phys.* 153 (10), 100903. doi:10.1063/5.0016163

Sorte, E. G., Paren, B. A., Rodriguez, C. G., Fujimoto, C., Poirier, C., Abbott, L. J., et al. (2019). Impact of hydration and sulfonation on the morphology and ionic conductivity of sulfonated poly(phenylene) proton exchange membranes. *Macromolecules* 52 (3), 857–876. doi:10.1021/acs.macromol.8b02013

Stacy, E. W., Gainaru, C. P., Gobet, M., Wojnarowska, Z., Bocharova, V., Greenbaum, S. G., et al. (2018). Fundamental limitations of ionic conductivity in polymerized ionic liquids. *Macromolecules* 51 (21), 8637–8645. doi:10.1021/acs.macromol.8b01221

Su, G. M., Cordova, I. A., Yandrasits, M. A., Lindell, M., Feng, J., Wang, C., et al. (2019). Chemical and morphological origins of improved ion conductivity in perfluoro ionene chain extended ionomers. *J. Am. Chem. Soc.* 141 (34), 13547–13561. doi:10.1021/jacs.9b05322

Sui, Y., Du, Y., Hu, H., Qian, J., and Zhang, X. (2019). Do acid–base interactions really improve the ion conduction in a proton exchange membrane? – a study on the effect of basic groups. *J. Mat. Chem. A* 7 (34), 19820–19830. doi:10.1039/c9ta06508c

Takaba, H., Hisabe, T., Shimizu, T., and Alam, M. K. (2017). Molecular modeling of OH− transport in poly(arylene ether sulfone ketone)s containing quaternized ammonio-substituted fluorenyl groups as anion exchange membranes. *J. Memb. Sci.* 522, 237–244. doi:10.1016/j.memsci.2016.09.019

Tarokh, A., Karan, K., and Ponnurangam, S. (2020). Atomistic MD study of nafion dispersions: Role of solvent and counterion in the aggregate structure, ionic clustering, and acid dissociation. *Macromolecules* 53 (1), 288–301. doi:10.1021/acs.macromol.9b01663

Taylor, M. E., Clarkson, D., Greenbaum, S. G., and Panzer, M. J. (2021). Examining the impact of polyzwitterion chemistry on lithium ion transport in ionogel electrolytes. *ACS Appl. Polym. Mat.* 3 (5), 2635–2645. doi:10.1021/acsapm.1c00229

Trigg, E. B., Gaines, T. W., Marechal, M., Moed, D. E., Rannou, P., Wagener, K. B., et al. (2018). Self-assembled highly ordered acid layers in precisely sulfonated polyethylene produce efficient proton transport. *Nat. Mat.* 17 (8), 725–731. doi:10.1038/s41563-018-0097-2

Tuckerman, M. E., Chandra, A., and Marx, D. (2010). A statistical mechanical theory of proton transport kinetics in hydrogen-bonded networks based on population correlation functions with applications to acids and bases. *J. Chem. Phys.* 133, 124108. doi:10.1063/1.3474625

Tuckerman, M. E., Marx, D., Klein, M. L., and Parrinello, M. (1997). On the quantum nature of the shared proton in hydrogen bonds. *Science* 275, 817–820. doi:10.1126/science.275.5301.817

Vishnyakov, A., Mao, R., Lee, M.-T., and Neimark, A. V. (2018). Coarse-grained model of nanoscale segregation, water diffusion, and proton transport in nafion membranes. *J. Chem. Phys.* 148, 2024108. doi:10.1063/1.4997401

Wang, R.-Y., and Park, M. J. (2020). Self-assembly of block copolymers with tailored functionality: From the perspective of intermolecular interactions. *Annu. Rev. Mat. Res.* 50 (1), 521–549. doi:10.1146/annurev-matsci-081519-020046

Wang, R., Liu, S., Wang, L., Li, M., and Gao, C. (2019a). Understanding of nanophase separation and hydrophilic morphology in nafion and speek membranes: A combined experimental and theoretical studies. *Nanomater. (Basel)* 9, 869. doi:10.3390/nano9060869

Wang, X., Chen, F., Girard, G. M. A., Zhu, H., Macfarlane, D. R., Mecerreyes, D., et al. (2019b). Poly(Ionic liquid)s-in-salt electrolytes with Co-Coordination-Assisted lithium-ion transport for safe batteries. *Joule* 3 (11), 2687–2702. doi:10.1016/j.joule.2019.07.008

Wang, Y., Fan, F., Agapov, A. L., Yu, X., Hong, K., Mays, J., et al. (2014). Design of superionic polymers—new insights from walden plot analysis. *Solid State Ion.* 262, 782–784. doi:10.1016/j.ssi.2013.09.026

Welch, C., Labouriau, A., Hjelm, R., Orler, B., Johnston, C., Kim, Y. S., et al. (2012). Nafion in dilute solvent systems: Dispersion or solution? *ACS Macro Lett.* 1 (12), 1403–1407. doi:10.1021/mz3005204

Wojnarowska, Z., Feng, H., Fu, Y., Cheng, S., Carroll, B., Kumar, R., et al. (2017). Effect of chain rigidity on the decoupling of ion motion from segmental relaxation in polymerized ionic liquids: Ambient and elevated pressure studies. *Macromolecules* 50 (17), 6710–6721. doi:10.1021/acs.macromol.7b01217

Xiao, J., Yan, D., Li, J., Li, Q., and Sun, H. (2018). Hydronium ions diffusion behavior in nafion membrane by mesoscopic simulation. *AIP Adv.* 8 (7), 075303. doi:10.1063/1.5035366

Xiao, W., Yang, Q., and Zhu, S. (2020). Comparing ion transport in ionic liquids and polymerized ionic liquids. *Sci. Rep.* 10, 7825. doi:10.1038/s41598-020-64689-8

Yandrasits, M. A., Lindell, M. J., and Hamrock, S. J. (2019). New directions in perfluoroalkyl sulfonic acid–based proton-exchange membranes. *Curr. Opin. Electrochem.* 18, 90–98. doi:10.1016/j.coelec.2019.10.012

Ye, Y., Choi, J.-H., Winey, K. I., and Elabd, Y. A. (2012). Polymerized ionic liquid block and random copolymers: Effect of weak microphase separation on ion transport. *Macromolecules* 45 (17), 7027–7035. doi:10.1021/ma301036b

Yoshida, K., Manabe, H., Takahashi, Y., and Furukawa, T. (2011). Correlation between ionic and molecular dynamics in the liquid state of polyethylene oxide/lithium perchlorate complexes. *Electrochim. Acta* 57, 139–146. doi:10.1016/j.electacta.2011.06.099

Zelovich, T., Long, Z., Hickner, M., Paddison, S. J., Bae, C., Tuckerman, M. E., et al. (2019a). *Ab initio* molecular dynamics study of hydroxide diffusion mechanisms in nanoconfined structural mimics of anion exchange membranes. *J. Phys. Chem. C* 123 (8), 4638–4653. doi:10.1021/acs.jpcc.8b10298

Zelovich, T., and Tuckerman, M. E. (2022). Controlling hydronium diffusivity in model proton exchange membranes. *J. Phys. Chem. Lett.* 13 (9), 2245–2253. doi:10.1021/acs.jpclett.1c04071

Zelovich, T., and Tuckerman, M. E. (2021). OH(-) and H3O(+) diffusion in model AEMs and PEMs at low hydration: Insights from ab initio molecular dynamics. *Membr. (Basel)* 11, 355. doi:10.3390/membranes11050355

Zelovich, T., and Tuckerman, M. E. (2020). Water layering affects hydroxide diffusion in functionalized nanoconfined environments. *J. Phys. Chem. Lett.* 11 (13), 5087–5091. doi:10.1021/acs.jpclett.0c01141

Zelovich, T., Vogt-Maranto, L., Hickner, M. A., Paddison, S. J., Bae, C., Dekel, D. R., et al. (2019b). Hydroxide ion diffusion in anion-exchange membranes at low hydration: Insights from ab initio molecular dynamics. *Chem. Mat.* 31 (15), 5778–5787. doi:10.1021/acs.chemmater.9b01824

Zelovich, T., Vogt-Maranto, L., Simari, C., Nicotera, I., Hickner, M. A., Paddison, S. J., et al. (2022). Non-monotonic temperature dependence of hydroxide ion diffusion in anion exchange membranes. *Chem. Mat.* 34 (5), 2133–2145. doi:10.1021/acs.chemmater.1c03594

Zelovich, T., Winey, K. I., and Tuckerman, M. E. (2021). Hydronium ion diffusion in model proton exchange membranes at low hydration: Insights from ab initio molecular dynamics. *J. Mat. Chem. A* 9 (4), 2448–2458. doi:10.1039/d0ta10565a

Zhang, W., and Van Duin, A. C. T. (2015). ReaxFF reactive molecular dynamics simulation of functionalized poly(phenylene oxide) anion exchange membrane. *J. Phys. Chem. C* 119 (49), 27727–27736. doi:10.1021/acs.jpcc.5b07271

Zhang, Z., Cui, Y., Vila, R., Li, Y., Zhang, W., Zhou, W., et al. (2021a). Cryogenic electron microscopy for energy materials. *Acc. Chem. Res.* 54 (18), 3505–3517. doi:10.1021/acs.accounts.1c00183

Zhang, Z., Krajniak, J., and Ganesan, V. (2021b). A multiscale simulation study of influence of morphology on ion transport in block copolymeric ionic liquids. *Macromolecules* 54 (11), 4997–5010. doi:10.1021/acs.macromol.1c00025

Zhang, Z., Krajniak, J., Keith, J. R., and Ganesan, V. (2019). Mechanisms of ion transport in block copolymeric polymerized ionic liquids. *ACS Macro Lett.* 8 (9), 1096–1101. doi:10.1021/acsmacrolett.9b00478

Zhang, Z., Nasrabadi, A. T., Aryal, D., and Ganesan, V. (2020a). Mechanisms of ion transport in lithium salt-doped polymeric ionic liquid electrolytes. *Macromolecules* 53 (16), 6995–7008. doi:10.1021/acs.macromol.0c01444

Zhang, Z., Wheatle, B. K., Krajniak, J., Keith, J. R., and Ganesan, V. (2020b). Ion mobilities, transference numbers, and inverse haven ratios of polymeric ionic liquids. *ACS Macro Lett.* 9 (1), 84–89. doi:10.1021/acsmacrolett.9b00908

Zhang, Z., Zofchak, E., Krajniak, J., and Ganesan, V. (2022). Influence of polarizability on the structure, dynamic characteristics, and ion-transport mechanisms in polymeric ionic liquids. *J. Phys. Chem. B* 126 (13), 2583–2592. doi:10.1021/acs.jpcb.1c10662

Zhao, L., Von Hopffgarten, M., Andrada, D. M., and Frenking, G. (2017). Energy decomposition analysis. *WIREs Comput. Mol. Sci.* 8, 3. doi:10.1002/wcms.1345

Zhu, L., Pan, J., Wang, Y., Han, J., Zhuang, L., Hickner, M. A., et al. (2016). Multication side chain anion exchange membranes. *Macromolecules* 49 (3), 815–824. doi:10.1021/acs.macromol.5b02671

Zhu, Z., Luo, X., and Paddison, S. J. (2022). Coarse-grained modeling of ion-containing polymers. *Chem. Rev.* 122 (12), 10710–10745. doi:10.1021/acs.chemrev.1c00913

Zhu, Z., Luo, X., and Paddison, S. J. (2019). DPD simulations of anion exchange membranes functionalized with various cationic groups and associated anions. *Solid State Ion.* 340, 115011. doi:10.1016/j.ssi.2019.115011

Zimudzi, T. J., and Hickner, M. A. (2016). Signal enhanced FTIR analysis of alignment in NAFION thin films at SiO2 and Au interfaces. *ACS Macro Lett.* 5 (1), 83–87. doi:10.1021/acsmacrolett.5b00800

communications chemistry

ARTICLE

https://doi.org/10.1038/s42004-023-00878-6 OPEN

Search for a Grotthuss mechanism through the observation of proton transfer

Ivan Popov[1,2], Zhenghao Zhu[3], Amanda R. Young-Gonzales[2], Robert L. Sacci[1], Eugene Mamontov[4], Catalin Gainaru[1], Stephen J. Paddison[3]✉ & Alexei P. Sokolov[1,2]✉

The transport of protons is critical in a variety of bio- and electro-chemical processes and technologies. The Grotthuss mechanism is considered to be the most efficient proton transport mechanism, generally implying a transfer of protons between 'chains' of host molecules via elementary reactions within the hydrogen bonds. Although Grotthuss proposed this concept more than 200 years ago, only indirect experimental evidence of the mechanism has been observed. Here we report the first experimental observation of proton transfer between the molecules in pure and 85% aqueous phosphoric acid. Employing dielectric spectroscopy, quasielastic neutron, and light scattering, and ab initio molecular dynamic simulations we determined that protons move by surprisingly short jumps of only ~0.5–0.7 Å, much smaller than the typical ion jump length in ionic liquids. Our analysis confirms the existence of correlations in these proton jumps. However, these correlations actually reduce the conductivity, in contrast to a desirable enhancement, as is usually assumed by a Grotthuss mechanism. Furthermore, our analysis suggests that the expected Grotthuss-like enhancement of conductivity cannot be realized in bulk liquids where ionic correlations always decrease conductivity.

[1] Chemical Sciences Division, Oak Ridge National Laboratory, Oak Ridge, TN, USA. [2] Department of Chemistry, University of Tennessee, Knoxville, TN, USA. [3] Department of Chemical & Biomolecular Engineering, University of Tennessee, Knoxville, TN, USA. [4] Neutron Scattering Division, Oak Ridge National Laboratory, Oak Ridge, TN, USA. ✉email: spaddison@utk.edu; sokolov@utk.edu

It is commonly accepted that there are two major mechanisms of proton transport[1–7]: (1) the vehicular mechanism, where a proton moves via a molecular entity (i.e., a vehicle); and (2) the structural diffusion mechanism[8], where protons are transferred between different molecules within a hydrogen bond network. The second mechanism provides more efficient proton transport because it does not require the mobility of entire molecules (vehicles). Furthermore, successive proton transfer enables the possibility of a collective mechanism extending over several molecules, originally proposed by Grotthuss to explain observations in the hydrolysis of water[9,10]. According to several prior studies,[9,11–15] the Grotthuss mechanism is considered to be the most efficient conductivity process because it implies the collective chain-like proton transfer, where the net charge, in principle, can be transported faster than a proton itself. However, the intensive pursuit to experimentally observe this mechanism has led to confusion along with speculation. Many authors assign the observation of a low energy barrier in ionic conductivity as a fingerprint of a Grotthuss-like mechanism[16,17]. However, a low energy barrier is not a sufficient condition, because vehicular transport of charge may also be governed by a low energy barrier for molecular diffusion, e.g., in dilute salt solutions[18]. Although proposed more than 200 years ago, there is still no direct experimental evidence of its existence in bulk systems.

Phosphoric acid (PA) is an excellent and important system for the examination of proton transport in the bulk, due to its highest intrinsic proton conductivity[19–25]. Indeed, nuclear magnetic resonance (NMR) studies of this liquid revealed proton diffusion significantly faster than phosphorus diffusion, clearly indicating the dominance of proton transfer[20]. Structural diffusion is also confirmed by the rather high proton conductivity of PA at temperatures below its glass transition temperature, where molecular (vehicle) motion is frozen while macroscopic proton transport remains active[26], and by the strong isotope effect upon hydrogen/deuterium substitution[27]. Moreover, extensive computational studies suggested the existence of correlated proton transfer between several PA molecules[25,28,29] along short chains of ~2–4 molecules[22]. However, the search for direct experimental evidence of structural diffusion as the principle phenomenon responsible for the high conductivity in PA has not been successful. Neutron scattering provides measurement of proton (or hydrogen) dynamics on molecular/atomistic time and length scales. However, several neutron scattering studies were only able to detect processes with proton displacements significantly larger than expected for proton transfer[23,30]. Moreover, recent NMR studies of ^{1}H, and ^{17}O diffusion[31] lead authors to the conclusion that structural diffusion dominates conductivity only in pure PA, while H_3O^+ diffusion provides a significant contribution to the conductivity in an 85 wt% aqueous PA solution (85 wt% of PA in water that corresponds to 1:1 molar ratio of PA and water; we label this sample as PA85).

To observe and characterize details of proton transport in pure PA and PA85, we performed Broadband Dielectric Spectroscopy (BDS) studies that extend into the sub-THz region, combined with Depolarized Light Scattering and Quasielastic Neutron Scattering (QENS) studies. Furthermore, ab initio molecular dynamics (AIMD) simulations were undertaken to secure insight into the proton transport mechanism. These studies revealed very short proton jump lengths proving the dominating role of the structural diffusion mechanism for the proton transport. Moreover, proton jumps were observed to be correlated. However, these correlations in proton jumps appear to suppress the conductivity, in contrast to the general expectation for a Grotthuss mechanism enhancement in the conductivity.

Results and discussion

Broadband dielectric spectroscopy measurements. The conductivity spectra of PA (Fig. 1a; data for PA85 are presented in Supplementary Fig. S1a in Supplementary Information (SI)) show two important regimes: (i) the frequency dependent alternative current (AC) regime at higher frequencies that crosses over to (ii) the frequency independent direct current (DC) conductivity plateau with the amplitude σ_{DC} at intermediate frequencies. The AC regime corresponds to the sub-diffusive regime, when the protons are trapped, rattling in Coulombic cages formed by the neighboring counter ions. Once a proton escapes from a cage and begins to diffuse, the conductivity becomes frequency independent and shows a plateau in the DC regime. This escape from a Coulombic cage leads to charge rearrangements that appear as a dipole relaxation also in the real part of the dielectric permittivity (Fig. 1b). Thus, the frequency of the DC-AC transition, $\nu_{DC\text{-}AC}$, and its characteristic conductivity relaxation time, $\tau_\sigma = 1/(2\pi\nu_{DC\text{-}AC})$, define the timescale for the transition of charge (i.e., protons) mobility from rattling behavior (in a cage) to a normal diffusion regime[32–38]. The Random Barrier Model (RBM)[32–38] is often used to describe the conductivity spectra. This model suggests that the transport of charge carriers occurs through hops over potential energy barriers. In the specific case, of a constant barrier height distribution, the model leads to[32,36]:

$$\ln\left(\frac{\sigma^*(\omega)}{\sigma_{DC}}\right) = \frac{i\omega\tau_\sigma\sigma_{DC}}{\sigma^*(\omega)}\left(1+\frac{8}{3}\frac{i\omega\tau_\sigma\sigma_{DC}}{\sigma^*(\omega)}\right)^{-1/3}. \quad (1)$$

Here $\sigma^*(\omega)$ is the complex conductivity; σ_{DC} is the DC-conductivity, and τ_σ is the conductivity relaxation time. The RBM also describes the process observed in the permittivity spectra (Fig. 1b). Figure 2 presents the temperature dependence of the DC-conductivity, while Fig. 3 presents the temperature dependence of the conductivity relaxation time estimated from the BDS spectra for pure PA and PA85.

Light Scattering Measurements. One may wonder whether the relaxation process identified in Fig. 1 may also reflect dipolar

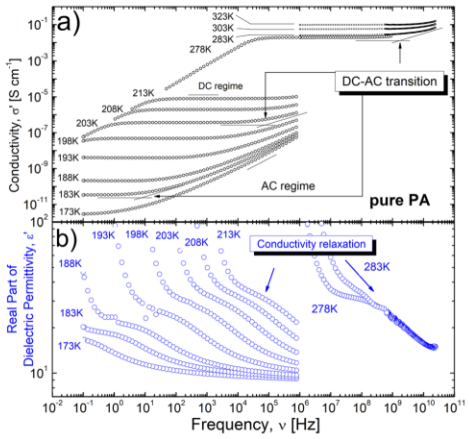

Fig. 1 Conductivity and storage permittivity spectra for PA. Conductivity **a** and storage permittivity **b** spectra for PA. Examples of DC-AC transitions **a**, and corresponding conductivity relaxations **b** at different temperatures are marked with arrows. The decrease in conductivity and the increase in storage permittivity at low frequencies are related to electrode polarization.

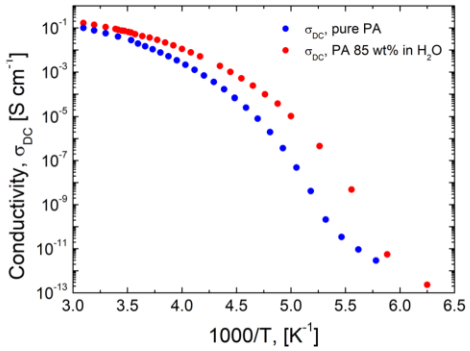

Fig. 2 Temperature dependence of the DC-conductivity. Temperature dependence of the DC conductivity, σ_{DC}, for pure PA (blue symbols) and PA85 (red symbols).

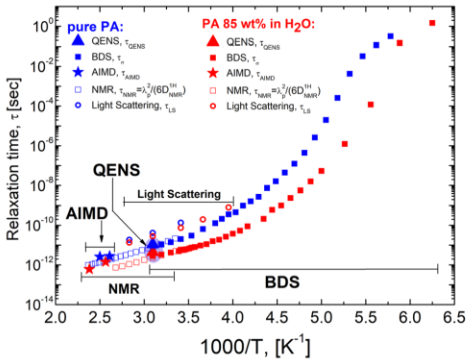

Fig. 3 Temperature dependence of the relaxation time. Temperature dependence of the relaxation time obtained with different methods for pure PA (blue symbols) and PA85 (red symbols): Conductivity relaxation time (closed squares); Structural relaxation time from Light Scattering (open circles); Characteristic relaxation time of proton jumps from QENS (triangles) and from AIMD simulations (stars). Characteristic NMR relaxation time for protons (open squares) are estimated from NMR diffusion data, $\tau_{NMR} = \langle\lambda_p\rangle^2/(6D^{1H}_{NMR})$, assuming a temperature independent $\langle\lambda_p\rangle$.

relaxation due to the rotation of the PA and water molecules (e.g., as a dielectric α-process). In this regard, several experimental observations must be considered: (i) In the highly viscous regime, this conductivity relaxation process is significantly faster than the structural relaxation of the matrix measured by rheology[26,39]; (ii) Despite the strong variation in water content, neat phosphoric acid (Fig. 1b) and its monohydrates (Supplementary Fig. S1b) display similar dielectric relaxation strength; (iii) The dielectric strength of the observed dielectric process decreases upon cooling (Fig. 1b and Supplementary Fig. S1b), this behavior is usual for conductivity relaxation[40–42] and is opposite to the Curie law (increase in the dielectric strength with cooling) for a dipolar relaxation process[43–46]. All these results suggest that the observed dielectric relaxation process is dominated by conductivity relaxation and is not related to molecular relaxation.

Nevertheless, to estimate the structural relaxation time in these systems, we performed Depolarized Light Scattering (LS) measurements which are not sensitive to the conductivity. The LS susceptibility spectra revealed a relaxation peak (Fig. 4a, b), and the characteristic structural relaxation time can be estimated from the frequency of its maximum, $\tau_{LS} = 1/2\pi f_{max}$. This estimated structural relaxation time is about one order slower than the conductivity relaxation time (Fig. 3). These results provide clear evidence that the conductivity process in PA and PA85 is significantly faster than the structural relaxation even at high temperatures, and is consistent with the well-known fact that phosphorus in PA moves much slower than protons[20,21].

Using a proton diffusion coefficient probed by NMR[20,21] we calculate the characteristic rearrangement length when 'normal' diffusion begins with:

$$\langle\lambda_p\rangle = \sqrt{6D^{1H}_{NMR}\tau_\sigma}. \quad (2)$$

The estimates show surprisingly small values $\langle\lambda_p\rangle = 0.7 \pm 0.2$ Å for pure PA and $\langle\lambda_p\rangle = 0.5 \pm 0.2$ Å for PA85. This is ~5–6 times smaller than observed in ionic liquids, where $\langle\lambda_{ion}\rangle \approx 2.5 - 3.5$Å is comparable to the distance between the ions in these systems[37]. However, the estimated $\langle\lambda_p\rangle$ agrees well with the equilibrium distance ~0.63 Å computed in simulations for proton transfer between PA molecules[25]. These results suggest that PA conductivity is indeed dominated by direct proton transfer between the molecules.

Furthermore, assuming that the rearrangement length is temperature independent, we can use Eq. (2) to determine the conductivity relaxation time of a proton jump at higher temperature based on diffusivity, where the AC-DC crossover in the conductivity spectra is beyond the frequency window. The temperature dependences of $\tau_{NMR} = \langle\lambda_p\rangle^2/(6D^{1H}_{NMR})$ and of $\tau_\sigma(T)$ agree well for both pure PA and PA85 (Fig. 3).

Quasielastic neutron scattering measurements. We emphasize, however, that the BDS method does not provide a direct estimate of the proton rearrangement length, only its characteristic rate, and the values of $\langle\lambda_p\rangle$ are therefore model dependent. In contrast, QENS can provide estimates of the characteristic rearrangement time and length, although the latter is model dependent. Neutrons scatter primarily on hydrogen atoms, and the contribution from oxygen and phosphorus atoms to the neutron scattering spectra of the systems in this study is below 8%. Moreover, oxygen and phosphorus scattering is mostly coherent, and their contribution to incoherent neutron scattering is negligibly small (below 0.1%). Thus, the studied QENS spectra are dominated by motions of protons (hydrogens). The QENS spectra revealed clear broadening that is Q dependent (see Fig. 5a, c), reflecting strong dynamics in the accessible energy range. To analyze the QENS spectra, we convert them to a susceptibility presentation (Fig. 5b, d). The susceptibility spectra reveal a strongly Q-dependent relaxation peak for both PA (Fig. 5b) and PA85 (Fig. 5d). This peak is well described using a Cole-Davidson distribution function with the stretching exponent $\beta \approx 0.68$ (for details of the fit procedure see Supplementary Methods in SI). The fit of the spectra (lines in Fig. 5) provides estimates of $E^X_{max}(Q)$, which corresponds to the position of the maximum of the relaxation peak in susceptibility format and is close to the Half-Width at the Half-Maximum (HWHM) of the QENS spectra but takes into account the distribution of relaxation processes as well. Analysis also revealed that the remaining elastic component is very small (below 6% for pure PA and below 3% for PA85, see Supplementary Fig. S2a), indicating that all protons in the system, including water protons in PA85, are mobile on the measured time scale. The small remaining elastic component might be

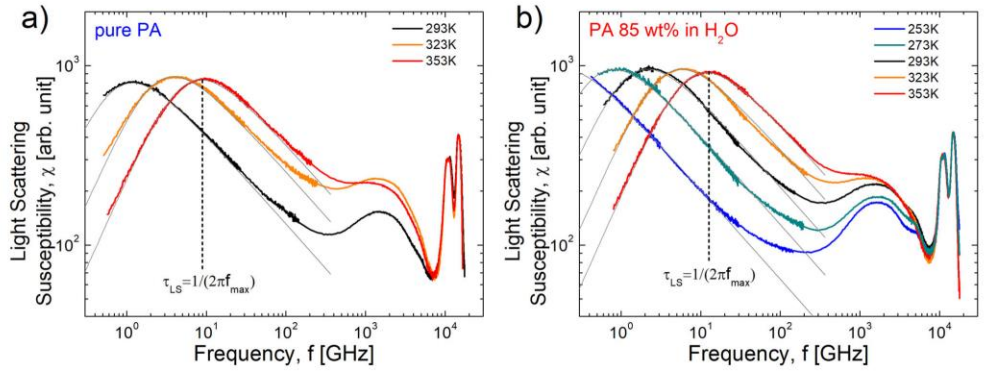

Fig. 4 Light scattering susceptibility spectra. Light scattering susceptibility spectra for **a** pure PA and **b** PA85. High frequency Raman modes were used to normalize the spectra at different temperatures. Gray line is the Cole-Davidson fit function[70]. The relaxation time was estimated from the maximum relaxation peak, $\tau_{LS} = 1/2\pi f_{max}$.

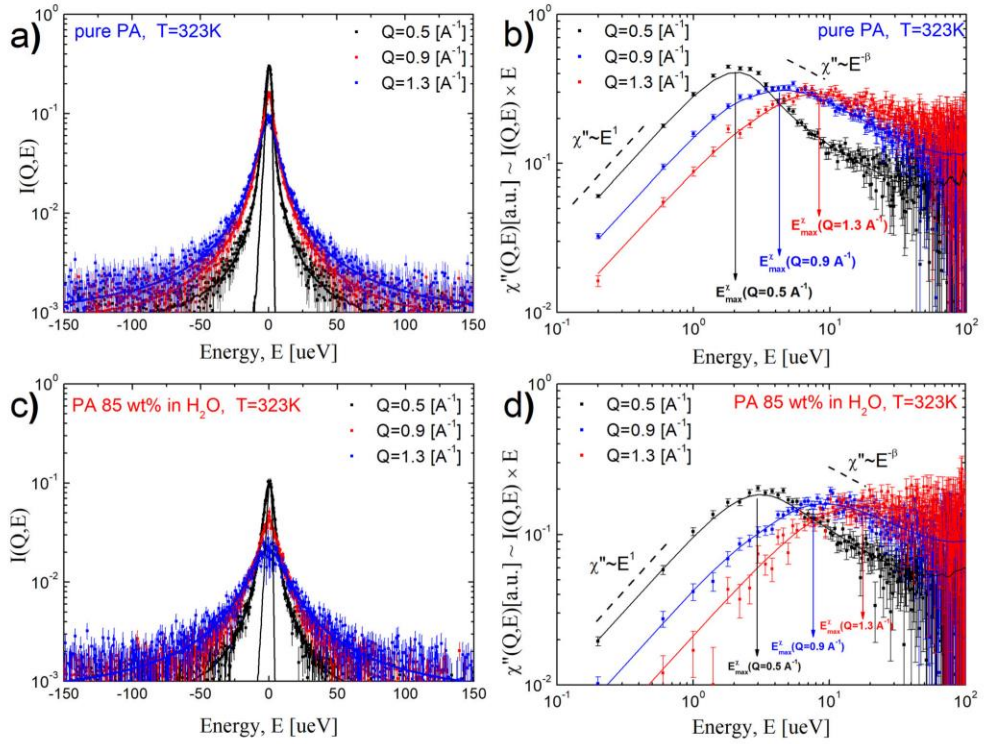

Fig. 5 QENS spectra in intensity and susceptibility format. Intensity and corresponding susceptibility presentation of the QENS data, respectively, for pure PA **a**, **b** PA 85 **c**, **d**. Lines present fit to the Cole-Davidson function. For a complete description of the fitting procedure see the SI. The arrows in **b**, **d** show the energies corresponding to the maximum of the relaxation peak in the susceptibility spectra, $E^{\chi}_{max}(Q)$. This value in the case of the Cole-Davidson function is close to HWHM, but takes into account the distribution of the relaxation processes. In plots **a** and **c** the resolution functions (measured at 20 K) are shown to demonstrate the broadening of the scattering peak. Error bars are standard deviation.

related to a scattering from oxygen and phosphorus that are slower than protons.

$E^{\chi}_{max}(Q)$ increases linearly with Q^2 at lower Q (Fig. 6), reflecting proton diffusion at long distances, and starts leveling off at higher Q corresponding to a finite jump length. This behavior can be well described by the Singwi-Sjolander jump-diffusion model (Fig. 6)[47]:

$$E^{\chi}_{max}(Q) = \frac{\hbar D_{QENS} Q^2}{(1 + D_{QENS}\tau_{QENS}Q^2)}, \lambda_p = \sqrt{6 D_{QENS}\tau_{QENS}} \quad (3)$$

Here ħ is the Planck constant divided by 2π, and τ_{QENS} and D_{QENS} are the characteristic relaxation time and diffusion coefficient of protons. The fit of $E^{\chi}_{max}(Q)$ to the jump-diffusion model (Fig. 6) results in a diffusion coefficient in good agreement with the NMR data (see Supplementary Fig. S3), confirming that QENS measures proton diffusion at lower Q. The most impressive aspect of this is that the estimated relaxation time, τ_{QENS}, is similar to the value of τ_σ estimated from the BDS spectra and is much faster than the structural relaxation estimated from the LS spectra in these systems (Fig. 3). The agreement of τ_{QENS} and τ_σ reveals that proton dynamics probed by QENS governs the conductivity of both PA and PA85. QENS also provides model dependent estimates of the jump length (Eq. 3), with $\langle\lambda_p\rangle = 0.7 \pm 0.2$ Å for pure PA and $\langle\lambda_p\rangle = 0.6 \pm 0.2$ Å for PA85, in excellent agreement with the estimates from combined BDS and NMR data.

Our results also explain why earlier neutron scattering studies of PA[23,30] could not detect the proton transfer process. In these previous studies, QENS spectra were measured in a much narrower energy transfer range (±15 or ±25 μeV) and analyzed using a single Lorentzian peak plus background, while HWHM obviously exceeds 20 - 40 μeV at higher Q (Fig. 5). As a result, the major part of the faster proton transfer events was missed. Our data clearly show that the proton transfer process is stretched (see Supplementary Methods in SI) and occurs with a characteristic energy $E \sim \hbar/\tau_{QENS} \sim 130$ μeV.

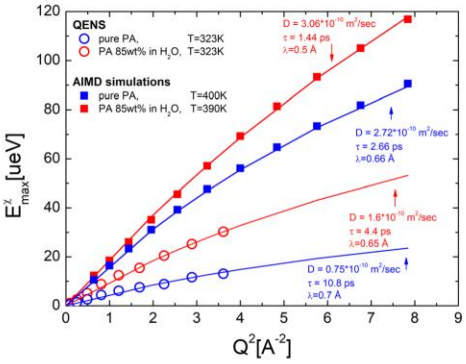

Fig. 6 Wave vector dependence of the HWHM. Wave vector dependence of the $E^{\chi}_{max}(Q)$ for PA (blue symbols) and PA85 (red symbols) estimated from the maximum of relaxation process in the QENS susceptibility spectra at $T = 323$ K (open circles) and from the AIMD simulations at higher T (closed squares). The lines show the fit of the AIMD and QENS results to the jump diffusion model (see Eq. (3)).

Ab Initio Molecular Dynamics Simulations. To unravel the molecular picture of the proton transport in PA we performed AIMD simulations (see Supplementary Methods in SI for a complete description). They allow one to calculate the Self-intermediate Scattering Function of the protons, *ISF*(*Q*,*t*), which provides similar information to that obtained from QENS data, but can access a much higher Q range. The *ISF(Q,t)* shows three processes (Fig. 7b, Supplementary Figs. S4a, S5, and Supplementary Tables S1-S6). The fastest process with Q-independent characteristic time occurs at a few femtoseconds. Examination of the vibrational density of state for protons in pure PA indicates that this process is due to the covalent vibration of the hydrogen atoms (Supplementary Fig. S4b). The intermediate process has a weak Q-independent time constant ~0.1−0.3 ps, suggesting a local process. Similar processes with characteristic times of ~0.1−0.3 ps were reported in simulations of water and imidazole and assigned to proton rattling between two oxygen/nitrogen atoms[48,49]. Following this idea, we also ascribe this process to the rattling of protons between oxygen atoms in PA and PA85. Furthermore, the proton transfer population correlation function

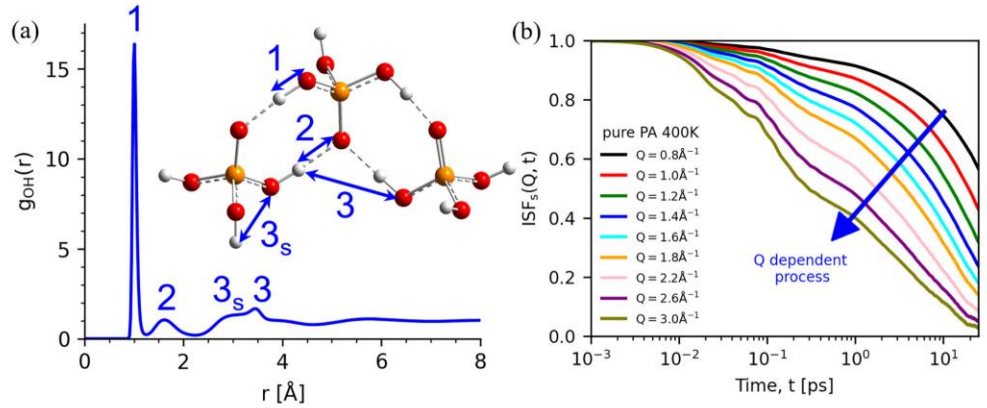

Fig. 7 The radial distribution function and self-intermediate scattering function. a The radial distribution function (g_{OH}) of oxygen-hydrogen in PA obtained from AIMD. The shoulder on the left side of the 3rd peak marked 3 s corresponds to the distance between the proton and the oxygen atoms in the same PA molecule. **b** Self-intermediate scattering function *ISF(Q, t)* of protons with different Q values at 400 K for pure PA.

(PCF) validates that the proton rattling process takes place at the sub-picosecond time scale (Supplementary Fig. S6a). The slow process, however, exhibits strong Q dependent relaxation time, τ_3, indicating its diffusive nature. It can be well described by a stretched exponential decay, $\propto exp[-(t/\tau_3)^{\beta}]$, with the stretching parameter $\beta \sim 0.7 \pm 0.2$. The latter agrees with the stretching determined from the QENS spectra. Moreover, the HWHM calculated from the obtained $\tau_3(Q)$, $E^{N}_{max}(Q) = \hbar\beta/[\tau_3\Gamma(1/\beta)]$, exhibits the same Q dependence as the process observed in QENS (Fig. 6). The fit of the AIMD simulation results (Fig. 6) provides estimates of the parameter $\langle\lambda_p\rangle = 0.7 \pm 0.2$ Å for pure PA and $\langle\lambda_p\rangle = 0.5 \pm 0.1$ Å for PA85, in excellent agreement with the QENS data analysis. The same fit provides the value of relaxation time and is plotted in the Fig. 3 in good agreement with our experimental results.

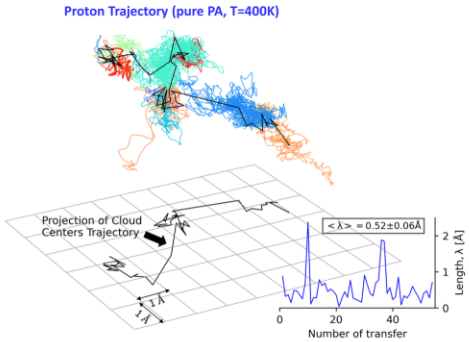

Fig. 8 Trajectory of an individual proton in pure PA. Trajectory lines of an individual proton in pure PA at 400 K. Each colored cloud reflects the proton vibrational and rotational motions as the proton is associated with the same oxygen atom. The trajectory changes color when the proton transfers to a different oxygen atom. The center of mass of each cloud is connected by a black line to the center of mass of the next cloud. These black lines present averaged jumps of the proton transfers between the oxygen atoms. (Inset) The length of each proton jump between oxygen atoms (the length of the black lines). The average jump length is very short ~ 0.5 Å, although there are a few larger (~2 Å) jumps that are associated with the large-angle jumps followed by a proton transfer.

Having established a clear relationship of the diffusive process in the simulations to the proton jumps observed in the QENS, we can now follow the trajectory of an individual proton during its diffusion over 40 ps (Fig. 8). Trajectories show the vibrational and rotational motion of the proton within the same color cloud and proton jumps are defined as the proton transfers from one oxygen atom to another oxygen atom (black lines). Analysis of these proton jumps reveals that they are very short ~ 0.5 Å with only a few (~2–3 out of 50) large scale jumps ~ 2 Å. This is smaller than that suggested much earlier jumps (~2.8 Å)[20]. Specifically, the short proton jumps are the proton transfers between the same pair of oxygen atoms although there are some trials of rotating motions. However, the long jumps are associated with a rotation of the OH bond followed by an effective proton transfer, which is a much rarer event than individual proton jumps. Examination of the other protons in the PA system shows a similar distribution and average jump length.

The AIMD simulations reveal that proton hopping plays a key role in the long-range proton diffusion through the breaking and forming of hydrogen bonds (Fig. 9). The structural characteristics of a proton with neighboring oxygen atoms show that the covalent OH bond and the hydrogen bond are the first peak at $r_{OH} = 1.01$ Å and the second peak at $r_{OH} = 1.61$ Å, respectively, in the radial distribution function g_{OH} (Fig. 7a). The proton (in green) first forms a strong hydrogen bond with a neighboring oxygen, which induces the proton associated with the neighboring oxygen to transfer to the solvent (neutral) PA molecule (Fig. 9a). Following the completion of the proton transfer from the neighboring oxygen to the solvent PA molecule, the proton transfers to the neighboring oxygen through a strong hydrogen bond (Fig. 9b). These successive proton hopping events take place at the sub-picosecond time scale, followed by a long quiescent period, in which the proton is trapped in a cage formed by adjacent oxygen atoms via strong hydrogen bonds. This quiescent period corresponds to the hydrogen bond reorganization relaxation time (a couple of picoseconds), which is also revealed

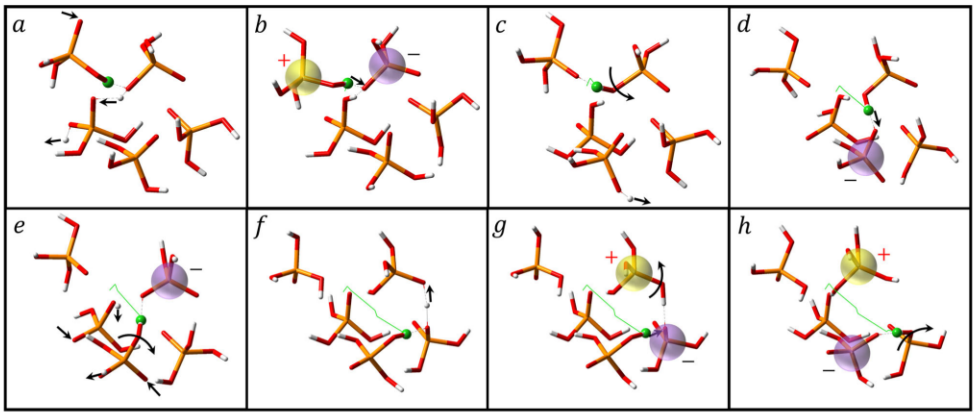

Fig. 9 Snapshots of proton transport. The length of each proton jump between oxygen atoms for a specific proton. The average jump length is very short ~0.5 Å. **a**–**h** Snapshots of the elementary steps of the mechanism for long-range proton diffusion in pure PA. The charged entities are highlighted. The collaboration of proton transfers **a**, **b**, **d**, **f**, **g** and large angular jumps **c**, **e**, **h** facilitates the long-range diffusion of protons. See the text for a detailed description.

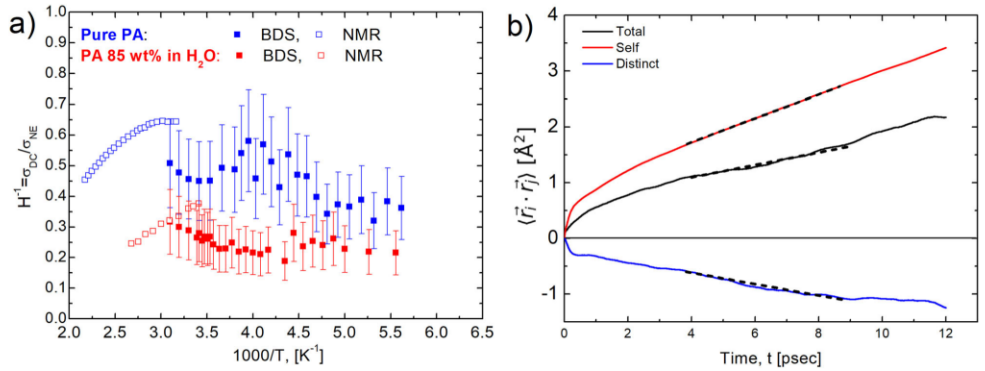

Fig. 10 Inverse Haven ratio and correlation functions of proton displacement vectors. a Temperature dependence of the inverse Haven ratio for PA (blue symbols) and PA85 (red symbols) estimated using diffusion coefficients obtained from NMR[20,21] (open squares) and BDS (closed squares). Error bars are standard deviation. **b** Correlation functions of proton displacement vectors for pure PA at 400 K and the linear fit to obtain self-, distinct, and total diffusion coefficients using Eq. (6).

by the proton transfer PCFs (Supplementary Fig. S6a). The large-angle proton jump due to the reorientation of the covalent OH bond causes the breaking of the original hydrogen bond and the forming of the nascent hydrogen bond with a new PA molecule (Fig. 9c, d), which facilitates protons escaping the local "trap" formed by the strong hydrogen bonds. Subsequently, proton transfer occurs via the new hydrogen bond followed by another large-angle reorientation of the covalent OH bond (Fig. 9e, f). The proton transfer through this newly formed hydrogen bond induces the cleavage of the other hydrogen bond between the next acceptor oxygen and the surrounding solvent PA molecules by a large reorientation of a covalent OH bond (Fig. 9g, h). This molecular mechanism indicates that the reorientation of an OH bond by large angular jumps is involved in the long-range diffusion of the protons.

Proton correlations. Once the molecular-level picture of the proton jumps and its averaged length are established, we can finally analyze the proton dynamics correlations and the existence of a Grotthuss-like mechanism in the conductivity. Historically, ion correlations in dilute solutions were described by Debye-Huckel-Onsager theory[50]. However, this approach is valid only for dilute solutions[50]. Traditionally, correlations in concentrated ionic systems are analyzed from comparison of the experimentally measured conductivity, σ_{DC}, to that expected for uncorrelated ion diffusion, i.e., conductivity estimated using the Nernst-Einstein (NE) equation, σ_{NE}[51,52]:

$$H^{-1} = \frac{\sigma_{DC}}{\sigma_{NE}},\ \text{where}\ \sigma_{NE} = \frac{nq^2D}{k_BT}. \tag{4}$$

Here n, q, and D are the concentration, charge, and diffusion coefficient of the mobile ions, respectively. The parameter H^{-1} is the inverse Haven ratio, often called 'ionicity', characterizes the ion transport correlations[53,54], and can be used as an indicator of the presence of a Grotthuss-like mechanism. Indeed, measured DC conductivity by definition depends on velocity-velocity correlations of all the ions[51,55,56]

$$\sigma_{DC} = \frac{1}{3Vk_BT}\int_0^\infty \left\langle \vec{\mathbf{J}}(0)\cdot\vec{\mathbf{J}}(t)\right\rangle \mathrm{d}t,\ \text{where}$$
$$\left\langle \vec{\mathbf{J}}(0)\cdot\vec{\mathbf{J}}(t)\right\rangle = \left\langle \textstyle\sum_i q_i\vec{\mathbf{v}}_i(0)\cdot\sum_j q_j\vec{\mathbf{v}}_j(t)\right\rangle. \tag{5}$$

Thus, DC conductivity can be presented as $\sigma_{DC} = \sigma_{NE} + \sigma_{++} + \sigma_{+-} + \sigma_{--}$, where the last three terms show contributions of distinct ion-ion correlations[57–59]. As a result, the inverse Haven ratio can be expressed as $H^{-1} = 1 + \sigma_{++}/\sigma_{NE} + \sigma_{+-}/\sigma_{NE} + \sigma_{--}/\sigma_{NE}$. The original idea of the Grotthuss-like mechanism implies that protons move in the same direction (chain-like)[12], enhancing conductivity and leading to $\sigma_{++} > 0$. Furthermore, in PA and PA85 we can neglect the contribution of σ_{+-} and σ_{--} in comparison to σ_{++} because of slow anion diffusion in comparison to proton diffusion. Thus, if Grotthuss-like mechanism takes place in PA or PA85, the inverse Haven ratio has to be larger than one, $H^{-1} > 1$[12,19,60]. The low value of the elastic component in QENS spectra (within the error bars) indicates that all protons are mobile and participate in conductivity, even the water protons in PA85 (Supplementary Fig. S2a). The DC conductivity σ_{DC} is directly extracted from the dielectric spectra and it is plotted in Fig. 2 as a function of temperature. To estimate σ_{NE}, we used proton diffusivities from NMR at higher temperatures[20,21], and estimations based on the relaxation time from BDS data at lower temperatures, assuming temperature independent $\langle\lambda_p\rangle$, $D = \langle\lambda_p\rangle^2/(6\tau_\sigma)$. Analysis reveals that $H^{-1} < 1$ in the entire temperature range (Fig. 10a). The obtained estimates of the inverse Haven ratio agrees with many earlier studies[19,20], and indicates that proton transfer between PA molecules is indeed correlated. However, in contrast to the expected enhancement in the conductivity due to a Grotthuss-like mechanism, the correlated proton transfer in PA leads to a decrease in conductivity (Fig. 10a).

To confirm this result, we also analyzed distinct proton-proton displacement vector correlations from the AIMD simulation trajectories. The self- and distinct- diffusivities of the protons may be obtained using the Einstein relation:

$$D_{ij} = \frac{1}{6}\lim_{t\to\infty}\frac{\mathrm{d}}{\mathrm{d}t}\left\langle \sum_{i=1}^{N}\sum_{j=1}^{N}[\vec{\mathbf{r}}_i(t) - \vec{\mathbf{r}}_i(0)]\cdot[\vec{\mathbf{r}}_j(t) - \vec{\mathbf{r}}_j(0)]\right\rangle, \tag{6}$$

where $\vec{\mathbf{r}}_i$ and $\vec{\mathbf{r}}_j$ are the coordinates of protons i and j, respectively. Equation (6) can be decomposed into the self- (D_{ii}^{self} for $i=j$) and distinct- ($D_{ii}^{\mathrm{distinct}}$ for $i\neq j$) diffusivity contributions. Assuming that the proton conductivity is the dominant contribution to the conductivity of the system, the inverse Haven ratio can be computed via $H^{-1}=(D_{ii}^{\mathrm{self}}+D_{ii}^{\mathrm{distinct}})/D_{ii}^{\mathrm{self}}$. These diffusivities were calculated from the linear fitting to the proton displacement vector correlations ($\langle\vec{\mathbf{r}}_i\cdot\vec{\mathbf{r}}_j\rangle$). Indeed, the distinct proton correlation is negative, $D_{ii}^{\mathrm{distinct}}=-1.53\times10^{-6}\mathrm{cm^2s^{-1}}$, leading to a negative contribution to the conductivity (Fig. 10b). Given that the negative distinct correlation of a proton may arise through the rotation of PA molecules, we calculated the distinct correlation function of the proton displacement vectors from the same PA molecule and the results show that the distinct diffusivity of protons from the same PA molecule are very small with a positive value (Supplementary Fig. S7). Notably, the self-diffusion coefficient of the protons is in good agreement with that obtained from the intermediate scattering function ($D_{ii}^{\mathrm{self}}=3.59\times10^{-6}\mathrm{cm^2s^{-1}}$). The anticorrelation between protons definitely gives rise to the suppression of the conductivity in pure PA at 400 K ($H^{-1}=0.58$). This combination of experimental and simulations results suggests that correlated proton transfer events in PA and PA85 form a kind of backflow with total charge displacement lower than in the case of uncorrelated proton transfer. The case where $H^{-1}<1$ is typically observed in ionic liquids[61,62] and is explained by momentum conservation between the moving ions. Thus, we suggest that a Grotthuss chain-like proton conductivity is impossible in a bulk liquid state. It usually leads to a suppression of conductivity by anion-anion and cation-cation correlations[57,58].

Conclusion

In summary, our results demonstrate that the proton jump length is much shorter than the distance between the hydrogen atoms in the system and is comparable to the distance of proton transfer between oxygen atoms forming a hydrogen bond either between two PA molecules, or PA and water molecules in the case of PA85. The strong similarity in the results for PA and PA 85 suggests that proton transfer is also the dominating conductivity mechanism in PA85. It is known that adding water to PA reduces viscosity and increases conductivity[26]. This indicates that water molecules assist in faster proton diffusion with respect to neat PA. However, also for PA85 this diffusion involves short proton jumps between molecules rather than vehicular diffusion (i.e., as H_3O+). To the best of our knowledge, the presented combination of several techniques provides the first experimental observation of proton jumps between molecules as the dominant proton diffusion mechanism in a bulk system.

Methods

Materials. Phosphoric acid (PA) (crystalline, ≥99.99% trace metal basis) was purchased from Sigma-Aldrich and 85 wt% phosphoric acid aqueous solution (i.e., 85% of the weight of PA in water) was purchased from Alfa Aesar. Both were used as purchased. The sample PA 85 wt% in H_2O was chosen for more detailed measurements due to its stability at ambient temperature and lower sensitivity to moisture. For BDS, QENS, and Light Scattering measurements pure PA samples were loaded into the cell in a glovebox under dry argon atmosphere. Pure PA, below crystallization temperature was measured only in a liquid supercooled state.

Broadband Dielectric Spectroscopy (BDS) measurements. Spectra of complex conductivity measurements were probed using three setups to cover the wide frequency range from 0.1 Hz up to 30 GHz. An Alpha-A analyzer from Novocontrol was utilized in the frequency range of 0.1 Hz to 10^6 Hz. An Agilent RF Impedance Material Analyzer, E4991A was used in the frequency range 10^6 Hz to 3×10^9 Hz. The Panoramic Network Analyzer, Agilent Technologies, E8364C with 85070E Dielectric Probe Kit were utilized for frequency measurements from 5×10^8 Hz up to 3×10^{10} Hz. The Slim Probe with the Agilent Electronic Calibration module (ECal) were used for measurements of real and imaginary part of dielectric permittivity. A Quattro temperature controller (Novocontrol) was used for temperature stabilization for the measurements from 10^{-1} Hz to 10^9 Hz. The samples were stabilized for 20 min at each temperature to reach precision ±0.2 K. The Presto, Julabo, W80 was used for temperature stabilization for the measurements from 5×10^8 Hz up to 3×10^{10} Hz. The samples were stabilized for 40 min at each temperature to reach precision ±0.2 K. Additional details of calibration and designs of the cells are presented in Supplementary Methods in SI.

Quasielastic neutron scattering (QENS) measurements. at the BASIS spectrometer (Spallation Neutron Source, ORNL)[63] were performed in the extended energy transfer mode to cover the energy transfer window of −200 μeV to +200 μeV at 323 K for pure PA and PA 85 wt% aqueous solution. This was achieved with the spectrometer's bandwidth choppers operated at 30 Hz and the incident neutron bandwidth centered at 6.15 Å. The energy resolution was ca. 3.7 μeV (Q-averaged full width at half maximum). The samples were placed in flat-plate gold-coated aluminum sample holders with sample space thickness of 0.25 mm to reduce multiple scattering. Samples were loaded in glovebox and sealed with indium. The sample holder was placed at 90° with respect to the incident beam. A closed-cycle refrigerator was used for temperature control within 0.5 K offset. The sample-specific resolution spectra were collected at a baseline temperature of 20 K. The QENS data were reduced and analyzed using Mantid[64] and DAVE[65] software, respectively. Additional details of data treatment are presented in Supplementary Methods in SI.

Light scattering (LS). was measured using Raman spectrometer and Tandem Fabry-Perot (TFP - 1) interferometer (JRS Scientific Instruments, Table Stable Ltd). The experiments were performed in backscattering geometry using laser wavelength 532 nm. To obtain wide frequency range, three mirror spacing were used in TFP interferometer: 0.4 mm, 3 mm, and 15 mm. Narrow interference filter was used to suppress higher order transmissions. Optical signal from the same spot in the sample was transferred by additional mirrors to the T64000 Raman spectrometer from Horiba Jobin Yvon. Raman spectra were measured in subtractive mode, and the optical Raman modes were used to normalize the spectra at different temperatures. A glovebox was used to load the samples in a glass vial and seal. The samples were measured in cryostat. After temperature stabilization for one hour, the light scattering spectra were collected. To remove the contribution of longitudinal modes from the light scattering spectra, the samples were measured in HV and HH polarizations at the same mirror spacing.

Ab initio molecular dynamics (AIMD) simulations. AIMD simulations of pure PA and 85 wt% aqueous PA were performed using the CPMD code[66]. The pure PA system was made up of 54 PA molecules in a cubic simulation box of side $L=16.696$ Å ($\rho=1.885\ \mathrm{g\,cm^{-3}}$), and the PA85 system consisted of 38 PA molecules and 38 H_2O molecules in a cubic simulation box of side $L=16.317$ Å ($\rho=1.685\ \mathrm{g\,cm^{-3}}$). The dispersion-corrected atomic core pseudopotentials (DCACP)[67,68] were employed to account for dispersion forces within the Kohn-Sham formulation of density functional theory and the B-LYP exchange-correlation functional[69]. A plane-wave basis set was used to expand the Kohn-Sham orbitals up to a kinetic energy cutoff of 80 Ry. In order to increase the adiabatic decoupling of nuclear and electronic dynamics, and allow a larger time step 4 au, the mass of deuterium was assigned to the hydrogen atoms and the fictitious electron mass was set to $\mu=500$ au. Each system was pre-equilibrated using a classical force field for 10 ns, followed by 15–20 ps equilibration with AIMD at the desired temperatures using a massive Nose-Hoover chain thermostat. Note that the temperature of the simulated system was increased to enhance proton dynamics without changing the physical mechanism and to avoid the formation of a glassy state because the expansive AIMD simulations limit the temporal and spatial scales. Subsequently, the equilibrated configuration was used for the ~60 ps production run in a microcanonical (NVE) ensemble.

Data availability

The data that support the plots within this paper and another finding of this study are available from the corresponding author upon reasonable request.

Code availability

The computer code used for simulations is available from the corresponding authors upon reasonable request.

Received: 3 March 2023; Accepted: 4 April 2023;
Published online: 22 April 2023

References

1. Tuckerman, M. E., Marx, D. & Parrinello, M. The nature and transport mechanism of hydrated hydroxide ions in aqueous solution. *Nature* **417**, 925–929 (2002).

2. Marx, D., Tuckerman, M. E., Hutter, J. & Parrinello, M. The nature of the hydrated excess proton in water. *Nature* **397**, 601–604 (1999).
3. Tuckerman, M., Laasonen, K., Sprik, M. & Parrinello, M. Ab initio molecular dynamics simulation of the solvation and transport of H3O+ and OH- ions in water. *J. Phys. Chem.* **99**, 5749–5752 (1995).
4. Agmon, N. The Grotthuss mechanism. *Chem. Phys. Lett.* **244**, 456–462 (1995).
5. Kreuer, K.-D., Rabenau, A. & Weppner, W. Vehicle mechanism, a new model for the interpretation of the conductivity of fast proton conductors. *Angew. Chem. Int. Ed. Engl.* **21**, 208–209 (1982).
6. Greenwood, N. N. & Thompson, A. Proton-switch as a mechanism for conduction in anhydrous phosphoric acid. *P. Chem. Soc. London*, 352–353, (1958).
7. Swanson, J. M. J. et al. Proton solvation and transport in aqueous and biomolecular systems: insights from computer simulations. *J. Phys. Chem. B* **111**, 4300–4314 (2007).
8. Eigen, M. & DeMaeyer, L. Self-dissociation and protonic charge transport in water and ice. *Proc. R. Soc. Lond., Ser. A* **247**, 505–533 (1958).
9. Cukierman, S. Et tu, Grotthuss! and other unfinished stories. *Biochim. Biophys. Acta (BBA) - Bioenerg.* **1757**, 876–885 (2006).
10. von Grotthuss, C. J. T. Sur la Décomposition de L'eau et des Corps Qu'elle Tient en Dissolution à L'aide de L'électricité Galvanique. *Ann. Chim.* **58**, 54–73 (1806).
11. Dellago, C., Naor, M. M. & Hummer, G. Proton transport through water-filled carbon nanotubes. *Phys. Rev. Lett.* **90**, 105902 (2003).
12. Wojnarowska, Z. & Paluch, M. Recent progress on dielectric properties of protic ionic liquids. *J. Phys.: Condens. Matter* **27**, 073202 (2015).
13. Cao, Z. et al. Mechanism of fast proton transport along one-dimensional water chains confined in carbon nanotubes. *J. Am. Chem. Soc.* **132**, 11395–11397 (2010).
14. Dellago, C. & Hummer, G. Kinetics and mechanism of proton transport across membrane nanopores. *Phys. Rev. Lett.* **97**, 245901 (2006).
15. Tunuguntla, R. H., Allen, F. I., Kim, K., Belliveau, A. & Noy, A. Ultrafast proton transport in sub-1-nm diameter carbon nanotube porins. *Nat. Nanotechnol.* **11**, 639–644 (2016).
16. Wu, X. et al. Diffusion-free Grotthuss topochemistry for high-rate and long-life proton batteries. *Nat. Energy* **4**, 123–130 (2019).
17. Yang, Y. et al. Grotthuss proton conductive covalent organic frameworks for efficient proton pseudocapacitors. *Angew. Chem.* **60**, 1–7 (2021).
18. Borodin, O. et al. Liquid structure with nano-heterogeneity promotes cationic transport in concentrated electrolytes. *ACS Nano* **11**, 10462–10471 (2017).
19. Schuster, M., Kreuer, K.-D., Steininger, H. & Maier, J. Proton conductivity and diffusion study of molten phosphonic acid H3PO3. *Solid State Ion.* **179**, 523–528 (2008).
20. Dippel, T., Kreuer, K. D., Lassègues, J. C. & Rodriguez, D. Proton conductivity in fused phosphoric acid; A 1H/31P PFG-NMR and QNS study. *Solid State Ion.* **61**, 41–46 (1993).
21. Aihara, Y., Sonai, A., Hattori, M. & Hayamizu, K. Ion conduction mechanisms and thermal properties of hydrated and anhydrous phosphoric acids studied with 1H, 2H, and 31P NMR. *J. Phys. Chem. B* **110**, 24999–25006 (2006).
22. Greenwood, N. N. & Thompson, A. The mechanism of electrical conduction in fused phosphoric and trideuterophosphoric acids. *J. Chem. Soc.*, 3485–3492 (1959).
23. Frick, B., Vilčiauskas, L., Deen, P. P. & Lyonnard, S. The nanosecond proton dynamics of phosphoric acid – from the solid to the melt – investigated by neutron backscattering. *Solid State Ion.* **252**, 26–33 (2013).
24. Tromp, R. H., Spieser, S. H. & Neilson, G. W. A neutron diffraction and computer modeling study of the interatomic structure of phosphoric acid. *J. Chem. Phys.* **110**, 2145–2150 (1999).
25. Vilčiauskas, L., Tuckerman, M. E., Bester, G., Paddison, S. J. & Kreuer, K.-D. The mechanism of proton conduction in phosphoric acid. *Nat. Chem.* **4**, 461–466 (2012).
26. Wang, Y. et al. Ionic conductivity and glass transition of phosphoric acids. *J. Phys. Chem. B* **117**, 8003–8009 (2013).
27. Heres, M., Wang, Y., Griffin, P. J., Gainaru, C. & Sokolov, A. P. Proton conductivity in phosphoric acid: the role of quantum effects. *Phys. Rev. Lett.* **117**, 156001 (2016).
28. Vilciauskas, L., Paddison, S. J. & Kreuer, K.-D. Ab initio modeling of proton transfer in phosphoric acid clusters. *J. Phys. Chem. A* **113**, 9193–9201 (2009).
29. Krueger, R. A., Vilčiauskas, L., Melchior, J.-P., Bester, G. & Kreuer, K.-D. Mechanism of efficient proton conduction in diphosphoric acid elucidated via first-principles simulation and NMR. *J. Phys. Chem. B* **119**, 15866–15875 (2015).
30. Melchior, J.-P. & Frick, B. On the nanosecond proton dynamics in phosphoric acid–benzimidazole and phosphoric acid–water mixtures. *Phys. Chem. Chem. Phys.* **19**, 28540–28554 (2017).
31. Melchior, J.-P., Kreuer, K.-D. & Maier, J. Proton conduction mechanisms in the phosphoric acid–water system (H4P2O7–H3PO4·2H2O): a 1H, 31P and 17O PFG-NMR and conductivity study. *Phys. Chem. Chem. Phys.* **19**, 587–600 (2017).
32. Dyre, J. C. The random free-energy barrier model for ac conduction in disordered solids. *J. Appl. Phys.* **64**, 2456–2468 (1988).
33. Dyre, J. C. Studies of ac hopping conduction at low temperatures. *Phys. Rev. B* **49**, 11709–11720 (1994).
34. Dyre, J. C. & Schrøder, T. B. Universality of ac conduction in disordered solids. *Rev. Mod. Phys.* **72**, 873–892 (2000).
35. Schrøder, T. B. & Dyre, J. C. Scaling and universality of AC conduction in disordered solids. *Phys. Rev. Lett.* **84**, 310–313 (2000).
36. Schrøder, T. B. & Dyre, J. C. AC hopping conduction at extreme disorder takes place on the percolating cluster. *Phys. Rev. Lett.* **101**, 025901 (2008).
37. Sangoro, J. R. et al. Charge transport and mass transport in imidazolium-based ionic liquids. *Phys. Rev. E* **77**, 051202 (2008).
38. Schrøder, T. B. & Dyre, J. C. Solid-like mean-square displacement in glass-forming liquids. *J. Chem. Phys.* **152**, 141101 (2020).
39. Ahlmann, S. et al. The relationship between charge and molecular dynamics in viscous acid hydrates. *J. Chem. Phys.* **155**, 014505 (2021).
40. Münzner, P., Hoffmann, L., Böhmer, R. & Gainaru, C. Deeply supercooled aqueous LiCl solution studied by frequency-resolved shear rheology. *J. Chem. Phys.* **150**, 234505 (2019).
41. Beerwerth, J., Bierwirth, S. P., Adam, J., Gainaru, C. & Böhmer, R. Local and global dynamics of the viscous ion conductors 2Ca(NO3)2-3KNO3 and 2Ca(NO3)2-3RbNO3 probed by 87Rb nuclear magnetic resonance and shear rheology. *J. Chem. Phys.* **150**, 194503 (2019).
42. Thomann, C. A. et al. Tuning the dynamics of imidazolium-based ionic liquids via hydrogen bonding. I. The viscous regime. *J. Chem. Phys.* **153**, 194501 (2020).
43. Kremer, F. & Schönhals, A. *Broadband dielectric spectroscopy*. 739 (Springer Science & Business Media, 2002).
44. Fröhlich, H. *Theory of dielectrics: dielectric constant and dielectric loss*. **180** (Clarendon Press, 1949).
45. Popov, I., Cheng, S. & Sokolov, A. P. In *Macromolecular Engineering* 1–39 (Wiley-VCH GmbH, 2022).
46. Popov, I. & Sokolov, A. P. In *Dynamics of Composite Materials* (eds Schönhals, A. & Szymoniak, P.) 35–61 (Springer International Publishing, 2022).
47. Singwi, K. S. & Sjölander, A. Diffusive motions in water and cold neutron scattering. *Phys. Rev.* **119**, 863–871 (1960).
48. Berkelbach, T. C., Lee, H.-S. & Tuckerman, M. E. Concerted hydrogen-bond dynamics in the transport mechanism of the hydrated proton: a first-principles molecular dynamics study. *Phys. Rev. Lett.* **103**, 238302 (2009).
49. Long, Z., Atsango, A. O., Napoli, J. A., Markland, T. E. & Tuckerman, M. E. Elucidating the proton transport pathways in liquid imidazole with first-principles molecular dynamics. *J. Phys. Chem. Lett.* **11**, 6156–6163 (2020).
50. Wright, M. R. *An Introduction to Aqueous Electrolyte Solutions*. 602 (John Wiley & Sons, Ltd, 2007).
51. Dyre, J. C., Maass, P., Roling, B. & Sidebottom, D. L. Fundamental questions relating to ion conduction in disordered solids. *Rep. Prog. Phys.* **72**, 046501 (2009).
52. Gainaru, C. et al. Mechanism of conductivity relaxation in liquid and polymeric electrolytes: direct link between conductivity and diffusivity. *J. Phys. Chem. B* **120**, 11074–11083 (2016).
53. Dyre, J. C. & Murch, G. E. Correlation effects in tracer diffusion and ionic conductivity. II. *Solid State Ion.* **21**, 139–142 (1986).
54. MacFarlane, D. R. et al. On the concept of ionicity in ionic liquids. *Phys. Chem. Chem. Phys.* **11**, 4962–4967 (2009).
55. Maass, P., Meyer, M. & Bunde, A. Nonstandard relaxation behavior in ionically conducting materials. *Phys. Rev. B* **51**, 8164–8177 (1995).
56. Roling, B., Martiny, C. & Brückner, S. Ion transport in glass: Influence of glassy structure on spatial extent of nonrandom ion hopping. *Phys. Rev. B* **63**, 214203 (2001).
57. Popov, I. et al. Strongly correlated ion dynamics in plastic ionic crystals and polymerized ionic liquids. *J. Phys. Chem. C* **124**, 17889–17896 (2020).
58. Kashyap, H. K., Annapureddy, H. V. R., Raineri, F. O. & Margulis, C. J. How is charge transport different in ionic liquids and electrolyte solutions? *J. Phys. Chem. B* **115**, 13212–13221 (2011).
59. Schoenert, H. J. Evaluation of velocity correlation coefficients from experimental transport data in electrolytic systems. *J. Phys. Chem.* **88**, 3359–3363 (1984).
60. Murch, G. E. The haven ratio in fast ionic conductors. *Solid State Ion.* **7**, 177–198 (1982).
61. Harris, K. R. Relations between the fractional Stokes−Einstein and Nernst −Einstein equations and velocity correlation coefficients in ionic liquids and molten salts. *J. Phys. Chem. B* **114**, 9572–9577 (2010).
62. Tokuda, H., Tsuzuki, S., Susan, M. A. B. H., Hayamizu, K. & Watanabe, M. How ionic are room-temperature ionic liquids? An indicator of the physicochemical properties. *J. Phys. Chem. B* **110**, 19593–19600 (2006).

63. Mamontov, E. & Herwig, K. W. A time-of-flight backscattering spectrometer at the Spallation Neutron Source, BASIS. *Rev. Sci. Instrum.* **82**, 085109 (2011).
64. Arnold, O. et al. Mantid—data analysis and visualization package for neutron scattering and μ SR experiments. *Nucl. Instrum. Methods Phys. Res. Sect. A: Accelerators, Spectrometers, Detect. Associated Equip.* **764**, 156–166 (2014).
65. Azuah, R. T. et al. DAVE: a comprehensive software suite for the reduction, visualization, and analysis of low energy neutron spectroscopic data. *J. Res Natl Inst. Stand Technol.* **114**, 341–358 (2009).
66. CPMD (IBM Corporation 1990−2009 and MPI für Festkörperforschung 1997−2001, 2009).
67. Aeberhard, P. C., Arey, J. S., Lin, I.-C. & Rothlisberger, U. Accurate DFT descriptions for weak interactions of molecules containing sulfur. *J. Chem. Theory Comput.* **5**, 23–28 (2009).
68. Lin, I.-C. et al. Library of dispersion-corrected atom-centered potentials for generalized gradient approximation functionals: elements H, C, N, O, He, Ne, Ar, and Kr. *Phys. Rev. B* **75**, 205131 (2007).
69. Becke, A. D. Density-functional exchange-energy approximation with correct asymptotic behavior. *Phys. Rev. A* **38**, 3098–3100 (1988).
70. Böttcher, C. J. F. & Bordewijk, P. *Theory of electric polarization. Volume II. Dilectric in time-dependent fields*. **2** (Elsevier Science Limited, 1978).

Acknowledgements

We thank Drs. Linas Vilčiauskas (Vilnius University), Klaus-Dieter Kreuer (MPI-Stuttgart) and Mark E. Tuckerman (NYU) for helpful discussions and insight comments. We acknowledge support by the National Science Foundation (awards CHE-1764409 and CHE-2102425) for dielectric and simulations work. I.P., R.L.S. and E.M. acknowledge support for neutron and some dielectric studies by the Fluid Interface Reactions, Structures and Transport (FIRST) Center, an Energy Frontier Research Center funded by the U.S. Department of Energy, Office of Science, Basic Energy Sciences. Research at the BASIS of the ORNL's Spallation Neutron Source was sponsored by the Scientific User Facilities Division, Office of Basic Energy Sciences, U.S. Department of Energy. Computing resources were provided through an XSEDE allocation DMR130078 on Stampede2 at the Texas Advanced Computing Center (TACC).

Author contributions

I.P., A.Y.G. performed the dielectric measurements over a wide range in frequency and analyzed the conductivity data. I.P. and A.P.S. performed and analyzed the light scattering measurements. E.M., I.P., and R.L.S. performed the QENS measurements and analyzed the neutron scattering data. Z.Z. performed and analyzed the AIMD simulations. C.G., S.J.P., and A.P.S. developed the idea and led the research. All authors contributed to the discussion of the results.

Competing interests

The authors declare no competing interests.

Additional information

Supplementary information The online version contains supplementary material available at https://doi.org/10.1038/s42004-023-00878-6.

Correspondence and requests for materials should be addressed to Stephen J. Paddison or Alexei P. Sokolov.

Peer review information *Communications Chemistry* thanks the anonymous reviewers for their contribution to the peer review of this work.

Reprints and permission information is available at http://www.nature.com/reprints

Publisher's note Springer Nature remains neutral with regard to jurisdictional claims in published maps and institutional affiliations.

Open Access This article is licensed under a Creative Commons Attribution 4.0 International License, which permits use, sharing, adaptation, distribution and reproduction in any medium or format, as long as you give appropriate credit to the original author(s) and the source, provide a link to the Creative Commons license, and indicate if changes were made. The images or other third party material in this article are included in the article's Creative Commons license, unless indicated otherwise in a credit line to the material. If material is not included in the article's Creative Commons license and your intended use is not permitted by statutory regulation or exceeds the permitted use, you will need to obtain permission directly from the copyright holder. To view a copy of this license, visit http://creativecommons.org/licenses/by/4.0/.

© The Author(s) 2023

Reprinted with permission from American Chemical Society
Copyright 2023 American Chemical Society

THE JOURNAL OF PHYSICAL CHEMISTRY B
A JOURNAL OF THE AMERICAN CHEMICAL SOCIETY

pubs.acs.org/JPCB Article

Effect of Ion Mass on Dynamic Correlations in Ionic Liquids

Md. Dipu Ahmed, Zhenghao Zhu, Airat Khamzin, Stephen J. Paddison, Alexei P. Sokolov, and Ivan Popov*

Cite This: J. Phys. Chem. B 2023, 127, 10411−10421 Read Online

ACCESS | Metrics & More | Article Recommendations | Supporting Information

ABSTRACT: Ionic liquids (ILs) are a class of liquid salts with distinct properties such as high ionic conductivity, low volatility, and a broad electrochemical window, making them appealing for use in energy storage applications. The ion−ion correlations are some of the key factors that play a critical role in the ionic conductivity of ILs. In this work, we present the study of the impact of ion mass on ion−ion correlations in ILs, applying a combination of broadband dielectric spectroscopy measurements and molecular dynamics simulations. We examined three ILs with the same cation but different anions to consider three different cases of cation−anion masses: $M_+ > M_-$, $M_+ \approx M_-$, and $M_+ < M_-$. We applied the momentum conservation approach to estimate the contribution of distinct ion−ion correlations from experimental data and obtained good agreement with direct calculations of distinct ion−ion correlations from molecular dynamics simulations. Our findings reveal that relative ion mass has a strong effect on the distinct ion−ion correlations, leading to swapping of the relative amplitude of distinct cation−cation and anion−anion correlations.

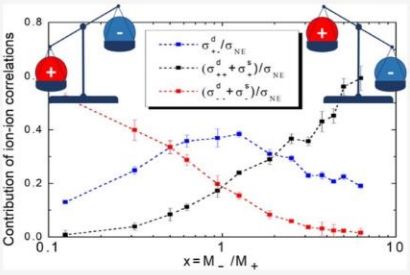

INTRODUCTION

Room-temperature ionic liquids (ILs) are promising materials for various electrochemical energy storage applications, including batteries and supercapacitors.[1−3] ILs demonstrate high intrinsic conductivity, low flammability, and higher thermal and electrochemical stabilities in comparison to conventional salt solutions with carbonate solvents.[4−7] Due to these characteristics, they meet most of the criteria for electrochemical devices with improved performance and safety.[8] One of the key fundamental properties of any ionic system is its ionic conductivity. In diluted salt solutions, ionic conductivity can be estimated using the Nernst−Einstein (NE) equation from information concerning the concentration, n_i, and self-diffusion coefficient, D_i^s, of the mobile ions[9,10]

$$\sigma_{NE} = \frac{q^2}{k_B T} \sum_i n_i D_i^s \tag{1}$$

where q is the charge of an ion. In diluted salt solutions, where ion−ion interactions are assumed to be negligible, the experimentally measured ionic conductivity (σ_{DC}) indeed is very close to the estimation from eq 1 ($\sigma_{DC} \approx \sigma_{NE}$). However, concentrated ionic systems, including ILs, have significant ion−ion interactions, leading to strong dynamic correlations of ions. As a result, the NE equation fails to describe the ionic conductivity of concentrated systems,[9−19] and the additional factor has to be introduced to the NE equation[9,20,21]

$$\sigma_{DC} = H^{-1}\sigma_{NE} = H^{-1}\frac{q^2}{k_B T} \sum_i n_i D_i^s \tag{2}$$

Here, the ratio $H^{-1} = \sigma_{DC}/\sigma_{NE}$ is known as ionicity or inverse Haven ratio.[13,22] The ionicity of ILs is always less than one (i.e., $H^{-1} < 1$),[13,15,16,23−26] and this has been traditionally ascribed to the presence of ion pairs due to the coupled motion of anion and cation.[1,27] However, recent simulations[28] and experiments[29−31] have revealed that the low value of H^{-1} for molten salts and ionic liquids is mostly caused by distinct anion−anion and cation−cation correlations, rather than the ion pairs. Even more interesting effects occur in the mixtures of salt and ionic liquids, where ion−ion correlations lead to clustering and surprising negative cation transport numbers,[32−35] or even superionic behavior[36] with $H^{-1} > 1$.

Molecular dynamics (MD) simulations have been the only method for estimating the contribution of distinct ion−ion correlations to conductivity. Recently, a method was proposed from experimental measurements.[37] However, the proposed approach is complex and challenging, requiring electrodes containing one ion (e.g., Li^+), and has been applied only to a

Received: August 17, 2023
Revised: November 13, 2023
Accepted: November 14, 2023
Published: November 27, 2023



ACS Publications © 2023 American Chemical Society

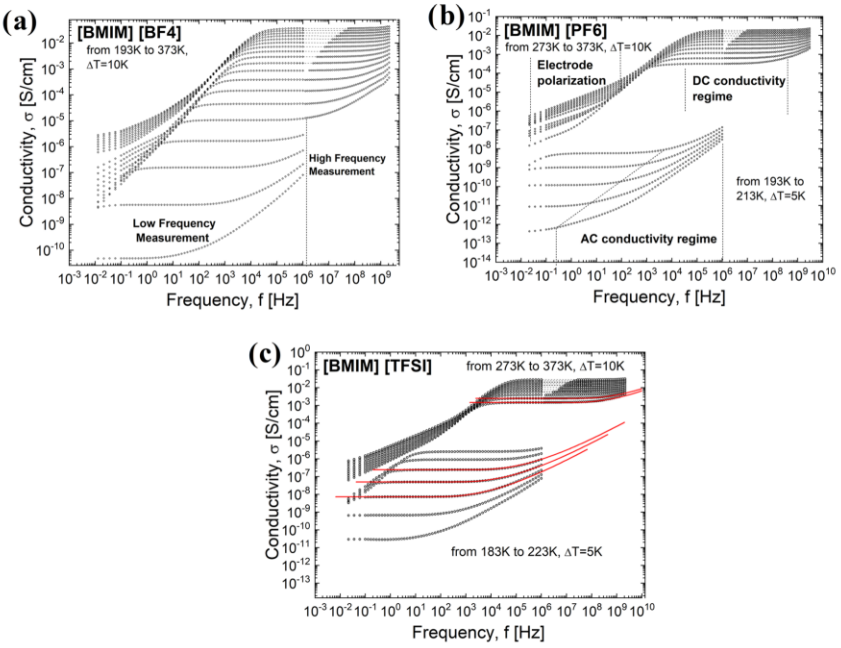

Figure 1. Conductivity spectra over a wide frequency range for the different ionic liquids: (a) [BMIM][BF4]; (b) [BMIM][PF6]; and (c) [BMIM][TFSI]. In panel (b), the different regimes are shown: (1) AC conductivity; (2) DC conductivity; and (3) electrode polarization. To determine the conductivity relaxation time, τ_σ, the conductivity spectra were fitted using eq 7. The example of fitting at different temperatures is shown in panel (c) by red solid lines. To match data from high- and low-frequency measurements, the electrode polarization regime in the high-frequency measurements was removed, and dashed lines are displayed only to guide the eye.

few lithium conductive systems. Another approach that was proposed in refs. 38,39 is based on a combination of experimental measurements of conductivity and diffusion and theoretical models and the assumption that the total momentum of all ions is conserved. Recently, this approach was used to estimate each term of the distinct ion−ion correlations in polymerized ionic liquids,[39] ionic liquids,[28,30] and concentrated solutions.[40] However, the estimations of the distinct ion−ion correlations from experimental data using this approach were never compared to the results of model-independent MD investigations.

To verify the validity of the momentum conservation approach, we performed experimental and computational studies of ILs with different ion masses. We chose ILs with the same cation, 1-butyl-3-methylimidazolium ([BMIM], M_+ ≈139 g/mol), but different anions, [BF_4] (M_- ≈ 87 g/mol), [PF_6] (M_- ≈145 g/mol), and bis(trifluoromethane)-sulfonimide [TFSI](M_- ≈280 g/mol). These ILs present the cases when $M_- < M_+$ [BMIM]-[BF4], $M_- \approx M_+$ [BMIM]-[PF6], and when $M_- > M_+$ [BMIM]-[TFSI]. Experimental data were used to estimate distinct ionic correlations based on the momentum conservation approach, and the results were compared to MD simulations, where distinct ion−ion correlations were directly computed. This comparison revealed a good quantitative agreement between experimental and simulation results. In particular, the cation−cation correlations provide a more negative contribution to conductivity than the anion−anion correlations in [BMIM]-[BF]4 with $M_- < M_+$, while in [BMIM]-[TFSI] with $M_- > M_+$, the anion−anion correlations contribute more negatively to conductivity than the cation−cation correlations. At the same time, the cation−anion correlation has a positive contribution to conductivity in all three ILs. We also discuss how the momentum conservation approach depends on the choice of coordinate system.

■ EXPERIMENTAL RESULTS

Materials. 1-Butyl-3-methylimidazolium tetrafluoroborate [BMIM][BF4], 1-butyl-3-methylimidazolium hexafluorophosphate [BMIM][PF6], and 1-butyl-3-methylimidazolium bis(trifluoromethylsulfonyl)imide [BMIM][TFSI] were purchased from Sigma-Aldrich and used as purchased. The samples were opened and loaded into a cell for conductivity measurements inside a glovebox in an inert atmosphere.

Broadband Dielectric Spectroscopy (BDS). BDS was used to perform conductivity spectra measurements. Two spectrometers were utilized to cover the wide frequency range from 0.1 Hz up to 3 GHz. An α-A analyzer from Novocontrol was utilized in the frequency range of 10^{-1}−10^6 Hz. A cell consists of a cap as the bottom electrode; the upper electrode is separated from the cap by a sapphire window to avoid electrical contact between them. The fixed electrode distance of 0.4 mm and a diameter of 10.2 mm were used. The samples were measured with a voltage amplitude of 0.1 V. The standard calibration procedure was used before measurements. An

https://doi.org/10.1021/acs.jpcb.3c05568
J. Phys. Chem. B 2023, 127, 10411−10421

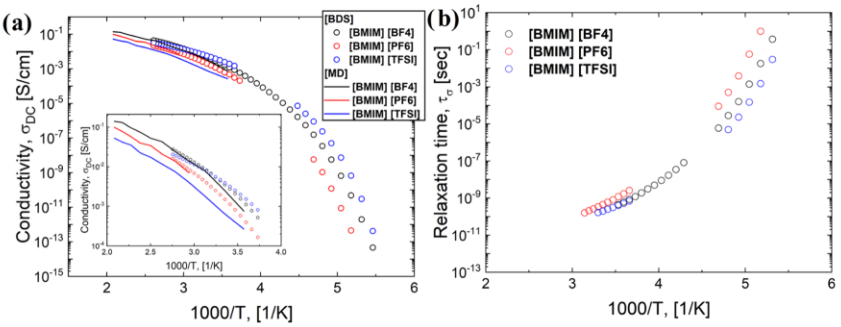

Figure 2. (a) Temperature dependence of the DC conductivity, σ_{DC}: symbols present experimental data, and lines are from the MD simulations results. The inset figure in panel (a) represents the comparison of MD results and experimental data on an expanded scale. (b) Temperature dependence of the conductivity relaxation time, τ_σ. The gap in the experimental data for σ_{DC} and τ_σ at low temperatures for [BMIM][PF6] and [BMIM][TFSI] is due to crystallization.

Agilent RF impedance material analyzer, E4991A, with WinDETA Software from Novocontrol, was used in the frequency range 10^6−3 × 10^9 Hz. The cell was constructed using two APC-7 connectors. For the upper electrode, the inner pin of one connector was replaced by a solid pin with a diameter of 3 mm, and the free space between the inner pin and outer part was filled by Teflon. For the lower electrode, the pin in the other connector was removed, and in the free central space, a movable metallic cylinder was inserted. As a result, the coaxial line was terminated by a plate capacitor with an adjustable distance between the electrodes. The coaxial line was calibrated using a standard procedure (Open/Short/50 Ω) to move the reference plane up to the cell terminating the line. The cell was also calibrated (open and short) for better precision. The samples were loaded between the two electrodes at 0.1 mm and measured with a voltage amplitude of 0.1 V. A Quattro temperature controller (Novocontrol) was used for temperature stabilization for the measurements from 10^{-1} to 10^9 Hz. The samples were stabilized for 20 min at each temperature to reach a precision of ±0.2 K. The samples were equilibrated at each temperature for 20 min to achieve a precision of ±0.2 K, followed by rapid quenching to prevent crystallization at low temperatures and to reach supercooled liquid states. However, the two ionic liquids [BMIM][PF6] and [BMIM][TFSI] crystallized upon heating and then melted back at higher temperatures. In our further analysis, the conductivity data corresponding to the crystalline states of the ILs were excluded.

The conductivity spectra for all studied systems exhibit three usual regions (Figure 1a−1c): (i) frequency-dependent AC conductivity regime at high frequencies, σ_{AC}; (ii) a plateau level of DC conductivity regime at the intermediate frequency range, σ_{DC}, and (iii) a decrease due to the accumulation of charge carriers at the surface of the electrode at a lower frequency (electrode polarization effect).[41] The temperature gap in the data for [BMIM][PF6] and [BMIM][TFSI] is caused by sample crystallization.

Molecular Dynamic (MD) Simulations. MD simulations were performed for a variety of molecular BMIM-based ILs. Each system consisted of 500 pairs of ions, providing an optimal balance between statistical reliability and computational efficiency.[42−44] The methodology was established by using the generalized AMBER force field (GAFF) utilizing a previously employed protocol.[45−48] Partial charges on all atoms were determined with the restrained electrostatic potential (RESP) algorithm[49] based on the optimized electronic structures of the isolated cation or anion. These *ab initio* calculations were carried out at the Hartree−Fock HF/6−31g(d) level of theory using the Gaussian 09 package.[50] The computed atomic partial charges were scaled by a factor of 0.8 to account for polarization and charge transfer, which has been proven to be an efficient and reliable approach in ion-containing systems.[48,51,52] A cutoff distance of 14 Å was used for the electrostatic and Lennard-Jones interactions with long-range corrections handled by the particle mesh Ewald (PME) method and appropriate tail corrections, respectively. The initial systems were equilibrated for over 50 ns within the NPT ensemble, following a ∼ 30 ns annealing process using the GROMACS code.[53] Following an additional 30 ns of equilibration under the NVT ensemble, a trajectory of 100 ns was collected every 1 ps. This length of trajectory ensured reliable ion−ion correlations in these IL systems.[12,54] Temperature and pressure were controlled by the Bussi thermostat[55] and the Parrinello-Rahman barostat[56] with coupling times of 0.5 and 5 ps, respectively. The MD simulations for all of the IL systems were conducted in a periodic cubic box with a time step of 2 fs. To assess the accuracy of the force fields applied to these systems, we compared the simulation and experimental densities, as illustrated in Figure S1. The density of [BMIM][TFSI] closely matches the experimental data. While the densities of the other two systems are slightly lower than the experimental values,[23] they still exhibit reasonable agreement. All dynamic correlations were compiled from 4 to 6 trajectories to provide average values, along with their corresponding standard deviations.

■ DISCUSSION

The conductivity spectra of ion conductive materials[10,11] are usually described by the random barrier model (RBM).[57−60] According to this model, charge carriers hop over potential energy barriers. When the barrier height distribution is constant, the model results in the following equation[61]

$$\ln\left(\frac{\sigma^*(\omega)}{\sigma_{DC}}\right) = \frac{i\omega\tau_\sigma\sigma_{DC}}{\sigma^*(\omega)}\left(1 + \frac{8}{3}\frac{i\omega\tau_\sigma\sigma_{DC}}{\sigma^*(\omega)}\right)^{-1/3} \quad (3)$$

https://doi.org/10.1021/acs.jpcb.3c05568
J. Phys. Chem. B 2023, 127, 10411−10421

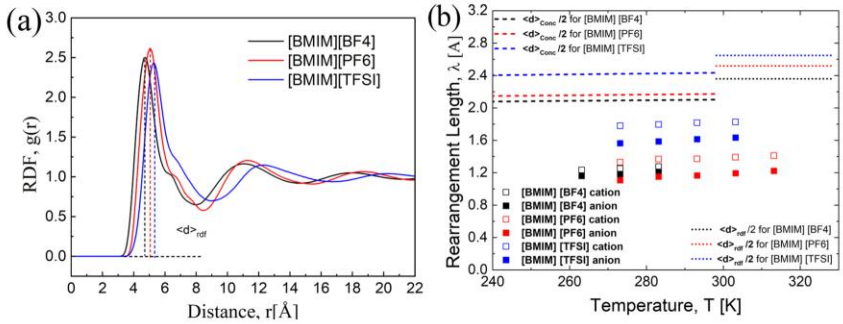

Figure 3. (a) Radial distribution functions of the center of mass of cations and anions in ILs to estimate half the average distance between the ions, $\langle d \rangle_{rdf}/2$. (b) Ions rearrangement length estimated from eq 8 for cations (open square symbols) and anions (closed square symbols). Estimated half distances between the ions from ion concentration, $\langle d \rangle_{conc}/2$, are represented by dashed lines. Estimated half distances between the ions from the radial distribution functions, $\langle d \rangle_{rdf}/2$, are represented by dotted lines.

Here, $\sigma^*(\omega)$ is a measured complex conductivity, σ_{DC} is a DC conductivity, and τ_σ is a conductivity relaxation time. The latter specifies the characteristic of AC−DC crossover time when charge mean-squared displacement crosses over from a subdiffusive regime, $\langle r^2(t) \rangle \sim t^\alpha$ with $\alpha < 1$ (corresponds to AC tail in conductivity spectra) to a normal diffusion regime $\langle r^2(t) \rangle \sim t$ (corresponds to DC-plateau in conductivity spectra). Both the conductivity spectra and the conductivity relaxation process in the real part of the dielectric permittivity are described by eq 3. The examples of conductivity spectra fits are shown in Figure 1c, and the temperature dependences of σ_{DC} and τ_σ obtained from the fits are plotted in Figure 2. The results for conductivity values from MD simulations are presented in the same Figure 2a and provide a good match with experimentally measured data for [BMIM][BF4] and [BMIM][PF6] but slightly underestimate the conductivity for [BMIM][TFSI].

As it was proposed in early studies,[10,11,16,27,40] the conductivity relaxation process corresponds to local ion rearrangements, and from knowledge of the conductivity relaxation time and diffusion coefficient, D, measured by pulsed field gradient nuclear magnetic resonance (PFG-NMR), we can estimate the ion rearrangement length, λ, with

$$\lambda = \sqrt{6D\tau_\sigma} \tag{4}$$

The parameter, λ, defines the characteristic length, where anomalous subdiffusion regime crosses over into a normal Fickian diffusion, and in typical ILs, its value is about $\lambda \approx 1-3$ Å.[27,62] Using the diffusion coefficients of the cation and anion,[23,63] we can estimate separately the rearrangement length for positive and negative charge carriers: $\lambda_+ = \sqrt{6D_+\tau_\sigma}$ and $\lambda_- = \sqrt{6D_-\tau_\sigma}$. These parameters for the studied ILs appear in the range ≈1.2−1.9 Å (Figure.3b). It was suggested[10] that the ion rearrangement length should be about half the average distance between the ions estimated from their concentration, $\langle d \rangle_{conc}/2 = [(3/4\pi n)^{1/3}]/2$. However, the distance estimated from ion concentration appears slightly larger than λ,$\langle d \rangle_{conc}/2 \sim 2.0-2.4$ Å (Figure 3b). The average distance between the ions can also be estimated from the radial distribution function (RDF) obtained from the MD simulations (Figure 3a). Half of the average distance between the ions estimated from the RDF is even slightly larger than $\langle d \rangle_{conc}/2$ (Figure 3b).

Although the estimated rearrangement length, λ, is slightly smaller than the average distance estimated from the ion concentration and RDFs, it is worth noting that its value is almost temperature-independent. This fact can be used for an estimation of the ion diffusion coefficient at low temperatures where slow ion dynamics is inaccessible from PFG-NMR measurements. Indeed, knowing the value of the parameter λ, we can invert eq 4 and use τ_σ from the BDS measurements to estimate the diffusivity of the ions even at low temperatures $D_\pm = \lambda_\pm^2/6\tau_\sigma$.[10,40] The result of these estimations is presented in Figure 4. In the same figure, we presented diffusion coefficients

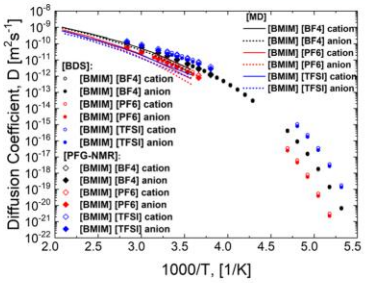

Figure 4. Temperature dependence of the diffusion coefficient for cations and anions of the ILs. Circle symbols represent our experimental data, which are in good agreement with previous studies (ref 23). PFG-NMR data are shown with diamond symbols, and the MD simulation results are shown as solid and dotted lines for the cations and anions, respectively.

from MD simulation, which has a good match with PFG-NMR data for [BMIM][BF4] and [BMIM][PF6] but slightly underestimates diffusion for [BMIM][TFSI]. This is consistent with an underestimated conductivity for the same IL (Figure 2a).

From the diffusion coefficient, we can estimate the expected NE ionic conductivity using eq 1 and calculate the inverse Haven ratio, $H^{-1} = \sigma_{DC}/\sigma_{NE}$, (eq 2) to reveal how ion−ion correlations depend on temperature. Analysis of the inverse Haven ratio in the studied systems (Figure 5) reveals that it remains almost constant ∼0.6−0.8 at higher temperatures and

https://doi.org/10.1021/acs.jpcb.3c05568
J. Phys. Chem. B 2023, 127, 10411−10421

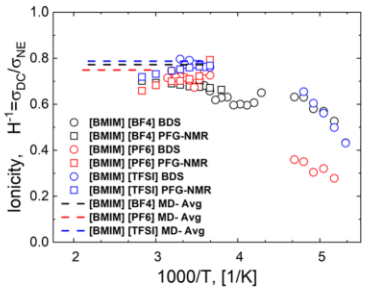

Figure 5. Temperature dependence of the ionicity or the inverse Haven ratio. Circle symbols represent our experimental data, where the diffusion coefficient was estimated from the ac−dc crossover and square symbols corresponds to data, where the diffusion coefficient was measured by PFG-NMR results. The dashed lines represent the average value of ionicity from the MD simulations, which are in good agreement with the experimental data. The complete data obtained from the MD simulations, along with computed standard deviations, are reported in Figure S1b.

then decreases to ∼0.4−0.25 upon cooling toward T_g. The decrease of H^{-1} upon cooling has been reported for many other systems,[10,27] and the mechanism behind this behavior remains unknown.

Although the inverse Haven ratio provides information about ion correlations, this parameter does not reveal any mechanistic details that dominate these correlations in the studied systems. At the same time, the direct experimental measurement of distinct ion−ion correlations is quite difficult.[37] However, the contributions of distinct ion−ion correlations to conductivity can be estimated based on the model proposed by Schonert and developed in several papers.[28,38,39] The model only assumes that the total momentum of all ions is conserved and that the velocities of the cations and anions obey the following equation (the validity of this assumption will be discussed later):

$$M_+ \sum_i \vec{v}_{i+}(0) + M_- \sum_i \vec{v}_{i-}(0) = 0 \tag{5}$$

Considering the case when all ions are mobile, we can multiply eq 5 by $\vec{v}_{j+}(t)$ and $\vec{v}_{j-}(t)$ and take the average to obtain the following pair of equations:

$$\begin{cases} M_+(D_+^s + D_{++}^d/2) = -M_- D_{+-}^d/2 \\ M_-(D_-^s + D_{--}^d/2) = -M_+ D_{+-}^d/2 \end{cases} \tag{6}$$

where D_+^s and D_-^s are self-diffusion coefficients and D_{++}^d, D_{--}^d, and D_{+-}^d are distinct diffusion coefficients defined by the relationships

$$\begin{aligned} D_+^s &= \frac{1}{3}\int_0^\infty \langle \vec{v}_{i+}(t)\vec{v}_{i+}(0)\rangle \mathrm{d}t, \\ D_-^s &= \frac{1}{3}\int_0^\infty \langle \vec{v}_{i-}(t)\vec{v}_{i-}(0)\rangle \mathrm{d}t \\ D_{++}^d &= \frac{\varphi}{3}\int_0^\infty \langle \vec{v}_{i+}(t)\vec{v}_{j+}(0)\rangle \mathrm{d}t, \\ D_{--}^d &= \frac{\varphi}{3}\int_0^\infty \langle \vec{v}_{i-}(t)\vec{v}_{j-}(0)\rangle \mathrm{d}t \\ D_{+-}^d &= \frac{\varphi}{3}\int_0^\infty \langle \vec{v}_{i+}(t)\vec{v}_{j-}(0)\rangle \mathrm{d}t = \frac{\varphi}{3}\int_0^\infty \langle \vec{v}_{i-}(t)\vec{v}_{j+}(0)\rangle \mathrm{d}t \end{aligned} \tag{7}$$

Here, the −/+ subscript refers to either anion/cation, φ is the total number of correlated ions in a local area, and $i \neq j$. Using the definition of conductivity as a current−current correlation function[9,20,21]

$$\begin{aligned} \sigma_{DC} &= \frac{1}{3VK_BT}\int_0^\infty \langle \vec{J}(0)\cdot\vec{J}(t)\rangle \mathrm{d}t, \text{ with } \langle \vec{J}(0)\cdot\vec{J}(t)\rangle \\ &= \langle \sum_i q_i\vec{v}_i(0)\cdot \sum_j q_j\vec{v}_j(t)\rangle \end{aligned} \tag{8}$$

we have, together with eqs 6 and 8, the closed system of equations for D_{++}^d, D_{--}^d, and D_{+-}^d. To find the contribution of distinct ion−ion correlations into conductivity we can write conductivity as[28,38,39]

$$\sigma_{DC} = \sigma_{NE} + \sigma_{+-}^d + \sigma_{++}^d + \sigma_{--}^d, \quad \sigma_{NE} = \sigma_+^s + \sigma_-^s \tag{9}$$

where we combined self-correlation to NE conductivity eq 1, and the last three terms define conductivity contribution from distinct anion−cation (σ_{+-}^d), cation−cation (σ_{++}^d), and anion−anion (σ_{--}^d) correlations. As a result, after solving[28,38−40] system of eqs 6 and 8, we can derive analytical expressions for the contribution of the ion−ion correlation in each term of eq 9

$$\begin{aligned} \sigma_{++}^d &= \frac{1}{2}\frac{e^2n}{k_BT}D_{++}^d = \sigma_{DC}\left(\frac{M_-}{M_- + M_+}\right)^2 - \sigma_+^s, \\ \sigma_+^s &= \frac{e^2n}{k_BT}D_+^s \\ \sigma_{--}^d &= \frac{1}{2}\frac{e^2n}{k_BT}D_{--}^d = \sigma_{DC}\left(\frac{M_+}{M_- + M_+}\right)^2 - \sigma_-^s, \\ \sigma_-^s &= \frac{e^2n}{k_BT}D_-^s \\ \sigma_{+-}^d &= -\frac{e^2n}{k_BT}D_{+-}^d = \sigma_{DC}\frac{2M_+M_-}{(M_- + M_+)^2} \end{aligned} \tag{10}$$

This result provides a simple means to estimate distinct ion−ion correlations if the DC conductivity and self-diffusion coefficients are experimentally measured. According to eq 10, the cation−anion correlations in ionic liquids always have a positive contribution to conductivity, unlike the systems with a solvent, where this type of correlation might change sign, depending on the solvent concentration.[40] This indicates that the conductivity of the ionic liquids is always improved by the correlated anion−cation motion. The distinct contributions to conductivity estimated by eq 10 and scaled by the expected NE conductivity for the three IL systems studied here are shown in Figure 6. These contributions appear in surprisingly good

https://doi.org/10.1021/acs.jpcb.3c05568
J. Phys. Chem. B 2023, 127, 10411−10421

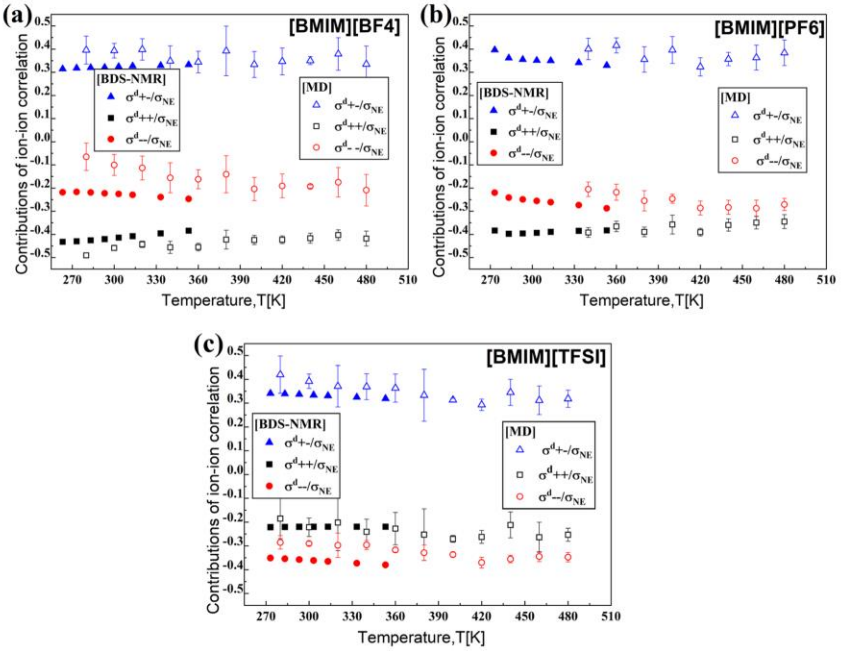

Figure 6. Distinct ion−ion contribution to conductivity normalized by σ_{NE} for the three ILs, where the closed symbols represent our experimental data and open symbols represent data from our MD simulations.

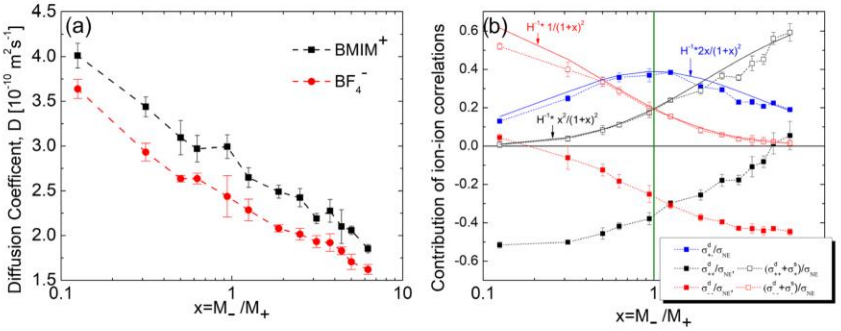

Figure 7. (a) Self-diffusion coefficient as a function of the anion-to-cation mass ratio, $x = M_-/M_+$, at 400 K obtained by MD simulations. (b) Contributions of distinct (closed symbols) and total (open symbols) ion−ion correlations to conductivity normalized by σ_{NE} of [BMIM][BF4] ionic liquids as a function of the artificially changed anion-to-cation mass ratio, $x = M_-/M_+$, at 400 K. The green vertical line indicates the case in which the masses of anion and cation are equal. The solid lines present the theoretical prediction from eq 10, where we used $H^{-1} = 0.78$.

agreement with the direct calculations of these correlations from our MD simulations (Figures 6 and S2). These important results suggest that momentum conservation likely plays an important role in ionic correlations in liquid electrolytes.

Both experimental and simulation results also revealed a significant role of the anion mass in these correlations (Figure 6). While the contribution of the anion−cation correlations to conductivity remains essentially the same, ∼+(0.3−0.4), distinct anion−anion correlations decrease from ∼−0.2 in the IL with (the light) BF_4 to ∼−(0.4−0.5) in the IL with the heavier TFSI, and distinct cation−cation correlations have opposite behavior with the increase of anion mass (Figure 6). Moreover, it can be seen from eq 10 that the mass of the ions has a direct relationship with the distinct ion−ion correlations. In BMIM-BF_4, the mass of the cation is larger than the mass of the anion, resulting in stronger negative cation−cation contributions to the conductivity (Figure 6a), but BMIM-TFSI, where the anion mass is larger than the cation mass, has

https://doi.org/10.1021/acs.jpcb.3c05568
J. Phys. Chem. B 2023, 127, 10411−10421

stronger negative anion−anion contributions to conductivity (Figure 6c). The independent MD simulations reveal a similar result of switching anion−anion and cation−cation correlations with the change of the anion mass (Figure 6). Surprisingly, in [BMIM][PF6], where the anion and cation have similar masses, the cation−cation correlations appear more negative (stronger). The same result is observed in the MD simulations (Figure 6b). This surprising result might be related to the difference in the size/geometry/structure of these ions and their diffusion. Indeed, it was shown[64] that in the case of [EMIM][TFSI], cation and anion diffusion coefficients have different dependence on the applied pressure, corresponding to the connection between TFSI conformational exchange and diffusion. It appears[23] that the diffusion of BMIM cation is faster than the diffusion of any studied here anions, regardless of their mass. The good agreement between the estimates of the distinct ionic correlations from the experimental data using eq 10 and the results of the MD simulations justifies a simple approach based on momentum conservation for the analysis of distinct ion−ion correlations in the various ionic systems.

To better understand the impact of the mass of the anion, we artificially manipulated the mass of BF_4^- in the MD simulations across a broad spectrum of molecular weight while maintaining the same force field. This approach enabled us to eliminate the influence of other factors, including the anion structure and charge distribution. As expected, the self-diffusion coefficient of the anion decreases with increasing mass. Similar behavior is observed for the cation (Figure 7a). It is worth noting that the self-diffusivity of the cation is consistently greater than that of the anion across all of the studied cases ($M_-/M_+ = 0.125 - 6.26$). This occurrence can be explained by the geometry of the cation, which leads to a preferential translational motion in the plane of the ring.[48,65] Spatial distribution functions (SDFs) of these ILs show that the anions preferentially present above/below the imidazolium ring generally close to the top carbon, while the area near the nonpolar alkyl tails remains vacant (Figure 8 top), leading to a preferential direction for the movement of the cation. In addition, the surfaces become larger with decreasing size of the anion. This characteristic has been observed previously in both experimental and computational studies.[24,65−72] In contrast, the SDFs of the BMIM cation around the three anions reveal that the BMIM cation distributes around the anions in a symmetric and well-ordered way, especially noticeable for the PF6 and BF4 anions (forming an octahedron for PF6 and a tetrahedron for BF4, respectively), as depicted in the bottom panel of Figure 8. It is worth noting that the BMIM cation resides around the linear TFSI anion, contributing to the fast movement of the anion in BMIM-TFSI system, despite TFSI being heavier than the other two anions. However, this specific phenomenon was not captured in our simulations due to the limitations in the force field, which could not adequately represent the multiple conformations of the TFSI anion.[73] Not surprisingly, changes in the anion mass have a negligible influence on the distribution of cations around the anion and the anions around the cation, as shown in Figure S3. This phenomenon elucidates why the [BMIM] cation exhibits diffusion faster than that of the anion across a wide range of anion-to-cation mass ratios (Figure 7a). The relaxation time of ion-association increases with an increase in the mass of the anion (Figure S4). This implies that heavier ions require more time to escape the cage formed by oppositely charged ions. In addition, our MD simulations reveal the heterogeneity of the nonpolar domains. The anion exhibits a minimal influence on the clustering of these nonpolar domains, which is represented by the tail groups of the imidazolium ring (Figure S5). However, previous reports indicate that increasing the tail length significantly increases the aggregation of nonpolar domains in coarse-grained modeling of $[C_xMIM][NO_3]$ (x = 1, 2, 3, 4, 6, and 8) systems.[74]

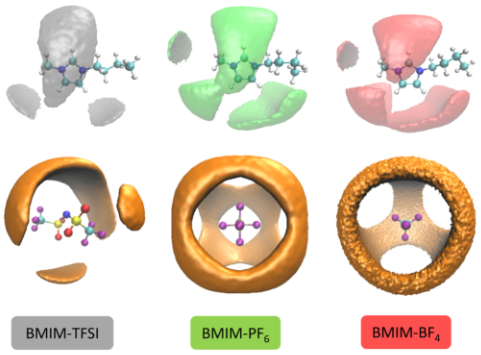

Figure 8. Spatial distribution functions of anions around the BMIM cation (top) and the BMIM cation around three anions (bottom). The SDFs were computed using the TRAVIS program[75] and visualized by the VMD program.[76] The contour surfaces are shown at the isovalues of 10 nm^{-3} and 6 nm^{-3} for the top and bottom ones, respectively.

The contribution of distinct ion−ion correlations normalized by σ_{NE} as a function of the anion-to-cation mass ratio were also examined (Figure 7b). We found that the correlated movement of the cations and anions positively contributes to the conductivity, while the distinct correlations between ions of the same charge result in negative contributions to the conductivity. More specifically, the negative contribution of distinct anion−anion correlation increases with an increase in the mass of the anion. In contrast, the distinct cation−cation correlation shows an opposite trend. Moreover, all of the distinct correlations quickly change when the anion-to-cation mass ratio is very small or very large. This is consistent with the difference between the distinct like-charged ion correlations in the case of an anion lighter than the cation (Figure 6a) and the opposite situation (Figure 6c). It is worth noting that the distinct anion−anion correlation coincides with the distinct cation−cation correlation when the ratio of the anion-to-cation mass (M_-/M_+) equals 1.25, rather than when the masses are identical, as indicated by the green vertical line in Figure 7b. This shift is consistent with stronger negative σ^d_{++} than σ^d_{--} in the [BMIM][PF6] system with $M_+ \sim M_-$ (Figure 6b). The shift of the crossing between the distinct ion correlations is related to the differences in diffusion coefficients of anion and cation, which may be due to the anisotropic diffusion of the cation compared to the isotropic movement of the anion, as discussed above. Indeed, if we take into account the self-correlations, we obtain that $\Delta_-^{total} = (\sigma^d_{--} + \sigma^s_-)/\sigma_{NE}$ and $(\Delta_-^d + \sigma^s_-)/\sigma_{NE}$ switch exactly at $M_- = M_+$ (Figure 7b), in agreement with eq 10. Furthermore, eq 10 correctly predicts how normalized cation−anion correlations $\sigma^d_{+-}/\sigma_{NE}$ and total contribution Δ_+^{total} and Δ_-^{total} depend on mass (solid lines in

https://doi.org/10.1021/acs.jpcb.3c05568
J. Phys. Chem. B 2023, 127, 10411−10421

Figure 7b). Surprisingly, the distinct like-charged ion correlations shift from negative to slightly positive values, as the ratio of anion-to-cation masses is either significantly small or sufficiently large. The reason for this remains unclear. These findings conclusively demonstrate that disparities in the anion and cation masses influence the magnitude of distinct correlations between ions. Remarkably, even the sign of these contributions can change when the masses of the ions are significantly different. However, the results (Figures 6 and 7b) also suggest that the ion mass is not the only parameter affecting these correlations. Apparently, the geometry and/or volume of the ions and their diffusion also play a role.

It is important to emphasize that the MD simulations explicitly assume momentum conservation (keeping no displacement for the center of mass). The law of momentum conservation in the form of eq 5 assumes that total momentum is conserved only for mobile ions and is not transferred to the environment, e.g., to the sample cell. It is equivalent when the coordinate system is linked to the center of mass, where the velocity of the center of mass of the system is zero, i.e.,

$$\vec{v}_{CM}(t) = \frac{M_+\vec{v}_+(t) + M_-\vec{v}_-(t)}{M_+ + M_-} = 0 \quad (11)$$

However, recent studies using electrophoretic NMR[77] suggest that momentum conservation might be broken in ILs, and instead, the conservation of local molar volumes of specific ions may play a critical role. In this case, the velocity of the center of mass of the system might not be equal to zero $\vec{v}_{CM}(t) \neq 0$, and we have to take into account the next type of correlations $\langle \vec{v}_{CM}(t)\vec{v}_{CM}(0)\rangle$, $\langle \vec{v}_+(t)\vec{v}_{CM}(0)\rangle$ and $\langle \vec{v}_-(t)\vec{v}_{CM}(0)\rangle$. The general equations in this case have been derived in refs.78,79. The effect of these three additional terms is difficult to estimate because it is quite challenging to measure how much momentum has passed to the environment due to the movement of the ions. One of the ways to measure this is to compare the MD simulations, which explicitly assume momentum conservation only between ions and experimentally measured distinct ion−ion correlations, as proposed in 37.

CONCLUSIONS

In this work, we studied three ILs with different anion/cation mass ratios. We have measured conductivity spectra over a wide frequency range and estimated DC conductivity and conductivity relaxation times over a wide temperature range. Based on the diffusion coefficient at high temperatures, we estimated the ion rearrangement length, marking a crossover from anomalous to normal diffusion regime. This length appears slightly shorter than half of the average distance of the ions assumed in earlier studies. It is important that in the accessible temperature range, this length scale appears essentially temperature-independent. This enables an estimate of ion diffusion at low temperatures, where it is too slow for PFG-NMR. As a result, it provides a way to estimate the inverse Haven ratio at very low temperatures. Our results indicate that H^{-1} decreases with decreasing temperature, but the mechanism of this temperature dependence requires additional investigation. Furthermore, we demonstrate that the distinct ion−ion contributions to conductivity can be estimated using a momentum conservation approach in the center of mass coordinate system. The results from this approach were validated by our MD simulations. It was discovered that the behavior of the anion−anion and cation−cation correlations depend strongly on the anion-to-cation mass ratio, M_-/M_+. In the case of $M_-/M_+ > 1$, the distinct anion−anion correlations show a stronger suppression effect in the conductivity in comparison to the distinct cation−cation correlation. The opposite effect is observed in the case of $M_-/M_+ < 1$. This switching effect was also verified by our MD simulations. A detailed analysis also revealed that not only mass but also the diffusivity of ions plays a role in these correlations, emphasizing the role of ion geometry.

ASSOCIATED CONTENT

Data Availability Statement

The data that support the plots within this paper and another finding of this study are available from the corresponding author upon reasonable request.

Supporting Information

The Supporting Information is available free of charge at https://pubs.acs.org/doi/10.1021/acs.jpcb.3c05568.

Comparison of simulated and experimental densities; simulated inverse Haven ratio; MD simulations of distinct ion−ion contribution to conductivity for all three systems; spatial distribution functions; continuous and intermittent time correlation functions at different mass ratios; snapshots of different groups and radial distribution functions (PDF)

AUTHOR INFORMATION

Corresponding Author

Ivan Popov − *Department of Chemistry, University of Tennessee, Knoxville, Tennessee 37996, United States; University of Tennessee—Oak Ridge Innovation Institute, University of Tennessee, Knoxville, Tennessee 37996, United States;* orcid.org/0000-0002-7235-2043; Email: ipopov@utk.edu

Authors

Md. Dipu Ahmed − *Department of Chemistry, University of Tennessee, Knoxville, Tennessee 37996, United States*

Zhenghao Zhu − *Department of Chemical Engineering, University of Tennessee, Knoxville, Tennessee 37996, United States;* orcid.org/0000-0001-9748-3894

Airat Khamzin − *Institute of Physics, Kazan Federal University, Kazan 420008, Russia;* orcid.org/0000-0001-9741-4346

Stephen J. Paddison − *Department of Chemical Engineering, University of Tennessee, Knoxville, Tennessee 37996, United States;* orcid.org/0000-0003-1064-8233

Alexei P. Sokolov − *Department of Chemistry, University of Tennessee, Knoxville, Tennessee 37996, United States; Chemical Sciences Division, Oak Ridge National Laboratory, Oak Ridge, Tennessee 37831, United States;* orcid.org/0000-0002-8187-9445

Complete contact information is available at: https://pubs.acs.org/10.1021/acs.jpcb.3c05568

Author Contributions

M.D.A. and I.P. performed the dielectric measurements over a wide range of frequencies and analyzed the conductivity data. Z.Z. and S.J.P. performed molecular dynamics simulations. All authors contributed to the discussion of the results and writing of the manuscript.

Notes

The authors declare no competing financial interest.
The computer code used for simulations is available from the corresponding authors upon reasonable request.

■ ACKNOWLEDGMENTS

This work was supported by the National Science Foundation (award CHE-2102425). Computing resources were provided through an ACCESS allocation DMR130078 on Purdue Anvil CPU. A.Kh. is grateful for support by the Kazan Federal University Strategic Academic Leadership Program (Priority-2030).

■ REFERENCES

(1) Watanabe, M.; Thomas, M. L.; Zhang, S.; Ueno, K.; Yasuda, T.; Dokko, K. Application of Ionic Liquids to Energy Storage and Conversion Materials and Devices. *Chem. Rev.* **2017**, *117*, 7190−7239.
(2) Goodenough, J. B.; Park, K.-S. The Li-Ion Rechargeable Battery: A Perspective. *J. Am. Chem. Soc.* **2013**, *135*, 1167−1176.
(3) Suo, L.; Hu, Y.-S.; Li, H.; Armand, M.; Chen, L. A new class of solvent-in-salt electrolyte for high-energy rechargeable metallic lithium batteries. *Nat. Commun.* **2013**, *4*, No. 1481, DOI: 10.1038/ncomms2513.
(4) Zeng, X.; Li, J. Innovative application of ionic liquid to separate Al and cathode materials from spent high-power lithium-ion batteries. *J. Hazard. Mater.* **2014**, *271*, 50−56.
(5) Shah, F. U.; An, R.; Muhammad, N. Editorial: Properties and Applications of Ionic Liquids in Energy and Environmental Science. *Front. Chem.* **2020**, *8*, No. 627213.
(6) Yoo, K. S. Synthesis of TiO2 Materials Using Ionic Liquids and Its Applications for Sustainable Energy and Environment. *J. Nanosci. Nanotechnol.* **2016**, *16*, 4302−4309.
(7) Sippel, P.; Lunkenheimer, P.; Krohns, S.; Thoms, E.; Loidl, A. Importance of liquid fragility for energy applications of ionic liquids. *Sci. Rep.* **2015**, *5*, No. 13922.
(8) Rauber, D.; Hofmann, A.; Philippi, F.; Kay, C. W. M.; Zinkevich, T.; Hanemann, T.; Hempelmann, R. Structure-Property Relation of Trimethyl Ammonium Ionic Liquids for Battery Applications. *Appl. Sci.* **2021**, *11*, No. 5679, DOI: 10.3390/app11125679.
(9) Maass, P.; Meyer, M.; Bunde, A. Nonstandard relaxation behavior in ionically conducting materials. *Phys. Rev. B* **1995**, *51*, 8164−8177.
(10) Gainaru, C.; Stacy, E. W.; Bocharova, V.; Gobet, M.; Holt, A. P.; Saito, T.; Greenbaum, S.; Sokolov, A. P. Mechanism of Conductivity Relaxation in Liquid and Polymeric Electrolytes: Direct Link between Conductivity and Diffusivity. *J. Phys. Chem. B* **2016**, *120*, 11074−11083.
(11) Stacy, E. W.; Gainaru, C. P.; Gobet, M.; Wojnarowska, Z.; Bocharova, V.; Greenbaum, S. G.; Sokolov, A. P. Fundamental Limitations of Ionic Conductivity in Polymerized Ionic Liquids. *Macromolecules* **2018**, *51*, 8637−8645.
(12) Vargas-Barbosa, N. M.; Roling, B. Dynamic Ion Correlations in Solid and Liquid Electrolytes: How Do They Affect Charge and Mass Transport? *ChemElectroChem* **2020**, *7*, 367−385.
(13) MacFarlane, D. R.; Forsyth, M.; Izgorodina, E. I.; Abbott, A. P.; Annat, G.; Fraser, K. On the concept of ionicity in ionic liquids. *Phys. Chem. Chem. Phys.* **2009**, *11*, 4962−4967.
(14) Murch, G. E. The haven ratio in fast ionic conductors. *Solid State Ionics* **1982**, *7*, 177−198.
(15) Noda, A.; Hayamizu, K.; Watanabe, M. Pulsed-Gradient Spin−Echo 1H and 19F NMR Ionic Diffusion Coefficient, Viscosity, and Ionic Conductivity of Non-Chloroaluminate Room-Temperature Ionic Liquids. *J. Phys. Chem. B* **2001**, *105*, 4603−4610.
(16) Sangoro, J. R.; Kremer, F. Charge Transport and Glassy Dynamics in Ionic Liquids. *Acc. Chem. Res.* **2012**, *45*, 525−532.
(17) Angell, C. A. Diffusion—Conductance Relations and Free Volume in Molten Salts. *J. Phys. Chem. A* **1965**, *69*, 399−403.
(18) Bockris, J. O. M.; Hooper, G. W. Self-diffusion in molten alkali halides. *Discuss. Faraday Soc.* **1961**, *32*, 218−236.
(19) Spedding, P. L.; Mills, R. Trace-Ion Diffusion in Molten Alkali Carbonates. *J. Electrochem. Soc.* **1965**, *112*, No. 594, DOI: 10.1149/1.2423614.
(20) Dyre, J. C.; Maass, P.; Roling, B.; Sidebottom, D. L. Fundamental questions relating to ion conduction in disordered solids. *Rep. Prog. Phys.* **2009**, *72*, No. 046501.
(21) Roling, B.; Martiny, C.; Brückner, S. Ion transport in glass: Influence of glassy structure on spatial extent of nonrandom ion hopping. *Phys. Rev. B* **2001**, *63*, No. 214203.
(22) Zhang, Z.; Wheatle, B. K.; Krajniak, J.; Keith, J. R.; Ganesan, V. Ion Mobilities, Transference Numbers, and Inverse Haven Ratios of Polymeric Ionic Liquids. *ACS Macro Lett.* **2020**, *9*, 84−89.
(23) Tokuda, H.; Hayamizu, K.; Ishii, K.; Susan, M. A. B. H.; Watanabe, M. Physicochemical Properties and Structures of Room Temperature Ionic Liquids. 1. Variation of Anionic Species. *J. Phys. Chem. B* **2004**, *108*, 16593−16600, DOI: 10.1021/jp047480r.
(24) Tokuda, H.; Hayamizu, K.; Ishii, K.; Susan, M. A. B. H.; Watanabe, M. Physicochemical Properties and Structures of Room Temperature Ionic Liquids. 2. Variation of Alkyl Chain Length in Imidazolium Cation. *J. Phys. Chem. B* **2005**, *109*, 6103−6110, DOI: 10.1021/jp044626d.
(25) Tokuda, H.; Ishii, K.; Susan, M. A. B. H.; Tsuzuki, S.; Hayamizu, K.; Watanabe, M. Physicochemical Properties and Structures of Room-Temperature Ionic Liquids. 3. Variation of Cationic Structures. *J. Phys. Chem. B* **2006**, *110*, 2833−2839, DOI: 10.1021/jp053396f.
(26) Tokuda, H.; Tsuzuki, S.; Susan, M. A. B. H.; Hayamizu, K.; Watanabe, M. How Ionic Are Room-Temperature Ionic Liquids? An Indicator of the Physicochemical Properties. *J. Phys. Chem. B* **2006**, *110*, 19593−19600, DOI: 10.1021/jp064159v.
(27) Sangoro, J. R.; Serghei, A.; Naumov, S.; Galvosas, P.; Kärger, J.; Wespe, C.; Bordusa, F.; Kremer, F. Charge transport and mass transport in imidazolium-based ionic liquids. *Phys. Rev. E* **2008**, *77*, No. 051202.
(28) Kashyap, H. K.; Annapureddy, H. V. R.; Raineri, F. O.; Margulis, C. J. How Is Charge Transport Different in Ionic Liquids and Electrolyte Solutions? *J. Phys. Chem. B* **2011**, *115*, 13212−13221.
(29) Harris, K. R. Relations between the Fractional Stokes−Einstein and Nernst−Einstein Equations and Velocity Correlation Coefficients in Ionic Liquids and Molten Salts. *J. Phys. Chem. B* **2010**, *114*, 9572−9577.
(30) Harris, K. R. Can the Transport Properties of Molten Salts and Ionic Liquids Be Used To Determine Ion Association? *J. Phys. Chem. B* **2016**, *120*, 12135−12147.
(31) Harris, K. R.; Kanakubo, M. Self-Diffusion Coefficients and Related Transport Properties for a Number of Fragile Ionic Liquids. *J. Chem. Eng. Data* **2016**, *61*, 2399−2411.
(32) Brinkkötter, M.; Mariani, A.; Jeong, S.; Passerini, S.; Schönhoff, M. Ionic Liquid in Li Salt Electrolyte: Modifying the Li+ Transport Mechanism by Coordination to an Asymmetric Anion. *Adv. Energy Sustainability Res.* **2021**, *2*, No. 2000078, DOI: 10.1002/aesr.202000078.
(33) McEldrew, M.; Goodwin, Z. A. H.; Molinari, N.; Kozinsky, B.; Kornyshev, A. A.; Bazant, M. Z. Salt-in-Ionic-Liquid Electrolytes: Ion Network Formation and Negative Effective Charges of Alkali Metal Cations. *J. Phys. Chem. B* **2021**, *125*, 13752−13766.
(34) Molinari, N.; Mailoa, J. P.; Craig, N.; Christensen, J.; Kozinsky, B. Transport anomalies emerging from strong correlation in ionic liquid electrolytes. *J. Power Sources* **2019**, *428*, 27−36.
(35) Molinari, N.; Mailoa, J. P.; Kozinsky, B. General Trend of a Negative Li Effective Charge in Ionic Liquid Electrolytes. *J. Phys. Chem. Lett.* **2019**, *10*, 2313−2319.
(36) Nürnberg, P.; Atik, J.; Borodin, O.; Winter, M.; Paillard, E.; Schönhoff, M. Superionicity in Ionic-Liquid-Based Electrolytes

Induced by Positive Ion−Ion Correlations. *J. Am. Chem. Soc.* **2022**, *144*, 4657−4666.
(37) Dong, D.; Sälzer, F.; Roling, B.; Bedrov, D. How efficient is Li+ ion transport in solvate ionic liquids under anion-blocking conditions in a battery? *Phys. Chem. Chem. Phys.* **2018**, *20*, 29174−29183.
(38) Schoenert, H. J. Evaluation of velocity correlation coefficients from experimental transport data in electrolytic systems. *J. Phys. Chem. A* **1984**, *88*, 3359−3363.
(39) Popov, I.; Biernacka, K.; Zhu, H.; Nti, F.; Porcarelli, L.; Wang, X.; Khamzin, A.; Gainaru, C.; Forsyth, M.; Sokolov, A. P. Strongly Correlated Ion Dynamics in Plastic Ionic Crystals and Polymerized Ionic Liquids. *J. Phys. Chem. C* **2020**, *124*, 17889−17896.
(40) Popov, I.; Khamzin, A.; Matsumoto, R. A.; Zhao, W.; Lin, X.; Cummings, P. T.; Sokolov, A. P. Controlling the Ion Transport Number in Solvent-in-Salt Solutions. *J. Phys. Chem. B* **2022**, *126*, 4572−4583.
(41) Ishai, P. B.; Talary, M. S.; Caduff, A.; Levy, E.; Feldman, Y. Electrode polarization in dielectric measurements: a review. *Meas. Sci. Technol.* **2013**, *24*, No. 102001.
(42) Liu, H.; Luo, X.; Sokolov, A. P.; Paddison, S. J. Quantitative Evidence of Mobile Ion Hopping in Polymerized Ionic Liquids. *J. Phys. Chem. B* **2021**, *125*, 372−381.
(43) Luo, X.; Liu, H.; Paddison, S. J. Molecular Dynamics Simulations of Polymerized Ionic Liquids: Mechanism of Ion Transport with Different Anions. *ACS Appl. Polym. Mater.* **2021**, *3*, 141−152.
(44) Mogurampelly, S.; Keith, J. R.; Ganesan, V. Mechanisms Underlying Ion Transport in Polymerized Ionic Liquids. *J. Am. Chem. Soc.* **2017**, *139*, 9511−9514.
(45) Sprenger, K. G.; Jaeger, V. W.; Pfaendtner, J. The General AMBER Force Field (GAFF) Can Accurately Predict Thermodynamic and Transport Properties of Many Ionic Liquids. *J. Phys. Chem. B* **2015**, *119*, 5882−5895.
(46) Slingsby, J. G.; Vyas, S.; Maupin, C. M. A charge-modified general amber force field for phospholipids: improved structural properties in the tensionless ensemble. *Mol. Simul.* **2015**, *41*, 1449−1458.
(47) Liu, H.; Maginn, E.; Visser, A. E.; Bridges, N. J.; Fox, E. B. Thermal and transport properties of six ionic liquids: An experimental and molecular dynamics study. *Ind. Eng. Chem. Res.* **2012**, *51*, 7242−7254.
(48) Liu, H.; Maginn, E. A molecular dynamics investigation of the structural and dynamic properties of the ionic liquid 1-n-butyl-3-methylimidazolium bis(trifluoromethanesulfonyl) imide. *J. Chem. Phys.* **2011**, *135*, No. 124507.
(49) Bayly, C. I.; Cieplak, P.; Cornell, W.; Kollman, P. A. A well-behaved electrostatic potential based method using charge restraints for deriving atomic charges: the RESP model. *J. Phys. Chem. A* **1993**, *97*, 10269−10280.
(50) Frisch, M. J.; Trucks, G. W.; Schlegel, H. B.; Scuseria, G. E.; Robb, M. A.; Cheeseman, J. R.; Scalmani, G.; Barone, V.; Mennucci, B.; Petersson, G. A.et al. *Gaussian 09*, Revision E.01; Gaussian, Inc.: Wallingford, CT, 2013.
(51) Zhang, Z.; Zofchak, E.; Krajniak, J.; Ganesan, V. Influence of Polarizability on the Structure, Dynamic Characteristics, and Ion-Transport Mechanisms in Polymeric Ionic Liquids. *J. Phys. Chem. B* **2022**, *126*, 2583−2592.
(52) Barbosa, G. D.; Liu, X.; O'Harra, K. E.; Bara, J. E.; Turner, C. H. Charge scaling parameter evaluation for multivalent ionic liquids with fixed point charge force fields. *J. Ionic Liq.* **2022**, *2*, No. 100020.
(53) Abraham, M. J.; Murtola, T.; Schulz, R.; Páll, S.; Smith, J. C.; Hess, B.; Lindahl, E. GROMACS: High performance molecular simulations through multi-level parallelism from laptops to supercomputers. *SoftwareX* **2015**, *1*−*2*, 19−25.
(54) Fong, K. D.; Self, J.; McCloskey, B. D.; Persson, K. A. Ion Correlations and Their Impact on Transport in Polymer-Based Electrolytes. *Macromolecules* **2021**, *54*, 2575−2591.
(55) Bussi, G.; Donadio, D.; Parrinello, M. Canonical sampling through velocity rescaling. *J. Chem. Phys.* **2007**, *126*, No. 014101.
(56) Parrinello, M.; Rahman, A. Crystal Structure and Pair Potentials: A Molecular-Dynamics Study. *Phys. Rev. Lett.* **1980**, *45*, 1196−1199.
(57) Dyre, J. C. The random free-energy barrier model for ac conduction in disordered solids. *J. Appl. Phys.* **1988**, *64*, 2456−2468.
(58) Dyre, J. C. Studies of ac hopping conduction at low temperatures. *Phys. Rev. B* **1994**, *49*, 11709−11720.
(59) Dyre, J. C.; Schrøder, T. B. Universality of ac conduction in disordered solids. *Rev. Mod. Phys.* **2000**, *72*, 873−892.
(60) Schrøder, T. B.; Dyre, J. C. Scaling and Universality of ac Conduction in Disordered Solids. *Phys. Rev. Lett.* **2000**, *84*, 310−313.
(61) Schrøder, T. B.; Dyre, J. C. ac Hopping Conduction at Extreme Disorder Takes Place on the Percolating Cluster. *Phys. Rev. Lett.* **2008**, *101*, No. 025901.
(62) Sangoro, J. R.; Iacob, C.; Naumov, S.; Valiullin, R.; Rexhausen, H.; Hunger, J.; Buchner, R.; Strehmel, V.; Kärger, J.; Kremer, F. Diffusion in ionic liquids: the interplay between molecular structure and dynamics. *Soft Matter* **2011**, *7*, 1678−1681.
(63) Popov, I.; Sacci, R. L.; Sanders, N. C.; Matsumoto, R. A.; Thompson, M. W.; Osti, N. C.; Kobayashi, T.; Tyagi, M.; Mamontov, E.; Pruski, M.; et al. Critical Role of Anion−Solvent Interactions for Dynamics of Solvent-in-Salt Solutions. *J. Phys. Chem. C* **2020**, *124*, 8457−8466.
(64) Suarez, S. N.; Rúa, A.; Cuffari, D.; Pilar, K.; Hatcher, J. L.; Ramati, S.; Wishart, J. F. Do TFSA Anions Slither? Pressure Exposes the Role of TFSA Conformational Exchange in Self-Diffusion. *J. Phys. Chem. B* **2015**, *119*, 14756−14765.
(65) Urahata, S. M.; Ribeiro, M. C. C. Single particle dynamics in ionic liquids of 1-alkyl-3-methylimidazolium cations. *J. Chem. Phys.* **2004**, *122*, No. 024511, DOI: 10.1063/1.1826035.
(66) Sarangi, S. S.; Zhao, W.; Müller-Plathe, F.; Balasubramanian, S. Correlation between Dynamic Heterogeneity and Local Structure in a Room-Temperature Ionic Liquid: A Molecular Dynamics Study of [bmim][PF6]. *ChemPhysChem* **2010**, *11*, 2001−2010.
(67) Kanakubo, M.; Harris, K. R.; Tsuchihashi, N.; Ibuki, K.; Ueno, M. Effect of Pressure on Transport Properties of the Ionic Liquid 1-Butyl-3-methylimidazolium Hexafluorophosphate. *J. Phys. Chem. B* **2007**, *111*, 2062−2069.
(68) Bhargava, B. L.; Balasubramanian, S. Refined potential model for atomistic simulations of ionic liquid [bmim][PF6]. *J. Chem. Phys.* **2007**, *127*, No. 114510.
(69) Rey-Castro, C.; Vega, L. F. Transport Properties of the Ionic Liquid 1-Ethyl-3-Methylimidazolium Chloride from Equilibrium Molecular Dynamics Simulation. The Effect of Temperature. *J. Phys. Chem. B* **2006**, *110*, 14426−14435.
(70) Cadena, C.; Zhao, Q.; Snurr, R. Q.; Maginn, E. J. Molecular Modeling and Experimental Studies of the Thermodynamic and Transport Properties of Pyridinium-Based Ionic Liquids. *J. Phys. Chem. B* **2006**, *110*, 2821−2832.
(71) Liu, Z.; Huang, S.; Wang, W. A Refined Force Field for Molecular Simulation of Imidazolium-Based Ionic Liquids. *J. Phys. Chem. B* **2004**, *108*, 12978−12989.
(72) Morrow, T. I.; Maginn, E. J. Molecular Dynamics Study of the Ionic Liquid 1-n-Butyl-3-methylimidazolium Hexafluorophosphate. *J. Phys. Chem. B* **2002**, *106*, 12807−12813.
(73) Fujii, K.; Fujimori, T.; Takamuku, T.; Kanzaki, R.; Umebayashi, Y.; Ishiguro, S.-I. Conformational Equilibrium of Bis(trifluoromethanesulfonyl) Imide Anion of a Room-Temperature Ionic Liquid: Raman Spectroscopic Study and DFT Calculations. *J. Phys. Chem. B* **2006**, *110*, 8179−8183.
(74) Wang, Y.; Voth, G. A. Unique Spatial Heterogeneity in Ionic Liquids. *J. Am. Chem. Soc.* **2005**, *127*, 12192−12193.
(75) Brehm, M.; Thomas, M.; Gehrke, S.; Kirchner, B. TRAVIS—A free analyzer for trajectories from molecular simulation. *J. Chem. Phys.* **2020**, *152*, No. 164105, DOI: 10.1063/5.0005078.
(76) Humphrey, W.; Dalke, A.; Schulten, K. VMD: Visual molecular dynamics. *J. Mol. Graphics* **1996**, *14*, 33−38.
(77) Lorenz, M.; Kilchert, F.; Nurnberg, P.; Schammer, M.; Latz, A.; Horstmann, B.; Schonhoff, M. Local Volume Conservation in

Concentrated Electrolytes Is Governing Charge Transport in Electric Fields. *J. Phys. Chem. Lett.* **2022**, *13*, 8761−8767.
(78) Pfeifer, S.; Ackermann, F.; Salzer, F.; Schonhoff, M.; Roling, B. Quantification of cation-cation, anion-anion and cation-anion correlations in Li salt/glyme mixtures by combining very-low-frequency impedance spectroscopy with diffusion and electrophoretic NMR. *Phys. Chem. Chem. Phys.* **2021**, *23*, 628−640.
(79) Roling, B.; Miß, V.; Kettner, J. J. E.; Materials, E. Ion Dynamics in Concentrated Electrolyte Solutions: Relating Equilibrium Fluctuations of the Ions to Transport Properties in Battery Cells. *Energy Environ. Mater.* **2022**, No. e12533, DOI: 10.1002/eem2.12533.

https://doi.org/10.1021/acs.jpcb.3c05568
J. Phys. Chem. B 2023, 127, 10411−10421

The preprint of manuscript for publication in the Journal of Chemical Physics:

Proton transport mechanisms in aqueous acids: Insights from *ab initio* molecular dynamics simulations

Zhenghao Zhu,[1] Alexei P. Sokolov,[2,3] and Stephen J. Paddison[1,a)]

AFFILIATIONS

[1]Department of Chemical & Biomolecular Engineering, University of Tennessee, Knoxville, Tennessee 37996, USA

[2]Department of Chemistry, University of Tennessee, Knoxville, Tennessee 37996, USA

[3]Chemical Sciences Division, Oak Ridge National Laboratory, Oak Ridge, Tennessee 37831, USA.

[a)]**Author to whom correspondence should be addressed:** spaddison@utk.edu

Abstract

The solvation and transport of protons in aqueous solutions of phosphoric acid (PA), sulfuric acid (SA), and nitric acid (NA) were studied using AIMD simulations. Systems with acid-to-water ratios of 1:1 and 1:3 were examined to understand the similarities and differences in transport mechanisms. The solvation structure of H_3O^+ in these systems is similar to that in slightly acidic water, with variations in the strength of hydrogen bonds (H-bonds) donated by acid molecules. In aqueous PA systems, strong H-bonds between PA molecules are slightly affected by water, leading to significantly greater H_3O^+ diffusion compared to aqueous SA and NA systems. This enhanced diffusion is attributed to the participation of PA molecules in H_3O^+ transport, where the PA molecule can shuttle a proton for H_3O^+, facilitating a large displacement via collective proton hopping. This shuttling mechanism is prominent in aqueous PA but rare in aqueous SA and absent in aqueous NA. Moreover, the decomposition of H_3O^+ diffusion into vehicular and structural components indicates that the higher diffusion in aqueous PA is primarily due to the structural mechanism with the aid of PA molecules. In the aqueous NA systems, the vehicular diffusion is dominant at low water contents and the increase of water content improves the structural diffusion by forming connected H-bonds with water molecules. Our findings elucidate the role of acid molecules in proton transport within their aqueous solutions, thereby advancing the fundamental understanding of proton transport mechanisms.

I. INTRODUCTION

The proton is the only cation without any electrons and thereby may readily be transferred along a hydrogen bond (H-bond). This simple chemical reaction plays a key role in various fields ranging from biochemical processes to electrochemical technologies.[1-4] To understand the mechanisms underlying proton transport, extensive research has been devoted to revealing the molecular structures and dynamics in different environments, especially in aqueous solutions.[5-19] Two protonic defects, i.e. hydronium H_3O^+ and hydroxide OH^-, serve as a charge carrier to provide ionic conductivity in many materials.[9, 20] These protonic defects can be transported via two major mechanisms: (1) a vehicular mechanism where the defect moves via a molecular vehicle; and (2) a structural diffusion mechanism, in which the defect diffuses structurally by sequentially transferring protons between molecules within a H-bond network.[4, 10-12, 21-23] The latter one may occur through collective proton transfers within a strong H-bond chain and this idea was originally proposed by Grotthuss.[2, 24] Recent studies reveal that there are several differences in the solvation structure and dynamics of these two ions. The hydroxide ion possesses four accepting and one donating H-bond forming a stable configuration that leads to slow transport.[25] However, the hydronium ion prefers to have three donating H-bonds forming an Eigen cation. Once a proton transfers to a neighboring water molecule from the H_3O^+, there is a transition state where a proton is shared by two water molecules equally (i.e., Zundel ion).[26] This transport mechanism is referred to as the Eigen-Zundel-Eigen (EZE) mechanism.[27, 28] However, more complex solvation structures of the hydronium have been observed in slightly acidic water[11, 12, 27, 29, 30] These results indicate that the Eigen ion is distorted with one strong and two weak H-bonds and the coordinated water in the strong H-bond is denoted as the "special pair". More importantly, this special pair is dynamically altering among the water molecules of the first solvation shell, referred to as the "special pair dance". Recently, Voth et al. deconvoluted the distorted structures of a H_3O^+ and resolved an anisotropy reorientation relaxation time of 1 – 2 ps.[13]

The solvation and transport properties of hydrated protons are influenced by the local environment including confinement and hydration.[6, 18, 31-36] Tuckerman et al. suggested that the functional group in model proton exchange membranes is capable of participating in H^+ transport at low hydration, facilitating H_3O^+ diffusion.[6, 31, 37] Paddison et al. illustrated the effects of the confinement with bare and fluorinated carbon nanotubes on the proton transfer.[33, 34] In addition, reactive molecular dynamics (MD) simulations were used to study the charge transport in proton exchange

membranes (PEMs) via vehicular and structural diffusion mechanisms.[17, 38-41] These prior studies provoke the following pair of questions: What is the solvation structure of H_3O^+ in the presence of either strong or weak acid molecules? How does the strength of the acid affect H^+ diffusion via vehicular and structural mechanisms?

In an aqueous acid system, the acid molecule acts as a proton donor and the water molecules as proton acceptors forming protonic defects that contribute to the protonic conductivity of the solution. There are a variety of factors controlling the diffusion of protons. One major factor is the relative strength of the acid. The stronger the acid, the more $H^+(H_2O)$ in the acid solution. Therefore, a strong acid solution may contain a greater number of H_3O^+ which may result in a significant vehicular component in the transport of protons. The water content also plays an important role in the conductivity of an acid solution, which suggests that there exists a maximum with regard to the acid concentration. This phenomenon has been observed in various acid solutions.[42] In contrast, when the acid is weak, the acid retains protons which may result in lower conductivity (e.g., acetic solution with a pK_a of 4.76). To understand the diffusion of protons, it is necessary to take into consideration the chemical structure, the acidity, and the ability of the acid species to exchange protons with a relatively low energy barrier.

Phosphoric acid (PA), sulfuric acid (SA), and nitric acid (NA) are three canonical acids, which are important chemicals in agriculture, food and cosmetic industries, and atmospheric science.[43-46] These acids possess distinct features including acidity, molecular structure, and proton donor/acceptor sites (see Fig. 1). PA is a weak acid (pK_a = 2.1) and has the highest intrinsic proton conductivity and a peculiar molecular structure (3 OH proton donors and one unprotonated oxygen proton acceptor). Pure PA and its solution have been extensively investigated with experiments and simulations.[42, 47-52] SA is widely considered a strong acid (pK_a = −3) and its dilute solution displays high conductivity.[53] NA is a monoprotic acid with a planar molecular structure and is also considered a strong acid (pK_a = −1.4). These acids are soluble in water forming protonic defects including H_3O^+ by dissociation and show high conductivity, and hence they and their derivatives are widely used in electrochemical devices, such as PA/SA/NA-doped polybenzimidazole (PBI).[54, 55] The transport of protons in these bulk solutions is important and has attracted substantial attention.

In this work, *ab initio* molecular dynamics (AIMD) simulations were utilized to examine the transport mechanisms aqueous H_3PO_4, H_2SO_4, and HNO_3 at two different ratios of the acid to water: 1:1 and 1:3. This paper is organized as follows. The computational methods are first described followed by the results and discussion about the solvation and transport of protons in these systems. Finally, major findings are summarized in the conclusion section.

II. SIMULATION DETAILS

All AIMD simulations were performed using the CPMD code.[56, 57] Aqueous acid systems were constructed consisting of ratios of 1:1 or 1:3 acid molecules to water molecules within a cubic simulation box with a side length of ~16 Å. The specifics of each system are presented in Table S1 in the Supplementary Information. To allow for dispersion forces within the Kohn-Sham formulation of density functional theory, we employed dispersion-corrected atomic core pseudopotentials (DCACP)[58, 59] and the B-LYP exchange-correlation functional.[60, 61] Kohn-Sham orbitals were expanded using a plane-wave basis set up with kinetic energy cutoff of 80 Ry. To enhance the adiabatic decoupling of nuclear and electronic dynamics, and allow a larger time step 4 au, we assigned the mass of deuterium to the hydrogen atoms and set the fictitious electron mass to $\mu = 500$ au. Each system was pre-equilibrated using a classical force field[62] for a duration of 10 ns, followed by 15-20 ps equilibration with AIMD at the desired temperatures using a massive Nose-Hoover chain thermostat.[63] Subsequently, the equilibrated configuration was utilized for the production run, lasting approximately 60 - 100 ps, within a microcanonical (NVE) ensemble. In addition to the aforementioned systems, we conducted a simulation of 104 H_2O molecules and an extra proton at the same level of theory for comparative analysis.

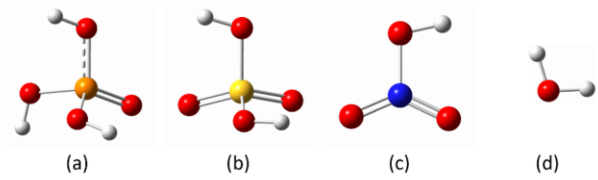

FIG. 1. Chemical structures of (a) phosphoric acid (PA), (b) sulfuric acid (SA), (c) nitric acid (NA), and (d) water (W). The p*K*a values for these acids are 2.1, −3, and −1.4, respectively.

III. RESULTS AND DISCUSSION

A. Distribution of protonated species

AIMD simulations explicitly allow for the breaking and forming of covalent bonds, leading to an equilibrium distribution of the various protonated/deprotonated states of the acid and water molecules. In order to identify the protonated species in these systems, each hydrogen atom is assigned to the nearest particular oxygen atom. Oxygen atoms associated with two hydrogen atoms are identified as a water oxygen, O_W, while oxygen atoms with three assigned hydrogen atoms are treated as hydronium ions denoted by O^*. Similarly, the oxygen atoms belonging to the acid molecules are denoted as O_A. The fraction of water and acid molecules in their various states of protonation were calculated and the results collected in Table I.

There is a small number of positively charged acidic species in the aqueous PA systems due to the similar proton affinity of PA and H_2O. For the strong acids, these species are negligible, but the water appears to trap protons as H_3O^+ ions, which may consequently retard the structural diffusion of the protons. The increase in the ratio of water to an acid has minimal influence on the neutral species in aqueous PA systems but significantly decreases the neutral species in aqueous SA and NA. Although SA is a strong acid, SA molecules tend to donate only one proton to the water molecules even when the ratio of water to acid is 3. It is worth noting that there are about 10% neutral species in the SA3H system, in contrast to the findings of a previous study[53] where the authors stated that all sulfuric acid molecules were dissociated although short-lived neutral sulfuric acid molecules were observed because the transiently shared protons are included. In contrast, the addition of water in PA systems gives rise to a slight increase in neutral phosphoric acid from 81.5 to 81.9% due to the reduction of self-dissociation of the PA molecules, suggesting that the self-dissociation of PA decreases with increasing water content. With respect to H_3O^+, there is a small number of H_3O^+ in the PA systems due to its weak acidity. However, most water molecules are protonated via the acid molecules in the SA systems and an increase in water further promotes the dissociation of protons by SA even facilitating dissociation of a second proton. The significant fraction of H_3O^+ in the aqueous SA systems contributes to the high conductivity via vehicular diffusion. The acidity of NA is moderately strong, which leads to a significant increase in the proton dissociation from NA molecules with the addition of water (i.e., NA3H).

TABLE I. Computed fractions (%) of acid and water molecules in their different states of protonation in the studied aqueous acid systems.

Species	$H_4PO_4^+$/ $H_3SO_4^+$/ $H_2NO_3^+$	H_3PO_4/ H_2SO_4/ HNO_3	$H_2PO_4^-$/ HSO_4^-/ NO_3^-	HPO_4^{2-}/ SO_4^{2-}	H_3O^+	H_2O
PA1H	5.6	81.5	12.8	0.06	7.3	92.7
PA3H	2.3	81.9	15.7	0.05	4.5	95.5
SA1H	0.03	46.7	53.0	0.26	53.5	46.5
SA3H	-	10.1	88.9	1.03	30.3	69.7
NA1H	-	88.3	11.7	-	11.7	88.3
NA3H	-	49.0	51.0	-	17.0	83.0

B. H-bond structure

The primary aim of this work is to provide insight into how the acid molecules affect the solvation structure of protons and H_2O and elucidating proton transport mechanisms in terms of the molecular structures and acidities. To this end, we start with exploring the structural properties of the hydrogen bonding. Fig. 2 shows the OO radial distribution functions (RDFs) excluding the intra-molecular pairs for clarity. To gain additional insight into the compositions of the peaks, we decomposed the OO RDFs into three pairs: both oxygen atoms from water molecules denoted by O_WO_W; one oxygen from water and the other from acid molecules denoted by O_WO_A; and both oxygen atoms from acid molecules denoted by O_AO_A. Note that all oxygen atoms are not distinguished based on their protonation states, namely, the O_W includes neutral water and hydronium ion oxygen atoms. Compared to the OO RDF for the protonated water system, the first peak becomes weaker but shifts to short or long distances to various extents. Specifically, the first peak is located at ~2.6 Å in the PA1H system while the first peak moves to 2.7 Å in PA3H which is identical to that in the protonated water system, indicating that the presence of water molecules at the ratio of 1:1 does not change the strong overall H-bonds but the addition of water molecules makes the overall H-bonds weaker.[64, 65] However, the corresponding peak for SA1H and NA1H systems is located at ~3.1 Å which is much longer than that in the protonated water system. Obviously, there is a shoulder on the left side of the peak in SA1H while the shoulder and the peak switch their roles in SA3H. A similar phenomenon occurs in the aqueous NA systems changing from a broad peak to two equivalent flat peaks.

In aqueous acids, hydrogen bonds exist between the different species, leading to distinct local environments for proton transfer. Figs. 2b-d depict the OO RDFs of different species for the 1:1 aqueous acid systems. For the H-bonds between water species (including H_3O^+), the positions of the first peak shifts to the left as the acidity increases, suggesting that there are more H_3O^+ ions in strong acids forming stronger H-bonds than between water molecules. The H-bond between water and NA molecules is the weakest one while the H-bonds between water and PA or SA molecules are similar despite the difference in their acidities. The scenarios are different in the strong H-bonds between aqueous species and PA or SA molecules. In aqueous PA systems, PA molecules donate protons to aqueous species (mainly H_2O) due to the high concentration of OH groups. SA molecules act as proton-acceptors in H-bonds with aqueous species (mainly H_3O^+) (see Fig. S1). It is commonly understood that neat PA has a high intrinsic proton conductivity because of the strong and polarizable H-bonds between the PA molecules.[42, 47, 50-52, 66] Fig. 2(d) shows that the position of the first peak is located at the shortest distance (2.62 Å) among these aqueous acids, implying that the strong H-bonds between the PA molecules are essentially not influenced by the presence of water molecules. Interestingly, the addition of water molecules alters the intensities of the first OO RDF peaks but not the positions of the corresponding peaks (Fig. 2(f-h)).

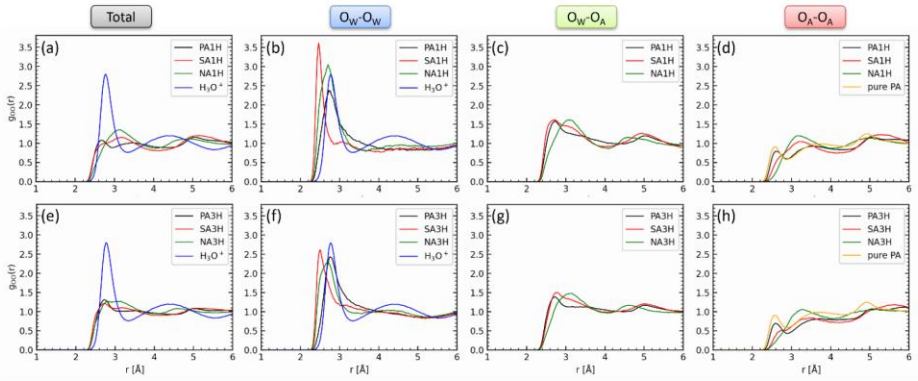

FIG. 2. RDFs of OO pairs from different species: Total (a and e); both from water species (b and f); oxygen atoms of water and acid molecules (c and g); and oxygen atoms of acid molecules (d and h). The oxygen atoms from the same molecule are excluded for clarity.

C. Solvation structure of H_3O^+

Of particular interest is the influence of the acid on the solvation structure of the hydronium ions. For this purpose, we calculated the O^*O and O^*H RDFs for these aqueous acid systems as shown in Fig. 3, in which O^* denotes the hydronium oxygen atoms, and O_W and O_A represent water and acid oxygen atoms, respectively. For comparison, the O_WO RDFs are also illustrated in Fig. 4. As seen in Fig. 4(a, d), the positions of the first peak for the three aqueous acid systems are similar but their intensities vary due to the different number of water molecules in these systems. The addition of water makes the difference in intensity smaller. The O^*H RDFs are shown in Fig. 3(c and f), in which the first sharp peak clearly indicates the covalent bond OH, and the second one represents the H-bond that is consistent with the trend as the O^*O_W RDFs (Fig. 3(a and d)). It is worth noting that there is a small shoulder on the second peak of O^*H RDFs corresponding to the weak accepting H-bond of the H_3O^+ ions. A significant difference in the H-bonds appears in the pair of hydronium ion oxygen and acid oxygen atoms due to the various protonated states of the acid molecules. Specifically, the H-bond is stronger in the PA systems than in the other two aqueous acid systems partially because of the potent proton-donating capability of neat PA. In the aqueous SA and NA systems, there are two characteristic peaks related to the H-bond, which are located at identical positions but clearly possess distinct features. The first peak is dominant in aqueous SA systems while the second one is dominant in the aqueous NA systems. The addition of water molecules weakens the difference between the two peaks in these two aqueous acid systems. These results clearly suggest that the H-bond structure is influenced by the acid molecules and the water content.

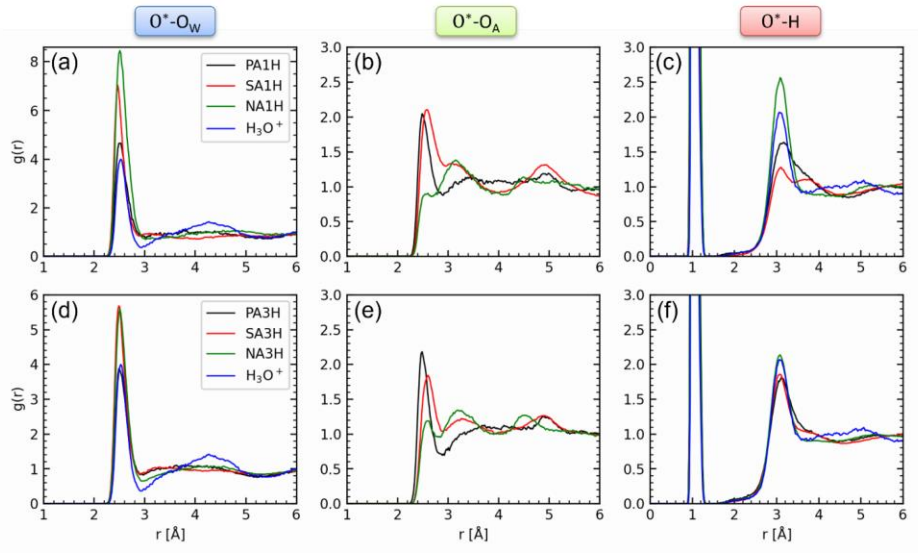

FIG. 3. RDFs of O^* with other atoms: oxygen atom of a water molecule (a and d); oxygen atom of an acid molecule (b and e); and all hydrogen atom (c and f).

Fig. 4 displays the RDFs of the water oxygen with other atoms from different molecular species. The position of the first peak of the O_WO_W RDFs is located at ~2.8 Å in good agreement with results from an X-ray diffraction experiment of 1.2 mol/L sulfuric acid solution at 20 °C,[67] indicating that the H-bonding between water molecules is weaker than that between H_3O^+ and H_2O. This phenomenon is consistent with previous studies.[11, 12, 53, 68, 69] The acid has a very small influence on the hydrogen bonding between the water molecules. Fig. 4(b and e) shows that the strength of the H-bonds between water and acid molecules is as follows: PA > SA > NA. It should be emphasized that this order is different from that of the acidity of these acid solutions (i.e., SA > NA >> PA). The first peak of the O_WH RDFs resembles that of the protonated water system where the covalent bonds in the water molecules is sharper than that of the H_3O^+ ion. However, the second peak moves a short distance to varying extents due to the number of H_3O^+ ions in the systems.

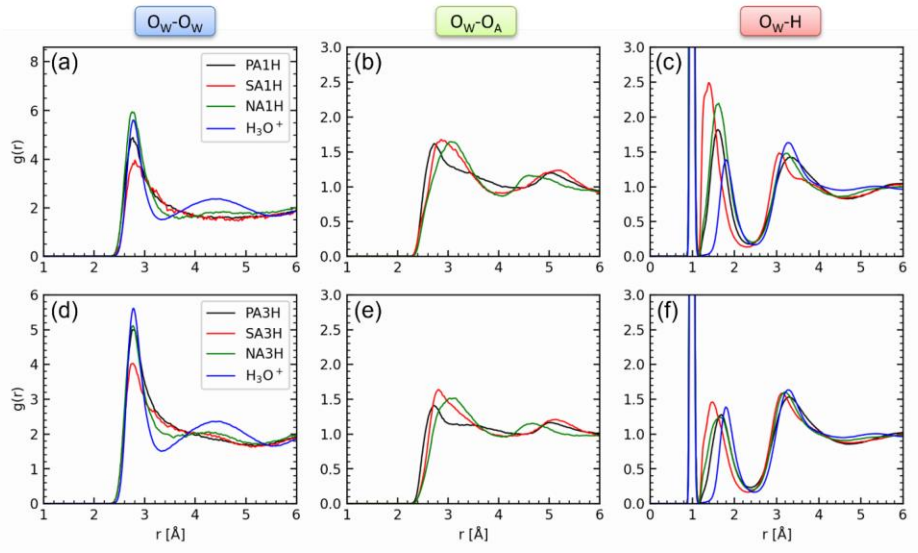

FIG. 4. RDFs of the water oxygen atom with other atoms: oxygen atom of the water molecule (a and d); oxygen atom of the acid molecule (b and e); and all hydrogen atoms (c and f).

D. Solvation patterns of H_3O^+ and H_2O

Proton transfer is significantly influenced by the solvation structure of H_3O^+ and its neighboring H_2O.[5, 12, 14, 25, 31] To elucidate the local surrounding H-bond network of H^+(aq), probability distribution functions for the solvation pattern were calculated as the probability of finding a H_3O^+ or H_2O that donates *m* H-bonds and accepts *n* H-bonds (denoted as *m*D*n*A) according to the H-bond criteria: the distance between donating oxygen (O_d) and accepting oxygen (O_a) O_dO_a < 3.5 Å; the distance between accepting oxygen and donating hydrogen (H_d) O_aH_d < 2.5 Å; and the angle $\angle O_aO_dH_d$ < 30°. Furthermore, a reaction coordinate is defined as $\delta = |r(O_aH) - r(O_dH)|$ for proton transfer events occurring along the H-bond $O_a\cdots H - O_d$. Previous studies[13, 27] revealed that H_3O^+ primarily forms three dynamic donating H-bonds with water or acid molecules in the first solvation shell, and one of the three H-bonds is stronger than the other two, referred to as the "special pair" (i.e., δ_{min}). The water molecule in this special pair, which acts as the proton acceptor, needs to adjust its coordination to readily receive the proton from the H_3O^+. These coordination fluctuations are the rate-limiting step for proton transport.[11, 12, 70] Therefore, it is also crucial to

analyze the solvation pattern distribution for the H_2O in the special pair at the proton transfer transition state ($\delta_{min} < 0.1$ Å). The results are presented in Tables II and III along with the representative solvation patterns for active H_3O^+ in these aqueous acid systems (Fig. S2).

In the slightly acidic water system, the solvation pattern of 3D0A is dominant (90.4%). This dominance of 3D0A is also evident in all aqueous acid systems, albeit with varying percentages lower than in the acidic water system. At the proton transfer transition state, the prevalent solvation pattern for H_3O^+ remains 3D0A, although the population becomes lower. Correspondingly, the special pair water exhibits the highest population of the 2D1A solvation pattern in all studied systems at the proton transfer transition state. This configuration corresponds to the Zundel ion, featuring two water molecules with the same solvation pattern (see Table III). In this scenario, proton transfer occurs readily between the two water molecules with a very low energy barrier. These findings indicate that the dominating solvation pattern 3D0A of the H_3O^+ persists in the aqueous acids even at the transition state, when compared to its prevalence in acidic water. However, the solvation pattern distribution of H_2O is influenced by the presence of acid molecules. Specifically, in acidic water, the dominant solvation configuration is 2D2A (54.8%), with 2D1A and 1D2A patterns having similar populations (16.7% and 12.2% respectively). In the aqueous PA systems, the population of the 2D2A configuration remains the highest, but their values decrease to 31.4 and 30.9% in PA1H and PA3H, respectively. Nevertheless, as the acid strength increases, the highest population shifts from 2D2A to 2D1A, with stronger acids favoring the dominance of the 2D1A solvation pattern. This trend is attributed to the reduced presence of water molecules in strong acid solutions and the steric hindrance imposed by the larger acid molecules, which hinders them from donating the second H-bond to H_2O. Interestingly, the active special pair water ($\delta_{min} < 0.1$ Å) consistently exhibits the highest population of the 2D1A pattern in all systems. This suggests the occurrence of the Eigen-Zundel-Eigen (i.e., EZE) mechanism, even though the H_3O^+ ion forms three H-bonds with either water or acid molecules (i.e., an Eigen-like ion). For this Eigen-like ion, the special patterner may involve acid molecules with various protonation states (see Table S2).

Table II. Probability distribution (%) of solvation patterns.

O*		1D	2D	3D	4D
PA1H	0A	0.09	8.86	85.54	0.26
	1A	0	0.29	4.96	0.01
PA3H	0A	0.07	7.28	83.56	0.2
	1A	0	0.46	8.4	0.01
SA1H	0A	0.36	14.09	83.31	0.62
	1A	0	0.17	1.44	0
SA3H	0A	0.08	7.4	87.74	0.32
	1A	0	0.27	4.18	0.02
NA1H	0A	0.13	9.27	84.55	2.09
	1A	0	0.26	3.62	0.07
NA3H	0A	0.03	5.38	86.16	1.64
	1A	0	0.24	6.45	0.08
H_3O^+	0A	0	1.09	90.44	0
	1A	0	0.09	8.37	0
O_W		0D	1D	2D	3D
PA1H	0A	0.16	0.5	0.47	0
	1A	2.96	19.28	29.76	0.32
	2A	1.33	13.07	31.43	0.27
	3A	0	0.11	0.32	0
PA3H	0A	0.29	1.05	0.89	0
	1A	2.63	18.13	29.41	0.25
	2A	1.28	13.27	30.94	0.24
	3A	0.03	0.4	1.18	0
SA1H	0A	0.07	0.12	0.11	0
	1A	3.81	25.92	41.6	0.63
	2A	1.05	8.27	18.06	0.31
	3A	0	0	0.03	0
SA3H	0A	0.11	0.39	0.36	0
	1A	2.27	19.58	41.01	0.48
	2A	0.88	9.59	24.72	0.26
	3A	0	0.08	0.23	0
NA1H	0A	0.17	0.54	0.38	0.01
	1A	4.77	23.26	26.46	0.83
	2A	2.28	15.61	24.57	0.8
	3A	0.02	0.11	0.18	0
NA3H	0A	0.18	0.82	0.71	0.02
	1A	2.54	18.54	32.68	0.93
	2A	1.14	12.33	28.38	0.82
	3A	0.02	0.21	0.67	0.02

H_3O^+	0A	0.08	0.41	0.45	0
	1A	0.65	7.59	16.73	0
	2A	0.48	12.18	54.82	0
	3A	0.01	0.68	5.71	0

Table III. Probability distribution (%) of solvation patterns at $\delta_{\min} < 0.1$ Å.

O*		1D	2D	3D	4D
PA1H	0A	0.31	15.02	73.93	0.31
	1A	0	0.78	9.61	0.04
PA3H	0A	0.2	11.32	73.88	0.29
	1A	0	1.16	13.01	0.04
SA1H	0A	1.3	22.44	71.84	0.87
	1A	0.02	0.6	2.9	0.02
SA3H	0A	0.31	12.83	78.21	0.47
	1A	0	0.79	7.34	0.02
NA1H	0A	0.49	18.25	72.22	2.14
	1A	0	0.76	5.94	0.15
NA3H	0A	0.16	10.2	76.07	1.8
	1A	0	0.82	10.74	0.17
H_3O^+	0A	0	2.38	80.12	0
	1A	0	0.15	17.35	0
O_W^{1x}		0D	1D	2D	3D
PA1H	1A	0.43	16.96	68.93	0.54
	2A	0.02	1.46	11.52	0.02
PA3H	1A	0.34	14.33	70.81	0.25
	2A	0	1.52	12.41	0
SA1H	1A	1.76	25.96	66.02	0.79
	2A	0.04	1.17	4.27	0.04
SA3H	1A	0.56	15.81	73.15	0.57
	2A	0.03	1.21	8.6	0.04
NA1H	1A	1.15	22.37	67.82	1.77
	2A	0.06	1.18	5.55	0.07
NA3H	1A	0.36	13.01	70.83	1.88
	2A	0	1.12	12.51	0.17
H_3O^+	1A	0.07	3.48	73.62	0.07
	2A	0	0.35	22.33	0.02

E. Energetics of proton transfer

The H-bond structure between different molecular species has been discussed above. Proton transfer along the H-bonds is an elementary step in the structural diffusion of protons. Energy profiles, $A(\delta)$, provides energetics of proton transfer along the reaction coordinate δ, which may be defined as:

$$A(\delta) = -k_B T \ln P(\delta)$$

where k_B is the Boltzmann constant, and T is the absolute temperature. The reaction coordinate is defined as $\delta = |r(\mathrm{O_aH}) - r(\mathrm{O_dH})|$ for proton transfer events occurring along the H-bond $\mathrm{O_a{\cdots}H-O_d}$. $P(\delta)$ is the probability distribution of δ, which is affected by the proton donor-acceptor distance $R_{\mathrm{O_aO_d}}$ (see Fig. S3). The computed free energy profiles for proton transfer are shown in Fig. 5. Generally, the free energy profiles are symmetrical double-well shaped with barriers at $\delta = 0$. In the PA1H system, the energetic barrier for proton transfer from hydronium ion to water molecule is ~1.1 kcal/mol while the barrier for proton transfer from an H_3O^+ ion to PA molecule is slightly lower (0.9 kcal/mol). Surprisingly, an increase in the number of water molecules per PA increases the barrier (1.2 kcal/mol) for proton transfer from H_3O^+ ion to H_2O but lowers the barrier (0.7 kcal/mol) for that from H_3O^+ to a PA molecule. The most probable δ values are almost identical (~0.48 Å). However, proton transfer barriers in proximity to PA molecules are much higher than those near H_3O^+ ions. It is interesting to note that the equilibrium distance for proton transfer between the PA molecules is ~0.65 Å which is similar to that in pure PA.[65] In the SA1H system, the proton transfer barrier from H_3O^+ to H_2O is the lowest amongst all aqueous acid systems (0.4 kcal/mol), while in the SA3H system, this energy barrier for proton transfer is ~0.8 kcal/mol which is twice as high as in SA1H system. Moreover, there is a large penalty for transferring a proton back to the SA molecule from H_3O^+ due to the strong acidity of SA and weak basicity of HSO_4^-. The strong acidity of the SA molecules also gives rise to a very high barrier for proton transfer between SA molecules. This phenomenon, not surprisingly, occurs in the aqueous NA systems although the NA is not as acidic as the SA. In addition, the aqueous NA system is the only one where the addition of water molecules slightly lowers the proton transfer barrier from H_3O^+ to H_2O.

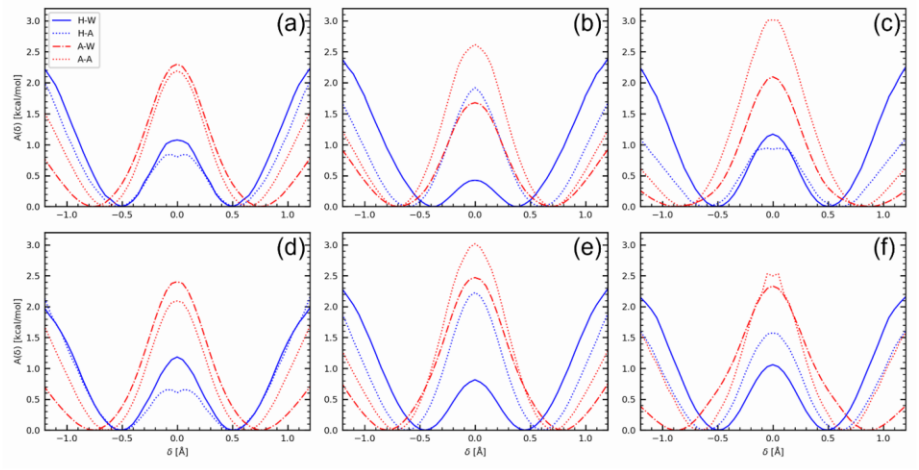

FIG. 5. Energy profiles for proton transfer between different molecular species in (a) PA1H, (b) SA1H, (c) NA1H, (d) PA3H, (e) SA3H, and (f) NA3H.

F. Relaxation time of H_3O^+

To elucidate the structural diffusion of the protons, it is important to estimate relaxation times, lifetimes, and reaction rates. Time-dependent population correlation functions have been extensively employed in a variety of systems.[7, 8, 13, 64, 71-73] Here the continuous correlation function for protons was calculated according to the following equation:

$$C_c(t) = \frac{\langle h(0) \cdot H(t) \rangle}{\langle h \rangle}$$

where $h(0)$ and $H(t)$ are the indicators for the H_3O^+ at initial time $t = 0$ and t, respectively. If the targeted hydronium ion O* retains its identity during the period from time 0 to t, then $H(t) = 1$; otherwise, $H(t) = 0$. This "history-dependent" correlation function includes fast proton rattling and long-range proton diffusion behavior. Since proton rattling does not contribute to long-range diffusion, this process can be excluded by defining the proton rattling event as a proton transferring between two oxygen atoms without visiting a third oxygen atom. The relaxation time of these different time-scale events may be extracted by fitting the function to a bi-exponential function:

$$C_c(t) = a_1 exp\left[-\left(\frac{t}{\tau_1}\right)\right] + a_2 exp\left[-\left(\frac{t}{\tau_2}\right)\right]$$

where a_1 and a_2 are weighting factors satisfying $a_1 + a_2 = 1$, and τ_1 and τ_2 represent two separate relaxation times. The lifetime, τ_{exch}, of H_3O^+ can be calculated with

$$\tau_{\text{exch}} = \int_0^\infty C_c(t)\, dt.$$

Fig. 6(a) presents the continuous population correlation functions for H_3O^+ by including proton rattling. The continuous population correlation function including rattling for the six systems decays very quickly (~ 2 ps). In the aqueous strong acid systems, the hydronium ion has a long lifetime, but the increase in water content makes it decay quickly. This may be because there are more acid molecules around the H_3O^+ in the 1:1 systems leading to a smaller probability for the hydronium ion to transfer a proton to a neighboring molecule. The addition of water molecules changes the local environment of the hydrated protons in which more water molecules coordinate with the H_3O^+ and the energetic penalty for proton transfer between an H_3O^+ ion and an H_2O is small as shown in Fig. 5. However, in the weak aqueous PA systems, the barriers for a hydronium ion to transfer a proton to water or PA molecules are identically low, which gives rise to the fastest decay occurring in aqueous PA systems. The short lifetime caused by the fast rattling does not mean that the proton can transport fast via the Grotthuss mechanism. Thus, the long timescale for proton diffusion is contained in the continuous population correlation functions excluding the rattling (Fig. 6(b)). In this case, the decay process becomes significantly slow (beyond 30 ps for some systems). For the aqueous PA systems, the lifetime of H_3O^+ is the longest (around 17 ps) among the studied systems (see Table IV). It is surprising to note that the lifetime of H_3O^+ in NA1H is equally long as that in the aqueous PA systems. The reasons for the long relaxation times in the three systems is likely different. In both aqueous PA systems, strong H-bonds trap the protons as H_3O^+, resulting in rapid rattling rather than effectively transferring to an adjacent molecule (~130 fs and ~17 ps for including and excluding rattling, respectively). Nevertheless, weak H-bonds and less coordinating water molecules give rise to the long lifetime of hydronium ions in NA1H when excluding rattling. This may lead to the dominant vehicular diffusion of protons in NA1H. An increase in the ratio of water to NA molecules significantly shortens the H_3O^+ lifetime, which may improve the structural diffusion of protons in NA3H. Interestingly, the opposite trend was observed in the aqueous SA systems. The relaxation time of H_3O^+ is very short in SA1H and the addition of water molecules slightly increases the relaxation time. This could be ascribed to a significant

number of H_3O^+ in the aqueous SA systems and a further increase of dissociated protons may cause the "traffic jam" of proton in which there are less productive and forward proton transfers from the H_3O^+ to the water molecule.[32]

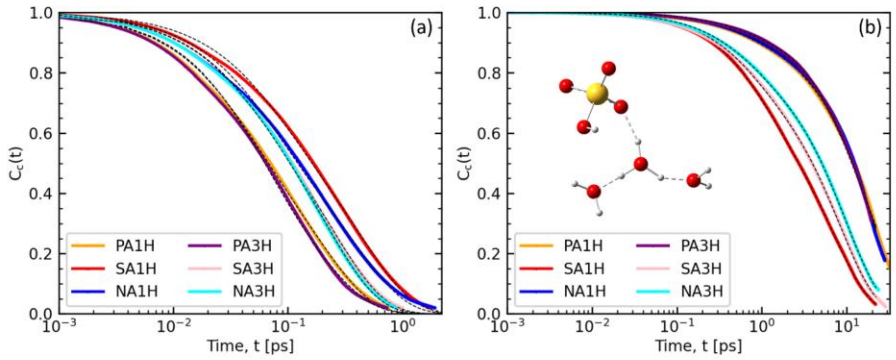

FIG. 6. Continuous population correlation functions $C_c(t)$ for H_3O^+ at two conditions: (a) including proton rattling; and (b) excluding proton rattling.

Table IV. Calculated relaxation times (in ps) including and excluding rattling for H_3O^+ in simulated aqueous acid systems. The fitting results for the function excluding rattling are listed in parentheses.

	a_1	τ_1	τ_2	τ_{exch}
PA1H	0.37 (0.07)	0.034 (0.570)	0.198 (19.223)	0.138 (17.861)
PA3H	0.36 (0.04)	0.034 (0.458)	0.170 (18.139)	0.121 (17.396)
SA1H	0.33 (0.28)	0.068 (0.866)	0.455 (7.080)	0.328 (5.315)
SA3H	0.28 (0.20)	0.043 (0.655)	0.260 (8.309)	0.199 (6.809)
NA1H	0.39 (0.05)	0.059 (0.408)	0.401 (18.067)	0.268 (17.131)
NA3H	0.24 (0.15)	0.038 (0.587)	0.229 (9.690)	0.184 (8.288)

Based on the above discussion, we cannot clearly correlate the local environment and energy barriers for proton transfer around H_3O^+ to the long-range diffusion of protons. It seems to be impossible for the aqueous PA systems to achieve high conductivity if an H_3O^+ is transported without the aid of PA molecules due to the long lifetime of H_3O^+ excluding rattling. To gain further insight into the dynamics of the proton, we will turn to study how an acid molecule plays a role in proton diffusion.

G. H^+ (aq.) transport mechanism

To glean the functionality of the acid molecules in the diffusion of the protons, we first verified the participation of the molecules in actual diffusion. The RDFs of AO* are presented in Fig. 7. The A represents the central acid atom in each system. Indeed, the first peaks are sharp and located at ~1.7 Å for the aqueous PA and SA systems, and ~1.4 Å for the aqueous NA systems, respectively. Such peaks correspond to A–H, in which the acid molecule accepts a proton from a neighboring H_3O^+, and their intensity indicates the relative time the proton remains with the acid molecule as shown in the inset of Fig. 7(a). The second peak is broad, ranging from 3.0 to 4.0 Å, which refers to the state of A^- and H_3O^+ resulting in strong interaction between the ions. It is worth noting that the protonated states of the PA molecules are dynamic and more than $H_2PO_4^-$ anion (or neutral H_3PO_4), implying that the interaction between H_3O^+ and the acid molecule is different from that observed in the other two acids. These results suggest that the reaction: $HA + H_2O \leftrightarrow A^- + H_3O^+$ may play a key role in the diffusion of the protons. This phenomenon has been observed in AIMD simulations of a model PEM represented by graphane bilayers functionalized with SO_3^- at low hydration.[31, 37] Compared to the model PEM systems, the difference comes from the protonated states of the acid molecules. For example, in the aqueous PA systems, a neutral PA molecule accepts a proton from a neighboring H_3O^+ forming $H_4PO_4^+$ ion, thereby possessing four identical protons. This feature enriches the possibilities for a different proton (not the proton accepted from H_3O^+) to transfer to an adjacent water or another acid molecule. Obviously, these possibilities do not exist in the aqueous NA system because NA can have at most one proton (see Table I).

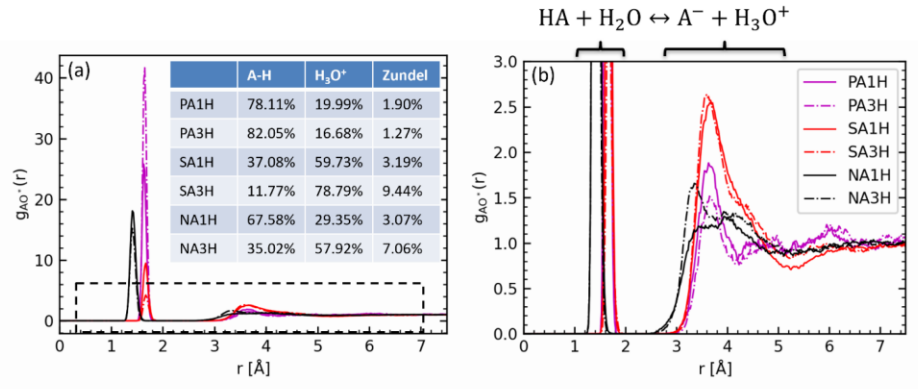

	A-H	H_3O^+	Zundel
PA1H	78.11%	19.99%	1.90%
PA3H	82.05%	16.68%	1.27%
SA1H	37.08%	59.73%	3.19%
SA3H	11.77%	78.79%	9.44%
NA1H	67.58%	29.35%	3.07%
NA3H	35.02%	57.92%	7.06%

FIG. 7. (a) RDFs of the central atom of the acid with the oxygen of H_3O^+ for the aqueous acid systems. The inset lists the percentage time the proton spends as A–H, H_3O^+, or Zundel ions. (b) A close-up view of the second peak seen in (a).

Furthermore, we calculated the percentage of time the proton exists as A–H, H_3O^+, or $H_5O_2^+$ (Zundel ion). It is not surprising to observe that proton appears in the A–H state for ~80% of the simulation time in the aqueous PA systems while this percentage decreases to ~37% in SA1H. Interestingly, the addition of water slightly increases the time percentage acting as A–H in aqueous PA systems, but significantly decreases the A–H time in strong acid systems (~37% to ~12% for SA and ~68% to ~35% for NA, respectively).

These results motivated us to observe the protons in each system recording the coordinates of the H^+(aq), which can be readily used to calculate the mean squared displacement (MSD) of the proton. Note that for the transition state, the position of the shared proton as a Zundel ion is taken as the coordinate of the proton, and the central acid atom's position is recorded when the proton is covalently bonded to the acid molecule. The calculated MSDs of H_3O^+ and H_2O are presented in Fig. S4 and the diffusion coefficients are listed in Table V. Water molecules diffuse only via a vehicular mechanism, which is governed by the hydrodynamics of the solution. The PA1H system has the lowest water diffusion coefficient but a very high H^+ diffusion coefficient. The increase in water content enhances the water diffusion by 3-fold (0.109 $Å^2/ps$ in PA3H vs. 0.03 $Å^2/ps$ in PA1H) but increases the proton diffusion by 50% (2.18 $Å^2/ps$ in PA3H vs. 1.4 $Å^2/ps$ in PA1H). These results suggest that structural diffusion dominates, and the water content has less influence

on H^+ diffusion than on H_2O diffusion in the aqueous PA systems. In the aqueous SA systems, the diffusion of water increases with increasing water content while the diffusion of H^+ has the opposite trend. The aqueous NA system has the highest water diffusion coefficient but the lowest H^+ diffusion coefficient, indicating that vehicular diffusion is the dominant contributor to the proton diffusion in aqueous NA. Compared to the proton diffusion in the slightly acidic water system, only the aqueous PA system has a higher H^+ diffusion. This clearly implies that PA enhances proton diffusion, but SA and NA impede the diffusion of protons.

To further glean insight into the mechanisms of proton transport, the MSDs were decomposed into continuous vehicular and discrete structural diffusion contributions as follows:

$$\Delta \boldsymbol{r}(t) = \Delta \boldsymbol{r}_{\mathrm{v}}(t) + \Delta \boldsymbol{r}_{\mathrm{s}}(t)$$

$$\langle |\Delta \boldsymbol{r}(t)|^2 \rangle = \langle |\Delta \boldsymbol{r}_{\mathrm{v}}(t)|^2 \rangle + \langle |\Delta \boldsymbol{r}_{\mathrm{s}}(t)|^2 \rangle + 2\langle \Delta \boldsymbol{r}_{\mathrm{v}}(t) \cdot \Delta \boldsymbol{r}_{\mathrm{s}}(t) \rangle$$

$$= \mathrm{MSD}_{\mathrm{v}} + \mathrm{MSD}_{\mathrm{s}} + 2\mathrm{Corr}$$

where $\mathrm{MSD}_{\mathrm{v}}$ and $\mathrm{MSD}_{\mathrm{s}}$ are the vehicular and structural components, respectively. The term $\langle \Delta \boldsymbol{r}_{\mathrm{v}}(t) \cdot \Delta \boldsymbol{r}_{\mathrm{s}}(t) \rangle$ is the correlation between the two components in which the bracket denotes the ensemble average over all configurations. In the period from 0 to time *t*, all elementary displacements due to PT are accumulated to $\Delta \boldsymbol{r}_{\mathrm{s}}(t)$, and the remaining are accumulated in $\Delta \boldsymbol{r}_{\mathrm{v}}(t)$. The time window for the elementary displacement is set as the sampling time of 0.97 fs, which ensures that the structural component is not overestimated. We note that a large time window (i.e., 100 fs) was selected in prior studies.[5, 14]

Table V. Diffusion coefficients of hydrated H^+ and H_2O (in $Å^2/ps$) and the computed conductivities of hydrated H^+ (in S/cm).

System	PA1H	PA3H	SA1H	SA3H	NA1H	NA3H	H_3O^+
$D_S^{\mathrm{O_W}}$	0.030	0.109	0.042	0.068	0.153	0.165	0.134
$D_S^{\mathrm{O^*}}$	1.40	2.18	0.31	0.29	0.22	0.28	0.77
$D_{\mathrm{veh.}}^{\mathrm{O^*}}$	0.043	0.089	0.054	0.119	0.145	0.159	0.177
$D_{\mathrm{stru.}}^{\mathrm{O^*}}$	1.408	1.908	0.291	0.303	0.112	0.249	0.586
$D_S^{\mathrm{O^*}}/D_S^{\mathrm{O_W}}$	46.7	20.0	7.4	4.3	1.4	1.7	4.9
$\sigma_{\mathrm{NE}}^{\mathrm{O^*}}$	0.426	0.823	0.790	0.840	0.143	0.504	0.102

Fig. 8 displays the decomposed MSDs including the vehicular and structural components along with the correlation term between these two components. As shown in Fig. 8(a and d), the total diffusivity is mainly due to structural diffusion in the aqueous PA system. Interestingly, the correlation between the structural and vehicular components slightly fluctuates around 0, and this correlation becomes slightly positive after a long time (> 15 ps) by increasing the water content (i.e., for PA3H). This may be ascribed to the participation of the PA molecule and the dynamic change of the protonated state of the neighboring PA molecules around the H_3O^+ although its state is generally as the neutral PA for most of the time. Meanwhile, the frustrated H-bond network facilitates the depolarization of the chain connecting two oppositely charged species. The conductivity of the PA1H system is mostly due to the conductivity of protons, and may be calculated via the Nernst-Einstein (NE) relationship:

$$\sigma_{\mathrm{NE}}^{0^*} = \frac{\rho}{k_B T} z^2 D$$

where ρ is the number density of H_3O^+, z the charge, and D the diffusion coefficient. The conductivity of PA1H is 0.426 S/cm in good agreement with the experimental conductivity, $\sigma_{\mathrm{exp}} = 0.43$ S/cm at 400 K.[42] Nevertheless, the estimated structural conductivity derived from experimental data is lower than that due vehicular transport,[42] in which the structural conductivity was approximately computed by subtracting the vehicular NE conductivity from the total measured conductivity. This trend is opposite to our results, which may arise from ignoring the distinct correlations between charge carriers in the vehicular diffusion. We note that the assumption of proton conductivity dominating the overall conductivity does not extend to the other aqueous acids.

However, the scenario is quite different in the strong acid solutions. In aqueous SA systems, there exists a theoretical possibility for the SA molecule to shuttle a proton for proton transport at low ratio of water to acid, although the H_3O^+ prefers to transfer a proton to an adjacent water molecule rather than a strong acid molecule due to the lower energetic barrier for proton transfer from H_3O^+ to H_2O than for H_3O^+ to an acid (Fig. 5). This situation would be altered by adding additional water leading to less participation of SA molecules in the H^+(aq) transport since the water molecules form a connected H-bond network. That is one important reason for the observation that the structural diffusion slightly increases with increasing water content (from 0.291 $\text{Å}^2/\text{ps}$ in SA1H

to 0.303 $Å^2/ps$ in SA3H). This analysis suggests that the maximum conductivity occurring as a function of the acid concentration may arise from a competition between the effective participation of acid molecules and the concentration of dissociated protons. In addition, the structural and vehicular components are anticorrelated due to the interaction with the anion. As a proton moves away from the anion through proton transfer, vehicular diffusion has the potential to pull it back toward the anion. Similarly, when the proton diffuses away from the anion via a vehicular mechanism, structural diffusion can counteract this movement by shuttling it back toward the anion. A similar anticorrelation between vehicular and structural diffusions was also observed in the AIMD and MS-EVB simulations of anion exchange membranes[5, 14] and the reactive MD and MS-EVB simulations of proton exchange membranes.[17, 40, 41] Nevertheless, this anticorrelation disappears in the slightly acidic water as shown in Fig. S5.

NA is of intermediate acidity (i.e., $pK_a = -1.4$) amongst these acids, and its molecular structure restricts its participation in proton transport. Indeed, vehicular diffusion is greater than structural diffusion in the NA1H system in part because the NA molecule appears to play a negative role in the transport of protons. This can be improved by increasing the water content to build up a connected H-bond network. As shown in Fig. 8(c and f), the addition of water significantly enhances H^+ diffusion via structural diffusion over vehicular. Anticorrelation also occurs in the aqueous NA system and this anticorrelation is slightly stronger than that in the SA1H system although the anion concentration is lower in the NA1H system (see Table I). This is because the NA molecule cannot effectively participate in H^+ diffusion as the SA molecule does in the SA1H system to mitigate the interaction between H_3O^+ and the anions. This difference in the anticorrelation between aqueous NA and SA systems decreases as the water content increases (see Fig. 8(e and f)).

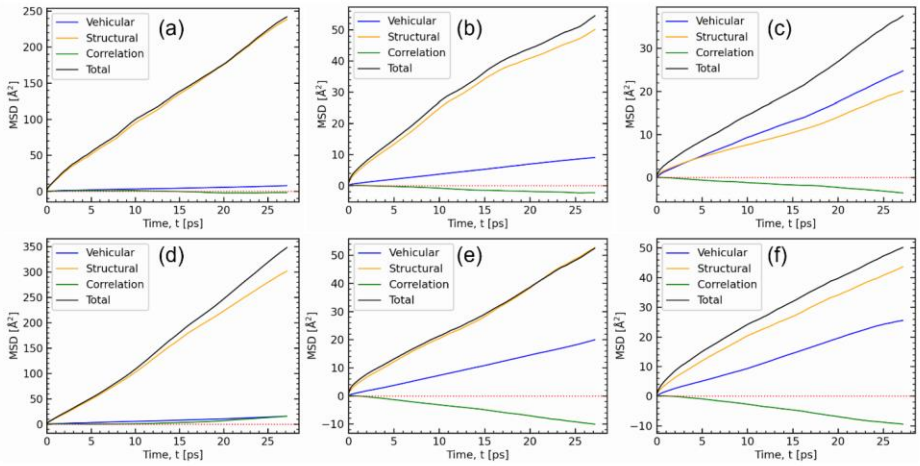

FIG. 8. The mean squared displacement (MSD) of H_3O^+ decomposed into the continuous vehicular component; the discrete structural component; and the correlation between the two components in (a) PA1H; (b) SA1H; (c) NA1H; (d) PA3H; (e) SA3H; and (f) NA3H.

Bearing that in mind, the acid molecule plays distinct roles in the diffusion of protons. Further insight into proton transport can be gained by accumulating the frequency of proton transfer events between the different species when following the H_3O^+. We classified proton transfer into three distinct types as follows: proton transfer from H_3O^+ to H_2O (Type 1), between H_3O^+ and an acid molecule (Type 2), and between acid molecules (Type 3). As shown in Fig. 9, the frequency for Type 1 is about half of that for the other two types in the PA1H system, suggesting that the PA molecule accepting a proton from H_3O^+ may pass another proton to another water or a PA molecule due to the similar proton affinity between PA and H_2O. However, the frequency for Type 1 increases to that for Type 2 in the SA1H system in contrast to Type 3 events that rarely occur. This indicates that the SA molecule obtaining a proton from a H_3O^+ prefers to return the proton to the previous H_3O^+ rather than transfer a different proton to an SA molecule. In the NA1H system, the Type 1 has an identical frequency as in the SA1H system, but the Type 2 has a relatively small frequency compared to the other two systems. This suggests that the NA molecule does not take an active part in the proton transport. The frequency for Type 1 significantly increases in the SA3H and NA3H systems but slightly decreases in the PA3H system when compared with the corresponding 1:1 systems leading to dominant structural diffusion through the H-bond formed by

the water molecules. The addition of water molecules decreases the frequency for Type 2 in the aqueous SA system but has only a minimal effect on that for Type 2 in the aqueous NA system.

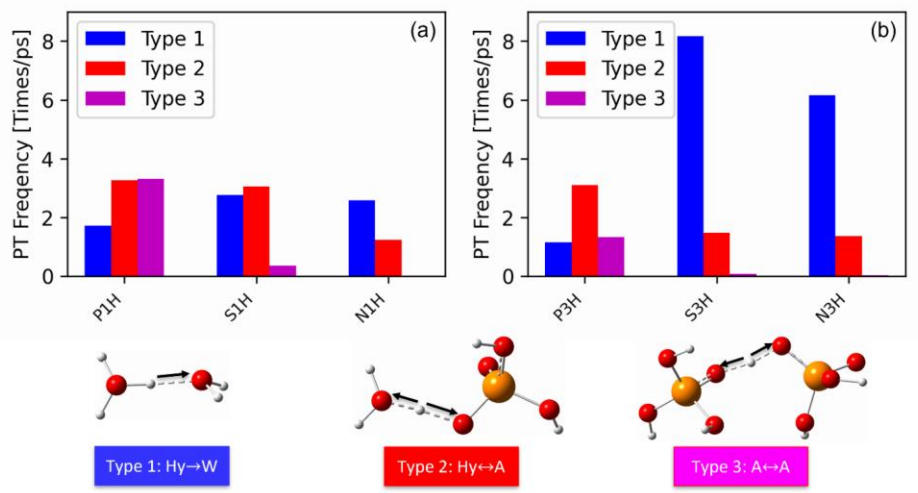

FIG. 9. The average occurrence times per picosecond for three types of proton transfer as defined at the bottom: proton transfer from H_3O^+ to H_2O; from H_3O^+ to acid molecule; and between acid molecules in the (a) 1:1 systems, and (b) 1:3 systems.

The frequency of these types of proton transfer events clearly indicates that the acid molecule plays a role in proton transport to varying extent. Remaining questions include: What roles does each acid molecule play in these aqueous systems? How do these acid molecules facilitate or impede proton transport? To shed light on these questions, we defined four functionalities of an acid molecule as shown in Fig. 10. The first one is defined as rattling if the acid molecule accepting a H^+ from a H_3O^+ returns the proton to the H_3O^+; Type 2 is a relay event where the acid molecule obtaining a H^+ of H_3O^+ transfers it to another H_2O by rotating the covalent OH bond; Type 3 is a rotation event as the acid molecule accepting a H^+ from a H_3O^+ transfers a different H^+ to the water which was previously in the form of H_3O^+ by rotating its molecular structure; and Type 4 is the most efficient shuttling process in which the acid molecule receives a proton from H_3O^+ and transfers another proton to a water molecule on the other side, resulting in a large charge displacement. Notice that Type 4 also includes the case where proton transfer events occur via a

collective H-bonding formed by several acid molecules before transferring to form a new H_3O^+. This collective proton transfer over several PA molecules was observed in AIMD simulations of pure PA.[65] The occurrence probability for these functionalities was calculated and is shown in Fig. 10. Obviously, most acid molecules just accept a proton and transfer the proton back (above 70 %), which thereby does not contribute to proton diffusion. A very small fraction of the acid molecules plays a relay role for H^+ transport. The rotation functionality of the acid molecules is negligible since the molecular rotation happens on a large timescale that exceeds the length of the simulations. Efficient shuttling events occur in aqueous PA and SA systems. The order of the fraction of shuttling is as follows: PA3H > PA1H > SA3H > SA1H, which is consistent with the structural diffusion of protons in these systems (Table V). Since NA is a monoprotic acid, the NA molecule does not act as a shuttle for H^+ transport.

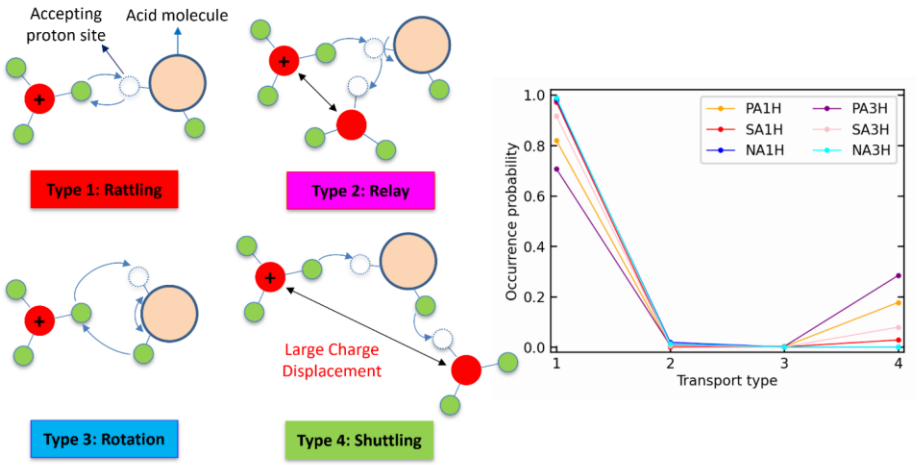

FIG. 10. The occurrence probability for the distinct types of the acid functionality as defined on the left: Type 1: the acid molecule accepts the dissociated proton and then returns the proton to the water molecule; Type 2: the acid molecule accepts the dissociated proton and then passes the proton to a different water molecule; Type 3: the acid molecule accepts the dissociated proton and then passes another proton to the water molecule by rotating OH bond; and Type 4: the acid molecule accepts the dissociated proton and then passes a different proton to another water molecule.

IV. CONCLUSIONS

The solvation and transport of protons in three different aqueous acids has been extensively investigated in this work using AIMD simulations. To reveal the mechanisms of H^+ in solutions of PA, SA, and NA, we performed simulations over 100 ps. The aqueous PA, SA, and NA systems were modeled with two ratios of acid to water 1:1 and 1:3 to study the effects of the acid and the water content on the solvation and transport of protons. We observed that self-dissociation between acid molecules appears only in the aqueous PA systems and that an increase in water content reduces the self-dissociation. PA solutions exhibit a small amount of H_3O^+ due to its weak acidity while SA solutions have a significant number of hydrated protons and very few sulfate anions. The H-bond structure is markedly influenced by the strength and character of the acid. In aqueous SA, strong hydrogen bonds form between the water due to the large population of H_3O^+ while only weak hydrogen bonds form between the SA molecules. The strong H-bonding between the PA molecules is only slightly affected by the presence of the water. The H_3O^+ ion has a similar solvation structure as observed in slightly acidic water except for the donating H-bond with an acid molecule that shows various strengths in these systems.

The H_3O^+ population correlation functions indicate that proton rattling occurs on a very short time scale (~50 fs) in all these systems and the addition of water enhances this process. However, the lifetime of dissociated protons excluding rattling is much longer. This lifetime plays an important role in the structural diffusion of H^+, but it ignores the participation of the acid molecules in proton transport. Indeed, the acid molecule takes part in proton diffusion when following the hydronium as shown in Fig. 7. Further inspection of proton transfer events reveals that the acid molecule can accept a proton from H_3O^+ and it either enhances the H^+ diffusion by shuttling the proton resulting in a large displacement via a collective proton hopping or impedes the transport of protons through rattling. The shuttling event occurs in aqueous PA systems leading to a significant contribution to proton transport. This is ascribed to the similar proton affinity as water and the peculiar proton donor and acceptor sites (3 OH proton donor and one unprotonated oxygen acceptor). In contrast, this shuttling rarely occurs in the aqueous SA system and is not observed in the aqueous NA. Moreover, the decomposition of the proton diffusion into vehicular and structural components indicates that a significant contribution to H^+ transport occurs via structural diffusion with the aid of the PA molecules. In the aqueous NA systems, vehicular diffusion is dominant at the low water

content and with an increase in hydration improves the structural diffusion by forming connected H-bonds within the water molecules.

SUPPLEMENTARY MATERIAL

See the supplementary material for details of AIMD simulation systems, the decomposed RDFs of OO pairs from water and acid molecules, the representative solvation patterns for active H_3O^+ ($\delta_{\min} < 0.1$ Å), the computed fraction of special pair acid molecules, contour plots of probability distribution for proton transfer between H_3O^+ and other species, the MSDs for H_2O and H_3O^+ and their decomposed MSDs of the vehicular and structural components.

ACKNOWLEDGEMENTS

We thank Dr. Klaus-Dieter Kreuer (MPI-Stuttgart) for helpful discussions and insightful comments. We acknowledge support by the National Science Foundation awards CHE-1764409. Computing resources were provided through an ACCESS allocation DMR130078 on Stampede2 at the Texas Advanced Computing Center (TACC).

AUTHOR DECLARATIONS

Author contributions

Z.Z. performed and analyzed the AIMD simulations and wrote the original draft. S.J.P. and A.P.S. developed the idea, led the research, and handled review and editing. All authors contributed to the discussion of the results.

Conflict of Interest

The authors declare no competing interests.

DATA AVAILABILITY

The data that support the findings of this study are available from the corresponding author upon reasonable request.

References

[1] C. A. Wraight, Biochim. Biophys. Acta, Bioenerg. **1757**, 886 (2006).
[2] S. Cukierman, Biochim. Biophys. Acta, Bioenerg. **1757**, 876 (2006).
[3] K. D. Kreuer, Solid State Ion. **97**, 1 (1997).
[4] K.-D. Kreuer, Chem. Mater. **8**, 610 (1996).
[5] Z. Long, and M. E. Tuckerman, J. Phys. Chem. C **127**, 2792 (2023).
[6] T. Zelovich, and M. E. Tuckerman, J. Phys. Chem. Lett. **13**, 2245 (2022).
[7] Z. Long, A. O. Atsango, J. A. Napoli, T. E. Markland, and M. E. Tuckerman, J. Phys. Chem. Lett. **11**, 6156 (2020).
[8] T. Zelovich, Z. Long, M. Hickner, S. J. Paddison, C. Bae, and M. E. Tuckerman, J. Phys. Chem. C **123**, 4638 (2019).
[9] D. Marx, A. Chandra, and M. E. Tuckerman, Chem. Rev. **110**, 2174 (2010).
[10] M. E. Tuckerman, D. Marx, and M. Parrinello, Nature **417**, 925 (2002).
[11] D. Marx, M. E. Tuckerman, J. Hutter, and M. Parrinello, Nature **397**, (1999).
[12] M. Tuckerman, K. Laasonen, M. Sprik, and M. Parrinello, J. Phys. Chem. **99**, 5749 (1995).
[13] P. B. Calio, C. Li, and G. A. Voth, J. Am. Chem. Soc. **143**, (2021).
[14] C. Chen, Y. L. S. Tse, G. E. Lindberg, C. Knight, and G. A. Voth, J. Am. Chem. Soc. **138**, 991 (2016).
[15] Y. Peng, J. M. J. Swanson, S.-g. Kang, R. Zhou, and G. A. Voth, J. Phys. Chem. B **119**, 9212 (2015).
[16] C. Knight, and G. A. Voth, Acc. Chem. Res. **45**, 101 (2012).
[17] S. Feng, and G. A. Voth, J. Phys. Chem. B **115**, 5903 (2011).
[18] Z. Cao, Y. Peng, T. Yan, S. Li, A. Li, and G. A. Voth, J. Am. Chem. Soc. **132**, 11395 (2010).
[19] Z. Zhu, and S. J. Paddison, Frontiers in Chemistry **10**, 981508 (2022).
[20] D. Marx, Chemphyschem **7**, (2006).
[21] N. Agmon, Chem. Phys. Lett. **244**, 456 (1995).
[22] K.-D. Kreuer, A. Rabenau, and W. Weppner, Angew. Chem., Int. Ed. Engl. **21**, 208 (1982).
[23] C. Arntsen, C. Chen, P. B. Calio, C. Li, and G. A. Voth, J. Chem. Phys. **154**, (2021).
[24] C. J. T. von Grotthuss, Ann. Chim. **58**, (1806).
[25] M. Chen, L. Zheng, B. Santra, H.-Y. Ko, R. A. DiStasio Jr, M. L. Klein, R. Car, and X. Wu, Nat. Chem. **10**, 413 (2018).
[26] G. Zundel, and H. Metzger, Z. für Phys. Chem. **58**, 225 (1968).
[27] O. Markovitch, H. Chen, S. Izvekov, F. Paesani, G. A. Voth, and N. Agmon, J. Phys. Chem. B **112**, 9456 (2008).
[28] H. Lapid, N. Agmon, M. K. Petersen, and G. A. Voth, J. Chem. Phys. **122**, 014506 (2004).
[29] J. M. J. Swanson, and J. Simons, J. Phys. Chem. B **113**, 5149 (2009).
[30] U. W. Schmitt, and G. A. Voth, J. Chem. Phys. **111**, 9361 (1999).
[31] T. Zelovich, K. I. Winey, and M. E. Tuckerman, J. Mater. Chem. A **9**, 2448 (2021).
[32] E. M. Adams, H. Hao, I. Leven, M. Rüttermann, H. Wirtz, M. Havenith, and T. Head-Gordon, Angew. Chem. **133**, 25623 (2021).
[33] J. K. Clark, 2nd, B. F. Habenicht, and S. J. Paddison, Phys. Chem. Chem. Phys. **16**, 16465 (2014).
[34] J. K. Clark Ii, and S. J. Paddison, Phys. Chem. Chem. Phys. **16**, 17756 (2014).
[35] B. F. Habenicht, and S. J. Paddison, J. Phys. Chem. B **115**, 10826 (2011).
[36] R. Liu, C. Zhang, X. Liang, J. Liu, X. Wu, and M. Chen, J. Chem. Phys. **157**, 024503 (2022).
[37] T. Zelovich, and M. E. Tuckerman, Membranes (Basel) **11**, (2021).
[38] J. Savage, Y.-L. S. Tse, and G. A. Voth, J. Phys. Chem. C **118**, (2014).
[39] K. Park, W. Lin, and F. Paesani, The Journal of Physical Chemistry B **116**, (2012).
[40] M. K. Petersen, and G. A. Voth, J. Phys. Chem. B **110**, 18594 (2006).
[41] Y.-L. S. Tse, A. M. Herring, K. Kim, and G. A. Voth, J. Phys. Chem. C **117**, 8079 (2013).
[42] J.-P. Melchior, K.-D. Kreuer, and J. Maier, Phys. Chem. Chem. Phys. **19**, 587 (2017).
[43] J. Elm, N. Myllys, and T. Kurtén, Mol. Phys. **115**, 2168 (2017).

[44] M. Sipilä, T. Berndt, T. Petäjä, D. Brus, J. Vanhanen, F. Stratmann, J. Patokoski, R. L. Mauldin, A.-P. Hyvärinen, H. Lihavainen, and M. Kulmala, Science **327**, 1243 (2010).
[45] R. P. Turco, R. C. Whitten, and O. B. Toon, Rev. Geophys. **20**, 233 (1982).
[46] J. N. Galloway, and G. E. Likens, Atmos. Environ. (1967) **15**, 1081 (1981).
[47] A. Mikalčiūtė, and L. Vilčiauskas, Phys. Chem. Chem. Phys. **23**, 6213 (2021).
[48] S. Ahlmann, P. Münzner, K. Moch, A. P. Sokolov, R. Böhmer, and C. Gainaru, J. Chem. Phys. **155**, 014505 (2021).
[49] B. Frick, L. Vilčiauskas, P. P. Deen, and S. Lyonnard, Solid State Ion. **252**, 26 (2013).
[50] Y. Aihara, A. Sonai, M. Hattori, and K. Hayamizu, J. Phys. Chem. B **110**, 24999 (2006).
[51] R. H. Tromp, S. H. Spieser, and G. W. Neilson, J. Chem. Phys. **110**, 2145 (1999).
[52] T. Dippel, K. D. Kreuer, J. C. Lassègues, and D. Rodriguez, Solid State Ion. **61**, 41 (1993).
[53] Y.-K. Choe, E. Tsuchida, and T. Ikeshoji, J. Chem. Phys. **126**, 154510 (2007).
[54] J. T. Wang, R. F. Savinell, J. Wainright, M. Litt, and H. Yu, Electrochim. Acta **41**, 193 (1996).
[55] J. S. Wainright, J. T. Wang, D. Weng, R. F. Savinell, and M. Litt, J. Electrochem. Soc. **142**, L121 (1995).
[56] D. M. J. Hutter, A. Alavi, T. Deutsch, M. Bernasconi, S. Goedecker, and M. T. M. Parrinello, (IBM Corporation 1990− 2009 and MPI für Festkörperforschung 1997−2001, 2009).
[57] D. Marx, and J. Hutter, *Ab Initio Molecular Dynamics: Theory and Implementation. In Modern Methods and Algorithms of Quantum Chemistry* (Forschungszentrum: Juelich, 2000), Vol. Vol. 1,
[58] P. C. Aeberhard, J. S. Arey, I.-C. Lin, and U. Rothlisberger, J. Chem. Theory Comput. **5**, 23 (2009).
[59] I.-C. Lin, M. D. Coutinho-Neto, C. Felsenheimer, O. A. von Lilienfeld, I. Tavernelli, and U. Rothlisberger, Phys. Rev. B **75**, 205131 (2007).
[60] C. Lee, W. Yang, and R. G. Parr, Phys. Rev. B **37**, 785 (1988).
[61] A. D. Becke, Phys. Rev. A **38**, 3098 (1988).
[62] K. G. Sprenger, V. W. Jaeger, and J. Pfaendtner, J. Phys. Chem. B **119**, 5882 (2015).
[63] G. J. Martyna, M. E. Tuckerman, and M. L. Klein, J. Chem. Phys. **97**, 2635 (1992).
[64] I. Popov, Z. Zhu, A. R. Young-Gonzales, R. L. Sacci, E. Mamontov, C. Gainaru, S. J. Paddison, and A. P. Sokolov, Commun. Chem. **6**, 77 (2023).
[65] L. Vilciauskas, M. E. Tuckerman, G. Bester, S. J. Paddison, and K. D. Kreuer, Nat. Chem. **4**, 461 (2012).
[66] I. Persson, M. Trublet, and W. Klysubun, J. Phys. Chem. A **122**, 7413 (2018).
[67] R. Caminiti, Chem. Phys. Lett. **96**, 390 (1983).
[68] M. D. Newton, J. Chem. Phys. **67**, 5535 (1977).
[69] R. Triolo, and A. H. Narten, J. Chem. Phys. **63**, 3624 (1975).
[70] M. Tuckerman, K. Laasonen, M. Sprik, and M. Parrinello, J. Chem. Phys. **103**, 150 (1995).
[71] T. Zelovich, L. Vogt-Maranto, M. A. Hickner, S. J. Paddison, C. Bae, D. R. Dekel, and M. E. Tuckerman, Chem. Mater. **31**, 5778 (2019).
[72] M. E. Tuckerman, A. Chandra, and D. Marx, J. Chem. Phys. **133**, 124108 (2010).
[73] A. Chandra, M. E. Tuckerman, and D. Marx, Phys. Rev. Lett. **99**, 145901 (2007).

The preprint of manuscript that has been submitted to the *Cell Reports Physical Science*:

Mechanisms of proton transport in aqueous acid solutions

Ivan Popov,[1*] Zhenghao Zhu,[2] Harmandeep Singh,[3,4] Mohanad Abdullah,[5] Robert L. Sacci,[4] Eugene Mamontov,[6] Joshua T. Damron,[4] Catalin Gainaru,[4] Stephen J. Paddison,[2*] and Alexei P. Sokolov[4,5*]

[1]University of Tennessee – Oak Ridge Innovation Institute, University of Tennessee, Knoxville, Tennessee 37996, USA

[2]Department of Chemical & Biomolecular Engineering, University of Tennessee, Knoxville, Tennessee 37996, USA

[3]Bredesen Center for Interdisciplinary Research and Graduate Education, University of Tennessee, Knoxville, Tennessee 37996, USA

[4]Chemical Sciences Division, Oak Ridge National Laboratory, Oak Ridge, Tennessee 37831, USA

[5]Department of Chemistry, University of Tennessee, Knoxville, Tennessee 37996, USA

[6]Neutron Scattering Division, Oak Ridge National Laboratory, Oak Ridge, Tennessee 37831, USA

Abstract

The fundamental understanding of proton transport, specifically the Grotthuss-like mechanism, is critical for many technological applications. The current study presents a comprehensive and comparative analysis of proton transport in well-known model systems: aqueous solutions of sulfuric and phosphoric acids and pure phosphoric acid. To analyze dynamics in these systems, we employed quasielastic neutron scattering, broadband dielectric spectroscopy, light scattering, rheology, and PFG-NMR measurements combined with *ab initio* molecular dynamic simulations. Analysis of the results shows that in all systems, proton transport occurs through very short 'jumps' about ~0.5 - 0.7 Å, and that structural relaxation is much slower than the proton jump rate. However, there are fundamental differences in proton transport in phosphoric and sulfuric acid systems. One of the key differences is that the proton hopping is coupled to structural relaxation in the aqueous solution of sulfuric acid, while these processes are decoupled in phosphoric acid. Furthermore, neutron scattering indicates that at least one proton per sulfuric molecule remains slower than other protons in the system, while all protons have the same fast mobility in phosphoric acid systems. Analysis also revealed correlated proton jumps, but these correlations suppress the conductivity in all these systems, suggesting that the expected Grotthuss-like enhancement of conductivity cannot be realized in bulk liquids.

Introduction

Understanding proton transport is crucial for various scientific disciplines such as chemistry and biology, and for different technologies including fuel cells or electrolyzes [1-3]. Unlike regular ion transport, where an ion moves as an individual unit through the diffusion process, protons spend

most of the time associated to a host molecule but also move between molecules through the hydrogen-bonded network. In general, there are two types of proton transport [4-11]: i) the vehicle mechanism when a proton moves with the host molecule (vehicle) and ii) the hopping or shuttling mechanism, where protons hop between host molecules The second mechanism is deemed to be more efficient because it does not require motion of the entire molecule. In general, both types of proton transport take place in proton conducting systems, where rotation and diffusion of the host molecules also impact the hopping mechanism [4]. This leads to the question of how strong is the coupling between proton hopping and rotation of the host molecule in various systems. Another important question is related to collective phenomena in proton transport. The idea, initially proposed by Grotthuss [12,13], suggests that proton jumps might be correlated, leading to charge displacement exceeding that of the individual protons. The 'Grotthuss-like' mechanism is considered to be the most efficient mode of protonic charge transport. However, a recent study [4] suggested that 'Grotthuss-like' enhancement of conductivity cannot be realized in bulk liquids where dynamic correlations always decrease conductivity.

One of the best candidates to study the properties of proton transport are acids and their aqueous solutions. Phosphoric acid (PA) and sulfuric acid (SA) along with their aqueous solutions are considered the systems with the highest intrinsic proton conductivity [4,14-21]. In particular, diffusion studies using nuclear magnetic resonance (NMR) and isotopic effect in conductivity, unambiguously indicate that proton transfer dominates the conductivity in PA [15,21]. In our recent publication [4] we presented a comprehensive study of proton transport in PA and 1:1 molar aqueous solution of PA (corresponding to 85 wt% PA and hereinafter we denote it as PA1). We found that the proton jump length is about 0.5 Å, and is comparable to the distance of proton transfer between oxygen atoms forming a hydrogen bond. Moreover, our studies revealed that all the protons, including the protons of the water molecules are involved in these short and fast jumps. We also showed that the proton conductivity process is decoupled from structural relaxation of the host molecule, indicating that proton hopping is only weakly coupled to diffusion and rotation of the PA and the water molecules in these systems.

The current manuscript presents a similar analysis of proton transport in 65 wt% aqueous solution of sulfuric acid (SA) (which corresponds to molar concentration SA:H_2O= 1:3, and hereinafter we denote it as SA3). We analyzed proton transport using Broadband Dielectric Spectroscopy (BDS) including sub-THz region, Quasielastic Neutron Scattering (QENS) and Pulse Field Gradient

Nuclear Magnetic Resonance (PFG-NMR). To study structural relaxation in wide frequency range we performed Light Scattering and Rheology measurements. Our experimental investigations are complemented by *ab initio* molecular dynamics (AIMD) simulations. Combined results from these techniques revealed the key differences in proton transport in aqueous solutions of phosphoric and sulfuric acids. We found that unlike the PA and PA1, in the SA3 system the proton hopping is coupled with rotation of the host molecule and one of the protons dissociates from SA at longer timescales in contrast with the PA systems where all protons move with the same rate. These results help to formulate a general picture of proton transport in aqueous acid solutions.

Material and experimental measurements details.

Materials. Sulfuric acid (≥ 98% trace metal basis, EMD Millipore Corporation) and distilled water was purchased from Sigma Aldrich. Then, the acid aqueous solution (SA3) was prepared in molar concentration of SA:H_2O = 1:3.

Broadband Dielectric Spectroscopy (BDS) measurements. The conductivity spectra were measured using three setups to cover the wide frequency range from 0.1 Hz up to 30 GHz. An Alpha-A analyzer from Novocontrol was utilized in the frequency range from 10^{-3} to 10^{6} Hz. A Quattro temperature controller (Novocontrol) was used for temperature stabilization for these lower frequency measurements. The samples were stabilized for 20 minutes at each temperature to reach precision ±0.2 K. The Panoramic Network Analyzer, Agilent Technologies, E8364C with 85070E Dielectric Probe Kit were utilized for frequency measurements from $5 \cdot 10^{8}$ Hz up to $3 \cdot 10^{10}$ Hz. The Slim Probe with the Agilent Electronic Calibration module (ECal) was used for measurements of real and imaginary part of dielectric permittivity. The Presto, Julabo, W80 was used for temperature stabilization for the high frequency measurements. The samples were stabilized for 40 minutes at each temperature to reach precision ±0.2 K. Additional details of calibration and designs of the cells are presented in similar measurements of PA systems [4].

Quasielastic Neutron Scattering (QENS) measurements at the BASIS spectrometer (Spallation Neutron Source, ORNL)[22] were performed in the extended energy transfer mode to cover the energy transfer window of -200 μeV to +200 μeV at 280K and 315K for aqueous solution of sulfuric acid SA3. This was achieved with the spectrometer's bandwidth choppers operated at 30 Hz and the incident neutron bandwidth centered at 6.15 Å. The energy resolution was ca. 3.7 μeV (Q-averaged full width at half maximum). The samples were placed in flat-plate gold-coated aluminum sample holders with sample space thickness of 0.25 mm to reduce multiple scattering. Samples were loaded in glovebox and sealed with indium. The sample holder was placed at 90° with respect to the incident beam. A closed-cycle refrigerator was used for temperature control within 0.5 K offset. The sample-specific resolution spectra were collected at a baseline temperature of 20 K. The QENS data were reduced and analyzed using Mantid[23] and DAVE[24] software, respectively. Additional details of data treatment are presented in SI.

Light Scattering (LS) was measured using Raman spectrometer and Tandem Fabry-Perot (TFP – 1) interferometer (JRS Scientific Instruments, Table Stable Ltd). The experiments were performed in backscattering geometry using laser wavelength 532 nm. To cover a wide frequency range, three mirror spacings were used: 0.4 mm, 3 mm, and 15 mm. Narrow interference filter was used to suppress higher order transmissions. Optical signal from the same spot in the sample was

transferred by additional mirrors to the T64000 Raman spectrometer from Horiba Jobin Yvon. Raman spectra were measured in subtractive mode, and the optical Raman modes were used to normalize the spectra at different temperatures. The samples were measured in a cryostat. After temperature stabilization for one hour, the light scattering spectra were collected. To remove the contribution of longitudinal modes from the light scattering spectra, the samples were measured in HV and HH polarizations at the same mirror spacing.

Oscillatory shear rheology covering a frequency range between 100 Hz and 0.01 Hz has been carried out with an ARES G2 rheometer from TA Instruments, employing a 4 mm parallel plate configuration. The thickness of the loaded liquid layer was 1 mm and the temperature stability during each frequency scan was kept within ±0.1 K. All mechanical spectra were probed in the linear-response regime, using strains with small amplitudes of 0.03%.

Pulse Field Gradient Nuclear Magnetic Resonance (PFG-NMR) Diffusometry was used at temperatures 298K and 280K, the latter at which QENS spectrum was also collected. Experiments were performed on a 400 MHz Bruker NEO spectrometer equipped with a diff50 H/X diffusion probe using the standard STE experiment with a gradient pulse of 1ms and diffusion time delay of 20ms. Different gradient strengths were used to ensure different timescales weren't missed along the diffusion curve.

***Ab Initio* Molecular Dynamics (AIMD) Simulations**

AIMD simulations of 65 wt% aqueous sulfuric acid (SA3) were conducted using the CPMD code [25,26]. The SA3 system comprised 26 sulfuric acid molecules and 78 water molecules within a cubic simulation box with a side length of 16.153 Å ($\rho = 1.56$ g/cm^3). Dispersion-corrected atomic core pseudopotentials (DCACP) [27,28] were utilized to account for dispersion forces within the Kohn-Sham formulation of density functional theory, employing the B-LYP exchange-correlation functional [29,30]. The Kohn-Sham orbitals were expanded using a plane-wave basis set with a kinetic energy cutoff of 80 Ry. To enhance the adiabatic decoupling of nuclear and electronic dynamics and allow a larger time step of 4 au, hydrogen atoms were assigned the mass of deuterium, and the fictitious electron mass was set to $\mu = 500$ au. The system was initially pre-equilibrated using a classical force field [31] for 10 ns, followed by 15-20 ps equilibration with AIMD at 360 K using a massive Nose-Hoover chain thermostat [32]. An elevated temperature was employed to enhance proton dynamics without altering the physical mechanism due to the temporal and spatial limitations of computationally expensive AIMD simulations. Subsequently, the equilibrated configuration was used for a ~60 ps production run in a microcanonical (NVE) ensemble.

Experimental results

Broadband dielectric spectroscopy (BDS) measurements. The conductivity spectra measured in a very broad frequency range (Fig. 1a) clearly show a DC-conductivity plateau and an AC-tail at higher frequencies. For measurements up to 10^6 Hz, the sample was quenched below the glass transition to prevent crystallization and measured on heating. Above T = 190K, the sample crystalized and melted again only at T = 245K, as a result the spectra between these temperatures are not presented in Figure 1a. The spectra in the frequency range between 10^6 – $5 \cdot 10^8$ Hz were not measured because aggressive behavior of sulfuric acid was corroding coaxial pin in the sample cell. The spectra of ion conductive systems are usually described by the Random Barrier Model [33-

[39]. The model assumes that ions hop over potential barriers, and in the case of constant distribution of barrier height the model predicts the simple but non-linear equation [33,37]

$$\ln\left(\frac{\sigma^*(\omega)}{\sigma_{DC}}\right) = \frac{i\omega\tau_\sigma\sigma_{DC}}{\sigma^*(\omega)}\left(1+\frac{8}{3}\frac{i\omega\tau_\sigma\sigma_{DC}}{\sigma^*(\omega)}\right)^{-1/3}. \quad (1)$$

where $\sigma^*(\omega)$ is a complex conductivity; σ_{DC} is the DC-conductivity, which can also be estimated from the DC plateau, and its temperature dependence is presented in the Figure 1b. The parameter τ_σ is the conductivity relaxation time and it defines the timescale when a proton overcomes the highest potential energy barrier, escaping from a Coulombic cage formed by the neighboring counter charges, and its mean-squared displacement crosses over from sub-diffusive to the normal diffusion regime. The conductivity relaxation time corresponds to the frequency, $f_{AC-DC} = 1/(2\pi\tau_\sigma)$, at which the AC-tail (defined by the sub-diffusion regime) in the conductivity spectra crosses over to the frequency independent DC-conductivity plateau (defined by the normal diffusion regime) (Fig. 1a). The temperature dependence of the conductivity relaxation time together with relaxation times obtained from other techniques is presented in Figure 2a.

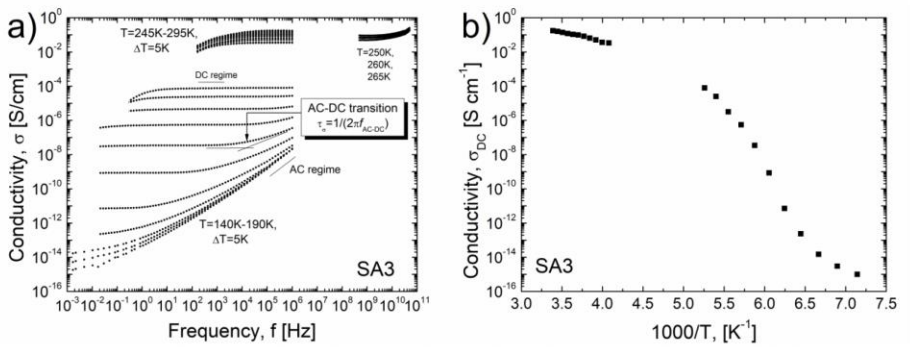

Figure 1. a) The frequency dependence of the conductivity measured over a wide frequency and temperature range. **B)** DC-conductivity estimated from the DC – plateau in the conductivity spectra.

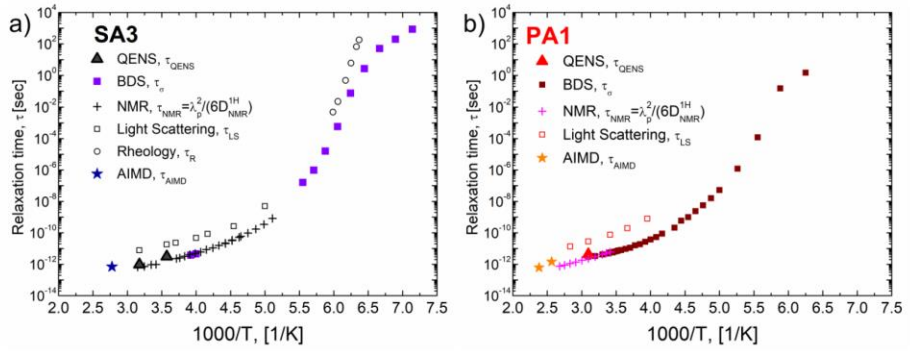

Figure 2. (a) Temperature dependence of the relaxation times collected from various techniques for SA3. The crosses are estimations based on the NMR diffusivity data reported in [21]. **(b)** For comparison we presented data for the relaxation times for aqueous solution of phosphoric acid PA1 taken from [4].

Quasielastic neutron scattering measurements (QENS). QENS spectra of the SA3 aqueous solution were measured at two temperatures T = 280K and 315K. The intensity spectra, $I(Q,E)$, show clear Q-dependent broadening (Figs. 3a and 3b). They also show residual elastic intensity, especially obvious at T = 315 K (Fig. 3b) at large Q values. To analyze the spectra, it is more informative to present the data in the susceptibility format $\chi''(Q,E)\sim I(Q,E)\ \times E$ (Figures 3c and 3d). Similar to the QENS spectra of PA and PA1 [4], the current QENS spectra show strong Q-dependence with the spectral shape follows $\chi''(Q,E)\sim E^1$ in the low energy range, and $\chi''(Q,E)\sim E^{-\beta}$ at high energy. The stretching parameter in the SA3 spectra is Q-independent and $\beta \approx 0.48$ at 280K and $\beta \approx 0.68$ at 315K. This shape is well described by the Cole-Davidson function [40]. Detailed analysis of the fitting procedure can be found in the SI. One of the major differences with the earlier PA studies is the amplitude of the Elastic Incoherent Structure Factor (EISF), $x(Q)$. As was emphasized above, the strong elastic contribution is evident in the measured spectra (Figs. 3a, b), and EISF has significant amplitude above 10% at higher Q (Fig. S1a). This is in strong contrast with our earlier studies of pure PA [4] where the elastic component was below 6% and below 3% for PA1. In the analysis of the Q-dependence of Half-Width at the Half-Maximum (HWHM), we considered the stretching of the relaxation peak by using the Cole-Davidson function in the fitting procedure and analyzed the peak positions in the susceptibility format $E_{max}^{\chi}(Q)$ (Figs. 3c, d). It corresponds to HWHM with time distributed relaxation processes (see

SI for details). The Q-dependence of $E_{max}^{\chi}(Q)$ is shown in Figure 4 and can be well described by the Singwi-Sjolander jump-diffusion model [41]:

$$E_{max}^{\chi}(Q) = \frac{\hbar D_{QENS} Q^2}{(1+D_{QENS}\tau_{QENS}Q^2)}, \quad \langle\lambda_{QENS}\rangle = \sqrt{6D_{QENS}\tau_{QENS}}, \tag{2}$$

where $\hbar$ is Planck's constant divided by 2π, and τ_{QENS} and D_{QENS} are the characteristic jump time and diffusion coefficient of the protons, respectively. The parameter $\langle\lambda_{QENS}\rangle$ corresponds to an averaged proton jump length. Figure 4 reveals a good fit to the jump-diffusion model. When estimated in this way τ_{QENS} agrees with τ_{σ} estimated from the BDS measurements (Fig. 2a). This suggests that the proton jumps observed in the QENS are responsible for the measured conductivity. The obtained diffusion coefficients agree reasonably well with the ones measured by PFG-NMR in this study and in previous work [21] (Fig. S2). The estimated proton jump length was about $\langle\lambda_{QENS}\rangle \approx 0.5$ Å comparable to the values estimated for PA and PA1 [4].

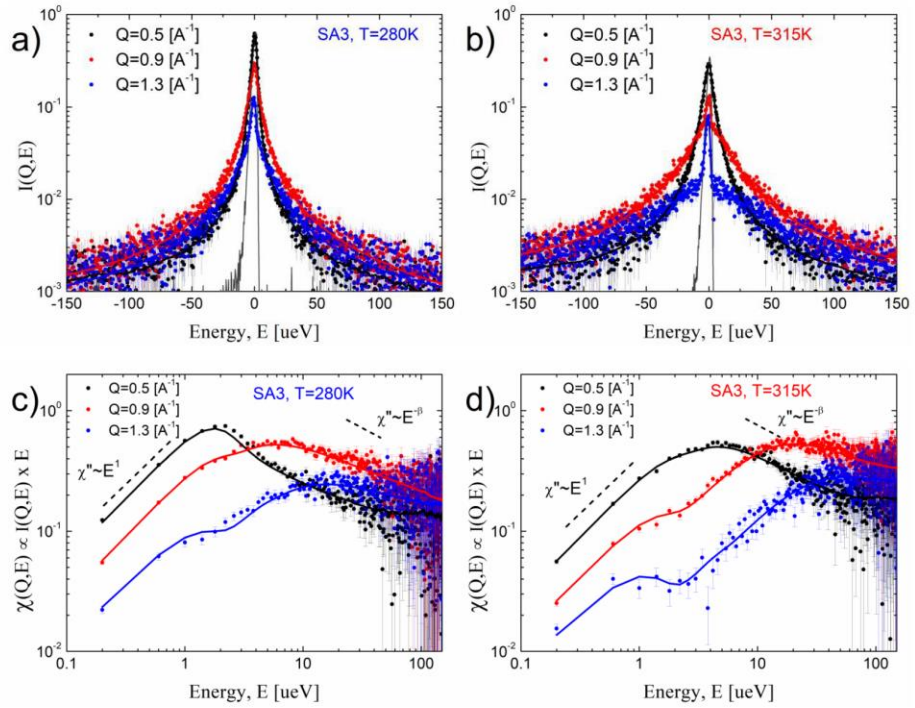

Figure 3. QENS spectra of aqueous solution of sulfuric acid with molar concentration SA3 (symbols) at two different temperatures: 280K and 315K in **(a, b)** intensity $I(Q,E)$ and **(c, d)**

susceptibility $\chi(Q,E) \propto I(Q,E) \times E$ format. In the intensity format (a, b) the resolution response (measured at 20 K) is displayed by the gray line in the center. The solid lines show fits of the spectra (for details see SI), while dashed lines in (c, d) indicate the slopes of the spectra.

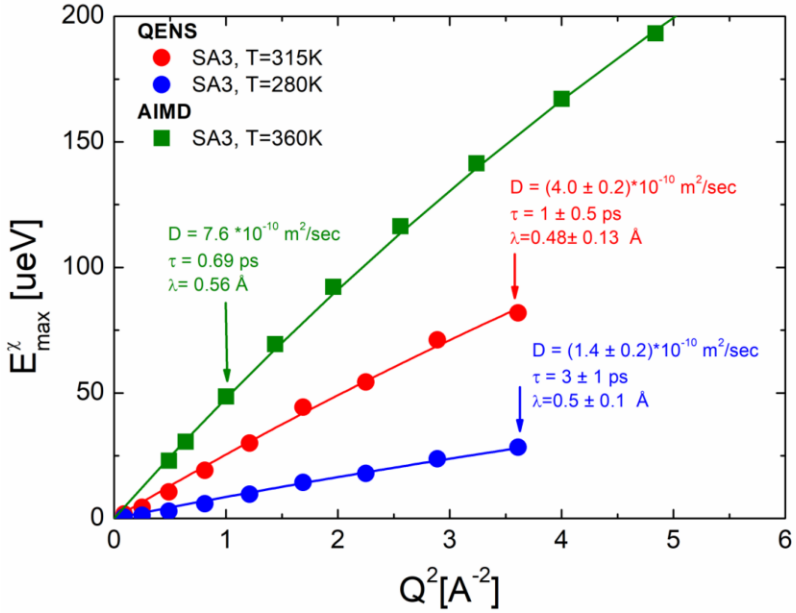

Figure 4. Dependence of the $E^{\chi}_{max}(Q)$ versus the square of the wave vector for aqueous sulfuric acid with a molar concentration SA3. At T=280K and T=315 K, $E^{\chi}_{max}(Q)$ was estimated from the maximum of the relaxation process in the QENS susceptibility. The $E^{\chi}_{max}(Q)$ for T = 360K was calculated from AIMD simulations using the $ISF_s(Q,t)$. The full Q range of $E^{\chi}_{max}(Q)$ calculated from the simulations is shown in Fig. S3b. Solid lines show fit the data to the jump diffusion model [41]. The estimate diffusion coefficient and relaxation time are shown in the Figure. See additional details in the SI for the fitting procedure of $ISF_s(Q,t)$.

Structural relaxation measured by Light Scattering (LS) and Rheology. To study structural relaxation at the picosecond time scale we perform depolarized light scattering (LS) measurements. The LS susceptibility spectra show a distinct relaxation process (Figure 5) with broadening at higher frequencies that can be well described by the Cole-Davidson function with the broadening parameter $\beta \approx 0.45$ independent of temperature. We estimated the characteristic structural relaxation time using the frequency at the relaxation process maximum, $\tau_{LS} = 1/(2\pi f_{max})$, and its temperature dependence is presented in Figure 2a. Similar to PA [4], the structural relaxation

process was significantly slower than τ_σ and τ_{QENS} observed in BDS and QENS experiments, respectively.

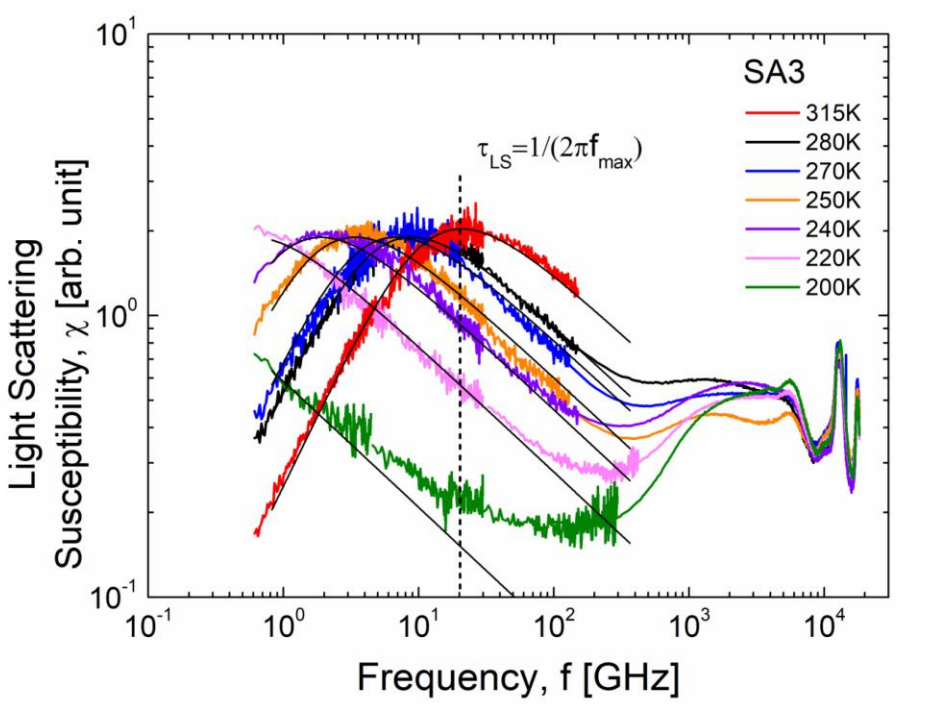

Figure 5. Light Scattering spectra of aqueous solution of sulfuric acid SA3 at different temperatures. Black lines represent the fitting of the relaxation process to the Cole-Davidson function. The relaxation time was estimated from the maximum of the relaxation process.

We utilized shear rheology to study structural relaxation at lower temperatures. This technique provides access to the frequency dependence of the real (G′) and imaginary (G″) parts of the complex shear modulus G* of the studied material. Their corresponding spectra are shown in Fig. 6, where their frequency responses probed at different temperatures have been superimposed to form master curves [42,43]. In this particular case the reference temperature is 160 K. This procedure is usually employed for the extraction of relaxation times in a model-independent manner and in a dynamic range exceeding that covered by the rheometer under isothermal conditions [44]. To this end, the inverse of the characteristic frequency of the loss modulus peak in Fig. 6 corresponds to

the rheological characteristic time, τ_R, at the chosen reference temperature. For the other temperatures, τ_R has been determined using the horizontal shift factors used for constructing the master scale and its temperature dependence as shown in Fig. 2a. The rheology relaxation time, τ_R, also appears slower than the conductivity relaxation process (Fig. 2a), and the decoupling of structural and conductivity relaxations appears only slightly stronger close to the glass transition temperature T_g than at high T. This result is in strong contrast to that observed in PA where the decoupling of structural and conductivity relaxations at high T is comparable to our SA data, but it ncreasees drastically as T_g is approached [4,45,46].

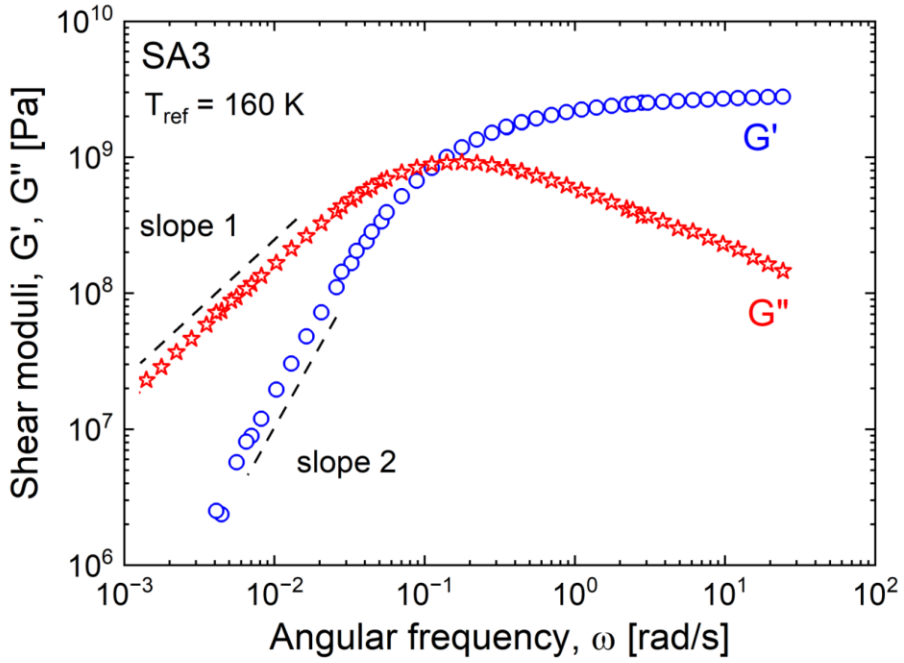

Figure 6. Master curves of the shear moduli (blue circles for G′ and red stars for G″) constructed for the SA3 system. The high value of the instantaneous shear modulus $G'(\omega \to \infty) = G_\infty > 1$ Gpa and the presence of terminal Maxwell regime [42,43] (revealed by $G'(\omega) \sim \omega^2$ and $G''(\omega) \sim \omega^1$ indicated by the dashed lines) demonstrates that the probed rheological response is governed by the structural relaxation of the investigated material.

Ab Initio Molecular Dynamics (AIMD) Simulations.

To deepen our understanding of proton transport mechanisms on the molecular level, we utilized AIMD simulations. The calculated self-intermediate scattering function of the protons, $ISF_s(Q,t)$, shows clear Q-dependent process associated with the proton diffusion (see Fig S3a). Analysis of $ISF_s(Q,t)$ provides (see SI for details) Q-dependent $E_{max}(Q)$ for a larger range of Q values at a higher temperature and is plotted in Figure 4 (and in Fig S3b) together with the QENS result. Applying jump-diffusion model to $E_{max}(Q)$, the relaxation time, τ_{AIMD}, diffusion coefficient and rearrangement length for proton hopping were obtained. Diffusion coefficient and relaxation time are in good agreement with the experimental results (see FigS2a, and Fig.2) proving the validity of the AIMD simulations. The proton jump length, obtained independently, from AIMD simulations, $\langle\lambda_{AIMD}\rangle = \sqrt{6D_{AIMD}\tau_{AIMD}}$, is in excellent agreement with QENS and BDS/NMR measurements $\langle\lambda_{AIMD}\rangle \approx \langle\lambda_{QENS}\rangle \approx 0.5$ Å.

Following an individual proton, we plotted the trajectories of a typical proton in Fig. S4. The "tracked" proton exhibits vibrational, rotational, and translational motions in the same color with proton transfer indicated by changes in color. Thick lines represent the trajectory of the center of mass of the proton clouds. The clouds associated with the SA molecule are smaller and more localized compared to those associated with the water molecule, due to the larger contribution of translational motion in the latter. Once the proton enters the connected hydrogen bond network within the water molecules, it diffuses rapidly through vehicular and structural diffusion mechanisms, depicted by thin solid lines and thick blue lines. Analysis of these jumps between the molecules shows that the average jump length between different species are similar (≈ 0.5 Å), except for a few large rotation-assisted jumps. Furthermore, as proton transfer occurs between the molecules, the proton associates with different entities, resulting in a distribution of protonated species. To identify various relaxation processes related to proton transfer, we used a "history-dependent" proton transfer correlation function for two protonated acidic species (i.e., H_2SO_4 and HSO_4^-). The results clearly indicate two distinct relaxation processes, as discussed in the following section.

Discussion

After analysis of all spectra from the various techniques, we plotted the relaxation time for SA3 (Fig. 2a), and for comparison, we also presented similar data for PA1 (Fig. 2b) from our previous work [4]. Similar to our earlier studies [4,47], we can also estimate the rearrangement characteristic

length of the protons when 'normal' diffusion leads to DC-conductivity, using the conductivity relaxation time and diffusion coefficient from NMR [21]:

$$\langle\lambda_p\rangle = \sqrt{6D_{NMR}^{1H}\tau_\sigma}. \quad (3)$$

This estimate gives $\langle\lambda_p\rangle \approx 0.5$ Å, in agreement with proton jump length obtained from QENS and AIMD, $\langle\lambda_p\rangle \approx \langle\lambda_{AIMD}\rangle \approx \langle\lambda_{QENS}\rangle$, and approximately equal to the distance the proton needs to move to switch between two oxygen atoms, i.e. to transfer between two host molecules. It means that a proton reaches a normal diffusion regime even after one jump between host molecules, in line with the results obtained for PA and PA1 [4]. This length differs from the one in regular ionic liquids, where an ion escapes from the Coulombic cage to reach a normal diffusion regime, and rearrangement length in this case is approximately equal to the size of the cage, ~1-2 Å [47-49]. We emphasize that earlier QENS studies of diluted (5 M) aqueous SA solution [50], estimated the proton jump length ~1.6 Å at room temperature and ~4.2 Å at a lower temperature. This discrepancy is probably caused by employing a Lorentzian [50] to fit these strongly stretched QENS spectra (Fig. 3). Moreover, the SA solution studied in [50] had significantly higher water content, and the QENS spectra were dominated by the dynamics of water. Good agreement in our estimates of the averaged jump length from QENS, BDS, NMR, and AIMD simulations provides strong confidence that protons indeed move mostly by very short jumps.

Inverting Eq.(3) as: $\tau_{\mathrm{NMR}} = \langle\lambda_p\rangle^2/6D_{NMR}^{1H}$, we can also estimate the proton relaxation time at higher temperatures, assuming that $\langle\lambda_p\rangle$ is temperature independent. We denote this time as, τ_{NMR}, pointing out that it was obtained from NMR diffusion (Figure 2a). A good match of the temperature dependences of τ_{NMR} with τ_σ indicates validity of the assumption about the temperature independence of $\langle\lambda_p\rangle$. Thus, all experimental methods and AIMD simulations independently provide consistent results about the timescale of proton transport and the proton jump length.

Analysis of the QENS results at higher Q reveals ~10-15% EISF contribution in the SA3 system versus 3% in PA1 and below 6% in pure PA [4]. The latter indicates that all protons in PA systems, including the protons of H_2O, have similar mobility on the measured picosecond time scale. Obviously, this is not the case in the SA3 system. In this system scattering of S and O atoms contributes only ~4.5% of the total scattering, and 95.5% of the scattering comes from the 8 hydrogen atoms. The high value of EISF suggests that approximately one of hydrogen atoms in SA3 has relatively slow mobility on the measured time (picoseconds) and length (~1 nm) scale.

AIMD simulations provide clear answers about the origin of the elastic component. The instantaneous distribution of concentration of different species presented in SA3 reveals that almost all SA molecules have a single proton (Fig. 7a, HSO_4^-) per $1{\cdot}SA{:}3{\cdot}H_2O$ unit, while 7 other protons are mostly attached to the water molecules. Moreover, the AIMD simulations provide estimates of the proton transfer population correlation function, $C_c^{n_j}(t)$, for two sulfuric acid protons (Fig. 7b):

$$C_c^{n_j}(t) = \frac{\langle h_{n_j}(0) \cdot H_{n_j}(t) \rangle}{\langle h_{n_j} \rangle} \tag{4}$$

here $h_{n_j}(0) = 1$ if a given SA molecule possesses $\geq n_j$ protons and 0 otherwise, $H_{n_j}(t) = 1$ if the protonated SA molecule keeps its identity up to time *t*. It was calculated from the trajectory and used to verify the various relaxation time scales of proton motion. The exchange time $\tau_{\text{exch}} = \int_0^\infty c_c^{n_j}(t)dt$ is equal $\tau_{\text{exch}_1} = 0.5$ ps for first proton and $\tau_{\text{exch}_2} = 17.6$ ps for second proton (HSO_4^-). The first time is comparable to the averaged time of the proton jumps in simulations (~0.69 ps, Fig.4), while the second time is ~30 times longer.

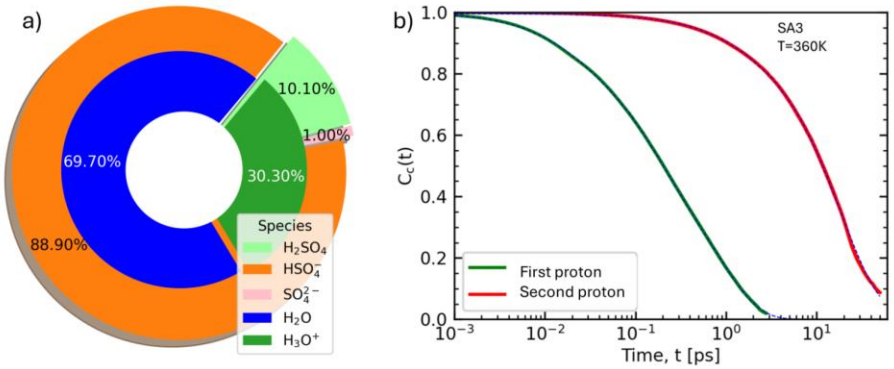

Figure 7. a) Instantaneous concentration distribution of the different species in SA3 per $1{\cdot}SA{:}3{\cdot}H_2O$ unit at 360 K. **b)** Proton transfer population correlation functions for SA3 at 360 K for two acid protons.

Combining this result with instantaneous species distribution (Fig 7a), we might conclude that the first proton dissociates from SA molecule forming H_3O^+ ion and is mobile on the same timescale as other protons. However, the second proton has ~30 times longer exchange time and remains with the SA molecule, moving much slower than the other 7 protons. This contributes to the EISF.

To compare the mobility of protons at longer length and time scales we conducted proton PFG-NMR measurements. Detailed analysis of the data reveals a single exponential behavior for the diffusion curves (see Figure S2), suggesting that all protons diffuse at a similar rate on the time (~ms) and length (microns) scale of the NMR experiment. This clearly indicates that all protons of sulfuric acid and water have been exchanged on these time scales leading to the same average mobility. This conclusion agrees with the time of the second SA proton exchange being much shorter than the characteristic PFG-NMR time.

From comparison of conductivity relaxation time, τ_σ (from BDS), and much slower structural relaxation time, τ_{Struct}, (from LS and Rheology) we can conclude that the proton conductivity of SA3 occurs via proton hopping rather than through a vehicle mechanism. It is in line with proton transport in PA and PA1 [4]. However, there are critical differences between the proton transport in SA3 and PA1. First, not all protons participate in the conductivity with the same rate in the SA3 system, while all protons are involved in the PA and PA1 systems. Second, the structural and conductivity relaxation times, in the case of PA1 diverges at low temperature (Fig. 2b) and even stronger decoupling is observed for pure PA [4]. However, in the case of SA3, the structural and conductivity relaxation times vary in a parallel way down to T_g (Fig. 2a). To make this point clearer, in Figure 8, we presented the schematic temperature behavior of the relaxation time from Figure 2a and 2b, indicating these differences. Thus, although the conductivity in SA3, is mostly defined by proton hopping, it is strongly coupled to structural relaxation, i.e. to the rotation of the host sulfuric or water molecule. In contrast, proton transport in the PA systems shows stronger decoupling from structural dynamics especially at lower temperatures close to T_g. It results in much faster conductivity relaxation time at T_g in PA ($\tau_\sigma \sim 10^{-2}$ s) and PA1 (~ 0.1 s) [4] than in SA3 (~ 10 s) (Fig. 2).

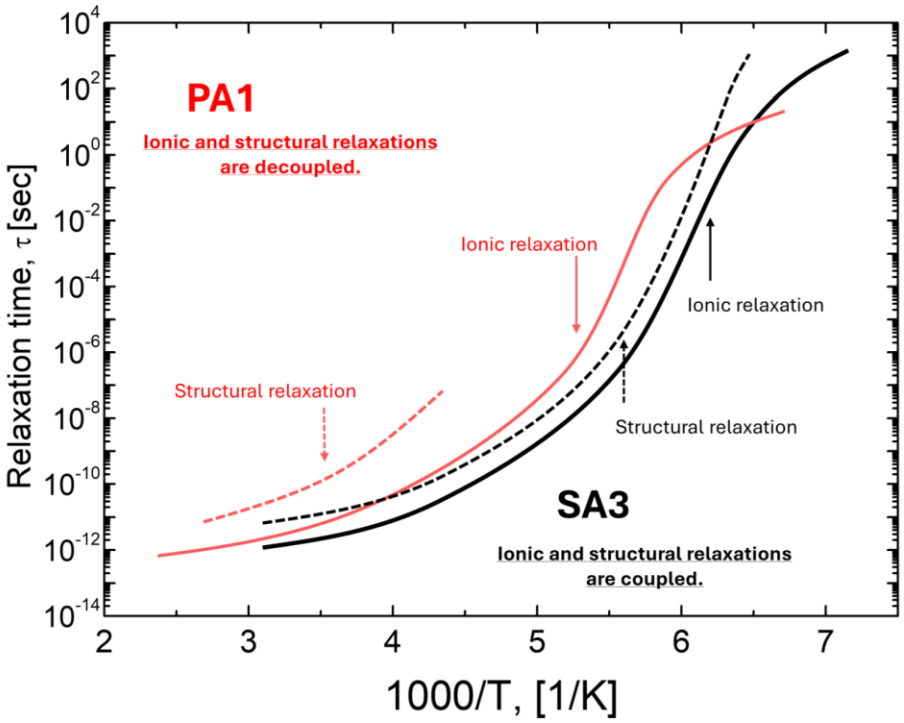

Figure 8. Schematic representation of the temperature dependence of the relaxation times presented in Figure 2a and b for aqueous solutions of phosphoric and sulfuric acids. Solid lines correspond to ionic relaxation, while dashed lines correspond to structural relaxation.

Having diffusion coefficient and the conductivity we can estimate the value of proton dynamic correlations to check the existence of the Grotthuss mechanism (positively correlated proton transport). The ion correlations can be characterized by the parameter called ionicity or inverse Haven ratio defined as [51,52]:

$$H^{-1} = \frac{\sigma_{DC}}{\sigma_{NE}}, \quad where \ \sigma_{NE} = \frac{nq^2D}{kT}. \tag{5}$$

where n, q, and D are the concentration, charge, and diffusion coefficient of the protons, respectively. In Eq. (5), σ_{NE} is the Nernst-Einstein (NE) conductivity estimated using the proton diffusion coefficient. The NE equation assumes independent contribution of all the protons. However, the DC- conductivity is defined by the current-current correlations that include self- and

cross- (distinct) correlations [52]. If cross-correlations are positive, as it is expected in the 'Grotthuss' mechanism, then $\sigma_{DC} > \sigma_{NE}$ and $H^{-1} > 1$. If cross-correlations are negative and suppress conductivity, then it leads to $H^{-1} < 1$. The latter is usually observed in ionic liquids [52]. To estimate the inverse Haven ratio, we used the proton diffusion coefficient from NMR at high temperatures, and diffusion coefficient estimated from conductivity relaxation time, Eq.(3) $D_{BDS}^{1H} = \langle\lambda_p\rangle^2/6\tau_\sigma$, at low temperatures, which are not accessible with the NMR measurements (Fig. 2a). In the latter case, we explicitly assumed that $\langle\lambda_p\rangle$ = 0.5 Å independent on temperature. If we assume that all protons participate in the conductivity, the analysis reveals that the measured conductivity is ~5 times lower than expected from the NE equation (Fig. 9a).

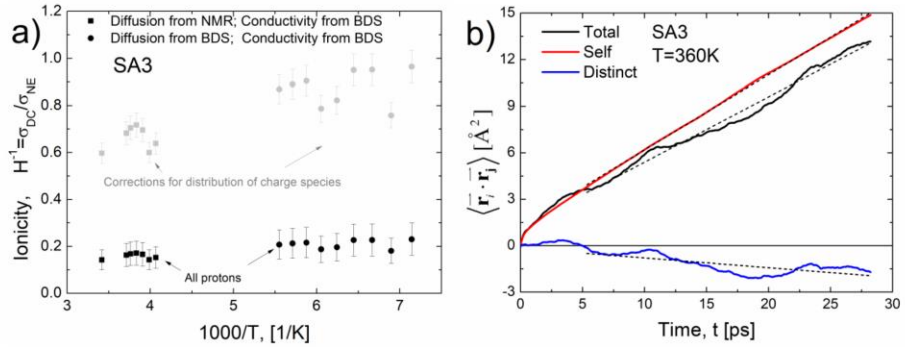

Figure 9 a) Temperature dependence of the inverse Haven ratio for SA3. For calculation of H^{-1} at high temperatures, the diffusion coefficients measured by PFG-NMR were taken from [21]. At low temperatures, the diffusion coefficient was estimated from the AC-DC crossover from the conductivity spectra (see text for details). Black symbols correspond to the case when we assume that all protons contribute to the conductivity, grey symbols correspond to the case when the number of charge species is corrected according to the species distribution (Fig.7a) **b)** Mean square displacement of protons for SA3 at 360 K (black line) and self (red line) and distinct (blue) contributions. The dashed line is the linear fit to estimate the diffusion coefficients.

AIMD simulations allow us to directly calculate the self- and distinct- proton displacement vector correlations and their time dependencies (Figure 9b). While the self-proton displacement vector correlation shows smooth variation, the total one (self + distinct) doesn't show a straight line due to strong fluctuations in the distinct one (Fig. 9b) This may be ascribed to different mobilities of protons that are associated with various species as well as the distinct frequencies of proton transfer between different pairs. Nevertheless, the average slopes provide rough estimate of the self- and total diffusion coefficients (dashed line in Fig.9b). In that case the inverse Haven ratio defined as

D_{total}/D_{self}, is about 0.85. This value is significantly higher than the value we obtained from the experimental data and the Eq. 5 (Fig. 9a). This difference can be explained by the fact that in Eq.(5) we took into account all protons, but most of them move with the water molecules without carrying any charge. The instantaneous species distribution (Fig. 7a) indeed shows that only about one proton (HSO_4^-) from a sulfuric acid molecule and one from H_3O^+ will contribute to the conductivity. This correction leads to $H^{-1} \sim 0.7\text{-}0.95$, which is close to the range predicted by the AIMD simulations. Thus, simulation and experimental data indicate that $H^{-1} < 1$, and this result clearly indicates that proton-proton correlations suppress conductivity also in SA3. All these results reinforced our previous suggestion [4] that 'Grotthuss' chain-like proton conductivity seems to be impossible in a bulk liquid state, most probably due to momentum or volume conservation laws [53,54].

Summarizing, we can propose the next scenario of proton transport in PA, PA1 and SA3 systems. PA molecules easily donate and accept protons, resulting in mostly neutral PA and water molecules in these systems [55]. As a result, all protons in PA systems jump at a similarly fast rate. In contrast, SA molecules easily donate one proton to the water network and are reluctant to accept protons. The donated proton is associated between water molecules forming H_3O^+. The dissociation of the second proton from the deprotonated SA molecule takes much longer, and this leads to much slower local diffusion of this proton in comparison to other protons in the SA3 system. This creates a population of two charged species in the system, HSO_4^- and H_3O^+, and stronger coupling between proton hopping and rotation of the SA and water molecules. As a result, both proton transfer and vehicular transport contribute to proton conductivity in SA3 [55]. In contrast, in the PA and PA1 systems, protons easily dissociate and associate with the PA molecules, resulting in the observation that all protons in the PA systems hop at a similar fast rate. This leads to decoupling between the rotation of the PA molecules and proton hopping. This facilitates smooth and fast proton transport throughout the whole sample without strong involvement of molecular motion. In this case, the proton transport dominates the conductivity of the PA systems making them the best intrinsic proton conductors. The readiness of a PA molecule to accept protons also means that it predominantly moves as a neutral species, resulting in lower pH levels in PA and PA1 systems and less chemical aggressive behavior in comparison to SA3.

Conclusions

We have undertaken a comprehensive study of proton transport in aqueous solution SA3 and compared it with previous study of proton transport in pure PA and aqueous solution PA1 [4]. Our results show that characteristics of proton transport in all these systems are generally quite similar, but there are fundamental differences in SA3 and in pure PA and PA1 systems. The protons in pure PA, PA1, and SA3 solutions are moving via very short (about 0.5 Å) and fast jumps between the molecules, and this proton hopping provides the major contribution to the DC-conductivity. However, unlike the PA systems, QENS measurements and AIMD simulations indicate that not all protons in the SA3 system participate in this fast proton hopping on a picosecond timescale. Our estimates suggest that at least one proton per host SA molecule is much slower on the picosecond timescale, versus all protons being mobile in PA systems. However, all protons in SA3 became identical on the time and length scale of the PFG-NMR experiments, clearly suggesting that proton transfers/exchanges even for HSO_4^-. Another similarity between the PA and SA systems is that structural relaxation is much slower than conductivity relaxation. However, in SA3 there is strong coupling between structural and conductivity relaxation in comparison to the PA systems, where these two processes are decoupled, especially at lower temperatures. This indicates that rotation of the host SA and water molecules plays a more important role in proton transport than that in PA systems. Furthermore, our results show that, the proton-proton correlations suppress the conductivity in sulfuric aqueous solutions and in PA, supporting our early suggestions that a 'Grotthuss-like' mechanism is apparently not possible in a bulk liquid state.

Acknowledgements

We acknowledge support of the National Science Foundation (awards CHE-1764409 and CHE-2102425). We also acknowledge support for the high frequency dielectric and rheology measurements from "Fast and Cooperative Ion Transport in Polymer-Based Materials (FaCT)", and Energy Frontier Research Center funded by the U.S. Department of Energy, Office of Science, Basic Energy Sciences. Research at the BASIS of the ORNL's Spallation Neutron Source was sponsored by the Scientific User Facilities Division, Office of Basic Energy Sciences, U.S. Department of Energy. Computing resources were provided through an ACCESS allocation DMR130078 on Stampede2 at the Texas Advanced Computing Center (TACC). J.T.D. acknowledges the U.S. Department of Energy, Office of Science, Basic Energy Sciences, Materials

Sciences and Engineering Division [FWP# ERKCK60], under contract DE-AC05-00OR22725 with UT-Battelle, LLC for the support of the NMR experiments.

Author contributions

I.P., H.S., A.M. performed the dielectric measurements over a wide range in frequency and analyzed the conductivity data. I.P. and A.P.S. performed and analyzed the light scattering measurements. E.M., C.G., I.P., and R.L.S. performed the QENS measurements and analyzed the neutron scattering data. C.G. and J.T.D. performed PFG-NMR measurements. Z.Z. and S.J.P. performed and analyzed the AIMD simulations. C.G. performed and analyzed rheological measurements. S.J.P. and A.P.S. developed the idea and led the research. All authors contributed to the discussion of the results.

Corresponding Authors

*E-mail: sokolov@utk.edu; spaddison@utk.edu; ipopov@utk.edu

Data Availability. The data that support the plots within this paper and another finding of this study are available from the corresponding author upon reasonable request.

Code Availability. The computer code used for simulations is available from the corresponding authors upon reasonable request.

Competing interests. The authors declare no competing interests.

References

1 Lim, D.-W. & Kitagawa, H. Proton Transport in Metal–Organic Frameworks. *Chemical Reviews* **120**, 8416-8467, (2020).

2 Ogiwara, N., Iwano, T., Ito, T. & Uchida, S. Proton conduction in ionic crystals based on polyoxometalates. *Coordination Chemistry Reviews* **462**, 214524, (2022).

3 Wang, X. R. et al. Review on water management methods for proton exchange membrane fuel cells. *International Journal of Hydrogen Energy* **46**, 12206-12229, (2021).

4 Popov, I. et al. Search for a Grotthuss mechanism through the observation of proton transfer. *Communications Chemistry* **6**, 77, (2023).

5 Tuckerman, M. E., Marx, D. & Parrinello, M. The nature and transport mechanism of hydrated hydroxide ions in aqueous solution. *Nature* **417**, 925-929, (2002).

6 Marx, D., Tuckerman, M. E., Hutter, J. & Parrinello, M. The Nature of the Hydrated Excess Proton in Water. *Nature* **397**, 601-604, (1999).

7 Tuckerman, M., Laasonen, K., Sprik, M. & Parrinello, M. Ab Initio Molecular Dynamics Simulation of the Solvation and Transport of H3O+ and OH- Ions in Water. *The Journal of Physical Chemistry* **99**, 5749-5752, (1995).

8 Agmon, N. The Grotthuss mechanism. *Chemical Physics Letters* **244**, 456-462, (1995).

9 Kreuer, K.-D., Rabenau, A. & Weppner, W. Vehicle Mechanism, A New Model for the Interpretation of the Conductivity of Fast Proton Conductors. *Angewandte Chemie International Edition in English* **21**, 208-209, (1982).

10 Greenwood, N. N. & Thompson, A. Proton-Switch as a Mechanism for Conduction in Anhydrous Phosphoric Acid. *P Chem Soc London*, 352-353, (1958).

11 Swanson, J. M. J. et al. Proton Solvation and Transport in Aqueous and Biomolecular Systems: Insights from Computer Simulations. *The Journal of Physical Chemistry B* **111**, 4300-4314, (2007).

12 Cukierman, S. Et tu, Grotthuss! and other unfinished stories. *Biochimica et Biophysica Acta (BBA) - Bioenergetics* **1757**, 876-885, (2006).

13 von Grotthuss, C. J. T. Sur la Décomposition de L'eau et des Corps Qu'elle Tient en Dissolution à L'aide de L'électricité Galvanique. *Ann. Chim.* **58**, 54– 73, (1806).

14 Schuster, M., Kreuer, K.-D., Steininger, H. & Maier, J. Proton conductivity and diffusion study of molten phosphonic acid H3PO3. *Solid State Ionics* **179**, 523-528, (2008).

15 Dippel, T., Kreuer, K. D., Lassègues, J. C. & Rodriguez, D. Proton Conductivity in Fused Phosphoric Acid; A 1H/31P PFG-NMR and QNS Study. *Solid State Ionics* **61**, 41-46, (1993).

16 Vilciauskas, L., Tuckerman, M. E., Bester, G., Paddison, S. J. & Kreuer, K. D. The Mechanism of Proton Conduction in Phosphoric Acid. *Nat Chem* **4**, 461-466, (2012).

17 Aihara, Y., Sonai, A., Hattori, M. & Hayamizu, K. Ion Conduction Mechanisms and Thermal Properties of Hydrated and Anhydrous Phosphoric Acids Studied With1H, 2H, And31P NMR. *J. Phys. Chem. B* **110**, 24999–25006, (2006).

18 Greenwood, N. N. & Thompson, A. The mechanism of electrical conduction in fused phosphoric and trideuterophosphoric acids. *J. Chem. Soc.*, 3485–3492, (1959).

19 Frick, B., Vilčiauskas, L., Deen, P. P. & Lyonnard, S. The nanosecond proton dynamics of phosphoric acid – from the solid to the melt – investigated by neutron backscattering. *Solid State Ionics* **252**, 26-33, (2013).

20 Tromp, R. H., Spieser, S. H. & Neilson, G. W. A neutron diffraction and computer modeling study of the interatomic structure of phosphoric acid. *The Journal of Chemical Physics* **110**, 2145-2150, (1999).
21 Frey, M., Didzoleit, H., Gainaru, C. & Böhmer, R. Dynamics in Glass Forming Sulfuric and Nitric Acid Hydrates. *The Journal of Physical Chemistry B* **117**, 12164-12174, (2013).
22 Mamontov, E. & Herwig, K. W. A time-of-flight backscattering spectrometer at the Spallation Neutron Source, BASIS. *Review of Scientific Instruments* **82**, 085109, (2011).
23 Arnold, O. et al. Mantid—Data analysis and visualization package for neutron scattering and μ SR experiments. *Nuclear Instruments and Methods in Physics Research Section A: Accelerators, Spectrometers, Detectors and Associated Equipment* **764**, 156-166, (2014).
24 Azuah, R. T. et al. DAVE: A Comprehensive Software Suite for the Reduction, Visualization, and Analysis of Low Energy Neutron Spectroscopic Data. *J Res Natl Inst Stand Technol* **114**, 341-358, (2009).
25 CPMD (IBM Corporation 1990− 2009 and MPI für Festkörperforschung 1997−2001, 2009).
26 Marx, D. & Hutter, J. *Ab Initio Molecular Dynamics: Theory and Implementation. In Modern Methods and Algorithms of Quantum Chemistry*. Vol. Vol. 1 (Forschungszentrum: Juelich, 2000).
27 Aeberhard, P. C., Arey, J. S., Lin, I.-C. & Rothlisberger, U. Accurate DFT Descriptions for Weak Interactions of Molecules Containing Sulfur. *J. Chem. Theory Comput.* **5**, 23−28, (2009).
28 Lin, I.-C. et al. Library of Dispersion-Corrected Atom-Centered Potentials for Generalized Gradient Approximation Functionals: Elements H, C, N, O, He, Ne, Ar, and Kr. *Phys. Rev. B* **75**, 205131, (2007).
29 Lee, C., Yang, W. & Parr, R. G. Development of the Colle-Salvetti Correlation-energy Formula into a Functional of the Electron Density. *Phys. Rev. B* **37**, 785-789, (1988).
30 Becke, A. D. Density-Functional Exchange-Energy Approximation with Correct Asymptotic Behavior. *Phys. Rev. A* **38**, 3098−3100, (1988).
31 Sprenger, K. G., Jaeger, V. W. & Pfaendtner, J. The General AMBER Force Field (GAFF) Can Accurately Predict Thermodynamic and Transport Properties of Many Ionic Liquids. *J. Phys. Chem. B* **119**, 5882-5895, (2015).
32 Martyna, G. J., Tuckerman, M. E. & Klein, M. L. Nose-Hoover Chains: The Canonical Ensemble via Continuous Dynamics. *J. Chem. Phys.* **97**, 2635−2643, (1992).
33 Dyre, J. C. The random free-energy barrier model for ac conduction in disordered solids. *Journal of Applied Physics* **64**, 2456-2468, (1988).
34 Dyre, J. C. Studies of ac hopping conduction at low temperatures. *Physical Review B* **49**, 11709-11720, (1994).
35 Dyre, J. C. & Schrøder, T. B. Universality of ac conduction in disordered solids. *Reviews of Modern Physics* **72**, 873-892, (2000).
36 Schrøder, T. B. & Dyre, J. C. Scaling and Universality of ac Conduction in Disordered Solids. *Physical Review Letters* **84**, 310-313, (2000).
37 Schrøder, T. B. & Dyre, J. C. ac Hopping Conduction at Extreme Disorder Takes Place on the Percolating Cluster. *Physical Review Letters* **101**, 025901, (2008).
38 Sangoro, J. R. et al. Charge transport and mass transport in imidazolium-based ionic liquids. *Physical Review E* **77**, 051202, (2008).

39 Schrøder, T. B. & Dyre, J. C. Solid-like mean-square displacement in glass-forming liquids. *The Journal of Chemical Physics* **152**, 141101, (2020).

40 Böttcher, C. J. F. & Bordewijk, P. *Theory of electric polarization. Volume II. Dilectric in time-dependent fields*. Vol. 2 (Elsevier Science Limited, 1978).

41 Singwi, K. S. & Sjölander, A. Diffusive Motions in Water and Cold Neutron Scattering. *Physical Review* **119**, 863-871, (1960).

42 Ferry, J. D. *Viscoelastic properties of polymers*. (John Wiley & Sons, 1980).

43 Roland, C. M. *Viscoelastic behavior of rubbery materials*. (OUP Oxford, 2011).

44 Bierwirth, S. P., Gainaru, C. & Böhmer, R. Communication: Correlation of terminal relaxation rate and viscosity enhancement in supramolecular small-molecule liquids. *The Journal of Chemical Physics* **148**, (2018).

45 Ahlmann, S. et al. The relationship between charge and molecular dynamics in viscous acid hydrates. *The Journal of Chemical Physics* **155**, 014505, (2021).

46 Wang, Y. et al. Ionic Conductivity and Glass Transition of Phosphoric Acids. *The Journal of Physical Chemistry B* **117**, 8003-8009, (2013).

47 Ahmed, M. D. et al. Effect of Ion Mass on Dynamic Correlations in Ionic Liquids. *The Journal of Physical Chemistry B* **127**, 10411-10421, (2023).

48 Popov, I. et al. Controlling ion transport number in Solvent-in-Salt Solutions. *The Journal of Physical Chemistry B* **4**, 3174-3182, (2022).

49 Popov, I. et al. Critical Role of Anion–Solvent Interactions for Dynamics of Solvent-in-Salt Solutions. *The Journal of Physical Chemistry C* **124**, 8457-8466, (2020).

50 Lassegues, J. C. & Cavagnat, D. Neutron scattering study of the proton dynamics in aqueous solutions of sulphuric acid and caesium sulphate. *Molecular Physics* **68**, 803-822, (1989).

51 Dyre, J. C., Maass, P., Roling, B. & Sidebottom, D. L. Fundamental questions relating to ion conduction in disordered solids. *Reports on Progress in Physics* **72**, 046501, (2009).

52 Gainaru, C. et al. Mechanism of Conductivity Relaxation in Liquid and Polymeric Electrolytes: Direct Link between Conductivity and Diffusivity. *The Journal of Physical Chemistry B* **120**, 11074-11083, (2016).

53 Kashyap, H. K., Annapureddy, H. V. R., Raineri, F. O. & Margulis, C. J. How Is Charge Transport Different in Ionic Liquids and Electrolyte Solutions? *The Journal of Physical Chemistry B* **115**, 13212-13221, (2011).

54 Schoenert, H. J. Evaluation of velocity correlation coefficients from experimental transport data in electrolytic systems. *The Journal of Physical Chemistry* **88**, 3359-3363, (1984).

55 Zhu, Z., Sokolov, A. P. & Paddison, S. J. Proton transport Mechanisms in Aqueous Acids: Insight from Ab Initio Molecular Dynamics Simulations. *J. Chem. Phys.* **JCP24-AR-MD602024-02497**, (2024).

The preprint of manuscript that is to be submitted to the Advanced Energy Materials:

Ion Transport in Polymerized Ionic Liquids: Effects of Sidechain Flexibility and Specific Interactions

Zhenghao Zhu,[1] Alexei P. Sokolov,[2,3] and Stephen J. Paddison[1*]

[1]Department of Chemical & Biomolecular Engineering, University of Tennessee, Knoxville, Tennessee 37996, USA

[2]Department of Chemistry, University of Tennessee, Knoxville, Tennessee 37996, USA

[3]Chemical Sciences Division, Oak Ridge National Laboratory, Oak Ridge, Tennessee 37831, USA.

Abstract

Atomistic molecular dynamics (MD) simulations were undertaken on polymerized ionic liquids (polyILs) consisting of a polymethylmethacrylate (PMMA) based backbone with attached imidazolium cations through a series of linker lengths and mobile anions: $TFSI^-$, PF_6^-, BF_4^-, and Br^-. Ionic correlations and the mechanisms of ion transport in these polyILs were systematically investigated to understand the effects of sidechain flexibility coupled with specific interactions. The simulations revealed that the linker length has only a minimal effect on cation-anion interactions particularly when compared to the change with the associated anion. An increase in the linker length enhances the anion diffusivity to a varying extent for the different anions arising from significant increases in diffusivity but a lesser reduction in ion hopping. Specifically, the small anions exhibit large increases in the anion diffusivity when the linker length is increased since the rigid "cage" appears to be strongly softened by increasing sidechain flexibility, suggesting a size-dependent effect. Dynamical heterogeneity in the anion mobility further confirms the softening effect of the long linkers. Moreover, only a small fraction of the anions was observed to travel farther than the characteristic distance determined by the self-part of the van Hove function within the characteristic time of the strongest heterogeneity. Fast mobile anions exhibit dominant interchain hopping associated with more cations from more chains compared with the slow anions. The stringlike cooperative motion was observed in these fast anions and the string length decreases as the linker length increases. More importantly, distinct anion-anion correlation suppresses the conductivity in a barycentric reference frame, while this correlation enhances the conductivity within a polycation-fixed reference frame. The cage escape seems to serve as the primary ion transport rate controlling mechanism in these systems. These findings

may lead to interesting implications for the design of polyILs with enhanced ionic conductivity for electrochemical applications.

1 Introduction

Polymerized ionic liquids (polyILs) continue to be of great interest as electrolytes in energy conversion and storage devices since they combine the ion transport behavior of ionic liquids (ILs) with the advantageous properties of polymers including robust mechanical integrity, low flammability, reduced leakage concerns, improved safety, and prolonged durability.[1-3] However, these materials exhibit low conductivity at room temperature, primarily stemming from the sluggish segmental dynamics of polymer chains, and limited dielectric constants, thus impeding their widespread applications.[4, 5] Substantial effort has been made to address this hurdle, aiming to enhance the ionic conductivity to ~10^{-3} S/cm by tailoring the architecture of the polymer chain and the chemical structure of the ions.[3, 4, 6-11] One direction is to accelerate segmental dynamics by lowering the glass transition temperature of the polyILs. Another avenue seeks to decouple the mobility of the ion from the segmental dynamics. Hence, the advancement of next-generation materials exhibiting superior properties strongly relies on securing a fundamental understanding of the role of molecular structure, morphology, and ionic correlations in the transport of charge.

Recent studies[10, 12-15] have unveiled a competition between electrostatic interaction and elastic force, which are strongly influenced by factors including: mobile ion size, dielectric constant, and polymer backbone rigidity. This competition manifests itself in a non-monotonic trend of the activation energy of the ion mobility vs the radius of the mobile ion within polyILs below their glass transition temperature.[10] Similar observations extend to other properties like glass transition temperature, segmental relaxation time, and counterion diffusivity, as evidenced by coarse-grained simulations.[13] These findings suggest that ion transport can potentially be enhanced by reducing the glass transition temperature via tailoring various parameters. Furthermore, a decoupling of mobile ion transport from polymer segmental dynamics has been observed in polyILs, as depicted in a Walden plot.[16-19] Particularly, rigid polymers with small counterions exhibit pronounced decoupling behavior.

To explore the ion transport characteristics from a molecular-level behind these intriguing phenomena, molecular dynamics (MD) simulations were leveraged to elucidate ion transport mechanisms in polyILs. Specifically, Ganesan et al.[20] proposed that mobile ions transport through

interchain, intrachain, and chain-to-free hopping pathways. Furthermore, these studies revealed that the PF_6^- diffusivity is directly correlated to the average lifetime of ion-dissociation in poly(1-butyl-3vinylimidazolium-hexafluorophosphate) electrolytes. This contrasts to the primary mechanism of ion transport in pure ILs, in which a linear correlation exists between PF_6^- diffusivity and the inverse structural relaxation time.[21] This universal correlation was consistently observed in the subsequent studies of the authors.[22-24] However, the linear correlation of ion mobilities also occurs for anion cage escape times in both imidazolium-based and ammonium-based polyILs.[25-28] Furthermore, dynamic heterogeneity and cooperative stringlike motion were observed in these polyILs.[25-27]

Regardless of the ion transport mechanism, another indicator that reveals the difference between ion transport and ionic conductivity is the inverse Haven ratio, $H^{-1} = D_\sigma/D_i$. Here, D_i represents the self-diffusivity of the ions, typically measured by NMR, while D_σ signifies charge diffusivity, including both self- and distinct correlations, obtained from impedance spectroscopy employing the Nernst-Einstein (NE) equation.[29-34] This indicator shows that the classical NE equation is valid only when distinct correlations are negligibly small. Typically, distinct correlations can be positive or negative leading to either enhancement or suppression of ion conductivity. In the case of ILs, correlations have been observed to notably suppress ionic conductivity by approximately 2-3 times.[35-42] This reduction, denoted by $H^{-1} < 1$, is traditionally attributed to the movement of cation-anion pairs contributing to ion diffusion but not conductivity.[41, 42] However, this interpretation fails in polyILs where polymerized ions are moving much slower than the mobile counter ions. Moreover, this interpretation faced challenges from atomistic MD simulations,[38, 43] in which no long-lived neutral ion pairs were observed to travel together. Our recent studies[35] suggested that distinct correlations between the like-ions are responsible for the reduction in ionic conductivity of various ILs, as estimated from both experimental data using the momentum conservation approach and MD simulations capable of directly calculating these correlations. These distinct correlations are strongly influenced by the mass of the ions. Furthermore, experimental investigations of polyILs revealed that the primary mechanism behind the suppression of ionic conductivity in these materials is also due to the highly correlated motion of the mobile ions.[30] Meanwhile, recent simulations of polyILs suggested that H^{-1} is dependent on the degree of polymerization (N), reaching a maximum at $N = 3$, which arises from the pronounced distinct correlations between adjacent cations within the polyIL backbone under a fixed center of

mass reference frame.[29] Of particular interest, ion-ion correlations have been found to enhance conductivity in superionic ceramics with charge displacement exceeding that of the ions.[33, 44, 45] This prompts the question: can negative ion-ion correlations be converted into positive ones through structural modifications of ion channels and tailored specific interactions between the ions and the lattice. Excitingly, superionicity has been achieved in IL-based electrolytes by incorporating ether oxygens into the sidechain of IL cations.[46] This modification serves to increase the correlation between Li and IL cations while reversing the sign of Li-anion correlation. Currently, it remains a puzzle why these correlations enhance conductivity in superionic ceramics while significantly impeding ionic conductivity in polyILs.

This study delves into the influence of sidechain flexibility coupled with the specific interactions between the ions on the transport mechanisms and ionic correlations within polyILs. We used a polymethylmethacrylate (PMMA)-based backbone to which imidazolium cations are attached via a series of linkers (x = 2 – 8), alongside mobile anions, including bis(trifluoromethane) sulfonimide ($TFSI^-$), PF_6^-, BF_4^-, and Br^- (see Figure 1). These anions differ not only in size but also in the degree of charge delocalization, resulting in diverse specific interactions between the ions. Another key factor in tuning ionic correlations in concentrated ionic systems is electrostatic interactions, whose role was investigated by changing the dielectric constant of the simulated systems. The Onsager transport theory can readily be adopted to quantify the effect of strong dynamical correlations on the ionic conductivity in these concentrated ionic systems, which has been highlighted in recently published papers.[8] In addition, the choice of the reference frame was also considered for these distinct correlations because of the important role as shown in recent studies.[47, 48] The results are systematically discussed in the following section followed by a concise summary of the major findings. In addition, the methodology is described at the end of the manuscript.

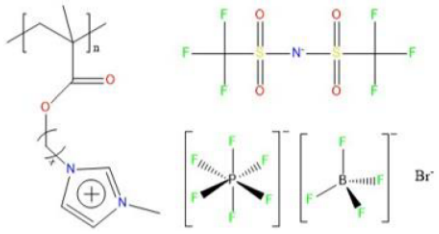

Figure 1. Chemical structures of the polyILs consisting of polycations PMMA-C_x-IM with various linker lengths (x = 2 – 8) and four associated anions.

2 Results and Discussion

2.1 Structural and Ion Association Analysis

To assess the flexibility of the sidechain, we initially analyzed the distribution of sidechain extension and projected distance as a function of the linker length (see Figure 2). For the shortest sidechain, two distinct peaks are evident, representing the two predominant configurations of the pendant imidazole ring. These configurations are influenced by interactions between the imidazole functional group and the acrylate group. As the alkyl linker length increases, these interactions weaken, leading to a transition from double peaks to a single peak with only minor shoulders. Consequently, both the extended and projected distances of the imidazole ring exhibit broad distributions, shifting towards longer distances with increasing linker length. This is indicative of enhanced flexibility with the longer linkers. Figure S1 further elucidates this trend, depicting detailed distributions of the extension and angle between the sidechain and the backbone, underscoring that longer linkers afford increased flexibility in both extension and angle.

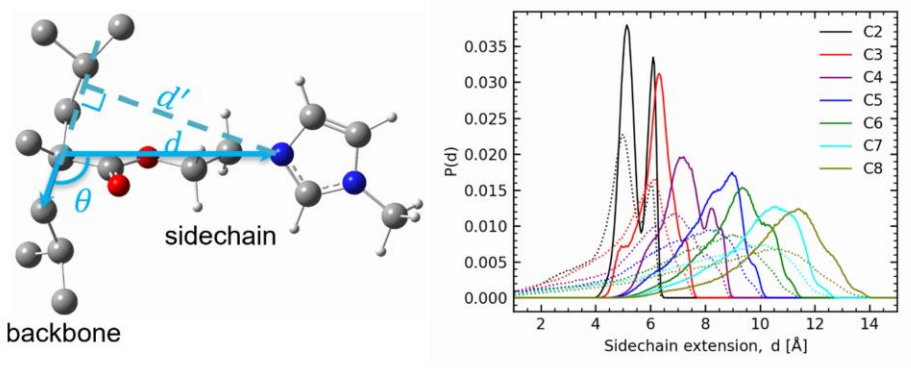

Figure 2. Distribution of the sidechain extended (solid lines) and projected (dotted lines) distances at 400 K.

In Figure 3, we present the radial distribution function (RDF) of the center of mass of the cations and anions for a broad range of linker lengths as well as a function of the various mobile anions. Figure 3(a) illustrates that increasing the sidechain length does not alter the position of the primary peak, instead, it enhances the intensity of this peak. This suggests that the increase of sidechain flexibility better accommodates anions in the nearest shell due to reduced steric hindrance from the backbone, although it has a slight impact on the strong electrostatic interactions between the cation and anion. In contrast, the position of the first peak shifts to shorter distance as the size of the anion decreases and is depicted in Figure 3(b). Small spherical anions exhibit sharp peaks compared to the linear anion $TFSI^-$, owing to the strong electrostatic interactions for small anions with less delocalized charge. This trend can be reproduced by simply tuning the dielectric constant of the PMMA-C_2-IM[TFSI] system, as shown in Figure S2. However, the positions of the first local minima remain unaffected by changes in the electrostatic interactions. The first local minima of these cation-anion RDFs were used to define ion association in the subsequent discussion.

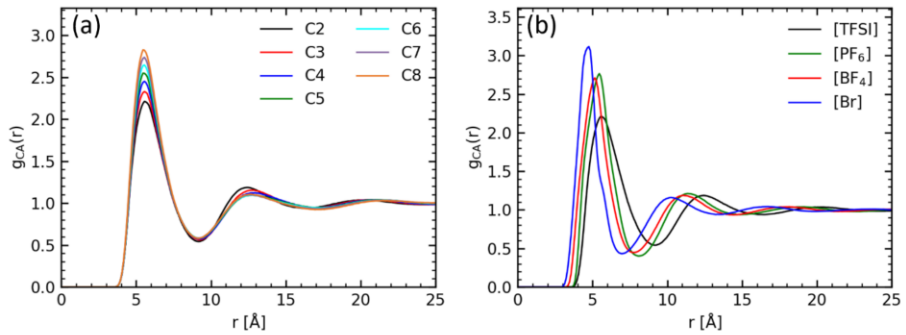

Figure 3. Cation-anion (CA) RDFs at 580 K for: (a) PMMA-C_x-IM[TFSI] (x = 2 – 8); and (b) PMMA-C_2-IM associated with various anions.

The RDFs demonstrate that all anions strongly interact with the polymerized cations. Furthermore, we examined the probabilities of the coordination numbers of the cations, $P(n)$, and of the polyIL chains, $P(N)$, with a given anion at 580 K (see Figure 4), which play an important role in the ion hopping mechanism. In Figure 4(a), the majority of the $TFSI^-$ anions associate with 4 – 7 cations. The peak of $P(n)$ was observed at $n = 6$ for the shortest linker length and at $n = 5$ for longer sidechains $(x = 4 - 8)$, with two comparable probabilities at $n = 5$ and 6 for the intermediate sidechain length $(x = 3)$. However, linker length has little influence on the distribution of coordinated chains, $P(N)$, especially when the linker is sufficiently long $(x \geq 5)$ (Figure 4(c)). An increase in the linker length slightly shifts $P(N)$ to the right with a maximum at $N = 3$. These results indicate that increased sidechain flexibility results in fewer cations associating with an anion but from more distinct chains, forming a loose "cage" around the anion. Figure 4(b) and (d) show the effect of the size of anions on the coordination characteristics at 580 K. Interestingly, $TFSI^-$ and BF_4^- exhibit a similar distribution of associated cations, with peaks at $n = 6$, while PF_6^- displays a broad peak and the small Br^- associates with fewer cations, featuring a sharp peak at $n = 5$. Regarding the probability distribution of associated chains, $P(N)$, the three spherical anions exhibit similar distributions with a sharp peak at $N = 3$, whereas the linear $TFSI^-$ features a broad peak with the distribution shifted to the left. This implies that the ion association is influenced by the interplay between electrostatic interactions and steric hindrance arising from both the shape of the anion and the backbone of the polycation.

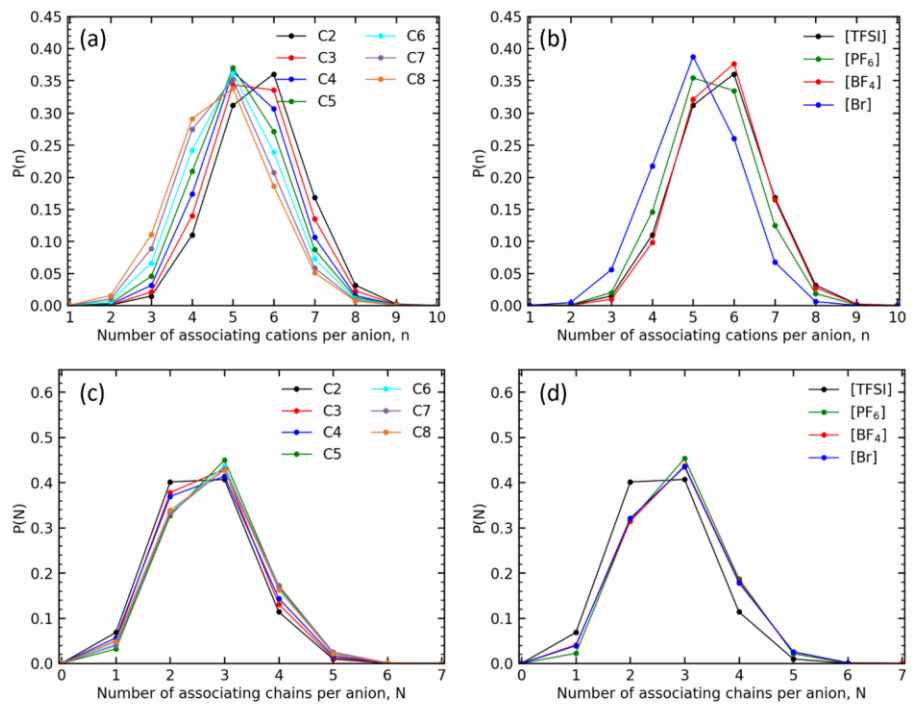

Figure 4. Probability of an anion coordinating with n cations, $P(n)$, for: (a) a broad range of linker lengths and (b) four anions at 580 K. Probability of an anion associating with N cations, $P(N)$, for: (c) a broad range of linker lengths; and (d) four anions at 580 K.

2.2 Anion Dynamical Correlations

Our previous MD simulation results revealed that anions associating with fewer cations from more coordinating polymers tend to exhibit higher mobility.[26] To explore the relationship between ion association and ion dynamics, the self-diffusivity of the anion was derived from the mean square displacement (MSD) using the Einstein relation:

$$D = \frac{1}{6}\lim_{t\to\infty}\frac{d}{dt}\langle\sum_{i=1}^{N}[\boldsymbol{r}_i(t_0+t)-\boldsymbol{r}_i(t_0)]^2\rangle, \quad (1)$$

where $\boldsymbol{r}_i(t_0 + t)$ and $\boldsymbol{r}_i(t_0)$ represent the positions of the ith particle at times $t_0 + t$ and t_0, respectively. Figure 5 illustrates the self-diffusion coefficients of the anions as a function of linker length for the various anions. In general, the self-diffusivity increases to a varying extent with increasing linker length for the studied anions. Specifically, the diffusivity of the smallest anion, Br^-, increases significantly fast from a linker length of C2 to that of C5, followed by a more gradual increase. This is the case for anion PF_6^-, although it has a larger volume than Br^-. Nevertheless, the increase in the linker length only marginally enhances the diffusion coefficients of anions BF_4^- and $TFSI^-$. As a result, the differences between these anions are substantial (exceeding one order of magnitude) in systems with short linkers, but diminish as the linker length increases. More interestingly, for the shortest linker, the diffusivity follows the order: $TFSI^- > BF_4^- > PF_6^- > Br^-$, consistent with observations in the poly(1-butyl-3-vinyl-imidazolium)[49] and poly(1-ethyl-3-vinyl-imidazolium)[27] systems where the imidazolium ring directly attaches to the backbone. However, the diffusivity of BF_4^- surpasses that of $TFSI^-$ with a sufficiently long linker.

To discern the effect of electrostatic interactions, the diffusivities of $TFSI^-$, BF_4^-, and Br^- as a function of the relative permittivity in the PMMA-C_2-IM systems at 500 K were plotted in Figure S3. At low dielectric constants, the diffusivities of the smaller BF_4^- and Br^- are lower than that of the larger $TFSI^-$. However, at high dielectric constants, the smaller anions exhibit higher diffusivities than the larger one. This shift occurs because, at high dielectric constants, the dominant factor changes from electrostatic interactions to the size/mass of the anon.

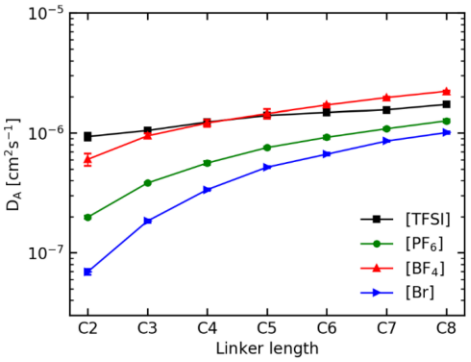

Figure 5. Diffusion coefficient of the four anions as a function of linker length at 580 K.

In concentrated ionic systems, distinct correlations between the ions play a critical role in ion transport mechanisms due to the strong electrostatic interactions. The Onsager transport coefficients can be readily obtained from the following equation:

$$L^{ij} = \frac{1}{6k_B TV} \lim_{t\to\infty} \frac{d}{dt} \langle \sum_{i=0}^{N} [\boldsymbol{r}_i(t) - \boldsymbol{r}_i(0)] \cdot \sum_{j=0}^{N} [\boldsymbol{r}_j(t) - \boldsymbol{r}_j(0)] \rangle, \quad (2)$$

where k_B is the Boltzmann constant, T is the temperature, and V is the volume. The ionic conductivity may then be related to L^{ij} with:

$$\sigma_{ij} = z_i z_j F^2 L^{ij} \quad (3)$$

where z_i and z_j are the charge valences of species i and j, respectively; and F is the Faraday constant. First, we assume that the polymerized cations are fixed, and only mobile anions contribute to the ionic conductivity. Figure 6(a) shows the contributions of ionic correlations between $TFSI^-$ normalized by the self-component σ_{an}^{s}, representing ideal and uncorrelated particle movement as a function of linker length. It is observed that the distinct anion correlation is always negative, although the magnitude slightly decreases and then increases along the linker length. As a result, the total contribution seems to reach a maximum at the linker length of C5. This normalized total contribution is also interpreted as the inverse Haven ratio H^{-1}, which lies in the range between 0.3 and 0.5, consistent with experimental data.[10, 15] Note that these data were derived from Equation (3) using a barycentric reference frame (RF). Additionally, electrostatic interactions influence these ionic correlations to varying extents. Specifically, changes in the dielectric constant have a more significant impact on the less delocalized anions (BF_4^- and Br^-) compared to the larger $TFSI^-$ (Figure S4).

A recent study[47] reveals that the choice of the RF plays an important role in certain dynamical properties including the transference number that exhibits a negative value in PEO-LiTFSI under certain conditions. This negative transference number was reproduced in MD simulations by transforming the Onsager coefficients to the solvent-fixed RF from the barycentric RF.[47, 50] One may naturally ask the question: does the RF affect the distinct correlations and the inverse Haven ratio? To verify this hypothesis, we calculated the distinct correlation between anions and cations as shown by blue upper triangles in Figure 6(a). Surprisingly, the magnitude of this anion-cation

correlation is nontrivial, suggesting that the movement of polycations may also have an influence on the inverse Haven ratio. We chose the center of mass of all polycations in the systems as the RF. Figure 6(b) illustrates the corresponding contributions of ionic correlations with a polycation-fixed RF. Indeed, the anticorrelated motion between the anions become positive, indicating that the distinct anion-anion correlation positively contributes to the ionic conductivity under the polycation-fixed RF. Simultaneously, the distinct anion-cation correlation becomes negligible. This transformation leads to $H^{-1} > 1$ in these polyILs. Such a phenomenon was also observed in poly(1-butyl-3-vinyl-imidazolium) associated with various anions in which the distinct anion-anion correlation was obtained from the self-diffusivity and the true conductivity based on the equilibrium and non-equilibrium simulations, respectively.[49] Given the principle of momentum conservation, the momentum of the anions is dissipated by removing the movement of the polymerized cations, leading to an intriguing implication of constraining the poly-ion motion by crosslinking the polymer chains or introducing solvent in the design of polyILs with improved ionic conductivity.

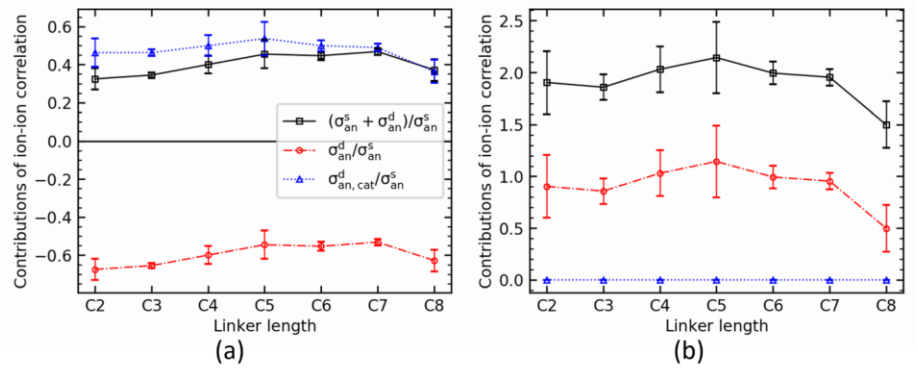

Figure 6. (a) Contribution of anion-anion correlations as a function of linker length under: (a) a barycentric reference frame; and (b) a polycation-fixed reference frame at 580 K.

Utilizing our prior categorization of ion hopping events,[26, 27] we classified four ion hopping types in Figure 7: Type 1 denotes instances where the anion changes its coordination of cationic groups from the same polymer chain during the hopping interval Δt; Type 2 occurs when the anion alters its coordination of cationic groups from the different polymers; Type 3 characterizes cases where the anion does not associate with any cations; and Type 4 is rattling events in which the anion gets

trapped in a "cage" formed by the cationic groups. It has been suggested that the choice of Δt within the range of 10 – 100 ps for polyILs makes little difference, although the best option is around 2 ps or smaller corresponding to the fastest ion jumping rates.[20] Therefore, we chose a sampling interval of 10 ps to strike a balance between accuracy and computational expense.

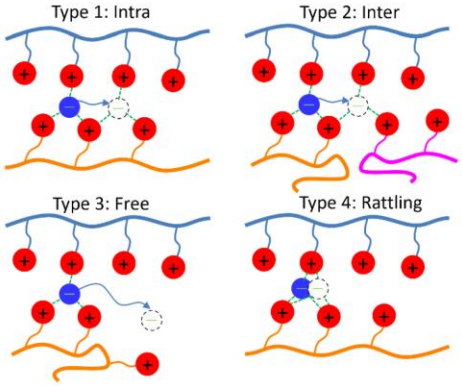

Figure 7. Categorization of the ion hopping types: type 1 (intrachain); type 2 (interchain); type 3 (free ions without associated ions); and type 4 (rattling).

Figure 8a demonstrates the percentage of the four types of ion hopping for PMMA-C_x-IM[TFSI] (x = 2 – 8). Surprisingly, the occurrence of rattling events is only affected slightly by the linker length with a minimum at the linker lengths of C5 and C6, although the self-diffusivity increases monotonically in Figure 5. It is observed that the rate of interchain hopping is consistently lower than that of intrachain hopping. However, as the linker length extends, the percentage of intrachain hopping decreases while the proportion of interchain hopping increases. Free anions are essentially not observed in these concentrated systems. These results indicate that intrachain and interchain hopping make different contributions to the diffusivity of the anions. In Figure 8b, the occurrence probability of the hopping types across various anions with the same linker C2 is presented. The largest anion, $TFSI^-$, exhibits the lowest rattling percentage coupled with the highest percentage of intrachain and interchain hopping types, while the smallest anion Br^- displays the highest rattling percentage along with the lowest percentage of intrachain and interchain hopping. Nevertheless, BF_4^- exhibits less rattling when compared to PF_6^- despite its smaller size, which underscores the competition between Coulomb interactions and the size of the mobile ion. These trends are similar at low temperature as shown in Figure S5.

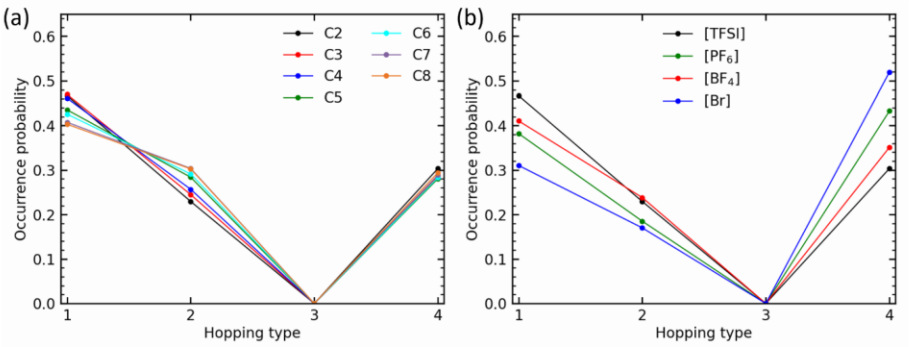

Figure 8. Occurrence probability of the hopping types for $TFSI^-$ with (a) different linker lengths; and (b) various anions with the linker length of C2 at 580 K.

One may wonder what causes the variations in intrachain and interchain hopping types. Ganesan et al. suggested that the increase in the interchain hopping type is linked to a reduction in distance between the nearest cationic groups from distinct chains, as observed in their simulation study of three different linkers devoid of the acrylate group.[23] We surmised that the nearest cation from the same chain may potentially compete with one from a different chain to associate with the hopping anion. To investigate this hypothesis, we computed the minimum distance between the cations from the same chain as shown in Figure 9. Interestingly, the average distance between the cations from different chains in the closest proximity decreases slightly with increasing linker length from C2 to C5, followed by a small increase from C5 to C8, despite the monotonical increase of the interchain hopping type illustrated in Figure 8a. However, the average distance between the nearest cations from the same chain exhibits a steady increase as the linker length is increased, resulting in a constant increase in the difference between these two average distances.

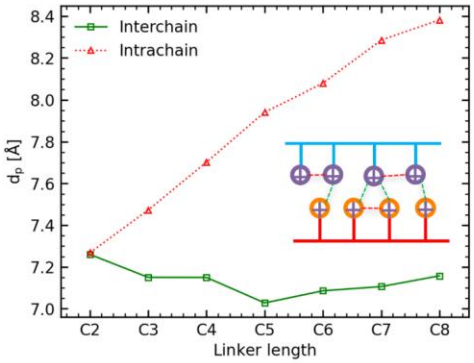

Figure 9. Average distance, d_p, between the nearest cationic group from the same polymer chain and the different polymers. Inset depicts the intermolecular distance (green dashed line) and the intramolecular distance (red dashed line) between the nearest cations, respectively.

2.3 Anion Dynamical Heterogeneity

Dynamical heterogeneity of the ions is indicative of a deviation from ideal Gaussian behavior, which has been observed in supercooled liquids,[51] ionic liquids,[52, 53] and polyILs[25-27, 49] at intermediate time scales. This deviation can be quantified by the non-Gaussian parameter α_2 defined as:

$$\alpha_2(t) = \frac{3\langle r^4(t)\rangle}{5\langle r^2(t)\rangle^2} - 1, \tag{4}$$

where $r(t)$ is the displacement of an ion at time t with respect to its position at time $t = 0$. Deviations from $\alpha_2(t) = 0$ provide insight into the degree and timescale of ion dynamical heterogeneity. The maximum of $\alpha_2(t)$ indicates the greatest dynamical heterogeneity of the anion at the intermediate timescale t^* as shown in the inset of Figure 10a. The time at which α_2 reaches its maximum value was extracted and plotted as a function of linker length for four anions to define the characteristic time t^* for ion hopping in these systems (see Figure 10a). It is observed that the difference in t^* for different anions is large for the linker of C2, while this difference diminishes with increasing linker length. Moreover, it does not exhibit a consistent correlation between t^* and anion size along with varying linker lengths. In Figure 10b, however, the maximum values $\alpha_2^{\max}$ are inversely correlated to the size of the anion across all the linker lengths, although the difference decreases as the linker length increases. Specifically, the smallest Br^- anion possessing the largest

$\alpha_2^{\max}$ exhibits the strongest heterogeneity by hopping from one Coulombic 'cage' to another formed by the polycations due to strong electrostatic interactions. The $\alpha_2^{\max}$ of Br^- sharply decreases with increasing linker length, while the linear and biggest anion, $TFSI^-$, consistently maintains the lowest $\alpha_2^{\max}$ values, typically below 0.5, which is slightly influenced by changes in linker length.

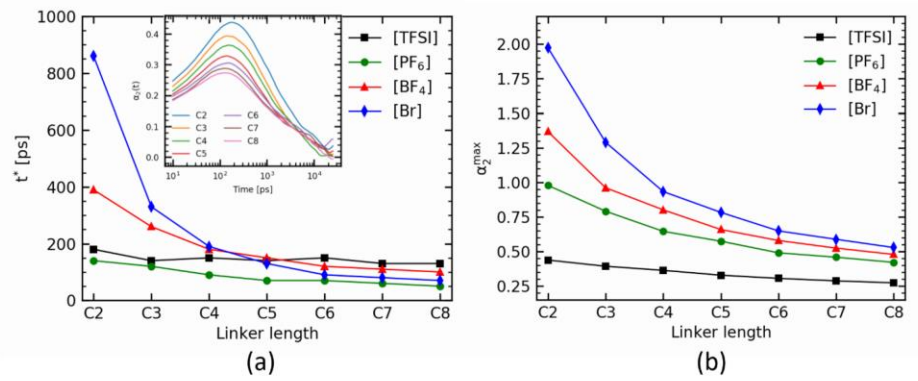

Figure 10. (a) The time scale (t^*) for the non-Gaussian parameter (α_2) reaching its maximum as a function of the linker length at 580 K. The inset shows the non-Gaussian parameter as a function of time for $TFSI^-$ with different linker lengths at 580 K. (b) Maxima of α_2 as a function of the linker length at 580 K.

To further demonstrate the motions of mobile anions with distinct extents of heterogeneities in terms of hopping types, we plotted trajectories of a typical anion from the system displaying the least heterogeneity, PMMA-C8-IM[TFSI], and the system with the largest degree of heterogeneity, PMMA-C2-IM[Br], respectively (Figure 11). Thin lines depict trajectories of the anion at intervals of 10 ps, while thick lines represent the anion hopping trajectory with the characteristic time scale of t^*. Over a period of 50 ns, $TFSI^-$ is highly mobile with over 1500 interchain hops and over 2000 intrachain hops or jumps. The trajectory with a timestep of $t^* = 130$ ps exhibits diffusive motion resembling a random walk, consistent with its small $\alpha_2^{\max}$ value (below 0.5). In contrast, Br^- experiences only a few intrachain and interchain jumps in comparison to more than 3000 rattling events (see Figure 11b and S6b). For the majority of the time, Br^- remains trapped within a Columbic 'cage', with occasional effective hops from one "cage" to another, primarily contributing to long-range diffusion. The motion between the two "cages" are discrete, indicating strong heterogeneity in the system. Analysis of these hopping events at the interval of t^* provides

the average hopping length of 2.22 Å for $TFSI^-$ and 1.13 Å for Br^-, respectively. The average hopping length for $TFSI^-$ and Br^- at the interval of 10 ps were plotted as a function of linker length in Figure S6c. The average jump length of $TFSI^-$ is consistently greater than that of Br^-. In addition, both anions exhibit a slight increase in the average jump length as the linker length increases.

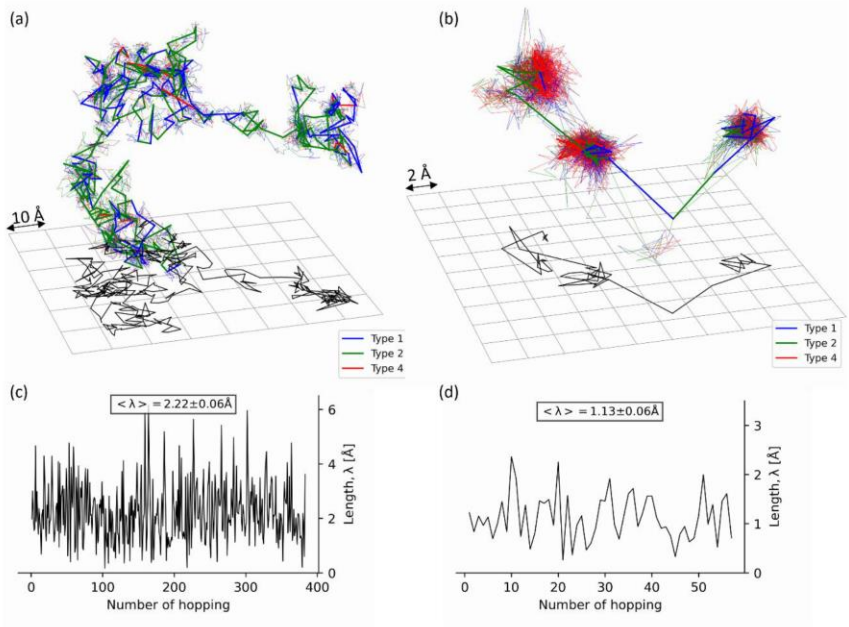

Figure 11. Trajectory lines of an individual anion in: (a) PMMA-C_8-IM[TFSI]; and (b) PMMA-C_2-IM[Br] at 580 K. Different color lines represent different types of ion hopping. Thin and thick lines refer to the trajectories with timesteps of 10 ps and the characteristic time, respectively (130 ps for (a) and 860 ps for (b), respectively). The length of each anion hopping from one "cage" to another at the interval of the characteristic time in (c) PMMA-C_8-IM[TFSI] and (d) PMMA-C_2-IM[Br] at 580 K.

To discern the correlation between mobile anions in terms of both time and space, we utilized the van Hove correlation function, which can be split into two parts, self and distinct:

$$G(r,t) = G_s(r,t) + G_d(r,t) \tag{5}$$

$$G_s(r,t) = \frac{1}{N}\sum_{i=1}^{N}\langle\delta(r - |\boldsymbol{r}_i(t) - \boldsymbol{r}_i(0)|)\rangle \tag{6}$$

$$G_d(r,t) = \frac{1}{N}\sum_{i\neq j}^{N}\langle\delta\big(r - |\boldsymbol{r}_i(t) - \boldsymbol{r}_j(0)|\big)\rangle \tag{7}$$

in which δ is the Dirac's delta function. Thus, the function $4\pi r^2 G_s(r,t)$ is the probability of finding a mobile ion at distance r provided that it was at the origin $r = 0$ when $t = 0$. The distinct part, $G_d(r,t)$, evaluates the probability distribution of a mobile ion at time t at a distance of r away from another ion at $t = 0$. Meanwhile, ideal Gaussian behavior can be readily described by

$$G_{s,0}(r,t) = \left(\frac{3}{2\pi\langle r^2(t)\rangle}\right)^{\frac{3}{2}} \exp\left(-\frac{3r^2}{2\langle r^2(t)\rangle}\right), \tag{8}$$

where $\langle r^2(t)\rangle$ is the MSD of mobile ion at time t. Figure 12 shows the self-part and the distinct part of the van Hove function at the characteristic time t^* at which $\alpha_2(t^*) = \alpha_2^{\max}$ for Br^-. Two peaks are evident when the linker is the shortest (i.e. C2), and this double-peak gradually disappears as the length of the linker is increased. Compared with the corresponding Gaussian distribution as shown by a dotted curve, the deviation remains, as seen by the tail at long distances. Therefore, anions that travel farther than the distance r^* within time t^*, for which $G_s(r^*,t^*) = G_{s,0}(r^*,t^*)$, are defined as fast "mobile" anions. Surprisingly, this distance criterion for distinguishing fast anions is not dictated by linker length (Figure 12a). However, Figure 12c reveals that the intersection between $G_s(r,t^*)$ and $G_{s,0}(r,t^*)$ varies with the associated anion and it seems to be correlated with the size of the anion. It is important to note that the crossing point coincides with the local minimum of $G_s(r,t^*)$ between two peaks in some systems, suggesting that this identification of fast anions is as effective as our previous definition of a fast anion in which the local minimum was selected,[26, 27] especially for the case where there is a single peak in the self-part of the van Hove function due to the weak heterogeneity ($\alpha_2^{\max} < 1.0$).[3] An alternative approach is to fit $G_s(r,t^*)$ with two separate Gaussian functions.[49]

Figures 12 (b and d) illustrate the distinct part of the van Hove function, $G_d(r,t)$, for PMMA-C_x-IM[Br] and PMMA-C_2 systems, respectively. It is worth noting that a sharp peak at $r = 0$ reflects the replacement of the original anion by another anion at time t^*. The intensity of this peak becomes weak with increasing flexibility of the sidechain. This result indicates that a more flexible sidechain permits movement of the "cage" formed by the polycations, resulting in a less precise replacement of anions. In Figure 12d, the distinct part of the van Hove function, $G_d(r,t)$, for different anions demonstrates that, compared to the smallest anion Br^-, the linear anion $TFSI^-$ exhibits a very low and flat peak when $r \cong 0$ Å, which arises from the loose "cage" due to the

weak Coulombic interactions between the anion and polycations. These peaks at $r = 0$ also indicate concerted motion of the anions and is discussed in the following section.

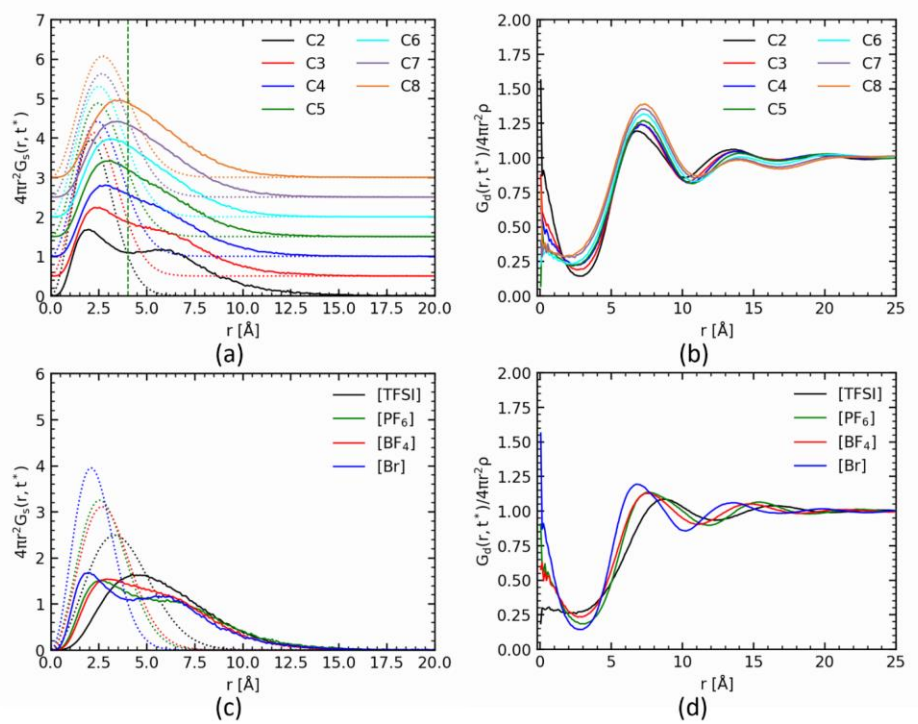

Figure 12. Self-part of the van Hove function, $G_s(r,t^*)$, for (a) PMMA-C$_x$-IM[Br] systems and (c) four anions in PMMA-C$_2$-IM systems at 580K. Each curve in (a) is vertically shifted 0.5 for clarity. The vertical line represents the intersection of $G_s(r,t^*)$ (solid lines) and $G_{s,0}(r,t^*)$ (dotted lines), which is used as the r^* criterion to determine fast and slow anion populations. Distinct-part of the van Hove function, $G_d(r,t^*)$, for (b) PMMA-C$_x$-IM[Br] systems and (d) four anions in PMMA-C$_2$-IM systems at 580 K.

To further elucidate the role of sidechain flexibility and specific interactions between the anions and polycations in ion hopping behaviors, we defined the tail of $G_s(r,t^*)$ (i.e., the green area) that deviates from the ideal Gaussian distribution (i.e. the orange area) as the ion hopping contribution (Figure 13a). The computed percentages of ion hopping contribution are presented in Figure 13b. Generally, the hopping contribution decreases with increasing linker length, although the largest anion $TFSI^-$ only exhibits a small reduction in the fraction of ion hopping. In terms of anion size,

the ion hopping fractions follow the order: $Br^- > PF_6^- > BF_4^- > TFSI^-$, and this trend is consistent across all the linkers in this investigation while the difference diminishes as the linker length increases.

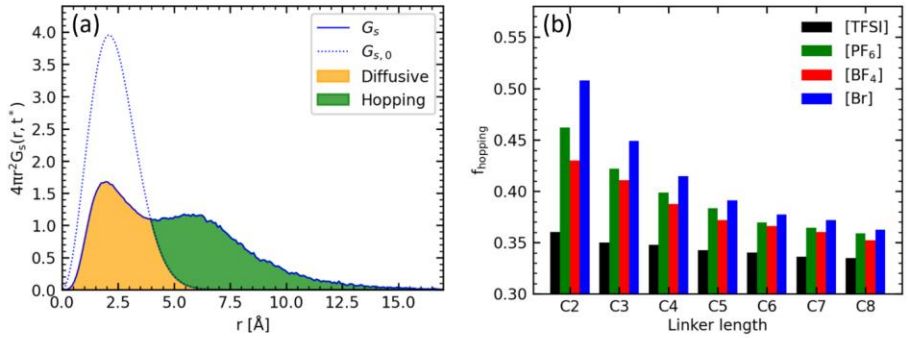

Figure 13. (a) Self-part of the van Hove function, $G_s(r, t^*)$, for PMMA-C_2-IM[Br] system to define the diffusive and hopping anions. (b) The fraction of hopping anions defined as the integral of the green area in (a) as a function of linker length for different anions.

Combining these findings with the self-diffusivity results, we may conclude that enhanced sidechain flexibility significantly improves the diffusive motions of anions but suppresses the ion hopping contribution to a lesser extent, resulting in an overall increase in the self-diffusivity constant. Moreover, a rigid Coulombic "cage" for less delocalized anions may be softened by increasing sidechain flexibility. However, for the strongly delocalized anion (i.e., $TFSI^-$), the relatively weak electrostatic interactions form a loose "cage", indicated by the primary contribution to anion diffusivity from diffusive motion that is slightly affected by changes in linker length. Interestingly, for intermediate-sized anions (i.e., BF_4^- and PF_6^-), the order of their diffusivities is not solely dictated by anion's size. The higher intensity of $g_{CA}(r)$ for PF_6^- relative to BF_4^- seems to imply that Coulombic interaction predominates over size (see Figure 3b), consistent with the findings of Zhang et al.[49] These findings underscore the intricate interplay between anion mobility and various additional factors, including mobile ion size, electrostatic interactions between ions, and linker length.

2.4 Stringlike Cooperative Motion

The results from the self- and distinct- parts of the van Hove function indicate that an ion "replacement" mechanism via a series of correlated and concerted ion hopping at the characteristic time t^* of the strongest heterogeneity appears to underlie the mobile ion transport in these polyILs. These mobile ions may form a "string", indicating a stringlike cooperative motion. This behavior may be quantified by:

$$\min\left[\left|\boldsymbol{r}_i(t^*) - \boldsymbol{r}_j(0)\right|, \left|\boldsymbol{r}_j(t^*) - \boldsymbol{r}_i(0)\right|\right] < r_s, \tag{9}$$

where $\boldsymbol{r}_i(t)$ and $\boldsymbol{r}_j(t)$ are the coordinates of the ith and j^{th} mobile ion at time t, and r_s is the distance criterion for ion "replacement". For the linear anion $TFSI^-$, r_s is determined as 2.5 Å, while for the spherical anions, it is set to 2.2 Å, based on their "hard core" radii.[26, 27] Figures 14a and 14b illustrate the probability distribution of string length, $P(n_s)$, that are greater than 10^{-4}. The string length $n_s = 0$ is referred to as the fraction of slow ions that travel less than r^* within time t^*. Only a small proportion of anions exhibit mobility sufficient to participate in stringlike motion. At 580 K, long strings containing over six anions are only observed in the PMMA-C_2-IM[Br] system. The probability distribution of string length shifts to the left as the linker length increases, suggesting that the flexibility of the sidechain impedes the formation of concerted string-like motion (Figure 14a). In addition, larger anions are less likely to form long strings. The average string length $\langle n_s \rangle$, presented in Figure 14c, decreases with increasing linker length for all the anions studied. Interestingly, there is no significant difference in the average string length among the anions except for Br^- when the linker exceeds a certain length (> C6).

According to both temporal and spatial criteria, the percentage of fast anions was accumulated in each system as shown in Figure 14d. $TFSI^-$ consistently exhibits the highest fraction of fast anions ($15 - 30\%$), and this fraction generally increases with linker length. However, the three spherical anions do not show discernible differences or even a consistent order. Given that ion transport is primarily due to the fast anions, despite their limited numbers, it is worth comparing the characteristics of ion association and hoping types between the fast ions and slow ions. Figure S7 illustrates that the fast anions tend to associate with more cations from more coordinating chains compared with the slow anions, in contrast to the findings in poly(C2Vim)TFSI, where fast anions associate with fewer cations from more chains when the imidazole ring is directly attached to the

backbone.[26] Moreover, interchain hopping predominates for fast anions, with only a slight influence from linker length. Conversely, linker length exerts a more pronounced effect on slow anions (see Figure S7c).

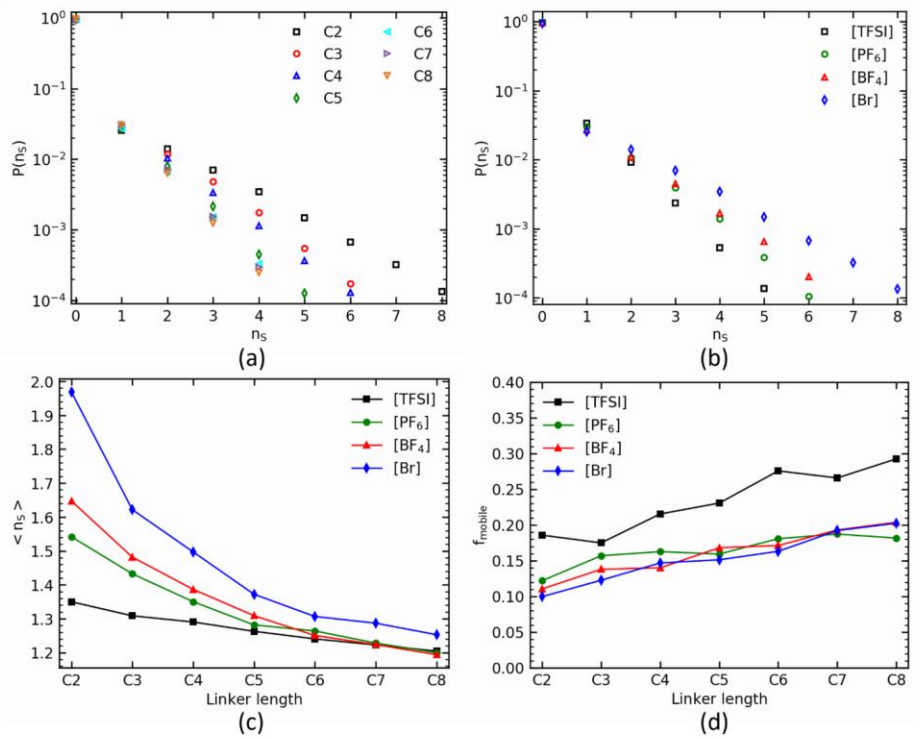

Figure 14. (a) The string length distribution for Br^- as a function of the length of the linker at 580 K. (b) The string length distribution for the various mobile anions. (c) The average string length $\langle n_S \rangle$ as a function of chain length for the four anions. (d) The fraction of mobile anions defined by both temporal and spatial scales (t^* and r^*).

2.5 Relaxation Time Underlying Anion Diffusivity

Ion diffusion has been correlated to the structural relaxation time, the ion association lifetime or ion cage lifetime in low molecular weight ILs[21] and polyILs.[20, 25-27, 54] To examine which relaxation process underlies ion diffusivity in these systems, we computed the intermittent correlation function, $C(t)$, and continuous time correlation function, $S(t)$, using the equations:

$$C(t) = \frac{\langle h(t)h(0)\rangle}{\langle h(0)\rangle} \tag{10}$$

$$S(t) = \frac{\langle H(t)h(0)\rangle}{\langle h(0)\rangle}, \tag{11}$$

where $h(t)$ is assigned unity if an ion association that was present at $t = 0$ will be present at time t independent of its occurrence in the interval $(0, t)$, and 0 otherwise, while $H(t)$ is unity if an ion association is retained up to time t, and 0 otherwise. The decay of $S(t)$ signifies the initial breaking of ion association, denoted by the ion association lifetime, τ_s, but the decay of $C(t)$ indicates the ultimate dissociation of an ion pair without recovery, where the ion leaves the cage and does not return, denoted as a cage relaxation time τ_c. It is worth noting that this relaxation time, was also called the structural relaxation time in earlier papers,[20, 25-27] and can be confused with the structural relaxation time in liquid and polymer systems, which is obtained from the decay of intermediate scattering function. The fitting of $C(t)$ and $S(t)$ to a stretched exponential function is presented in Figure S8, and the corresponding relaxation times as a function of temperature are shown in Figure 15a. Cage relaxation times are over one order of magnitude larger than the average lifetime of ion association, and both decrease with temperature. An increase in the sidechain length gives rise to shorter τ_c and τ_s, particularly for the short linkers (C2 – C4). Figure 15b displays the correlation between anion self-diffusion coefficients and relaxation times for different linker lengths associated with four anions in the temperature range of 400 to 600 K. The fitting of the data to a power law $D_\mathrm{A} \sim \tau^{-\lambda}$ reveals that D_A exhibits a better linear correlation with τ_c^{-1} than τ_s^{-1} ($\lambda = 0.94$ for τ_c and $\lambda = 1.28$ for τ_s, respectively), which is consistent with our previous studies of other polyILs.[25-27] Notably, at low temperatures, the average lifetime of ion association significantly deviates from the power law. Such results confirm that the transient dissociation of an anion is necessary but not sufficient for the long-range diffusivity of anions. It is worth mentioning that recent work suggested that the time a mobile ion remains trapped inside a cage is associated with the mobility of the ion.[54]

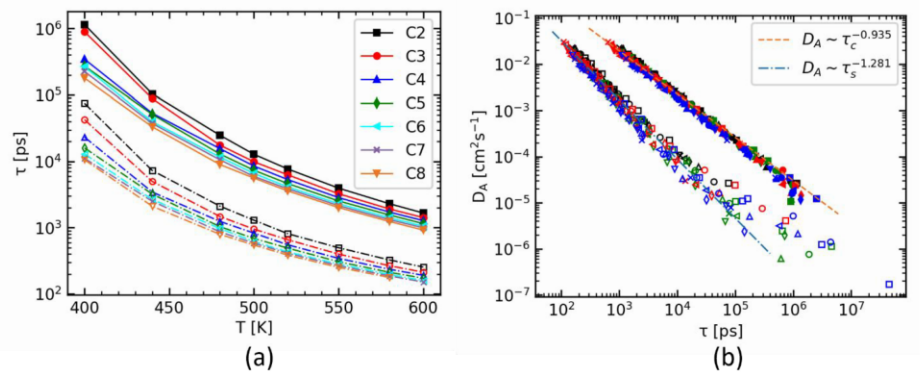

Figure 15. (a) Temperature dependence of the cage relaxation time and average lifetime of ion association for various linker lengths. (b) Correlations of self-diffusivity and cage relaxation time or average lifetime of ion association for all studied systems.

3 Conclusions

In this study, classical MD simulations were performed for PMMA-C_x-IM with varying linker lengths (x = 2 – 8) and associated with various anions, including a linear $TFSI^-$, and three spherical anions: PF_6^-, BF_4^-, and Br^-. We have systematically explored the effects of sidechain flexibility coupled with the specific interactions between anion and cation on ion transport. Initially, we verified that longer linkers afford greater flexibility to the pendant cations, enabling them to extend over larger distances and explore wider angular ranges. This enhanced flexibility could potentially influence the interaction between the imidazole ring and the acrylate groups within the sidechain. However, the sidechain flexibility has minimal impact on the interactions between cations and anions compared to changes in the associated anion.

Furthermore, our results demonstrate that the diffusion coefficients of smaller anions exhibit a more pronounced increase with increasing linker length compared to larger ones. This enhancement of anion diffusivity is ascribed to significant increases in diffusive motion, albeit with less pronounced reductions in ion hopping. To further quantify the contribution of ion hopping to the diffusion of the anions, we defined the ion hopping as the deviated area of the self-part of the van Hove function from ideal Gaussian distribution. The results demonstrate that the contribution of ion hopping is smaller than that of diffusive motion and this ion hopping fraction decreases as the linker length increases. In addition, the smallest anion Br^- exhibits the largest

portion of ion hopping from one “cage” to another amongst these anions because of the strongest specific interaction between the less charge delocalized Br^- and the cations. Fortunately, the rigid “cage” can be significantly softened by increased sidechain flexibility.

Dynamical heterogeneity in anion mobility further supports the softening effect of longer linkers, in which both the maximum of the non-Gaussian parameter and the time of the strongest heterogeneity swiftly decrease when the linker is varied from C2 to C4 followed by a much slower decrease when the linker is further increased. Moreover, our findings reveal that only a small fraction of anions travel beyond the characteristic distance determined by the distance at which the self-part of van Hove function at the characteristic time of the strongest heterogeneity intersects with its corresponding Gaussian distribution. Notably, the criteria for fast anions are not affected by the sidechain flexibility.

Regarding the ion hopping mechanism, fast mobile anions primarily engage in interchain hopping, with a higher involvement of cations from multiple chains compared to slow anions. A long linker promotes interchain hopping but reduces intrachain hopping. Our results also identified stringlike cooperative motion in the fast anions, with decreasing string length as linker length increases. More interestingly, distinct anion-anion correlations were observed to suppress conductivity in a barycentric reference frame but to enhance conductivity under a polycation-fixed reference frame. This highlights the importance of considering different reference frames in analyzing ion transport phenomena in polyILs. Ultimately, our findings underscore that cage escape plays a pivotal role as the primary mechanism governing anion transport in these systems. Overall, these results improve our understanding of ion transport mechanisms in polyILs, which may pave the way for tailored design strategies aimed at optimizing the transport properties of polyILs for various applications, ranging from energy storage devices to electrochemical sensors.

4 Methodology

Molecular dynamics (MD) simulations were conducted using GROMACSS (2021.2)[55] for the various molecular PMMA-based polyILs. Each system was comprised of 10 polycation chains, consisting of 40 monomers, and 400 anions, ensuring an optimal balance between statistical accuracy and computational efficiency.[56-58] The methodology followed an established protocol.[25-27, 35, 52] The generalized AMBER force field (GAFF) was utilized for bonded and nonbonded interactions.[59, 60] Partial charges on the atoms were calculated using the Restrained Electrostatic

Potential (RESP) algorithm,[61] derived from optimized electronic structures of the repeat unit of the polycation or isolated anion at the Hartree-Fock HF/6-31g(d) level of theory using the GAUSSIAN 09 suite of programs.[62] To accommodate polarization and charge transfer effects, the computed atomic partial charges on both polycations and anions were scaled by a factor of 0.8, known for its efficiency and reliability in ion-containing systems. This approach has been validated in prior studies.[35, 52, 63, 64] Electrostatic and Lennard-Jones interactions were truncated at a distance of 14 Å, with long-range corrections handled by the particle mesh Ewald (PME) method and appropriate tail corrections, respectively. Initial configurations were generated by randomly packing polycation chains and associated anions in a cubic box using the Packmol software,[65] and force field assignments were made in the topology files with the aid of ACPYPE and antechamber tools.[66] Initial systems were equilibrated for over 50 ns in the NPT ensemble, preceded by an annealing process at higher temperature (750 K – 950 K) and 1.0 bar for ~55 ns. Subsequently, an additional 30 ns equilibration under the NVT ensemble was performed, followed by the collection of trajectories at 10 ps intervals for 50 ns, along with longer trajectories of 300 – 500 ns saved every 100 ps to ensured reliable ion-ion correlations in these polyIL systems.[8, 67] Temperature and pressure were controlled using the Bussi thermostat[68] and the Parrinello-Rahman barostat[69] with coupling times of 0.5 and 5 ps, respectively. The MD simulations for all polyIL systems were conducted in periodic cubic boxes with a time step of 2 fs. Furthermore, to mitigate statistical uncertainty, dynamic correlations were computed from 4 – 6 trajectories to provide average values and corresponding standard deviations.

References

1. Popov, I.; Biernacka, K.; Zhu, H.; Nti, F.; Porcarelli, L.; Wang, X.; Khamzin, A.; Gainaru, C.; Forsyth, M.; Sokolov, A. P., Strongly Correlated Ion Dynamics in Plastic Ionic Crystals and Polymerized Ionic Liquids. *J. Phys. Chem. C* **2020,** *124* (33), 17889-17896.
2. H. Zhu; D.R. MacFarlane; J.M. Pringle; M. Forsyth, Organic Ionic Plastic Crystals as Solid-State Electrolytes. *Trends in Chemistry* **2019,** *1*, 126-140.
3. Zhu, Z.; Paddison, S. J., Perspective: Morphology and Ion Transport in Ion-Containing Polymers from Multiscale Modeling and Simulations. *Frontiers in Chemistry* **2022,** *10*, 981508.
4. Bocharova, V.; Sokolov, A. P., Perspectives for Polymer Electrolytes: A View from Fundamentals of Ionic Conductivity. *Macromolecules* **2020,** *53* (11), 4141-4157.
5. Son, C. Y.; Wang, Z.-G., Ion Transport in Small-Molecule and Polymer Electrolytes. *J. Chem. Phys.* **2020,** *153* (10), 100903.
6. Li, Q.; Yan, F.; Texter, J., Polymerized and Colloidal Ionic Liquids—Syntheses and Applications. *Chemical Reviews* **2024,** *124* (7), 3813-3931.
7. Zhu, Z.; Luo, X.; Paddison, S. J., Coarse-Grained Modeling of Ion-Containing Polymers. *Chem. Rev.* **2022,** *122* (12), 10710-10745.
8. Fong, K. D.; Self, J.; McCloskey, B. D.; Persson, K. A., Ion Correlations and Their Impact on Transport in Polymer-Based Electrolytes. *Macromolecules* **2021,** *54* (6), 2575-2591.
9. Ganesan, V., Ion Transport in Polymeric Ionic Liquids: Recent Developments and Open Questions. *Mol. Syst. Des. Eng.* **2019,** *4* (2), 280-293.
10. Stacy, E. W.; Gainaru, C. P.; Gobet, M.; Wojnarowska, Z.; Bocharova, V.; Greenbaum, S. G.; Sokolov, A. P., Fundamental Limitations of Ionic Conductivity in Polymerized Ionic Liquids. *Macromolecules* **2018,** *51* (21), 8637-8645.
11. Mogurampelly, S.; Borodin, O.; Ganesan, V., Computer Simulations of Ion Transport in Polymer Electrolyte Membranes. *Annu. Rev. Chem. Biomol. Eng.* **2016,** *7*, 349-71.
12. Iacob, C.; Matsumoto, A.; Brennan, M.; Liu, H.; Paddison, S. J.; Urakawa, O.; Inoue, T.; Sangoro, J.; Runt, J., Polymerized Ionic Liquids: Correlation of Ionic Conductivity with Nanoscale Morphology and Counterion Volume. *ACS Macro Lett.* **2017,** *6* (9), 941-946.
13. Fu, Y.; Bocharova, V.; Ma, M.; Sokolov, A. P.; Sumpter, B. G.; Kumar, R., Effects of counterion size and backbone rigidity on the dynamics of ionic polymer melts and glasses. *Phys. Chem. Chem. Phys.* **2017,** *19* (40), 27442-27451.
14. Bocharova, V.; Wojnarowska, Z.; Cao, P.-F.; Fu, Y.; Kumar, R.; Li, B.; Novikov, V. N.; Zhao, S.; Kisliuk, A.; Saito, T.; Mays, J. W.; Sumpter, B. G.; Sokolov, A. P., Influence of Chain Rigidity and Dielectric Constant on the Glass Transition Temperature in Polymerized Ionic Liquids. *J. Phys. Chem. B* **2017,** *121* (51), 11511-11519.
15. Kisliuk, A.; Bocharova, V.; Popov, I.; Gainaru, C.; Sokolov, A. P., Fundamental parameters governing ion conductivity in polymer electrolytes. *Electrochim. Acta* **2019,** *299*, 191-196.
16. Wojnarowska, Z.; Feng, H.; Fu, Y.; Cheng, S.; Carroll, B.; Kumar, R.; Novikov, V. N.; Kisliuk, A. M.; Saito, T.; Kang, N.-G.; Mays, J. W.; Sokolov, A. P.; Bocharova, V., Effect of Chain Rigidity on the Decoupling of Ion Motion from Segmental Relaxation in Polymerized Ionic Liquids: Ambient and Elevated Pressure Studies. *Macromolecules* **2017,** *50* (17), 6710-6721.
17. Fan, F.; Wang, W.; Holt, A. P.; Feng, H.; Uhrig, D.; Lu, X.; Hong, T.; Wang, Y.; Kang, N.-G.; Mays, J.; Sokolov, A. P., Effect of Molecular Weight on the Ion Transport Mechanism in Polymerized Ionic Liquids. *Macromolecules* **2016,** *49* (12), 4557-4570.

18. Fan, F.; Wang, Y.; Hong, T.; Heres, M. F.; Saito, T.; Sokolov, A. P., Ion Conduction in Polymerized Ionic Liquids with Different Pendant Groups. *Macromolecules* **2015,** *48* (13), 4461-4470.
19. Sangoro, J. R.; Iacob, C.; Agapov, A. L.; Wang, Y.; Berdzinski, S.; Rexhausen, H.; Strehmel, V.; Friedrich, C.; Sokolov, A. P.; Kremer, F., Decoupling of ionic conductivity from structural dynamics in polymerized ionic liquids. *Soft Matter* **2014,** *10* (20), 3536-3540.
20. Mogurampelly, S.; Keith, J. R.; Ganesan, V., Mechanisms Underlying Ion Transport in Polymerized Ionic Liquids. *J. Am. Chem. Soc.* **2017,** *139* (28), 9511-9514.
21. Zhang, Y.; Maginn, E. J., Direct Correlation between Ionic Liquid Transport Properties and Ion Pair Lifetimes: A Molecular Dynamics Study. *The Journal of Physical Chemistry Letters* **2015,** *6* (4), 700-705.
22. Keith, J. R.; Ganesan, V., Ion transport in backbone-embedded polymerized ionic liquids. *The Journal of Chemical Physics* **2019,** *151* (12), 124902.
23. Keith, J. R.; Mogurampelly, S.; Wheatle, B. K.; Ganesan, V., Influence of side chain linker length on ion-transport properties of polymeric ionic liquids. *J. Polym. Sci., Part B: Polym. Phys.* **2017,** *55* (23), 1718-1723.
24. Keith, J. R.; Mogurampelly, S.; Aldukhi, F.; Wheatle, B. K.; Ganesan, V., Influence of molecular weight on ion-transport properties of polymeric ionic liquids. *Phys. Chem. Chem. Phys.* **2017,** *19* (43), 29134-29145.
25. Luo, X.; Paddison, S. J., Molecular Dynamics Simulations of Ammonium-Based Acrylate Polymerized Ionic Liquids. *Journal of The Electrochemical Society* **2023,** *170* (10), 106502.
26. Liu, H.; Luo, X.; Sokolov, A. P.; Paddison, S. J., Quantitative Evidence of Mobile Ion Hopping in Polymerized Ionic Liquids. *J. Phys. Chem. B* **2021,** *125* (1), 372-381.
27. Luo, X.; Liu, H.; Paddison, S. J., Molecular Dynamics Simulations of Polymerized Ionic Liquids: Mechanism of Ion Transport with Different Anions. *ACS Appl. Polym. Mater.* **2020,** *3* (1), 141-152.
28. Keith, J. R.; Rebello, N. J.; Cowen, B. J.; Ganesan, V., Influence of Counterion Structure on Conductivity of Polymerized Ionic Liquids. *Acs Macro Lett* **2019,** *8* (4), 387-392.
29. Zhang, Z.; Wheatle, B. K.; Krajniak, J.; Keith, J. R.; Ganesan, V., Ion Mobilities, Transference Numbers, and Inverse Haven Ratios of Polymeric Ionic Liquids. *ACS Macro Lett.* **2020,** *9* (1), 84-89.
30. Popov, I.; Biernacka, K.; Zhu, H.; Nti, F.; Porcarelli, L.; Wang, X.; Khamzin, A.; Gainaru, C.; Forsyth, M.; Sokolov, A. P., Strongly Correlated Ion Dynamics in Plastic Ionic Crystals and Polymerized Ionic Liquids. *J. Phys. Chem. C* **2020,** *124* (33), 17889-17896.
31. Gainaru, C.; Stacy, E. W.; Bocharova, V.; Gobet, M.; Holt, A. P.; Saito, T.; Greenbaum, S.; Sokolov, A. P., Mechanism of Conductivity Relaxation in Liquid and Polymeric Electrolytes: Direct Link between Conductivity and Diffusivity. *J Phys. Chem. B* **2016,** *120* (42), 11074-11083.
32. J.C. Dyre; P. Maass; B. Roling; D.L. Sidebottom, Fundamental questions relating to ion conduction in disordered solids. *Rep. Prog. Phys.* **2009,** *72*, 046501.
33. B. Roling, C. M., S. Brückner, , Ion transport in glass: Influence of glassy structure on spatial extent of nonrandom ion hopping. *Phys Rev B* **2001,** *63* (21), 214203.
34. P. Maass; M. Meyer; A. Bunde, Nonstandard relaxation behavior in ionically conducting materials. *Phys Rev B* **1995,** *51* (13), 8164.
35. Ahmed, M. D.; Zhu, Z.; Khamzin, A.; Paddison, S. J.; Sokolov, A. P.; Popov, I., Effect of Ion Mass on Dynamic Correlations in Ionic Liquids. *The Journal of Physical Chemistry B* **2023,** *127* (48), 10411-10421.

36. K.R. Harris; M. Kanakubo, Self-Diffusion Coefficients and Related Transport Properties for a Number of Fragile Ionic Liquids. *Journal of Chemical & Engineering Data* **2016,** *61*, 2399-2411.
37. K.R. Harris; M. Kanakubo, Revised and Extended Values for Self-Diffusion Coefficients of 1-Alkyl-3-methylimidazolium Tetrafluoroborates and Hexafluorophosphates: Relations between the Transport Properties. *The Journal of Physical Chemistry B* **2016,** *120*, 12937-12949.
38. Zhao, W.; Leroy, F.; Heggen, B.; Zahn, S.; Kirchner, B.; Balasubramanian, S.; MUeller-Plathe, F., Are There Stable Ion-Pairs in Room-Temperature Ionic Liquids? Molecular Dynamics Simulations of 1-n-Butyl-3-methylimidazolium Hexafluorophosphate. *J. Am. Chem. Soc.* **2009,** *131*, 15825-15833.
39. Tokuda, H.; Ishii, K.; Susan, M. A. B. H.; Tsuzuki, S.; Hayamizu, K.; Watanabe, M., Physicochemical Properties and Structures of Room-Temperature Ionic Liquids. 3. Variation of Cationic Structures. *The Journal of Physical Chemistry B* **2006,** *110* (6), 2833-2839.
40. Tokuda, H.; Hayamizu, K.; Ishii, K.; Susan, M. A. B. H.; Watanabe, M., Physicochemical Properties and Structures of Room Temperature Ionic Liquids. 2. Variation of Alkyl Chain Length in Imidazolium Cation. *The Journal of Physical Chemistry B* **2005,** *109* (13), 6103-6110.
41. Tokuda, H.; Hayamizu, K.; Ishii, K.; Susan, M. A. B. H.; Watanabe, M., Physicochemical Properties and Structures of Room Temperature Ionic Liquids. 1. Variation of Anionic Species. *J. Phys. Chem. B* **2004,** *108* (42), 16593-16600.
42. Every, H. A.; Bishop, A. G.; MacFarlane, D. R.; Orädd, G.; Forsyth, M., Transport properties in a family of dialkylimidazolium ionic liquids. *Phys. Chem. Chem. Phys.* **2004,** *6* (8), 1758-1765.
43. Kashyap, H. K.; Annapureddy, H. V.; Raineri, F. O.; Margulis, C. J., How is Charge Transport Different in Ionic Liquids and Electrolyte Solutions? *J. Phys. Chem. B* **2011,** *115* (45), 13212-21.
44. Z. Zhang, H. L., K. Kaup, L. Zhou, P.-N. Roy, L.F. Nazar, , Targeting Superionic Conductivity by Turning on Anion Rotation at Room Temperature in Fast Ion Conductors. *Matter* **2020,** *2* (6), 1667.
45. E. Bychkov, Superionic and ion-conducting chalcogenide glasses: Transport regimes and structural features. *Solid State Ionics* **2009,** *180* (6), 510.
46. Nürnberg, P.; Atik, J.; Borodin, O.; Winter, M.; Paillard, E.; Schönhoff, M., Superionicity in Ionic-Liquid-Based Electrolytes Induced by Positive Ion–Ion Correlations. *Journal of the American Chemical Society* **2022,** *144* (10), 4657-4666.
47. Shao, Y.; Gudla, H.; Brandell, D.; Zhang, C., Transference Number in Polymer Electrolytes: Mind the Reference-Frame Gap. *Journal of the American Chemical Society* **2022,** *144* (17), 7583-7587.
48. Pfeifer, S.; Ackermann, F.; Sälzer, F.; Schönhoff, M.; Roling, B., Quantification of cation–cation, anion–anion and cation–anion correlations in Li salt/glyme mixtures by combining very-low-frequency impedance spectroscopy with diffusion and electrophoretic NMR. *Phys. Chem. Chem. Phys.* **2021,** *23* (1), 628-640.
49. Zhang, Z.; Krishna, R.; Zofchak, E. S.; Marioni, N.; Sachar, H. S.; Ganesan, V., The influence of counterion structure identity on conductivity, dynamical correlations, and ion transport mechanisms in polymerized ionic liquids. *The Journal of Chemical Physics* **2023,** *159* (8), 084902.

50. Wheatle, B. K.; Lynd, N. A.; Ganesan, V., Effect of Polymer Polarity on Ion Transport: A Competition between Ion Aggregation and Polymer Segmental Dynamics. *Acs Macro Lett* **2018,** *7* (10), 1149-1154.
51. Kob, W.; Donati, C.; Plimpton, S. J.; Poole, P. H.; Glotzer, S. C., Dynamical Heterogeneities in a Supercooled Lennard-Jones Liquid. *Physical Review Letters* **1997,** *79* (15), 2827-2830.
52. Liu, H.; Maginn, E., A molecular dynamics investigation of the structural and dynamic properties of the ionic liquid 1-n-butyl-3-methylimidazolium bis(trifluoromethanesulfonyl) imide. *J. Chem. Phys.* **2011,** *135*, 124507.
53. Del Pópolo, M. G.; Voth, G. A., On the Structure and Dynamics of Ionic Liquids. *The Journal of Physical Chemistry B* **2004,** *108* (5), 1744-1752.
54. Xiao, W.; Yang, Q.; Zhu, S., Comparing Ion Transport in Ionic Liquids and Polymerized Ionic Liquids. *Sci. Rep.* **2020,** *10* (1), 7825.
55. Abraham, M. J.; Murtola, T.; Schulz, R.; Páll, S.; Smith, J. C.; Hess, B.; Lindahl, E., GROMACS: High performance molecular simulations through multi-level parallelism from laptops to supercomputers. *SoftwareX* **2015,** *1-2*, 19-25.
56. Liu, H.; Luo, X.; Sokolov, A. P.; Paddison, S. J., Quantitative Evidence of Mobile Ion Hopping in Polymerized Ionic Liquids. *J Phys Chem B* **2021,** *125* (1), 372-381.
57. Luo, X.; Liu, H.; Paddison, S. J., Molecular Dynamics Simulations of Polymerized Ionic Liquids: Mechanism of Ion Transport with Different Anions. *ACS Applied Polymer Materials* **2020,** *3* (1), 141-152.
58. Mogurampelly, S.; Keith, J. R.; Ganesan, V., Mechanisms Underlying Ion Transport in Polymerized Ionic Liquids. *J Am Chem Soc* **2017,** *139* (28), 9511-9514.
59. Sprenger, K. G.; Jaeger, V. W.; Pfaendtner, J., The General AMBER Force Field (GAFF) Can Accurately Predict Thermodynamic and Transport Properties of Many Ionic Liquids. *J. Phys. Chem. B* **2015,** *119* (18), 5882-5895.
60. Slingsby, J. G.; Vyas, S.; Maupin, C. M., A charge-modified general amber force field for phospholipids: improved structural properties in the tensionless ensemble. *Mol Simulat* **2015,** *41* (18), 1449-1458.
61. Bayly, C. I.; Cieplak, P.; Cornell, W.; Kollman, P. A., A well-behaved electrostatic potential based method using charge restraints for deriving atomic charges: the RESP model. *The Journal of Physical Chemistry* **1993,** *97* (40), 10269-10280.
62. Frisch, M. J.; Trucks, G. W.; Schlegel, H. B.; Scuseria, G. E.; Robb, M. A.; Cheeseman, J. R.; Scalmani, G.; Barone, V.; Mennucci, B.; Petersson, G. A.; Nakatsuji, H.; Caricato, M.; Li, X.; Marenich, A.; Bloino, J.; Janesko, B. G. *Gaussian 09*, Revision E.01; Gaussian, Inc.: Wallingford, CT, 2013.
63. Zhang, Z.; Zofchak, E.; Krajniak, J.; Ganesan, V., Influence of Polarizability on the Structure, Dynamic Characteristics, and Ion-Transport Mechanisms in Polymeric Ionic Liquids. *J. Phys. Chem. B* **2022,** *126* (13), 2583-2592.
64. Barbosa, G. D.; Liu, X.; O'Harra, K. E.; Bara, J. E.; Turner, C. H., Charge scaling parameter evaluation for multivalent ionic liquids with fixed point charge force fields. *Journal of Ionic Liquids* **2022,** *2* (1), 100020.
65. Martinez, L.; Andrade, R.; Birgin, E. G.; Martinez, J. M., PACKMOL: A Package for Building Initial Configurations for Molecular Dynamics Simulations. *J. Comput. Chem.* **2009,** *30* (13), 2157-2164.

66. Sousa da Silva, A. W.; Vranken, W. F., ACPYPE - AnteChamber PYthon Parser interfacE. *BMC Research Notes* **2012,** *5* (1), 367.
67. Vargas-Barbosa, N. M.; Roling, B., Dynamic Ion Correlations in Solid and Liquid Electrolytes: How Do They Affect Charge and Mass Transport? *ChemElectroChem* **2020,** *7* (2), 367-385.
68. Bussi, G.; Donadio, D.; Parrinello, M., Canonical sampling through velocity rescaling. *The Journal of Chemical Physics* **2007,** *126* (1), 014101.
69. Parrinello, M.; Rahman, A., Crystal Structure and Pair Potentials: A Molecular-Dynamics Study. *Physical Review Letters* **1980,** *45* (14), 1196-1199.

Vita

Zhenghao Zhu received his B.S. and M.S. degrees in Chemical Engineering from East China University of Science and Technology. His M.S. research primarily focused on investigating the thermodynamic properties of polymer solutions using the COSMO-SAC Model and Lattice Model, providing significant guidance for membrane preparation. Following his journey as an engineer specializing in wastewater treatment at Shanghai Sep-Bio Engineering Co., LTD, he joined the Ph.D. program at the University of Tennessee under the supervision of Prof. Stephen Paddison. His research centers on understanding the interplay between molecular structure, morphology, and proton/ion transport in electrolytes for clean energy applications through multiscale modeling and simulations. Throughout his Ph.D. studies, he has been recognized with several accolades, including the Volunteer of Distinction Award from Office of the Provost, the Award for Excellence in Graduate Research from Graduate Student Senate, the Outstanding Achievement CBE Graduate Student Award (twice) and the CBE Graduate Teaching Assistant Award from the department. Additionally, he was honored with the prestigious SSI Award for the Best Paper Published in 2019.